SEA ICE: BRIDGING SPATIAL-TEMPORAL SCALES AND DISCIPLINES

EDITED BY: Hauke Flores, Benjamin Allen Lange, Giulia Castellani, Jeff Shovlowsky Bowman and Janne-Markus Rintala

PUBLISHED IN: Frontiers in Earth Science and Frontiers in Marine Science

frontiers Research Topics

frontiers

ISSN 1664-8714
ISBN 978-2-88963-805-5
DOI 10.3389/978-2-88963-805-5

About Frontiers

Frontiers is more than just an open-access publisher of scholarly articles: it is a pioneering approach to the world of academia, radically improving the way scholarly research is managed. The grand vision of Frontiers is a world where all people have an equal opportunity to seek, share and generate knowledge. Frontiers provides immediate and permanent online open access to all its publications, but this alone is not enough to realize our grand goals.

Frontiers Journal Series

The Frontiers Journal Series is a multi-tier and interdisciplinary set of open-access, online journals, promising a paradigm shift from the current review, selection and dissemination processes in academic publishing. All Frontiers journals are driven by researchers for researchers; therefore, they constitute a service to the scholarly community. At the same time, the Frontiers Journal Series operates on a revolutionary invention, the tiered publishing system, initially addressing specific communities of scholars, and gradually climbing up to broader public understanding, thus serving the interests of the lay society, too.

Dedication to Quality

Each Frontiers article is a landmark of the highest quality, thanks to genuinely collaborative interactions between authors and review editors, who include some of the world's best academicians. Research must be certified by peers before entering a stream of knowledge that may eventually reach the public - and shape society; therefore, Frontiers only applies the most rigorous and unbiased reviews.
Frontiers revolutionizes research publishing by freely delivering the most outstanding research, evaluated with no bias from both the academic and social point of view. By applying the most advanced information technologies, Frontiers is catapulting scholarly publishing into a new generation.

What are Frontiers Research Topics?

Frontiers Research Topics are very popular trademarks of the Frontiers Journals Series: they are collections of at least ten articles, all centered on a particular subject. With their unique mix of varied contributions from Original Research to Review Articles, Frontiers Research Topics unify the most influential researchers, the latest key findings and historical advances in a hot research area! Find out more on how to host your own Frontiers Research Topic or contribute to one as an author by contacting the Frontiers Editorial Office: researchtopics@frontiersin.org

SEA ICE: BRIDGING SPATIAL-TEMPORAL SCALES AND DISCIPLINES

Topic Editors:
Hauke Flores, Alfred Wegener Institute Helmholtz Centre for Polar and Marine Research (AWI), Germany
Benjamin Allen Lange, Norwegian Polar Institute, Norway
Giulia Castellani, Alfred Wegener Institute Helmholtz Centre for Polar and Marine Research (AWI), Germany
Jeff Shovlowsky Bowman, University of California, San Diego, United States
Janne-Markus Rintala, University of Helsinki, Finland

Citation: Flores, H., Lange, B. A., Castellani, G., Bowman, J. S., Rintala, J.-M., eds. (2020). Sea Ice: Bridging Spatial-Temporal Scales and Disciplines. Lausanne: Frontiers Media SA. doi: 10.3389/978-2-88963-805-5

Table of Contents

frontiers in Earth Science

EDITORIAL
published: 29 April 2020
doi: 10.3389/feart.2020.00119

Editorial: Sea Ice: Bridging Spatial-Temporal Scales and Disciplines

Benjamin A. Lange[1]*, *Hauke Flores*[2], *Jeff S. Bowman*[3], *Janne-Markus Rintala*[4] and *Giulia Castellani*[2]

[1] Norwegian Polar Institute, Fram Centre, Tromsø, Norway, [2] Alfred-Wegener-Institute Helmholtz Center for Polar and Marine Research, Bremerhaven, Germany, [3] Scripps Institution of Oceanography, University of California, San Diego, San Diego, CA, United States, [4] INAR—Institute for Atmospheric and Earth System Research, University of Helsinki, Helsinki, Finland

Keywords: Arctic Ocean, Southern Ocean, remote sensing, sea ice algae, interdisciplinary, polar regions, biogeochemistry, cryosphere

Editorial on the Research Topic

Sea Ice: Bridging Spatial-Temporal Scales and Disciplines

The ice-covered Arctic Ocean has undergone rapid changes, including pronounced sea ice thinning and volume loss, a rapidly declining sea ice extent and a shift toward a seasonally dominated ice cover (Kwok, 2018; Stroeve and Notz, 2018). In the Southern Ocean, there is large regional and interannual variability in sea ice extent (Parkinson and Cavalieri, 2012; Holland et al., 2017). Although there has been an overall slightly increasing trend in Antarctic sea ice extent, some regions have experienced drastic changes comparable to the Arctic (Stammerjohn et al., 2012; Hobbs et al., 2016). Yet the impact of these strong changes in sea ice habitat properties on polar marine ecosystems is not fully understood (Gerland et al., 2019; IPCC, 2019).

Innovative technologies, improved methods and novel experimental approaches increase the reliability and accuracy of observations while at the same time enable us to bridge multiple spatial-temporal scales across disciplines in logistically challenging environments. In combination with remote sensing and numerical models of sea-ice ecosystems, an increasingly comprehensive understanding of biogeochemical processes and interaction of ice-associated organisms with the sea ice environment can be scaled in time and space. Further development and the integration of these various approaches and technologies across disciplines will solidify predictions of the impact of changing sea ice habitats on biodiversity and ecosystem functions.

In this Research Topic we focused on field-based research, modeling studies and laboratory-based experiments, which provided novel approaches, innovative technologies, and/or new interdisciplinary perspectives to sea ice research.

Campbell et al. investigated ice algal photophysiology from ^{14}C incubations of sea ice samples prepared by three different melt procedures. They extended their experimental investigation using a common sea ice diatom *N. frigida* as a model organism. Observed large differences in several photophysiological parameters were related to relative changes in salinity resulting from the different melt procedures. Thus, the approach chosen to melt ice samples almost certainly contributed to the variability in production reported across polar regions.

Janssens et al. conducted the first laboratory-controlled sea-ice growth experiment, with trace metal clean conditions, to investigate the role of organic matter in incorporating iron into sea ice. They showed that biogenic particulate iron was preferentially incorporated into sea ice compared to lithogenic particulate iron and that the incorporation of dissolved iron is favored by the presence of organic ligands.

OPEN ACCESS

Edited and reviewed by:
Regine Hock,
University of Alaska Fairbanks, United States

***Correspondence:**
Benjamin A. Lange
blange.sea.ice@gmail.com

Specialty section:
This article was submitted to Cryospheric Sciences, a section of the journal Frontiers in Earth Science

Received: *17 March 2020*
Accepted: *30 March 2020*
Published: *29 April 2020*

Citation:
Lange BA, Flores H, Bowman JS, Rintala J-M and Castellani G (2020) Editorial: Sea Ice: Bridging Spatial-Temporal Scales and Disciplines. Front. Earth Sci. 8:119. doi: 10.3389/feart.2020.00119

König et al. present controlled laboratory experiments which investigated the dynamics of the total inorganic carbon budget (TIC) in an experimental seawater tank. Their experiment showed that the bulk of the TIC remained in the under-ice water rather than in the newly formed sea ice. König et al. conclude that brine drainage is a key process transporting inorganic carbon into the surface water during ice formation.

Kauko et al. followed the ice algal species succession in young Arctic sea ice during spring. They showed that the seeding source varied between algal groups, with dinoflagellates originating from the water column and diatoms from the surrounding older ice. Their results provide further evidence that the surrounding ice is an important seeding source, particularly over deep oceanic regions and in early spring when water column algal biomass is low. The successional patterns evolved into ice-associated algae independent of environmental conditions, which highlights the importance of biological traits in the colonization of the sea ice environment.

Limoges et al. investigated the dynamics of the paleo-oceanographic sea-ice marker IP25 in relation to ice algae community structure both in sea ice and in sediments from Young Sound, Greenland. They showed that only three rare species of sea-ice diatoms produced IP25, causing only limited concentrations of the biomarker in both sea ice and sediments. The ice algae community changed between freezing and melting conditions, and the melt- and post-melt algae assemblages dominated in the sediment. The results of this study demonstrate that concentrations of IP25 in seafloor sediments largely depend on the productivity of sea-ice diatoms.

Uhlig et al. investigated concentrations of Dimethylsulfide (DMS) and its precursor Dimethylsulfoniopropionate (DMSP) in relation to sea-ice exposure and hydrographic properties. In Atlantic-influenced open waters DMS concentrations were higher and positively correlated with DMSP concentrations and chlorophyll concentration, whereas in polar- and sea ice-influenced waters DMS and DMSP concentrations were low, showing no relationship between the two compounds or chlorophyll. This indicates decoupling of DMSP production from microbial conversion to DMS, suggesting that DMS production in the ice-covered Central Arctic Ocean is lower than expected from DMSP concentrations or phytoplankton biomass.

Forrest et al. deployed an AUV fitted with multispectral sensors to remotely estimate ice-algal biomass along ∼500 m transects beneath land-fast sea ice in McMurdo Sound, Antarctica. Bio-optical algorithms developed using local measurements explained 40% of the biomass variability. The poor performance of the algorithm was attributed to difference in footprint size of the optical sensor compared to ice core samples. Nevertheless, their results support continued development of bottom-ice biophysical remote sensing techniques.

König et al. provided an evaluation of five currently available atmospheric correction processors (ACOLITE, ATCOR, iCOR, Polymer, and Sen2Cor) for Sentinel-2 multispectral observations using *in situ* spectral measurements over snow, sea ice and open water. They showed that Polymer performed best over open water while ACOLITE, ATCOR and iCOR performed well over sea ice. ATCOR, iCOR, and Sen2Cor failed in retrieval of aerosol optical thickness and water vapor while ACOLITE was within the range of uncertainty for these parameters. They conclude that the choice of correction processor can have a large influence on secondary products.

Steiner et al. integrate scientific methods with indigenous knowledge by synthesizing results from models, observations and laboratory experiments in order to better understand current and future changes to Arctic marine ecosystems, how these changes impact society and how can we better manage and plan for climate change. They focus on a key forage species in the Arctic Ocean, Arctic cod (*Boreogadus saida*). Their model simulations showed a 17% decrease in Arctic cod populations over the next 80 years as a result of migration limits and temperature increases. Furthermore, they highlight the need for more extensive, unified community- and science-based monitoring programs to improve knowledge-based management and planning.

Logistical difficulties will undoubtedly remain as some of the largest hurdles in polar research. Nevertheless, we should continue to strive for improved spatial and temporal coverage of observations and monitoring programs throughout both polar regions. There remain large geographical and seasonal knowledge gaps in sea ice related research, such as observations within the central Arctic Ocean, year-long observation and monitoring programs and winter studies (e.g., MOSAiC, Nansen Legacy, among others). Satellite and airborne remote sensing have provided unprecedented detail of the snow and ice physical properties, but as of yet still cannot penetrate the snow and ice matrix to observe the under-ice habitat, making ecologically relevant observations of polar marine environments nearly impossible from air/space. Improving our understanding of sea ice biogeochemical processes and biophysical linkages can foster rapid improvements in our understanding of projected changes in polar marine environments through approaches that couple experimental results, observations and models at different spatial and temporal scales.

AUTHOR CONTRIBUTIONS

BL coordinated the writing of the editorial. BL and HF made original plans for the Research Topic and edited several published papers in this Research Topic. JB, J-MR, and GC provided substantial input for the initial submitted Research Topic proposal, edited manuscripts, and commented on the editorial.

FUNDING

BL, HF, and GC were supported by the Alfred-Wegener-Institute Helmholtz Center for Polar and Marine Research and funding from the Helmholtz Association Young Investigators Group Iceflux: Ice ecosystem carbon flux in polar oceans (VH-NG-800). BL was also supported by a Visiting Fellowship from the Natural Science and Engineering Research Council of Canada (NSERC) supported by Fisheries and Oceans Canada International Governance Strategy, in addition to current support from NPI and funding from the Research Council of Norway (CAATEX [280531] and HAVOC [280292]). GC was currently supported

by the EcoLight project (grant number 03V01465), part of the Changing Arctic Ocean program, jointly funded by the UKRI Natural Environment Research Council (NERC) and the German Federal Ministry of Education and Research (BMBF). JB was supported through the National Science Foundation (NSF-OPP 1821911, NSF-OPP 1846387), and by an Early Career Marine Microbial Investigator award from these Simons Foundation.

REFERENCES

Gerland, S., Barber, S., Meier, W., Mundy, C. J., Holland, M., Kern, S., et al. (2019). Essential gaps in the understanding of the roles and functions of Arctic sea ice. *Environ. Res. Lett.* 14:043002. doi: 10.1088/1748-9326/ab09b3

Hobbs, W. R., Massom, R., Stammerjohn, S., Reid, P., Williams, G., and Meier, W. (2016). A review of recent changes in Southern Ocean sea ice, their drivers and forcings. *Global. Planet. Change* 143, 228–250. doi: 10.1016/j.gloplacha.2016.06.008

Holland, M. M., Landrum, L., Raphael, M., and Stammerjohn, S. (2017). Springtime winds drive Ross Sea ice variability and change in the following autumn. *Nat. Commun.* 8:731. doi: 10.1038/s41467-017-00820-0

IPCC (2019). *IPCC Special Report on the Ocean and Cryosphere in a Changing Climate*, eds H.-O. Pörtner, D. C. Roberts, V. Masson-Delmotte, P. Zhai, M. Tignor, E. Poloczanska, K. Mintenbeck, A. Alegría, M. Nicolai, A. Okem, J. Petzold, B. Rama, and N. M. Weyer. Available online at: https://www.ipcc.ch/site/assets/uploads/sites/3/2019/12/SROCC_FullReport_FINAL.pdf

Kwok, R. (2018). Arctic sea ice thickness, volume, and multiyear ice coverage: losses and coupled variability (1958–2018). *Environ. Res. Lett.* 13:105005. doi: 10.1088/1748-9326/aae3ec

Parkinson, C. L., and Cavalieri, D. J. (2012). Antarctic sea ice variability and trends, 1979-2010. *Cryosphere* 6, 871–880. doi: 10.5194/tc-6-871-2012

Stammerjohn, S., Massom, R., Rind, D., and Martinson, D. (2012). Regions of rapid sea ice change: an inter-hemispheric seasonal comparison. *Geophys. Res. Lett* 39:L06501. doi: 10.1029/2012GL050874

Stroeve, J., and Notz, D. (2018). Changing state of Arctic sea ice across all seasons. *Environ. Res. Lett.* 13:103001. doi: 10.1088/1748-9326/aade56

Conflict of Interest: The authors declare that the research was conducted in the absence of any commercial or financial relationships that could be construed as a potential conflict of interest.

frontiers in Earth Science

ORIGINAL RESEARCH
published: 10 July 2019
doi: 10.3389/feart.2019.00179

Sea Ice and Water Mass Influence Dimethylsulfide Concentrations in the Central Arctic Ocean

Christiane Uhlig[1], Ellen Damm[1], Ilka Peeken[1], Thomas Krumpen[1], Benjamin Rabe[1], Meri Korhonen[2] and Kai-Uwe Ludwichowski[1]*

[1] Alfred-Wegener-Institut Helmholtz-Zentrum für Polar- und Meeresforschung, Bremerhaven, Germany, [2] Finnish Meteorological Institute, Helsinki, Finland

Dimethylsulfide (DMS) is a biogenic trace gas with importance to aerosol formation. DMS is produced by microbial degradation of dimethylsulfoniopropionate (DMSP), an abundant metabolite in marine microalgae. We analyzed DMS and DMSP concentrations in surface water in the central Arctic Ocean during two expeditions north of 79°N in 2011 and 2015. We identified three regions, which were characterized by different DMS and DMSP concentrations, dependent on the regional water masses and the relative movement of sea ice and water to each other. In addition, correlations between DMS and DMSP and correlation of the two sulfur compounds to autotrophic biomass (as chlorophyll *a*) differed in the regions. In the area of the nutrient rich Atlantic water inflow and short contact of this water with sea ice, DMS is present in high concentrations and correlates to DMSP as well as chlorophyll *a*. At two stations, particularly high DMS concentrations were found in conjunction with under-ice phytoplankton biomass peaks. In contrast, in mixed Atlantic and Pacific water with strong polar influence, where long-term contact between sea ice and water causes persistent stratification, only little DMS is found. Further, the correlations to DMSP and chlorophyll *a* are lost and the ratio of DMS to DMSP is about one order of magnitude lower, pointing toward consumption of DMSP without the production of DMS. We conclude that the duration of sea ice influence and source of the surface water do not only lead to differences in phytoplankton productivity, resulting in different DMSP concentrations, but also influence microbial recycling of DMSP to DMS or other compounds. DMS production, as possible source for aerosols, is thus presumably lower in the strongly sea ice influenced central Arctic areas than what could be expected from DMSP concentration or biomass.

Keywords: DMS, DMSP, aerosol, Arctic Ocean, sea ice

OPEN ACCESS

Edited by:
Jeff Shovlowsky Bowman, University of California, San Diego, United States

Reviewed by:
Mar Fernández-Méndez, GEOMAR Helmholtz Centre for Ocean Research Kiel, Germany
Jacqueline Stefels, University of Groningen, Netherlands

****Correspondence:***
Ellen Damm
ellen.damm@awi.de

Specialty section:
This article was submitted to Cryospheric Sciences, a section of the journal Frontiers in Earth Science

Received: *01 November 2018*
Accepted: *24 June 2019*
Published: *10 July 2019*

Citation:
Uhlig C, Damm E, Peeken I, Krumpen T, Rabe B, Korhonen M and Ludwichowski K-U (2019) Sea Ice and Water Mass Influence Dimethylsulfide Concentrations in the Central Arctic Ocean. Front. Earth Sci. 7:179. doi: 10.3389/feart.2019.00179

INTRODUCTION

Dimethylsulfide (DMS) represents the most important natural source of sulfur to the atmosphere, accounting for up to 80% of global biogenic sulfur emissions (Keller et al., 1989; Liss et al., 1997; Kettle and Andreae, 2000). In the atmosphere DMS can be oxidized to sulfate aerosols which serve as cloud condensation nuclei and thus influence solar radiation income (Charlson et al., 1987; Andreae, 1990). The contribution of DMS to cloud condensation nuclei is particularly

important in remote oceanic regions, such as the Southern Ocean that is little affected by anthropogenic sources of sulfate (Vallina et al., 2007). In the Arctic, several studies show a coincidence or strong contribution of DMS to aerosol formation. This is particularly pronounced during phytoplankton blooms (Park et al., 2017) and in the summer, when other condensation nuclei, e.g., from anthropogenic sources or sea salts, are low (Chang et al., 2011; Leaitch et al., 2013; Ghahremaninezhad et al., 2016).

Dimethylsulfide is produced by degradation of dimethylsulfoniopropionate (DMSP), which is an abundant metabolite produced by marine microalgae. Different taxonomic groups of microalgae produce different amounts of DMSP per biomass. Dinoflagellates, prymnesiophytes, and chrysophytes are high DMSP producers, whereas diatoms, prasinophytes and chlorophytes produce lower amounts of DMSP (Keller et al., 1989; Stefels et al., 2007). In the polar regions, sea ice algae are important DMSP producers, for whom it probably serves as osmoregulator and cryoprotectant (Kirst et al., 1991). Marine bacteria have recently been shown to produce DMSP, but the physiological role and contribution to overall DMSP production is unknown so far (Curson et al., 2017). Phytoplankton as well as bacteria cleave DMSP to DMS with enzymes (e.g., Ishida, 1968; Kiene, 1990; Stefels and Van Boekel, 1993; Ledyard and Dacey, 1994). DMSP is further released into the seawater by active exudation or by disruption of cells, e.g., by autolysis, viral lysis, or grazing (Malin et al., 1998; Simó, 2001; Kasamatsu et al., 2004). Dissolved DMSP is then available for microbial consumption, serving as an important carbon and sulfur source, covering up to 15% of the carbon and 100% of the sulfur demand (Kiene et al., 2000). Bacteria either lyse DMSP to assimilate the carbon and produce DMS as side product, or demethylate DMSP to assimilate both carbon and sulfur. The balance between both pathways is controlled by the sulfur demand of the bacterial community. Major removal processes of DMS from seawater are bacterial uptake and degradation, photo-oxidation and sea-air flux (Kiene and Bates, 1990; Simó, 2004; del Valle et al., 2009).

The central Arctic Ocean is influenced by Atlantic water (AW) entering through Fram Strait and Pacific water (PW) entering through Bering Strait (**Figure 1A**). AW and PW differ in their nitrate-to-phosphate ratios, with PW being depleted in nitrate compared to AW (Jones et al., 1998). Both water masses mix while drifting from the Laptev Sea toward Fram Strait in the Transpolar Drift, which is also the primary drift direction of sea ice (Kwok et al., 2013; **Figure 1A**). In addition, in the central Arctic sea-ice melt and freeze influence the surface stratification. This limits winter vertical mixing and thus the resupply of nutrients from deeper water (e.g., Rudels et al., 1991).

Most of the studies on DMS and DMSP in the Arctic have been performed in the Canadian Archipelago, coastal regions and some in Greenland and Barents Sea (see references in Levasseur, 2013). Only three studies (Gosselin et al., 1996; Leck and Persson, 1996; Matrai et al., 2008) were conducted in the central Arctic Ocean, covering a slim corridor along 0–10°E and continuing on 170°W (**Figure 1B**). Our study covers regions extending further eastward toward the Laptev Sea and toward the Beaufort Sea, which have not been investigated in previous studies. We hypothesize that DMSP and DMS concentrations differ by region, despite a full sea ice cover. We define three regions with influence of different sea ice – ocean interaction and water mass signatures. We analyzed DMS and DMSP concentrations with respect to chlorophyll *a*, as a marker for autotrophic biomass, as well as group-specific marker pigments, macronutrients and overlying sea-ice types. The objective of our study is to quantify DMS in the three regions and to explain how different DMSP and DMS production and consumption processes could lead to the observed findings.

MATERIALS AND METHODS

Water Column Properties and Water Sampling

Samples were collected in the central Arctic Ocean during Transark I (13 August–22 September 2011) and Transark II (20 August–24 September 2015) cruises of RV Polarstern (**Figure 1B** and **Supplementary Table 1**; Schauer, 2012, 2016). The two cruises covered an area north of 79°N between 30° E and 130° W. Water column salinity and temperature were recorded with a conductivity-temperature-density (CTD) system (SBE911+, Sea-Bird Electronics Inc., Washington, DC, United States) mounted on a carousel water sampler/rosette (SBE32). Water samples from the upper 100 m of the water column were either collected with 12 L Niskin bottles mounted onto a rosette sampler during the up-cast or with 6.4 L Kemmerer bottles through a hole in the sea ice in several meters distance from the ship. Details on CTD measurement and Niskin water sampling procedures are described in Schauer (2012, 2016) and Damm et al. (2018).

At the time of observations in August/September, the depth of the Winter Mixed Layer (WML) can be identified as a temperature minimum below the much shallower summer mixed layer and the summer halocline (Rudels et al., 1996; Korhonen et al., 2013). This estimation is based on the assumption that the temperature minimum, often with temperature close to the freezing point temperature, is a remnant of the haline convection during previous winter. Since the summer warming and ice melting quickly establish strong density stratification near the surface, their effect is restricted to the shallow surface layer and the warming does not reach as deep as the winter convection.

Analysis of Inorganic Nutrients and Calculations of Pacific Water Fractions

In 2011, inorganic nutrients nitrate, phosphate and silicate were determined on an Evolution III Autoanalyzer (Alliance Instruments GmbH, Salzburg, Austria). Methods were modified after Grasshoff et al. (1998) and manufacturers instructions (Seal Analytical, https://seal-analytical.com, accessed June 27, 2019). In 2015, nutrients were analyzed colorimetrically as described in Van Ooijen et al. (2016). Data can be accessed at PANGEA (Kattner and Ludwichowski, 2014; Van Ooijen et al., 2016). Pacific water fractions (f_{PW}) were calculated from nitrate and phosphate concentrations according to Jones et al. (2008), using

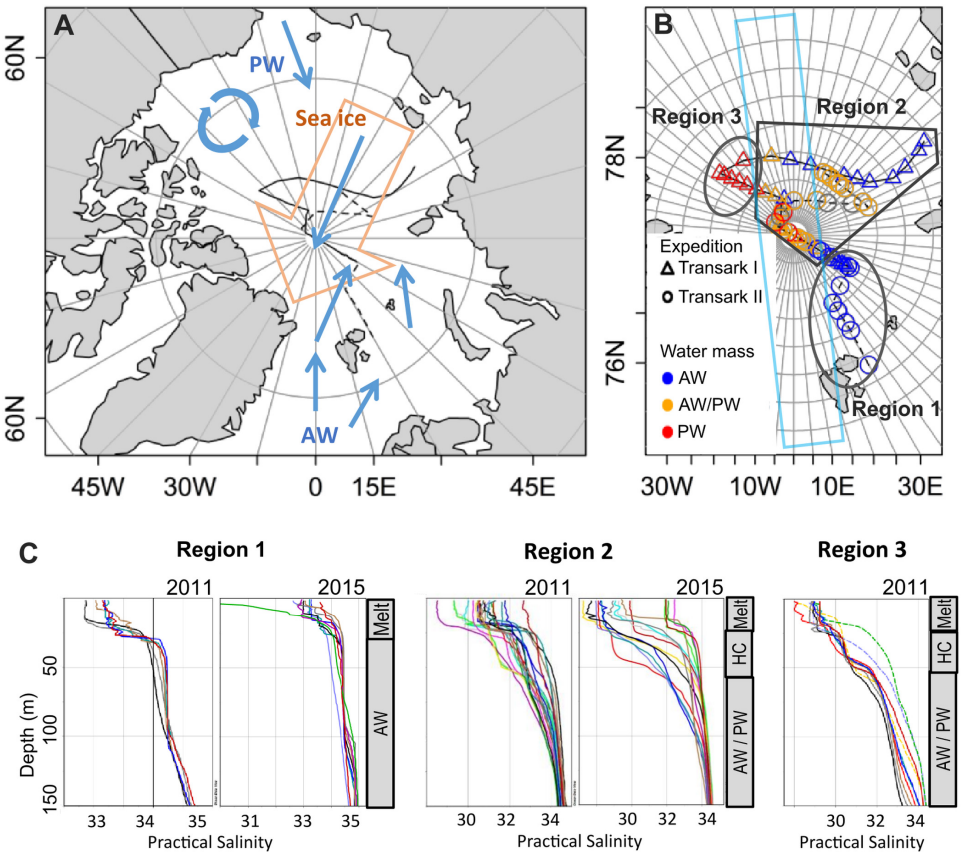

FIGURE 1 | Study area **(A)**, station map **(B)**, and salinity profiles in the upper 150 m of the water column **(C)**. **(A)** Schematic of general surface water (blue arrows) and sea ice (orange arrow) movement relevant for our study. Atlantic water (AW) enters the central Arctic via Fram Strait, Pacific water (PW) via the Bering Strait. The black lines indicate the cruise tracks Transark I 2011 (solid) and Transark II 2015 (dashed). Adapted from Ulfsbo et al. (2014) and Damm et al. (2018). **(B)** Stations during expeditions Transark I 2011 (triangles) and Transark II 2015 (circles), covered a broad area of the central Arctic Ocean spanning different water masses. Colors show the water mass dominating in the surface layer (<25 m). Region 1 is dominated by AW, Region 2 is characterized by a mix of nutrient signatures, while Region 3 is dominated by PW. The light blue box indicates the approximate coverage of previous studies in the central Arctic from Levasseur (2013). **(C)** Salinity profiles in the different regions for both years. Sea ice melt from the current season (Melt) causes the lower salinity in the upper 25 m. In Region 1, directly beneath is the AW. In Regions 2 and 3, the mixed AW/PW water is separated from the meltwater layer by a second halocline (HC). The gray bars on the right show the general structure of the water column. Note the different *x*-axis scales.

endmember correlations of selected Atlantic water and Pacific water dominated stations from our study.

To express macronutrient limitations and deviations from the Redfield ratio the quasi-conservative tracer $N^* = (N - 16 \times P + 2.9\ \mu mol\ kg^{-1}) \times 0.87$ was calculated according to Gruber and Sarmiento (1997). Values of 0 reflect that Redfield ratio is retained, while $N^* > 0$ indicates a depletion of phosphate relative to nitrate (Atlantic influenced waters) and $N^* < 0$ indicates a depletion of nitrate relative to phosphate (Pacific waters).

Quantification of DMS and DMSP

Dimethylsulfide was analyzed on a gas chromatograph (Varian 450C) which was coupled to a purge and trap system slightly modified from the method described in Kiene and Slezak (2006). Aliquots of 3 mL seawater were sampled directly into 5 mL glass vials, sealed with Teflon-coated rubber septa and crimp lids, and analyzed within 3 h after sampling. Samples were purged with helium for 10 min at a flow rate of 60 mL min^{-1} and dried while passing a Nafion^{TM} tube (Perma Pure LLC, NH, United States). DMS was cryo-trapped in teflon tubing immersed in liquid nitrogen, desorbed in a water bath heated to 70°C and transferred into the gas chromatograph equipped with a CP-Sil 5CB column (25 m, 0.32 mm, 0.25 µm) and a pulsed flame photometric detector (PFPD). Helium was used as carrier gas at a flow rate of 1.7 mL min^{-1}, the oven temperature was 130°C isotherm and the detector was run at 200°C.

Since samples were not filtered prior to measurements, we cannot exclude that fragile phytoplankton cells like prymnesiophytes might have been disrupted during purging, releasing DMSP followed by conversion to DMS. As detailed in the **Supplementary Material** this might have led to a overestimation of DMS concentrations of up to 1.5 nM and an according underestimation of DMSP in samples with high haptophyte content (e.g., Station Transark II/54).

Total DMSP was analyzed as DMS after alkali cleavage (Dacey and Blough, 1987) with the same analytical procedure as described above. For DMSP analysis, approximately 30 mL seawater was sampled into 50 mL centrifuge tubes and stored refrigerated. Within 12 h the tubes were inverted several times to resuspend particles and 1–3 mL seawater were subsampled into 5 mL glass vials. To initiate alkali lysis of DMSP, 2 mL of 10 M NaOH were added, the vial sealed, and incubated at room temperature for 2 h. DMS and DMSP were analyzed from separate aliquots. Since DMS was not purged from the DMSP aliquot before alkali lysis, the measured DMSP concentration ($DMSP_{gross}$) also contained DMS. DMSP data presented in this publication were corrected for DMS as follows: $DMSP = DMSP_{gross} - DMS$.

The system was calibrated with DMS (>99%, Sigma-Aldrich) for concentrations from 0.8 to 763 pmol in 3 mL Milli-Q in 2011 (Transark I). In 2015 (Transark II) the calibration spanned 2.4–315 pmol in 3 mL Milli-Q. The limit of quantification (LOQ) was defined to the lowest calibration level. Considering the sample volume, this resulted in LOQ of 0.16 nM DMS and 0.27 nM DMSP in 2011 and 0.8 nM for DMS and DMSP in 2015. Samples below LOQ but >0 were normally distributed and treated as ½ of the LOQ for calculation of the mean and standard deviation. For further analysis (e.g., correlations, means) values <LOQ were omitted. Standard deviation on replicate standard measurements was 12% on average, while sample replicates had average standard deviations of 19% for DMS and 14% for DMSP.

Pigment Analysis

For pigment analyses, 1–2 L seawater samples were taken from Niskin bottles attached to the CTD rosette from 6 to 8 depths in the upper 100 m. During Transark I, occasionally only the upper 50 m were sampled. In addition, samples from a hand held Kemmerer bottle were taken through an ice hole. The seawater was immediately filtered on GF/F filters, frozen in liquid nitrogen, and stored at −80°C until further analyses by high performance liquid chromatography (HPLC) at the home laboratory. Pigment samples were measured with reverse-phase HPLC with a VARIAN Microsorb-MV3 C8 column (4.6 mm × 100 mm), using HPLC-grade solvents (Merck), a Waters 1525 binary pump equipped with an autosampler (OPTIMAS^{TM}), a Waters 2996 PDA (photodiode array detector) and the EMPOWER software. For further details see Tran et al. (2013). The ratio of respective marker pigments to chlorophyll *a* was calculated to serve as indication of the dominant phytoplankton communities observed during this study.

Sea Ice Trajectories

To determine pathways, age and source area of sampled sea ice, a Lagrangian approach (ICETrack) was used that traces sea ice backward in time using a combination of satellite-derived low-resolution drift products. ICETrack has been used in a number of publications to examine sea ice sources, pathways, thickness changes and atmospheric processes acting on the ice cover (e.g., Krumpen et al., 2016, 2019; Damm et al., 2018; Peeken et al., 2018). The tracking approach works as follows: An ice parcel is tracked backward in time on a daily basis starting at Fram Strait. Tracking is stopped if (a) ice hits the coastline or fast ice edge, or (b) ice concentration at a specific location drops below 25% and we assume the ice to be formed.

Statistics

Data processing and analyses were performed with the software package R version 3.2.3 (R Core Team, 2015) in RStudio Version 1.0.163. Figures, except for **Figures 1C**, **3**, were prepared with base and ggplot2 packages. Sample groups in **Figures 2**, **5**, **6** were compared to each other applying Welch's *t*-test (Welch, 1938; Andrade and Estévez-Pérez, 2014, Eqs. 5 and 5c). Boxplots in those figures show the median, the 25th and 75th percentiles, as well as 1.5 times the interquartile range as whiskers. Pearson correlation coefficients (Pearson, 1895; Hollander et al., 2015) in **Figure 4** were calculated in R package Hmisc version 4.0-3. **Figure 1C** was created using Ocean Data View (Schlitzer, 2018). **Figure 3** was created with Sigma plot 10 displaying the median, the 10th, 25th, 75th, and 90th percentiles as vertical boxes with error bars.

RESULTS

We can distinguish three different regions (**Figure 1**), based on the dominating water masses at depths <25 m and the influence of sea ice processes on the upper water column. For each of the regions we describe the respective water mass, nutrients and ice conditions, followed by DMSP and DMS as well as the biomass and taxonomy of the phototrophic community.

Region 1

In 2011 all stations in Region 1 were sampled between 13 and 17 August, while in 2015 Region 1 was sampled between 20 August and 2 September. For both years Region 1 was characterized by northeastward directed inflow of Atlantic water from the Fram Strait with fractions of Pacific Water (f_{PW}) smaller than 25% (**Figure 1B**). Salinity was high with 31.8–34.3 PSU in the upper 25 m and 34.1–34.8 PSU at 50–100 m depth (**Figure 1C**). The corresponding seawater densities of 1026.7 ± 0.4 kg m^{-3} in the upper 25 m and 1027.7 ± 0.1 kg m^{-3} at 50–100 m depth indicate weak stratification caused by meltwater in the upper 25 m. The Winter Mixed Layer, describing the depth of the haline convection during the previous winter, is 60–100 m deep in Region 1. Macronutrients nitrate, phosphate and silicate in Region 1 were lowest in the upper 25 m, increasing downward (**Table 1**). Nitrate was replete with 2.2 ± 1.6 (0–25 m) to 8.4 ± 2.4 μmol L^{-1} (50–100 m) compared to relatively low phosphate of 0.2 ± 0.1 to 0.6 ± 0.2 μmol L^{-1}. The nitrate to phosphate ratio deviated slightly from the Redfield ratio toward phosphate limitation as indicated by N* of 1.3 ± 0.7 μmol kg^{-1}. Silicate concentrations were the lowest of all three regions with values of 2.3 ± 0.9 μmol L^{-1}.

A loose cover of melting summer sea ice characterized Region 1 except for one station at the ice edge in 2011 and one in open water toward Fram Strait in 2015. In both years, most of the sea

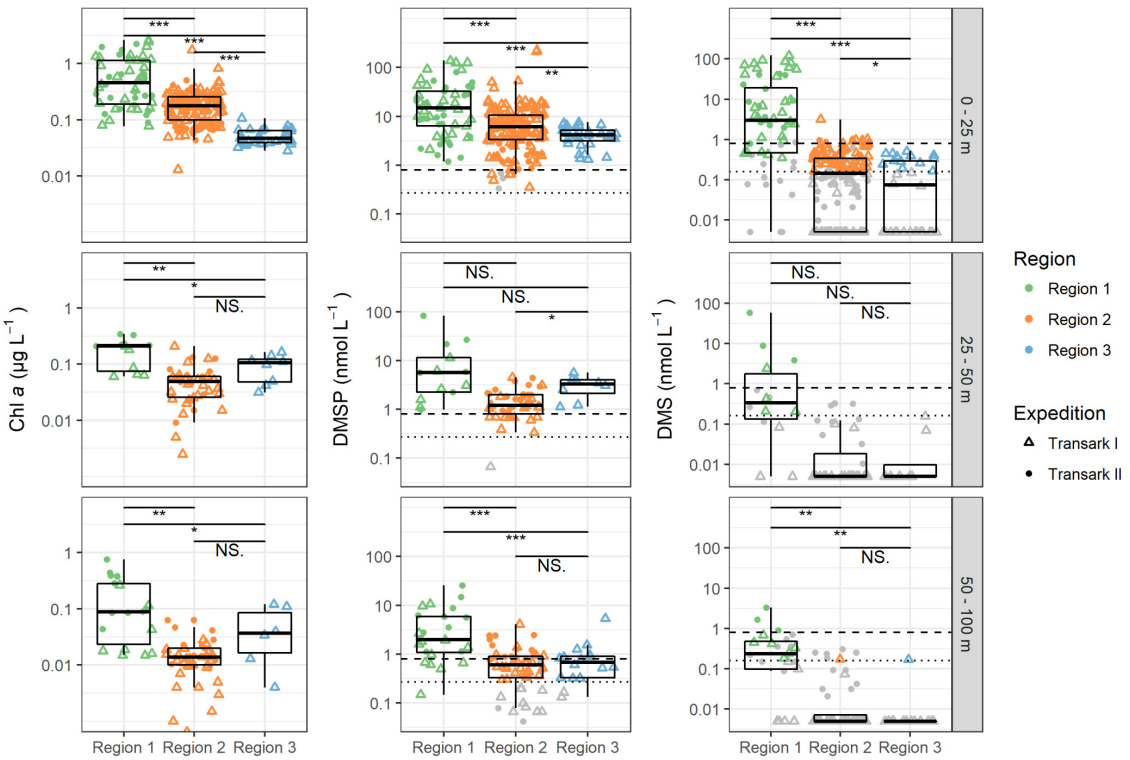

FIGURE 2 | Chlorophyll *a* (Chl *a*), dimethylsulfoniopropionate (DMSP), and dimethylsulfide (DMS) concentrations in the upper 100 m water column during expeditions Transark I (triangles) and Transark II (circles) in the three regions. Data, of which the measured value was below the limit of quantification (LOQ), is shown in gray (Transark I: 0.16 nmol L^{-1} DMS and 0.27 nmol L^{-1} DMSP, dotted lines; Transark II: 0.8 nmol L^{-1} DMS and DMSP, dashed lines). In Region 1 depth 0–25 m, 25% of the DMS measurements were <LOQ, while for all other regions and depths ≥50% were <LOQ. This value was even higher with >93% for regions 2 and 3 for depths below 25 m. DMSP or DMS = 0 are shown as 0.005 due to logarithmic *y*-axis. Confidence levels of Welch's *t*-test for significant differences between sample groups: $0.0001 \leq ^{***}p < 0.001 \leq ^{**}p < 0.01 \leq ^{*}p \leq 0.05 <$ NS. ≤ 1.

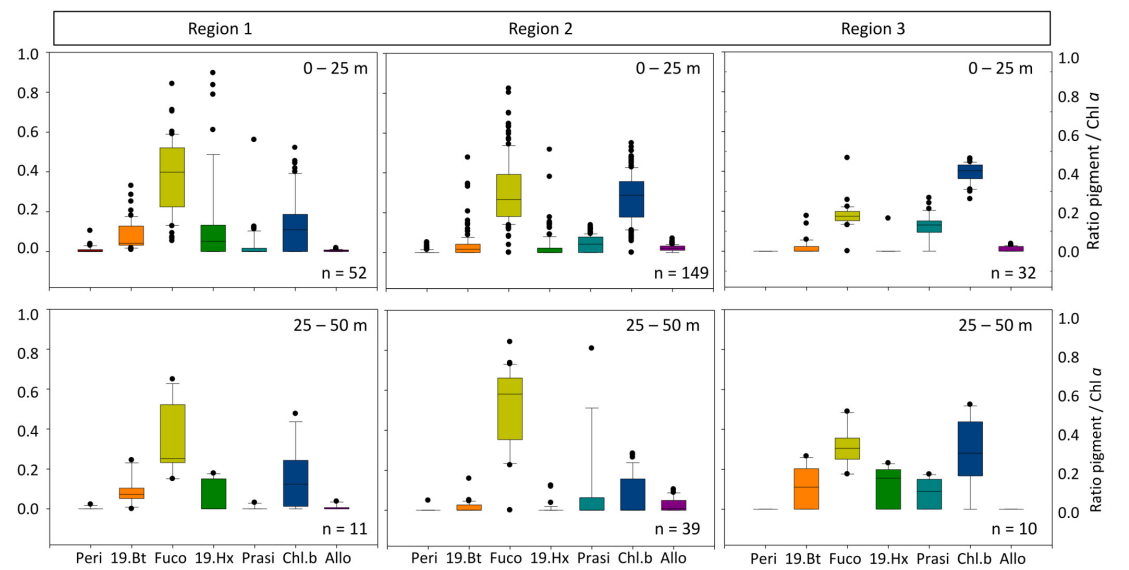

FIGURE 3 | Marker pigment ratio to chlorophyll *a* for the various regions (upper panel 0–25 m; lower panel 25–50 m). Peri, Peridinin; 19.Bt, 19-butanoyloxyfucoxanthin; Fuco, fucoxanthin; 19.Hx, 19-Hexanoyloxyfucoxanthin; Prasi, Prasinoxanthin; Chl.*b*, Chlorophyll *b*; Allo, Alloxanthin indicative for Dinoflagellates, Crysophytes, Diatoms, Prymnesiophytes, Prasinophytes, Chlorophytes, and Cryptophytes, respectively.

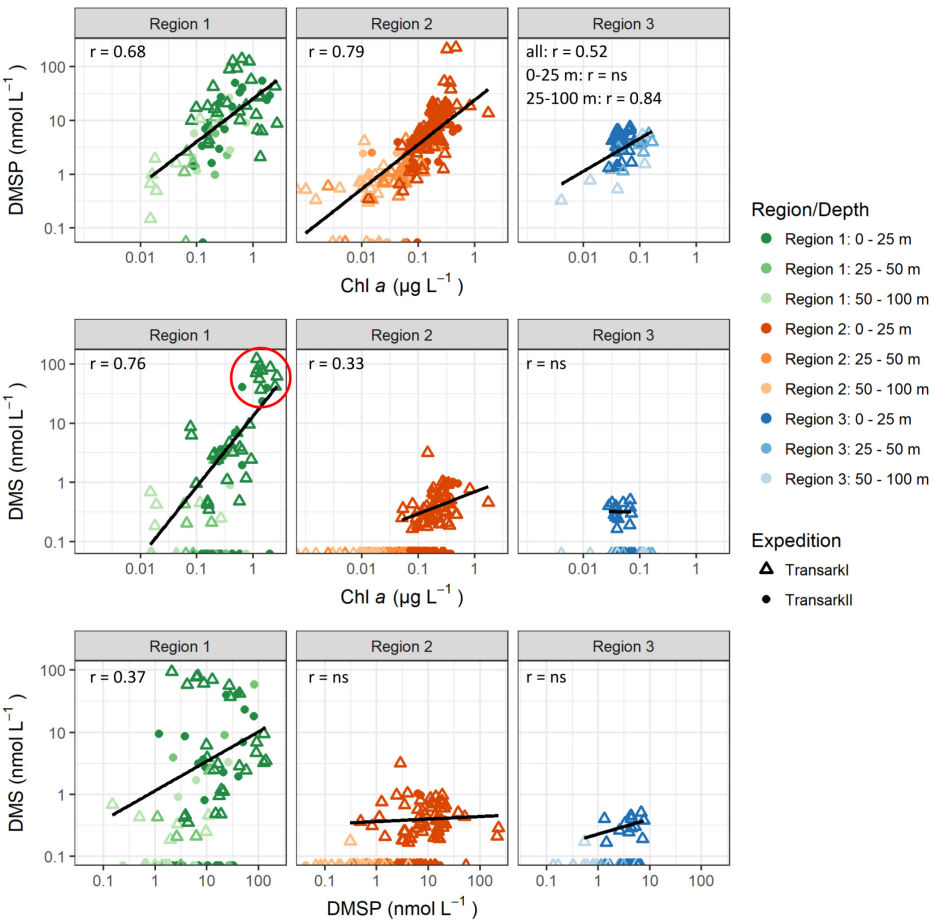

FIGURE 4 | Correlations between DMSP and DMS to chlorophyll *a* and DMS to DMSP. DMS and DMSP values <LOQ are shown at the *x*-axis. Correlations were calculated with DMS and DMSP values >LOQ. Outliers were omitted for correlations: Region 2 DMSP >200 nmol L^{-1}, DMS >2 nmol L^{-1}. Pearson correlation coefficients (r) are shown for *p*-value <0.05. For *p*-value >0.05 "ns" indicates that those were not statistically significant. Stations with high DMS concentration in Region 1 (red circle) are PS78/203 (n = 10, depth <11 m), PS94/34 (n = 2, depth: 20 m, 28 m), and PS94/54 (n = 2, depth: 2 m, 10 m).

ice (87%) had drifted to Region 1 from the Laptev Sea area. In 2011 all stations were covered by 2 year ice, which had formed in polynyas close to the coast. In 2015, on the other hand, most of the ice was 1-year-old and had formed during sea ice freeze-up in deeper waters.

Chlorophyll *a* concentration, describing total autotrophic biomass, was highest in the upper 25 m of the water column throughout all regions, with concentrations between 0.077 and 2.65 µg L^{-1} (0.72 ± 0.67 µg L^{-1}, **Figure 2**). Below 25 m chlorophyll *a* concentrations were homogeneous with means of 0.18 ± 0.10 µg L^{-1} at 25–50 m, and 0.18 ± 0.20 µg L^{-1} at 50–100 m depth. Corresponding to chlorophyll *a*, DMSP was also high in the upper 100 m of the water column in Region 1, with concentrations of up to 139.4 nM. However, concentrations decreased from the surface layer to 100 m with mean values of 38.6 ± 37.2 nM (0–25 m), over 21.3 ± 39.3 nM (25–50 m) to 4.7 ± 5.7 nM (50–100 m). We observed maximal DMS concentrations of 122 nM in the surface layer, with a mean of 17.6 nM (±29.1 nM), while at 25–50 m DMS was only 5.4 ± 15.5 nM, with 42.8% of the samples below the LOQ (**Supplementary Table 2**). At 50–100 m concentrations were even lower with a maximum of 3.3 nM, and 54% of the samples below the LOQ.

In the high biomass region 1 the phytoplankton community (0–50 m) was dominated by diatoms as indicated by the high ratio of fucoxanthin to chlorophyll *a*. Other important groups were prymnesiophytes (19-hexanoyloxyfucoxanthin) and chlorophytes (chlorophyll *b*) (**Figure 3**). Overall, the communities in the surface <25 m and the 25–50 m range were similar except for sporadic high contributions of prymnesiophytes in the surface layer.

Region 2

Region 2 was sampled from 19 to 30 August and 6 to 22 September in 2011. In 2015, sampling in this region was performed from 4 to 24 September. Generally, Region 2 is characterized by the Transpolar Drift transporting Polar surface water from the Siberian shelf toward Fram Strait. Pacific water (f_{PW}) fractions were largely between 25 and 60%, although some reached values outside that range (**Figure 1B**).

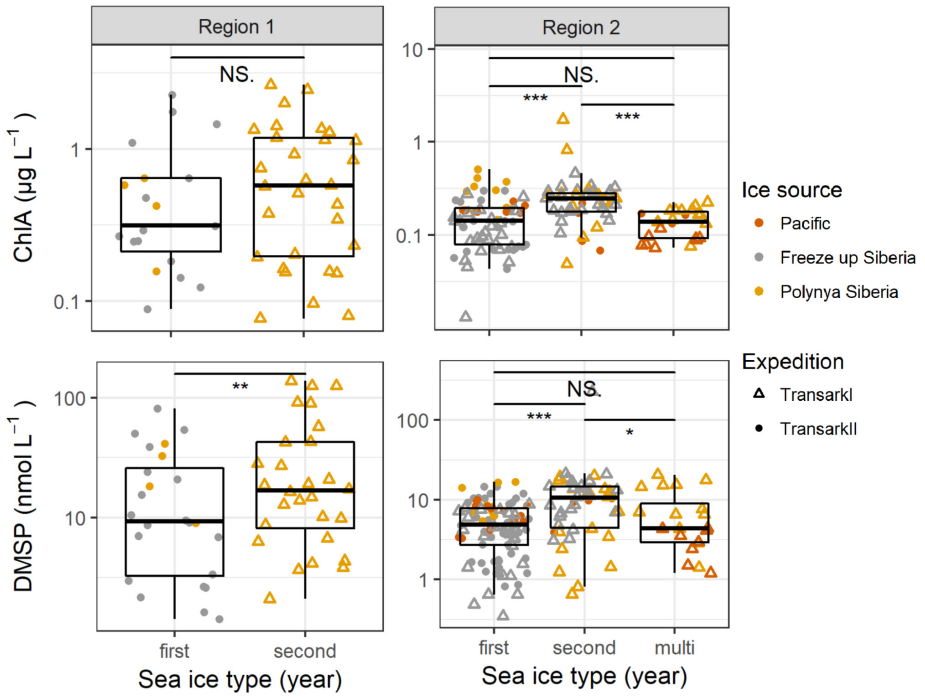

FIGURE 5 | Chlorophyll *a* and DMSP concentrations in the upper 25 m water column in Regions 1 and 2. The *x*-axis shows different age of sea ice, color indicates the source region and symbols the two different expeditions/years. Note the different *y*-axis scales. Confidence levels of Welch's *t*-test for significant differences between sample groups: $0.0001 \leq ^{***}p < 0.001 \leq ^{**}p < 0.01 \leq ^{*}p \leq 0.05 <$ NS. ≤ 1.

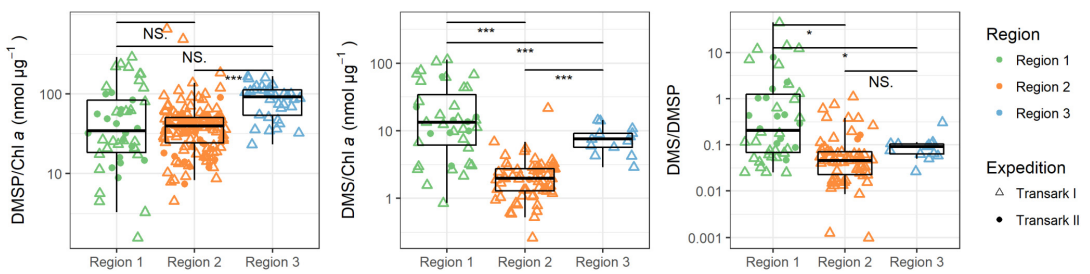

FIGURE 6 | Ratios of DMSP and DMS to chlorophyll *a* (Chl *a*), and between DMS and DMSP in the upper 25 m water column during expeditions Transark I (triangles) and Transark II (circles) in the three regions. Confidence levels of Welch's *t*-test for significant differences between means: $0.0001 \leq ^{***}p < 0.001$, $0.01 \leq ^{*}p \leq 0.05 <$ NS. ≤ 1.

Salinity spread from 27.2 to 34.5 PSU in the upper 25 m, and had a narrower range of 32.0 to 34.7 PSU at 50–100 m depth (**Figure 1C**). Corresponding seawater densities of 1024.3 ± 1.3 kg m^{-3} near the surface and 1027.1 ± 0.5 kg m^{-3} at depth show a moderate to strong influence of sea ice melt in the upper 25 m of the water column. The WML in Region 2 is approximately 50 m deep (Korhonen et al., 2013). Nitrate was particularly depleted near the surface, with 1.1 ± 1.2 µmol L^{-1} (0–25 m), increasing to 7.5 ± 2.2 µmol L^{-1} (50–100 m). This compares to homogeneous phosphate concentrations of 0.6 ± 0.09 µmol L^{-1} (**Table 1**). Deviation from the Redfield ratio toward nitrate limitation was strongest near the surface with N* of −3.3 ± 2.8 µmol kg^{-1} (0–25 m) but lower in the deeper water layers −0.7 ± 2.1 µmol kg^{-1} (50–100 m). Silicate concentrations were homogeneous at 8.1 ± 4.7 µmol L^{-1}.

A loose cover of melting summer sea ice characterized Region 2 except for three ice-free stations in the Laptev Sea in 2011 (14%). Source regions and types of the ice were diverse in both years, but dominated by ice from the Laptev Sea region. Whereas 57 and 52% was freeze-up sea ice from the interior Laptev Sea, sea ice originated in the shallow Siberian polynya region made up 24 and 14% in 2011 and 2015, respectively. In 2015, 33% of the ice had formed in the Pacific Arctic during freeze-up or in shallow polynya regions close to coast in the Beaufort Sea. In 2011, the age of ice was mixed with 24% one-year, 43% two-year, and 14% multi-year ice. In 2015, one-year ice dominated with 86%, over two and multi-year ice.

TABLE 1 | Salinity, concentrations of macronutrients and N* (mean ± standard deviation).

	Depth	Salinity	Nitrate	Phosphate	Silicate	N*
Region 1	0–25 m	33.2 ± 0.5	2.2 ± 1.6	0.2 ± 0.1	1.5 ± 0.9	1.1 ± 0.7
Region 1	25–50 m	34.2 ± 0.3	5.5 ± 1.5	0.4 ± 0.1	2.3 ± 0.6	1.2 ± 0.8
Region 1	50–100 m	34.5 ± 0.2	8.4 ± 2.5	0.6 ± 0.2	3.3 ± 1.1	1.6 ± 0.7
Region 2	0–25 m	30.3 ± 1.6	1.1 ± 1.2	0.5 ± 0.2	7.4 ± 3.8	−3.3 ± 2.8
Region 2	25–50 m	32.3 ± 1.2	4.2 ± 1.9	0.6 ± 0.2	9.1 ± 5.0	−2.6 ± 2.4
Region 2	50–100 m	33.7 ± 0.6	7.5 ± 2.2	0.7 ± 0.2	7.8 ± 5.2	−0.7 ± 2.1
Region 3	0–25 m	29.2 ± 0.5	0.1 ± 0.1	0.6 ± 0.0	2.1 ± 1.0	−6.3 ± 0.5
Region 3	25–50 m	30.9 ± 0.6	4.6 ± 3.5	1.1 ± 0.3	9.8 ± 5.9	−8.8 ± 1.5
Region 3	50–100 m	32.0 ± 0.8	13.1 ± 4.0	1.8 ± 0.4	27.7 ± 9.8	−11.0 ± 2.0

Chlorophyll *a* concentrations were 0.20 ± 0.17 μg L^{-1} in the upper 25 m decreasing to 0.16 ± 0.14 μg L^{-1} in the deeper layers (**Figure 2**). In the upper 25 m DMSP had a wide spread of concentrations with the highest observed value in this study being 227.8 nM, but averaged lower than Region 1 to 11.0 ± 26.1 nM. Deeper in the water column, DMSP concentrations were small with 1.4 ± 1.0 nM in 25–50 m and 0.8 ± 0.8 nM in 50–100 m depth. DMS concentration in the upper 25 m ranged up to 3.1 nM, but averaged below the LOQ. In the upper 25 m 58% of the samples were below the LOQ, while in the deeper water layers (50–100 m) over 96% were not quantifiable in Region 2.

In the upper 50 m water column in Region 2, diatoms (marker pigment fucoxanthin) dominated the phytoplankton community (**Figure 3**). Chlorophytes (marker pigment chlorophyll *b*) were the second most abundant group. Compared to Region 1, a slightly higher contribution of prasinophytes and cryptophytes was indicated by the marker pigments prasinoxanthin and alloxanthin, while the prymnesiophyte signal 19-hexanoyloxyfucoxanthin was lower than in Region 1.

Region 3

Region 3 was sampled from 31 August to 4 September in 2011. Region 3 was characterized by Pacific water (f_{PW}) fractions >60% (**Figure 1B**). Salinity was 29.2 ± 0.5 PSU in the upper 25 m, and had a narrower range of 32.0 ± 0.8 PSU at 50–100 m depth (**Figure 1C**). Corresponding seawater densities showed a strong stratification and decrease gradually from 1023.4 ± 0.4 kg m^{-3} in the surface layer to 1025.7 ± 0.6 kg m^{-3} at depth. The Winter Mixed Layer was relatively shallow at approximately 40 m in Region 3. The range of macronutrient concentrations was largest in Region 3 increasing from surface to deeper waters. Nitrate was fully depleted (0.09 ± 0.1 μmol L^{-1}) in the upper 25 m of the water column, increasing toward 13.1 ± 4.0 μmol L^{-1} at 50–100 m depth (**Table 1**). Phosphate increased from 0.6 ± 0.03 μmol L^{-1} to 1.8 ± 0.4 μmol L^{-1}. The strong deviation from the Redfield ratio with N* of −6.3 ± 0.5 μmol kg^{-1} increased with depth to −11.0 ± 2.0 μmol kg^{-1}. Silicate ranged between 2.2 ± 1.0 and 27.66 ± 9.8 μmol L^{-1} from surface to deeper waters, respectively.

Sea-ice cover was 90% for Region 3, which was only sampled in 2011. The ice consisted to 86% of 2-year freeze-up ice from the Canadian Arctic. Only the northernmost station of this region was covered by multi-year sea ice that had formed during freeze-up in the East Siberian Sea.

Chlorophyll *a* was generally low in Region 3 but in contrast to the other two regions, there was no downward gradient (**Figure 2**). Highest concentrations were observed at 25–50 m water depth with 0.09 ± 0.05 μg L^{-1}, while the above and below concentrations were 0.05 μg L^{-1}. DMSP was 4.2 ± 1.8 nM at 0–25 m, 3.0 ± 1.5 nM at 25–50 m and 0.9 ± 1.2 nM at 50–100 m. In the surface layer DMS was present at concentration of 0.2 ± 0.2 nM, while in the underlying water 93% of the DMS samples were below LOQ.

In the upper 50 m water column, the marker pigments in Region 3 represented a community dominated by chlorophytes and prasinophytes (chlorophyll *b* and prasionoxanthin, **Figure 3**). Within the deep chlorophyll maximum, also chrysophytes (19-butanoyloxyfucoxanthin) and prymnesiophytes were present, indicating an overall flagellate dominated community. Dinoflagellates (peridinin) were almost absent, as in all other regions.

DISCUSSION

Overall, seawater DMS and DMSP concentrations in our study (**Figure 2**) are similar to concentrations reported in the few previous studies north of 79°N (<10 nM DMS, <40 nM DMSP) (Gosselin et al., 1996; Leck and Persson, 1996; Matrai et al., 2008; Levasseur, 2013). However, we observe pronounced regional differences in DMS and DMSP concentrations, which match differences in water masses, the intensity of sea ice – ocean interaction, as well as differences in the phototrophic biomass. This complexity might point to different mechanisms for DMSP and DMS production and degradation processes in the regions, which eventually control the overall budget of DMSP and DMS in the central Arctic. In the following we discuss in detail the physical as well as biological drivers on the patterns of DMSP and DMS distribution.

Region 1

Influence by Inflowing AW and Short Time Sea Ice – Ocean Contact

The upper 100 m water column in Region 1 is characterized by a high fraction of Atlantic water (**Figure 1A**) due to the AW inflow

into the Eurasian Basin via Fram Strait. While the AW circulates northeastward toward the Laptev Sea (Jones et al., 1998), wind drives sea ice drift in the opposite direction from the Siberian shelf toward Fram Strait (Kwok et al., 2013). Because of the opposite movements of water and ice (**Figure 1A**), the seawater in Region 1 has been in contact with sea ice for a relatively short time only. Thus, the influence of sea ice is low (Damm et al., 2018) and ice melt forms a slightly less saline, shallow (approximately 25 m) meltwater layer on top of the AW body. The presence of nitrate and phosphate (0–50 m) shows that winter mixing reaches deep enough (approximately 75 m; **Supplementary Figure 1A**) to resupply the surface layers with fresh nutrients before the next growth season.

The drawdown of nutrients, however, observed in mid to late August in the meltwater layer (0–25 m) compared to the deeper water, as well as high chlorophyll *a* concentrations (**Figure 2** and **Table 1**), point to recent or ongoing phytoplankton growth. Due to reduced mixing between the lower saline meltwater and the underlying higher saline AW, the majority of the phytoplankton was found in the meltwater lens directly under the ice, where it receives the highest incoming radiation to support primary production (Laney et al., 2017). About 75% of the chlorophyll *a* signal was found in the upper 25 m of the water column.

That phytoplankton was actively growing in Region 1 during our study is corroborated by net community production rates (approximately 1 mol C m^{-2}) derived from carbon dioxide partial pressure (pCO_2) for the same region in 2011 (Ulfsbo et al., 2014). Generally, during late summer, these latitudes of the Eurasian Arctic (82–87°N) – ice covered, yet in proximity to the ice edge – show higher integrated net primary production estimates (20–30 mg C m^{-2} d^{-1}) compared to higher latitudes (Fernández-Méndez et al., 2015).

DMS Production Controlled by Phytoplankton Abundance

Concurrent with the highest concentrations of chlorophyll *a*, we observed the highest concentration of DMSP and DMS in Region 1 (**Figure 2**). The strong positive correlation of DMSP to chlorophyll *a* (r = 0.68, **Figure 4**) shows, that the DMSP in this region is largely controlled by the biomass of photosynthetic microalgae in the water column. The tight correlation is striking considering the spread in species composition within Region 1 (**Figure 3**). The influence of species composition was identified as one of the reasons for a missing global correlation between DMSP and chlorophyll *a* (Stefels et al., 2007).

Beside the production of DMSP through phytoplankton, sea ice melt might release ice algal-sourced DMSP into the under ice water. Galindo et al. (2014) report maximum concentrations of 20 nM ice-sourced DMSP in the under ice water in the Canadian Archipelago. Due to the lower DMSP stocks in sea ice of the central Arctic (Levasseur, 2013 and unpublished own data) and the short time of sea ice – ocean contact, we assume that in Region 1 the effect of DMSP release from sea ice is negligible compared to the production by phytoplankton.

However, considering the sea ice-influence it is worth having a closer look on the different ice types influencing the water column. Damm et al. (2018) found that sea ice formed in the shallow shelf region transports methane from the shelf which is released to the underlying water column during the common drift into the central Arctic. Indeed, the source region of sea ice seems also be applicable to other dissolved compounds or particles. In the sea ice-influenced upper 25 m water column DMSP concentrations were significantly higher in 2011 beneath 2-year sea-ice, which had formed in polynyas close to the Siberian coast, than in 2015 beneath 1-year sea-ice, which had formed offshore in the Laptev Sea (**Figure 5**). In addition, nitrate and phosphate concentration were lower in 2011 below second year ice compared to 2015 below first year ice. This circumstance might also refer to the effect of different sea ice types to the sea ice influenced water underneath (**Supplementary Figure 2**).

Further, we also find DMS strongly correlated with chlorophyll *a* and DMSP (**Figure 4**) in Region 1. This is typical for ice edge blooms and ice-free regions in the Arctic (Galí and Simó, 2010; Levasseur, 2013; Park et al., 2013). DMS is produced by enzymatic cleavage of DMSP by phytoplankton as well as bacteria. The latter can also take up DMSP or degrade it via demethylation/demethiolation, which does not result in the production of DMS, and is usually the dominant pathway for bacterial DMSP assimilation (Kiene et al., 2000). Although unfortunately no microbiological data is available for this study, previous studies support that also in Arctic waters bacterial conversion processes of both sulfur compounds are likely to be an important factor for the final DMS and DMSP concentrations. For example, alpha-proteobacteria been reported from Arctic surface water (Motard-Côté et al., 2012; Rapp et al., 2018). The alpha-proteobacteria include the typical DMSP degrading groups SAR11 and Roseobacter (Kiene et al., 2000; Reisch et al., 2008). In addition, alpha- and gamma-proteobacteria have been shown to incorporate DMSP-sulfur in Arctic waters (Motard-Côté et al., 2012). The balance between the DMSP lysis and demethylation pathways is controlled by the sulfur demand of the bacterial community. Once the sulfur demand is saturated, lysis of DMSP becomes dominant (Kiene et al., 2000). Based on the findings by Kiene et al. (2000) we hypothesize that the high DMSP availability in Region 1 leads to a dominance of the lysis pathway over the demethylation pathway resulting in high DMS concentrations.

Since sea-air exchange of gasses as well as incoming radiation is reduced by the sea ice cover (Loose et al., 2011; Nicolaus et al., 2012), we assume that sea-air efflux as well as photo-oxidation of DMS were low and bacterial consumption of DMS was the most important sink for dissolved DMS in the under ice water in our study. An equilibrium between microbial DMS production and consumption rates has been suggested to keep the dissolved DMS pool steady at relatively low concentrations (Wolfe et al., 1999; Galí and Simó, 2010). However, the high concentrations of DMS or DMSP found in Region 1 might overwhelm DMS consumption and allow for accumulation of high amounts of dissolved DMS. Concentrations in the range of 11–32 nM DMS or dissolved DMSP were found to saturate DMS consumption (Kiene, 1992; Wolfe

et al., 1999). In the Labrador Sea, a particularly low DMS consumption rate was found at the coldest temperature of −0.1°C (Wolfe et al., 1999). Considering that the temperatures in our study are between −1.2° and −1.8°C, saturation as well as low consumption rates might cause the observed high DMS concentrations.

Under-Ice Biomass Peaks as Hotspots for DMS Production

The particularly high DMS concentrations of up to 122 nM in surface water of Region 1 (**Figure 4**, red circle and **Supplementary Figure 3**) are the highest observed in latitudes above 79°N (Gosselin et al., 1996; Leck and Persson, 1996; Matrai et al., 2008; Galí and Simó, 2010). For the ice-edge station Transark II/34 the depth of the DMS- and DMSP-peak at 28 m resembles the depth of biomass peaks previously observed in open water in vicinity to the ice edge (Arrigo et al., 2012). Chlorophyll *a* and other pigment data is not available for this station. At the other two stations (Transark II/54, Transark I/203) maximal DMS and DMSP values were located at a depth ≤10 m in the meltwater layer, concurrent with high phytoplankton biomass (chlorophyll *a* 0.6–2.6 μg/L) and a drawdown of nitrate, phosphate and silicate. These characteristics are typical for under-ice blooms that can develop, if structures like melt ponds or leads in the sea ice allow for increased incoming radiation to the underlying water column compared to an uninterrupted ice cover without ponds (Arrigo et al., 2012; Assmy et al., 2017).

In 2011, the under-ice-biomass peak was located at 86°N (station Transark I/203), 353 km from the ice edge (83°N, 14.8.2011) in an area with 92% ice cover (50 km average) and a high melt pond fraction of 25–50%. Both, the broken ice cover and melt ponds, likely allowing for light transmission to the under ice water (Nicolaus et al., 2012). The mixed community was dominated by diatoms (41 ± 3%), but also contained considerable fractions of prymnesiophytes (13 ± 2%) and chlorophytes (14 ± 2%). This resembles the average species composition in Region 1 (**Figure 3** and **Supplementary Figure 3**). We thus conclude that the high DMS signal at station 203 in 2011 is driven by the high biomass (Chlorophyll *a*: 1.1–2.6 μg/L).

In 2015, the under-ice biomass peak was located at 85°N (Transark II/54), 260 km from the ice edge (83°N, 28.8.2015) in an area with 100% ice cover (50 km average). The fractions of prymnesiophytes (90 ± 14%) and crysophyte (23 ± 10%) specific pigments were distinctly higher, and the fraction of diatoms lower (13 ± 5%), compared to other stations in Region 1 (**Figure 3** and **Supplementary Figure 3**). In the same year in May, the prymnesiophyte *Phaeocystis pouchettii* was reported form under-ice blooms north of Svalbard at 81°N (Assmy et al., 2017; Wollenburg et al., 2018). Prymnesiophytes and crysophytes are known to be strong DMSP producers (Keller et al., 1989; Stefels et al., 2007). However, the fraction of prymnesiophytes was neither correlated to DMSP nor DMS, while the fraction of crysophytes showed a weak negative correlation to DMSP and no correlation to DMS (**Supplementary Table 3**).

We conclude that in Region 1 the concentration of DMS is primarily controlled by phytoplankton biomass which controls DMSP concentration (Wolfe and Kiene, 1993; Wolfe et al., 1999; Galí and Simó, 2010), while the species composition has a minor influence on DMS concentrations. Overall, DMSP as precursor for the climate cooling gas DMS seems to be high in this Atlantic water-influenced region of the central Arctic.

Region 2

Influence by Recurrent AW/PW Mixed Water and Long-Time Sea Ice – Ocean Contact

In Region 2, Atlantic dominated waters mix with Pacific waters. While AW completes its anti-clockwise circulation in the southern Eurasian Basin, PW enters the Arctic Basin through Bering Strait (Jones et al., 1998). Surface waters as well as sea ice thus move from the Siberian shelf toward Fram Strait in a southwestward direction (**Figure 1A**). Because of this common drift direction, the sea water in Region 2 is strongly influenced by sea ice melt and freezing processes over one or more seasons (Damm et al., 2018). During freezing events in winter, brine release leads to haline convection in the upper water column (Rudels et al., 1996; Kikuchi, 2004). Despite the brine rejection, the resulting WML has a lower salinity than the underlying Atlantic water (**Figure 1C** and **Table 1**) and seasonal sea ice melt forms an even less saline meltwater layer in the upper 25 m of the water column. The meltwater halocline reduces downward mixing, retaining most of the phytoplankton in the meltwater layer.

Comparable to Region 1, the highest chlorophyll *a* signal was found at depths <25 m, below 25 m less than 25% of the surface layer chlorophyll *a* signal was found, and only 8% of the surface layer signal below 50 m. A similar distribution with decreasing concentrations toward depth was observed for DMSP and DMS. At depths >25 m DMS was either too low to be quantified or absent. In the AW/PW mixed water nitrate was close to depletion, while phosphate was still available, causing a deviation from the Redfield ratio toward nitrate limitation. When nitrate is depleted in late summer, primary production in the central Arctic has been found to be predominantly supported by a regenerated system based on ammonium as nitrogen source (Martin et al., 2012). Supporting this, Ulfsbo et al. (2014) found low net community production (approximately 0.25 mol C m^{-2}) in highly ice covered areas in 2011. As a result, chlorophyll *a* and DMSP concentrations are lower in Region 2 compared to Region 1 (**Figure 2**).

As laid out for Region 1, sea ice melt might also be a source of DMSP to the water column. Since the amount of DMSP produced by phytoplankton is presumably lower in Region 2 due to the lower biomass, the relative influence of sea ice sourced DMSP might be higher assuming that the same amount is released during melting. In addition to melt, brine rejection during sea ice freezing transports dissolved compounds like salts and gasses (Rudels et al., 1996; Damm et al., 2015), but also particulates like sea ice algae (Hardge et al., 2017) from the sea ice system to the underlying water. Particularly the biogeochemical signals in the WML can still be observed in the next summer (Damm et al.,

2015), since downward mixing is reduced by a strong halocline (Rudels et al., 1996). Some of the DMSP observed in 25–100 m might thus be sourced from the previous sea ice freeze up.

As in Region 1, we find significantly higher DMSP concentrations beneath 2-year sea-ice, this time accompanied by higher chlorophyll *a* concentrations (**Figure 5**). Under one-year as well as multi-year ice DMSP concentrations were lower and not significantly different from each other. Source regions were not clearly separated between the 2 years and different ice types. However, like in Region 1, the water under sea ice formed in the coastal Siberian polynyas mostly contained higher DMSP and chlorophyll *a* concentrations, compared to water under sea ice formed in the other source regions. Differences in nutrient availability might also contribute to the differences in DMSP concentrations (**Supplementary Figure 2**).

DMS Budget Controlled by Secondary Processes

Similar to Region 1, the amount of DMSP in Region 2 is tightly coupled to phytoplankton biomass indicated by the strong correlation between DMSP and chlorophyll *a* (r = 0.79, **Figure 4**). On the contrary, DMS is neither correlated to chlorophyll *a* nor DMSP (**Figure 4**). Furthermore, DMS was over-proportionally lower in Region 2 when comparing to DMSP and chlorophyll *a*. In the upper 25 m, chlorophyll *a* and DMSP were about 25% of the amount in Region 1, while this ratio was only 2% for DMS. Thus, either DMS is not produced in the first place, or DMS is removed faster or more complete than in Region 1.

Abiotic removal by photo-oxidation and sea-air efflux was supposedly low due to the high sea ice cover and in a similar magnitude than in Region 1. Microbial consumption of DMS, however, might be more complete than in Region 1, since 90% of the DMS concentrations in Region 2 were lower than the saturation concentration of 18 nM DMS determined in the Labrador Sea (Wolfe et al., 1999). This might have allowed DMS consumption to match DMS production, resulting in overall low DMS concentrations.

Second, the production of DMS via DMSP lysis might be reduced. Considering a similar sulfur demand for the bacterial communities in Region 1 and Region 2 and the lower DMSP concentrations in Region 2, a higher fraction of the DMSP would be demethylated to assimilate the sulfur. This would result in a lower fraction of DMSP being cleaved to DMS. Pinhassi et al. (2005) found higher contribution of DMSP sulfur to bacterial sulfur demand under oligotrophic conditions than under phytoplankton senescence in microcosm experiments with water from the Gulf of Mexico. The authors conclude that nutrient limitation leads to a limitation in S-containing organic molecules in dissolved organic matter, which could serve as alternate sulfur source to the bacteria besides DMSP. This might also apply to Region 2 where nitrate limitation leads to low phytoplankton biomass. In the same experiment, Pinhassi et al. (2005) identify DMSP as an important carbon source to the microbial community. Damm et al. (2010) found evidence that in nitrate limited waters of the central Arctic and when phosphate is available, bacteria use DMSP as carbon-source via the demethylation pathway and produce methane as side product. The same process might have lead to the low DMS concentrations in Region 2 in our study.

Concluding, in Region 2, phytoplankton production is low and DMSP and DMS production is decoupled. We hypothesize that DMS concentrations are mainly controlled by secondary processes like bacterial DMS production or consumption.

Region 3

Influence by PW and Intense Sea Ice – Ocean Interaction

Like in Region 2, the upper 100 m of the water column in Region 3 are strongly influenced by sea ice melting and freezing processes. However, Region 3 is mainly influenced by Pacific water. Since Pacific water has a lower salinity than Atlantic water (Jones et al., 1998) all water layers are less saline than in Region 2. In addition, the higher phosphate concentrations and low nitrate concentrations typical for Pacific Water (Jones et al., 1998), lead to a strong deviation from the Redfield ratio toward excess phosphate. At 0–25 m nitrate was fully depleted, resulting in very low concentrations of phytoplankton biomass indicated by low chlorophyll *a* concentrations (**Figure 2**).

In contrast, the underlying water still contained nitrate at similar concentrations than the other two regions and chlorophyll *a* peaked between 25 and 50 m in Region 3 (**Supplementary Figure 1B**). This deep chlorophyll *a* maximum could be caused by phytoplankton growth at the shallowest depth where nitrate becomes available with sufficient light to support primary production (Carmack et al., 2004). This is typically observed in very oligotrophic regions where nutrient depletion near the surface inhibits phytoplankton growth in the well illuminated surface layer (Takahashi and Hori, 1984; Agustí and Duarte, 1999) and also on the arctic shelves when the spring bloom exhausted the nutrients in the surface layer (e.g., Carmack et al., 2004; Martin et al., 2010). Since algal cells contain a higher chlorophyll *a* content to balance the low light levels available for photosynthesis (Beardall and Morris, 1976), the actual phytoplankton concentration is supposedly very low at this depth. In contrast to chlorophyll *a*, depth profiles of DMSP, showed two peaks of similar concentration, one near the surface and one at 50 m suggesting multiple sources for this compound (**Figure 2** and **Supplementary Figure 1B**).

Low DMS Concentrations Controlled by Low Phytoplankton and Secondary Processes

Surprisingly, in Region 3 a strong positive correlation between DMSP and chlorophyll *a* is observed only below 25 m water depth (r = 0.84, **Figure 4**), pointing toward phytoplankton as major control on DMSP concentration in these deep water layers. Coinciding with the WML depth at 44 ± 3 m (**Supplementary Figure 1B**), the deep chlorophyll as well as DMSP maxima could be affected by brine rejection during sea-ice freeze-up in previous winter. Above 25 m, DMSP and chlorophyll *a* are not correlated and other factors than phytoplankton abundance must control DMSP concentration. For example, bacteria could

constitute a DMSP-fraction unrelated to chlorophyll *a*, as marine bacteria were found to take up and accumulate DMSP intracellularly before metabolizing it (Kiene et al., 2000), and being capable of producing DMSP (Curson et al., 2017). Further, zooplankton and fecal pellets can contain DMSP (Kwint et al., 1996; Tang et al., 1999) adding to this chlorophyll *a*-unrelated DMSP-pool.

While the chlorophyll *a*-unrelated DMSP-pool might also be present in the other two regions, it is masked by the higher signal of phytoplankton derived DMSP. The low nanomolar DMSP concentrations in Region 3 are similar to concentrations previously reported under Arctic sea ice if there was no phytoplankton bloom present (Simó, 2001; Galindo et al., 2014). They are likely to be a result of a quick turnover of dissolved DMSP by the microbial community (Kiene et al., 2000). The very low DMS concentrations and DMS/DMSP ratios in Region 3 could either be the result of a high DMS turnover or of a dominance of the demethylation pathway over the lysis pathway in bacterial DMSP metabolism.

As a result DMSP as precursor for the climate cooling gas DMS seems to be low in this strongly oligotrophic Pacific influenced waters of the central Arctic. Secondary processes seem to mainly control DMS concentrations in Region 3. Additionally, and contrary to Region 1 and 2, in the surface layer (<25 m) DMSP appears to be controlled by other factors than phytoplankton biomass.

CONCLUSION AND OUTLOOK

Our study shows strong heterogeneity of DMS and DMSP concentrations in ice covered surface waters between different regions of the central Arctic. These differences are driven by physical as well as biological drivers, i.e., variations in water mass composition, sea ice cover, phytoplankton abundance and bacterial processes. High DMS and DMSP concentrations are found in the less ice-influenced region in the western Eurasian Basin (Region 1) where Atlantic water inflow provides nutrients for phytoplankton growth and light penetrates through the thinner or broken sea ice cover. In contrast, little DMS and DMSP are found in the eastern Eurasian Basin (Region 2) and the region influenced by Pacific waters (Region 3). Here sea ice strongly influences the underlying water causing oligotrophic conditions, which probably lead to different microbial cycling of DMSP and DMS, resulting in a 10- and 25-fold reduced DMS concentration per amount of chlorophyll *a* and DMSP, respectively (**Figure 6** and **Supplementary Table 4**).

These regional patterns of DMS are likely to change with future changes in the ocean-ice system in the Arctic due to climate warming, particularly in the Eurasian Arctic. Here, "Atlantification," is a term used to summarize the increased importance of surface Atlantic inflow further eastward into the Eurasian Basin (Polyakov et al., 2017). It reflects the increased depth of winter mixing leading to upward mixing of the warmer and nutrient rich deeper waters coupled with loss of sea ice. Decreases in sea ice extent and duration, as well as changing properties of the sea ice cover, like higher dynamics, i.e., opening of leads are currently observed, and predicted to become more pronounced in the future (Stroeve and Notz, 2015; Comiso et al., 2017; Kwok, 2018). Further intensified melt in the marginal ice zone interrupts the transarctic conveyer belt and reduces long-ranged transport of sea ice (Krumpen et al., 2019). Extension of these conditions, i.e., less sea ice especially from the shelves, more nutrients, and warmer water could change the distinct conditions for the western and eastern part of the Eurasian basin, to more homogeneous conditions. This might enhance biological production with the potential of increased DMSP and DMS production in these ice-covered waters. A thinner and more dynamic ice cover with frequent opening of leads might allow for enhanced exchange of gasses, e.g., DMS release from the seawater to the atmosphere. On the other hand predicted stronger stratification due to higher freshwater input, e.g., by ice melt, might lead to increased oligotrophic conditions in the surface, limiting primary production (Slagstad et al., 2015). This could result in a shift of the system observed in the eastern Eurasian basin toward low DMSP and DMS production in the surface as observed in the region influenced by Pacific waters.

In light of the ongoing changes in the Arctic, our observations provide a status quo for projections of the DMS concentration and can be used in modeling approaches to access its contribution to aerosol production in the Arctic. Our study suggests that in the central Arctic macronutrient concentrations in the euphotic zone, controlled by water mass and sea ice influenced stratification, regulate not only the abundance of DMSP producing phytoplankton but also the heterotrophic cycling of DMSP to DMS and recycling of DMS itself. While our study lacks rate measurements of the suggested processes, those will be essential to confirm the autotrophic and heterotrophic processes in DMSP and DMS cycling suggested in this study and should be included in future studies. Improving the understanding of the regulation of heterotrophic processes, such as DMSP and DMS cycling, will help to build appropriate parametrizations for model studies. Already the currently available seasonally limited studies in the central Arctic, which were all performed in summer to autumn (July to October), show seasonality in DMS concentration and suggest that sea-ice melt and freeze processes are important for DMS concentrations in the upper water column. In future studies observations should be extended to a full year, ideally analyzing the same water mass to capture possible exchange of these compounds between the upper water column and sea ice particularly during freezing and melting.

DATA AVAILABILITY

Data on sulfur compounds and HPLC pigments are available in the database of the Data Publisher for Earth and Environmental Science, PANGAEA (https://www.pangaea.de/; doi: 10.1594/PANGAEA.901742). Further, physical oceanography data by Schauer et al. (2012; doi: 10.1594/PANGAEA.774181), and Rabe et al. (2016; doi: 10.1594/PANGAEA.859558) can be accessed in

PANGEA. The datasets generated for this study are available on request to the corresponding author.

AUTHOR CONTRIBUTIONS

ED and CU designed the study, and collected and analyzed the DMS and DMSP data. IP processed and analyzed the HPLC data. TK analyzed the sea ice trajectories. BR and MK collected and analyzed the physical oceanography data. K-UL collected the inorganic nutrient data in 2011. CU wrote the manuscript with contributions from all authors.

FUNDING

This study was funded by the PACES (Polar Regions and Coasts in the Changing Earth System) Program of the Helmholtz Association. Backtracking of sea ice was carried out as part of the Russian–German cooperation QUARCCS funded by the BMBF under the grant 03F0777A. This study used samples and data provided by the Alfred-Wegener-Institut Helmholtz-Zentrum für Polar- und Meeresforschung in Bremerhaven (Grant Nos. ARK-XXVI/3 and AWI-PS94_00).

ACKNOWLEDGMENTS

We would like to acknowledge the support of the captain and crew of the R/V Polarstern cruises ARK-XXVI/3 (Transark I) and PS94 (Transark II) as well as the chief scientist Ursula Schauer for facilitating the presented measurements. We are grateful to Laura Wischnewski and Elena Vinogradova for supporting sampling during ARK-XXVI/3 and PS94, respectively. Further, we would like to thank Jan van Ooijen for measurements of inorganic nutrients during PS94.

SUPPLEMENTARY MATERIAL

The Supplementary Material for this article can be found online at: https://www.frontiersin.org/articles/10.3389/feart.2019.00179/full#supplementary-material

REFERENCES

Agustí, S., and Duarte, C. M. (1999). Phytoplankton chlorophyll a distribution and water column stability in the central Atlantic Ocean. *Oceanol. Acta* 22, 193–203. doi: 10.1016/S0399-1784(99)80045-0

Andrade, J. M., and Estévez-Pérez, M. G. (2014). Statistical comparison of the slopes of two regression lines: a tutorial. *Anal. Chim. Acta* 838, 1–12. doi: 10.1016/j.aca.2014.04.057

Andreae, M. O. (1990). Ocean-atmosphere interactions in the global biogeochemical sulfur cycle. *Mar. Chem.* 30, 1–29. doi: 10.1016/0304-4203(90)90059-L

Arrigo, K. R., Perovich, D. K., Pickart, R. S., Brown, Z. W., van Dijken, G. L., Lowry, K. E., et al. (2012). Massive phytoplankton blooms under Arctic Sea Ice. *Science* 336, 1408–1408. doi: 10.1126/science.1215065

Assmy, P., Fernández-Méndez, M., Duarte, P., Meyer, A., Randelhoff, A., Mundy, C. J., et al. (2017). Leads in Arctic pack ice enable early phytoplankton blooms below snow-covered sea ice. *Sci. Rep.* 7:40850. doi: 10.1038/srep40850

Beardall, J., and Morris, I. (1976). The concept of light intensity adaptation in marine phytoplankton: some experiments with *Phaeodactylum tricornutum*. *Mar. Biol.* 37, 377–387. doi: 10.1007/BF00387494

Carmack, E., Macdonald, R., and Jasper, S. (2004). Phytoplankton productivity on the Canadian Shelf of the Beaufort Sea. *Mar. Ecol. Prog. Ser.* 277, 37–50. doi: 10.3354/meps277037

Chang, R. Y.-W., Sjostedt, S. J., Pierce, J. R., Papakyriakou, T. N., Scarratt, M. G., Michaud, S., et al. (2011). Relating atmospheric and oceanic DMS levels to particle nucleation events in the Canadian Arctic. *J. Geophys. Res.* 116:D17. doi: 10.1029/2011JD015926

Charlson, R. J., Lovelock, J. E., Andreae, M. O., and Warren, S. G. (1987). Oceanic phytoplankton, atmospheric sulphur, cloud albedo and climate. *Nature* 326, 655–661. doi: 10.1038/326655a0

Comiso, J. C., Meier, W. N., and Gersten, R. (2017). Variability and trends in the Arctic Sea ice cover: results from different techniques: trends in the Arctic Sea Ice Cover. *J. Geophys. Res. Oceans* 122, 6883–6900. doi: 10.1002/2017JC012768

Curson, A. R. J., Liu, J., Bermejo Martínez, A., Green, R. T., Chan, Y., Carrión, O., et al. (2017). Dimethylsulfoniopropionate biosynthesis in marine bacteria and identification of the key gene in this process. *Nat. Microbiol.* 2:17009. doi: 10.1038/nmicrobiol.2017.9

Dacey, J. W. H., and Blough, N. V. (1987). Hydroxide decomposition of dimethylsulfoniopropionate to form dimethylsulfide. *Geophys. Res. Lett.* 14, 1246–1249. doi: 10.1029/gl014i012p01246

Damm, E., Bauch, D., Krumpen, T., Rabe, B., Korhonen, M., Vinogradova, E., et al. (2018). the transpolar drift conveys methane from the Siberian Shelf to the central Arctic Ocean. *Sci. Rep.* 8:4515. doi: 10.1038/s41598-018-22801-z

Damm, E., Helmke, E., Thoms, S., Schauer, U., Nöthig, E., Bakker, K., et al. (2010). Methane production in aerobic oligotrophic surface water in the central Arctic Ocean. *Biogeosciences* 7, 1099–1108. doi: 10.5194/bg-7-1099-2010

Damm, E., Rudels, B., Schauer, U., Mau, S., and Dieckmann, G. (2015). Methane excess in Arctic surface water- triggered by sea ice formation and melting. *Sci. Rep.* 5:16179. doi: 10.1038/srep16179

del Valle, D. A., Kieber, D. J., Toole, D. A., Bisgrove, J., and Kiene, R. P. (2009). Dissolved DMSO production via biological and photochemical oxidation of dissolved DMS in the Ross Sea. *Antarct. Deep Sea Res. Part Oceanogr. Res. Pap.* 56, 166–177. doi: 10.1016/j.dsr.2008.09.005

Fernández-Méndez, M., Katlein, C., Rabe, B., Nicolaus, M., Peeken, I., Bakker, K., et al. (2015). Photosynthetic production in the central Arctic Ocean during the record sea-ice minimum in 2012. *Biogeosciences* 12, 3525–3549. doi: 10.5194/bg-12-3525-2015

Galí, M., and Simó, R. (2010). Occurrence and cycling of dimethylated sulfur compounds in the Arctic during summer receding of the ice edge. *Mar. Chem.* 122, 105–117. doi: 10.1016/j.marchem.2010.07.003

Galindo, V., Levasseur, M., Mundy, C. J., Gosselin, M., Tremblay, J. -É, Scarratt, M., et al. (2014). Biological and physical processes influencing sea ice, under-ice algae, and dimethylsulfoniopropionate during spring in the Canadian Arctic Archipelago. *J. Geophys. Res. Oceans* 119, 3746–3766. doi: 10.1002/2013JC009497

Ghahremaninezhad, R., Norman, A.-L., Abbatt, J. P. D., Levasseur, M., and Thomas, J. L. (2016). Biogenic, anthropogenic and sea salt sulfate size-segregated aerosols in the Arctic summer. *Atmos. Chem. Phys.* 16, 5191–5202. doi: 10.5194/acp-16-5191-2016

Gosselin, M., Levasseur, M., Simard, N., Michaud, S., Sharma, S., Brickell, P., et al. (1996). in *The 1994 Arctic Ocean Section: The First Major Scientific Crossing of the Arctic Ocean*, eds T. Tucker and D. Cate (Hanover, NH: US Army Cold Regions Research and Engineering Laboratory). doi: 10.5194/acp-16-5191-2016

Grasshoff, K., Kremling, K., and Ehrhardt, M. (eds) (1998). *Methods of Seawater Analysis, Third, Completely Revised and Extended Edition*. Weinheim: Wiley-VCH Verlag GmbH.

Gruber, N., and Sarmiento, J. L. (1997). Global patterns of marine nitrogen fixation and denitrification. *Glob. Biogeochem. Cycles* 11, 235–266. doi: 10.1029/97GB00077

Hardge, K., Peeken, I., Neuhaus, S., Lange, B. A., Stock, A., Stoeck, T., et al. (2017). The importance of sea ice for exchange of habitat-specific protist communities in the Central Arctic Ocean. *J. Mar. Syst.* 165, 124–138. doi: 10.1016/j.jmarsys.2016.10.004

Hollander, M., Wolfe, D. A., and Chicken, E. (2015). *Nonparametric Statistical Methods*, 1st Edn. Hoboken, NJ: Wiley.

Ishida, Y. (1968). *Physiological Studies on the Evolution of Dimethyl- Sulfide*. Kyoto: Mem Coll Agric Kyoto Univ., 47–82.

Jones, E. P., Anderson, L. G., Jutterström, S., Mintrop, L., and Swift, J. H. (2008). Pacific freshwater, river water and sea ice meltwater across Arctic Ocean basins: results from the 2005 Beringia expedition. *J. Geophys. Res.* 113:C08012. doi: 10.1029/2007JC004124

Jones, E. P., Anderson, L. G., and Swift, J. H. (1998). Distribution of Atlantic and Pacific waters in the upper Arctic Ocean: implications for circulation. *Geophys. Res. Lett.* 25, 765–768. doi: 10.1029/98GL00464

Kasamatsu, N., Kawaguchi, S., Watanabe, S., Odate, T., and Fukuchi, M. (2004). Possible impacts of zooplankton grazing on dimethylsulfide production in the Antarctic Ocean. *Can. J. Fish. Aquat. Sci.* 61, 736–743. doi: 10.1139/f04-072

Kattner, G., and Ludwichowski, K.-U. (2014). *Inorganic Nutrients Measured on Water Bottle Samples During POLARSTERN Cruise ARK-XXVI/3 (TransArc)*. Bremerhaven: Alfred Wegener Institute, Helmholtz Centre for Polar and Marine Research.

Keller, M., Bellows, W., and Guillard, R. (1989). "Dimethyl Sulfide Production in Marine Phytoplankton," in *Biogenic Sulfur in the Environment ACS Symposium Series*, eds E. S. Saltzman and W. J. Cooper (Washington, DC: American Chemical Society), 167–182. doi: 10.1021/bk-1989-0393.ch011

Kettle, A. J., and Andreae, M. O. (2000). Flux of dimethylsulfide from the oceans: a comparison of updated data sets and flux models. *J. Geophys. Res. Atmos.* 105, 26793–26808. doi: 10.1029/2000JD900252

Kiene, R. P. (1990). Dimethyl sulfide production from dimethylsulfoniopropionate in coastal seawater samples and bacterial cultures. *Appl. Environ. Microbiol.* 56, 3292–3297.

Kiene, R. P. (1992). Dynamics of dimethyl sulfide and dimethylsulfoniopropionate in oceanic water samples. *Mar. Chem.* 37, 29–52. doi: 10.1016/0304-4203(92)90055-F

Kiene, R. P., and Bates, T. S. (1990). Biological removal of dimethyl sulphide from sea water. *Nature* 345, 702–705. doi: 10.1038/345702a0

Kiene, R. P., Linn, L. J., and Bruton, J. A. (2000). New and important roles for DMSP in marine microbial communities. *J. Sea Res.* 43, 209–224. doi: 10.1016/S1385-1101(00)00023-X

Kiene, R. P., and Slezak, D. (2006). Low dissolved DMSP concentrations in seawater revealed by small volume gravity filtration and dialysis sampling. *Limnol. Oceanogr. Methods* 4, 80–95. doi: 10.4319/lom.2006.4.80:

Kikuchi, T. (2004). Distribution of convective Lower Halocline Water in the eastern Arctic Ocean. *J. Geophys. Res.* 109:C12030. doi: 10.1029/2003JC002223

Kirst, G. O., Thiel, C., Wolff, H., Nothnagel, J., Wanzek, M., and Ulmke, R. (1991). Dimethylsulfoniopropionate (DMSP) in ice-algae and its possible biological role. *Mar. Chem.* 35, 381–388. doi: 10.1016/S0304-4203(09)90030-5

Korhonen, M., Rudels, B., Marnela, M., Wisotzki, A., and Zhao, J. (2013). Time and space variability of freshwater content, heat content and seasonal ice melt in the Arctic Ocean from 1991 to 2011. *Ocean Sci.* 9, 1015–1055. doi: 10.5194/os-9-1015-2013

Krumpen, T., Belter, H. J., Boetius, A., Damm, E., Haas, C., Hendricks, S., et al. (2019). Arctic warming interrupts the Transpolar Drift and affects long-range transport of sea ice and ice-rafted matter. *Sci. Rep.* 9:5459. doi: 10.1038/s41598-019-41456-y

Krumpen, T., Gerdes, R., Haas, C., Hendricks, S., Herber, A., Selyuzhenok, V., et al. (2016). Recent summer sea ice thickness surveys in Fram Strait and associated ice volume fluxes. *Cryosphere* 10, 523–534. doi: 10.5194/tc-10-523-2016

Kwint, R., Irigoien, X., and Kramer, K. (1996). "Copepods and DMSP," in *Biological and Environmental Chemistry of DMSP and Related Sulfonium Compounds*, eds R. P. Kiene, P. T. Visscher, M. D. Keller, and G. O. Kirst (New York, NY: Plenum Press), 239–252. doi: 10.1007/978-1-4613-0377-0_21

Kwok, R. (2018). Arctic sea ice thickness, volume, and multiyear ice coverage: losses and coupled variability (1958–2018). *Environ. Res. Lett.* 13:105005. doi: 10.1088/1748-9326/aae3ec

Kwok, R., Spreen, G., and Pang, S. (2013). Arctic sea ice circulation and drift speed: decadal trends and ocean currents: ARCTIC SEA ICE MOTION. *J. Geophys. Res. Oceans* 118, 2408–2425. doi: 10.1002/jgrc.20191

Laney, S. R., Krishfield, R. A., and Toole, J. M. (2017). The euphotic zone under Arctic Ocean sea ice: vertical extents and seasonal trends: the euphotic zone under Arctic sea ice. *Limnol. Oceanogr.* 62, 1910–1934. doi: 10.1002/lno.10543

Leaitch, W. R., Sharma, S., Huang, L., Toom-Sauntry, D., Chivulescu, A., Macdonald, A. M., et al. (2013). Dimethyl sulfide control of the clean summertime Arctic aerosol and cloud. *Elem. Sci. Anthr.* 1:000017. doi: 10.12952/journal.elementa.000017

Leck, C., and Persson, C. (1996). The central Arctic Ocean as a source of dimethyl sulfide Seasonal variability in relation to biological activity. *Tellus B* 48, 156–177. doi: 10.3402/tellusb.v48i2.15834

Ledyard, K. M., and Dacey, J. W. H. (1994). Dimethylsulfide production from dimethyl-sulfoniopropionate by a marine bacterium. *Mar. Ecol. Prog. Ser.* 100, 95–103. doi: 10.3354/meps110095

Levasseur, M. (2013). Impact of Arctic meltdown on the microbial cycling of sulphur. *Nat. Geosci.* 6, 691–700. doi: 10.1038/ngeo1910

Liss, P. S., Hatton, A. D., Malin, G., Nightingale, P. D., Turner, S. M., and Liss, P. S. (1997). Marine sulphur emissions. *Philos. Trans. Biol. Sci.* 352, 159–169.

Loose, B., Schlosser, P., Perovich, D., Ringelberg, D., Ho, D. T., Takahashi, T., et al. (2011). Gas diffusion through columnar laboratory sea ice: implications for mixed-layer ventilation of CO2 in the seasonal ice zone. *Tellus B* 63, 23–39. doi: 10.1111/j.1600-0889.2010.00506.x

Malin, G., Wilson, W. H., Bratbak, G., Liss, P. S., and Mann, N. H. (1998). Elevated production of dimethylsulfide resulting from viral infection of cultures of *Phaeocystis pouchetii*. *Limnol. Oceanogr.* 43, 1389–1393. doi: 10.4319/lo.1998.43.6.1389

Martin, J., Tremblay, J., Gagnon, J., Tremblay, G., Lapoussière, A., Jose, C., et al. (2010). Prevalence, structure and properties of subsurface chlorophyll maxima in Canadian Arctic waters. *Mar. Ecol. Prog. Ser.* 412, 69–84. doi: 10.3354/meps08666

Martin, J., Tremblay, J. É, and Price, N. M. (2012). Nutritive and photosynthetic ecology of subsurface chlorophyll maxima in Canadian Arctic waters. *Biogeosciences* 9, 5353–5371. doi: 10.5194/bg-9-5353-2012

Matrai, P. A., Tranvik, L., Leck, C., and Knulst, J. C. (2008). Are high Arctic surface microlayers a potential source of aerosol organic precursors? *Mar. Chem.* 108, 109–122. doi: 10.1016/j.marchem.2007.11.001

Motard-Côté, J., Levasseur, M., Scarratt, M. G., Michaud, S., Gratton, Y., Rivkin, R. B., et al. (2012). Distribution and metabolism of dimethylsulfoniopropionate (DMSP) and phylogenetic affiliation of DMSP-assimilating bacteria in northern Baffin Bay/Lancaster Sound. *J. Geophys. Res. Oceans* 117:C00G11. doi: 10.1029/2011JC007330

Nicolaus, M., Katlein, C., Maslanik, J., and Hendricks, S. (2012). Changes in Arctic sea ice result in increasing light transmittance and absorption: light in A changing Arctic Ocean. *Geophys. Res. Lett.* 39:L24501. doi: 10.1029/2012GL053738

Park, K.-T., Jang, S., Lee, K., Yoon, Y. J., Kim, M.-S., Park, K., et al. (2017). Observational evidence for the formation of DMS-derived aerosols during Arctic phytoplankton blooms. *Atmos. Chem. Phys.* 17, 9665–9675. doi: 10.5194/acp-17-9665-2017

Park, K.-T., Lee, K., Yoon, Y.-J., Lee, H.-W., Kim, H.-C., Lee, B.-Y., et al. (2013). Linking atmospheric dimethyl sulfide and the Arctic Ocean spring bloom: atmospheric dms in the arctic spring bloom. *Geophys. Res. Lett.* 40, 155–160. doi: 10.1029/2012GL054560

Pearson, K. (1895). Note on regression and inheritance in the case of two parents. *Proc. R. Soc. Lond.* 58, 240–242. doi: 10.1098/rspl.1895.0041

Peeken, I., Primpke, S., Beyer, B., Gütermann, J., Katlein, C., Krumpen, T., et al. (2018). Arctic sea ice is an important temporal sink and means of transport for microplastic. *Nat. Commun.* 9:1505. doi: 10.1038/s41467-018-03825-5

Pinhassi, J., Simo, R., Gonzalez, J. M., Vila, M., Alonso-Saez, L., Kiene, R. P., et al. (2005). Dimethylsulfoniopropionate turnover is linked to the composition and dynamics of the bacterioplankton assemblage during a microcosm phytoplankton bloom. *Appl. Environ. Microbiol.* 71, 7650–7660. doi: 10.1128/AEM.71.12.7650-7660.2005

Polyakov, I. V., Pnyushkov, A. V., Alkire, M. B., Ashik, I. M., Baumann, T. M., Carmack, E. C., et al. (2017). Greater role for Atlantic inflows on sea-ice loss in the Eurasian Basin of the Arctic Ocean. *Science* 356, 285–291. doi: 10.1126/science.aai8204

R Core Team (2015). *R: A Language and Environment for Statistical Computing*. Vienna: R Foundation for Statistical Computing.

Rabe, B., Schauer, U., Ober, S., Horn, M., Hoppmann, M., Korhonen, M., et al. (2016). *Physical Oceanography During POLARSTERN Cruise PS94 (ARK-XXIX/3)*. Bremerhaven: Alfred Wegener Institute, Helmholtz Centre for Polar and Marine Research. doi: 10.1594/PANGAEA.859558

Rapp, J. Z., Fernández-Méndez, M., Bienhold, C., and Boetius, A. (2018). Effects of ice-algal aggregate export on the connectivity of bacterial communities in the central Arctic Ocean. *Front. Microbiol.* 9:1035. doi: 10.3389/fmicb.2018.01035

Reisch, C. R., Moran, M. A., and Whitman, W. B. (2008). Dimethylsulfoniopropionate-dependent demethylase (DmdA) from ıtPelagibacter ubique and ıtSilicibacter pomeroyi. *J. Bacteriol.* 190, 8018–8024. doi: 10.1128/JB.00770-08

Rudels, B., Anderson, L. G., and Jones, E. P. (1996). Formation and evolution of the surface mixed layer and halocline of the Arctic Ocean. *J. Geophys. Res. Oceans* 101, 8807–8821. doi: 10.1029/96JC00143

Rudels, B., Larsson, A.-M., and Sehlstedt, P.-I. (1991). Stratification and water mass formation in the Arctic Ocean: some implications for the nutrient distribution. *Polar Res.* 10, 19–32. doi: 10.1111/j.1751-8369.1991.tb00631.x

Schauer, U. (2012). *The Expedition of the Research Vessel Polarstern to the Arctic in 2011 (ARK-XXVI/3 - TransArc)*. Bremerhaven: Alfred Wegener Institute, Helmholtz Centre for Polar and Marine Research. doi: 10.2312/BzPM_0649_2012

Schauer, U. (2016). *The Expedition PS94 of the Research Vessel POLARSTERN to the Central Arctic Ocean in 2015*. Bremerhaven: Alfred Wegener Institute, Helmholtz Centre for Polar and Marine Research. doi: 10.2312/BzPM_0703_2016

Schauer, U., Rabe, B., and Wisotzki, A. (2012). *Physical Oceanography During POLARSTERN Cruise ARK-XXVI/3 (TransArc)*. Bremerhaven: Alfred Wegener Institute, Helmholtz Centre for Polar and Marine Research. doi: 10.1594/PANGAEA.774181

Schlitzer, R. (2018). *Ocean Data View*. Available at: https://odv.awi.de (accessed March 18, 2019).

Simó, R. (2001). Production of atmospheric sulfur by oceanic plankton: biogeochemical, ecological and evolutionary links. *Trends Ecol. Evol.* 16, 287–294. doi: 10.1016/S0169-5347(01)02152-8 doi: 10.1016/s0169-5347(01)02152-8

Simó, R. (2004). From cells to globe: approaching the dynamics of DMS(P) in the ocean at multiple scales. *Can. J. Fish. Aquat. Sci.* 61, 673–684. doi: 10.1139/f04-030

Slagstad, D., Wassmann, P. F. J., and Ellingsen, I. (2015). Physical constrains and productivity in the future Arctic Ocean. *Front. Mar. Sci.* 2:85. doi: 10.3389/fmars.2015.00085

Stefels, J., Steinke, M., Turner, S., Malin, G., and Belviso, S. (2007). Environmental constraints on the production and removal of the climatically active gas dimethylsulphide (DMS) and implications for ecosystem modelling. *Biogeochemistry* 83, 245–275. doi: 10.1007/s10533-007-9091-5

Stefels, J., and Van Boekel, W. H. M. (1993). Production of DMS from dissolved DMSP in axenic cultures of the marine phytoplankton species Phaeocystis sp. *Mar. Ecol. Prog. Ser.* 97, 11–18. doi: 10.3354/meps097011

Stroeve, J., and Notz, D. (2015). Insights on past and future sea-ice evolution from combining observations and models. *Glob. Planet. Change* 135, 119–132. doi: 10.1016/j.gloplacha.2015.10.011

Takahashi, M., and Hori, T. (1984). Abundance of picophytoplankton in the subsurface chlorophyll maximum layer in subtropical and tropical waters. *Mar. Biol.* 79, 177–186. doi: 10.1007/BF00951826

Tang, K., Dam, H., Visscher, P., and Fenn, T. (1999). Dimethylsulfoniopropionate (DMSP) in marine copepods and its relation with diets and salinity. *Mar. Ecol. Prog. Ser.* 179, 71–79. doi: 10.3354/meps179071

Tran, S., Bonsang, B., Gros, V., Peeken, I., Sarda-Esteve, R., Bernhardt, A., et al. (2013). A survey of carbon monoxide and non-methane hydrocarbons in the Arctic Ocean during summer 2010. *Biogeosciences* 10, 1909–1935. doi: 10.5194/bg-10-1909-2013

Ulfsbo, A., Cassar, N., Korhonen, M., van Heuven, S., Hoppema, M., Kattner, G., et al. (2014). Late summer net community production in the central Arctic Ocean using multiple approaches: NCP in the central Arctic Ocean. *Glob. Biogeochem. Cycles* 28, 1129–1148. doi: 10.1002/2014GB004833

Vallina, S. M., Simó, R., Gassó, S., de Boyer-Montégut, C., del Río, E., Jurado, E., et al. (2007). Analysis of a potential "solar radiation dose-dimethylsulfide-cloud condensation nuclei" link from globally mapped seasonal correlations: global "solar radiation dose-DMS-CCN" link. *Glob. Biogeochem. Cycles* 21:GB2004. doi: 10.1029/2006GB002787

Van Ooijen, J. C., Rijkenberg, M. J. A., Gerringa, L. J. A., Rabe, B., and Rutgers Van Der Loeff, M. M. (2016). *Inorganic Nutrients Measured on Water Bottle Samples During POLARSTERN Cruise PS94 (ARK-XXIX/3)*. Texel: Royal Netherlands Institute for Sea Research. doi: 10.1594/PANGAEA.868396

Welch, B. L. (1938). The significance of the difference between two means when the population variances are unequal. *Biometrika* 29, 350–362. doi: 10.1093/biomet/29.3-4.350

Wolfe, G., and Kiene, R. (1993). Radioisotope and chemical inhibitor measurements of dimethyl sulfide consumption rates and kinetics in estuarine waters. *Mar. Ecol. Prog. Ser.* 99, 261–269. doi: 10.3354/meps099261

Wolfe, G., Levasseur, M., Cantin, G., and Michaud, S. (1999). Microbial consumption and production of dimethyl sulfide (DMS) in the Labrador Sea. *Aquat. Microb. Ecol.* 18, 197–205. doi: 10.3354/ame018197

Wollenburg, J. E., Katlein, C., Nehrke, G., Nöthig, E.-M., Matthiessen, J., Wolf-Gladrow, D. A., et al. (2018). Ballasting by cryogenic gypsum enhances carbon export in a Phaeocystis under-ice bloom. *Sci. Rep.* 8:7703. doi: 10.1038/s41598-018-26016-0

Conflict of Interest Statement: The authors declare that the research was conducted in the absence of any commercial or financial relationships that could be construed as a potential conflict of interest.

frontiers in Earth Science

ORIGINAL RESEARCH
published: 25 February 2019
doi: 10.3389/feart.2019.00021

Melt Procedure Affects the Photosynthetic Response of Sea Ice Algae

Karley Campbell[1], C. J. Mundy[2], Andrew R. Juhl[3], Laura A. Dalman[2], Christine Michel[2,4], Ryan J. Galley[2], Brent E. Else[5], Nicolas X. Geilfus[2] and Søren Rysgaard[2,6,7]*

[1] Bristol Glaciology Centre, University of Bristol, Bristol, United Kingdom, [2] Centre for Earth Observation Science, University of Manitoba, Winnipeg, MB, Canada, [3] Lamont-Doherty Earth Observatory, Columbia University, Palisades, NY, United States, [4] Fisheries and Oceans Canada, University Crescent, Winnipeg, MB, Canada, [5] Department of Geography, University of Calgary, Calgary, AB, Canada, [6] Arctic Research Centre, Department of Bioscience, University of Aarhus, Aarhus, Denmark, [7] Greenland Institute of Natural Resources, Nuuk, Greenland

The accuracy of sea ice algal production estimates is influenced by the range of melting procedures used in studies to obtain a liquid sample for incubation, particularly in relation to the duration of melt and the approach to buffering for osmotic shock. In this research, ice algal photophysiology from ^{14}C incubations was compared in field samples prepared by three melt procedures: (i) a rapid $\leq$ 4 h melt of the bottommost ($<$ 1 cm) ice algal layer scraped into a large volume of filtered seawater (salinity 27–30), (ii) melt of a bottom 5 cm section diluted into a moderate volume of filtered seawater over 24 h (salinity 20–24), and (iii) melt of a bottom 5 cm section without any filtered seawater dilution over about 48 h (salinity 10–12). Maximum photosynthetic rate, photosynthetic efficiency and production at zero irradiance were significantly affected by the melt treatment employed in experiments. All variables were greatest in the highly diluted scrape sample and lowest in the bulk-ice samples melted in the absence of filtered seawater. Laboratory experiments exposing cultures of the common sea ice diatom *Nitzschia frigida* to different salinities and light conditions suggested that the field-based responses can be attributed to the rapid ($<$ 4 h) adverse effects of exposing cells to low salinities during melt without dilution. The observed differences in primary production between melt treatments were estimated to account for over 60% of the variability in production estimates reported for the Arctic. Future studies are strongly encouraged to replicate salinity conditions representative of *in situ* values during the melting process to minimize hypoosmotic stress, thereby most accurately estimating primary production.

Keywords: sea ice, algae, salinity stress, photophysiology, sample melt, Arctic

OPEN ACCESS

Edited by:
Janne-Markus Rintala, University of Helsinki, Finland

Reviewed by:
Jonna Piiparinen, Finnish Environment Institute (SYKE), Finland
Andrew Mcminn, University of Tasmania, Australia

****Correspondence:***
Karley Campbell
kc17823@bristol.ac.uk

Specialty section:
This article was submitted to Cryospheric Sciences, a section of the journal Frontiers in Earth Science

Received: *01 October 2018*
Accepted: *04 February 2019*
Published: *25 February 2019*

Citation:
Campbell K, Mundy CJ, Juhl AR, Dalman LA, Michel C, Galley RJ, Else BE, Geilfus NX and Rysgaard S (2019) Melt Procedure Affects the Photosynthetic Response of Sea Ice Algae. Front. Earth Sci. 7:21. doi: 10.3389/feart.2019.00021

INTRODUCTION

Algae colonizing the brine network and bottom layer of sea ice are estimated to account for 3–25% of annual primary production in the Arctic Ocean (Subba Rao and Platt, 1984; Legendre et al., 1992), although greater contributions have been documented in high Arctic regions (Gosselin et al., 1997). In particular, a bloom of largely photosynthetic diatoms in spring provides a concentrated

food resource for aquatic grazers (Leu et al., 2011), which also influences the flux of CO_2 between the atmosphere and ocean (Brown et al., 2015). The availability of light and nutrients are understood to be important controls of ice algal abundance and productivity (Leu et al., 2015), but the magnitude of variability in production estimates reported across the Arctic, even between studies of seemingly comparable environments, requires further investigation (Leeuwe et al., 2018). There are renewed efforts to expand the spatial coverage of sea ice production measurements as recent studies have shown that ice algae in previously under sampled regions may be greatly underestimated (Lange et al., 2017; Fernandez-Mendez et al., 2018). Timely completion of such assessments of sea ice algal communities are required to predict the consequences of climate warming on ice algae, including the impact of ongoing changes to sea ice volume, seasonality and areal coverage (Vihma, 2014; Simmonds, 2015).

Effective studies of sea ice biogeochemistry rely on accurate measurements of ice algal production, which can be done by monitoring oxygen evolution or carbon uptake *in situ* or via incubation of samples in a closed system. *In situ* approaches, such as quantifying oxygen flux across the ocean-ice diffusive boundary layer (McMinn et al., 2000; Rysgaard et al., 2001; McMinn and Hegseth, 2007), arguably provide estimates under the most natural conditions. However, these methods can be costly, time consuming, and dangerous if divers are required for the deployment of sensors (Bates and Cota, 1986). Furthermore, the corresponding biomass, areal footprint, as well as the role of physical processes (e.g., ice melt) on flux measurements is often uncertain (Kuhl et al., 2001). There are also concerns related to gas and tracer diffusion when measuring algal production within the solid ice matrix (Mock and Gradinger, 1999).

For these reasons, sea ice productivity studies typically use melted sections of sea ice cores (Leeuwe et al., 2018) or, to a lesser extent, sea ice brine (McMinn et al., 2014). Incorporation of liquid samples into specialized incubators further permits a range of assessments, such as construction of photosynthesis-irradiance (PE) curves to assess algal photophysiology (Cota and Horne, 1989) that have been widely used in studies of sea ice algal production across the Arctic (e.g., Michel et al., 1988; Bergmann et al., 1991; Søgaard et al., 2010; Campbell et al., 2016). It is more common to incubate melted bulk-ice samples than collecting sea ice brine because all cells, independent of size, are obtained from a known section of an ice core (Norrman and Anderson, 1994). This is also a practical approach when studying the Arctic spring bloom given that sea ice algae are predominantly concentrated in the bottommost skeletal layer of first-year ice during this time (Leu et al., 2015). Furthermore, sampling the growth interface rather than the brine network collects the majority of biomass for subsequent analysis. Despite widespread measurement of primary productivity on melted ice samples, there is a lack of consensus in the scientific community on the specific melt procedure to employ (Miller et al., 2015). Samples are consistently melted in darkness to avoid light stress on the shade acclimated algae; however, approaches vary in the temperature and duration of melt used, as well as whether the sample is buffered for the decrease in salinity that occurs with melting of the solid ice matrix.

Carbon-fixation of ice algal communities is greatest between 4 and 14°C (Kottmeier and Sullivan, 1988; Arrigo and Sullivan, 1992), which is significantly warmer than the subzero temperatures experienced by cells in the ice environment. Ice algae are thus capable of functioning over a wide range of temperatures. However, recent assessments of sea ice sample melt temperatures have shown conflicting results, likely due to the inherent link between temperature and duration of melt. For example, Rintala et al. (2014) demonstrated no significant difference in algal productivity between samples melted at room temperature (∼12 h) or at 4°C (36 h) and advocated for a rapid melt to limit the influence of biological impacts (e.g., growth of algae and bacteria) that are likely to increase over time. In contrast, Mikkelson and Witkowski (2010) showed that melting over approximately 14 h at room temperature (20°C) caused significantly lower abundances of non-diatom cells that often dominate ice communities outside of the bloom period, concluding that rapid melt at temperatures warmer than 4°C should be avoided.

Sea ice algae have the capacity to survive a broad range of salinities, with maximum photosynthetic rates typically found at salinities comparable to ocean surface water (Grant and Horner, 1976; Kottmeier and Sullivan, 1988). Nevertheless, studies have shown that sea ice algae are susceptible to osmotic shock, particularly if not given sufficient time to gradually acclimate to decreasing salinity (Kirst, 1990; Ryan et al., 2004). This can include damage to cell pigments and the potential release of intracellular carbon and nutrient pools, although the impact on diatoms is thought to be less than algae of other functional groups (Kirst, 1990).

To avoid the potential effects of hypoosmotic shock, adding filtered seawater at about 3–4 times the volume of ice collected has been encouraged by a number of studies to buffer salinity during the melting process (Garrison and Buck, 1986; Ryan et al., 2004; Mikkelson and Witkowski, 2010; Thomas et al., 2010; Campbell et al., 2018). Still others have employed higher-dilution methods, like the 'scrape' sampling approach that melts the bottommost skeletal layer into much greater volumes of seawater (Smith et al., 1988; Cota and Horne, 1989; Bergmann et al., 1991), or diver-operated suction-type samplers (Welch et al., 1988) that collect algal cells from the ice-ocean interface and ice bottom in a mix of ambient (unfiltered) interface and brine water (Welch and Bergmann, 1989; Gosselin et al., 1990, 1997; Johnsen and Hegseth, 1991; Hegseth, 1998). One potential drawback of adding filtered seawater during the melting process is that it may introduce additional constituents which artificially enhance photosynthesis (Rintala et al., 2014), though these external inputs are likely to be insignificant relative to intracellular pools of nutrients unless standing stocks are high (Thomas et al., 2010). As a result, a number of studies on sea ice communities have melted ice samples without buffering for salinity (e.g., Kaartokallio et al., 2007; Søgaard et al., 2010; Fernandez-Mendez et al., 2018). Conflicting recommendations for melting sea ice have resulted in the use of different approaches in different studies. The array of techniques employed raises concerns regarding the accuracy of measurements relative to *in situ* communities and may contribute to variability in

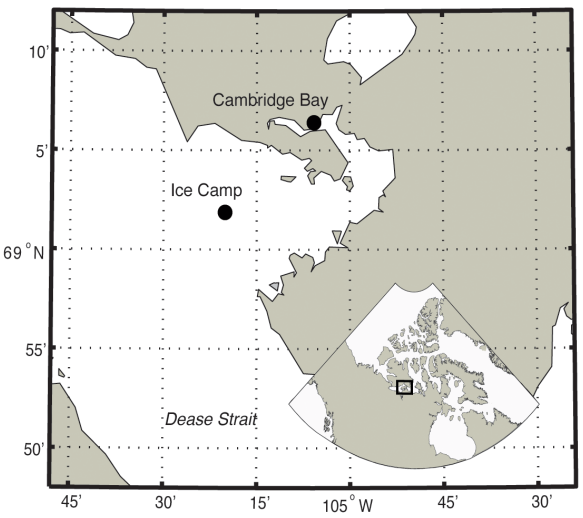

FIGURE 1 | Location of ice camp-based sampling location (69.03°N, 105.33°W) in Dease Strait, Nunavut, Canada.

production estimates across polar regions (Arrigo et al., 1997; Leeuwe et al., 2018).

The main objective of this study was to investigate how different sample melting procedures may impact subsequent measurements of primary productivity. First, we conducted field-based experiments to test the hypothesis that melt procedure had a significant impact on the productivity and photophysiology of sea ice algae in Dease Strait of the Canadian Arctic Archipelago. We then conducted laboratory experiments on cultures of the prevalent ice diatom species *Nitzschia frigida* to investigate the relative importance of conditions that cells experience during different melt procedures. Based on the results of these experiments we provide recommendations for melt procedure in future studies of sea ice algal photophysiology.

MATERIALS AND METHODS

Collection and Processing of Dease Strait Samples

Site Characteristics and Description of Field-Based Melt Treatments

Field data were collected from the first-year sea ice in Dease Strait, Canada, on five occasions between 17 May and 9 June 2014 (**Figure 1**). Areas of thin snow cover ($<$ 10 cm) were selected for sampling approximately every 4 days in this region. During four of the five sampling events a scrape melt treatment was obtained by collecting the bottom ∼1 cm of six ice cores using a Mark II Kovacs core barrel. These scrape samples were pooled by placing scrapes directly into filtered seawater (FSW), for a dilution factor of approximately eight. Total volume of FSW and scrape samples was not measured directly and was instead estimated assuming that 1 cm of ice was collected per core ($FSW_{8:1}$). On each date of sample collection, the bottom 5 cm of 12–16 different cores were also collected and core segments were split into two separate insulated containers before transport back to the field laboratory for processing under two other melt treatments that included: (i) diluted melt with filtered seawater added at a volumetric ratio of three parts filtered seawater to one part ice ($FSW_{3:1}$), and (ii) undiluted melt without the addition of filtered seawater (FSW_{zero}). With each replicate representing an individual sampling event, the result is a total of four sample replicates for $FSW_{8:1}$ scrapes and five replicates for $FSW_{3:1}$ and FSW_{zero} melt treatments. All filtered seawater was collected from 2.5 m depth 24–48 h prior to ice collection using a Kemmerer sampler deployed through the ice and was prepared at room temperature using 0.2 μm polycarbonate filters. Filtered seawater added to ice for melt was also at room temperature. Melting of all samples took place within the insulated containers that were stored in a dark room at approximately 20°C. Samples were periodically checked for complete ice melt, about 4 h for $FSW_{8:1}$, 24 h for $FSW_{3:1}$, and 48 h for FSW_{zero}. Samples were analyzed as soon as possible (within ∼1 h) after complete melt to prevent significant warming above the melting point of sea ice in containers. These melt treatments of pooled cores for each sampling event were used for all field-based measurements presented.

Sampling of Biological and Chemical Variables in Dease Strait

Chlorophyll *a* concentration (chl *a*) was determined by filtering two subsamples from each of the three melted core treatments onto GF/F filters (Whatman), and measuring fluorescence (Turner Designs Trilogy Fluorometer) of pigments extracted into 10 ml of 90% acetone for 18–24 h before and after acidification with 5% HCl (Holm-Hansen et al., 1965; Parsons et al., 1984). The resultant concentrations of chl *a* reported were further corrected for melt dilution. Salinity of each melted ice sample was measured using an Orion Star A212 conductivity meter upon complete melt. On average (± SD) the salinity of $FSW_{8:1}$, $FSW_{3:1}$, and FSW_{zero} samples were 27.0 ± 0.2, 24.1 ± 0.3, 9.6 ± 1.1, respectively. The salinity of melted ice samples was proportional to volume of seawater added, where the salinity of filtered seawater averaged 28.3 ± 0.4 during the sampling period.

During each coring event, the bottom 5 cm of a separate ice core (melted without dilution at room temperature in the dark) and water sample collected from the base of a cored hole via submersible pump, were taken to measure nutrients in the bottom-ice and at the ice-ocean interface, respectively. Filtered seawater collected for melt treatments was also subsampled for nutrients within 24–48 h of collection. Nutrient samples were processed using acid sterilized syringes (HCl) and GF/F filters (Whatman) previously combusted at 450°C for 5 h. Filtrate was frozen at –20°C prior to analysis of nitrate (NO_3) and nitrite (NO_2), phosphate (PO_4) and silicic acid ($Si(OH)_4$) concentrations using a Seal Analytical auto analyzer within 6 months of collection (Grasshoff et al., 1983).

Pseudo-duplicate samples of the melted bulk-sea ice, filtered seawater and interface water were collected in 12-ml Exetainers and fixed with 20 μl of saturated mercury chloride ($HgCl_2$) solution for later analysis of dissolved inorganic carbon (DIC).

Average DIC concentration was measured within 6 months of sample collection using an Apollo Scitech Inc. infrared CO_2 analyzer. Routine analysis of Certified Reference Materials provided by A. G. Dickson, Scripps Institution of Oceanography, verified that DIC were analyzed within $\pm$ 3 μmol kg^{-1}.

Measurement of Gross Primary Production on Field Samples

Photosynthesis-irradiance curves of gross primary production relative to chl *a* were calculated for each of the melt treatments using the ^{14}C tracer method (Strickland and Parsons, 1972). This consisted of incubating subsamples of pooled cores in 60 ml polystyrene culture flasks (Corning) over a range of 10 different light intensities from 8 to 200 μmols m^2 s^{-1}, and in two dark bottles that were spiked with 50 μl of 3-3,4-dichlorophenyl-1,1-dimethylurea (DCMU; Legendre et al., 1983). Once inoculated with 1 ml of ^{14}C (4 μCi ml^{-1}), for a final concentration of ∼0.07 μCi ml^{-1} per culture flask, samples were incubated in chambers modeled after Babin et al. (1994) for 3 h at −1.5°C to represent approximate *in situ* temperatures. During this time, chambers were placed on a shaker table to promote cell suspension, while also being illuminated by a full spectrum halogen lamp (Phillips Ceramalux). The average light intensity (n = 3) at each bottle position was determined prior to incubations by measuring integrated photosynthetically active radiation (PAR) (μmol photons m^{-2} s^{-1}) using a scalar PAR probe (Walz model US-SQS/L) and data logger (LI-COR LI-1000) in a water-filled incubation flask, while keeping surrounding sample-filled flasks in place. Incubations of photosynthesis-irradiance curves were typically started $\pm$ 2 h of 1300 local time.

Following incubation, samples were filtered onto 25 mm GF/F filters (Whatman), placed into 7 ml glass scintillation vials, and acidified with 200 μl 0.5 N HCl to remove any unfixed carbon. Once dry, 5 ml of Ecolume scintillation cocktail was added to each vial, followed by an extraction period of 24–48 h before measurement of activity on a Hidex Triathler liquid scintillation counter. Initial ^{14}C activity was determined from the average of 3–50 μl aliquots of spiked sample that had been randomly removed from clear flasks prior to the start of incubation. These samples were placed into a solution of 5 ml scintillation cocktail and 50 μl ethanolamine (to prevent degassing) for extraction prior to counting. Gross primary productivity of ^{14}C incubations was calculated from scintillation counts, initial ^{14}C activity, and DIC concentrations (see Section "Sampling of biological and chemical variables in Dease Strait") of sample melt following the equation of potential primary productivity outlined in Søgaard et al. (2010).

Photosynthesis-irradiance curves were modeled using an exponential function in the absence of photoinhibition (Platt et al., 1980; Arrigo et al., 2010), as it was not observed, to determine photophysiological parameters that include: maximum photosynthetic rate, P^B_s (mg C mg chl a^{-1} h^{-1}), photosynthetic efficiency, α^B (mg C mg chl a^{-1} h^{-1} (μmol photons m^{-2} $s^{-1})^{-1}$), production at zero irradiance, P_0 (mg C mg chl a^{-1} h^{-1}), the compensation point, E_c (μmol photons m^{-2} s^{-1}) and the photoacclimation index, E_s (μmol photons m^{-2} s^{-1}) (Cota and Smith, 1991; Arrigo et al., 2010).

Laboratory-Based Culture Experiments

Growth and Preparation of Diatom Cultures

The large differences in several photophysiological parameters observed between the three melt treatments applied to field samples appeared to be related to the relative change in salinity experienced by ice algae during each melt procedure. To support this hypothesis, lab experiments were designed to test whether salinity changes comparable to those that occurred during the different melt procedures (or the change in salinity plus darkness) could by themselves produce photophysiological changes in ice algae of comparable magnitude to those observed in the field samples. Because the three melt procedures also vary in their duration, the experiments assessed the potential for temporal changes in photophysiological parameters during exposure of cells to low salinity and darkness over 48 h.

The pennate diatom species *N. frigida* was selected for these experiments due to its known abundance in spring ice algal communities across the Arctic (Różańska et al., 2009; Poulin et al., 2011), including in the region of Dease Strait where species of *Nitzschia* comprised 24% and *N. frigida* 10% of the algal community between 17 May and 5 June 2014 (Campbell et al., 2018). Cultures of *N. frigida* originally isolated from landfast sea ice of the nearshore Chukchi Sea (Aumack and Juhl, 2015), were transferred to the University of Manitoba for experiments. Stock and experimental cultures were grown in sterile L1 medium (Guillard and Hargraves, 1993) made using artificial seawater (Instant Ocean). When grown at 1°C in media with a salinity of 33 and exposure to photosynthetically active radiation of 30 μmol m^{-2} s^{-1}, exponential phase growth rates of approximately 0.4 d^{-1} were comparable to others of *N. frigida* under similar conditions (Suzuki et al., 1997; Juhl and Krembs, 2010).

Procedure for Experimentation on Diatom Cultures

Experiments tested the photophysiological responses of *N. frigida* to salinities similar to the three field-based melt treatments ($FSW_{8:1}$, $FSW_{3:1}$, and FSW_{zero}), under near growth saturating light and darkness. L1 media of three different salinities comparable to the three field-based melt treatments (30, 20, and 12, respectively) were created by modifying the amount of Instant Ocean dissolved to make the artificial seawater base. The resultant experimental treatments at salinity 30, 20, and 12 are hereafter referred to as S30, S20, and S12, respectively. Initial nutrient, trace metal and vitamin concentrations were consistent for all salinities. For a given salinity treatment, 40 ml of stock *N. frigida* were transferred into each of eight-1 L polystyrene culture flasks (Thermo Scientific) containing 800 ml of experimental L1 growth media, previously cooled to 1°C (**Figure 2**). Samples were gently mixed and then 10 ml of inoculated media from each of the 8 flasks were pooled to provide an average initial (T_0) sample. Flasks were then sealed and placed into one of the two light conditions (30 or 0 μmol photons m^{-2} s^{-1}, n = 4 for each light treatment) in a 1°C incubator. Thirty μmol photons m^{-2} s^{-1} was expected to result in nearly maximal growth rate in *N. frigida* (Suzuki et al., 1997; Juhl and Krembs, 2010). To assess the

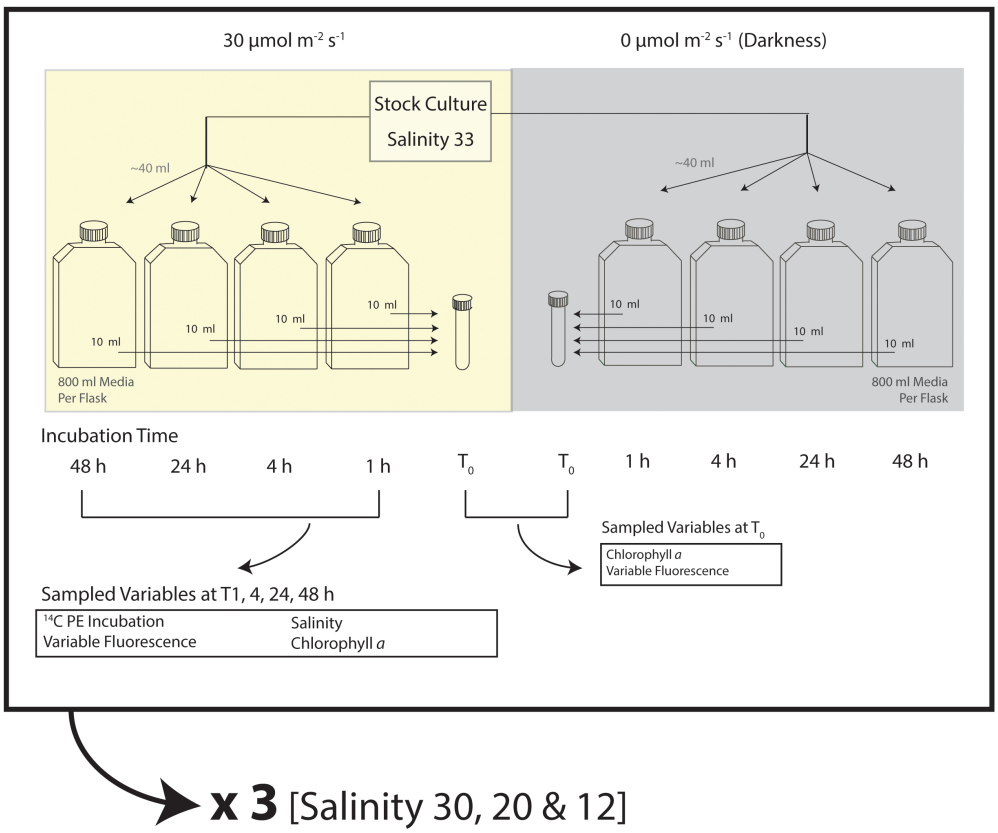

FIGURE 2 | Outline of experimental design for a given treatment of salinities 30, 20, or 12 under 30 or 0 µmol m^{-2} s^{-1}, showing analytical measurements at the beginning (T_0) of experiments and after 1, 4, 24, and 48 h.

potential time-dependence of photophysiological responses, one flask from each combined salinity/light treatment was sacrificed for measurements (see Section "Analysis of data from culture experiments") at each designated time interval of 1, 4, 24, or 48 h. These time intervals were specifically chosen to assess short and long-term responses that correspond to field-based melt times of $FSW_{8:1}$ (4 h), $FSW_{3:1}$ (24 h), and FSW_{zero} (48 h) samples. The result was measurements of photophysiology in 48 flasks in a given experimental run, with each flask representing a single treatment combination of salinity, light and time. Two experimental runs were completed, providing duplicate measurements for each treatment combination.

Analysis of Data From Culture Experiments

Experimental samples of T_0 and time intervals 1, 4, 24, and 48 h were processed immediately after removal from the incubator for maximum quantum efficiency of PSII, chl *a* and salinity (**Figure 2**). A total of five measurements of *in vivo* fluorescence were first measured on each of the duplicate-5 ml subsamples taken from each melt treatment flask (Turner Designs Trilogy Fluorometer), before (F_0) and after (F_m) 20 µl DCMU ($< 0.1\%$) was added to induce maximum fluorescence. Each sample was gently mixed to suspend cells in solution prior to *in vivo* fluorescence measurements. The maximum quantum yield of photosystem II (Fv/Fm) was calculated as $[(F_m\text{-}F_0)/F_m]$ (Maxwell and Johnson, 2000; Parkhill et al., 2001), and is reported hereafter as a combined average of duplicate Fv/Fm measurements for the two experimental runs. Chlorophyll *a* and salinity were measured following the protocols described previously, as was ^{14}C-derived primary production that was measured on samples from time intervals 1, 4, 24, and 48 h (**Figure 2**). Since DIC could not be directly measured for the experimental solutions, the concentration of DIC used to calculate primary production was based on experimental temperature and salinity, assuming 100% saturation (Parsons et al., 1984).

Statistical Analyses for Field and Laboratory-Based Results

Matlab (R2016a) was used for fitting of all exponential photosynthesis-irradiance curves. SPSS statistical software (IBM Version 20) was used for all statistical analyses. When comparing photophysiological parameters of the three field-based melt procedures, one-way ANOVA was performed with Fisher's *post hoc* test. Parametric linear regression was used to test for temporal trends in experimental results. Photophysiological data found to be not normally distributed by a Shapiro–Wilk test or have inhomogeneous variances via Levene test were first log transformed prior to statistical analyses, but are otherwise

reported as original values with units defined in the text. ANOVA results are reported with the F statistic ($F(df_1, df_2)$, where df_1 is the degrees of freedom for melt treatments and df_2 is the number of observations less the number of melt treatments, overall *p*-value for the model, as well as the *p*-values for the respective *post hoc* tests. Regression results are reported with the r^2 and *p*-value. Significance of statistical analyses in this research was concluded for $p < 0.05$ for a given test unless otherwise specified.

RESULTS

Sea Ice Experiments of Dease Strait

Biological and Chemical Characteristics of the Sampling Location

The physical and biological characteristics of sites in Dease Strait sampled from 17 May to 9 June 2014 are summarized in **Table 1**. Selection of thin snow cover resulted in a relatively constant snow and ice thickness throughout the sample period. Stable ice thickness combined with observations of low bulk-ice salinity and bottom-ice (5 cm) temperatures around the −1.5°C freezing point of seawater at salinity 28 also indicate that sampling took place near the onset of spring melt. Average $NO_2 + NO_3$ concentrations in the bottom-ice and water immediately below the sea ice were low, generally less than 1 μmol L^{-1}. The ice algal community was largely comprised of *Attheya* and *Nitzschia* diatom species, which over a given 24 h day, were exposed to light intensities averaging 29 μmol m^{-2} s^{-1} during our study period (Campbell et al., 2016).

TABLE 1 | Average values with standard deviation (brackets) for environmental and oceanographic parameters at the study location in Dease Strait, sampled between 17 May and 9 June (*n* = 5).

	Parameter	Average (SD)
General	Snow thickness (cm)	9.40 ± 5.15
	Ice thickness (cm)	197.7 ± 3.86
	Transmitted irradiance (μmol m^{-2} s^{-1}) [Campbell et al., 2017]	28.8 ± 7.87
Filtered seawater	DIC (μmol kg^1)	2000 ± 30
	Salinity	28.3 ± 0.4
	$NO_2 + NO_3$ (μmol L^{-1})	0.25 ± 0.29
	PO_4 (μmol L^{-1})	1.07 ± 0.24
	$Si(OH)_4$ (μmol L^{-1})	6.40 ± 1.30
Bulk-ice	Temperature (°C)	−1.44 ± 0.15
	Salinity	8.37 ± 0.76
	$NO_2 + NO_3$ (μmol L^{-1})	0.32 ± 0.07
	PO_4 (μmol L^{-1})	3.64 ± 1.41
	$Si(OH)_4$ (μmol L^{-1})	2.68 ± 0.93
Sea ice-Ocean Interface	Salinity	28.2 ± 0.13
	$NO_2 + NO_3$ (μmol L^{-1})	0.94 ± 0.14
	PO_4 (μmol L^{-1})	0.90 ± 0.04
	$Si(OH)_4$ (μmol L^{-1})	5.42 ± 0.38

Field-Based Melt Treatments

Salinity and DIC concentration were greatest in the $FSW_{8:1}$ melt treatment, followed by the $FSW_{3:1}$ and FSW_{zero} treatments (**Supplementary Table S1**). The salinity and DIC of the highly diluted $FSW_{8:1}$ treatment were most similar to concentrations measured in filtered seawater that had an average salinity of 28.3 ± 0.4 and DIC concentration of 2000 ± 30 μmol kg^1. Inorganic nutrient content of the filtered seawater has been summarized in **Table 1**.

Primary production at a given light level was consistently highest in the $FSW_{8:1}$ samples, followed by $FSW_{3:1}$ and FSW_{zero} samples, respectively (**Figure 3A**). This is highlighted by significantly different P^B_s, α^B, and P_0 between FSW_{zero} and all other melt treatments, which were greatest in $FSW_{8:1}$ and lowest in FSW_{zero} melt treatments. Photophysiological parameters E_c and E_s were not significantly different between melt treatments (**Table 2**). Modeled production for $FSW_{3:1}$ on 14 June did not intercept the x-axis at zero irradiance, and as a result, P_0 and E_c were not calculated for this sample date.

Laboratory Experiments on *Nitzschia frigida* Cultures

Lab experiments were run to determine whether changes in salinity alone, or salinity with darkness, could produce changes in photophysiology that were comparable to those observed in field samples under the different melt conditions (**Figure 3**).

Chlorophyll *a* and Maximum Quantum Efficiency of PSII of Cultures

Conditions of laboratory experiments on *N. frigida* cultures are summarized in **Supplementary Table S2**. The concentration of chl *a* in treatments ranged between 17.5 and 52.0 μg L^{-1} (**Figure 4A**) and exhibited no apparent relationship with salinity treatment or light condition. The concentration of chl *a* increased over the duration of experiments in S30 and S20 samples exposed to 30 μmol m^{-2} s^{-1}, but decreased over time at S12 under illuminated or dark conditions (**Figure 4A**). The maximum quantum efficiency of PSII of S12 samples under light or dark conditions were lower than S30 and S20 salinity treatments, respectively (**Figure 4B**). At S30 and S20, Fv/Fm of light and dark samples appeared to increasingly deviate over incubation time, with fluorescence at 30 μmol following similar trends as chl *a* described previously (**Figure 4B**).

Photosynthesis-Irradiance (PE) Curves of Salinity Treatments in Culture Experiments

Photophysiological parameters P^B_s, α^B and P_0 within each experimental light condition (i.e., light or dark) were highest at S30, followed by S20 and S12, respectively (**Figures 3B**, **5**). Parameters P^B_s, α^B, and P_0 at S12 showed the greatest differences in responses between light and dark conditions (**Supplementary Table S3**). In comparison, the response of E_c and E_s was similar for algae grown in the three melt treatments; although, average measurements were consistently lower in dark versus light conditions (**Supplementary Table S3**). The majority of photophysiological parameters showed no significant temporal

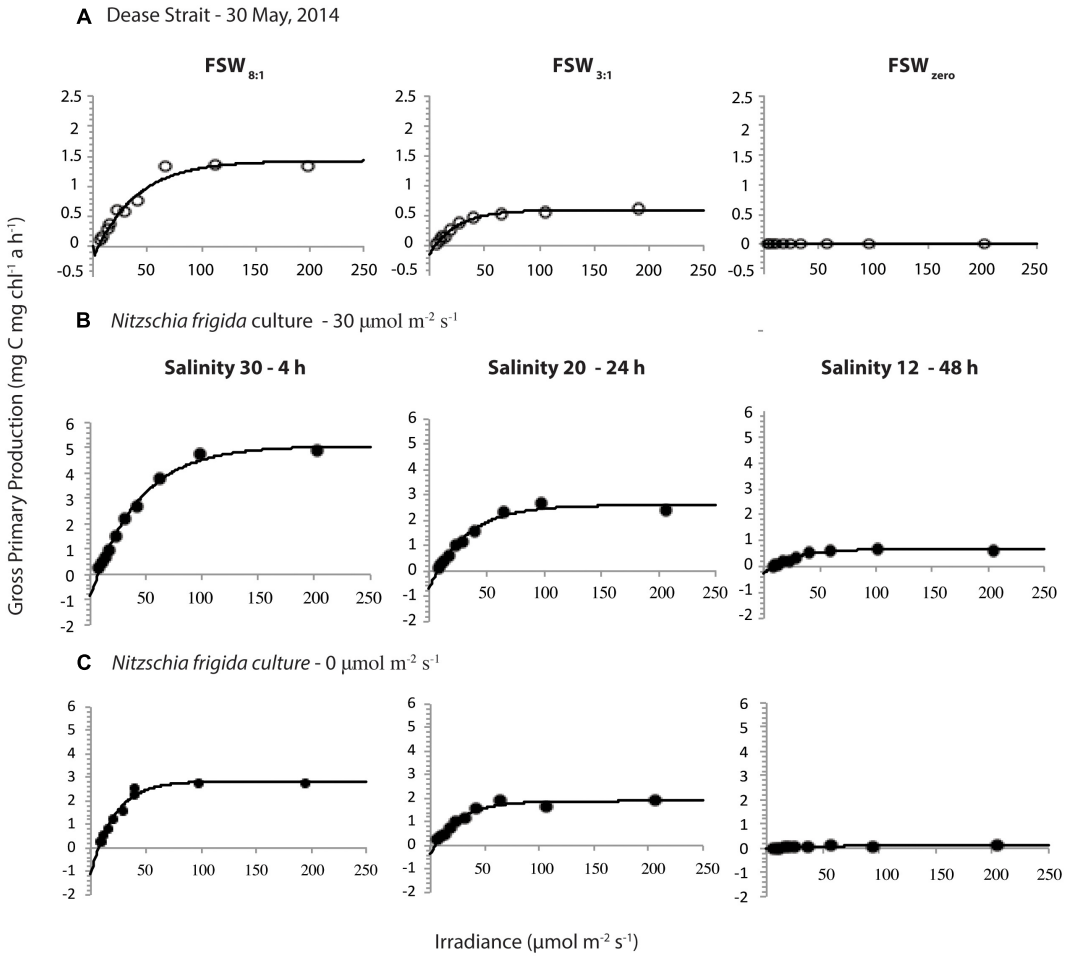

FIGURE 3 | Selected photosynthesis-irradiance curves from samples collected on 30 May in Dease Strait melted in different volume-based ratios of filtered seawater (FSW) to ice **(A)**, and laboratory cultured samples of *Nitzschia frigida* grown under 30 µmol m^{-2} s^{-1} **(B)** or in the dark **(C)** for defined time intervals (hour, h) at salinities of 30, 20, or 12. Laboratory experimental curves shown represent the times of exposure and salinity treatments most comparable to melt procedures of field samples.

TABLE 2 | Average values with standard deviation (brackets) of photosynthesis-irradiance parameters (see text for definitions) for samples melted in filtered sea water added at a ratio of eight parts water to one part ice ($FSW_{8:1}$), three parts water to one part ice ($FSW_{3:1}$), and melted without filtered seawater added (FSW_{zero}).

		Average			ANOVA	Fisher's *post hoc* test of significance		
		$FSW_{8:1}$	**$FSW_{3:1}$**	**FSW_{zero}**	**F Statistic *p*-value *(df)***	**$FSW_{8:1}$ vs. $FSW_{3:1}$**	**$FSW_{8:1}$ vs. FSW_{zero}**	**$FSW_{3:1}$ vs. FSW_{zero}**
PE Parameters	P^B_s	2.03 (0.661)	0.762 (0.121)	0.077 (0.112)	**34.730 <0.001 (2, 11)**	0.108	**<0.001**	**<0.001**
	α^B	0.062 (0.021)	0.024 (0.005)	0.004 (0.007)	**18.741 <0.001 (2, 11)**	0.147	**0.001**	**<0.001**
	P_0	0.295 (0.132)	0.097 (0.043)	0.016 (0.026)	**16.378 0.001 (2, 10)**	0.158	**0.003**	**<0.001**
	E_c	4.63 (0.735)	2.80 (2.56)	4.59 (1.28)	0.681 0.528 (2, 10)	0.306	0.365	0.854
	E_s	33.4 (5.29)	40.8 (20.5)	32.1 (18.0)	0.532 0.602 (2, 11)	0.670	0.325	0.604

The ANOVA test statistic F (top), p-value (bottom), and Fisher's post hoc p-value are presented. Significant values ($p < 0.05$) are in bold. Degrees of freedom (df) in the ANOVA model is also shown.

trends between hour 1 and 48 of the experiments, with the exception of increases of illuminated sample P^B_S at S12 ($r^2 = 0.988$), P_0 at S12 ($r^2 = 0.917$), and E_c at S30 ($r^2 = 0.928$), as well as α^B of darkened samples at S20 ($r^2 = 0.461$) (**Figure 5**). Nevertheless, we note that in many instances (e.g., α^B at S30) the difference in P^B_s, α^B and P_0 parameters between individual time points of the experiment is greatest between hours 1 and 4, followed by more consistent values thereafter.

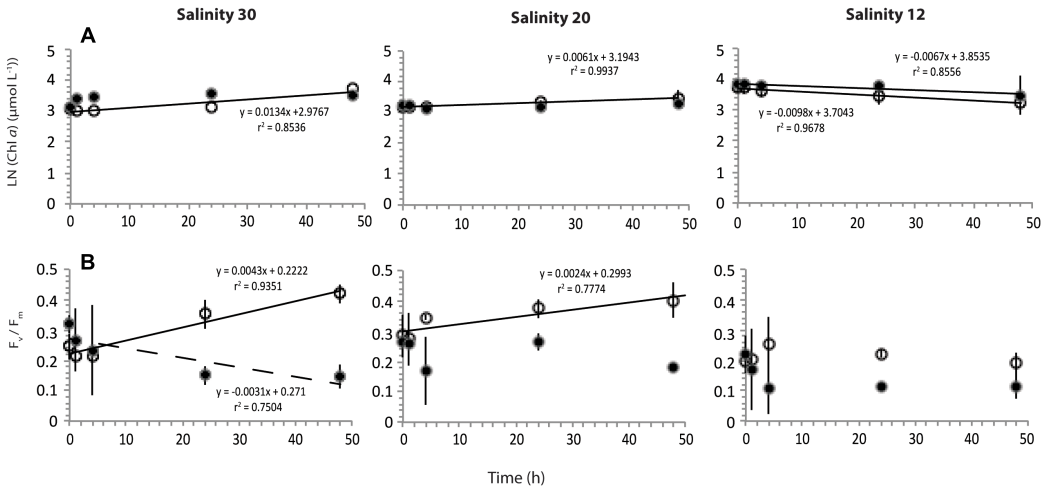

FIGURE 4 | Change in average (n = 2) values with standard deviation of **(A)** LN transformed chlorophyll *a* (chl *a*) and **(B)** maximum quantum efficiency of PSII (Fv/Fm) over time (hour) of cells in treatments of 30, 20, and 12 salinity, incubated under 30 (white) or 0 (black) µmol m^{-2} s^{-1} light intensities. Linear regressions significant to $p < 0.05$ (solid) or $p < 0.10$ (dashed) with associated equations and coefficients of determination are also shown.

DISCUSSION

Differences in the Physical Characteristics and Production of Algal Communities in Dease Strait Melt Treatments

Observations of higher chl *a* in $FSW_{8:1}$ than the other melt treatments (**Supplementary Table S1**), indicates that algal abundance likely increased toward the bottom-ice interface. That is, there is more algal pigment in the bottom 1 cm than the bottom 5 cm per liter of melted sea ice. Based on areal concentrations, chl *a* in the bottom 1 cm ($FSW_{8:1}$) of sea ice accounted for 145 ± 50 % of total chl *a* in the bottom 5 cm (FSW_{zero}) of sea ice during this study. Alternatively, if dilution corrected measurements of chl *a* in the bottom 1 cm of ice ($FSW_{8:1}$) are divided by five to simulate distributing the bottom 1 cm layer over a 5 cm core segment, the resultant average concentration (115.0 ± 14.1 µg L^{-1}) would be similar to the chlorophyll values observed in the $FSW_{3:1}$ treatment (**Supplementary Table S1**). This agrees with previous observations that the majority of biomass in first-year sea ice is near the very bottom due to greater nutrient availability with proximity to interface water (Smith et al., 1990; McMinn et al., 1999), especially under relatively thin snow cover (Aumack et al., 2014). Thus the majority of algal chl *a* in this study was located in the bottom 0 to 1 cm section of ice, while negligible concentrations of chl *a* existed 1 to 4 cm from the ice-water interface.

The collection of a 1 cm scrape for the $FSW_{8:1}$ melt treatment versus 5 cm core sections for $FSW_{3:1}$ and FSW_{zero} melt treatments introduces some uncertainty in the statistical comparison of field samples, as the different sections of sea ice could have contained physiologically unique communities. This includes potentially different algal species under greater nutrient stress with distance from the ocean-ice interface. However, the overwhelming proportion of biomass in the 0 to 1 cm horizon would dominate the production signal and therefore, the effect of algal cells from 1 to 5 cm ice core section on the observed photophysiological parameters would be limited. Concentration of algae in the bottom centimeter of ice also supports that the three melt treatments in Dease Strait contained largely the same algal population, and thus their comparison may be used to highlight the collective response of the ice algal community to the conditions of sample melt. Finally, we note that the proportion of dominant pennate and centric functional groups was very similar between all three melt treatments (**Supplementary Table S4**), indicating that the melt treatments were likely of similar species composition.

Independent of this potential sampling bias, a difference of > 50% in chl *a* between $FSW_{3:1}$ and FSW_{zero} samples from similar 0 to 5 cm core sections (**Supplementary Table S1**) reaffirms that the ice algal community was affected by the melt technique. Differences in P^B_s and α^B between the three melt treatments measured on Dease Strait samples further supports the important influence of melting procedure. In particular, values for P^B_S, α^B, and P_0 were consistently higher in the $FSW_{8:1}$ sample, followed by $FSW_{3:1}$ and FSW_{zero}, respectively (**Table 2**), illustrating that the magnitude of parameters likely increased with the proportion of filtered seawater added, or alternatively, decreased with the duration of ice melt. In comparison, differences in the E_c and E_s between melt treatments were not observed, suggesting these photophysiological parameters that characterize the light dependent mechanisms of photosynthesis are less sensitive to the stresses produced by melting. Similarly, sample melt did not appear to affect the composition of the ice algal community, as the proportion of pennate versus centric diatoms was relatively constant between melt treatments (**Supplementary Table S4**).

The results of this study largely contrast with those reported by Rintala et al. (2014) for sample of Baltic Sea ice, where

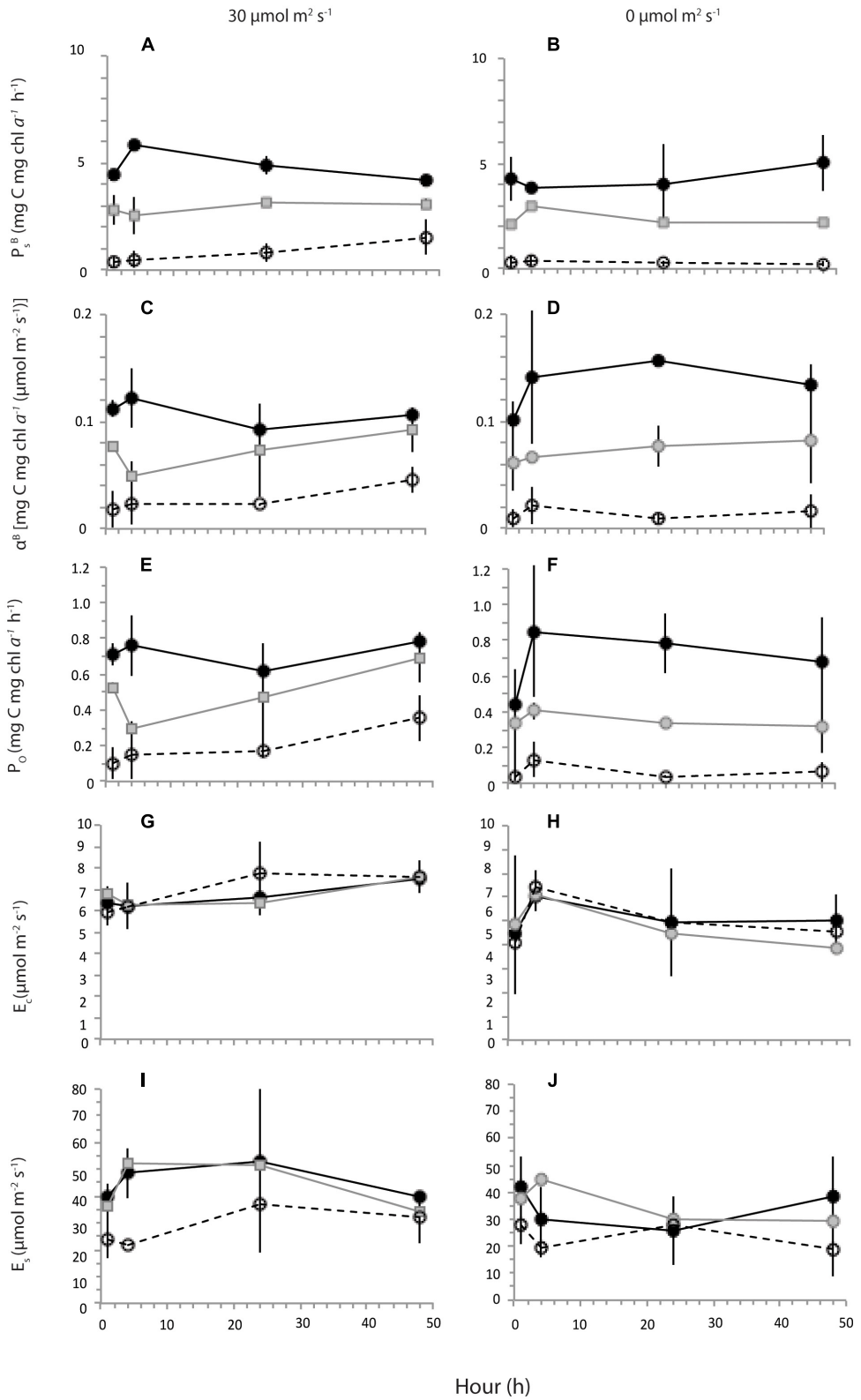

FIGURE 5 | Average (n = 2) photosynthetic parameters (see text for definitions) with standard deviation of algae grown in treatments of 30 (black), 20 (gray) and 12 (white) salinities for time intervals 1, 4, 24, and 48 h under 30 µmol m^{-2} s^{-1} **(A,C,E,G,I)** or in the dark **(B,D,F,H,J)**.

no significant difference in ice algal net production (relative to chl *a*) was found between samples melted with or without the addition of naturally derived filtered seawater. However, Baltic Sea surface water salinities can range from 2 to 24 (Leppäkoski et al., 2002), much lower than in this study (**Table 1**). It is possible that brackish waters of the Baltic Sea minimized a melt-processing effect due to acclimation of the local ice algal community to fresher *in situ* conditions. This suggestion supports conclusions by Rintala et al. (2014) that their results should only be directly applied to the Baltic Sea study region.

Rintala et al. (2014) also advocated for rapid ice melt overnight at room temperature versus at 4°C for 36 h, despite lower net production and chl *a*, as it was believed to limit algal growth during melting. In this research, we found that under conditions of stable temperature around the melting point of sea ice, faster ice melt was associated with greater maximum production (P^B_S). However, algal growth was not a factor in this study, as chl *a* was greater in $FSW_{8:1}$ and $FSW_{3:1}$ samples with shorter melt times, respectively. The Baltic Sea was also dominated by flagellated species (Rintala et al., 2014), while the ice algal community of Dease Strait was almost exclusively diatoms during this late-spring study period (Campbell et al., 2018). Differences in community composition could have contributed to variable responses between the studies, as individual species of algae are known to exhibit varying salinity tolerances (Ryan et al., 2004; Søgaard et al., 2011). Indeed, Balzano et al. (2011) showed that even different strains of the same marine diatom can exhibit varying sensitivities to decreases in salinity, where *Skeletonema marinoi* sourced from the moderately saline (7.5) North Sea exhibited greater sensitivity to experimental freshening than *S. marinoi* from the more brackish (2.5) conditions of the Baltic Sea. Similar to this study of sea ice in Dease Strait, algal blooms at the ice-ocean interface across the Arctic are typically characterized by diatoms like *N. frigida* growing at surface water salinities around 30 (Brandon et al., 2010; Poulin et al., 2011). As a result, the negative impact of unbuffered sample melt on algal photophysiology that we observed is likely more representative of bottom-ice algal communities in the Arctic than studies on non-diatom functional groups, or indeed algae from brackish environments.

Response of *Nitzschia frigida* Cultures to Experimental Treatments

Photosynthetic Responses of Algal Cultures

Variability in production between the melt treatments of Dease Strait samples as a result of time and/or salinity may have been driven by one or a combination of factors that include (i) optimal salinity ranges for growth and production (Arrigo and Sullivan, 1992), (ii) cell death or stress associated with melt time, darkness, and processing (Mikkelson and Witkowski, 2010; Rintala et al., 2014), (iii) inorganic nutrient (Rintala et al., 2014) and organic matter availability (Vähätalo and Järvinen, 2007), and (iv) the concentration of DIC (Rintala et al., 2014). The relationship between photophysiological parameters and final sample salinity suggested that the change in salinity was a key factor in the difference between the three melt methods, but the field-based sample melt experiments employed in this study did not distinguish between salinity and other possible mechanisms. The lab experiments were designed to determine whether changes in salinity alone, or in combination with darkness, could produce changes in photophysiological parameters that were comparable to those seen in the field samples. The time duration for any changes in photophysiology to occur were also assessed.

The similarity of our experimental results to the field observations supports our hypothesis that the photophysiology of sea ice algae is affected by sample melt procedure. The experimental results indicate that decreasing salinity alone caused the greatest observed changes in P^B_s, α^B, and P_0. Similar to the field observations, E_c and E_s did not change between treatments. While darkness enhanced the effects on P^B_s, α^B, and P_0, and there were temporal trends in some parameters, these impacts were comparatively minor relative to the salinity effects. In addition, given that the concentration of nutrients were consistent in all lab treatments, we note that photophysiological changes similar to those seen in the field samples can occur due to changes in salinity independent of nutrients.

Influence of Salinity in Driving Photosynthetic Responses of Algal Cultures

Previous studies have found that ice algal growth is optimized at salinities between 30 and 50 (Arrigo and Sullivan, 1992; Søgaard et al., 2011), while cells can survive under more extreme conditions between 10 and 60 with reduced metabolism (Grant and Horner, 1976; Vargo et al., 1986; Kottmeier and Sullivan, 1988). In particular, hypoosmotic (low salinity) conditions are thought to have a greater impact on ice algal cell functioning than hyperosmotic (high salinity) conditions due to cumulative impacts of osmotic stress following water uptake, salt stress with release of ions, and changes to the ion permeability of cell membranes (Kirst, 1990). These insights may thus in part explain the greater P^B_s and α^B in S30 and S20 laboratory samples as they were closest to the optimal salinity range described above. In comparison, the S12 laboratory sample was farthest from this range and had the lowest measurements of P^B_s, α^B, and P_0. By contrast, the consistently low values of photophysiological parameters, combined with low Fv/Fm and decreasing chlorophyll concentration, suggest that the cells in the S12 treatment were highly stressed, and probably dying.

Influence of Exposure Time on Photosynthetic Response of Algal Cultures

Longer melt times can promote gradual changes in salinity that limit the extent of osmotic shock to cells (Mikkelson and Witkowski, 2010), although, sea ice algae can take days to weeks to fully acclimate to altered growth salinities (Grant and Horner, 1976; Vargo et al., 1986). As a result, it is possible that the near-immediate changes to growth salinity during culture

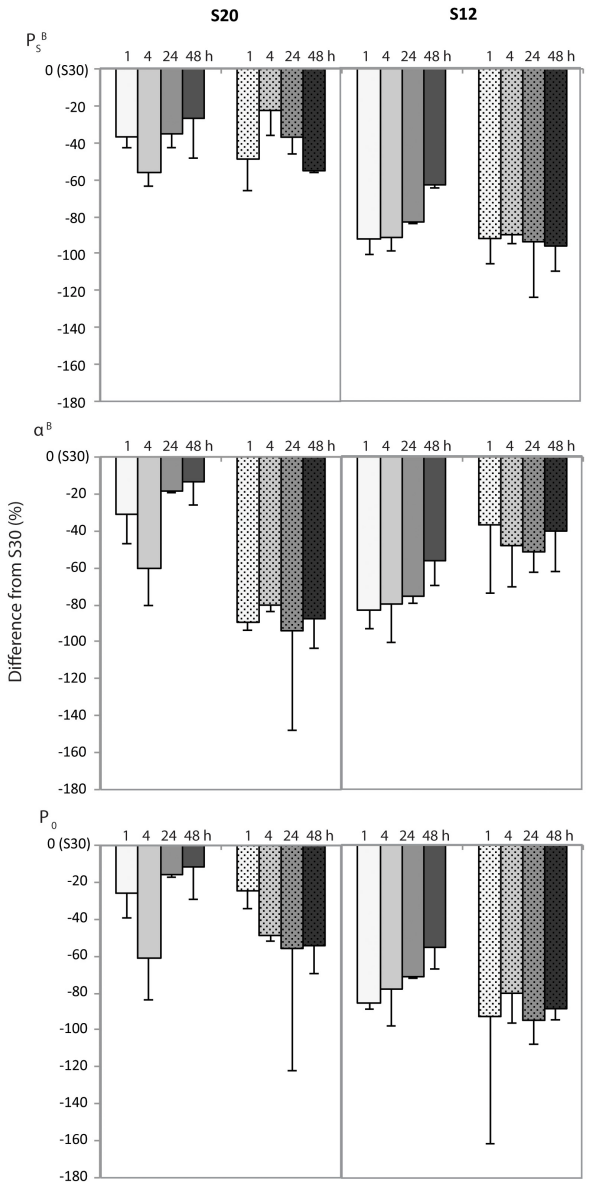

FIGURE 6 | Percent difference in the average (n = 2) of select photosynthetic parameters (see text for definitions) with standard deviation between algae grown in salinity 30 (S30) versus 20 (S20) and 12 (S12). Differences are plotted over experimental time intervals 1, 4, 24, and 48 h for samples grown at 30 μmol m^{-2} s^{-1} (solid fill) or in the dark (patterned fill).

experiments produced more severe responses than field-based melt treatments that had more gradual exposure times (4–48 h). Nevertheless, the documented differences in P^B_s, α^B, and P_0 between salinity treatments within 4 h of exposure support a measurable impact of salinity on algal photophysiology that was quite rapid. Further calculation of the percent difference in these parameters at S20 and S12 from the reference values at S30 also indicates that after an initial 4 h shock period, algal photophysiology of illuminated samples become more similar to the S30 treatment (**Figure 6**). The duration of this experiment was too short to assess whether these algae would have fully recovered from the initial salinity shock; however, our results demonstrate that the ability of cells to recover from hypoosmotic shock was likely hindered in the absence of photosynthesis. That is, ice algae did not acclimate to changes in salinity as well when in darkness, and in some instances, their photophysiological response actually continued to decline (e.g., P_0 at S20).

Greater differences in P^B_s, α^B, and P_0 parameters between light and dark experimental conditions in the S12 sample (**Figure 6** and **Supplementary Table S3**) supports that the combination of low light intensity and hypoosmotic stress was detrimental to algal production, more so than the impact of darkness alone. This finding contradicts the light dependency of ice algal photosynthetic responses to low salinity stress documented by Ralph et al. (2007) but could highlight the cause of exceptionally low production in regions of thick snow (low light) and low surface salinity, like Greenland fjords (Rysgaard et al., 2001; Søgaard et al., 2010; Leu et al., 2015). Future studies should investigate the potential for such additive responses of sea ice algae to their growth environments.

Influence of Dissolved Inorganic Carbon (DIC) Availability on Photosynthetic Response of Algal Cultures

Greater inventories of DIC may stimulate algal photosynthesis in carbon-limited systems (Riebesell et al., 1993), although this influence is not certain, as other studies have also documented a negligible impact on production (Hoppe et al., 2018). DIC was not constant across our experimental treatments and instead increased with the salinity of growth media. The higher concentrations of DIC calculated for S30 and S20 treatments, in comparison to S12, could have thus contributed to the measurement of greater production with salinity. However, recent studies on Arctic phytoplankton have also shown that production of particulate carbon following increased supply of DIC is time-dependent and requires a generation or more before the impact is pronounced (Schulz et al., 2013). Given the short-term (< 4 h) and arguably severe nature of responses to altered growth conditions in this study, we maintain that hypoosmotic shock was still a significant factor in driving variability in production response.

Drivers of Algal Response in Dease Strait Sea Ice

The majority of ice algae in Dease Strait were concentrated in the bottommost centimeter of the sea ice, suggesting that the majority of algae in this study were acclimated to the salinity of interface water infiltrating the skeletal layer. The scrape method of collecting $FSW_{8:1}$ samples produced melt water salinities most similar to interface water, limiting osmotic shock as detailed by our laboratory experiments. The scrape method also had the shortest duration of melt (< 4 h), which reduces the duration of exposure to any additive effects salinity stress and darkness may have had. We note that limiting melt duration

likely reduces the potential impact of predation (Rintala et al., 2014), although aquatic grazers were not explicitly observed in samples following taxonomic analysis (Campbell et al., 2018). In comparison, we attribute the lower estimates of P^B_s, α^B, and P_0 of $FSW_{3:1}$ and FSW_{zero} samples to greater levels of hypoosmotic shock. Based on these results it is our recommendation that bottom- ice samples be melted in filtered seawater volumes at minimum four times the volume of ice collected. Despite the number of perceived benefits to short melt times associated with the scrape treatment we believe that further work is required to ascertain an optimal duration of melt for ice samples, as shorter melt times could feasibly limit the potential for gradual acclimation of algae back-to true *in situ* levels of production and photophysiology. Algal photophysiology in S30 and S20 laboratory treatments varied little between zero and 30 μmol m^2 s^{-1} light intensities. However, for ease of sampling we also suggest the diluted ice melt should be undertaken in darkness versus at low light intensities that would be characteristic of conditions at the growth interface.

Although nutrients were controlled for during laboratory experiments, it is possible that the magnitude of variability in photophysiological response between field-based melt treatments was enhanced by additions of nutrients, organic constituents and DIC within the filtered seawater (Rintala et al., 2014). The average phosphate (PO_4), nitrate + nitrite ($NO_2 + NO_3$), and silicic acid ($Si(OH)_4$) in filtered seawater generated from Dease Strait was comparable to interface and bulk-ice estimates, where the concentration of nitrate + nitrite was found to be a limiting factor of algal production throughout the spring (Campbell et al., 2016). Due to low nitrogen concentrations in the region, it is thus unlikely that the addition of filtered seawater substantially increased ice algal production via enhanced nitrogen supply.

SUMMARY AND CONCLUSION

The photophysiological responses of ice algae were investigated following three possible methods of sample melt: (i) $\leq$ 4 h melt of the bottommost ($<$ 1 cm) ice in a large volume of filtered seawater, (ii) 24 h melt of the bottom 5 cm ice section with moderate dilution of filtered seawater, and (iii) 48 h melt of the bottom 5 cm section with no filtered seawater dilution. Our field-based measurements clearly demonstrate that sample melting procedure affects the magnitude of many photophysiological parameters subsequently measured on the incubated meltwater. Lab experiments indicated that the differences observed between melting procedures can be primarily attributed to different levels of hypoosmotic stress. Of particular significance for estimates of primary production were decreases in P^B_S, α^B and P_0 in response to hypoosmotic stress experienced during unbuffered melt treatments with final salinities of approximately 10.

Based on the average intensity of PAR available to bottom-ice algae and photophysiological parameters calculated in this study, we estimate that the differences in production between melt procedures may account for between 7 and 64% of production variability in the Arctic. That is, the percent difference in production between melt treatments in this study over a possible range in ice algal production of 0.01 to 5.2 mg C mg chl a^{-1} h^{-1} across the Arctic (Arrigo et al., 2010) is 1–1.5 orders of magnitude. This exercise emphasizes that in addition to environmental controls driving variability in ice algal production around the Arctic (Leu et al., 2015), differences in sample melt methodology can impact calculations of production by over an order of magnitude. In turn, the approach chosen by scientists to melt ice samples almost certainly contributes to the variability in production reported across the Arctic.

Standardization of melt procedures in studies of sea ice production would help reduce uncertainty of method-related error. However, rather than adopting one single protocol for sample melt across the discipline, we advocate that efforts to replicate *in situ* conditions should be made as much as possible. The strong influence of salinity documented in this research indicates that maintaining salinity conditions is of particular importance for accurate production estimates, especially given that ice algae appear to rapidly respond to changes in salinity within a 4 h time period. Following this rationale, ice samples with organisms predominantly inhabiting the brine network prior to spring melt (e.g., upper ice profile), should be melted at higher salinities than those readily exposed to ocean surface waters (e.g., skeletal layer).

AUTHOR CONTRIBUTIONS

This work was led by KC and is based on the scientific design of KC, CJM, SR, and AJ. All co-authors provided in-field and/or laboratory-based support, as well as input during the composition and editing of the manuscript that was written by KC.

FUNDING

Research support was given by the UK's Natural Environment Research Council (NERC) and Germany's Federal Ministry of Education and Research (BMBF) via Diatom-ARCTIC (NE/R012849/1), a Northern Scientific Training Program grant, Natural Sciences and Engineering Research Council of Canada (NSERC) Canadian Graduate Scholarship to KC, as well as Canada Foundation for Innovation (CFI) and the Canada Excellence Research Chair grants to SR, an NSERC Discovery and Northern Research Supplement Grants to CJM, and in-kind support from the Canadian High Arctic Research Station (CHARS). Collection, isolation and maintenance of the *N. frigida* culture was partly supported by the US National Science Foundation (ARC10-23348 to AJ). RG also thanks the NSERC Discovery Grant program. This work represents a contribution to the research programs of NERC-BMBF Changing Arctic Ocean (CAO) Diatom-ARCTIC, the ArcticNet, MEOPAR, the Arctic Science Partnership (ASP), the Canada Excellence Research Chair unit at the Centre for Earth Observation Science (CEOS) at the

University of Manitoba. This paper is a contribution to SCOR Working Group 152 - Measuring Essential Climate Variables in Sea Ice (ECV-Ice).

ACKNOWLEDGMENTS

KC would like to acknowledge Aurelie Delaforge for her efforts in collecting field data, as well as Emmelia Stainton, Megan Shields, Kyle Holden, Dr. John Iacozza, and Dr. Marcos Lemes for their support during laboratory experiments. Underlying data to support conclusions in this work are provided in the paper or Supplementary Information.

SUPPLEMENTARY MATERIAL

The Supplementary Material for this article can be found online at: https://www.frontiersin.org/articles/10.3389/feart.2019.00021/full#supplementary-material

REFERENCES

Arrigo, K. R., Mills, M. M., Kropuenske, L. R., van Dijken, G. L., Alderkamp, A. C., and Robinson, D. H. (2010). Photophysiology in two major Southern Ocean phytoplankton taxa: photosynthesis and growth of *Phaeocystis antarctica* and *Fragilariopsis cylindrus* under different irradiance levels. *Integr. Comp. Biol.* 50, 950–966. doi: 10.1093/icb/icq021

Arrigo, K. R., and Sullivan, C. W. (1992). The influence of salinity and temperature covariation on the photophysiological characteristics of Antarctic sea ice microalgae. *J. Phycol.* 28, 746–756. doi: 10.1111/j.0022-3646.1992.00746.x

Arrigo, K. R., Worthen, D. L., Lizotte, M. P., Dixon, P., and Dieckmann, G. (1997). Primary production in Antarctic sea ice. *Science* 276, 394–397. doi: 10.1126/science.276.5311.394

Aumack, C. F., and Juhl, A. R. (2015). Light and nutrient effects on the settling characteristics of the sea ice diatom Nitzschia frigida. *Limnol. Oceanog.* 60, 765–776. doi: 10.1002/lno.10054

Aumack, C. F., Juhl, A. R., and Krembs, C. (2014). Diatom vertical migration within land-fast Arctic sea ice. *J. Mar. Syst.* 139, 496–504. doi: 10.1016/j.jmarsys.2014.08.013

Babin, M., Morel, A., and Gagnon, R. (1994). An incubator designed for extensive and sensitive measurements of phytoplankton photosynthetic parameters. *Limnol. Oceanog.* 39, 694–702. doi: 10.4319/lo.1994.39.3.0694

Balzano, S., Sarno, D., Wiebe, H. C., and Kooistra, F. (2011). Eggects of salinity on the growth rate and morphology of ten Skeletonema strains. *J. Plank. Res.* 33, 937–945. doi: 10.1093/plankt/fbq150

Bates, S. S., and Cota, G. F. (1986). Fluorescence induction and photosynthetic responses of Arctic ice algae to sample treatment and salinity. *J. Phycol.* 22, 421–429. doi: 10.1111/j.1529-8817.1986.tb02484.x

Bergmann, M. A., Welch, H. E., Butler-Walker, J. E., and Siferd, T. D. (1991). Ice algal photosynthesis at resolute and saqvaqjuac in the Canadian Arctic. *J. Mar. Syst.* 2, 43–52. doi: 10.1016/0924-7963(91)90012-J

Brandon, M. A., Cottier, F. R., and Nilsen, F. (2010). "Chapter 3: sea ice and oceanography," in *Sea Ice*, eds D. N. Thomas and G. S. Dieckmann (Hoboken, NJ: Wiley-Blackwell), 97–130.

Brown, K. A., Miller, L., Mundy, C. J., Francois, R., Gosselin, M., Carnat, G., et al. (2015). Inorganic carbon system dynamics in landfast Arctic sea ice during the early-melt period. *J. Geophys. Res. Oceans* 120, 3542–3566. doi: 10.1002/2014JC01062

Campbell, K., Mundy, C. J., Belzile, C., Delaforge, A., and Rysgaard, S. (2018). Seasonal dynamics of algal and bacterial communities in Arctic sea ice under variable snow cover. *Polar Biol.* 41, 41–58. doi: 10.1007/s00300-017-2168-2

Campbell, K., Mundy, C. J., Gosselin, M., Landy, J. C., Delaforge, A., and Rysgaard, S. (2017). Net community production in the bottom of first-year sea ice over the Arctic spring bloom. *Geophys. Res. Lett.* 44, 8971–8978. doi: 10.1002/2017GL074602

Campbell, K., Mundy, C. J., Landy, J. C., Delaforge, A., Michel, C., and Rysgaard, S. (2016). Community dynamics of bottom-ice algae in Dease Strait of the Canadian Arctic. *Prog. Oceanog.* 149, 27–39. doi: 10.1016/j.pocean.2016.10.005

Cota, G., and Smith, R. E. H. (1991). Ecology of bottom ice algae: III. Comparative physiology. *J. Mar. Syst.* 2, 297–315. doi: 10.1016/0924-7963(91)90038-V

Cota, G. F., and Horne, E. P. W. (1989). Physical control of arctic ice algal production. *Mar. Ecol. Prog. Ser.* 52, 111–121. doi: 10.3354/meps052111

Fernandez-Mendez, M., Olsen, L. M., Kauko, H. M., Meyer, A., Rosel, A., Merkouriadi, I., et al. (2018). Algal hot spots in a changing arctic ocean: sea-ice ridges and the snow-ice interface. *Front. Mar. Sci.* 5:75. doi: 10.3389/fmars.2018.00075

Garrison, D. L., and Buck, K. R. (1986). Organism losses during ice melting: a serious bias in sea ice community studies. *Polar Biol.* 6, 237–239. doi: 10.1007/BF00443401

Gosselin, M., Legendre, L., Therriault, J.-C., and Demers, S. (1990). Light and nutrient limitation of sea-ice microalgae (Hudson Bay, Canadian Arctic). *J. Phycol.* 26, 220–232. doi: 10.1111/j.0022-3646.1990.00220.x

Gosselin, M., Levasseur, M., Patricia, A. W., Horner, R. A., and Booth, B. C. (1997). New measurements of phytoplankton and ice algal production in the Arctic Ocean. *Deep Sea Res.* 44, 1623–1644. doi: 10.1016/S0967-0645(97)00054-4

Grant, W. S., and Horner, R. A. (1976). Growth responses to salinity variation in four Arctic ice diatoms. *J. Phycol.* 261, 180–185. doi: 10.1111/j.1529-8817.1976.tb00498.x

Grasshoff, K., Ehrhardt, M., and Kremling, K. (1983). *Methods of Seawater Analysis*. Weinheim: Chemie.

Guillard, R. R. L., and Hargraves, P. E. (1993). *Stichochrysis* immobilis is a diatom, not a chrysophyte. *Phycolog.* 32, 234–236. doi: 10.2216/i0031-8884-32-3-234.1

Hegseth, E. N. (1998). Primary production of the northern Barents Sea (1998). *Polar Res.* 17, 113–123. doi: 10.1111/j.1751-8369.1998.tb00266.x

Holm-Hansen, O., Lorenzen, C. J., Holmes, R. W., and Strickland, J. D. H. (1965). Fluorometric Determination of Chlorophyll. *ICES J. Mar. Sci.* 30, 3–15. doi: 10.1093/icesjms/30.1.3

Hoppe, C. J. M., Wolf, K. E. K., Schuback, N., Tortell, P. D., and Rost, B. (2018). Compensation of ocean acidification effects in Arctic phytoplankton assemblages. *Nat. Clim. Change* 8, 529–533. doi: 10.1038/s41558-018-0142-9

Johnsen, G., and Hegseth, E. N. (1991). Photoadaptation of sea-ice microalgae in the Barents Sea. *Polar Biol.* 11, 179–184. doi: 10.1007/BF00240206

Juhl, A. R., and Krembs, C. (2010). Effects of snow removal and algal photoacclimation on growth and export of ice algae. *Polar Biol.* 33, 1057–1065. doi: 10.1007/s00300-010-0784-1

Kaartokallio, H., Kuosa, H., Thomas, D. N., Granskog, M. A., and Kivi, K. (2007). Biomass, composition and activity of organism assemblages along a salinity gradient in sea ice subjected to river discharge in the Baltic Sea. *Polar Biol.* 30, 183–197. doi: 10.1007/s00300-006-0172-z

Kirst, G. O. (1990). Salinity tolerance of eukaryotic marine algae. *Ann. Rev. Plant Physiol. Plant Mol. Biol.* 42, 21–53. doi: 10.1146/annurev.pp.41.060190.000321

Kottmeier, S. T., and Sullivan, C. W. (1988). Sea ice microbial communities (SIMCO). effects of temperature and salinity on rates of metabolism and growth of autotrophs and heterotrophs. *Polar Biol.* 8, 293–304. doi: 10.1007/BF00263178

Kuhl, M., Glud, R. N., Borum, J., Roberts, R., and Rysgaard, S. (2001). Photosynthetic performance of surface-associated algae below sea ice as measured with a pulse-amplitude-modulated (PAM) fluorometer and O2 microsensors. *Mar. Ecol. Progr. Ser.* 223, 1–14. doi: 10.3354/meps223001

Lange, B. A., Flores, H., Michel, C., Beckers, J. F., Bublitz, A., Casey, J. A., et al. (2017). Pan-Arctic sea ice-algal chl a biomass and suitable habitat are largely underestimated for multi-year ice. *Glob. Change Biol.* 23, 4581–4597. doi: 10.1111/gcb.13742

Leeuwe, M. V., Tedesco, L., Arrigo, K. R., Assmy, P., Campbell, K., Meiners, K. M., et al. (2018). Microalgal community structure and primary production in Arctic and Antarctic sea ice: a synthesis. *Elem. Sci. Anth.* 6:25. doi: 10.1525/elementa.267

Legendre, L., Ackley, S. F., Dieckmann, G. S., Gullicksen, B., Horner, R., Hoshiai, T., et al. (1992). Ecology of sea ice biota: part 2, global significance. *Polar Biol.* 12, 429–444. doi: 10.1007/BF00243113

Legendre, L., Demers, S., Yentsch, C. M., and Yentsch, C. S. (1983). The 14C method: patterns of dark CO2 fixation and DCMU correction to replace the dark bottle. *Limnol. Oceanog.* 28, 996–1003. doi: 10.4319/lo.1983.28.5.0996

Leppäkoski, E., Gollasch, S., and Olenin, S. (2002). *Invasive Aquatic Species of Europe. Distribution, Impacts and Management*. Dordrecht: Kluwer. doi: 10.1007/978-94-015-9956-6

Leu, E., Mundy, C. J., Assmy, P., Campbell, K., Gabrielsen, T. M., Gosselin, M., et al. (2015). Arctic spring awakening – steering principles behind the phenology of vernal ice algae blooms. *Prog. Oceanog.* 139, 151–170. doi: 10.1016/j.pocean.2015.07.012

Leu, E., Soreide, J. E., Hessen, D. O., Falk-Peterson, S., and Berge, J. (2011). Consequences of changing sea-ice cover for primary and secondary producers in the European Arctic shelf seas: timing, quantity, and quality. *Prog. Oceanog.* 90, 18–32. doi: 10.1016/j.pocean.2011.02.004

Maxwell, K., and Johnson, G. N. (2000). Chlorophyll fluorescence—a practical guide. *J. Exp. Bot.* 51, 659–668. doi: 10.1093/jexbot/51.345.659

McMinn, A., Ashworth, C., and Ryan, K. G. (2000). In situ net primary productivity of an Antarctic fast ice bottom algal community. *Aquat. Microb. Ecol.* 21, 177–185. doi: 10.3354/ame021177

McMinn, A., and Hegseth, E. N. (2007). Sea ice primary productivity in the northern Barents Sea, spring 2004. *Polar Biol.* 30, 289–294. doi: 10.1007/s00300-006-0182-x

McMinn, A., Muller, M. N., Martin, A., and Ryan, K. G. (2014). The response of antarctic sea ice algae to changes in pH and CO2. *PLoS One* 9:e86984. doi: 10.1371/journal.pone.0086984

McMinn, A., Skerrstt, J., Trull, T., Ashworth, C., and Lizotte, M. (1999). Nutrient stress gradient in the bottom 5 cm of fast ice, McMurdo Sound, Antarctica. *Polar Biol.* 21, 220–227. doi: 10.1007/s003000050

Michel, C., Legendre, L., Demers, S., and Therriault, J.-C. (1988). Photoadaptation of sea-ice microalgae in springtime: photosynthesis and carboxylating enzymes. *Mar. Ecol. Prog. Ser.* 50, 177–185. doi: 10.3354/meps050177

Mikkelson, D. M., and Witkowski, A. (2010). Melting sea ice for taxonomic analysis: a comparison of four melting procedures. *Polar Res.* 29, 451–454. doi: 10.1111/j.1751-8369.2010.00162.x

Miller, L. A., Fripiat, F., Else, B. G. T., Bowman, J. S., Brown, K. A., Collins, R. E., et al. (2015). Methods for biogeochemical studies of sea ice: the state of the art, caveats, and recommendations. *Elem. Sci. Anth.* 3:38. doi: 10.12952/journal.elementa.000038

Mock, T., and Gradinger, R. (1999). Determination of Arctic ice algal production with a new in situ incubation technicrue. *Mar. Ecol. Prog. Ser.* 177, 15–26. doi: 10.3354/meps177015

Norrman, B., and Anderson, A. (1994). Developement of ice biota in temperate sea area (Gulf of Bothnia). *Polar Biol.* 14, 531–537. doi: 10.1007/BF00238222

Parkhill, J., Maillet, G., and Cullen, J. J. (2001). Fluorescence-based maximum quantum yield for PSII as a diagnostic for nutrient stress. *J. Phycol.* 37, 517–529. doi: 10.1046/j.1529-8817.2001.037004517.x

Parsons, T. R., Maita, Y., and Lalli, C. M. (1984). *Manual of Chemical and Biological Methods for Seawater Analysis*. New York, NY: Pergamon Press.

Platt, T., Gallegos, C. L., and Harrison, W. G. (1980). Photoinhibition of photosynthesis in natural assemblages of marine phytoplanton. *J. Mar. Res.* 38, 687–701.

Poulin, M., Daugbjerg, N., Gradinger, R., Ilyash, L., Ratkova, T., and Quillf, C. (2011). The pan-Arctic biodiversity of marine pelagic and sea-ice unicellular eukaryotes: a first-attempt assessment. *Mar. Biodiv.* 41, 13–28. doi: 10.1007/s12526-010-0058-8

Ralph, P. J., Ryan, K. G., Martin, A., and Fenton, G. (2007). Melting out of sea ice causes greater photosynthetic stress in algae than freezing in. *J. Phycol.* 43, 948–956. doi: 10.1111/j.1529-8817.2007.00382.x

Riebesell, U., Wolf- Gladrow, D. A., and Smetacek, V. (1993). Carbon dioxide limitation of marine phytoplankton growth rates. *Nature* 361, 249–251. doi: 10.1038/361249a0

Rintala, J.-M., Piiparinen, J., Blomster, J., Majaneva, M., Muller, S., Uusikivi, J., et al. (2014). Fast direct melting of brackish sea-ice samples results in biologically more accurate results than slow buffered melti. *Polar Biol.* 37, 1811–1822. doi: 10.1007/s00300-014-1563-1

Różańska, M., Gosselin, M., Poulin, M., Wiktor, J. M., and Michel, C. (2009). Influence of environmental factors on the development of bottom ice protist communities during the winter-spring transition. *Mar. Ecol. Prog. Ser.* 386, 43–59. doi: 10.3354/meps08092

Ryan, K. G., Ralph, P., and McMinn, A. (2004). Acclimation of Antarctic bottom-ice algal communities to lowered salinities during melting. *Polar Biol.* 27, 679–686. doi: 10.1007/s00300-004-0636-y

Rysgaard, S., Kuhl, M., Glud, R. N., and Hansen, J. W. (2001). Biomass, production and horizontal patchiness of sea ice algae in a high-Arctic fjord (Young Sound, NE Greenland). *Mar. Ecol. Prog. Ser.* 223, 15–26. doi: 10.3354/meps223015

Schulz, K. G., Bellerby, R. G. J., Brussaard, C. P. D., Büdenbender, J., Czerny, J., Engel, A., et al. (2013). Temporal biomass dynamics of an Arctic plankton bloom in response to increasing levels of atmospheric carbon dioxide. *Biogeosci.* 10, 161–180. doi: 10.5194/bg-10-161-2013

Simmonds, I. (2015). Comparing and contrasting the behaviour of Arctic and Antarctic sea ice over the 35 year period 1979–2013. *Ann. Glaciol.* 56, 18–28. doi: 10.3189/2015AoG69A909

Smith, R. E., Harrison, W. G., Harris, L. R., and Herman, A. W. (1990). Vertical fine structure of particuate matter and nutrients in sea ice of the high Arctic. *Can. J. Fish. Aquat. Sci.* 47, 1348–1355. doi: 10.1139/f90-154

Smith, R. E. H., Anning, J., Clement, P., and Cota, G. (1988). Abundance and production of ice algae in resolute passage, Canadaian Arctic. *Mar. Ecol. Prog. Ser.* 48, 251–253. doi: 10.3354/meps048251

Søgaard, D. H., Hansen, P. J., Rysgaard, S., and Glud, R. N. (2011). Growth limitation of three Arctic sea ice algal species: effects of salinity, pH, and inorganic carbon availability. *Polar Biol.* 34, 1157–1165. doi: 10.1007/s00300-011-0976-3

Søgaard, D. H., Kristensen, M., Rysgaard, S., Glud, R. N., Hansen, P. J., and Hilligsoe, K. M. (2010). Autotrophic and heterotrophic activity in Arctic first-year sea ice: seasonal study from Malene Bight, SW Greenland. *Mar. Ecol. Prog. Ser.* 419, 31–45. doi: 10.3354/meps08845

Strickland, J. D. H., and Parsons, T. R. (1972). *A Practical Handbook of Seawater Analysis*. Ottawa: Fisheries Board of Canada.

Subba Rao, D. V., and Platt, T. (1984). Primary production of arctic waters. *Polar Biol.* 3, 191–201. doi: 10.1007/BF00292623

Suzuki, Y., Kudoh, S., and Takahashi, M. (1997). Photosynthetic and respiratory characteristics of an Arctic ice algal community living in low light and low temperature conditions. *J. Mar. Syst.* 11, 111–121. doi: 10.1016/S0924-7963(96)00032-2

Thomas, D. N., Papadimitriou, S., and Michel, C. (2010). "Chapter 12: biogeochemistry of sea ice," in *Sea Ice*, eds D. N. Thomas and G. S. Dieckmann (Hoboken, NJ: Wiley-Blackwell), 425–468.

Vähätalo, A. V., and Järvinen, M. (2007). Photochemically produced bioavailable nitrogen from biologically recalcitrant dissolved organic matter stimulates production of a nitrogen-limited microbial food web in the Baltic Sea. *Limnol. Oceang.* 52, 132–143. doi: 10.4319/lo.2007.52.1.0132

Vargo, G. A., Fanning, K., Heil, C., and Bell, L. (1986). Growth rates and the salinity response of an Antarctic ice microflora community. *Polar Biol.* 5, 241–247. doi: 10.1007/BF00446092

Vihma, T. (2014). Effects of Arctic sea ice decline on weather and climate: a review. *Surv. Geophys.* 35, 1175–1214. doi: 10.1007/s10712-014-9284-0

Welch, H. E., and Bergmann, M. A. (1989). Seasonal development of ice algae and its prediction from environmental factors near resolute, NWT, Canada. *Can. J. Fish. Aquat. Sci.* 46, 1793–1804. doi: 10.1139/f89-227

Welch, H. E., Bergmann, M. A., Jorgenson, J. K., and Burton, W. (1988). A sub ice suction corer for sampling epontic ice algae. *Can. J. Fish. Aquat. Sci.* 45, 562–568. doi: 10.1139/f88-067

Conflict of Interest Statement: The authors declare that the research was conducted in the absence of any commercial or financial relationships that could be construed as a potential conflict of interest.

frontiers in Marine Science

ORIGINAL RESEARCH
published: 10 April 2019
doi: 10.3389/fmars.2019.00179

Impacts of the Changing Ocean-Sea Ice System on the Key Forage Fish Arctic Cod (*Boreogadus Saida*) and Subsistence Fisheries in the Western Canadian Arctic—Evaluating Linked Climate, Ecosystem and Economic (CEE) Models

Nadja S. Steiner[1], William W. L. Cheung[2], Andres M. Cisneros-Montemayor[2], Helen Drost[1,3], Hakase Hayashida[4,5], Carie Hoover[6,7], Jen Lam[8], Tessa Sou[1], U. Rashid Sumaila[2], Paul Suprenand[9], Travis C. Tai[2] and David L. VanderZwaag[10]*

[1] Institute of Ocean Sciences, Fisheries and Oceans Canada, Sidney, BC, Canada, [2] Institute for the Oceans and Fisheries, University of British Columbia, Vancouver, BC, Canada, [3] Sheluqun Environmental, Saltspring, BC, Canada, [4] School of Earth and Ocean Sciences, University of Victoria, Victoria, BC, Canada, [5] Institute for Marine and Antarctic Studies, University of Tasmania, Hobart, TAS, Australia, [6] Centre for Earth Observation Science, University of Manitoba, Winnipeg, MB, Canada, [7] Freshwater Institute, Fisheries and Oceans Canada, Winnipeg, MB, Canada, [8] Joint Secretariat, Inuvialuit Settlement Region, Inuvik, NWT, Canada, [9] Mote Marine Laboratory, Sarasota, FL, United States, [10] Schulich School of Law, Dalhousie University, Halifax, NS, Canada

OPEN ACCESS

Edited by:
Benjamin Allen Lange, Freshwater Institute, Fisheries and Oceans Canada, Canada

Reviewed by:
Maria Vernet, University of California, San Diego, United States
Ute Daewel, Helmholtz Centre for Materials and Coastal Research (HZG), Germany

***Correspondence:**
Nadja S. Steiner
nadja.steiner@dfo-mpo.gc.ca

Specialty section:
This article was submitted to Global Change and the Future Ocean, a section of the journal Frontiers in Marine Science

Received: *26 September 2018*
Accepted: *20 March 2019*
Published: *10 April 2019*

Citation:
Steiner NS, Cheung WWL, Cisneros-Montemayor AM, Drost H, Hayashida H, Hoover C, Lam J, Sou T, Sumaila UR, Suprenand P, Tai TC and VanderZwaag DL (2019) Impacts of the Changing Ocean-Sea Ice System on the Key Forage Fish Arctic Cod (Boreogadus Saida) and Subsistence Fisheries in the Western Canadian Arctic—Evaluating Linked Climate, Ecosystem and Economic (CEE) Models. Front. Mar. Sci. 6:179. doi: 10.3389/fmars.2019.00179

This study synthesizes results from observations, laboratory experiments and models to showcase how the integration of scientific methods and indigenous knowledge can improve our understanding of (a) past and projected changes in environmental conditions and marine species; (b) their effects on social and ecological systems in the respective communities; and (c) support management and planning tools for climate change adaptation and mitigation. The study links climate-ecosystem-economic (CEE) models and discusses uncertainties within those tools. The example focuses on the key forage species in the Inuvialuit Settlement Region (Western Canadian Arctic), i.e., Arctic cod *(Boreogadus saida)*. Arctic cod can be trophically linked to sea-ice algae and pelagic primary producers and are key vectors for energy transfers from plankton to higher trophic levels (e.g., ringed seals, beluga), which are harvested by Inuit peoples. Fundamental changes in ice and ocean conditions in the region affect the marine ecosystem and fish habitat. Model simulations suggest increasing trends in oceanic phytoplankton and sea-ice algae with high interannual variability. The latter might be linked to interannual variations in Arctic cod abundance and mask trends in observations. CEE simulations incorporating physiological temperature limits data for the distribution of Arctic cod, result in an estimated 17% decrease in Arctic cod populations by the end of the century (high emission scenario), but suggest increases in abundance for other Arctic and sub-Arctic species. The Arctic cod decrease is largely caused by increased temperatures and constraints in northward migration, and could directly

impact key subsistence species. Responses to acidification are still highly uncertain, but sensitivity simulations suggests an additional 1% decrease in Arctic cod populations due to pH impacts on growth and survival. Uncertainties remain with respect to detailed future changes, but general results are likely correct and in line with results from other approaches. To reduce uncertainties, higher resolution models with improved parameterizations and better understanding of the species' physiological limits are required. Arctic communities should be directly involved, receive tools and training to conduct local, unified research and food chain monitoring while decisions regarding commercial fisheries will need to be precautionary and adaptive in light of the existing uncertainties.

Keywords: climate change, Arctic cod, subsistence fisheries, Canadian Arctic, Arctic change, Arctic ecosystems

1. INTRODUCTION

The Inuvialuit peoples maintain the link to their traditional way of life through their harvesting practices. Hunting, fishing and trapping are both subsistence and economic activities. The foods harvested from the land and ocean are an integral dimension of their diet and the harvest byproducts support thriving economies based on arts and cultural activities. Hence, potential changes to subsistence harvest species are highly relevant to them.

The Arctic Monitoring and Assessment Program (AMAP) report on Adaptation Actions in a Changing Arctic (AACA) in the Bering, Chukchi and Beaufort Sea (AMAP, 2017) states that, based on scientific observations and Indigenous knowledge (IK), the region is moving toward conditions never witnessed before. Environmental drivers related to seasonal loss of sea ice and water temperature have led to changes in the distribution of ice-dependent or ice-associated marine mammals and birds and initiated changes in migratory pathways and phenologies of mammals and fish, causing changes in species composition and season of harvests. Some coastal communities are impacted as availabilities of subsistence species are changing or have changed or moved beyond the geographic reach of harvesters (Loseto et al., 2018). Access complications are also linked to changes in weather, storms and sea state (e.g., Steiner et al., 2015a) which have made the sea rougher, less predictable and more dangerous for small boat travel. AMAP (2017) lists human health issues, such as obesity, diabetes and heart disease, which have already impacted coastal communities due to loss of the subsistence life style (see also Inuit health survey, e.g., Galloway et al., 2010; Egeland et al., 2011; Zhou et al., 2011; Saudny et al., 2012; Zienczuk and Egeland, 2012). AMAP (2017) suggests that restructuring of harvesting strategies in response to changes in the species composition and availability of the subsistence food resources might be inevitable (see also Ford, 2009; Ford and Pearce, 2010; Ford et al., 2014).

This study synthesizes previous (section 2) and new results (section 4) from observations, laboratory experiments and model tools to help understand how Arctic cod *(Boreogadus saida)*, a key forage fish for subsistence species in Arctic communities, might be affected by climate change and ocean acidification. The example provided focuses on the Inuvialuit Settlement Region (ISR) in the Western Canadian Arctic and highlights how the combination of multiple tools based on Scientific Methods (SM) and Indigenous knowledge can improve our understanding of (a) past and projected changes in environmental conditions and marine species, (b) how these might affect specific social and ecological systems in the communities of a particular region, and (c) how to inform management and planning tools for adaptation and mitigation. The study includes an effort to directly link available climate-ecosystem-economic (CEE) models (e.g., Sumaila et al., 2019) and discusses uncertainties within those models.

2. BACKGROUND

2.1. Study Area

The ISR was established in 1984 under the Inuvialuit Final Agreement by the Government of Canada and the Inuvialuit. The ISR includes the north slope of the Yukon and northern North West Territory, the inland delta communities Inuvik and Aklavik on the mainland, Tuktoyaktuk and Paulatuk along the mainland coast, Ulukhaktok on the northwestern coast of Victoria Island and Sachs Harbour on the western coast of Banks Island (**Figure 1**). The associated oceanic regions include the Beaufort Sea, composed of shallow shelves and the deep (up to 3,600 m) Canada Basin, and the western part of the Canadian Polar Shelf (CPS), which includes the Amundsen and Coronation Gulf. While sea ice shows significant reductions in the Beaufort Sea, the CPS in many areas acts as a repository or reservoir of thick ice. An overview of the oceanography of the region and recent and projected future environmental changes is provided in Steiner et al. (2015a). The active collaboration between the Inuvialuit and the Government of Canada includes a network planning process for marine protected areas (MPAs) which supported the recent establishment of the Anguniaqvia niqiqyuam, ANMPA, (est. 2016) in addition to the Tarium Niryutait, TNMPA, (est. 2010) (**Figure 1**, Loseto et al., 2018). The TNMPA is an important summer habitat for the Eastern Beaufort Sea beluga and a diverse range of fish species. Both MPAs have the conservation objective to maintain habitat and support populations of key species such as beluga whales, Arctic char, and ringed and bearded seals. The

co-management structure of the ISR together with the ecological importance of the area which is exhibiting some of the largest changes in sea-ice and other environmental factors within the Arctic, makes this an ideal case study area.

2.2. Focus Species Arctic Cod *(Boreogadus saida)*

In order to bridge model projections of sea-ice and other environmental changes to the impacts on harvested subsistence species, particular emphasis was given to the key forage fish species Arctic cod. Arctic cod is considered an ecological key species, because of its high stock biomasses and its importance as a carbon source for seabirds, fish and marine mammals in high Arctic ecosystems (Bradstreet et al., 1986; Coad and Reist, 2004; Kohlbach et al., 2017), many of which are key subsistence species harvested by Inuvialuit communities and are included in the MPA conservation objectives. Studies in the Beaufort Sea have reported Arctic cod as the most abundant demersal species across a range of habitats (Rand and Logerwell, 2010; Majewski et al., 2013; Walkusz et al., 2013). A recent assessment of fish assemblages in the Beaufort Shelf and Slope (Beaufort Sea Marine Fishes Project) indicates that Arctic cod typifies each of the four species assemblages (near-shore shelf, off-shore shelf, upper slope, lower slope) to varying degrees. High abundance of Arctic cod ($\approx$ 80%) at upper-slope stations was a major structuring feature of the fish community (Majewski et al., 2013, 2015, 2017). Under-sea ice habitats host unique food webs that Arctic cod can access due to their cold adaptation. Arctic cod survive in ice-covered, sub-zero waters due to the presence of anti-freeze glycoproteins, specialized kidney function (Osuga and Feeney, 1978; Christiansen et al., 1996) and the ability to digest food at -1.4°C water temperatures (Hop and Tonn, 1998). Arctic cod are generalist feeders and will eat what is available and digestible. Young Arctic cod (1–2 years) are often associated with the underside of sea ice where ice-associated (sympagic) amphipods and copepods (at all life stages) are key prey species (Bradstreet and Cross, 1982; Lønne and Gulliksen, 1989; David et al., 2015, 2016; Kohlbach et al., 2016, 2017). Under ice Arctic cod larvae mainly feed on copepod eggs and naupli (Walkusz et al., 2011) but 26% of their stomach contents can comprise of ice algal cells (Gilbert et al., 1992). Fatty acid profiles of Arctic cod further indicate that (ice algal) diatoms are the primary carbon source, indirectly obtained via amphipods and copepods (Kohlbach et al., 2017). This indicates a high importance of ice-algae produced carbon in early Arctic cod development, but also suggests a particular vulnerability to changes in the distribution and structure of sea-ice habitats. Arctic cod predation efficiently moves a large proportion of the energy and nutrients from Arctic algae and invertebrates to higher trophic levels (Bain and Sekerak, 1978; Welch et al., 1993; Crawford and Jorgenson, 1996; Christiansen et al., 2012; Hop and Gjøsæter, 2013). Due to the key role of Arctic cod, changes at the base of the sea ice-associated food web are likely to affect the higher trophic levels of high-Arctic ecosystems and hence the communities harvesting those species.

2.3. Aquatic Species Physiological Limits

A major gap in determining ecosystem risks and fisheries impacts of climate change (e.g., increased temperature, sea ice/habitat loss, noise, pollution) and ocean acidification is the limited information on physiological limits of key Arctic marine species to single and multiple stressors. As part of this project, we synthesized available literature into a database of Aquatic Species Physiological Limits (ASPL) for Arctic and sub-Arctic species indicating available information on species thresholds, lethal limits and acclimation potential for several stressors as well as sub-chronic thresholds that are termed "pejus" limits (tipping points when metabolic performance begins to decline). The ASPL database has been summarized in a technical report (Steiner et al., 2018) and entries for Arctic cod and capelin are shown in **Table 1**. The database includes data for cardio-respiratory performance of ectotherm species which is a powerful tool to quantify the impact of environmental stress upon animal health (Farrell et al., 2008; Anttila et al., 2013; Ferreira et al., 2014; Drost et al., 2016; Farrell, 2016). The impact of global warming on the physiology of ectotherm marine species (e.g., fish, copepods, bivalves) is of particular concern due to an ectotherms total reliance on habitat temperature to maintain body heat. Temperature drives metabolism and hence basic performance including development, growth, reproduction and survival (Brown et al., 2004). In addition the physiology and ecology of fish can also be impacted by other factors such as sea water pH (i.e., ocean acidification), e.g., acid excretion across gills is dependent upon water pH.

Only few laboratory-based thermal tolerance studies of Arctic cod exist and even fewer quantify the impact of multi-stressors (Kunz et al., 2016, 2018; Leo et al., 2017). **Table 1** indicates the known physiological limits for Arctic cod and capelin, in comparison. Drost et al. (2016) showed that after 1 month acclimation at 6.5°C water temperature, Arctic cod can actually improve their cardio-respiratory performance, essentially increasing aerobic scope capacity in water warmer than expected. Clearly these fish have some capacity for thermal acclimation and a greater than expected thermal performance of larvae and adult Arctic cod, which suggests that temperature may not be the sole dictator of their biogeographic range. It appears that the under-ice ecosystem they are associated with serves as a critical component of their biographic distribution and survival.

2.4. Observed Changes in Forage and Subsistence Species

Empirical observations already indicate a northward retreat of Arctic cod from their southern-most distributions, e.g., waters off Disko Bay, Greenland, Iceland-East Greenland waters, the Barents Sea, Cooper Island, Bering Sea and in the ISR (Hansen et al., 2012; Farrell et al., 2013; Astthorsson, 2015; Divoky et al., 2015; Harwood et al., 2015, and pers. comm. Rubin, 2017). Analyzing body condition since the late 1980s in five marine vertebrate species, Harwood et al. (2015) identified ringed seal, beluga, black guillemot chicks, all consumers with a dietary preference for Arctic cod, experience declines in condition, growth and/or production. Over the same time period they found

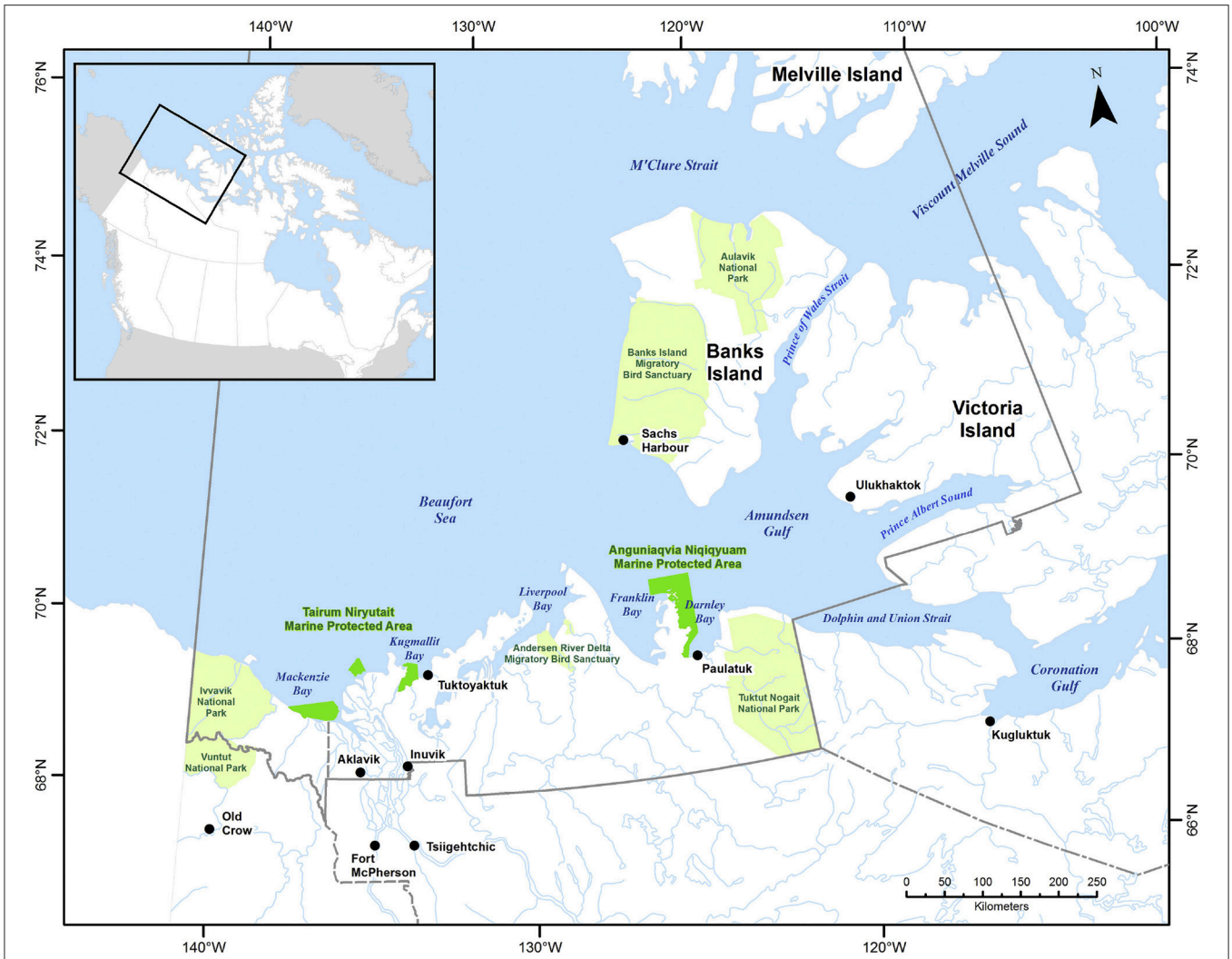

FIGURE 1 | Geographic representation of the Western Canadian Arctic and the Inuvialuit Settlement Region (ISR). The Tarium Niryutait Marine Protected Area (TN MPA, made up of three separate parcels in the Mackenzie Estuary) and the Anguniaqvia Niqiqyuam Marine Protected Area (AN MPA, located in Darnley Bay are indicated in dark green, national parks and park reserves are shown in light green. The ISR boundary is shown in solid gray. Reproduced from Loseto et al. (2018) with permission from Elsevier.

increasing body condition in bowhead whale (sub-adults) and (Arctic char), in both cases influenced by sea ice. Reductions of summer sea ice extent, including increased duration of open water, changes in upwelling potential (wind stress), and possibly higher primary production in the marine ecosystem favor herbivorous zooplankton that are targeted by bowheads (e.g., Lowry et al., 1978; Walkusz et al., 2012; Nelson et al., 2014). Northward spread of Pacific zooplankton into the Beaufort Sea has also been recognized (Nelson et al., 2009, 2014). Stomach contents indicate the diet of Arctic char includes a substantial number of Arctic cod in some years and is dominated by zooplankton in other years (Harwood, Drost, unpublished data). Harwood et al. (2015) state that the proximate causes of the observed changes in body condition remain unknown, but may reflect an upward trend in secondary productivity (zooplankton), and a concurrent downward trend in the availability of forage fishes, such as the preferred Arctic cod. Among other factors, the body condition of marine vertebrates is directly linked to the total annual availability and quality of their prey, with nutritional stress ultimately linked to health of individuals and populations (Moore and Gulland, 2014).

2.5. Foodweb Structure Around Arctic Cod

An analysis of past ecosystem and foodweb changes in the Beaufort Sea with the Ecopath with Ecosim (EwE) modeling tool (see section 3) has been performed by Suprenand et al. (2018), indicating already occurring food-web shifts and tipping points relevant to Arctic cod and higher trophic level species.

The EwE results suggest increases in biomass for both the Arctic cod and capelin model groups (Suprenand et al., 2018). These increases in model biomass are primarily driven by increases in primary production caused by warmer temperatures

TABLE 1 | Physiological limits extract from Aquatic Species Physiological Limits database (Steiner et al., 2018).

Common name	Critical lower temperature	Lower pejus temperature	Optimum temperature	Upper pejus temperature	Critical upper temperature	Critical lower pH	References
Arctic cod	-1.9 (assumed)	Adults: 0.2 (AT:0.5) 1.6 (AT:3.5) 5.4 (AT:6.5)	Adults: 1.0 (AT:0.5) 3.5 (AT:3.5) 5.4 (AT:6.5) Larvae: 3.3 (AT:3.5)	Adults: 10.8 (AT:0.5) 12.3 (AT:3.5) 10.9 (AT:6.5) Spawning 3.5	LOE-Adults: 14.9 (AT:0.0) 15.5 (AT:3.5) 17.1 (AT:6.5)	Similar proton leak and ATP production for ACO_2 of 400 μatm and 1170 μatm	Drost et al. (2014), Kunz et al. (2016), Laurel et al. (2015), Leo et al. (2017)
Capelin	-1.5	0.0	Adults:(-1)-6 Juveniles: 5-7 Larvae:4.5-9 Hatching:1-19 Spawning: 2.5-10.8	Adults: 14 Juveniles: 10			Rose (2005), Rose and Leggitt (1990), Fortier and Leggett (1985)

Temperatures are given in °C, AT indicates acclimation temperature and ACO_2 indicates acclimation partial pressure of CO_2. LOE indicates loss of equilibrium.

and longer open water seasons, which increase the trophic pathways for species favoring warmer water. Arctic cods' biomass is positively influenced by small primary producers (< 5 μm in the model), microzooplankton, and some mesozooplankton functional groups as Arctic cod consume these functional groups. According to the model's historic reconstruction from 1970 to 2014, ringed seals (whose diet is 12% Arctic cod) are becoming increasingly reliant on Arctic cod as prey, which constitute a large percentage of their overall diets. In addition, polar bears, who consume ringed seals, act to limit ringed seals predatory pressure on Arctic cod, thus yielding an indirect positive influence overall. If a sudden decrease in the ecosystem energetic contributions from Arctic cod occurs as the Beaufort Sea warms, higher trophic level predators (beluga whales, ringed seals, Arctic char) reliant on Arctic cod (Bradstreet et al., 1986; DFO, 1999; Loseto et al., 2009) will have to alter their prey, possibly to include sub-Arctic species such as capelin (Rose, 2005; Walkusz et al., 2013). Capelin are still considered low abundance in the region (1970 EwE model biomass 0.105t km^{-2}), compared to Arctic cod (1970 EwE model biomass 0.651t km^{-2}); however, they co-occur across the Beaufort Sea and have dietary overlaps with Arctic cod (Panasenko and Soboleva, 1980; Cobb et al., 2008; Mcnicholl et al., 2016). In the Beaufort Sea, both species are modeled to increase in both biomass and trophic level (TL), with these increases attributed to bottom-up changes in the food web, primarily driven by increases in sea surface temperature, a longer open water season, and increases in warm-water lower TL species. Slight increases in TL from 1970-2014 for cods (3.45 to 3.46) and capelin (3.45 to 3.51) are due to larger proportions of the diet from herring and smelt (TL = 3.08), macro-zooplankton (TL = 2.64), and reductions of colder-water species such as large copepods (TL = 2.306). Note, in the EwE model, primary producers and detrital groups are assigned a TL of 1, and consumers with a diet comprised entirely of primary producers have a TL of 2 (primary consumers). Each predator TL is calculated based on the proportion (X) of each prey item (a,b,c) and the TL of these prey items (TLa, TLb, TLc). Furthermore, while capelin are consumed by marine mammals in other Arctic regions (Bluhm and Gradinger, 2008), their importance to marine mammals (beluga whales and ringed seals) in the Beaufort Sea has not been noted until recently (Choy et al., 2016). Increases in capelin as a forage fish have occurred in Hudson Bay (Gaston et al., 2003) and the Barents Sea (Hop and Gjøsæter, 2013), with the potential to at least partially replace Arctic cod (Hoover et al., 2013a,b), highlighting the potential for large increases in the Beaufort Sea. However, the energetic contributions of Arctic cod and capelin are similar (5-7 $kJ\ g^{-1}\ ww$ vs. 4-5 $kJ\ g^{-1}\ ww$, respectively (Hop and Gjøsæter, 2013), with higher values up to 8.4 $kJ\ g^{-1}\ ww$ reported by Lawson et al. (1998) meaning energetic impacts from shifting diets to capelin from Arctic cod may not be as extreme as expected, assuming there are no ecological (predator-prey) barriers.

2.6. Fisheries in the Canadian Arctic

Fisheries harvest in Canada's Arctic is largely for subsistence purposes, providing key sources of food and nutrition for Inuit communities (Zeller et al., 2011). Information on the magnitude of seafood (and other country food) consumption by Arctic communities is critical for evaluating public health trade-offs between traditional subsistence harvest and imported (often processed) foods. Limited studies in the region indicate unclear recent (last 50 years) patterns in traditional food use in the communities (Berkes, 1990), but it is clear that their seafood consumption is markedly higher than in the general population. Based on a meta-analysis using available population and harvest data, in the Canadian Arctic some 70,000 people in 60 communities eat around 2,600 metric tonnes of seafood per year (Cisneros-Montemayor et al., 2016). While such studies help provide a sense of magnitude to coastal Indigenous seafood consumption, they also highlight the need for joining appropriate local research and observations with interdisciplinary modeling efforts in order to better inform climate and policy scenarios. Arctic commercial fisheries are very minor in Canada, but the increase in accessibility with ocean warming and decreasing sea-ice cover may encourage such development.

2.7. Climate Change and Acidification in the Western Canadian Arctic Ocean

Past environmental changes in the Western Canadian Arctic have been highlighted in recent assessments (e.g., Steiner et al., 2015a; AMAP, 2017) and show atmospheric and oceanic temperature increases, intense summer sea-ice retreat and thinning, particularly in the Beaufort Sea, as well as changes in stratification. In the Western Canadian Arctic the progression of ocean acidification is indicated by a significant northward expansion of waters with low aragonite saturation state, and upper halocline waters and deep waters now regularly showing aragonite undersaturation particularly in the off-shelf waters (Miller et al., 2014; Qi et al., 2016; AMAP, 2018).

Global Earth System Model (ESM) projections suggest the marine environment in the western Arctic is likely to experience large changes with suggested atmospheric temperature increases of 0–3°C in summer and 3–7°C in winter over the next 50 years (Steiner et al., 2015a). A multi-model analysis indicates different rates of sea-ice retreat in the region which cause differences in stratification and mixing, affecting exchanges with the atmosphere, such as heat uptake in summer. The models suggest reduced vertical mixing in the central Beaufort Sea, but increases to different degrees in the shelf areas (e.g., Steiner et al., 2014). Localized processes are likely to affect coastal regions much differently than the overall average over the Arctic region, causing some areas with greater or lesser changes in environmental conditions. The ESM projections also consistently show enhanced ocean acidification in the region with continuation over the next century, including accelerated reductions in calcium carbonate saturation state at least until the sea-ice cover reaches a new steady state with largely ice-free summers (Steiner et al., 2014). Projections with the high emission scenario (Representative Concentration Pathway, RCP8.5, see section3.1) forcing for the Canada Basin show reductions in the bidecadal mean surface pH from about 8.1 in 1986–2005 to 7.7 by 2066–2085, closely linked to reductions in the saturation states ($\Omega_{A,C}$) from about 1.4 (2.0) to 0.7 (1.0) for aragonite (calcite). The changes coincide with a decrease in sea-ice concentration (98% to 96% in winter and 60% to 3% in summer) and maximum mixed layer depth (by 5–10 m with high variability among the models) (Steiner et al., 2014). An analysis of future nutrients and primary production including 11 models (Vancoppenolle et al., 2013) indicates a consistent decrease in nutrients but increase in light for the area. The respective multi-model mean response shows an increase in the Beaufort Sea and even stronger increase in most of the CPS, however the models are inconsistent in their responses for primary production, depending on which of the two factors (light increase and nutrient decrease) has a more pronounced effect on the production. (Note that not all models have adequate resolution to resolve the CPS).

3. MATERIALS AND METHODS

The development of modeling tools in climate, ecosystem and fisheries research has made significant progress over the last two decades. Coupling and linking those tools can highlight impacts from climate change and other stressors for specific social-ecological contexts. In anticipation of significant changes in Arctic marine ecosystems, a co-production of knowledge (incorporating scientific methods, SM, and indigenous knowledge, IK) framework has been developed. This framework aims at improving the understanding of recent and forthcoming climate and ecosystem changes and their impacts at a community level, and identifying and supporting potential mitigation and adaptation measures. The framework represents a multi-step process combining modeling and analysis tools to both synthesize available knowledge and create new information. **Figure 2** indicates the various components with IK contributions in red, SM in blue, and a combination thererof indicated in purple. The steps include:

- Monitoring efforts providing information on past observed trends;
- Model simulations with global and regional climate models including future projections;
- Assessment of physiological responses and thresholds in marine species to help understand observed changes and provide input into models;
- Species distribution/habitat suitability, higher trophic level Ecosim/Ecopath models;
- Bio-economic models;
- Analysis of current subsistence fishery and economic activities in communities;
- Review of relevant laws and policies to assess how, e.g., adaptation measures on global, regional and national scales may impact the communities.

Observational monitoring efforts from SM and IK methods (ideally longterm) provide critical information of environmental conditions (including temperature, salinity, sea ice, nutrients, primary production etc.), which are used in regional and global climate models for validation and model development. In addition, monitoring efforts provide information on current species habitat as well as current fisheries-economic activities. Projection simulations with global and regional climate models provide information on potential future environmental and biogeochemical changes which can be used to assess potential physiological responses and thresholds in marine species. Simulated environmental changes, physiological responses and fisheries activities can then be fed into species distribution/habitat suitability and higher trophic level (EwE) models to assess potential changes in species distribution and abundance, species community structure and predator-prey interactions. Combining the output and information of all the above allows us to assess potential impacts of a changing ocean climate to socio-economic impacts on the community level. The latter can both influence and be affected by policy and governance, e.g., via fisheries regulations or conservation measures. Note that international policy decisions, e.g., related to carbon emissions can in turn affect the input into global climate projections (link not indicated in **Figure 2** for clarity).

Within the CEE model tool box, all the required tools have been developed, however due to their high complexity and computational demands not all components have been run out

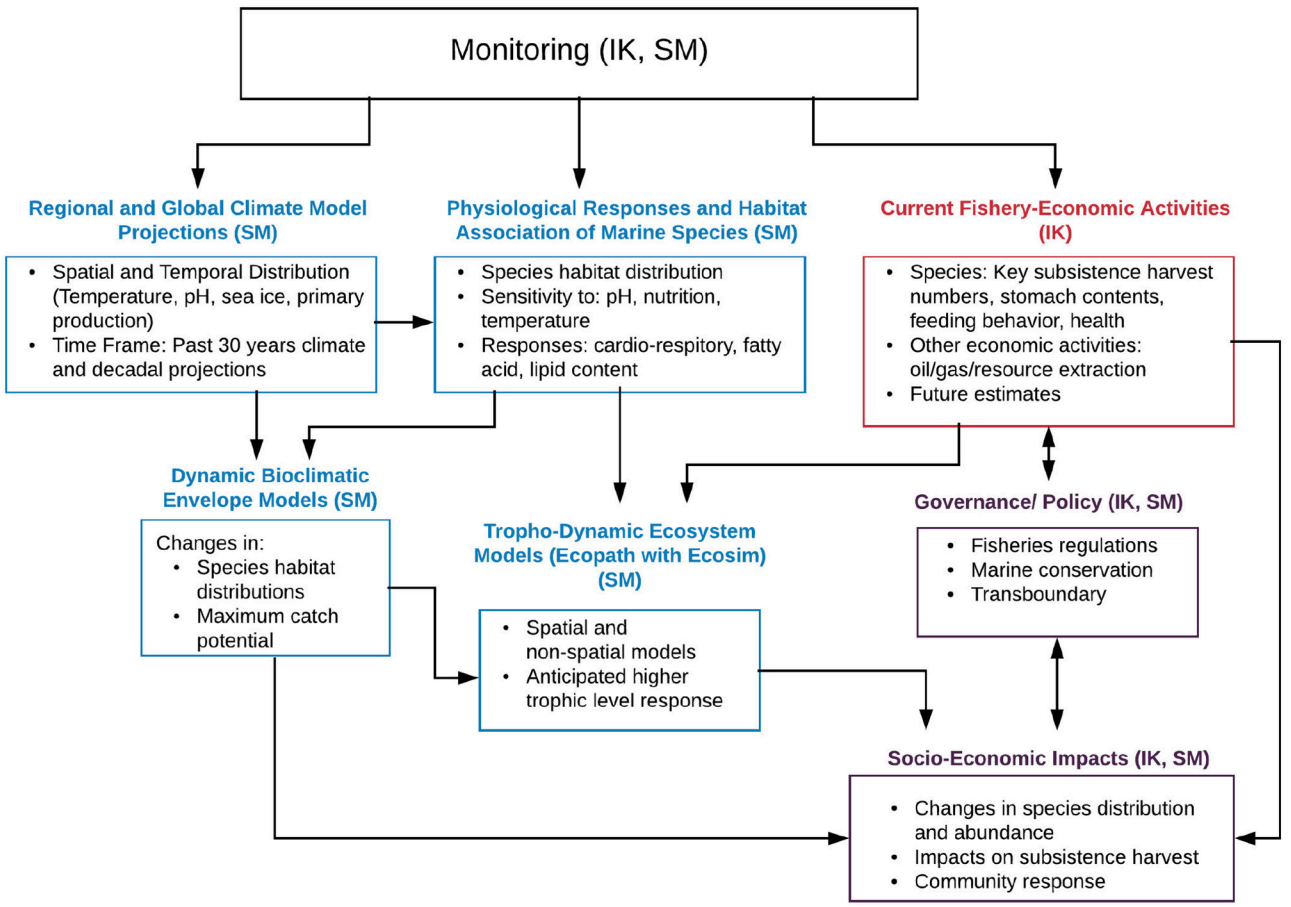

FIGURE 2 | Flow chart indicating a multi-step framework based on indigenous knowledge (IK, indicated in red) and scientific methods (SM, indicated in blue, efforts including both IK and SM input are indicated in purple). Monitoring efforts leading to observed trends are feeding into regional and global climate models for validation and model development, provide information on current species habitat as well as current fisheries-economic activities. Projection simulations with global and regional climate models in turn provide information on potential environmental and biogeochemical changes which can be used to assess physiological responses and thresholds in marine species. Simulated changes, physiological responses and fisheries activities can then be fed into species distribution/habitat suitability and higher trophic level (Ecopath with Ecosim) models. Combined output of all the above allows for the evaluation of socio-economic impacts on the community level. Additional impacts can be linked to or mitigated by policy and governance. Note that international policy decisions, e.g., related to carbon emissions can in turn affect the input into global climate projections (link not indicated in the schematic). Figure modified from AMAP (2018) with permission from AMAP.

for future simulations and/or adequately coupled yet, e.g., while higher resolution model projections are presented for the area, the habitat suitability and economic models are still driven by global climate models, the regional climate model with sea-ice algal representation as well as the Ecopath model have not yet been run out into the future and physiological responses are only limitedly reflected in the higher trophic level models. An uncertainty analysis and discussion of required refinements are provided in section 5. A summary of the applied model tools is provided in **Table 2**, indicating type and name of the model, resolution, timeperiod, ecosystem model components (for marine biogeochmistry models only). Also indicated is which other model the stated model is driving or feeding into. Links that have not yet been performed within this study, but will be included in future iterations are indicated in italics. Note that the food web model (EwE) has been implemented for the Beaufort Sea and evaluated in a previous study (Suprenand et al., 2018), but is included here, since it represents an essential component of the CEE tool box. The EwE model is currently being updated and will be directly linked in the next iteration to address potential future food web changes. The following sections provide some details of the CEE model components with additional detail in the **Supplementary Material**.

3.1. Global Earth System Models

Projecting future ecosystem responses to climate change, ocean acidification and other potential stressors requires the application of numerical ecosystem models. The 5th Coupled Model Intercomparison Project (CMIP5) included for the first time a variety of Earth System Models (ESMs, model systems with fully coupled atmosphere, ocean, sea ice, and land components including interactive biogeochemical modules for all components). Simulations from three different ESMs (Geophysical Fluid Dynamics Laboratory ESM, GFDL-ESM2G,

TABLE 2 | Description of models used in this study.

Model type	Model name	Resolution (ocean)	Ecosystem[a]	References	Time period	Source[b]	Feeds into[c]
ESM	MPI-ESM-MR	0.4°, 40 level	N3PZD	Giorgetta et al., 2013; Ilyina et al., 2013	2006–2100	CMIP5	DBEM
ESM	GFDL-ESM2M	0.3°-1°, 50 level	N4P3D	Dunne et al., 2012, 2013	2006–2100	CMIP5	DBEM
ESM	IPSL-CM5A-MR	0.5°-2°, 31 level	N5P2Z2D	Aumont et al., 2003; Dufresne et al., 2013	2006–2100	CMIP5	DBEM
ESM	CanESM2	1.4/0.9°, 40 level	NPZD	Christian et al., 2010; Arora et al., 2011	2006–2085	CMIP5, CCCma	CanRCM,NAA
Regional (ocean)	NAA-CMOC	0.25°, 40 level	NPZD	Steiner et al., 2015b	2006–2085	This study	*DBEM,EwE*
Regional (ocean)	NAA-CanOE-CSIB	0.25°, 40 level	N2P2Z2D2+N2P[d]	Hayashida et al., 2018	1979–2015	This study	*DBEM,EwE*
Regional (atmos.)	CanRCM4	0.5°	–	Scinocca et al., 2015	2006–2086	CORDEX,CCCma	NAA
Foodweb	EwE[e]	0.5°	–	Suprenand et al., 2018	2006–2100	Previous study	*DBEM, Economic*
DBEM	–	0.5°	–	Cheung et al., 2008, 2011, 2016	2005–2100	This study	Economic
Economic	Fish price database	0.5°	–	Sumaila et al., 2007		2006–2100	This study

[a]Ecosystem complexities are indicated via numbers of nutrient (N), phytoplankton (P), zooplankton (Z) and detritus (D) groups.

[b]If model output is obtained from a data repository, links are provided in data availability information.

[c]Indicates which other model the stated model is driving or feeding into. Indicated in italics are links that have not yet been performed within this study, but will be included in the future.

[d]Includes sea-ice biogeochemistry.

[e]Foodweb model implemented and evaluated in previous study.

Institut Pierre Simon Laplace low-resolution ESM, IPSL-CM5A-MR, Max Planck Institute for Meteorology, MPI-ESM-MR) and two different scenarios were used as environmental input data for the dynamic bioclimatic envelope model (DBEM) to provide projections of species distribution and abundance. Multiple models and scenarios were used to estimate uncertainty ranges (see section 5.1.1). The three ESMs differ in their resolution, parameterizations and model structure (see **Table 2**) resulting in dissimilarities in key biophysical drivers, i.e., primary production (Stock et al., 2011; Vancoppenolle et al., 2013), sea-ice cover and acidification (Steiner et al., 2014). With each ESM, two contrasting Representative Concentration Pathways (RCPs Moss et al., 2010) with differing greenhouse gas concentration forcings were used to evaluate biophysical responses of marine organisms. The first is the current "business-as-usual" trajectory, projecting to increase global sea surface temperature by 3.5°C by the end of the century relative to pre-industrial temperatures (RCP 8.5), while the second conforms to the Paris Agreement targets of limiting temperature increases to 1.5°C (RCP 2.6). We refer to the RCP 2.6 and RCP 8.5 scenarios as low and high CO_2 scenario, respectively. In addition, output from the Canadian Earth System Model version 2 (CanESM2, **Table 2**) for the high CO_2 scenario (RCP8.5) serves as boundary condition for the atmosphere-only Canadian regional climate model (CanRCM4), which in turn provides the amospheric forcing for the regional ocean model discussed below. The CanESM2 and CanRCM4 modules for the atmosphere use the same dynamical core, but different resolution which allows for consistency in the boundary forcing. CanESM2 does not provide output for oxygen, hence could not be included in the DBEM projections.

3.2. Ocean Ecosystem Models

The fairly coarse horizontal and vertical resolution of ESMs restricts the ability to resolve biological or chemical processes happening in the euphotic zone and on coastal shelves as well as small-scale physical processes important for biogeochemistry. Hence regional climate models (RCM) and basin-scale models need to be developed. So far these models are only limitedly available. We are presenting results from the North Atlantic Arctic (NAA) Model, a regional model for the Arctic with highest resolution in the Canadian Arctic. The model is based on the Nucleus for European Modeling of the Ocean (NEMO) coupled to the Louvain-la-Neuve sea Ice Model version 2 (LIM2) in the configuration by Hu and Myers (2013, 2014). The model is coupled to a low and a high complexity ecosystem model. The low complexity ecosystem component is the Canadian Model for Ocean Carbon (CMOC; Zahariev et al., 2008) which is the same module as in CanESM2. CMOC shows good correspondence with observed chlorophyll features in the Canada Basin for the NAA and CanESM2 configuration (Steiner et al., 2015b). NAA-CMOC has been forced with output from CanRCM4 with 22 km resolution to simulate the years 2006–2085.

NAA has now also been coupled with the higher complexity pelagic Canadian ocean ecosystem model (CanOE) and the Canadian sea-ice biogeochemistry model (CSIB) (Hayashida, 2018; Hayashida et al., 2018), which allows a more direct link to ice associated species feeding directly or indirectly (via

sympagic zooplankton grazers) on ice algae, i.e., Arctic cod. NAA-CanOE-CSIB has been run from 1969 to 2015 to investigate the interannual variability and trends in sea-ice and pelagic primary production in recent decades in the Arctic Ocean. The spin-up years 1969–1978 were excluded from the analysis. This model version has not yet been run out for future scenarios. Additional details for model, forcing and input data are provided in the **Supplementary Material**.

3.3. Food Web Model (Ecopath)

In order to link environmental drivers with impacts to the food web as a whole, the Ecopath with Ecosim (EwE) modeling software provides a suitable tool. The EwE model enables impacts to species or species groups within the food web to be assessed including multiple stressors such as direct (harvest and predation mortality) and indirect (environmental changes or shifts in prey items) impacts (Pauly et al., 2000; Christensen and Walters, 2004). The EwE software is comprised of three main components: The Ecopath component provides the instantaneous snap-shot of the energy balance between predator-prey relationships, the Ecosim component performs temporal simulations utilizing multiple drivers at once if necessary, and the Ecospace allows for spatial and temporal simulations for the ecosystem model (Christensen and Walters, 2004; Christensen et al., 2007).

The Beaufort Sea EwE model was created for an area containing the ISR and the eastern portion of the Alaskan Beaufort Sea) for the 1970s time frame (Suprenand et al., 2018). It considers 36 functional groups, including single species and aggregated groups of species, ranging from top predators (marine mammals) to primary producers and detritus, covering taxa throughout the food web. The Ecopath "snap-shot" of material fluxes are used to account for the energy of the system using a mass-balance approach, whereby production of a species group is determined for all components of the food web, and linked through diet proportions connecting species through predator-prey interactions. Adding in layers to account for harvest and environmental changes allows users to account for responses by functional or species groups to multiple stressors simultaneously. We are currently developing the protocol to directly link the NAA-CanOE-CSIB model with the EwE and species distribution models, however, no new analysis of the EwE model has been performed within this study. As an intermediate step, information on how the ecosystem structure and function changed over time with relevance to this study and Arctic cod in particular has been extracted from Suprenand et al. (2018) and summarized in section 2.5 above.

3.4. Species Distribution Model

A dynamic bioclimatic envelope model (DBEM, Cheung et al., 2008, 2011, 2016) was used to project the spatial and temporal change in species distributions and abundances due to changes in habitat and environmental conditions. ESMs are used as inputs for environmental change. The DBEM integrates ecophysiological growth (Cheung et al., 2011) and population growth (Pauly, 1980) models to simulate changes in biomass, while advection-diffusion (Sibert et al., 1999) and habitat suitability (Cheung et al., 2008) models determine spatial movements. It uses a global grid with a resolution of 0.5° longitude by 0.5° latitude. Thus, populations grow and move based on gradients of environmental suitability (e.g., temperature, oxygen, acidification, salinity, primary production) and carrying capacity, and we can expect population to shift in space and time to optimize areas where habitat is more suitable and potential for population growth is higher.

The full DBEM model version spans the Chuckchi Sea, Beaufort Sea, Canadian Polar Shelf, and Baffin Bay, and includes a total of 82 marine species (57 finfish and 25 invertebrate species). Species-specific data to parameterize the DBEM were collected from FishBase (Froese and Pauly, 2018) and SeaLifeBase (Palomares and Pauly, 2018). Invertebrates were modeled to respond to changes in acidity, in addition to other climate-related drivers such as temperature and oxygen concentration. Meta-analyses have shown evidence of negative (Munday et al., 2009; Baumann et al., 2012) and small to negligible (Kroeker et al., 2013) effects of acidification on growth and survival in marine finfish species, but most invertebrate species groups showed some level of sensitivity to acidification (Kroeker et al., 2013). (Additional details on the DBEM are provided in the **Supplementary Material**.)

Current evidence shows that there are negligible to minimal effects of ocean acidification on Arctic cod growth or survival (Kunz et al., 2016). However, similar studies have found evidence of behavioral and biochemical changes with acidification, especially when combined with other stressors such as temperature (Leo et al., 2017; Schmidt et al., 2017). Due to this uncertainty surrounding effects of acidification, we tested the sensitivity of Arctic cod abundance to changes in acidity. For every 100% increase in acidity (hydrogen concentration), ocean acidification was modeled to negatively affect both growth and survival by 10, 20, and 30%. While these values may be greater than what has been observed in Arctic cod growth and survival, it provides a measure of the relative weight of ocean acidification effects on abundance and distribution in a multistressor context.

The DBEM assesses shifts in species distribution based on (a) the change in environmental conditions which are favorable to each species, and (b) the carrying capacity (maximum attainable biomass) in each grid cell. The DBEM is developed on a grid and resolutions similar to climate models, but it does not include trophic interaction among species. It can be used to inform economic models which assign a monetary value to the fisheries changes or potential. In comparison, the EwE model assesses potential changes across the food web based on (a) changes in environmental conditions, (b) fisheries impacts, and (c) how these impacts are propagated throughout the food web. EwE models are often regionally averaged (1-dimensional) or include a very coarse spatial separation, which essentially applies the same food-web linkages on smaller domains and combines the results afterwards in a spatial map. The two methods complement each other and can provide different aspects of change. They can also be combined when spatial components of the EWE model are developed and linked to the DBEM, which then incorporates how the entire food web could change spatially.

In it's current state the DBEM has not yet been set up to run with input from the higher resolution model due to

inconsistencies in the grid and areal coverage. This will be addressed in a second iteration of the process.

3.5. Economic Model

Changes in distribution and abundance from the DBEM for each species were used to estimate changes in fisheries catch potential, which assumes that annual catch potential is equal to the maximum sustainable yield. The DBEM results were used to assess downstream effects to Arctic communities as drivers of socioeconomic indicators such as food security (i.e., catch potential) and revenues (i.e., landed values) and to provide an assessment of the potential scale of Arctic fisheries in the reference time period (2001–2010), as well as the potential change expected in the future (2091–2100). Ex-vessel prices (i.e., price of catch at the first point of sale) were weighted and averaged across the countries that reported respective catch and averaged for the 2001–2010 reference period to estimate the potential value of present and future Arctic fisheries. Prices for species were taken from a global ex-vessel fish price database (Sumaila et al., 2007; Tai et al., 2017). We used global average annual prices from the years 2001–2010, and corrected the prices to reflect inflation, purchasing power, and exchange rates. These prices were applied to estimates of annual landed value for the 2001–2010 and the 2091–2100 period.

4. RESULTS

4.1. Ocean Ecosystem Model Results: Recent Past

The pan-Arctic representation of NAA-CanOE-CSIB model has been evaluated in detail in Hayashida et al. (2018) and Hayashida (2018) and shows good correspondence with available observations. A more detailed analysis with respect to recent changes in the Western Canadian Arctic is included in the **Supplementary Material** (section S1.2). Arctic cod are tightly linked to the sea-ice habitat with young Arctic cod feeding under the ice on small zooplankton species that are feeding on ice algae. Hence, changes in ice algae production and distribution have direct impacts on the recruitment and distribution of Arctic cod. Models which include ice algae explicitly might therefore provide information that directly affects the distribution and abundance of Arctic cod. Simulated changes which might affect forage fish distribution and abundance and impact subsistence fisheries are evaluated here. The NAA-CanOE-CSIB simulations indicate the ISR as productive with respect to both ice algal and pelagic production. **Figures 3a,b** show the simulated production averaged from 1979 to 2015. Higher values are shown within the CPS than in the open Beaufort Sea (which is known for its low nutrient content). Averaged over the CPS, Beaufort Shelf and Beaufort Basin (**Figure 3c**), ice algae are suggested to increase in the CPS, but show little change in the Beaufort Shelf and Basin. Interannual variability over the CPS is high and seems to be increasing (**Figure 3d**). This might be a significant contributor to interannual changes in forage fish distribution and abundances. A regional trend analysis for the model suggests an increase in ice algae on the Beaufort Shelf and some part of the CPS in spring, but a decrease in some other parts over the period 1979–2015 (**Figure 4d**). This seems to a large part be related to a decrease in sea ice (**Figure 4b**) and snow thickness (**Figure 4a**) allowing enhanced light transmission. In the CPS several areas show increases in snow coverage in hand with a decrease in ice algae. Ice algae show hardly any change in summer which is not unexpected, since the ice algae bloom tends to be limited to spring season (**Figure 4d**). Phytoplankton production is suggested to have increased everywhere in the region both in spring and in summer (**Figures 4e,k**), particularly since the early 2000s (**Figure 3e**). This domain-wide increase appears to be tightly coupled to the vertical thinning (**Figures 4b,h**) and horizontal shrinking (**Figures 4c,i**) of sea ice, both of which lead to more light penetration into the water column. A consistent increase in ice mobility is indicated in spring (**Figure 4f**) and in some regions in summer (**Figure 4l**). In addition to the ice thinning and weakening, increased ice mobility further impedes cross-ice travel and hence access to traditional fishing grounds.

4.2. Ocean Ecosystem Model Results: Future Projections

Figure 5 shows some of the DBEM input variables for sea surface (upper panels) and sea bottom (lower panels) derived from the three ESMs (GFDL, IPSL, MPI) introduced above. Shown are regional averages across the region (shown in **Figure 9**) for all three models (thin lines) and the mean over all models (thick lines) for the high (RCP8.5, red) and low (RCP2.6, blue) emission scenarios. As expected the high emission scenario shows a much stronger response with significant temperature increases ($\approx$ 2.5°C for the surface and $\approx$ 0.8° for the bottom, **Figures 5A,D**), oxygen declines , likely related to temperature related decreases in solubility ($\approx$ -20μmol-L^{-1} and $\approx$-10μmol-L^{-1}, **Figures 5B,E**), and pH reductions ($\approx$ -0.5 and $\approx$ -0.2 for surface and bottom, respectively, **Figures 5C,F**). The NAA-CMOC is run under high CO_2 conditions (RCP8.5) and available from 2006 to 2085 (a portion of the ESM timeseries). An anomaly calculation for the NAA-CMOC using the regionally averaged values from 2006 to 2010 indicates the change in surface temperature and pH is within the range of the ESM models. Bottom temperature show a somewhat larger increase (1.2°C) and the NAA-CMOC bottom pH decrease is consistent with the ESM model mean. In the NAA-CMOC run, O_2 has been initialized with a value too low for the Arctic (177.6 mmol-O_2m^{-3}), hence surface O_2 increases until year 2046 when it starts to decline similar to the ESMs. As the deep ocean adjusts slower, the bottom O_2 increases the entire 80 year run. This error in the O_2 initialization does not affect the discussed NAA-CMOC results and has been corrected for NAA-CanOE-CSIB.

ESM results for the low emission scenarios show initially a similar change but level out after 2050 when interannual variability dominates any trends. The range among the models indicates the model uncertainty which needs to be taken into account when evaluating the DBEM outcomes. Projections performed with higher resolution ocean only models provide more detailed projections for the region, while showing very similar trends and Pan-Arctic patterns. NAA-CMOC simulations suggest a combination of changes which potentially affect the

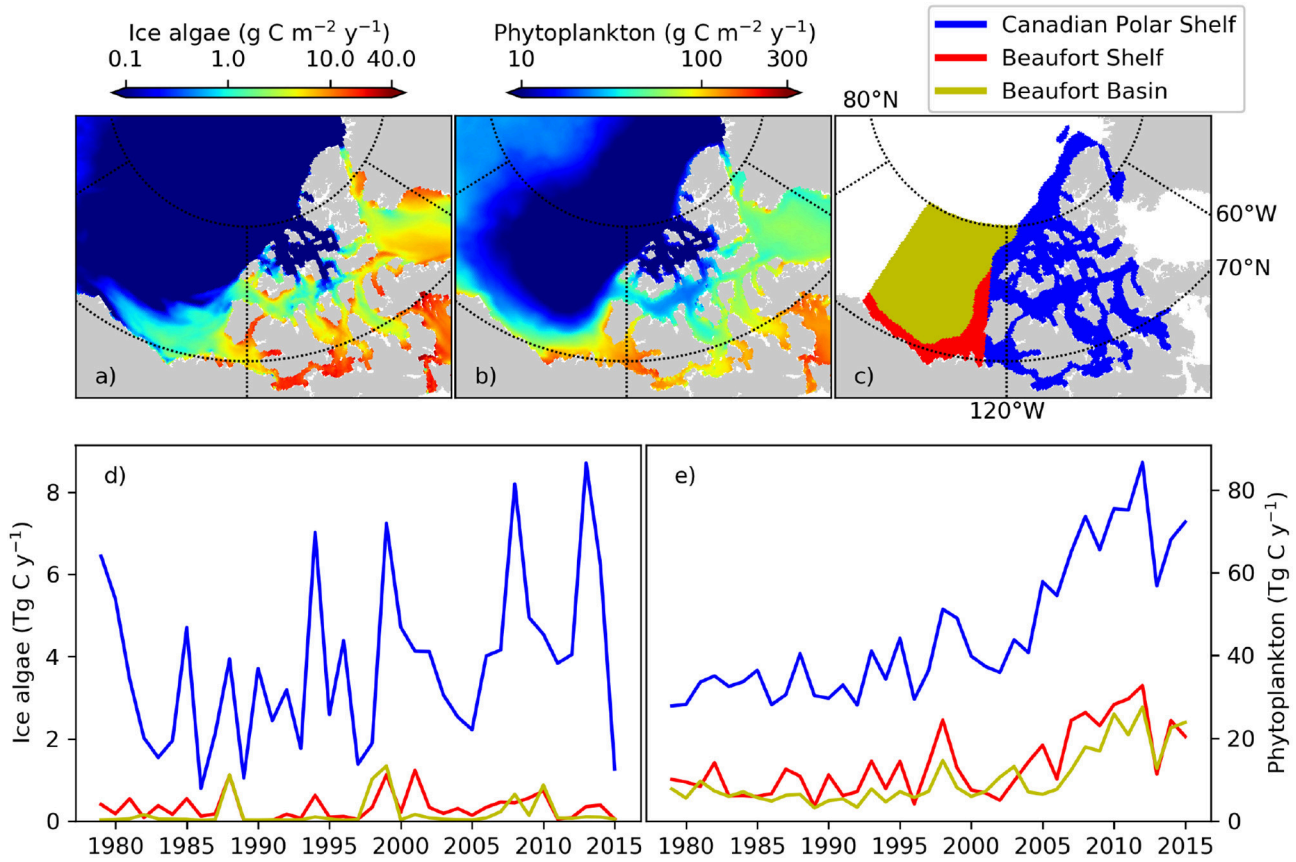

FIGURE 3 | (a) ice algal and **(b)** phytoplankton annual primary production in the Western Canadian Arctic averaged over the period 1979–2015 as simulated with the regional high resolution model NAA-CanOE-CSIB. **(c)** Areal definitions of three oceanographic subregions used for regional averaging. Time series of simulated **(d)** ice algal and **(e)** phytoplankton annual primary production integrated for each of the three subregions.

performance, abundance and phenology of marine species. **Figure 6** shows simulated ice concentration for the high emission scenario (RCP8.5) from 2010 to 2086 for winter (JFM) and summer (JAS) averaged over the (A) Northern Beaufort Sea, (B) Southern Beaufort Sea, and (C) the CPS. Ice concentration is projected to decrease mostly in summer (by -7%/decade), but also by some fraction (-2%/decade) in winter, which might have both positive and negative effects on species due to effects on habitat and primary production. Changes in the southern Beaufort Sea are much lower than in the other regions, since the area is already mostly ice free in summer by 2010. Ice thickness is simulated to continue decreasing at a rate of -(0.15–0.2)m/decade for all seasons, but with strongest declines in winter (not shown). Regional changes within the ISR, simulated with the same model (NAA-CMOC), are shown in **Figure 7**. Changes in summer over the 60 year time period from 2006–2025 to 2066–2085 are very low (**Figures 7a,b**), since the area already experienced significant ice thinning in the 90s and early 2000s. A continuous increase in sea surface temperature is simulated in the region and occurs across all depths in the Canadian Polar Shelf. The model suggest summer temperatures to increase by 4-6 °C within all of the ISR over a 60 year time period (**Figures 7c,d**). Progressing acidification is simulated in the ISR with decreases of −(0.3-0.4) for pH, −(0.6-0.9) for Ω_C, and −(0.4-0.6) for Ω_A (**Figures 7e,f**, Ω_a only). This indicates aragonite undersaturation for the whole region but surface waters remain supersaturated with respect to calcite. The projections also show a continuous decline across all depths over time for both $\Omega_{A,C}$. By 2066–2085 all of the central CPS is projected to be undersaturated with respect to Ω_A.

4.3. DBEM Results—Arctic Cod Distribution and Abundance

In the DBEM, projected changes are expressed in terms of Maximum catch potential (MCP). MCP is equal to the maximum sustainable yield of the projected abundance in the DBEM, equal to $rK/4$ where r is the intrinsic rate of population growth, and K is the carrying capacity. Projected changes in the overall MCP for the 82 modeled species are discussed in AMAP (2018) and indicate increases across the Canadian Arctic for the high emission scenario (overall increase by 35% from 2001–2010 to 2090–2100 for RCP8.5) and negligible effects for RCP2.6. Effects of ocean acidification on invertebrates reduced

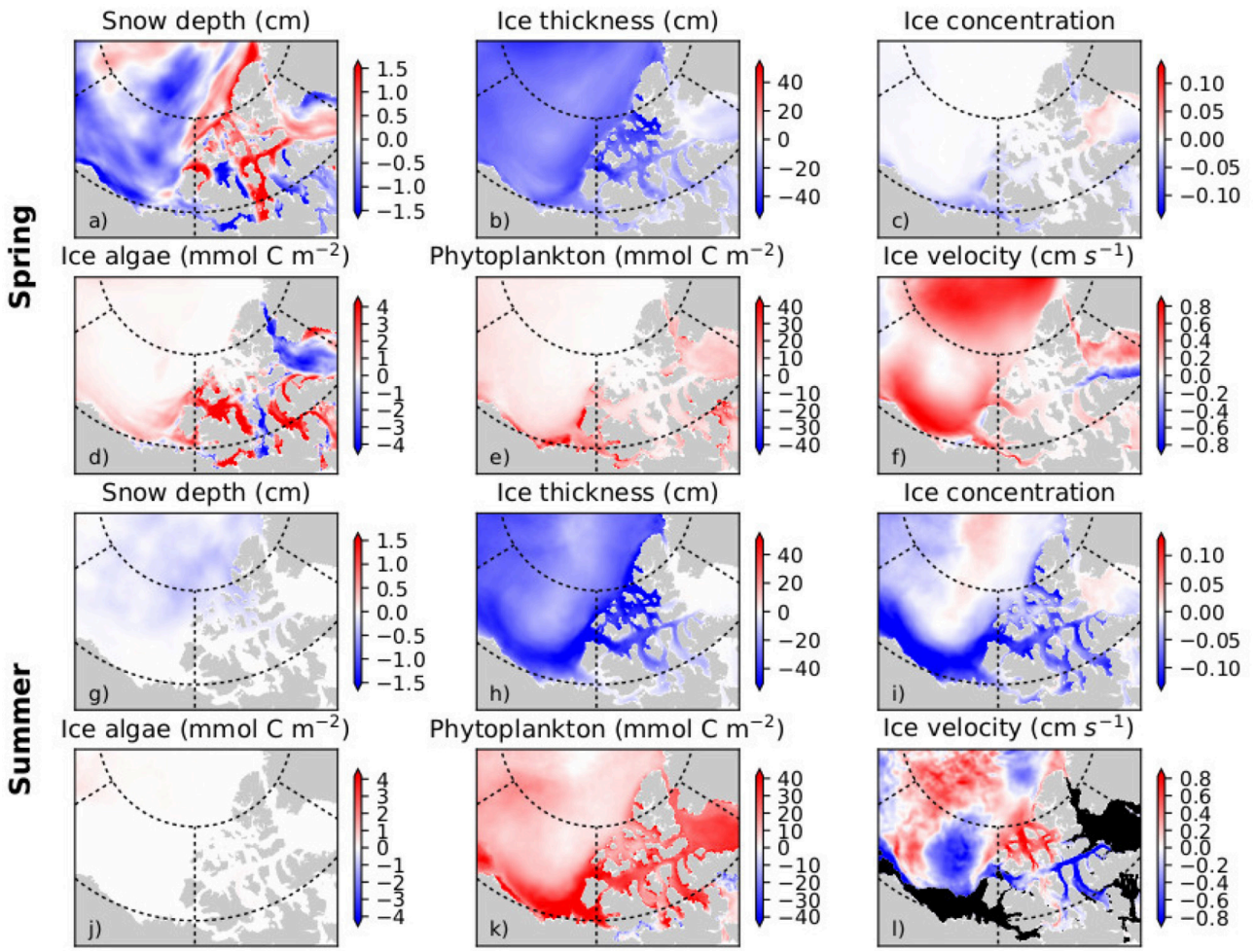

FIGURE 4 | Mean trend (per decade) in the spring (April-June; **a–f**) and summer (July-September; **g–l**) for snow depth, ice thickness, ice concentration, ice algal biomass, phytoplankton biomass, and ice velocity in the Western Canadian Arctic over the period 1979–2015 as simulated with the regional high resolution model NAA-CanOE-CSIB.

the projected increase in MCP by >10%, suggesting that ocean acidification reduces any gains from temperature-driven shifts in distributions. Increases in MCP occur due to increases in primary production and increases in northward moving species. DBEM results for Arctic cod populations show largely negative effects to climate change mainly due to temperature and sea-ice related habitat reductions. In the high emission scenario abundance decreases by more than 17% without the effects of ocean acidification (**Figure 8**). Changes in Arctic cod abundance (by 2100 relative to the averaged abundance from 2001 to 2010 shown in **Figure 9A**) shows significant decreases in the more southerly regions, and increases in northern regions, suggesting a northward shift for the species (**Figure 9B**). Note, however, that the large range in the simulated ESM input variables leads to a large standard deviation among the projected changes, indicating significant uncertainty. The model suggests that adding an ocean acidification effect by reducing growth and survival of Arctic cod by 10, 20, and 30% For every 100% increase in acidity has a consistent negative effects across much of the species range (**Figure 9C**), but the estimated effects of ocean acidification are small and amount to only an additional ≈1% decrease in abundance. Note only the 20% effect is shown in **Figures 8**, **9**.

4.4. Economic Model Results

Using current prices, the economic model estimates the current value for Beaufort Sea fisheries for all species to be $4.5 million USD. Under the low CO_2 scenario this landed value is projected to marginally increase to $5.3 million USD, but under the high CO_2 scenario it is expected to increase to $15.7 million USD (AMAP, 2018). This increased landed value is largely due to substantial increases in capelin, a comparatively low-priced species. This explains the 5-fold increase in catch potential but only a 3-fold increase in landed value: **Table 3** shows catch potential and landed values for Arctic cod and capelin in the Beaufort Sea. Arctic char is added for comparison to highlight the large biomass contribution from forage species. The summary indicates significant increases

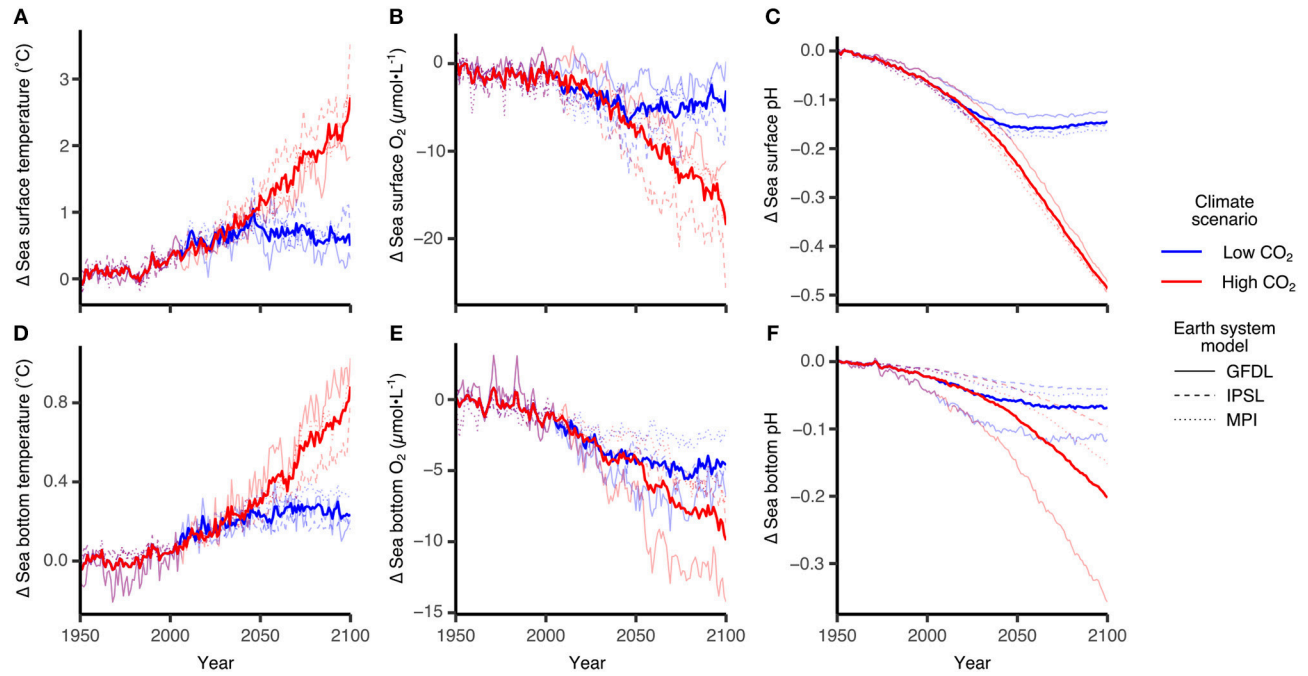

FIGURE 5 | Projected changes in sea surface and bottom ocean variables using three ESMs GFDL-ESM2G, IPSL-CM5A-MR and MPI-ESM-MR. Individual panels show changes in sea surface **(A)** temperature, **(B)** oxygen concentration and **(C)** pH and in bottom **(D)** temperature, **(E)** oxygen concentration and **(F)** pH. Bold lines represent multi-model averages and trajectories are relative to the 1951–1960 average. Blue lines are trajectories following climate scenarios where carbon emissions are mitigated and Paris Agreement targets are met (RCP2.6, +1.5°C global sea surface temperature), while red lines are climate scenarios along our current emissions trajectory (RCP8.5,+3.5°C). Reproduced from AMAP (2018) with permission from AMAP.

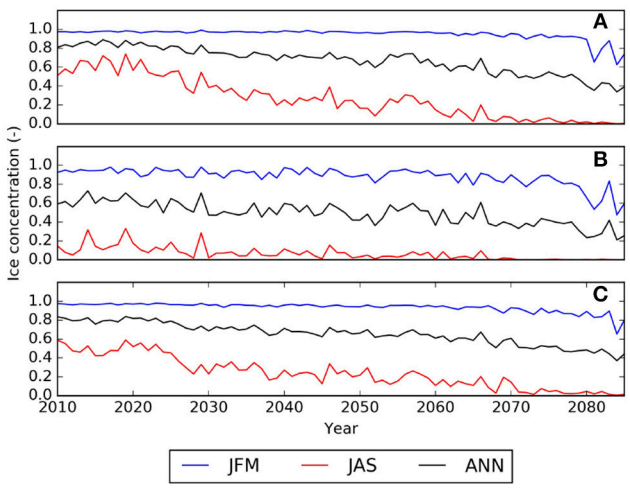

FIGURE 6 | Temporal evolution of the ice concentration (values between 0.0 and 1.0 representing 0–100% ice coverage) averaged over the **(A)** Northern Beaufort Sea, **(B)** Southern Beaufort Sea, and **(C)** the Canadian Polar Shelf (CPS) as simulated with the regional NAA-CMOC model. JFM indicates averages over January, February, March, JAS averages over July, August, September, ANN indicates the annual mean.

in capelin and slight reductions in Arctic cod for the high emission scenario, but also an increase in the subsistence species Arctic char.

5. DISCUSSION

5.1. Uncertainties

All applied model tools are prone to a variety of uncertainties which are highlighted below. **Table 4** summarizes those uncertainties and indicates ways to estimate the range and reduce those uncertainties. Coupling those model tools sequentially can lead to propagation and amplification of uncertainties, hence ways to reduce uncertainties need to be evaluated for each model component.

5.1.1. Uncertainty in Climate Model Projections

The issue of uncertainty in climate model projections is discussed in detail within the Intergovernmental Panel on Climate Change (IPCC) 5th Assessment report (AR5) and focused research papers (e.g., Collins et al., 2013; Cubasch et al., 2013; Kirtman et al., 2013; Knutti and Sedláçek, 2013). Kirtman et al. (2013), indicate three main sources of uncertainty. (1) Natural internal variability which is intrinsic to the climate system and places fundamental limits on the precision with which future climate variables can be projected. (2) Uncertainty concerning the past, present and future forcing of the climate system by natural and anthropogenic forcing agents (emission uncertainty). (3) Uncertainty related to the response of the climate system to the specified forcing agents (model uncertainty). The forcing-related uncertainty is estimated using the spread of projections for different emission scenarios (e.g., RCPs), while the spread among different models for

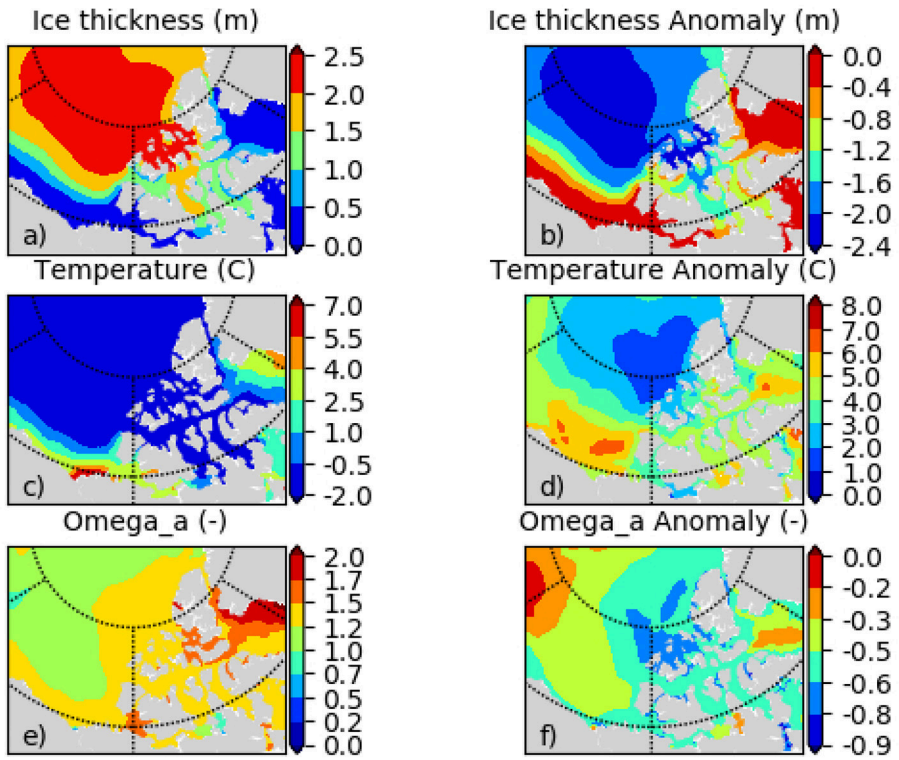

FIGURE 7 | (a) sea ice thickness h_{ice} , **(c)** temperature Ts, and **(e)** aragonite saturation state Ω_A for the bidecade 2006–2025, and respective change (2066–2085) minus (2006–2025) for **(b)** h_{ice}, **(d)** Ts, **(f)** Ω_A for July, August, September (JAS) as simulated with the regional NAA-CMOC model.

individual scenarios is used as a measure of the model response uncertainty. However, due to their natural internal variability, ESMs have limitations and cannot reliably simulate interannual and decadal variability, which might overlay and sometimes mask or enhance a longer term trend (Taylor et al., 2012; Loder and van der Baaren, 2013; Swart et al., 2015). Dynamical or statistical downscaling procedures introduce an additional dimension of model uncertainty.

Biogeochemical models of the Arctic are still under development and show inconsistent results with respect to the amount of primary production at current and future times (Popova et al., 2012; Vancoppenolle et al., 2013; Steiner et al., 2015b). Differences are related to the opposing impacts of increased light vs. decreased nutrient supply, and the representation thereof in the models, but also to our limited understanding of ecosystem functions such as the light-growth response in Arctic marine phytoplankton. Many biogeochemical processes are still insufficiently parameterized. The different pace in the projected ice retreat in the ESMs further affects light availability and exchange processes at the ocean surface, increasing model uncertainty (see e.g., **Figure 5** results for oxygen and pH). Models representing sea-ice algae which are closely linked to the diet of young Arctic cod have only recently been developed for regional Arctic models, and current models do not differentiate between sympagic and pelagic zooplankton species.

Many processes which are responsible for mixing and nutrient supply are smaller scale processes (e.g., coastal upwelling, local mixing and tidal mixing) and require higher resolution modeling and adequate bathymetry information. (The current model bathymetry is shown in the **Supplementary Material**). The Canadian Arctic is still not very well charted with main hydrographic surveys focusing on main shipping routes and only few models include tides.

5.1.2. Uncertainty in Physiological Responses for Key Marine Species

Traditionally critical limits were the focus of many early physiological research. However, sub-chronic limits to performance are potentially more important as drivers of marine species distribution and much more research on those lower threshold temperature limits is needed. Also required are studies that quantify the cumulative impacts of multi-stressors such as temperature, ocean acidification, hypoxia, contaminants and even underwater noise on aquatic species. The EwE model and DBEM include physiological species responses to environmental changes. Uncertainties and lacking information transfers into uncertainties in those models and or leads to rough estimates for potential impacts (e.g., acidification response of Arctic cod). Acclimation potential to changing conditions is generally not included in models of species distribution based on thermal limits. Arctic cod have the ability to acclimate to

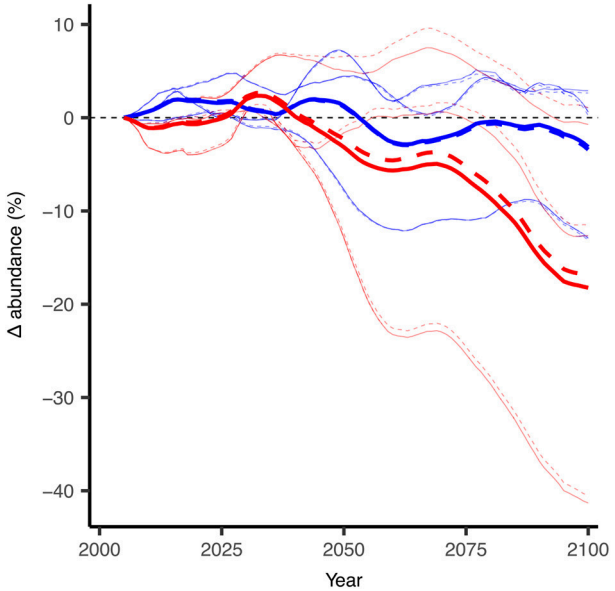

FIGURE 8 | Projected changes in abundance for Arctic cod (*B. saida*) with and without the modeled effects of ocean acidification as simulated with the DBEM. Thin lines indicate the individual DBEM results with forcing input from each of the three earth system models (GFDL, IPSL, MPI). Thick lines represent the averaged results from the respective three runs. Dashed lines indicate DBEM results which include impacts of ocean acidifcation on Arctic cod (For every 100% increase in acidity, i.e., hydrogen concentration, ocean acidification was modeled to negatively affect both growth and survival by 20%), solid lines include no acidification effect on the species. Changes in abundance are 10-year running means and relative to the 2001–2010 average. Red indicates the DBEM results forced with ESMs using the high CO_2 emission scenario (RCP8.5) and blue indicates results for the low emission scenario (RCP2.6). Modified from AMAP (2018) with permission from AMAP.

different temperatures depending on the duration of exposure (Drost et al., 2016). This finding is not unexpected as it has been shown that even true stenothermal Antarctic fish species are able to acclimate to warmer temperatures (Pörtner et al., 2000; Seebacher et al., 2005; Franklin et al., 2007; Robinson and Davison, 2008; Peck et al., 2014; Lanning et al., 2015). However, there may be a significant cost to acclimation and the subsequent alterations in respiratory and cardiac performance to maintain fundamental physiological demands (Pörtner and Farrell, 2008). The challenge is quantifying acclimation potential as well as the cost and benefits of acclimation on ectotherms, both for individuals and populations. Existing research suggests that the cost of acclimation may, in some cases, outweigh the benefits (Woods and Harrison, 2001; Seebacher et al., 2005; Deutsch et al., 2015; Pershing et al., 2015; Drost et al., 2016). The potential to acclimate (e.g., thermal plasticity in fish) requires further study and this potential should be included in ecosystem models that project climate change impacts on food webs (Farrell and Franklin, 2016).

5.1.3. Uncertainty in Food Web and Species Distribution

From the EwE perspective, uncertainties are based on assumptions made to calculate or estimate parameters in the initial model, and changes over time. Considering the initial Ecopath model, input parameters are ranked based on how they were calculated using a pedigree analysis available in EwE (Christensen et al., 2007). Each input parameter is ranked based on the level of assumptions made when setting initial parameters. An estimate of the uncertainty representing 6 categories for biomass and 8 categories for production and consumption is indicated in AMAP (2018) (their Figure A6.22). High uncertainty is associated with simple estimates from Ecopath or other models and the lowest uncertainty is associated with high precision local sampling (similar species/same system). Much of the information about links in the food web comes from research on higher trophic levels (stable isotopes and fatty acid analysis), giving insight into the structure and function of the lower trophic levels. Fish groups are some of the biggest uncertainty in terms of ecosystem research in the ISR, as only recently large scale assessments on numbers of local species have been collected under the Beaufort Regional Environmental Assessment (BREA)-Marine Fishes program (2012–2015) (Majewski et al., 2017). The Arctic and Polar cod group is marked as estimated from Ecopath (for biomass) and via empirical relationships (for production and consumption). Zooplankton and production studies on abundance, distribution, and food web role have occurred more recently, providing more relevant information on these groups. Previously, expert knowledge was relied upon for an understanding of these groups. As sampling of species diets occurs in the summer months due to logistics of working in the Arctic, there is a potential lack of understanding of annual diets from the food web perspective, so switching from specialists to generalists adds uncertainty to individual species and ecosystem impacts. Uncertainties in the species distribution model also come from limited and seasonally biased observations of species distributions from which their environmental preferences are derived. Uncertainties are also transferred from the driving climate models (e.g., **Figure 5** compared to **Figure 8**).

5.1.4. Uncertainty in the Economic Model

Estimates of the value of current and future fisheries are derived from current/recent (2001–2010) average global prices of each species and weighted by catch tonnage. This assumes that prices received for landings in the Arctic would be comparable to the global market. Constant average 2001–2010 prices were applied to estimate future potential landed values of Arctic commercial fisheries. Therefore, this estimate does not take into account changes in real prices due to supply-demand effects. In addition, landed values are gross revenues collected at the first point of sale; estimating profits would require estimates of the cost of fishing, including fuel, labor, and maintenance (Lam et al., 2011). While the economic model estimates potential amounts and values of the fishing resources, feasibility of fisheries in the Arctic depends on several other factors, including the potentially increased costs due to more difficult access, limited capacity (shipping, processing), resource rights, governance and policies.

5.2. Law and Governance Context

Laws and policies relevant to addressing the potential impacts of climate change and ocean acidification on marine species and

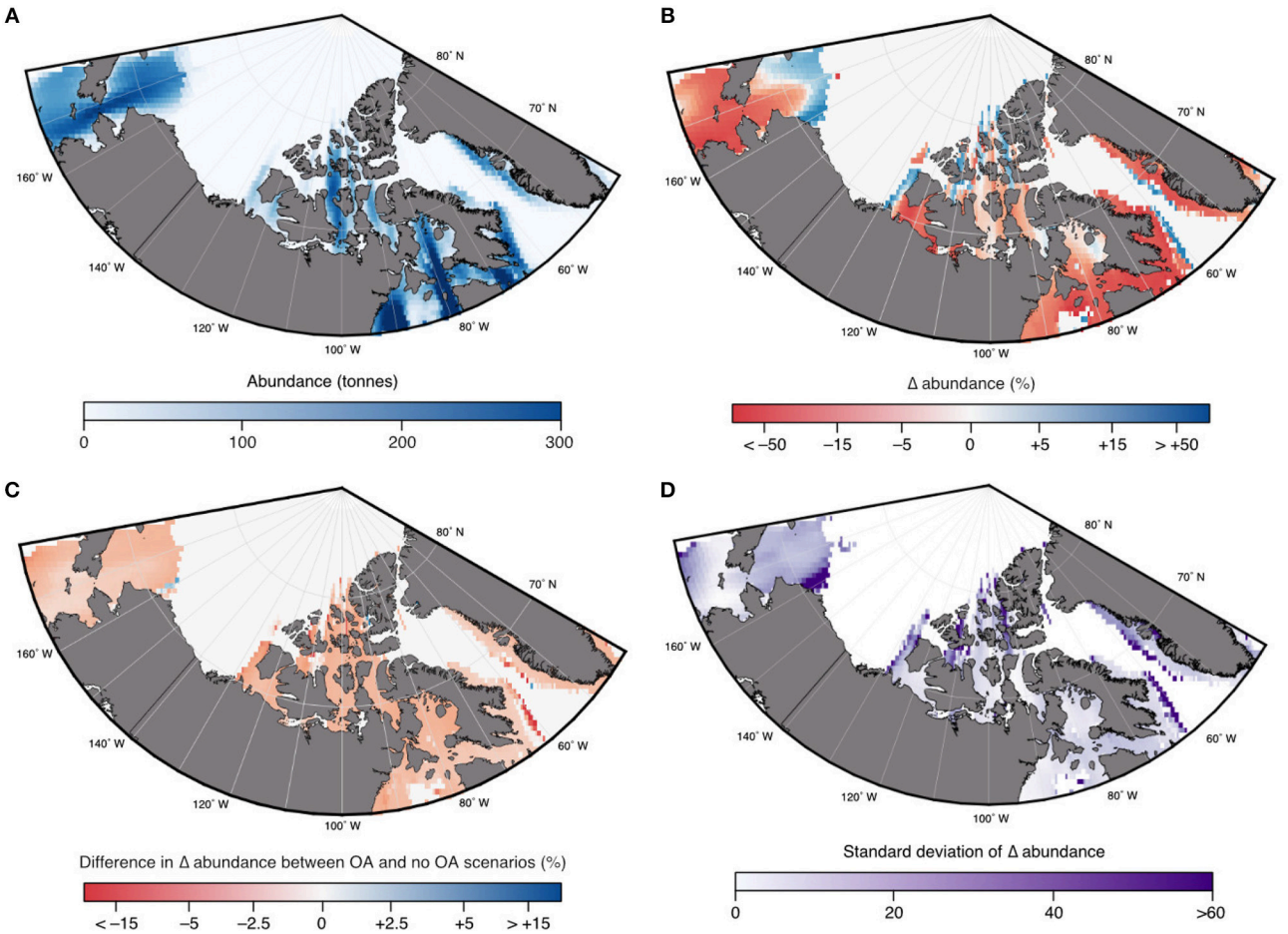

FIGURE 9 | Projected multimodel mean (of the 3 ESMs) changes in abundance for Arctic cod (*B. saida*) under the high emission (RCP8.5) scenario: **(A)** 2001–2010 abundance; **(B)** relative changes in abundance by 2100 compared to 2001–2010 in response to multiple stressors (i.e., ocean acidification, temperature, oxygen); and **(C)** changes in abundance due to additional effects of ocean acidification (OA) using a 20% negative effect on growth and survival (see text); and **(D)** the standard deviation of the changes in abundance shown in B, based on the three input ESMs. Modified from AMAP (2018) with permission from AMAP.

TABLE 3 | Examples for estimates of catch (tonnes) and landed value (USD) of potential current fisheries and future projections under RCP 2.6 and 8.5 scenarios in the Beaufort Sea.

	Current catch	**(2001–2010) Landed value**	**RCP 2.6 catch**	**(2091–2100) Landed value**	**RCP 8.5 catch**	**(2091–2100) Landed value**
Arctic cod	4,600	3,240,000	4,820	3,400,000	4,390	3,090,000
(*Boreogadus saida*)	(2,810–5,800)	(1,980,000–4,090,000)	(3,670–6,610)	(2,580,000–4,660,000)	(2,610–6,510)	(1,840,000–4,590,000)
Capelin	4,310	1,150,000	6,230	1,670,000	46,300	12,400,000
(*Mallotus villosus*)	(1,260–6,490)	(337,000–1,740,000)	(3,850–7,810)	(1,030,000–2,090,000)	(41,900–48,800)	(11,200,000–13,000,000)
Arctic char	3.50	13,200	4.80	18,100	7.36	27,800
(*Salvelinus alpinus alpinus*)	(1.17–5.39)	(4,410–20,300)	(0.794–9.47)	(2,990–35,700)	(1.51–14.8)	(5,690–55,700)

Values are multi-model means from simulations using three earth system models (GFDL, IPSL, MPI) and values in parentheses are the minimum and maximum results from simulations. Average global ex-vessel prices from 2001-2010 were used to estimate landed values (Tai et al., 2017). For an expanded table see AMAP (2018, Table A6.2).

TABLE 4 | Uncertainties in coupled climate-ecosystem-economic (CEE) models.

Model type	Type of uncertainty	Cause of uncertainty	Estimate of uncertainty	Measures to reduce uncertainty
Climate	Scenario uncertainty	Future emissions	Multiple scenarios	International commitments
Climate	Parameter uncertainty	Limited process understanding	Multi-model runs Sensitivity studies	Enhanced process understanding
Climate	Internal variability	Natural variability	Multiple ensembles	–
Food web (EwE), DBEM	Parameter uncertainty/ Structural uncertainty	Natural variability Lack of precise measurements for high amount of parameters	Monitoring, Parameter sensitivity studies, Different structures assessed in previous literature	Monitoring, Including advances from experimental literature
Physiological	Response uncertainty	Knowledge gaps	Monitoring, Laboratory testing	Monitoring, Laboratory testing
Economic	Market price	Variability in supply and demand	Price elasticity	–
Economic	Feasibility	Variable input parameters and circumstances	Scenario development	Feasibility studies

coastal communities in the Western Canadian Arctic appear on global, regional and national levels. Globally, the Paris Agreement continues to set the agenda for advancing mitigation and adaptation responses to climate change and ocean acidification (Klein et al., 2017; Oral, 2018). This agreement establishes an overall objective of keeping the global average temperature rise this century to well below 2°C above pre-industrial levels and to pursue efforts to limit the temperature increase even further to 1.5°C above pre-industrial levels, which is represented as low emission scenario (RCP2.5) in this study. A key to mitigation is the requirement for Parties to submit nationally determined contributions (NDCs) which set out planned domestic mitigation measures; successive NDCs are expected to become increasingly progressive and ambitious (Winkler, 2017).

National mitigation commitments to date have been lagging. Current NDCs submitted by Parties imply a global warming of about 3°C by 2100 (Masson-Delmotte et al., 2018; UNEP, 2018). While Canada has pledged a reduction of greenhouse gas emissions by 30% below 2005 levels by 2030 and has adopted the Pan-Canadian Framework on Clean Growth and Climate Change (Canada, 2016), Canada is reportedly not on track to meet its reduction target (UNEP, 2018), and Canada is facing considerable opposition from some provinces to the federal government's role and decision to impose a price on carbon pollution across Canada (McGregor, 2018).

The research results of this paper indicate that effective implementation and future strengthening of national mitigation commitments under the Paris Agreement are critical for decreasing the potential negative effects on Arctic cod based on temperature related habitat loss and for reducing the impact of the northwards-expanding lower-priced capelin species (**Table 3**). Arctic ocean acidification might be significantly reduced, although at this point the effects on Arctic cod are suggested to be minor albeit with high uncertainties in physiological species responses.

Climate change and ocean acidification impacts in the Arctic threaten various internationally recognized human and Indigenous rights (Duyck, 2015; de Windt et al., 2016). These rights, some set out in the United Nations Declaration on the Rights of Indigenous Peoples (2007) include, among others, the rights to food, subsistence, culture and human health (McCrimmon, 2016; Rapporteur, 2017). Hence, projects assessing potential climate change impacts on subsistence fisheries as presented in this study are highly relevant.

The study highlights that effects of temperature and sea-ice retreat alone cause significant changes in the distribution and abundance of forage species, however uncertainties are high with respect to ocean acidification impacts. The impacts on subsistence species are still unclear, as reductions in one species might mean increased availability of another species, but their nutritional value might be different. E.g., in 2014 beluga whales appeared at unusual locations in the Amundsen Gulf with sandlance in their stomachs rather than Arctic cod and Inuvialuit harvesters indicated lower body conditions for those whales (Loseto et al., 2018). Harvesters also indicated different flesh color and taste in Arctic char. Changes in ice conditions currently seem to favor zooplankton production, which could lead to an overall positive impact on subsistence fisheries, if they can provide a suitable food base for those species. However, ocean acidification might pose negative effects on some Arctic zooplankton species, suggesting an uncertain future. E.g., Arctic pteropods are suggested to be negatively impacted by temperature and ocean acidification (Comeau et al., 2010, 2012; Bednaršek et al., 2012; Lischka and Riebesell, 2012) and for the Arctic copepod *Calanus glacialis* ocean acidification effects seem to vary with developmental stage. Earlier copepodite stages show increases in metabolic rates and decreased scope for growth at high pCO_2 levels (Thor et al., 2017).

The inclusion of impacted communities into such assessments is highly important to understand the full impacts and to develop effective mitigation and adaptation strategies. In the ISR,

collaboration with local communities is active and evolving. The CEE model approach has been presented to and received support from the Inuvialuit Game Council and Inuvialuit Regional Corporation. A continued collaborative effort to assess climate and other stressor impacts on Arctic Marine ecosystems in the ISR is now linked to the Beaufort Sea Regional Strategic Environmental Assessment (RSEA) and intends to synthesize indigenous and scientific knowledge of forage species, links to higher trophic levels and observed changes due to a rapidly changing Arctic, and expand community based monitoring.

Adaptation initiatives have been encouraged on a regional level. They include the recent Agreement to Prevent Unregulated High Seas Fisheries in the Central Arctic Ocean, opened for signature in October 2018 (Schatz et al., 2018), the Arctic Council's Framework for a Pan-Arctic Network of Marine Protected Areas (PAME, 2015), and the promotion of other area-based conservation measures (PAME, 2017).

In Canada, pursuant to an Oceans Act mandate, the Beaufort Sea region was chosen as a pilot site for a large ocean management area integrated planning initiative. The resulting Integrated Ocean Management Plan for the Canadian Beaufort Sea was a collaborative work of people representing aboriginal, territorial and federal governmental departments, management bodies, and northern coastal community residents with interests in the Beaufort Sea, and includes input also from industry and other interested parties. The plan is voluntary and is intended to facilitate integrated planning and sustainability among all Beaufort Sea resource users and managers. The plan has served as a support tool for MPA network planning in the region (Cobb et al., 2008). Canada's commitment to protecting 10% of marine and coastal areas by 2020 under the Convention on Biological Diversity provides further support for MPA development. In Canada the establishment of MPAs includes the implementation of monitoring and management plans, which are currently being developed for the two MPAs in the ISR, TNMPA and ANMPA. Both MPAs have been established to support the conservation of beluga populations and led to enhancement of the existing longterm beluga harvest monitoring program (Loseto et al., 2018). Results of the monitoring program indicate that shifts in beluga metrics such as relative abundance, arrival to summering locations, diet and health appear to be responding to habitat changes and a shifting prey base (with lower Arctic cod content) resulting from climate change drivers. While these shifts have been identified, the underlying ecosystem processes and mechanisms that drive those shifts remain poorly known and hence provide only limited guidance for management actions (Loseto et al., 2018). Hence, Loseto et al. (2018) and Harwood et al. (2015) highlight the need to pair higher trophic species monitoring with concurrent direct (stomach contents) or indirect (isotopes, fatty acids) monitoring of diet, detailed studies of movements and seasonal ranges, as well as monitoring of ecosystem parameters. Continued food chain monitoring is also essential to track adaptation capacity of higher trophic levels to shifts in prey species and hence evaluate their adaptation capacity to environmental changes.

The ongoing marine conservation planning efforts are aiming at including climate change and ocean acidification into their assessments. The presented high resolution model represents a tool to identify high risk areas (areas likely experiencing high change under a changing climate, e.g., temperature, acidification, sea-ice loss), climate change refugia (areas likely experiencing limited change under a changing climate), as well as changes to hotspots of biodiversity and primary production. Current uncertainties in the designations of priority conservation areas arise from limited data availability and potential biases toward socially, culturally and economically important species and areas. Hence the presented CEE model approach linking changing environmental conditions to species distribution, abundance and fisheries catch potential provides valuable additional information to be used in MPA as well as community planning processes.

Finally, Canada has established a policy framework to ensure future commercial fisheries in the Western Beaufort Sea Bioregion would be subject to precautionary and adaptive approaches. The Beaufort Sea Integrated Fisheries Management Framework for the Inuvialuit Settlement Region (BSP, 2014) establishes a multi-step decision process for any future commercial fisheries applications, which would consider, among other factors, possible adverse affects on existing Inuvialuit subsistence fisheries and preferential rights of the Inuvialuit to harvest fish in the ISR (Ayles et al., 2016). Future commercial fisheries would be subject to other DFO sustainable fisheries policies including those on the precautionary approach (DFO, 2009a) and on managing the impacts of fishing on sensitive benthic areas (DFO, 2009b). Underpinning any such decisions requires solid research on environmental changes and species impacts in the region. The outlined approach is designed to provide such input.

Another issue is the unresolved ocean boundary dispute between Canada and the United States in the Beaufort Sea. Canada maintains the 141st west meridian line serves as both a land and maritime boundary while the U.S. argues for an equidistance line (Byers, 2013). An area of some 6250 square nautical miles is contested (McDorman, 2009). Thus, which country has jurisdiction over the disputed area and corresponding responsibilities for climate change adaptation in that area remains uncertain.

6. SUMMARY

In this case study a framework combining multiple modeling and analysis tools has been introduced and applied to identify potential climate change and ocean acidification effects on forage fish and impacts on subsistence fisheries in the Western Canadian Arctic. Since lower trophic level prey species such as copepods and forage fish respond more directly to primary production, they allow linkages with regional climate models that can aid in our understanding of causalities for observed shifts in distribution, abundance and prey shifts in higher trophic level species.

Arctic regions and communities are some of the most susceptible to climate changes. Changing environmental conditions affect marine species distribution and abundance as well as access to fishing grounds. Ocean acidification is

progressing here faster than anywhere in the world and adds a high factor of uncertainty to marine species responses in this fast changing environment, i.e., the model suggests that by 2066–2085 all of the central CPS is projected to be undersaturated with respect to Ω_A. These changes may potentially alter associated cultural and traditional practices.

Regional climate model results provide information on longterm trends and interannual variability and indicate increasing trends for ice algae and pelagic primary production with large interannual variability particularly for ice algae on the Canadian Polar Shelf. These fundamental changes are linked to decreases in ice and snow thickness allowing more light to penetrate the ice. More ice algae suggest larger amphipod abundance and good conditions for Arctic cod early life stages, hence high interannual variability in ice algal vs. pelagic primary production might be a significant contributor to interannual changes in forage fish distribution and abundances and might partially mask a longer term trend. Such interannual variability in forage species abundance has been indicated in scientific and Indigenous observations (pers. communication, Inuvialuit Game Council). The regional climate model also indicates increases in ice mobility which impedes cross-ice travel and hence access to traditional fishing grounds.

Species distribution (DBEM) simulations suggest that northward migration constrains Arctic cod to the higher Arctic, but leads to an influx of other forage species such as capelin, sandlance and zooplankton. The large decline in abundance of Arctic cod projected by the DBEM suggests that they may already be at their northern limits and thus their distributional range may be shrinking as it is compressed from the south (Frainer et al., 2017). The DBEM predicts spatial movements based solely on habitat and environmental suitability/preference and does not include trophic interactions. However, the Ecopath model also shows a reduction in Arctic cod, based primarily on changes in prey and predation, suggesting that both habitat changes and trophic interactions play a role in the Arctic cod decline.

So far empirical evidence of the effects of ocean acidification on Arctic cod remains limited. DBEM simulations which include potential effects of ocean acidification on life history traits, such as growth and survival suggest only an additional -1% decrease for Arctic cod on top of a 17% decrease based on habitat loss. However, much higher decreases are simulated for invertebrate species (AMAP, 2018).

Harwood et al. (2015) suggest higher trophic level species with a high preference for Arctic cod already exhibit a decrease in body condition, including beluga whales and ringed seals, while species with more flexibility in food choices including bowhead whales and Arctic char exhibit increased body condition. These are all important subsistence species in the ISR. While the simulated impact on Arctic cod is projected to be negative for the high emission scenario, other forage species are suggested to increase, e.g., zooplankton species and capelin. Hence, a demise of Arctic cod populations could impact subsistence and commercial fisheries (Thorsteinson and Love, 2016) but if subsistence species can adapt to alternative prey, the overall impact on the species may be reduced or even positive.

Some optimism for the Arctic to serve as a possible refugia for many species and fisheries relies heavily on the assumption that species will invade and integrate successfully to new regions. The caveat is our still very limited knowledge of physiological responses to temperature increases, acidification and cumulative stressors. Enhanced monitoring and physiological testing on local species is required to better understand physiological species responses and improve predictive models. Developing the CEE modeling system further with strong links among the components will allow for more integrated results and understanding of key stressors for each species group within the ecosystem.

The application of multiple models as well as multiple emission scenarios allows for estimates of the range of uncertainty. Global earth system models still show large differences in their projections of e.g., primary production which affects the DBEM and Ecopath projections. These model uncertainties can be reduced with enhanced process understanding and parameterization development which is an active area of research. Scenario uncertainty in climate models also remains high. While international commitments to reduce carbon emissions, as proposed in the Paris Agreement, suggest a more unified pathway, implementation time lines are still uncertain.

In addition to uncertainties linked to model assumptions and the representation of complex ecological dynamics, data availability and quality can be highly variable across regions and research themes. The Arctic in particular has less available scientific assessments compared to other Canadian oceans (Canada, 2015), with a particular lack of information regarding resource use by Indigenous communities (Cisneros-Montemayor et al., 2017). These challenges are partly due to operational difficulties for research, but also to historical marginalization of Indigenous communities. In the near future continued and culturally-appropriate collaboration between academics, communities, and managers is essential to integrate existing indigenous and scientific knowledge into relevant policies (Friddell et al., 2013). In the ISR researchers and communities are slowly moving toward this goal. E.g., longterm monitoring programs such as the beluga monitoring program (running since 1970, Loseto et al., 2018) are now including IK data collections (Ostertag et al., 2018). In addition, the Joint Secretariat, Fisheries Joint Management Council and Inuvialuit Regional Corporation are actively working toward accessible databases for Indigenous Knowledge and collaborative studies (e.g., via the ISR traditional and local knowledge catalogue, ISRTLK.com). Larger scale efforts also exist, e.g., via ArcticNet (http://www.arcticnet.ulaval.ca/), to include indigenous knowledge in research projects and use common data repositories such as the Polar Data Catalogue (https://www.polardata.ca/) for scientific and indigenous data.

Adaptation actions in the Arctic should be directed toward funding collaborative climate change and ocean acidification research, expediting and establishing pan-Arctic MPA networks and supporting unified monitoring programmes. Arctic communities should be provided with the tools and training to conduct local, unified research and food chain monitoring. Future decisions regarding commercial fisheries will need to be precautionary and adaptive in light of the many uncertainties still surrounding ocean acidification and species responses to cumulative changes.

AUTHOR CONTRIBUTIONS

NS lead the project and writing of the article and contributed to the climate modeling efforts and analysis. WC and URS contributed to the DBEM and economic models and evaluation. AC-M contributed information on indigenous Arctic fisheries and databases. HD contributed specific information on Arctic cod and physiological species responses. HH contributed to the development and analysis of the high resolution regional model and created figures. CH implemented the EwE model for the Beaufort Sea and contributed to the analysis, provided the EwE uncertainty analysis uncertainty, and created the CEE figure. JL provided community input for the ISR. TS contributed to the development and analysis of the high resolution regional model and future projections and created figures. TT contributed to the development and analysis of the DBEM and economic models and created figures. PS implemented the Ecopath model and contributed to the analysis. DV contributed the law and policy component. All authors contributed to the writing and review of the paper.

FUNDING

The authors acknowledge funding from the Canadian Social Sciences and Humanities Research Council (SSHRC) partnership grant *OceanCanada*, the Marine Environmental Observation Prediction and Response (MEOPAR) Network, ArcticNet, the Manitoba Centre of Excellence Funding, the Fisheries Joint Management Committee, and the Departments of Fisheries and Oceans Canada and Environment and Climate Change Canada.

ACKNOWLEDGMENTS

The publication is a product of the *OceanCanada* partnership. The analysis was inspired and guided by the Arctic Monitoring and Assessment Program (AMAP) 2nd assessment on Arctic Ocean Acidification. We acknowledge the valuable input from two reviewers which greatly helped to improve the structure of the manuscript. We also would like to thank Adam Monahan and Eric Mortenson for helpful discussion and contributions to supplementary figures. Figures modified or reproduced from AMAP (2018) are following the AMAP Usage Policy (https://www.amap.no/swipa2017). Extracts from Suprenand et al. (2018) relevant to this study are derived from Http://scholarcommons.usf.edu/msc_facpub/261.

SUPPLEMENTARY MATERIAL

The Supplementary Material for this article can be found online at: https://www.frontiersin.org/articles/10.3389/fmars.2019.00179/full#supplementary-material

REFERENCES

AMAP (2017). *Adaptation Actions for a Changing Arctic: Perspectives from the Bering-Chukchi-Beaufort Region*. Tech. rep., Arctic Monitoring and Assessment Programme (AMAP), Oslo.

AMAP (2018). *Arctic Ocean Acidification. Arctic Monitoring and Assessment Program (AMAP)*. Tech. rep., AMAP Secretariat.

Anttila, K., Casselman, M., Schulte, P., and Farrell, A. (2013). Optimum temperature in juvenile salmonids: connecting subcellular indicators to tissue function and whole-organism thermal optimum. *Physiol. Biochem. Zool.* 86, 245–256. doi: 10.1086/669265

Arora, V. K., Scinocca, J., Boer, G. J., Christian, J. R., Denman, K. L., Flato, G. M., et al. (2011). Carbon emission limits required to satisfy future representative concentration pathways of greenhouse gases. *Geophys. Res. Lett.* 38:L05805. doi: 10.1029/2010GL046270

Astthorsson, O. (2015). Distribution, abundance and biology of polar cod, boreogadus saida, in iceland-east greenland waters. *Polar Biol.* 39, 995–1003. doi: 10.1007/s00300-015-1753-5

Aumont, O., Maier-Reimer, E., Blain, S., and Monfray, P. (2003). An ecosystem model of the global ocean including Fe, Si, P colimitations. *Global Biogeochem. Cycles* 17:1060. doi: 10.1029/2001GB001745

Ayles, B., Porta, L., and Clarke, R. M. (2016). Development of an integrated fisheries co-management framework for new and emerging commercial fisheries in the Canadian Beaufort Sea. *Mar. Policy* 72, 246–254. doi: 10.1016/j.marpol.2016.04.032

Bain, H., and Sekerak, A. (1978). *Aspects of the biology of arctic cod, Boreogadus saida, in the central Canadian Arctic*. Tech. Rep. 104, Unpubl. Rep. by LGL Ltd, Toronto, ON. For Polar Gas Project.

Baumann, H., Talmage, S., and Gobler, C. (2012). Reduced early life growth and survival in a fish in direct response to increased carbon dioxide,. *Nat. Clim. Chang.* 2, 38–41. doi: 10.1038/nclimate1291

Bednaršek, N., Tarling, G., Bakker, D., Fielding, S., Cohen, A., Kuzirian, A., et al. (2012). Description and quantification of pteropod shell dissolution: a sensitive bioindicator of ocean acidification. *Global Change Biol.* 18, 2378–2388. doi: 10.1111/j.1365-2486.2012.02668.x

Berkes, F. (1990). Native subsistence fisheries: a synthesis of harvest studies in Canada. *Arctic* 43, 35–42. doi: 10.14430/arctic1588

Bluhm, B., and Gradinger, R. (2008). Regional variability in food availability for arcticx marine mammals. *Ecol. Appl.* 18, S77-S96. doi: 10.1890/06-0562.1

Bradstreet, M., and Cross, W. (1982). Trophic relationships at high arctic ice edges. *Arctic* 35, 1–2. doi: 10.14430/arctic2303

Bradstreet, M., Finley, K., Sederak, A., Griffiths, W., Evans, C., Fabijan, M., et al. (1986). *Aspects of the Biology of Arctic Cod (Boreogaduc saida) and Its Importance in Arctic Marine Food Chains*. Canadian technical report of fisheries and aquatic sciences, DFO.

Brown, J., Gillooly, J., Allen, A., Savage, V., and West, G. (2004). Toward a metabolic theory of ecology. *Ecology* 85, 1771–1789. doi: 10.1890/03-9000

BSP (2014). *Beaufort Sea Integrated Management Framework for the Inuvialuit Settlement Region*. Tech. rep., Fisheries and Oceans Canada and Fisheries Joint Management Committee and Inuvialuit Game Council and Inuvialuit Regional Corporation, Inuvialuit Settlement Region, 64.

Byers, M. (2013). *International Law and the Arctic*. Croydon: CPI Group Ltd.

Canada (2015). *State of Environmental Monitoring in Canada*. Tech. rep., Government of Canada, Polar Knowledge Canada. Available online at: https://www.canada.ca/en/polar-knowledge/publications/cpc-stateofenv.html. (accessed January, 2019).

Canada (2016). *Pan-Canadian Framework on Clean Growth and Climate Change: Canada's Plan to Address Climate Change and Grow the Economy*. Tech. rep., Government of Canada, Ottawa, ON, 77.

Cheung, W., Dunne, J. P., Sarmiento, J. L., and Pauly, D. (2011). Integrating ecophysiology and plankton dynamics into projected maximum fisheries catch potential under climate change in the Northeast Atlantic. *ICES J. Mar. Sci.* 68, 1008–1018. doi: 10.1093/icesjms/fsr012

Cheung, W., Jones, M., Reygondeau, G., Stock, C., Lam, V., and Froelicher, T. (2016). Structural uncertainty in projecting global fisheries catches under climate change. *Ecol. Modell.* 325, 57–66. doi: 10.1016/j.ecolmodel.2015.12.018

Cheung, W., Lam, V. W., and Pauly, D. (2008). Modelling present and climate-shifted distribution of marine fishes and invertebrates. *Fish. Cent. Res. Rep.* 16:72.

Choy, E., Roth, J., and Loseto, L. (2016). Lipid removal and acidification affect nitrogen and carbon stable isotope ratios of beluga whales *(delphinapterus leucas)* and their potential prey species in the Beaufort Sea ecosystem. *Mar. Biol.* 163. doi: 10.1007/s00227-016-2992-x

Christensen, V., and Walters, C. (2004). Ecopath with ecosim: methods, capabilities and limitations. *Ecol. Model.* 172, 109–139. doi: 10.1016/j.ecolmodel.2003.09.003

Christensen, V., Walters, C., Pauley, D., and Forrest, R. (2007). *Ecopath With Ecosim Version 6.0: User Manual/Help Files Guide.* Lenfest Oceans Futures Project, University of British Columbia, British Columbia.

Christian, J. R., Arora, V. K., Boer, G. J., Curry, C. L., Zahariev, K., Denman, K. L., et al. (2010). The global carbon cycle in the Canadian Earth System Model (CanESM1): preindustrial control simulation. *J. Geophys. Res.* 115:G03014. doi: 10.1029/2008JG000920

Christiansen, J., Dalmo, R., and Ingebrigtsen, K. (1996). Xenobiotic excretion in fish with aglomerular kidneys. *Mar. Ecol. Prog. Ser.* 136, 303–304. doi: 10.3354/meps136303

Christiansen, J., Hop, H., Nilssen, E., and Joensen, J. (2012). Trophic ecology of sympatric arctic gadoids, arctogadus glacialis (Peters, 1872) and boreogadus saida (Lepechin, 1774), in NE Greenland. *Polar Biol.* 35, 1247–1257. doi: 10.1007/s00300-012-1170-y

Cisneros-Montemayor, A., Pauly, D., Weatherdon, L., and Ota, Y. (2016). A global estimate of seafood consumption by coastal indigenous peoples. *PLoS ONE* 11:e0166681. doi: 10.1371/journal.pone.0166681

Cisneros-Montemayor, A. M., Cheung, W. W., Bodtker, K., Teh, L., Steiner, N. S., Bailey, M., et al. (2017). Towards an integrated database on canadian ocean resources: benefits, current states, and research gaps. *Can. J. Fish. Aquat. Sci.* 74, 65–74. doi: 10.1139/cjfas-2015-0573

Coad, B., and Reist, J. (2004). "Annotated list of the arctic marine fishes of canada," in *Canadian Manuscript Reports Fish and Aquatic Science*, 2674.

Cobb, D., Fast, H., Papst, M., Rosenberg, D., Rutherford, R., and Sareault, J. (2008). *Beaufort Sea Large Ocean Management Area: Ecosystem Overview and Assessment Report.* Canadian Technical Report of Fisheries and Aquatic Sciences 2780, DFO, 188.

Collins, M., Knutti, R., Arblaster, J., Dufresne, J.-L., Fichefet, T., Friedlingstein, P., et al. (2013). "Long-term climate change: projections, commitments and irreversibility," in *Climate Change 2013: The Physical Science Basis. Contribution of Working Group I to the Fifth Assessment Report of the Intergovernmental Panel on Climate Change* (New York, NY: Cambridge University Press).

Comeau, S., Alliouane, S., and Gattuso, J.-P. (2012). Effects of ocean acidification on overwintering juvenile arctic pteropods limacina helicina. *Mar. Ecol. Prog. Ser.* 456, 279–284. doi: 10.3354/meps09696

Comeau, S., Jeffree, R., Teyssié, J.-L., and Gattuso, J.-P. (2010). Response of the arctic pteropod limacina helicina to projected future environmental conditions. *PLoS ONE* 5:e11362. doi: 10.1371/journal.pone.0011362

Crawford, R., and Jorgenson, J. (1996). Quantitative studies of arctic cod (*Boreogadus saida*) schools: important energy stores in the arctic food web. *Arctic* 49, 181–193. doi: 10.14430/arctic1196

Cubasch, U., Wuebbles, D., Chen, D., Facchini, M., Frame, D., Mahowald, N., et al. (2013). "Introduction," in *Climate Change 2013: The Physical Science Basis. Contribution of Working Group I to the Fifth Assessment Report of the Intergovernmental Panel on Climate Change* (New York, NY: Cambridge University Press).

David, C., Lange, B., Krumpen, T., Schaafsma, F., van Franeker, J., and Flores, H. (2016). Under-ice distribution of polar cod *Boreogadus saida* in the central arctic ocean and their association with sea-ice habitat properties. *Polar Biol.* 39, 981–994. doi: 10.1007/s00300-015-1774-0

David, C., Lange, B., Rabe, B., and Flores, H. (2015). Community structure of under-ice fauna in the eurasian central arctic ocean in relation to environmental properties of sea-ice habitats. *Mar. Ecol. Prog. Ser.* 522, 15–32. doi: 10.3354/meps11156

de Windt, C., Campos, M., Peña, A. S., and Jimenez, E. (2016). *Climate Change: A Comparative Overview of the Rights Based Approach in the Americas*. Tech. rep., Department of Sustainable Development, General Secretariat of the Organization of American States, Washington, DC.

Deutsch, C., Ferrel, A., Seibel, B., Pörtner, H.-O., and Huey, R. (2015). Climate change tightens a metabolic constraint on marine habitats. *Science* 348, 1132–1135. doi: 10.1126/science.aaa1605

DFO (1999). *Hornaday River Arctic Charr*. DFO stock status report, Fisheries and Oceans Canada.

DFO (2009a). *A Fishery Decision-Making Framework Incorporating the Precautionary Approach*. Tech. rep., Fisheries and Oceans Canada, Ottawa, ON.

DFO (2009b). *Policy for Managing the Impacts of Fishing on Sensitive Benthic Areas*. Tech. rep., Fisheries and Oceans Canada, Ottawa, ON.

Divoky, G., Lukacs, P., and Druckenmiller, M. (2015). Effects of recent decreases in arctic sea ice on an ice-associated marine bird. *Prog. Oceanogr.* 136, 151–161. doi: 10.1016/j.pocean.2015.05.010

Drost, H., Carmack, E., and Farrell, A. (2014). Upper thermal limits of cardiac function for Arctic cod *boreogadus saida*, a key food web fish species in the Arctic Ocean. *J. Fish Biol.* 84, 1781–1792. doi: 10.1111/jfb.12397

Drost, H., Carmack, E., and Farrell, A. (2016). Acclimation potential of Arctic cod *Boreogadus saida* from the rapidly warming Arctic Ocean. *J. Exp. Biol.* 219, 3114–3125. doi: 10.1242/jeb.140194

Dufresne, J.-L., Foujols, M.-A., Denvil, S., Caubel, A., Marti, O., Aumont, O., et al., (2013). Climate change projections using the IPSL-CM5 earth system model: from CMIP3 to CMIP5. *Clim. Dyn.* 40, 2123–2165. doi: 10.1007/s00382-012-1636-1

Dunne, J. P., John, J., Shevliakova, E., Stouffer, R. J., Krasting, J. P., Malyshev, S., et al. (2013). GFDL's ESM2 global coupled climate-carbon earth system models part II: Carbon system formulation and baseline simulation characteristics. *J. Clim.* 26, 2247–2267. doi: 10.1175/JCLI-D-12-00150.1

Dunne, J. P., John, J. G., Adcroft, A. J., Griffies, S. M., Hallberg, R. W., Shevliakova, E., et al. (2012). GFDL's ESM2 global coupled climate-carbon earth system models. Part I: physical formulation and baseline simulation characteristics. *J. Clim.* 25, 6646–6665. doi: 10.1175/JCLI-D-11-00560.1

Duyck, S. (2015). The Paris Agreement and the protection of human rights in a changing climate. *Yearb. Int. Environ. Law* 26, 3–45. doi: 10.1093/yiel/yvx011

Egeland, G., Johnson-Down, L., Cao, Z., Sheikh, N., and Weiler, H. (2011). Food insecurity and nutrition transition combine to affect nutrient intakes in canadian arctic communities. *J. Nutr.* 141, 1746–1753. doi: 10.3945/jn.111.139006

Farrell, A. (2016). Pragmatic perspective on aerobic scope: peaking, plummeting, pejus and apportioning. *J. Fish Biol.* 88, 322–343. doi: 10.1111/jfb.12789

Farrell, A., Altimiras, J., Franklin, C., and Axelsson, M. (2013). Niche expansion of the shorthorn sculpin to Arctic waters is supported by a thermal independence of cardiac performance at low temperature. *Can. J. Zool.* 91, 1–8. doi: 10.1139/cjz-2013-0038

Farrell, A., and Franklin, C. (2016). Recognizing thermal plasticity in fish. *Science* 351, 132–133. doi: 10.1126/science.351.6269.132-b

Farrell, A., Hinch, S., Cooke, S., Crossin, D. P. G., Lapointe, M., and Mathes, M. (2008). Pacific salmon in hot water: applying aerobic scope models and biotelemetry to predict the success of spawning migrations. *Physiol. Biochem. Zool.* 81, 697–708. doi: 10.1086/592057

Ferreira, E., Anttila, K., and Farrell, A. (2014). Thermal optima and tolerance in the eurythermic goldfish (*Carassius auratus*): relationships between whole-animal aerobic capacity and maximum heart rate. *Physiol. Biochem. Zool.* 87, 599–611. doi: 10.1086/677317

Ford, J. (2009). Dangerous climate change and the importance of adaptation for the arctic's inuit population. *Environ. Res. Lett.* 4:9. doi: 10.1088/1748-9326/4/2/024006

Ford, J., McDowell, G., and Jones, J. (2014). The state of climate change adaptation in the arctic. *Environ. Res. Lett.* 9:104005. doi: 10.1088/1748-9326/9/10/104005

Ford, J., and Pearce, T. (2010). What we know, do not know, and need to know about climate change vulnerability in the western canadian arctic: a systematic literature review. *Environ. Res. Lett.* 5:9. doi: 10.1088/1748-9326/5/1/014008

Fortier, L., and Leggett (1985). A drift study of larval fish survival. *Mar. Ecol. Prog. Ser.* 25, 245–257. doi: 10.3354/meps025245

Frainer, A., Primicerio, R., Kortsch, S., Aune, M., Dolgov, A., Fossheim, M., et al. (2017). Climate-driven changes in functional biogeography of arctic marine fish communities. *Proc. Natl. Acad. Sci. U.S.A.* 114, 12203–12207. doi: 10.1073/pnas.1706080114

Franklin, C., Davison, W., and Seebacher, F. (2007). Antarctic fish can compensate for rising temperatures: thermal acclimation of cardiac performance in pagothenia borchgrevinki. *J. Exp. Biol.* 210, 3068–3074. doi: 10.1242/jeb.003137

Friddell, J., Michaud, J., Warwick, V., and LeDew, E. (2013). "The polar data catalogue: best practices for sharing and archiving Canada's polar data," in *Proceedings of the International Forum on Polar Data Activities in Global Data Systems*, ed W. I. P. Office (Tokyo), 6–8.

Froese, R., and Pauly, D. (2018). *Fishbase*. World Wide Web Electronic Publication. version (02/2018). Available online at: https://www.fishbase.org. (accessed February, 2018).

Galloway, T., Young, K., and Egeland, G. (2010). Emerging obesity among preschool-aged canadian inuit children: results from the nunavut inuit child health survey. *Int. J. Circumpolar Health* 69, 151–157. doi: 10.3402/ijch.v69i2.17437

Gaston, A., Woo, K., and Hipfner, J. (2003). Trends in forage fish populations in northern hudson bay since 1981, as determined from the diet of nestling thick-billed murres uria lomvia. *Arctic* 56, 227–233. doi: 10.14430/arctic618

Gilbert, M., Fortier, L., and Ponton, D. (1992). Feeding ecology of marine fish larvae across the great whale river plume in seasonally ice-covered southeastern hudson bay. *Mar. Ecol. Prog. Ser.* 84, 19–30. doi: 10.3354/meps084019

Giorgetta, M. A., Jungclaus, J. H., Reick, C. H., Legutke, S., Brovkin, V., Bader, J., et al. (2013). Climate and carbon cycle changes from 1850 to 2100 in MPI-ESM simulations for the coupled model intercomparison project phase 5. *J. Adv. Model. Earth Syst.* 5, 572–597. doi: 10.1002/jame.20038

Hansen, M., Nielsen, T., Stedmon, C., and Munk, P. (2012). Oceanographic regime shift during 1997 in Disko Bay, Western Greenland. *Limnol. Oceanogr.* 57, 634–644. doi: 10.4319/lo.2012.57.2.0634

Harwood, L., Smith, T., George, J., Sandstrom, S., Walkusz, W., and Divoky, G. (2015). Change in the beaufort sea ecosystem: diverging trends in body condition and/or production in five marine vertebrate species. *Prog. Oceanogr.* 136, 263–273. doi: 10.1016/j.pocean.2015.05.003

Hayashida, H. (2018). *Modelling Sea-Ice and Oceanic Dimethylsulfide Production and Emissions in the Arctic*. Ph.D. thesis, School of Earth and Ocean Sciences, University of Victoria.

Hayashida, H., Christian, J., Holdsworth, A., Hu, X., Monahan, A., Mortenson, E., et al. (2018). CSIB v1: a sea-ice biogeochemical model for the NEMO community ocean modelling framework. *Geosci. Model Dev. Discuss.* doi: 10.5194/gmd-2018-191

Hoover, C., Pitcher, T., and Christensen, V. (2013a). Effects of hunting, fishing and climate change on the Hudson Bay marine ecosystem: I. re-creating past changes 1970-2009. *Ecol. Modell.* 264, 130–142. doi: 10.1016/j.ecolmodel.2013.02.005

Hoover, C., Pitcher, T., and Christensen, V. (2013b). Effects of hunting, fishing and climate change on the hudson bay marine ecosystem: II. Ecosystem model future projections. *Ecol. Modell.* 264, 130–142.

Hop, H., and Gjøsæter, H. (2013). Polar cod (boreogadus saida) and capelin (*Mallotus villosus*) as key species in marine food webs of the arctic and the barents sea. *Mar. Biol. Res.* 9, 878–894. doi: 10.1080/17451000.2013.775458

Hop, H., and Tonn, W. (1998). Gastric evacuation rates and daily rations of arctic cod (*Boreogadus saida*) at low temperatures. *Polar Biol.* 19, 293–330. doi: 10.1007/s003000050249

Hu, X., and Myers, P. (2013). A lagrangian view of pacific water inflow pathways in the arctic ocean during model spin-up. *Ocean Model.* 71, 66–80. doi: 10.1016/j.ocemod.2013.06.007

Hu, X., and Myers, P. (2014). Changes to the Canadian Arctic Archipelago sea ice and freshwater fluxes in the 21st century under the IPCC A1B climate scenario. *Atmosphere-Ocean* 52, 331–350. doi: 10.1080/07055900.2014.942592

Ilyina, T., Six, K. D., Segschneider, J., Maier-Reimer, E., Li, H., and Nunez-Riboni, I. (2013). The global ocean biogeochemistry model HAMOCC: model architecture and performance as component of the MPI-Earth System Model in different CMIP5 experimental realizations. *J. Adv. Model. Earth Syst.* 5, 287–315. doi: 10.1029/2012MS000178

Kirtman, B., Power, S., Adedoyin, J., Boer, G., Bojariu, R., Camilloni, I., et al. (2013). "Near-term climate change: projections and predictability," in *Climate Change 2013: The Physical Science Basis. Contribution of Working Group I to the Fifth Assessment Report of the Intergovernmental Panel on Climate Change* (New York, NY: Cambridge University Press).

Klein, D., Carazo, M., Doelle, M., Bulmer, J., and Higham, A. (eds.) (2017). *The Paris Agreement on Climate Change: Analysis and Commentary*. New York, NY; Croydon: CPI Group Ltd.

Knutti, R., and Sedláçek, J. (2013). Robustness and uncertainties in the new CMIP5 climate model projections. *Nat. Clim. Change* 3, 369–373. doi: 10.1038/nclimate1716

Kohlbach, D., Graeve, M., Lange, B., David, C., Peeken, I., and Flores, H. (2016). The importance of ice algae- produced carbon in the central arctic ocean ecosystem: food web relationships revealed by lipid and stable isotope analyses. *Limnol. Oceanogr.* 61, 2027–2044. doi: 10.1002/lno.10351

Kohlbach, D., Schaafsma, F., Graeve, M., Lebreton, B., Lange, B., David, C., et al. (2017). Strong linkage of polar cod (*Boreogadus saida*) to sea ice algae-produced carbon: evidence from stomach content, fatty acid and stable isotope analyses. *Prog. Oceanogr.* 152, 62–74. doi: 10.1016/j.pocean.2017.02.003

Kroeker, K., Kordas, R., Crim, R., Hendriks, I., Ramajo, L., Singh, G., et al. (2013). Impacts of ocean acidification on marine organisms: quantifying sensitivities and interaction with warming. *Glob. Chang. Biol.* 19, 1884–1896. doi: 10.1111/gcb.12179

Kunz, K., Claireaux, G., Pörtner, H.-O., Knust, R., and Mark, F. (2018). Aerobic capacities and swimming performance of polar cod (*Boreogadus saida*; lepechin) under ocean acidification and warming conditions. *J. Exp. Biol.* 221:jeb184473. doi: 10.1242/jeb.184473

Kunz, K., Frickenhaus, S., Hardenberg, S., Johansen, T., Leo, E., Pörtner, H.-O., et al. (2016). New encounters in arctic waters: a comparison of metabolism and performance of polar cod (*Boreogadus saida*) and atlantic cod (*Gadus morhua*) under ocean acidification and warming. *Polar Biol.* 39, 1137–1153. doi: 10.1007/s00300-016-1932-z

Lam, V., Sumaila, U., Dyck, A., Pauly, D., and Watson, R. (2011). Construction and potential applications of a global cost of fishing database. *ICES J. Mar. Sci.* 68, 1–9. doi: 10.1093/icesjms/fsr121

Lanning, G., Storch, D., and Pörtner, H. (2015). Aerobic mitochondrial capacities in antarctic and temperate eelpout (zoarcidae) subjected to warm versus cold acclimation. *Polar Biol.* 28, 575–584. doi: 10.1007/s00300-005-0730-9

Laurel, B., Spencer, M., Iseri, P., and Copema, L. (2015). Temperature-dependent growth and behavior of juvenile arctic cod (*boreogadus saida*) and co-occurring north pacific gadids. *Polar Biol.* 39, 1127–1135. doi: 10.1007/s00300-015-1761-5

Lawson, J., Magalhaes, A., and Miller, E. (1998). Important prey species of marine vertebrate predators in the northwest atlantic: proximate composition and energy density. *Mar. Ecol. Prog. Ser.* 164, 13–20. doi: 10.3354/meps164013

Leo, E., Kunz, K., Schmidt, M., Storch, D., Pörtner, H.-O., and Mark, F. (2017). Mitochondrial acclimation potential to ocean acidification and warming of polar cod (*Boreogadus saida*) and atlantic cod (*Gadus morhua*). *Front. Zool.* 14:21. doi: 10.1186/s12983-017-0205-1

Lischka, S., and Riebesell (2012). Synergistic effects of ocean acidification and warming on overwintering pteropods in the arctic. *Global Change Biol.* 18, 3517–3528. doi: 10.1111/gcb.12020

Loder, J., and van der Baaren, A. (2013). *Climate Change Projections for the Northwest Atlantic From Six CMIP5 Earth System Models*. Canadian Technical Report of Hydrography and Ocean Sciences 286; Fisheries and Oceans Canada.

Lønne, O., and Gulliksen, B. (1989). Size, age and diet of polar cod, boreogadus saida (lepechin 1773), in ice covered waters. *Polar Biol.* 9, 187–191. doi: 10.1007/BF00297174

Loseto, L., Hoover, C., Ostertag, S., Whalen, D., Pearce, T., Paulic, J., et al. (2018). Beluga whales (*delphinapterus leucas*), environmental change and marine protected areas in the Western Canadian Arctic. *Estuar. Coast. Shelf Sci.* 212, 128–137. doi: 10.1016/j.ecss.2018.05.026

Loseto, L., Stern, G., Connelly, T., Deibel, D., Gemmill, B., Prokopowicz, A., et al. (2009). Summer diet of beluga whales inferred by fatty acid analysis of the eastern beaufort sea food web. *J. Exp. Mar. Biol. Ecol.* 374, 12–18. doi: 10.1016/j.jembe.2009.03.015

Lowry, L., Frost, K., and Burns, J. (1978). Food of ringed seals and bowhead whales near point barrow, Alaska. *Can. Field-Naturalist* 92, 67–70.

Majewski, A., Atchison, S., MacPhee, S., Eert, J., Niemi, A., Michel, C., et al. (2017). Marine fish community structure and habitat associations on the Canadian Beaufort shelf and slope. *Deep-Sea Res. Part I* 121, 169–182. doi: 10.1016/j.dsr.2017.01.009

Majewski, A., Lynn, B., Lowdon, M., Williams, W., and Reist, J. (2013). Community composition of demersal marine fishes on the Canadian Beaufort shelf and at Herschel Island, Yukon Territory. *J. Mar. Syst.* 127, 55–64. doi: 10.1016/j.jmarsys.2013.05.012

Majewski, A., Walkusz, W., Lynn, B., Atchison, S., Eert, J., and Reist, J. (2015). Distribution and diet of demersal arctic cod, (*Boreogadus saida*), in relation to habitat characteristics in the Canadian Beaufort Sea. *Polar Biol.* 39, 1087–1098. doi: 10.1007/s00300-015-1857-y

Masson-Delmotte, V., Zhai, P., Pörtner, H., Roberts, D., Skea, J., Shukla, P., et al. (eds.) (2018). "Summary for policymakers," in *Global Warming of 1.5°C. An IPCC Special Report on the Impacts of Global Warming of 1.5°C Above Pre-industrial Levels and Related Global Greenhouse Gas Emission Pathways, in the Context of Strengthening the Global Response to the Threat of Climate Change, Sustainable Development, and Efforts to Eradicate Poverty* (Geneva: World Meteorological Organization), 32.

McCrimmon, D. (2016). The athabaskan petition to the inter- american human rights commission: Using human rights to respond to climate change. *Polar J.* 6, 398–416. doi: 10.1080/2154896X.2016.1241484

McDorman, T. (2009). *Salt Water Neighbours: International Ocean Law Relations Between Canada and the United States*. New York, NY: Oxford University Press.

McGregor, J. (2018). *Premiers Vent Over Climate Change 'Goal Posts' and Internal Trade at First Ministers Meeting*. CBC News. Available online at: https://www.cbc.ca/news/politics/friday-first-ministers-montreal-1.4936364. (accessed January, 2019).

Mcnicholl, D., Walkusz, W., Davoren, G., Majewski, A., and Reist, J. (2016). Dietary characteristics of co-occurring polar cod (*Boreogadus saida*) and capelin (*Mallotus villosus*) in the Canadian arctic. *Polar Biol.* 39, 1099–1108. doi: 10.1007/s00300-015-1834-5

Miller, L., Macdonald, R., Mucci, A., Yamamoto-Kawai, M., Giesbrecht, K., McLaughlin, F., et al. (2014). Changes in the marine carbonate system of the western arctic: patterns in a rescued data set. *Polar Res.* 33:20577. doi: 10.3402/polar.v33.20577

Moore, S., and Gulland, F. (2014). Linking marine mammal and ocean health in the 'new normal' arctic. *Ocean Coast. Manag.* 102, 55–57. doi: 10.1016/j.ocecoaman.2014.08.011

Moss, R. H., Edmonds, J. A., Hibbard, K. A., Manning, M. R., Rose, S. K., van Vuuren, D. P., et al. (2010). The next generation of scenarios for climate change research and assessment. *Nature* 463, 747–756. doi: 10.1038/nature08823

Munday, P., Crawley, N., and Nilsson, G. (2009). Interacting effects of elevated temperature and ocean acidification on the aerobic performance of coral reef fishes. *Mar. Ecol. Prog. Ser.* 388, 235–242. doi: 10.3354/meps08137

Nelson, R., C.J, C. A., Bluhm, N., Conlan, K., and Gradinger, R. (2014). "Biodiversity and biogeography of the lower trophic taxa of the Pacific Arctic region: sensitivities to climate change," in *The Pacific Arctic Region: Ecosystem Status and Trends in a Rapidly Changing Environment* eds J. M. Grebmeier and W. Maslowski (Dordrecht: Springer Publishing), 269–336.

Nelson, R., Carmack, E., McLaughlin, F., and Cooper, G. (2009). Penetration of pacific zooplankton into the western arctic ocean tracked with molecular population genetics. *Mar. Ecol. Prog. Ser.* 381, 129–138. doi: 10.3354/meps07940

Oral, N. (2018). Ocean acidification: falling between the legal cracks of UNCLOS and the UNFCCC? *Ecol. Law Q.* 45, 10–30.

Ostertag, S., Loseto, L., Snow, K., Lam, J., Hynes, K., and Gillman, D. (2018). "that's how we know they're healthy": the inclusion of traditional ecological knowledge in beluga health monitoring in the inuvialuit settlement region. *Arctic Sci.* 4, 292–320.

Osuga, D., and Feeney, R. (1978). Antifreeze glycoproteins from arctic fish. *J. Biol. Chem.* 253, 5338–5343

Palomares, M., and Pauly, D. (2018). *Sealifebase*. World Wide Web Electronic Publication. Available online at: https://www.sealifebase.org. (accessed February, 2018) .

PAME (2015). *Framework for a Pan-Arctic Network of Marine Protected Areas*. Tech. rep., PAME International Secretariat, Akureyri.

PAME (2017). *PAME MPA-network Toolbox (2015-2017): Area-Based Conservation Measures and Ecological Connectivity*. Tech. rep., PAME International Secretariat, Akureyri.

Panasenko, L., and Soboleva, M. (1980). Food interrelations between the barents sea capelin and polar cod. *ICES* CM 1980:15

Pauly, D. (1980). On the interrelationships between natural mortality, growth parameters, and mean environmental temperature in 175 fish stocks. *J. du Cons. CIEM* 39, 175–192. doi: 10.1093/icesjms/39.2.175

Pauly, D., Christensen, V., and Walters, C. (2000). Ecopath, ecosim, and ecospace as tools for evaluating ecosystem impact of fisheries. *ICES J. Mar. Sci.* 57, 697–706. doi: 10.1006/jmsc.2000.0726

Peck, L., Morley, S., Richard, J., and Clark, M. (2014). Acclimation and thermal tolerance in antarctic marine ectotherms. *J. Exp. Biol.* 217, 16–22. doi: 10.1242/jeb.089946

Pershing, A., Alexander, M., Hernandez, C., Kerr, L., Bris, A. L., Mills, K., et al. (2015). Slow adaptation in the face of rapid warming leads to collapse of the gulf of maine cod fishery. *Science* 350, 809–812. doi: 10.1126/science.aac9819

Popova, E., Yool, A., Coward, A., Dupont, F., Deal, C., Elliott, S., et al. (2012). What controls primary production in the arctic ocean? Results from an intercomparison of five general circulation models with biogeochemistry. *J. Geophys. Res.* 117:C00D12. doi: 10.1029/2011JC007112

Pörtner, H. O., and Farrell, A. P. (2008). Ecology, physiology and climate change. *Science* 322, 690–692. doi: 10.1126/science.1163156

Pörtner, H. O., van Dijk, P. L. M., Hardewig, I., and Sommer, A. (2000). "Levels of metabolic cold adaptation: tradeoffs in eurythermal and stenothermal ectotherms," in *Antarctic Ecosystems: Models for Wider Ecological Understanding*, eds W. Davison and C. Howard Williams (Christchurch: Caxton Press).

Qi, D., Chen, L., Chen, B., Gao, Z., Zhong, W., Feely, R. A., et al. (2016). Increase in acidifying water in the Western Arctic Ocean. *Nat. Clim. Change* 7, 195–199. doi: 10.1038/nclimate3228

Rand, K., and Logerwell, E. (2010). The first demersal trawl survey of benthic fish and invertebrates in the Beaufort Sea since the late 1970s. *Polar Biol.* 34, 475–488. doi: 10.1007/s00300-010-0900-2

Rapporteur, S. (2017). *Report of the Special Rapporteur on the Issue of Human Rights Obligations Relating to the Enjoyment of a Safe, Clean, Healthy and Sustainable Environment*. Tech. Rep. A/HRC/34/49.

Robinson, E., and Davison, W. (2008). Antarctic fish can survive prolonged exposure to elevated temperatures. *J. Fish Biol.* 73, 1676–1689. doi: 10.1111/j.1095-8649.2008.02041.x

Rose, G. (2005). Capelin (*Mallotus villosus*) distribution and climate: a sea "canary" for marine ecosystem change. *ICES J. Mar. Sci.* 62, 1524–1530. doi: 10.1016/j.icesjms.2005.05.008

Rose, G., and Leggitt, W. (1990). Predicting variability in catch-per-unit effort in atlantic cod, gadus morhua, trap and gillnet fisheries. *J. Fish Biol.* 35, 155–161. doi: 10.1111/j.1095-8649.1989.tb03057.x

Saudny, H., Leggee, D., and Egeland, G. (2012). Design and methods of the adult inuit health survey 2007-2008. *Int. J. Circumpolar Health* 71:19752. doi: 10.3402/ijch.v71i0.19752

Schatz, V., Proelss, A., and Liu, N. (2018). The 2018 agreement to prevent unregulated high seas fisheries in the central arctic ocean: a primer. *Eur. J. Int. Law*. Available online at: https://www.ejiltalk.org/the-2018-agreement-to-prevent-unregulated-high-seas-fisheries-in-the-central-arctic-ocean-a-primer/ (accessed January, 2019).

Schmidt, M., Gerlach, G., Leo, E., Kunz, K., Swoboda, S., Pörtner, H.-O., et al. (2017). Impact of ocean warming and acidification on the behaviour of two co-occurring gadid species, boreogadus saida and gadus morhua, from svalbard. *Mar. Ecol. Prog. Series* 571, 183–191. doi: 10.3354/meps12130

Scinocca, J., Kharin, V., Jiao, Y., Qian, M., Lazare, M., Solheim, L., et al. (2015). Coordinated global and regional climate modelling. *J. Clim.* 29, 17–35. doi: 10.1175/JCLI-D-15-0161.1

Seebacher, F., Davison, W., Lowe, C., and Franklin, C. (2005). A falsification of the thermal specialization paradigm: compensation for elevated temperatures in antarctic fishes. *Biol. Lett.* 1, 151–154. doi: 10.1098/rsbl.2004.0280

Sibert, J., Hampton, J., Fournier, D., and Bills, P. (1999). An advection-diffusion-reaction model for the estimation of fish movement parameters from tagging data, with application to skipjack tuna (*Katsuwonus pelamis*). *Can. J. Fish. Aquat. Sci.* 56, 925–938.

Steiner, N., Azetsu-Scott, K., Hamilton, J., Hedges, K., Hu, X., Janjua, M., et al. (2015a). Observed trends and climate projections affecting marine ecosystems in the canadian arctic. *Environ. Rev.* 23, 191–239. doi: 10.1139/er-2014-0066

Steiner, N., Drost, H., and Hunter, K. (2018). *A Physiological Limits Database for Arctic and Subarctic Aquatic Species*. Can. Tech. Rep. Fish. Aquat. Sci. 3256, Fisheries and Oceans Canada.

Steiner, N., Sou, T., Deal, C., Jackson, J., Jin, M., Popova, E., et al. (2015b). The future of the subsurface chlorophyll-a maximum in the canada basin - a model intercomparison. *JGR Oceans* 121, 387–409.

Steiner, N. S., Christian, J. R., Six, K., Yamamoto, A., and Yamamoto-Kawai, M. (2014). Future ocean acidification in the canada basin and surrounding arctic ocean from cmip5 earth system models. *JGR Oceans* 119, 332–347. doi: 10.1002/2013JC009069

Stock, C., Alexander, M., Bond, N., Brander, K., Cheung, W., Curchitser, E., et al. (2011). On the use of ipcc-class models to assess the impact of climate on living marine resources. *Prog. Oceanogr.* 88, 1–27. doi: 10.1016/j.pocean.2010.09.001

Sumaila, U., Marsden, A., Watson, R., and Pauly, D. (2007). A global ex-vessel fish price database: construction and applications. *J. Bioeconomics* 9, 39–51. doi: 10.1007/s10818-007-9015-4

Sumaila, U., Tai, T., Lam, V., Cheung, W., Bailey, M., Cisneros-Montemayor, A., et al. (2019). Benefits of the paris agreement to ocean life, economies, and people. *Sci. Adv.* 5:eaau3855. doi: 10.1126/sciadv.aau3855

Suprenand, P. M., Ainsworth, C. H., and Hoover, C. (2018). *Ecosystem Model of the Entire Beaufort Sea Marine Ecosystem: A Temporal Tool for Assessing Food-Web Structure and Marine Animal Populations from 1970 to 2014*. Marine Science Faculty Publications. 261. Available online at: https://scholarcommons.usf.edu/msc_facpub/261

Swart, N. C., Fyfe, J. C., Hawkins, E., Kay, J. E., and Jahn, A. (2015). Influence of internal variability on arctic sea-ice trends. *Nat. Clim. Change* 5, 86–89. doi: 10.1038/nclimate2483

Tai, T., Cashion, T., Lam, V., Swartz, W., and U.R.Sumaila (2017). Ex-vessel fish price database: disaggregating prices for low-priced species from reduction fisheries. *Front. Mar. Sci.* 4:363. doi: 10.3389/fmars.2017.00363

Taylor, K. E., Stouffer, R. J., and Meehl, G. A. (2012). An overview of CMIP5 and the experiment design. *Bull. Amer. Meteor. Soc.* 93, 485–498. doi: 10.1175/BAMS-D-11-00094.1

Thor, P., Bailey, A., Dupont, S., Calosi, P., Søreide, J., Wit, P. D., et al. (2017). Contrasting physiological responses to future ocean acidification among arctic copepod populations. *Global Change Biol.* 24, e365–e377. doi: 10.1111/gcb.13870

Thorsteinson, L., and Love, M. (2016). *Alaska Arctic Marine Fish Ecology Catalog: Scientific Investigations Report 2016-*. Tech. rep., Bureau of Ocean Energy Management. doi: 10.3133/sir20165038

UNEP (2018). *The Emissions Gap Report 2018*. Tech. rep., United Nations Environment Programme, Nairobi.

Vancoppenolle, M., Bopp, L., Madec, C., Dunne, J., Ilyina, T., Halloran, P., et al. (2013). Future Arctic primary productivity from CMIP5 simulations: uncertain outcome, but consistent mechanisms. *Global Biogeochem. Cycles* 27, 605–619. doi: 10.1002/gbc.20055

Walkusz, W., Majewski, A., and Reist, J. (2013). Distribution and diet of the bottom dwelling arctic cod in the canadian beaufort sea. *J. Mar. Syst.* 127, 65–75. doi: 10.1016/j.jmarsys.2012.04.004

Walkusz, W., Paulic, J., WJ, W. W., Kwasniewski, S., and Papst, M. (2011). Distribution and diet of larval and juvenile arctic cod (*Boreogadus saida*) in the shallow canadian beaufort sea. *J. Mar. Syst.* 84, 78–84. doi: 10.1016/j.jmarsys.2010.09.001

Walkusz, W., Williams, W., Harwood, L., Moore, S., Stewart, B., and Kwasniewski, S. (2012). Composition, biomass and energetic content of biota in the vicinity of feeding bowhead whales (*Balaena mysticetus*) in the cape bathurst upwelling region (south eastern beaufort sea). *Deep-Sea Res. I* 69, 25–35. doi: 10.1016/j.dsr.2012.05.016

Welch, H., Crawford, R., and Hop, H. (1993). Occurrence of arctic cod (*Boreogadus saida*) schools and their vulnerability to predation in the canadian high arctic. *Arctic* 46, 331–339. doi: 10.14430/arctic1361

Winkler, H. (2017). "Mitigation," in *The Paris Agreement on Climate Change: Analysis and Commentary* (New York, NY; Croydon: CPI Group Ltd.), 141–165.

Woods, H., and Harrison, J. (2001). The beneficial acclimation hypothesis versus acclimation of specific traits: physiological change in water-stressed manduca sexta caterpillars. *Physiol. Biochem. Zool.* 74, 32–44. doi: 10.1086/319302

Zahariev, K., Christian, J., and Denman, K. (2008). A global ocean carbon model with parameterizations of iron limitation, calcification and N_2 fixation; preindustrial, historical and fertilization simulations. *Prog. Oceanogr.* 77, 56–82. doi: 10.1016/j.pocean.2008.01.007

Zeller, D., Booth, S., Pakhomov, E., Swartz, W., and Pauly, D. (2011). Arctic fisheries catches in Russia, USA, and Canada: baselines for neglected ecosystems. *Polar Biol.* 34, 955–973. doi: 10.1007/s00300-010-0952-3

Zhou, Y., Kubow, S., and Egeland, G. M. (2011). Highly unsaturated n-3 fatty acids status of canadian inuit: international polar year inuit health survey, 2007-2008. *Int. J. Circumpolar Health* 70, 498–510. doi: 10.3402/ijch.v70i5.17864

Zienczuk, N., and Egeland, G. M. (2012). Association between socioeconomic status and overweight and obesity among inuit adults: international polar year inuit health survey, 2007-2008. *Int. J. Circumpolar Health* 71:18419. doi: 10.3402/ijch.v71i0.18419

Conflict of Interest Statement: The authors declare that the research was conducted in the absence of any commercial or financial relationships that could be construed as a potential conflict of interest.

frontiers in Earth Science

ORIGINAL RESEARCH
published: 10 July 2019
doi: 10.3389/feart.2019.00169

Exploring Spatial Heterogeneity of Antarctic Sea Ice Algae Using an Autonomous Underwater Vehicle Mounted Irradiance Sensor

Alexander L. Forrest[1], Lars C. Lund-Hansen[2], Brian K. Sorrell[2], Isak Bowden-Floyd[3], Vanessa Lucieer[4], Remo Cossu[5], Benjamin A. Lange[6,7] and Ian Hawes[8]*

[1] Civil and Environmental Engineering, University of California, Davis, Davis, CA, United States, [2] Department of Bioscience, Aquatic Biology and Arctic Research Centre, Aarhus University, Aarhus, Denmark, [3] Australian Maritime College, University of Tasmania, Launceston, TAS, Australia, [4] Institute for Marine and Antarctic Studies, University of Tasmania, Hobart, TAS, Australia, [5] School of Civil Engineering, The University of Queensland, St Lucia, QLD, Australia, [6] Alfred-Wegener-Institut, Helmholtz-Zentrum für Polar- und Meeresforschung (AWI), Bremerhaven, Germany, [7] Fisheries and Oceans Canada, Freshwater Institute, Winnipeg, MB, Canada, [8] Coastal Marine Field Station, University of Waikato, Hamilton, New Zealand

Sea ice algae represent a key energy source for many organisms in polar food webs, but estimating their biomass at ecologically appropriate spatiotemporal scales remains a challenge. Attempts to extend ice-core derived biomass to broader scales using remote sensing approaches has largely focused on the use of under-ice spectral irradiance. Normalized difference index (NDI) based algorithms that relate the attenuation of irradiance by the snow-ice-algal ensemble at specific wavelengths to biomass have been used to explain up to 79% of the biomass of algae in limited areas. Application of these algorithms to datasets collected using tethered remotely operated vehicles (ROVs) has begun, generating methods for spatial sampling at scales and spatial resolution not achievable with ice-core sampling. Successful integration of radiometers with untethered autonomous underwater vehicles (AUVs) offers even greater capability to survey broader regions to explore the spatial heterogeneity of sea ice algal communities. This work describes the pilot use of an AUV fitted with a multispectral irradiance sensor to estimate ice-algal biomass along transects beneath land-fast sea ice (~2 m thick with minimal snow cover) in McMurdo Sound, Antarctica. The AUV obtained continuous, repeatable, multi-band irradiance data, suitable for NDI-type approaches, over transects of 500 m, with an instrument footprint of 4 m in diameter. Algorithms were developed using local measurements of ice algae biomass and spectral attenuation of sea ice and were able to explain 40% of biomass variability. Relatively poor performance of the algorithms in predicting biomass limited the confidence that could be placed in biomass estimates from AUV data. This was attributed to the larger footprint size of the optical sensors integrating small-scale biomass variability more effectively than the ice core in the platelet-dominated ice algal habitat. Our results support continued development of remote-sensing of sea ice algal biomass at m–km spatial scales using optical methods, but caution that footprint sizes of calibration data (e.g., coring) must be compatible with optical sensors used. AUVs offer autonomous survey techniques that could be applied to better understand the horizontal variability of sea ice algae from nearshore ice out to the marginal ice zone.

Keywords: ice algae, Antarctica, McMurdo, autonomous underwater vehicles, biomass, normalized difference indices

OPEN ACCESS

Edited by:
Alun Hubbard,
UiT The Arctic University of Norway, Norway

Reviewed by:
Ramesh Raju,
National Institute of Ocean Technology, India
Pedro Duarte,
Norwegian Polar Institute, Norway

****Correspondence:***
Alexander L. Forrest
alforrest@ucdavis.edu

Specialty section:
This article was submitted to Cryospheric Sciences, a section of the journal Frontiers in Earth Science

Received: *25 September 2018*
Accepted: *19 June 2019*
Published: *10 July 2019*

Citation:
Forrest AL, Lund-Hansen LC, Sorrell BK, Bowden-Floyd I, Lucieer V, Cossu R, Lange BA and Hawes I (2019) Exploring Spatial Heterogeneity of Antarctic Sea Ice Algae Using an Autonomous Underwater Vehicle Mounted Irradiance Sensor. Front. Earth Sci. 7:169. doi: 10.3389/feart.2019.00169

INTRODUCTION

A significant proportion of primary production in ice-covered oceans is associated with ice algal cells living within or attached to sea ice (Arrigo et al., 1997, 2010; Lizotte, 2001). Sea ice reaches a yearly maximum extent of 20 million km^2 of Antarctic waters (Holland et al., 2014) and conservative estimates attribute approximately 20% of primary productivity to algae that grow on or in sea ice (Arrigo et al., 1991; McMinn et al., 1999; Arrigo and Thomas, 2004). Sea ice algae are particularly important to marine ecosystems as they are a spatially constrained source of fixed carbon available to higher trophic levels during spring before the onset of significant pelagic productivity (Arrigo and Thomas, 2004; Flores et al., 2012; Kohlbach et al., 2017; Schaafsma et al., 2017). During ice break-up and melt, sea ice algae may also play an important role in the export of fixed carbon from the photic zone (Boetius et al., 2013) and potentially in seeding planktonic production in marginal ice zones (Mangoni et al., 2009).

The existence of patchiness on millimeter (Lund-Hansen et al., 2017) and meter spatial scales in sea ice algae is well known from traditional ice coring approaches (Rysgaard et al., 2001) and imagery obtained from divers (Mundy et al., 2007) and under-ice vehicles (Ambrose et al., 2005). Cimoli et al. (2017) provides a complete review of the spatial scales associated with ice algae and emerging observational techniques. This review highlights how the quantitative sampling of sea ice algal biomass using traditional ice coring methods remains a laborious and spatially constrained approach (e.g., Mundy et al., 2007; Campbell et al., 2015), that fails to resolve the distribution of sea ice algal biomass at larger (>100 m) spatial scales (Lange et al., 2016, 2017; Meiners et al., 2017). The lack of reliable broad-scale data on ice algae biomass distribution makes the contribution of algae to regional food webs difficult to quantify, and thus creates a problem when trying to model the potential consequences of climate-driven changes to sea ice dynamics on ecosystem functionality.

To fully understand sea ice ecosystem function, it is critical to develop techniques that capture measurements of the variability of ice algal distribution and abundance at appropriate spatial scales. Such techniques may include underwater vehicles equipped with irradiance sensors to spatially map the spectra associated with the presence of ice algae growing at the ice-water interface (e.g., Lange et al., 2016, 2017; Meiners et al., 2017). This technique relies on suitably sensitive sensor arrays deployed beneath the ice surface and development of robust correlation algorithms between the spectral irradiance data and algal biomass.

While radiative transfer models for sea ice bio-optics have been available for many years (Arrigo et al., 1991; Zeebe et al., 1996), the range of optical attributes that are needed to generate and validate such models are difficult to obtain. For these reasons, most attempts to link under-ice irradiance with biomass involve empirical modeling of relationships between under-ice irradiance spectra, ice and snow properties, and algal biomass (Mundy et al., 2007; Fritsen et al., 2011; Ehn and Mundy, 2013; Melbourne-Thomas et al., 2015; Lange et al., 2016). A variety of algorithms have been used in these investigations and normalized difference indices (NDI) have consistently emerged as the most successful to date (Melbourne-Thomas et al., 2015). A review of published NDI values shows prediction models with coefficients of determination values (R^2) ranging from 0.64 to 0.89, with wavelengths in the 420–490 nm band, proving the most useful in field-based research (Melbourne-Thomas et al., 2015). Optical methods for estimating ice algal biomass have been attempted for Antarctic pack ice (Fritsen et al., 2011) and Arctic land-fast ice (Mundy et al., 2007; Campbell et al., 2015), Arctic pack ice (Lange et al., 2016), Antarctic land-fast ice (Wongpan et al., 2018), and in pack ice for two sectors of the Southern Ocean (Melbourne-Thomas et al., 2015). These applications have been individually successful on a regional scale but other large scale variations between ice types have confounded development of a "universal algorithm" to date.

Routine use of optical methods for estimating sea ice algal biomass would greatly benefit from under-ice vehicles equipped with optical sensors able to obtain spatially resolved estimates of biomass across a wide range of length scales. To meet this need there have been several deployments of spectroradiometers on remotely operated vehicles (ROVs) under sea ice (e.g., Nicolaus and Katlein, 2013; Lund-Hansen et al., 2018). ROVs are generally limited by the tether length, platform stability and vehicle positioning. To further develop this approach, we mounted a multispectral radiometer on an autonomous underwater vehicle (AUV) to be flown along pre-programmed transects of up to 500 m in length under sea ice in November 2014. In contrast to ROVs, AUVs provide a more stable platform capable of making measurements over longer distances with greater spatial precision (e.g., Doble et al., 2009). In this research, we present a spatially explicit dataset showing transmitted spectral irradiance at different wavelengths across three separate transects from a single deployment hole. We present algorithms used to convert optical data to estimated biomass concentrations, specific to our study site through correlation and regression analyses of a dataset comprising under-ice spectra and algal biomass estimates within the survey area collected from an ice coring survey. The survey region was first year, land-fast ice off of Cape Evans, Antarctica, selected because it is: (1) a relatively deep region (>220 m water depth) of McMurdo Sound; (2) is well known for its near uniform first-year ice; (3) exhibits dense algal growth; and (4) often has minimal snow cover (McMinn et al., 2000; Remy et al., 2008). All of these variables were anticipated to optimize the chances of a successful first attempt at documenting variability of ice algal biomass using our AUV-based approach.

MATERIALS AND METHODS

Field Sampling

Field sampling was conducted in early November 2014 at Cape Evans, McMurdo Sound, Antarctica (77° 38.2 S, 166° 20.8 E) (**Figure 1A**). The study design involved AUV-based optical sampling along three transects (CE1, CE2, and CE3) radiating at about 50° to each other from the deployment hole. AUV-collected under-ice topography from these transects are shown in **Figure 1B** (after Lucieer et al., 2016). A concurrent ice-coring campaign occupied 15 stations close to the transects

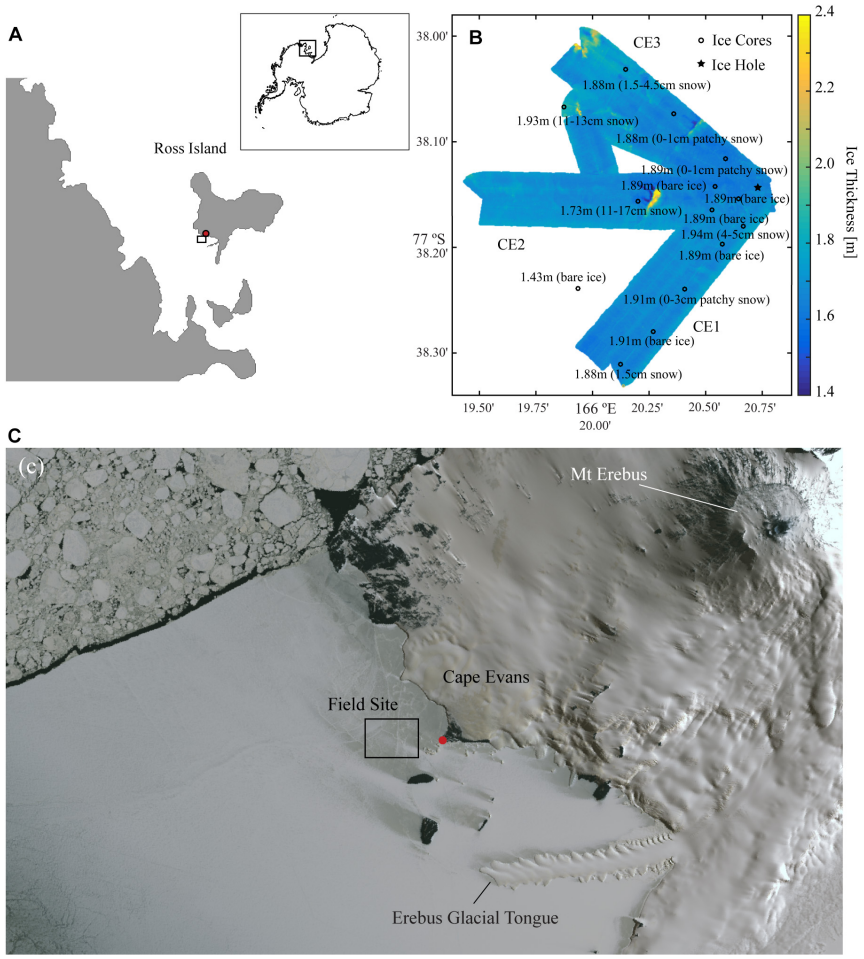

FIGURE 1 | (A) Location of Cape Evans, McMurdo Sound within the Antarctic continent (inset); **(B)** Ice thickness as mapped across 60 m swaths using the interferometric Geoswath *plus* sonar onboard the AUV on the three transects where spectral irradiance measurements were made (CE1, CE2, and CE3) with point measurements of ice thicknesses and snow condition measured at each of the coring stations (open circle) in addition to the ice hole (filled star) from which the vehicle was deployed; and **(C)** a WorldView-1 satellite image collected on 2 November 2014 showing the snow coverage in the region around Cape Evans and the location of the main field camp (red dot).

covered by the AUV (**Figure 1B**) and an additional 5 within a 3 km radius of the deployment hole (positions not shown). Ice coring stations were selected to avoid any multi-year ice inclusions, and were largely free of snow because the entire AUV survey region had nearly no snow cover. Sampling outside the AUV area and between transects included targeting of small patches of snow cover, thought to be from the previous winter, to provide a range of snow thicknesses for subsequent analyses to explore the relationship of snow and presence of chl-a. Water depth at the site was in excess of 100 m.

Under-Ice Spectral Irradiance From Ice Coring

At each of the 20 ice coring stations (15 shown in **Figure 1B**) we deployed a spectroradiometer (TriOS Ramses ACC-UV/VIS cosine-corrected hyperspectral radiometer) with no pressure or tilt sensor, through a 250-mm diameter hole drilled through the sea ice after the AUV transects had been completed. The zenith angle was controlled by using a cable connected at the bottom of the sensor and the weight of the cable kept the sensor vertically positioned below the ice. This design was tested in a water tank in a laboratory before the field work. No data were excluded from the data-set and it was all corrected for the immersion effect. The light field below the ice is entirely diffuse whereby the effects of any possible tilt of the sensor is at a minimum.

The radiometer was mounted on an articulated arm that positioned the sensor 10–15 cm under the ice surface, 1.2 m from the outer edge of the access hole, to avoid the interference of light from the hole. The holes were also filled with snow and pieces of ice to avoid light interference. Transmitted spectra of downwelling irradiance (E_d, mW m^{-2} nm^{-1}) had a nominal spectral resolution of 3.34 nm from 320 to 950 nm, though only values from 400 to 700 nm (i.e., photosynthetically active radiation – PAR) were used in this analysis. Once the radiometer was positioned under the ice, three replicate spectra were taken

at each of three positions of the arm; toward the sun and at right angles left and right. All spectra were obtained under clear skies, within 4 h of solar noon. At each station, the exact position where each spectrum was obtained was marked on the ice surface. In addition, three incident spectra (E_d) were obtained above the ice surface. This was done by making 3 consecutive measurements of down welling irradiance in air immediately followed be 3 measurements of reflected irradiance at 50 cm above the ice. Spectrally resolved vertically downwelling attenuation coefficients [$K_d(\lambda)$] for the water column was estimated at one location by lowering the TriOS sensor to a maximum depth of 16.5 m and recording spectra at 1 m vertical intervals. Spectrally resolved vertical attenuation coefficients for downwelling irradiance [$K_d(\lambda)$] were calculated from these depth profiles using log-linear regression (Kirk, 2011).

Biological Parameters and Laboratory Analysis

At each of the ice coring stations, snow thickness was measured and an ice core was recovered from each of the three positions of the light arm using a 76 mm diameter SIPRE ice corer. Ice cores frequently had platelet ice frozen onto the bottom of the ice layer and were withdrawn with care to preserve as much of the platelet structure as possible, though at times some plates were dislodged. The thickness of the ice was measured for each core sample. Cores were photographed and the lower 50 mm of each, plus attached platelets, were cut off using a stainless-steel hacksaw, and transferred to a shore laboratory in a dark, insulated box for processing which occurred within 2 h of collection.

In the laboratory, ice core sections were thawed in the dark at 4°C for pigment analysis. Immediately after thawing, the final melt volume was measured and vigorously mixed to break up cell aggregates. Aliquots were filtered onto Whatman GF/F filters for: (1) chl-a, (2) other algal pigments (HPLC), and (3) absorption characteristics of the sea ice algae. Filters were stored individually wrapped and frozen in liquid nitrogen for up to 4 weeks during return to New Zealand or Denmark for longer term storage at −80°C.

To determine chl-a, filters were extracted in 95% ethanol and pigment concentration was determined using a Shimadzu UV2401 twin-beam spectrophotometer following Lund-Hansen et al. (2014). Phaeopigments were estimated by acidification, but no phaeopigment was detectable. One sample from the three chl-a samples at each station was selected at random for HPLC analysis. HPLC analyses were conducted on a Shimadzu HPLC equipped with an online photodiode array detector (SPD-M10Avp) and fluorescence detector (RF-10Axl) with excitation set at 350 nm and emission set at 450 nm (for identification purposes only). Injection of 25–100 µl was conducted using a Shimadzu SIL-10AF auto-sampler with sample cooler set at 4°C. A reverse phase Supelcosil LC-18 column (5 µm particle size; length 25 cm × 4.6 mm ID) with a guard column, was used for separation. Mobile phases used in the separation were 80:20 Methanol:0.5 M ammonium acetate, 90:10 Acetonitrile:UV-pure milli-q water and 100% ethylacetate. All chromatograms were integrated using Class VP 7.2 software. Identification of individual pigments was based on a combination of retention time and absorbance spectra, compared to commercial standards. Quantification of chlorophylls were based on absorbance at 662 nm and carotenoids at 449 nm. Here we focus on fucoxanthin (fuco), diadinoxanthin and xanthin (DDX), as dominant carotenoids within the sea ice diatom community. The concentrations of diatoxanthin and diadinoxanthin were added together (hereafter DDX) as these two pigments interconvert through epoxidation within cells. For comparison between samples, HPLC quantified pigments were normalized to chl-a.

Ice-Algae Absorption

Measurements of spectral absorption characteristics of the ice algae are based on a known volume of filtered ice melt collected onto a GF/F filter. We assumed that particulate absorption showed a similar spectrum as by the algae and did not measure particulate absorption. This might have introduced errors but these are considered to be minimum in light of the dominant chl-a absorptions. The filters were placed in front of the aperture of an integrating sphere attached to the Shimadzu spectrophotometer to measure absorption of wavelengths from 380 to 800 nm. The blank was a similar filter soaked in filtered seawater and the chlorophyll-specific absorption coefficient a^*_λ was subsequently defined as:

$$a^*_\lambda = \left(2.303 \cdot A_f / \left(\beta \cdot V_f \cdot OD_\lambda\right)\right) / \text{chl-a} \quad (1)$$

where, A_f is the effective area of the filter (m^2), V_f is the volume filtered (m^3), OD_λ is the optical density of the filter at wavelength λ, β is a correction for path length amplification within the glass fiber filter (Cleveland and Weidemann, 1993), and chl-a is the estimated concentration of chlorophyll. The specific absorption coefficient a^*_λ was used in the optical modeling (see below) and normalized to a^*_{672} to allow the shape of the algal absorption spectra from all samples to be compared (Lund-Hansen et al., 2014). The ice algae species composition was determined on Lugol-fixed samples and enumerated according to Uthermöhl (1958) and identified based on the work by Tomas (1997). More details are provided in Lund-Hansen et al. (2014).

Linking Under-Ice Spectra to Chl-a

Relationships between chl-a concentration and under-ice spectral irradiance measurements were then compared using two methods: (1) the normalized difference index (NDI), and (2) the empirical orthogonal function analysis (EOF). Three ice core samples and three L-arm surveys were carried out at each of the 20 stations, and each L-arm deployment consisted of three irradiance spectra that were averaged to give a total of 60 samples. The same methodologies and model selection criteria, with averaged triplicate TriOS spectra for each of the 60 samples as the input dataset (three samples for each of 20 stations), were used as detailed in Lange et al. (2016).

For the first method, a correlation surface matrix between all possible (301 × 301) NDI wavelength combinations, as the spectra were interpolated to 1 nm from 400 to 700 nm following Nicolaus et al. (2010), and the associated chl-a concentrations

was generated with a moving average of a 3 × 3 nm grid centered at each value (e.g., Lange et al., 2016). This ensured that the maximum correlation value was not chosen at the edge of regions with an abrupt change between high and low correlations. The maximum correlation NDI wavelength combination was chosen with at least one wavelength within the range of 400 to 480 nm, which corresponds to the ∼440 nm chl-a absorption peak. A generalized linear model (GLM; McCullagh and Nelder, 1989) was constructed with chl-a concentrations and the maximum correlation NDI as the response and predictor variables, respectively. These took the log-link form defined in Eq. 2:

$$\ln\left(F\left(\text{chl-a}\right)\right) = \alpha + \beta\,(\text{NDI}) \quad (2)$$

where α is the intercept and β the regression coefficient. Consistent with Taylor et al. (2013) and Lange et al. (2016), we applied a log-link function for the prediction of chl-a [i.e., *F*(chl-a)] for both NDI and EOF GLM prediction models.

For the second method, a covariance matrix of the standardized spectra was submitted to an Eigen decomposition, which produces the EOF modes used as predictor variables. A GLM was constructed with chl-a as a response variable and the EOF modes and their squares as the predictor variables. Only the first 9 EOF modes, and their squares, were included to reduce the size of analysis and subsequently resulted in a total of 18 possible predictor variables. The "R" package *glmulti* (Calcagno and de Mazancourt, 2010) was applied to select the top 100 most reliable set of GLMs from all possible unique combinations. The bayesian information criterion (BIC) was used in the selection of robust models as it includes a penalty for both the number of predictor variables and the resulting estimated sample size (Schwarz, 1978). Finally, one reference model was selected based on the lowest BIC and in which all coefficients were significant ($p \leq 0.05$). These GLM models have the following form defined by Eq. 3:

$$\ln\left(F\left(\text{chl-a}\right)\right) = \alpha + \beta_1 s_1 + \beta_2 s_2^2 + \ldots + \beta_m s_m + \beta_n s_n^2 \quad (3)$$

where *F*(chl-a) is the log-link function for the prediction of chl-a, $s_{1,2,m,n}$ are the EOF modes or the EOF modes squared from S determined from the GLM model selections, α is the intercept and $\beta_{1,2,m,n}$ are the regression coefficients. In addition to determining the optimum NDI and EOF from the full suite of wavelength combinations available from the TriOS dataset to solve Eq. 3, we also undertook a limited analysis to focus on developing an NDI based on the wavelength data available from a multispectral cosine corrected radiometer (Satlantic OCR-507-ICSW) with 6 channels (412, 470, 532, 565, 655, and 670 nm) mounted on the AUV. The TriOS spectroradiometer-derived irradiance closest to the wavelength in the Satlantic bands was used in a pairwise fashion to derive all possible NDI values. Recognizing that the footprint of the AUV-mounted instrument was substantially larger than that of the ice corer or the TriOS itself, an averaged NDI for the three values measured at each of the 20 stations was used. These measurements were taken on the same day (although not concurrent) within a spatial distance of 1.7–2.4 m of each other. Likewise, we calculated average chl-a for the three cores from each station. We used a Pearson correlation to determine which NDI best predicted chl-a content.

Modeling Chl-a Concentration From Under-Ice Spectra

An unexpected feature was that the variability of chl-a concentration in the triplicate cores from each station was found to be higher than that of the chl-a concentration estimated from the corresponding irradiance spectra. To address concerns that we were failing to fully recover biomass from the fragile platelet component of the ice cores, a simple radiative transfer model was used with the specific goal of determining any evidence of undersampling of chl-a by coring. The iterative approach, modified from that of Mundy et al. (2007), was to use literature values of snow and ice spectral attenuation to first estimate, for each core, the spectral irradiance that would be expected under the ice, in the absence of algae. We then added in the effects of measured algal biomass using the chl-a concentration and a_λ^* for each site to develop a "predicted" under-ice spectrum. We then compared the predicted and observed spectra and, where they differed, iteratively changed the chl-a concentration used in modeling of the under-ice spectrum until the predicted most closely matched the observed. Observed and "required" chl-a concentrations could then be compared.

Specifically, following Mundy et al. (2007), we considered the sea ice was compartmentalized into snow, ice and ice/algae layer. Light entering this layer was estimated by subtracting measured reflectance from incident irradiance, and the attenuation by snow, then by ice, was based on attenuation coefficients for dry snow and cold ice given by Perovich (1990) and measured thicknesses. This allowed an estimate of the spectral irradiance reaching the ice/algae layer. To estimate the attenuation within the ice/algae layer (assuming no internal ice algae at this site) the approach of Ehn and Mundy (2013) was followed in Eq. 4:

$$\mathrm{K_d}\,(\lambda)\,(\text{ice/algae}) = 1/\mu_\mathrm{d}\sqrt{\left[\left(\mathrm{a_\lambda^{ice}} + \mathrm{C}\cdot\mathrm{a_\lambda^*}\right)^2 + 0.238\left(\mathrm{a_\lambda^{ice}} + \mathrm{C}\cdot\mathrm{a_\lambda^*}\right)\left(\mathrm{b^{tot}}\right)\right]} \quad (4)$$

where a_λ^{ice} is the wavelength-specific absorption coefficient (measured in $\mathrm{m^{-1}}$) for ice taken from Perovich (1990), μ_d is the dimensionless average cosine of the downwelling hemisphere of the light field (taken as 0.7 after Ehn and Mundy, 2013), and b^{tot} is a scattering coefficient for ice taken as 413 $\mathrm{m^{-1}}$ after Ehn and Mundy, 2013). C is the site specific chl-a concentration and a site specific a_λ^* that were used in these calculations and we assumed that the addition of algae to the ice did not change the scattering properties of the ice (Mundy et al., 2007; Ehn and Mundy, 2013). We iteratively changed the values of chl-a in these calculations until a least squares regression between observed and predicted irradiance was maximal across wavelengths from 400 to 600 nm (irradiance at wavelengths longer than 600 nm was too low to be included).

Autonomous Underwater Vehicle Irradiance Measurements

Irradiance measurements were made with a Satlantic OCR507 multispectral radiometer, along with its battery pack and a Satlantic STOR-X datalogger, mounted on a *Gavia*-class AUV (produced by Teledyne Gavia). The vehicle was pre-programmed to run three separate out and back 500 m return transects from a single deployment hole (recall lines CE1, CE2, and CE3; **Figure 1C**). As a result of the logistics of deploying, each transect was run approximately 2 h after the last. At a running speed of $\sim$1.5 m s^{-1} and a sampling frequency of 25 Hz, this corresponds to a single measurement every 6–8 cm, although the cone of acceptance (i.e., the field of view) of the sensor meant that, at the depth of travel ($\sim$6 m water depth), 75% of the irradiance sampled came from an under-ice footprint of approximately 4 m diameter. This water depth was selected as an estimated tradeoff between a safe operating envelope for the AUV and the quality of the collected data. The sampling frequency of the spectra data was subsequently downsampled to 1 Hz to match the navigation logging frequency of the vehicle.

Measurements of irradiance below the ice were collected at six, 10 nm wavelength bands centered on 412, 470, 532, 565, 625, and 670 nm. Known absorption properties of sea ice and ice algae suggested that attenuation of lower wavelengths (412–532 nm) would result from snow, ice and ice/algae whereas at 565–670 nm attenuation would primarily result from snow and ice (Hawes et al., 2012). To account for minor variations in AUV depth and ice cover thickness, the spectral irradiance at each wavelength was calculated for the ice-water interface using a vertical exponential attenuation model using data from the TriOS instrument deployments described above, and the water column length between the vehicle and the ice. Ice thickness was derived from collected sonar data and the recorded vehicle operating depth (Lucieer et al., 2016).

Statistical Treatment of Data

Relationships between snow, PAR transmittance (ratio of under-ice PAR irradiance to incident PAR irradiance represented as a percentage) and chl-a were examined using quantile regression analysis (QRA) techniques. QRA provides estimates of the relationship between the maximum chl-a concentration and snow depth, independent of data outliers and increasing/decreasing variance homogeneity over the snow depth range (Cade and Noon, 2003). Data were not transformed for QRA as it is a non-parametric test that makes no assumptions regarding normality of distribution or variance homogeneity.

To group samples by similarity of the spectral absorption of algae particulates on filters, a hierarchical cluster analysis based on a^*_λ normalized to a^*_{672} was used through Primer 7. After grouping samples, snow cover, chl-a, fucoxanthin and DDX from sites within clusters were compared. As normality could not be established by transformation, non-parametric Mann–Whitney Rank Sum tests, within Sigmaplot 13, were run.

Correlograms were used to examine for spatial autocorrelation in the AUV-based NDI-derived estimates of chl-a along transects. Correlations were done based on offsets of 0–100 m, over transects of up to 475 m, and plotted Pearson's correlation coefficient against offset distance to examine for periodicities in chl-a concentrations.

RESULTS

Ice Coring

Across the study site, snow thickness was generally quite low (0–20 cm) with only one site having more (41 cm), and chl-a ranged from 9.7 to 81.7 mg m^{-2} (**Figure 2A**). Concentrations of chl-a were log-normally distributed, with a geometric mean of 32.7 mg m^{-2}, and 95% C.I. of 11.4–62.5 mg m^{-2}. An apparent trend for high chl-a values under thinner snow depths was measured using QRA (**Figure 2A**), which became significant ($p < 0.05$) at the >80% quantile level. However, no simple relationship was found between transmittance, and chl-a (**Figure 2B**). The transmittance of total PAR through the ice varied between 0.12 and 0.90% of incident irradiance. This equates to 1.4–10.8 μmol photons m^{-2} s^{-1} at ice/ocean interface at a measured maximum surface irradiance of 1200 μmol photons m^{-2} s^{-1}. As expected, thicker snow depth (up to 10 cm) tended to be associated with reduced transmittance, but further increases in snow thickness up to 40 cm made little further difference to the light transmittance (**Figure 2C**). These thicker snow patches tended to be only several meters in size, and horizontal transfer of scattered light within the ice may have enhanced irradiance under such patches. The snow patches were very compact and appeared to be old snow from the winter some months ago. Ice thickness varied little, ranging from 1.87 to 1.93 m, with the exception of a single station where a thickness of 1.43 m was recorded and no effect of ice thickness on transmittance was evident (data not shown).

As was expected, based on previous visits to the site, ice cores contained large amounts of platelet ice embedded on the underside of the sea ice. The ice algae occurred both within the congelation ice that was cementing the platelets into the ice, as well as associated with the platelets themselves. Despite care being taken to ensure that the core-platelet assembly was extracted as intact as possible, some biomass was likely lost. Differences in pigment composition with snow thickness were evident in responses of accessory pigments normally associated with light harvesting (fuco) and with light protection (DDX). The fuco:chl-a ratio increased toward a maximum value with increasing snow thickness, while DDX:chl-a ratio was low under thick snow cover and increased as snow decreased (**Figures 2C,D**). Ice-algae species were dominated by diatoms in all samples, particularly *Fragilariopsis obliquecostata* which represented 80% of abundances, with *Nitzschia frigida* and *Navicula directa* as subdominants.

Algal Absorption Spectra

Algal absorption spectra showed the typical large peak absorption by chl-a and carotenoids in the region of the blue wavelengths (400–500 nm) and a secondary chl-a peak at 665 nm (**Figure 3** – Inset). Cluster analysis of normalized absorption

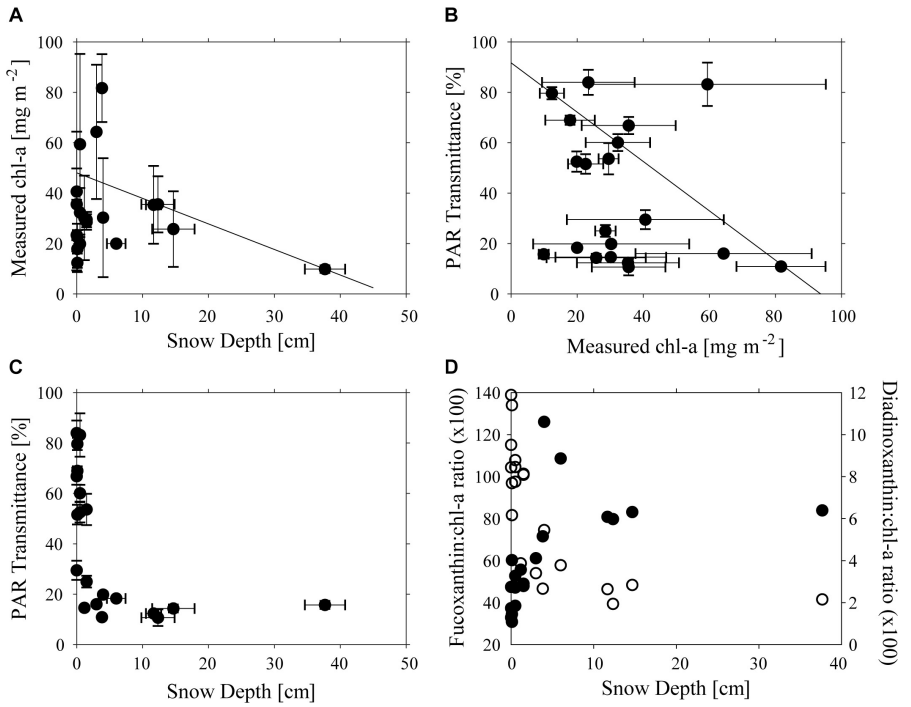

FIGURE 2 | Relationships between **(A)** Snow Depth (cm) and chl-a concentration (mg m^{-2}), **(B)** chl-a concentration (mg m^{-2}) and PAR transmittance (%), **(C)** Snow Depth (cm), and PAR transmission **(D)** Fucoxanthin:chl-a ratio and Snow Depth (cm) (filled circles) and Diadinoxanthin:chl-a ratio (unfilled circles). Lines in **(A,B)** show significant 80% quantile regression lines and error bars are shown in **(A–C)**.

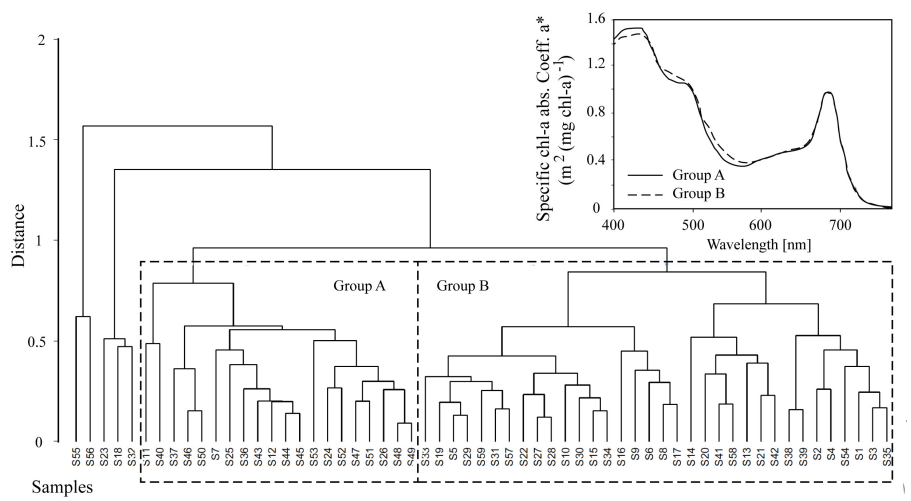

FIGURE 3 | Hierarchical cluster analysis of absorption spectra from 60 samples where Groups A and B are shown for subsequent analysis. The average algae particulate absorption spectra normalized to the 670 nm peak for each of the two main Groups A and B is also shown for reference (inset).

spectra identified two distinct groups of core samples based on their absorption spectra, hereafter termed Group A (21 cores) and Group B (34 cores), with five outliers (**Figure 3**). The average absorption spectra of the two large groups differed only slightly, mostly in the 400 to 550 nm region (**Figure 3** – Inset). These groups differed significantly in ratios of fucoxanthin and DDX to chl-a, with significantly higher proportions of photoprotective pigments in the low snow cover Group B, even though chl-a was similar in both groups (**Table 1**).

Estimations of NDI and EOF

Both empirical methods of linking under-ice spectra with measured chl-a explained a portion of the variance, but 95% prediction intervals were wide (**Figure 4**). The optimal

TABLE 1 | Mean values (range in brackets) of snow thicknesses and pigment properties for the two groups of core samples identified by cluster analysis.

Parameter	Group A (n = 21)	Group B (n = 34)
Snow thickness (cm)	*8.5 (3.6–12.5)*	*0.5 (0.5–1.5)*
chl-a (mg m^{-2})	26.0 (11.4–36.5)	24.9 (19.2–31.2)
Fuco:chl-a ratio	*0.79 (0.66–0.83)*	*0.48 (0.38–0.58)*
DDX:chl-a ratio	*0.03 (0.03–0.05)*	*0.08 (0.06–0.09)*

Parameters with significant differences (Mann–Whitney rank sum tests, $P < 0.05$) shown in italics).

combination of wavelengths for the NDI was 402:530 nm, which yielded a weak but significant coefficient of determination (R^2 = 0.31; $p < 0.001$) between predicted and observed chl-a (**Figure 4A**). The NDI residual showed no correspondence to snow cover, chl-a or to the two separate clusters of sites derived from a^*_λ analysis described below. The empirical orthogonal function (EOF, using modes S_2, S_3, and S_9) analyses produced a slightly better prediction of chl-a, (R^2 = 0.39; $p < 0.001$; N = 60), though the improvement on NDI was small (**Figure 4B**). As with NDI, examination of prediction residuals did not show a correspondence to snow cover, chl-a or site clustering.

The NDI derived values using the restricted set of wavelengths, after averaging sites within stations, showed a significant correlation between ln(chl-a) and ln(NDI 412:532) (**Figure 5**). A predictive relationship of ln(chl-a) = 1.76·ln(NDI 412:532) + 5.30 was evident (R^2 = 0.47; $p < 0.05$; N = 18). NDI values were then estimated for each point along the AUV transects using the collected on-board Satlantic data, and this relationship used to estimate footprint chl-a. It should be noted that running the AUV at ∼6 m water depth translates to ∼4 m from the ice-ocean interface. Testing the sensitivity showed that errors in depth of ± 0.11 m identified by Lucieer et al. (2016) translate to a 0.3% error in estimation of NDI at the ice-ocean interface if a constant $K_d(\lambda)$ is assumed. This assumption of a constant vertically downwelling attenuation coefficient across the study site was based on the fact that there were very short distances between coring sites and the AUV transects themselves were only a maximum of 500 m.

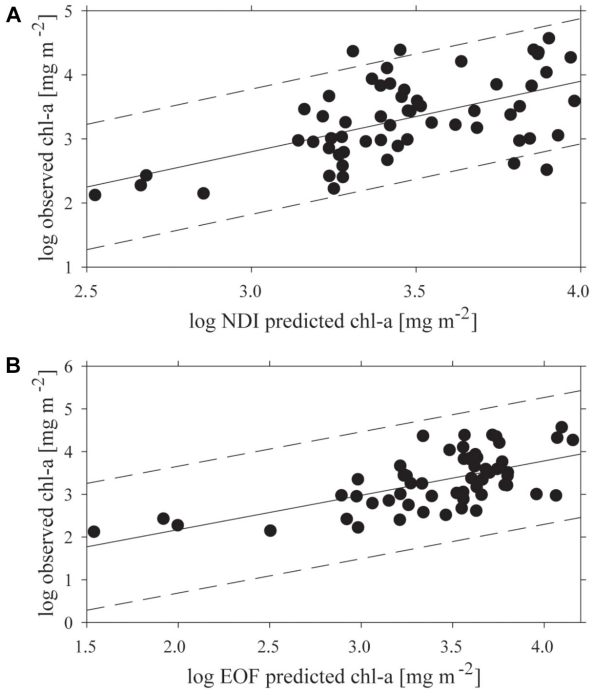

FIGURE 4 | The relationship between predicted and observed chl-a concentrations (mg m^{-2}) applying: **(A)** the normalized difference indices (NDI) 402:530 nm, and **(B)** the empirical orthogonal function analysis (EOF) both with a 95% confidence interval.

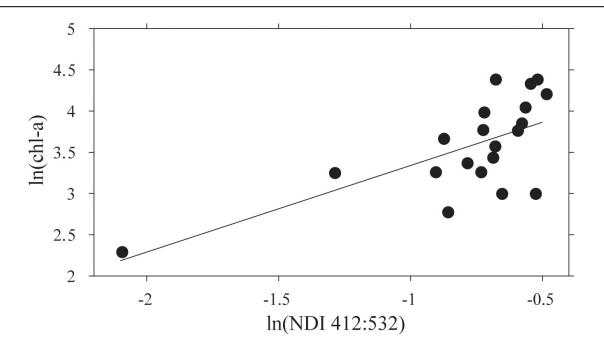

FIGURE 5 | The relationship between ln(NDI 412:532) and ln(chl-a) for means of the three sample cores collected at each of 20 stations. The regression line fitted is ln(chl-a) = 1.05 ln(NDI)+4.39 (R^2 = 0.44; N = 20; F = 14.15; p = 0.001).

Modeling Chl-a Concentration From Under-Ice Spectra

Above the ice surface, all downwelling irradiance spectra were relatively constant (**Figure 6A**), but below the ice, distinctively shaped transmitted spectra, with lowered values between 400 to 550 nm and a dip at 670 nm were evident (**Figure 6B**). The modifications to spectra under ice were consistent with the areas of maximum absorption seen in algae particulates (Hawes et al., 2012). Synthetic under-ice spectra, derived from the model of ice and algae spectral attenuation, showed similar shaped spectra (e.g., **Figure 6B**). In the example given in **Figure 6B**, the optical model output was based on the measured chl-a and agreed well with the observed under-ice spectrum, but this was not consistent across all transects in this study. In most cases, the observed under-ice spectra could not be replicated using the measured chl-a to drive the model. In these cases, a close match between observed and modeled spectra was possible only by iteratively changing the chl-a concentration used in Eq. 4, to derive the chl-a concentration required to reproduce the observed spectrum. Required chl-a showed a similar range of average values across stations compared to measured chl-a, from 10 to 50 mg m^{-2}. Variance within each station was, however, much lower for required than observed values (**Figure 6C**). Three samples had similar modeled chl-a and measured chl-a concentrations (i.e., were in close proximity to the 1:1 line in **Figure 6C**), whereas required chl-a was larger than measured

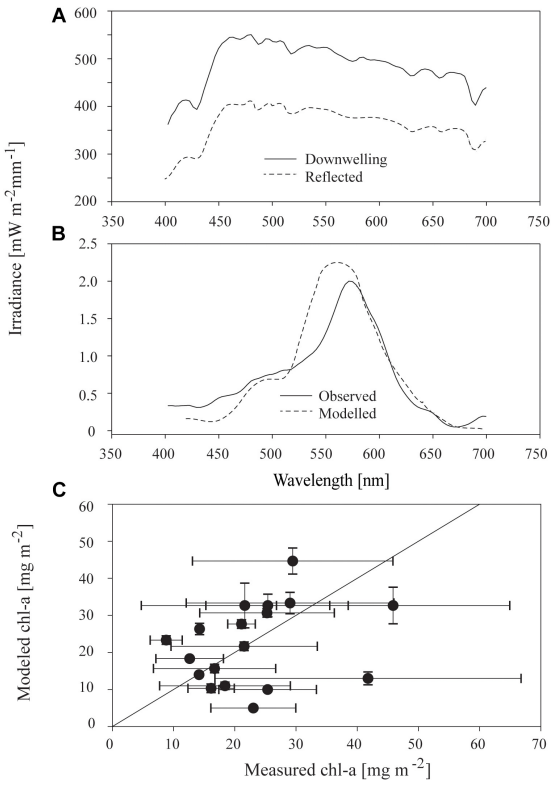

FIGURE 6 | (A) Incident downwelling and reflected irradiance spectrum at the surface of sea ice at a representative sample site free of snow; **(B)** observed irradiance spectrum 10–15 cm underneath the sea ice, and modeled irradiance; and, **(C)** relationship between measured chl-a and modeled chl-a at the 18 stations for which sufficient data were available. Modeled chl-a is defined as the concentration necessary to reproduce the observed under-ice irradiance spectrum using the optical model. Points and bars are the mean and standard deviation of the three replicate samples at each of 20 stations and the solid black line is the 1:1 line between the two variables.

for nine of the samples, and lower than measured chl-a for six of the stations.

AUV-Derived Spatial Variability

Autonomous underwater vehicle measurements were made along CE1, CE2, and CE3 close to solar noon, with a repeat of CE1 being conducted 12 h later to examine diurnal variability. Each of these transects consisted of an out and back leg separated by ∼20 m. Examples of derived spatial variability in chl-a concentrations from repeat runs along transect CE1 at different incident irradiance at 23:45 04 November 2014 and 09:00 05 November 2014 (local times) are shown below (**Figure 7A**). The NDI derived chl-a using the established relationship (recall **Figure 5**) values agree closely at the spatial sampling scales, though the noise is enhanced in the run undertaken at midnight (local time), when the sensors were often approaching detection limits. Results from CE2 demonstrate the lack of relationship between minor variations in the first-year ice topography (shown in gray) and the observed variations in ice algae biomass (**Figure 7B**). While there is not enough evidence to be conclusive, there are reduced concentrations at the ice stalactite (observed ∼175 m along track) and increased concentrations around the greater ice thickness at around 360 m. Measurements along parallel tracks, approximately 20 m apart, show similar amplitudes and length scales of variation (e.g., CE3; **Figure 7C**) that would be expected to be poorly sampled using surface-based techniques. Average chl-a estimates from the AUV were lower than those from coring (18.7 vs. 26.7 mg m^{-2}). We suggest that this is because the wavelength response of the multispectral Satlantic sensor does not follow that of the hyperspectral TriOS instrument and is integrating a larger footprint. In hindsight, the relationship between NDI and chl-a should be determined using the instrumentation to be deployed on under-ice vehicles. Nevertheless, we consider that the AUV provides a useful insight into spatial pattern of chl-a biomass in sea ice.

Correlograms showed some degree of periodicity in estimated chl-a in most tracks, with apparent spatial autocorrelation length scales of 20–100 m for each of the transect runs (various colors; **Figure 8**). While the highest correlation is seen at the lower length scales (e.g., <20 m), longer length scales are evident in some of the transects (e.g., peaks of 50 and 110 m in the burgundy trace). The fact that these peaks were not evident in all of the data is an indicator of the spatial heterogeneity of these ice algal communities.

DISCUSSION

The main purpose of this study was to develop a methodology to assess a compact, multispectral optical sensor, configured for AUV deployments for estimating spatial variability of sea ice algal communities. While similar approaches using an ROV and under-ice sleds have been demonstrated (e.g., Lange et al., 2016, 2017; Meiners et al., 2017; Lund-Hansen et al., 2018), this is the first attempt to our knowledge to make such irradiance measurements using an AUV. It is well documented that sea ice algae are optically active and make a significant contribution to the spectral attenuation in ice (e.g., Mundy et al., 2007; Ehn and Mundy, 2013; Melbourne-Thomas et al., 2015) making this type of remote sensing possible. Our data showed that it was possible to develop NDI and EOF correlations though with low correlations (R^2 = 0.31 and 0.39, respectively, N = 60) between predicted and observed chl-a, with broad 95% prediction intervals. These relationships are less reliable than previous studies, which developed predictive relationships with R^2-values of up to 0.89 (see summary in Melbourne-Thomas et al., 2015) possibly due to the presence of platelet ice increasing the complexity of the ice structure where predictive relationships are weaker (e.g., R^2 = 0.07; Wongpan et al., 2018). When using the averaged values for each site to generate the NDI for use with the AUV, correlation was increased to R^2 = 0.41 (N = 19). A study based on radiance measurements below the platelet-rich ice in McMurdo Sound showed an even lower R^2 of 0.07 for correlation of NDI (471, 416) and chl-a concentrations (Wongpan et al., 2018). The relatively poor performance of the Wongpan et al. (2018) sampling was attributed to a relatively small range in chl-a that corresponded to a large change in optics, and the difficulty in

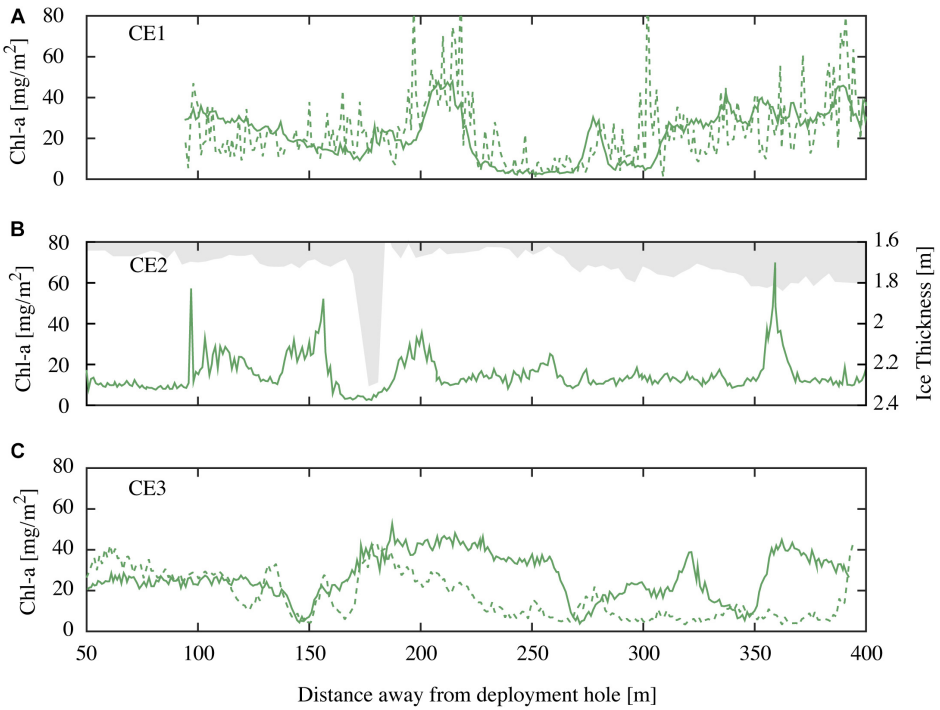

FIGURE 7 | (A) Chl-a values for repeat runs of the outgoing transit leg of CE1 at local time 23:45 04 November 2014 (green dashed line) and 09:00 05 November 2014 (green solid line); **(B)** chl-a values for CE2 at local 10:45 05 November 2014 (green line) and overhead ice keel depth (bin averaged in 5 m intervals; grayed out) for the incoming transit leg; and **(C)** chl-a values for outgoing (green line) and incoming (green dashed line) transit legs (spaced at 20 m) for CE3 recorded at local time 09:45 05 November 2014.

sampling the fragile platelet ice, similar to our experience. Clearly this type of ice and location is relatively difficult for remote sensing. The difference in within-station variability between observed and required chl-a, and the high variance as observed by Wongpan et al. (2018) of measured chl-a may indicate the main reason for the inability of our EOF and NDI models to provide a robust prediction of biomass. Firstly, it is possible that biomass was playing a minor role in attenuation of light within the sea ice. This seems unlikely, as the spectral qualities of under-ice light showed distinctive shapes typical of sea ice algae, with rapid attenuation in the blue (440 nm) and red (675 nm), affected by chl-a and carotenoids (Fritsen et al., 2011).

A second possibility is that the fragile nature of the platelet ice that was present on site resulted in incomplete and variable collection of biomass. This would be consistent with the high variability in observed chl-a compared to observed under-ice spectra in station replicates. To address this possibility, we undertook the simple modeling exercise that compared the concentrations of chlorophyll observed with those required to reproduce the observed spectra. Estimation of missing parameters using optical models has previously been used by Mundy et al. (2007), who derived a^*_λ from under ice spectra, ice properties and chl-a biomass. In our case, we have independent estimates of a^*_λ, and use these to estimate required chl-a to achieve observed spectra. This approach is limited by the sensitivity of such models to scattering (Ehn and Mundy, 2013). The scattering environment for ice with high amounts of embedded and extending platelets, as seen at Cape Evans, is poorly constrained and quantitative estimates of required chl-a may be difficult to achieve.

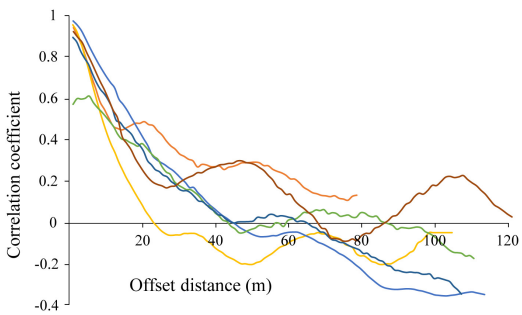

FIGURE 8 | Correlogram for estimated chl-a derived from optical measurements made along each of the out and back AUV transects CE1, CE2, and CE3 (6 total; shown in individual colors). Repeat mission of CE1 at night not shown.

A third option thus relates to the footprint size of the irradiance sensor and the ice corer. While the core samples have a diameter of 75 mm, the TriOS spectroradiometer, would have an effective footprint diameter of 350–500 mm when positioned 100–150 mm below the ice (Nicolaus et al., 2010). The difference in sampling footprint size may be important in sea ice of the type described here, if a high degree of small-scale variability

in biomass is related to the heterogenous matrix of the sub-ice platelet layer. The low variance in the required chl-a compared to measured chl-a for replicates at each station supports the view that, by sampling over a larger area, optical measurements are integrating variance, whereas under the conditions encountered at Cape Evans cores are not. Therefore, we suggest that when conducting these types of field observations under heterogeneous ice properties (i.e., a high probability of platelet ice) that multiple replicate cores are extracted from a region equivalent to the bottom-ice footprint size of the spectroradiometer.

Noise in the relationship between chl-a and NDI could be generated if there were substantial differences in the absorption spectra of ice algae across the sampling sites. However, while we did find significant differences between two groups of sites, the selected wavelengths did coincide with the selected NDI bands and differences were minor. These differences were systematic in that the two groups corresponded to sites with low (<5 μM photons m^{-2} s^{-1}) and very low (<1 μM photons m^{-2} s^{-1}) irradiances, and the shifts in carotenoid complements between these groups are consistent with a shift from energy harvesting (fuco) in low-light environments, to photoprotection (DDX) in higher light environments. Similar light-dependent carotenoid shifts have previously been reported in sea ice communities (Alou-Font et al., 2013). Robinson et al. (1997) also found that the diatoxanthin:chl-a ratio increased at higher irradiances in McMurdo Sound.

The shifts in absorption spectra and pigmentation of sea ice algal at Cape Evans occurred even though the highest light experienced by ice algae was low in absolute terms (e.g., average under-ice PAR was 2.61 μmol photons m^{-2} s^{-1}). Models suggested that 1 to 23 μmol photons m^{-2} s^{-1} at a median incident irradiance of 720 μmol photons m^{-2} s^{-1} penetrated to the ice-algal layer, depending on snow cover. It is within, or slightly above, the range of previously reported critical minimum under-ice irradiance levels for algal growth of 2 to 9 μmol photons m^{-2} s^{-1} (e.g., Horner and Schrader, 1982; Gosselin et al., 1985, 1986; Lange et al., 2015). Active ice algae photosynthesis have recently been measured at 0.17 μmol photons m^{-2} s^{-1} (Hancke et al., 2018). In locations where ice and snow conditions allow a greater range of under-ice irradiance, more extensive divergence of pigmentation and absorption properties may be expected. We note that, while not significant in our study, this could potentially confound the development of NDIs based on carotenoid-specific wavebands, especially where there was a correlation between biomass, irradiance and carotenoids.

Our study region was dominated by a snow free ice cover with small snow patches (qualitatively observed to be <5 m) which did not alter the bottom-ice light levels below the snow patches due to the horizontal propagation/scattering of light from the surrounding snow-free regions. Because our study site was dominated by a snow free ice cover, there is a smaller decrease in the spatial coverage of sufficient bottom ice light levels for ice algal growth than expected. However, this finding has perhaps more significant implications for regions with thicker snow cover and less coverage of snow-free/thin-snow regions. In thicker snow regions the horizontal propagation of light may substantially increase the areal coverage of suitable light levels at the ice bottom around these sparse snow-free/thin-snow features. A future hypothesis to test is whether the scales of spatial variability in the algae compare to observed scales of snow cover.

If our failure to produce a robust NDI for use with the AUV data is due to the mismatch between footprint sizes of the ice corer and the spectroradiometer, our procedural difficulties relate to our calibration exercise rather than the performance of the AUV-mounted instrument. The AUV itself collected repeatable transects of multispectral optical data. NDIs can provide robust estimates of ice-algal biomass (Mundy et al., 2007; Fritsen et al., 2011; Melbourne-Thomas et al., 2015) and while our estimated chl-a concentration may have very wide confidence intervals, within the limitations of the large footprint of the AUV sensors, then patterns of variability of biomass seen at scales of several decimeters to meters appears to be reliable. Within this constraint, the observed pattern of spatial variation of biomass, with its patchiness on scales of 50–100 m, provides insight into the dynamics of sea ice algal communities and the design of sampling campaigns that need to be carried out to obtain area-representative samples. At Cape Evans, for example, the length scale of autocorrelation suggests that coring would need to be undertaken at ∼10 m intervals along 200 m transects to obtain adequate representation. The mechanisms underlying this broad scale pattern of biomass are as yet unclear. However, our data suggest that at present no single approach is adequate to fully understand multi-scale variability in sea ice algal biomass.

CONCLUSION

In this study, we endeavored to determine whether AUV-mounted sensors could obtain systematic, transect-based information on sea ice algae from their optical signature. To achieve this, we attempted to develop a predictive model linking the under ice irradiance spectra to the biomass of bottom-ice algae and then applied this to AUV-derived data. Such approaches are now well accepted, but, while we were able to show a statistically significant relationship (R^2 = 0.41), this had a higher prediction error than other models produced using similar approaches in other ice-covered environments. We found some variability in the absorption characteristics of ice algae due to shifting pigment complements but conclude that the most likely challenge to development of a robust algorithm may be the small-scale variability of ice algal biomass. This is a feature of sea ice algae in general, but is particularly acute in our example as the under-ice environment at Cape Evans provided a physically complex structure, where variable amounts of platelet ice were frozen into first year sea ice and formed part of the ice-algal habitat.

Optical methods to estimate ice-algal biomass produced a smaller variance than coring, which we suggest reflects its ability to integrate biomass over a larger footprint than coring. Thus, our results suggest that remote assessment of biomass based on optical properties may, with suitable calibration for local algal attenuation, provide an estimate of the ice algal resource over spatial scales that is more robust

than coring approaches where small-scale variability of ice algal biomass is present. We used this approach, coupled to an AUV, to demonstrate what appear to be autocorrelated patterns of sea ice algal biomass on length scales of 10's to 100's m.

While sea ice imposes logistical challenges on the use of underwater technologies, the development of sensor arrays and the platforms that carry them offer a way forward to better understand sea ice algae communities. The development of such non-invasive techniques to measure environmental conditions under ice at scales commensurate with the inherent variability of these algal communities allows new understanding that would not be achievable with traditional methods and this alone represents a step change in our approach to studying these communities.

AUTHOR CONTRIBUTIONS

All authors listed have made a substantial, direct and intellectual contribution to the work, and approved it for publication.

FUNDING

This work was supported by the Air New Zealand through the New Zealand Antarctic Research Institute (Project NZARI-2014-3). In addition, the authors would like to thank the ongoing support of the Danish Council for Independent Research (Project DFF – 1323-00335) and the Australian Research Council's Special Research Initiative for the Antarctic Gateway Partnership (Project ID SR140300001). Griffiths University and the Defense Science and Technology Group (Australia) also contributed through equipment support. BL was partly funded during this study by a visiting fellowship from the Natural Sciences and Engineering Research Council of Canada (NSERC).

ACKNOWLEDGMENTS

We thank the Antarctica New Zealand for the provision of logistic support to ensure that this research was possible. Final thanks goes to Rowan Frost (Australian Maritime College Search) and the K081 Team for all of their work to make this project a success.

REFERENCES

Alou-Font, E., Mundy, C. J., Roy, S., Gosselin, M., and Agustí, S. (2013). Snow cover affects ice algal pigment composition in the coastal Arctic Ocean during spring. *Mar. Ecol. Prog. Ser.* 474, 89–104. doi: 10.3354/meps10107

Ambrose, W. G., von Quillfeldt, C., Clough, L. M., Tilney, P. V. R., and Tucker, T. (2005). The sub-ice algal community in the Chukchi sea: large- and small-scale patterns of abundance based on images from a remotely operated vehicle. *Polar Biol.* 28, 784–795. doi: 10.1007/s00300-005-0002-8

Arrigo, K. R., Mock, T., and Lizotte, M. P. (2010). Primary producers and sea ice. *Sea ice* 2, 283–325. doi: 10.1002/9781444317145.ch8

Arrigo, K. R., Sullican, C. W., and Kremer, J. N. (1991). A bio-optical model of Antarctic sea ice. *J. Geophys. Res.* 96, 10581–10592. doi: 10.1029/91JC00455

Arrigo, K. R., and Thomas, D. N. (2004). Large scale importance of sea ice biology in the Southern Ocean. *Antarctic Sci.* 16, 471–486. doi: 10.1017/S0954102004002263

Arrigo, K. R., Worthen, D. L., Lizotte, M. P., Dixon, P., and Dieckmann, G. (1997). Primary production in Antarctic sea ice. *Science* 276, 394–397. doi: 10.1126/science.276.5311.394

Boetius, A., Abrecht, S., Bakker, K., Beinhold, C., Felden, J., Fernandéz-Méndez, M., et al. (2013). Export of algal biomass from melting Arctic sea ice. *Science* 339, 1430–1432. doi: 10.1126/science.1231346

Cade, B. S., and Noon, B. R. (2003). A gentle introduction to quantile regression for ecologists. *Front. Ecol. Environ.* 1:412–420. doi: 10.1890/1540-9295(2003)001%5B0412:agitqr%5D2.0.co;2

Calcagno, V., and de Mazancourt, C. (2010). glmulti: an R package for easy automated model selection with (generalized) linear models. *J. Stat. Softw.* 34, 1–29. doi: 10.18637/jss.v034.i12

Campbell, K., Mundy, C. J., Barber, D. G., and Gosselin, M. (2015). Characterizing the sea ice algae chlorophyll a–snow depth relationship over Arctic spring melt using transmitted irradiance. *J. Mar. Syst.* 147, 76–84. doi: 10.1016/j.jmarsys.2014.01.008

Cimoli, E., Meiners, M. K., Lund-Hansen, L. C., and Lucieer, V. (2017). Spatial variability in sea-ice algal biomass: an under-ice remote sensing perspective. *Adv. Polar Sci.* 4, 268–296. doi: 10.13679/j.advps.2017.4.00268

Cleveland, J. S., and Weidemann, A. D. (1993). Quantifying absorption by aquatic particles: a multiple scattering correction for glass-fiber filters. *Limnol. Oceanogr.* 38, 1321–1327. doi: 10.4319/lo.1993.38.6.1321

Doble, M. J., Forrest, A. L., Wadhams, P., and Laval, B. E. (2009). Through-ice AUV deployment: operational and technical experience from two seasons of Arctic fieldwork. *Cold Reg. Sci. Technol.* 56, 90–97. doi: 10.1016/j.coldregions.2008.11.006

Ehn, J. K., and Mundy, C. J. (2013). Assessment of light absorption within highly scattering bottom sea ice from under-ice light measurements: implications for arctic ice algae primary production. *Limnol. Oceanogr.* 58, 893–902. doi: 10.4319/lo.2013.58.3.0893

Flores, H., van Franeker, J. A., Siegel, V., Haraldsson, M., Strass, V., Meesters, E. H., et al. (2012). The association of Antarctic krill *Euphausia superba* with the under-ice habitat. *PLoS One* 7:e31775. doi: 10.1371/journal.pone.0031775

Fritsen, C. H., Wirthlin, E. D., Momberg, D. K., Lewis, M. J., and Ackley, S. F. (2011). Bio-optical properties of Antarctic pack ice in the early austral spring. *Deep-Sea Res 2 Top. Stud. Oceanogr.* 58, 1052–1061. doi: 10.1016/j.dsr2.2010.10.028

Gosselin, M., Legendre, L., Demers, S., and Ingram, R. G. (1985). Responses of sea-ice microalgae to climatic and fortnightly tidal energy inputs (Manitounuk Sound, Hudson Bay). *Can. J. Fish. Aquat. Sci.* 42, 999–1006. doi: 10.1139/f85-125

Gosselin, M., Legendre, L., Therriault, J. C., Demers, S., and Rochet, M. (1986). Physical control of the horizontal patchiness of sea-ice microalgae. *Mar Ecol Prog Ser* 29, 289–298. doi: 10.3354/meps029289

Hancke, K., Lund-Hansen, L. C., Lamare, M. L., Pedersen, S. H., King, M. D., Andersen, P., et al. (2018). Extreme low light requirement for algaee growth underneath sea ice: a case study from station nord, NE Greenland. *J. Geophys. Res. Oceans* 123, 985–1000. doi: 10.1002/2017/JC013263

Hawes, I., Lund-Hansen, L. C., Sorrell, B., Nielsen, M. H., Borzák, R., and Buss, I. (2012). Photobiology of sea ice algae during initial spring growth in Kangerlussuaq, West Greenland: insights from imaging variable chlorophyll fluorescence of ice cores. *Photosynth. Res.* 112, 103–115. doi: 10.1007/s11120-012-9736-9737

Holland, P. R., Bruneau, N., Enright, C., Losch, M., Kurtz, N. T., and Kwok, R. (2014). Modeled trends in Antarctic sea ice thickness. *J. Clim.* 27, 3784–3801. doi: 10.1175/JCLI-D-13-00301.1

Horner, R., and Schrader, G. C. (1982). Relative contributions of ice algae, phytoplankton, and benthic microalgae to primary production in nearshore regions of the Beaufort Sea. *Arctic* 35, 485–503. doi: 10.14430/arctic2356

Kirk, J. T. (2011). *Light and Photosynthesis in Aquatic Ecosystems*, 3rd Edn. Cambridge: Cambridge University Press, 662.

Kohlbach, D., Lange, B. A., Schaafsma, F. L., David, C., Vortkamp, M., Graeve, M., et al. (2017). Ice algae-produced carbon is critical for overwintering of Antarctic krill *Euphausia superba*. *Front. Mar. Sci.* 4:310. doi: 10.3389/fmars.2017.00310

Lange, B., Katlein, C., Nicolaus, M., Peeken, I., and Hauke, F. (2016). Sea ice algae chlorophyll *a* concentrations derived from under-ice spectral radiation profiling platforms. *J. Geophysical Res.* 121, 8511–8534. doi: 10.1002/2016JC011991

Lange, B. A., Katlein, C., Castellani, G., Fernandez-Mendez, M., Nicolaus, M., Peeken, I., et al. (2017). Characterizing spatial variability of ice algal chlorophyll a and net primary production between sea ice habitats using horizontal profiling platforms. *Front. Mar. Sci.* 4:349. doi: 10.3389/fmars.2017.00349

Lange, B. A., Michel, C., Beckers, J. F., Casey, J. A., Flores, H., Hatam, I., et al. (2015). Comparing springtime ice-algal chlorophyll a and physical properties of multi-year and first-year sea ice from the Lincoln Sea. *PLoS One* 10:e0122418. doi: 10.1371/journal.pone.0122418

Lizotte, M. P. (2001). The contributions of sea ice algae to Antarctic marine primary production. *Am. zool.* 41, 57–73. doi: 10.1093/icb/41.1.57

Lucieer, V., Nau, A. W., Forrest, A. L., and Hawes, I. (2016). Fine-scale sea ice structure characterized using underwater acoustic methods. *Remote Sens.* 8:821. doi: 10.3390/rs8100821

Lund-Hansen, L. C., Hawes, I., Juul, T., Thor, P., Sorrell, B., and Hancke, K. (2018). A low-cost remotely operated vehicle (ROV) with an optical positioning system for under-ice measurements and sampling. *Cold Reg. Sci. Technol.* 151, 148–155. doi: 10.1016/j.coldregions.2018.03.017

Lund-Hansen, L. C., Hawes, I., Nielsen, M. H., and Sorrell, B. K. (2017). Is colonization of sea ice by diatoms facilitated by increased surface roughness in growing ice crystals? *Polar Biol.* 40, 593–602. doi: 10.1007/s00300-016-1981-1983

Lund-Hansen, L. C., Hawes, I., Sorrell, B. K., and Nielsen, M. H. (2014). Removal of snow cover inhibits spring growth of Arctic ice algae through physiological and behavioral effects. *Polar Biol.* 37, 471–481. doi: 10.1007/s00300-013-1444-z

Mangoni, O., Carrada, G. C., Modigh, M., Catalano, G., and Saggiomo, V. (2009). Photoacclimation in Antarctic bottom ice algae: an experimental approach. *Polar Biol.* 32, 325–335. doi: 10.1007/s00300-008-0517-x

McCullagh, P., and Nelder, J. A. (1989). "Log-linear models," in *Generalized Linear Models*, eds P. McCullagh and J. A. Nelder (New York, NY: Springer), 193–244.

McMinn, A., Ashworth, C., and Ryan, K. (1999). Growth and productivity of Antarctic sea ice algae under PAR and UV irradiances. *Botanica Marina* 42, 401–407. doi: 10.1515/BOT.1999.046

McMinn, A., Ashworth, C., and Ryan, K. G. (2000). In situ primary productivity of an Antarctic fast ice bottom algae community. *Aqua. Microbial. Ecol.* 21, 177–185. doi: 10.3354/ame021177

Meiners, K. M., Arndt, S., Bestley, S., Krumpen, T., Ricker, R., Milnes, M., et al. (2017). Antarctic pack ice algal distribution: floe-scale spatial variability and predictability from physical parameters. *Geophys. Res. Lett.* 44, 7382–7390. doi: 10.1002/2017GL074346

Melbourne-Thomas, J., Meiners, K. M., Mundy, C. J., Schallenber, C., Tatterhal, K. L., and Dieckman, G. S. (2015). Algorithms to estimate Antarctic sea ice algal biomass from under-ice irradiance spectra at regional scales. *Mar. Ecol. Prog. Ser.* 536, 107–121. doi: 10.3354/meps11396

Mundy, C. J., Ehn, J. K., Barber, D. G., and Michel, C. (2007). Influence of snow cover and algae on the spectral dependence of transmitted irradiance through Arctic landfast first year sea ice. *J. Geophys. Res. Oceans* 112, C3. doi: 10.1029/2006JC003683

Nicolaus, M., Hudson, S. R., Gerland, S., and Munderloh, K. (2010). A modern concept for autonomous and continuous measurements of spectral albedo and transmittance of sea ice. *Cold Reg. Sci. Technol.* 62, 14–28. doi: 10.1016/j.coldregions.2010.03.001

Nicolaus, M., and Katlein, C. (2013). Mapping radiation transfer through sea ice using a remotely operated vehicle (ROV). *Cryosphere* 7, 763–777. doi: 10.5194/tc-7-763-2013

Perovich, D. K. (1990). Theoretical estimates of light reflection and transmission by spatially complex and temporally varying sea ice covers. *J. Geophys. Res. Oceans* 95, 9557–9567. doi: 10.1029/JC095iC06p09557

Remy, J. P., Becquevort, S., Haskell, T. G., and Tison, J.-L. (2008). Impact of the B-15 iceberg "stranding event" on the physical and biological properties of sea ice in McMurdo Sound. *Ross Sea Antarct., Antarct. Sci.* 20, 593–604. doi: 10.1017/S0954102008001284

Robinson, D. H., Kolber, Z., and Sullivan, C. W. (1997). Photophysiology and photoacclimation in surface sea ice algae from McMurdo Sound, Antarctica. *Mar. Ecol. Prog. Ser.* 147, 243–256. doi: 10.3354/meps147243

Rysgaard, S., Kühl, M., Glud, R. N., and Hansen, J. W. (2001). Biomass, production and horizontal patchiness of sea ice algae in a high-Arctic fjord (Young Sound, NE Greenland). *Mar. Ecol. Prog. Ser.* 223, 15–26. doi: 10.3354/meps223015

Schaafsma, F. L., Kohlbach, D., David, C., Lange, B. A., Graeve, M., Flores, H., et al. (2017). Spatio-temporal variability in the winter diet of larval and juvenile Antarctic krill, *Euphausia superba*, in ice-covered waters. *Mar. Ecol. Prog. Ser.* 580, 101–115. doi: 10.3354/meps12309

Schwarz, G. (1978). Estimating the dimension of a model. *Ann. stat.* 6, 461–464. doi: 10.1214/aos/1176344136

Taylor, M. H., Losch, M., and Bracher, A. (2013). On the drivers of phytoplankton blooms in the Antarctic marginal ice zone: a modeling approach. *J. Geophys. Res. Oceans* 118, 63–75. doi: 10.1029/2012JC008418

Tomas, C. R. (1997). *Identifying Marine Phytoplankton*. New York, NY: Academic Press, 855.

Uthermöhl, H. (1958). Zur vervollkommung der quantitativen phytoplankton-methodik. *Mitt. D. Internat. Vere.Limnol.* 9, 1–39. doi: 10.1080/05384680.1958.11904091

Wongpan, P., Meiners, K. M., Longhorne, P., Heil, P., Smith, I. J., Leonard, G. H., et al. (2018). Estimation of Antarctic land-fast ice algal biomass and snow thickness from under-ice radiance spectra in two contrasting areas. *J. Geophys. Res. Oceans.* 123, 1907–1923. doi: 10.1002/2017/JCO13711

Zeebe, R. E., Eicken, H., Robinson, D. H., Wolf-Gladrow, D., and Dieckmann, G. S. (1996). Modeling the heating and melting of sea ice through light absorption by microalgae. *J. Geophys. Res. Oceans* 101, 1163–1181. doi: 10.1029/95JC02687

Conflict of Interest Statement: The authors declare that the research was conducted in the absence of any commercial or financial relationships that could be construed as a potential conflict of interest.

The reviewer PD declared a past co-authorship with one of the authors BS to the handling Editor.

frontiers in Earth Science

ORIGINAL RESEARCH
published: 18 December 2018
doi: 10.3389/feart.2018.00234

Carbon Dynamics During the Formation of Sea Ice at Different Growth Rates

Daniela König[1]*, *Lisa A. Miller*[2], *Kyle G. Simpson*[2] and *Svein Vagle*[2]

[1] Department of Environmental Systems Science, Institute of Biogeochemistry and Pollutant Dynamics, ETH Zurich, Zurich, Switzerland, [2] Institute of Ocean Sciences, Fisheries and Oceans Canada, Sidney, BC, Canada

Controlled laboratory experiments have shed new light on the potential importance of brine rejection during sea-ice formation for carbon dioxide sequestration in the ocean. We grew ice in an experimental seawater tank (1 m^3) under abiotic conditions at three different air temperatures (−40°C, −25°C, −15°C) to determine how different ice growth rates affect the allocation of carbon to ice, water, or air. Carbonate system parameters were determined by discrete sampling of ice cores and water, as well as continuous measurements by multiple sensors deployed mainly in the water phase. A budgetary approach revealed that of the initial total inorganic carbon (TIC) content of the water converted to ice, only 28–29% was located in the ice phase by the end of the experiments run at the warmest temperature, whereas for the coldest ambient temperature, 46–47% of the carbon remained in the ice. Exchange with air appeared to be negligible, with the majority of the TIC remaining in the under-ice water (53–72%). Along with a good correlation between salinity and TIC in the ice and water samples, these observations highlight the importance of brine drainage to TIC redistribution during ice formation. For experiments without mixing of the under-ice water, the sensor data further suggested stronger stratification, likely related to release of denser brine, and thus potentially larger carbon sequestration for ice grown at a colder temperature and faster growth rate.

Keywords: sea ice, growth rates, CO_2 system, brine drainage, tank experiment

OPEN ACCESS

Edited by:
Jeff Shovlowsky Bowman, University of California, San Diego, United States

Reviewed by:
Soren Rysgaard, Aarhus University, Denmark
Sebastien Moreau, Norwegian Polar Institute, Norway
Daiki Nomura, Hokkaido University, Japan

***Correspondence:**
Daniela König
daniela.koenig@liverpool.ac.uk

Specialty section:
This article was submitted to Cryospheric Sciences, a section of the journal Frontiers in Earth Science

Received: *27 July 2018*
Accepted: *03 December 2018*
Published: *18 December 2018*

Citation:
König D, Miller LA, Simpson KG and Vagle S (2018) Carbon Dynamics During the Formation of Sea Ice at Different Growth Rates. Front. Earth Sci. 6:234. doi: 10.3389/feart.2018.00234

INTRODUCTION

While the polar regions are generally considered an important sink for atmospheric carbon dioxide (CO_2), the influence of sea ice on air-sea carbon dynamics is unclear. Originally assumed to be an impermeable lid hindering air-sea gas exchange (e.g., Stephens and Keeling, 2000; Tison et al., 2002), sea ice has since been recognized to play an active role in the marine carbon cycle, as both biological and physico-chemical processes take place within and around the ice (Vancoppenolle et al., 2013). The sea-ice zone is believed to act as a sink for atmospheric CO_2 on an annual basis (Rysgaard et al., 2011), although the direction and magnitude of the carbon flux differ between the different stages of the seasonal sea-ice growth and decay cycle and also appear to depend on the methods used (Miller et al., 2015).

During the period of ice formation, the conceptual model developed by Rysgaard et al. (2011) predicts CO_2 release to the atmosphere. When ice is formed, the majority of ions and gases present in the original sea water are expelled from the crystal lattice, whereby liquid brine intrusions with high salinities and gas concentrations are formed between ice crystals (Petrich and Eicken, 2016).

A small part of the brine supersaturated in CO_2 is then predicted to be expelled to the sea-ice surface and to release CO_2 to the atmosphere (Rysgaard et al., 2011). Small, positive CO_2 fluxes out of young, newly formed sea ice have indeed been detected in the field (Else et al., 2011; Geilfus et al., 2013; Barber et al., 2014; Nomura et al., 2018) and in artificial sea ice (Nomura et al., 2006; Geilfus et al., 2016; Kotovitch et al., 2016). However, while the CO_2 flux out of the young ice itself is likely positive (upward), the overall CO_2 flux during ice formation in the marginal sea ice zone may be negative, depending on the presence of open water, including leads and polynyas, which may enhance CO_2 uptake from the air (e.g., Anderson et al., 2004; Loose et al., 2011).

Sea-ice formation also has the potential to export carbon to deeper water layers (Rysgaard et al., 2007, 2011). Carbon dioxide-enriched brine produced during sea-ice formation could sink to levels below the surface mixed layer and lead to a net annual uptake of atmospheric CO_2 of up to 33 Tg C yr^{-1}, according to Rysgaard et al. (2011). This uptake could be further enhanced by the precipitation of calcium carbonate ($CaCO_3$) minerals, namely ikaite. During the formation of ikaite, CO_2 is produced, and the ratio of total alkalinity (A_T) to dissolved inorganic carbon (DIC) of the brine is reduced (DIC refers here to the dissolved fraction of TIC; we use TIC for the remainder of this manuscript since our samples were unfiltered and may have contained solid carbonates). Assuming that the CO_2 enriched brine sinks to deeper water levels while the ikaite crystals stay in the ice, this would lead to an enrichment of surface water alkalinity during ice melt (Rysgaard et al., 2007). This, in turn, could result in a higher uptake of atmospheric CO_2, on the order of 83 Tg C yr^{-1}, globally (Rysgaard et al., 2011). This effect might be more pronounced at lower ice temperatures, since ikaite precipitation is more likely (in an open system) at the higher brine salinities encountered at lower temperatures (Papadimitriou et al., 2013). Differences in ice temperatures have thus been suggested to explain different A_T to TIC ratios observed at multiple field locations (Rysgaard et al., 2007, 2009). However, the importance of ikaite precipitation for atmospheric CO_2 uptake is debatable, as is transport below the mixed layer. The latter almost certainly does not occur in all sea-ice environments (Loose et al., 2011), and according to a recent modeling study (Moreau et al., 2016), the fraction of DIC exported to depth could be no more than 2% (about 4 Tg C yr^{-1}) of all DIC rejected during sea ice growth. This fraction was found to be even lower for a global warming scenario in a similar study conducted by Grimm et al. (2016) due to changes to the oceanic overturning circulation. However, Parmentier et al. (2013) also stressed the importance of open water in the sea-ice cover (i.e., leads and polynyas) for the formation of dense water needed for export to depth, which may not have been adequately represented in their model. Thus, as such open water areas may be more prevalent in a warming future (Parmentier et al., 2013), the export of carbon may also be enhanced.

The influence of the ice growth rate on TIC export from the forming ice has received little attention so far, but some insight might be gained from desalination studies, given that inorganic carbon is mostly present in dissolved form in seawater. Our understanding of sea-ice brine drainage processes is rapidly evolving, and mushy layer theory has been suggested as a useful model to explain the underlying mechanisms of sea-ice desalination (Feltham et al., 2006; Notz and Worster, 2009). This theory predicts gravity drainage to be the dominant desalination process during ice growth (Notz and Worster, 2009). Gravity drainage results from the temperature gradient across the ice, as high salinity brine formed at the lower temperatures in the upper layers of the ice overlies less saline, and thus less dense brine formed at the warmer temperatures closer to the sea ice-water interface. This unstable brine density profile eventually leads to convective overturning within the ice, when the density gradient and the ice thickness are large enough to provide the required potential energy to overcome the energy loss due to dissipation during convection (Wettlaufer et al., 1997). Thus, mushy layer theory predicts a delayed onset of desalination, which has been observed in laboratory ice growth studies (Wettlaufer et al., 1997; Notz and Worster, 2009).

The impact of different ice growth rates on gravity drainage is not straightforward. While the dependence of gravity drainage on the temperature gradient would suggest more effective desalination at colder ambient temperatures, desalination is hindered by lower ice permeability at these colder temperatures, which can limit the convection to the ice layers close to the ice-water interface (Notz and Worster, 2009). Both laboratory and numerical studies found that for constant boundary conditions (i.e., constant cooling), an inverse relationship between salt flux and growth rates holds, i.e., increased bulk ice salinity at faster growth rates as a result of the decreased permeability (Cox and Weeks, 1975; Wettlaufer et al., 1997; Griewank and Notz, 2013). Similarly, results from field studies comparing salinity profiles of ice cores to their growth rate history suggest that faster ice growth leads to higher retention of salt in sea ice (Nakawo and Sinha, 1981; Eicken, 1992; Gough et al., 2012). Assuming the TIC redistribution during ice formation is dominated by brine drainage, a higher retention of TIC in ice at faster ice growth rates is thus predicted.

The correlation between TIC and salinity could be disturbed by multiple abiotic and biological processes. Apart from biological transformations of TIC into organic substances, the precipitation of ikaite or the nucleation of CO_2 bubbles both lead to inorganic forms of carbon that could migrate within ice differently from dissolved salts (Vancoppenolle et al., 2013). Furthermore, both processes are dependent on the *in-situ* temperature and salinity conditions and are possibly interconnected: increased CO_2 partial pressure (pCO_2) at high salinities could lead to the formation of gas bubbles, which in turn could promote the precipitation of ikaite by lowering the CO_2 concentration in the brine (Papadimitriou et al., 2014). Therefore, TIC and salinity decoupling could be more pronounced in colder, and thus more saline, brine. Nevertheless, experimental and model studies on newly forming sea ice have found that ikaite precipitation and CO_2 outgassing to the atmosphere are small compared to the efflux of dissolved inorganic carbon with brine to the underlying water (Rysgaard et al., 2007; Sejr et al., 2011; Moreau et al., 2015; Kotovitch et al., 2016). This indicates that the transport in dissolved form is predominant, and the TIC signal should largely follow salinity. However, past laboratory experiments have been conducted

at a single, relatively high temperature, and might not be representative of faster ice growth conditions.

In the context of the large uncertainties in the air-ice and ice-water carbon fluxes, transformation and transport processes within the ice, and the impact of different ice growth rates, further insight into carbon dynamics during sea-ice formation is needed. Therefore, we conducted laboratory experiments simulating ice formation at three different growth rates with discrete and continuous measurements of CO_2 system parameters in ice and water. In addition, we estimated the air-ice CO_2 flux using a carbon budget approach. In addition to discrete sample analyses, the installation of sensors in the ice and water, including thermistors, Dopbeam sonars, and a water salinity probe, allowed us to further investigate brine drainage processes.

MATERIALS AND METHODS

Ice Growth Experiments

The ice growth experiments were conducted in a walk-in freezer at the Institute of Ocean Sciences in Sidney, BC, which is equipped with three separate refrigeration condensers. The condensers can be set to keep the ambient temperature of the freezer stable anywhere between 0°C and −45°C, apart from regular defrost intervals, when the temperature can increase by up to 10°C over a period of 1 h (in the case of the coldest experiments). Three ambient temperatures (−15°C, −25°C, and −40°C) were chosen to cover a wide range of ice growth rates within a temperature range observable in nature, and to be sufficiently cold to reach the desired thickness. The ambient conditions in the cold lab were monitored by a weather station (König, 2017), mean air temperatures and their standard deviations are listed in **Table S2**.

The cold lab contained a water tank (ca. 105 × 95 × 99 cm; **Figure 1A**) holding natural, open ocean seawater, which was collected on June 16, 2016, at Ocean Station P20 in the Northeast Pacific (50°N, 145°W) at a depth of 5 m. To minimize biological activity, the experiments were run in the dark and the water was filtered through a 1 μm filter and sterilized with a UV lamp for 24 h before the start of the experiment and whenever new seawater was added to the tank. Whereas in general, the seawater was re-used for the different experimental runs and additional seawater was only added on two occasions, tap water was added to the tank after each experiment, to counteract the increase in salinity due to evaporation and the removal of ice cores. This had a minor impact on the chemical composition of the seawater, observable as a slight increase in TIC relative to A_T. The tank was insulated on the sides, to prevent ice growth on the walls, and open at the top. To enable water sampling from underneath the ice, a sampling system with adjustable heating was installed in the tank, connecting multiple Tygon® tubes from within the tank to a port outside the freezer (**Figure 1A**).

The first set of experiments was conducted with stirring to prevent stratification and ensure that all deployed sensors would measure seawater representative of the whole body of water. For a second set of experiments, the water was not stirred (except during water sampling to avoid sampling stratified layers) to allow brine plume detection, as well as to test the impact of mixing on the results of the previous runs. Each experiment was stopped (i.e., water and ice were sampled) once the ice thickness had reached about 20 cm. The stirring system was made up of a pump connected to PVC pipes arranged in a rectangle at the bottom (**Figure 1A**), which generated an observable vortex through the entire depth of the tank. In addition, two pumps were installed vertically at a depth of ca. 30 cm in order to prevent stratification.

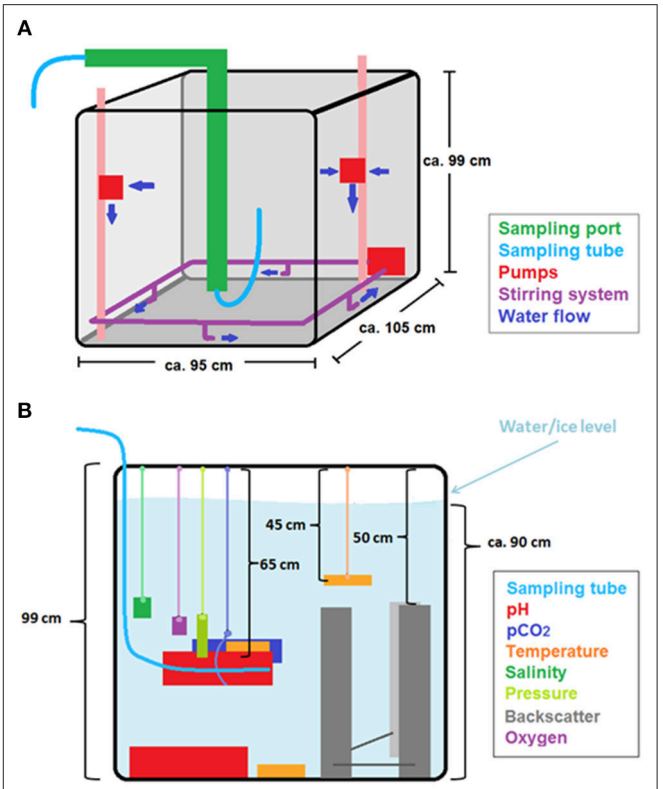

FIGURE 1 | Schematic illustration of the experimental tank with its stirring and sampling systems **(A)** and all sensors discussed in this manuscript **(B)**.

An overview of all successful experimental runs is shown in **Table 1**, including ambient temperatures and whether or not the tank was stirred. A more comprehensive overview, including all (attempted) runs is given by König (2017).

Water and Ice Melt Samples

In order to calculate a carbon budget, seawater and sea-ice melts were analyzed for TIC content, A_T, and salinity. In addition, the seawater was analyzed for pH.

For each run, water was sampled before the ice formed ("pre-ice" samples), and once the ice had reached a thickness of 20 cm ("under-ice" samples). All pre-ice samples were taken once water temperatures were close to or below 0°C, and while the tank was well-mixed. For some runs, two pre-ice samples were collected to determine the impact of the rapid cooling before each run on the carbon dynamics. For the stirred runs, we collected some pre-ice samples while the water was cooling down relatively quickly, which may have contributed to poor precision between replicates.

TABLE 1 | Overview of experimental runs.

Name	Dates	Air temp. (°C)	Stirring	Comments
Run 5	01.12–07.12.2016	−25	Yes	- Gaps in some sensor data due to power bumps - Slightly higher temperature in second half of experiment (+3°C) due to icing of condenser
Run 6	13.12–15.12.2016	−40	Yes	- Gaps and EM interference in some sensor data
Run 8	07.01–30.01.2017	−15	Yes	- Seawater added before - Contros and SeaFET operated without pump - Only 16–20 cm of ice
Run 10	11.02–16.02.2017	−25	No	- New improved thermistor string - Up to 24 cm of ice - Slightly higher temperature in second half of experiment (+3°C) due to icing of condenser
Run 11	21.02–23.02.2017	−40	No	- First 2 h only−30°C
Run 12	02.03–10.03.2017	−15	No	- Seawater added before

In the case of the unstirred runs, water was stirred while cooled relatively slowly to about −1°C before pre-ice samples were collected. Only after sampling was the stirring system turned off, and the water left to stratify. For the under-ice samples of these runs, the stirring system was turned on at least 2 h before sampling, to ensure adequate mixing of the stratified water column. For all sampling periods, the sampling port was heated beforehand. In the case of the colder runs, the heating power had to be increased, and the heating period extended. In general, 0.5–2 h of heating was required to open the port and allow sampling. The system was flushed before sampling to remove residual water from the sample port tubing. In the case of under-ice sampling, a significant number of bubbles formed in the sample tubing due to decreased solubility caused by decreased pressure and warming of the water during sampling. While we tried to avoid bubble entrainment during sampling, it could account for some of the differences between replicates sampled during these periods.

Samples were collected in the following order: salinity, TIC and A_T (duplicates), and pH (quadruplicates). In the case of the last three runs, additional salinity samples were collected after TIC and A_T, as salinity appeared to change slightly during the under-ice water sampling (possibly due to some residual stratification in the tank, despite the stirring). Salinity samples were collected into 200 ml borosilicate bottles rinsed three times with sample before filling. Samples for TIC and A_T were tapped into 250 ml borosilicate glass bottles, following a short initial rinse and an overflow of at minimum one bottle volume. Subsequently, the headspace was adjusted, samples were poisoned with 100 µl of saturated mercuric chloride, and the bottles closed using a greased glass stopper and electrician's tape, in accordance with standard operating procedures (Dickson et al., 2007). All TIC and A_T samples were stored in the dark at 4°C before analysis. Samples taken for pH analyses were collected directly into 10-cm spectrophotometric cells, which were rinsed, flushed for approximately 15 s, and closed without a headspace using two Teflon® stoppers, as described by Dickson et al. (2007). The cells were immediately placed in a 25°C incubator for 1 h before analysis.

Ice cores were collected after the under-ice water sampling and melted for subsequent chemical analyses. For all runs, we took four ice cores from approximately the same locations in the tank (König, 2017), except for Run 6, when only three cores were retrieved. The sampling spots were chosen so that different regions of the tank were sampled to best capture any horizontal variability. The ice was cored manually using a Kovacs Mark II corer (9 cm diameter). After a short visual inspection and determination of core length inside the cold lab (still at the pre-set temperature), the cores were placed in gas-impermeable ALTEF® bags which were then taken outside the lab and immediately sealed with C-clamps. The bags were closed outside the cold lab, because they became brittle and the clamps were difficult to close at low temperatures. The bags were evacuated immediately after sealing, using a hand-held pump to minimize excessive suction and potential loss of gases trapped inside the core, as suggested by Miller et al. (2015). The cores from the final three experiments were weighed after evacuation so as to determine the ice density, using an Ohaus GT4100 balance.

After evacuation, the cores were placed into a dark container and melted overnight at room temperature. All cores took approximately 24 h to melt completely. Once fully melted, the ice melts were mixed and allowed to warm up until all visible solid particles were dissolved, so as to assure homogeneity. The high reproducibility of TIC and A_T in the ice melt sub-samples (**Table S2**) confirms that this procedure was indeed adequate. Before sampling the melts, accumulated air inside bags was removed using a syringe. The air volume differed between the melts (ca. 40–200 ml), possibly due to natural heterogeneity, inconsistent evacuation, or, in the case of the highest air volume, a leaky bag or valve leading to uptake of air during melting. However, TIC, A_T, salinity, and the ratios between these parameters were no different in the ice melt sample with the largest air volume (200 ml) than those from the replicate cores without a large head-space. Ice melt samples were sub-sampled by connecting a short Tygon® tube to the valves of the bags. First, two TIC/A_T samples were tapped, preserved, and sealed like the water samples, except for a slightly smaller overflow (0.5–1 bottle volume) due to the limited ice melt volumes. The rest of

the ice melt was used for 1-2 salinity samples, depending on the remaining volume.

Chemical Analyses

Total inorganic carbon was measured coulometrically on a SOMMA system (Johnson et al., 1993), run in combination with a UIC coulometer, using standard operating protocols (Dickson et al., 2007). To ensure the accuracy of the measurements, certified reference materials (CRM batch 152 and 160, provided by Andrew Dickson, Scripps Institute of Oceanography) were measured daily, and all values were corrected accordingly. The analytical precision, calculated from differences between duplicate samples, was about 1 µmol/kg for water samples, and 0.5 µmol/kg for ice melt samples.

Total alkalinity was determined by open cell, potentiometric titration, using a custom built system following the procedure outlined by Dickson et al. (2007). The accuracy of this system was ensured by calibrating against reference materials (CRM batch 152, 160, and 161) at the beginning and end of each day. The analytical precision (determined as for TIC) was about 4 µmol/kg for water samples, and 3 µmol/kg for ice melt samples. Both TIC and A_T analyses were conducted within 4 weeks of collection.

Water sample pH was determined spectrophotometrically within 2 h of collection with an Agilent 8453 spectrometer, using *m*-cresol purple as an indicator dye, following Dickson et al. (2007). Each absorption measurement was conducted four times and averaged. All values were corrected for a potential pH perturbation by the dye addition. The temperature within the cell was recorded immediately after each spectrophotometric measurement using a hand-held temperature probe (Fluke 5611T). Since some of the under-ice water salinities were outside the range for which the dye pK_a was defined by Clayton and Byrne (1993), pH was calculated (on the free pH scale) following Miller et al. (2011), using the parameterization by Millero et al. (2009). The pH values were then converted back to the total scale using the HSO_4^- acidity constant of Dickson (1990), assuming the sulfate concentrations of the samples were proportional to salinity.

Salinity of water and ice melt samples was determined from conductivity using a Guildline 8400B salinometer, after at least 24 h of acclimatization at the laboratory temperature, which was kept constant at 1°-2°C below the salinometer bath temperature (24°C). The instrument's accuracy was confirmed by the daily measurement of a certified standard (IAPSO Seawater Standard). The salinity analyses were conducted within maximum 6 weeks of collection, and the analytical precision was 0.0003 (on the practical salinity scale).

Carbon Budget

We used a budgetary approach to estimate how TIC in the initial, pre-ice seawater was distributed between the air, water, and ice by the end of each experiment. For this purpose, the absolute TIC content (i.e., moles of carbon) of the formed ice ($absTIC_{ice}$) and drained brine ($absTIC_{drain}$; calculated from differences in TIC concentration between pre-ice and under-ice water) was compared to the absolute TIC content ($absTIC_{sw,\,ini}$) of the volume of seawater which was converted into ice. Any differences between these three values were assumed to originate from exchange with air:

$$absTIC_{sw,\,ini} = absTIC_{ice} + absTIC_{drain} + absTIC_{air}$$

The net TIC exchanged with the air over the course of the experiment ($absTIC_{air}$) was thereby not determined directly and could be either positive or negative, as carbon could be released to or taken up from the air, respectively.

To calculate the absolute TIC content of water that eventually froze and the resulting ice, the TIC content measured for the corresponding water ($TIC_{sw,\,ini}$) and ice melt samples (TIC_{ice}), both in µmol/kg, was multiplied by the final ice mass (m_{ice}), so as to consider only the pre-ice seawater from which the ice had formed. To account for TIC drained from the ice to the under-ice seawater, the difference between the TIC content in pre-ice and under-ice water samples ($TIC_{sw,\,fin} - TIC_{sw,\,ini}$) was multiplied by the total mass of the under-ice water, which was determined by subtracting the final ice mass from the initial water mass ($m_{sw.ini}$).

$$TIC_{sw,\,ini} * m_{ice} = TIC_{ice} * m_{ice} + (TIC_{sw,\,fin} - TIC_{sw,\,ini}) * (m_{sw.ini} - m_{ice}) + absTIC_{air}$$

The initial water mass was calculated from seawater density, determined from salinity and *in-situ* temperature according to Millero and Poisson (1981), and the initial water volume based on water depth after sampling and tank dimensions, corrected for estimated sensor volumes (König, 2017). Due to rather large uncertainties regarding ice volume and density, the ice mass was derived from a salinity budget set up in a similar way as the above outlined carbon budget. For this purpose, we replaced the TIC concentrations with the salinities measured in water and ice melt samples in the budget, assuming these practical salinity values represent the mass concentration of salt in water. As we assumed the exchange of salt with air during ice growth to be negligible (thereby neglecting evaporation and sublimation), we set the air fraction of the budget to zero, and could thus determine the ice mass.

The overall uncertainties in the carbon budgets were propagated from analytical errors in TIC and salinity and from estimated errors in the tank volume, seawater density, and sensor volumes. Details of the error analysis are given by König (2017).

Sensors

The sensors installed in the seawater tank with relevance for this study are described in **Table 2** and shown in **Figure 1B**. The three temperature probes were installed at different depths to confirm that the tank was well-mixed, and the majority of the other sensors were installed in the middle of the tank, with an extra pH sensor at the bottom. Dopbeam sonars were deployed at the bottom of the tank. Additional details about sensor configurations during each experiment, including additional sensors installed, are given by König (2017).

Sensor CO_2 System

The CONTROS HydroC pCO_2 probe (Fietzek et al., 2014) we deployed was connected to an external pump (SBE 5M, Sea-Bird

TABLE 2 | Overview of sensors deployed in the seawater tank. Additional sensors installed but not discussed in this paper are described in König (2017).

Sensor	Variables(s)	Measurement interval	Location in tank (avg. depth)
CONTROS HydroC/CO2 II	pCO_2	1 min/1 s (Run 5)	55 cm
2 × SeaFET pH Sensor	pH	10 min/5 min (Runs 9-12)/2 min (Run 5)	55 cm/85 cm
3 × RBR T 1050	Temperature	1 s/2 s (Runs 9-12)	30 cm/55 cm/85 cm
AANDERAA Conductivity Sensor 4319	Salinity	5 s/1 s (Run 5)	55 cm
RBR Solo Pressure	Pressure	10 s	55 cm
Sontek Dopbeam sonars	Ice thickness	2 MHz	40 cm
AANDERAA Oxygen Optode 4330	Oxygen, Temperature	1 min/5 s (Run 5)	55 cm

TABLE 3 | Average ice growth rates of all six runs, calculated from the runtime (duration) of each experiment and the average final ice thickness.

Name	Air temp. (°C)	Stirring	Duration (d)	Ice thickness (cm)	Growth rate (cm/d)
Run 5	−25	Yes	5.8	21.1 ± 0.6	3.6 ± 0.1
Run 6	−40	Yes	1.8	21.2 ± 0.8	11.8 ± 0.4
Run 8	−15	Yes	22.5	18.4 ± 1.5	0.8 ± 0.1
Run 10	−25	No	4.7	21.6 ± 1.3	4.6 ± 0.3
Run 11	−40	No	2.0	20.9 ± 0.8	10.6 ± 0.4
Run 12	−15	No	8.0	21.5 ± 0.7	2.7 ± 0.1

Scientific) for all experiments except Run 8, when the connection cable to the pump was broken, giving a longer sensor response time for that experiment. The sensor was programmed to zero every 12 h (24 h in the case of Run 8) (Fietzek et al., 2014), and pCO_2 values calculated from pH and TIC of the pre-ice water samples were used to correct for a (generally small) offset in the pCO_2 curve (König, 2017). For pH measurements, we deployed two SeaFET sensors (Martz et al., 2010). As for pCO_2, the pH data were calibrated using the measurements of discrete water samples. Further details about signal correction and data processing are given by König (2017).

Other Parameters

Three RBR TR 1050 probes were installed in the tank at different depths to measure water temperatures. These data were used to check for stratification, correct the SeaFET pH data, and for the sensor CO_2 system calculations. In addition, we obtained temperature data from an O_2 optode (Aanderaa Data Instruments AS, model 4330) deployed in the tank to monitor potential contaminating biological activity.

Seawater salinity was measured by a conductivity sensor (Aanderaa Data Instruments AS, model 4319). This inductive measurement was likely influenced by the sensors and tank walls around it, and therefore, we applied an offset to the data using the discrete water samples (König, 2017).

A pressure sensor (RBR Solo Pressure) was installed in the tank to monitor the potential pressure increase in the water during ice formation and for the CO_2 system calculations. This sensor was calibrated against ambient pressure, as described by König (2017).

Ice Thickness and Brine Release (Dopbeam Sonars)

Three 20 MHz single-beam Dopbeam sonars (Sontek) were deployed in the tank, facing upwards, to survey the growing ice. These sonars record the backscatter of the emitted sonar signal, as well as a velocity profile (Vagle et al., 2012) and were primarily installed to test whether they could provide information on the timing and extent of brine released from the growing ice layer, but we also used them to measure the thickness of the growing ice. This was possible thanks to the density differences between the high-salinity brine, the growing ice, and the underlying water layer, which lead to the reflection of the emitted sonar signals at these interfaces. Further information on the backscatter data collection is given by König (2017).

CO_2 System

The aqueous CO_2 system in the tank was fully characterized using water sample data and the program of van Heuven et al. (2011), with temperature and pressure from sensors deployed in the tank, the borate-to-salinity ratio of Uppström (1974), and KSO_4 dissociation constants of Dickson (1990). Total silicate and phosphate were assumed to be negligible for the calculations. We used the carbonic acid dissociation constants of Cai and Wang (1998), because they gave to the smallest discrepancies between calculated and measured values of the over-determined carbonate system (König, 2017).

We found that after the initial sampling point (before the experiments were started), calculated and measured alkalinity in the water diverged. We suspect that alkalinity was contaminated by an unknown process (possibly electrochemical) associated with the complex configuration of sensors (some of which were new) in the relatively small-volume tank during the initial trial

runs. The relative contamination decreased when more seawater was added to the tank. As this A_T increase occurred in a single step at the beginning of our experiments, the relative changes in A_T during each experiment are still useful.

Carbonate system calculations were also conducted with sensor pH (SeaFET 245) and pCO_2 data (HydroC), which allowed us to compute high-resolution TIC and A_T time series. These calculations were only implemented for the stirred runs, since for the unstirred experiments the water was likely stratified, and therefore the sensors did not evaluate the same water.

RESULTS AND DISCUSSION

Average Growth Rates

Except at the coldest temperature, the average growth rates were lower for the stirred than the unstirred runs (**Table 3**), and the largest difference was observed between the slow growth experiments at −15°C. These findings are not surprising, as the stratified water during unstirred runs allowed for quicker freezing due to decreased heat transfer from below. Ice growth during Runs 6 and 11 (coldest conditions, −40°C), appeared to be faster with stirring, but we think this is the result of a delayed start of the main condenser units during the unstirred experiment (Run 11; **Table 1**), which led to higher temperatures (−30°C) during the first hours of the experiment.

Fate of TIC, A_T, and Salinity During Ice Growth

Water and Ice Melt Samples

The relationship between salinity, A_T, and TIC for all water and ice melt samples is illustrated in **Figures 2**, **3**. We included A_T in this analysis, despite the potential contamination (section CO_2 system), since this contamination appeared to be consistent for all discussed runs, and therefore the change in the A_T signal in ice and water can still help identify potential ikaite precipitation in the ice.

The excellent fit of the linear regression to the data points in **Figure 2** shows that both TIC and A_T are closely coupled with salinity. This indicates that the TIC (and A_T) allocation in the air-ice-water system is strongly dominated by brine processes, and that gas exchange or precipitation processes within the ice are relatively minor. However, closer examination reveals additional differences between the different sample types and experiments (**Figure 3**). For this comparison, ratios between the variables (e.g., TIC to salinity) were calculated for each data point and subsequently normalized to the ratio of the pre-ice water sample from the same experiment, accounting for dilution (in the case of ice melts) and evaporation effects. For all experiments, changes in the parameter ratios were much more distinct for the ice melt samples than for the under-ice water. Even between ice cores from the same experiment, large discrepancies could be observed, particularly in the stirred runs. The TIC-to-salinity ratio in ice appeared to decrease slightly in most experiments (up to 5% decrease compared to pre-ice water), while A_T seemed to generally increase in the ice, relative to salinity and TIC (increases up to 4 and 9%, respectively). The decoupling of the TIC and salinity signals implies a release of CO_2 from the ice, either to the air above or water below, but through a different mechanism from the salinity release. No significant increase in TIC relative to salinity was identified in the under-ice water, suggesting release to the atmosphere. However, the change in the under-ice water TIC concentration relative to salinity would have been very small, and might have not been detectable within our sampling and analytical uncertainties.

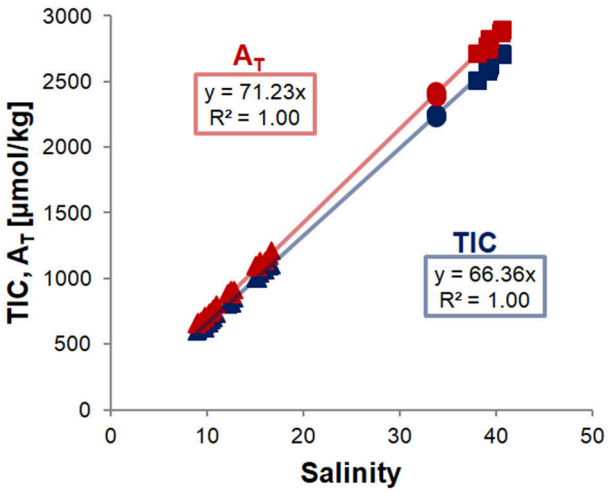

FIGURE 2 | Correlations of TIC (blue) and A_T (red) with salinity in water and ice melt samples of all runs. Replicates of water and ice melt samples were averaged for each sampling point and ice core, respectively, and trend lines were fit through all data points, and forced through zero. Error bars are smaller than the symbols. Analytical data are given in **Table S2**.

The detected increase in ice melt A_T compared to both TIC and salinity implies precipitation and retention of $CaCO_3$ minerals (e.g., ikaite) in some of the sampled ice. Since such minerals dissolve during the melting of the ice, they contribute twice as much A_T as TIC to the resulting solution. The observed relative decrease in A_T in some of the under-ice water samples might also be related to this process, as it leads to an increase in TIC (relative to A_T) in the remaining brine, which can then influence the underlying water by drainage (Jones and Coote, 1981). When examining the melting ice cores, white particles, which could have been $CaCO_3$, were visible for all cores from all experiments. No quantitative analysis of these particles was conducted, and we cannot confirm whether they were indeed $CaCO_3$ and not some other salt precipitates or contamination. Even though ikaite may have precipitated during all our experiments, its impact on the carbon distribution was small, given the small relative increase in the A_T to TIC ratio in the ice melt samples (mostly less than 5%, apart from one sample with a 10% increase).

Comparing the different experiments, it is difficult to find a clear pattern between the deviations in ice carbonate chemistry and the ice growth rates (**Table 3**). Nevertheless, it appears as if the A_T to TIC ratio in ice is higher for experiments with slower ice growth (**Figure 3C**), indicating that $CaCO_3$ precipitation may be enhanced at slower growth rates. In particular, the experiment with (by far) the slowest ice growth rate displayed an increase

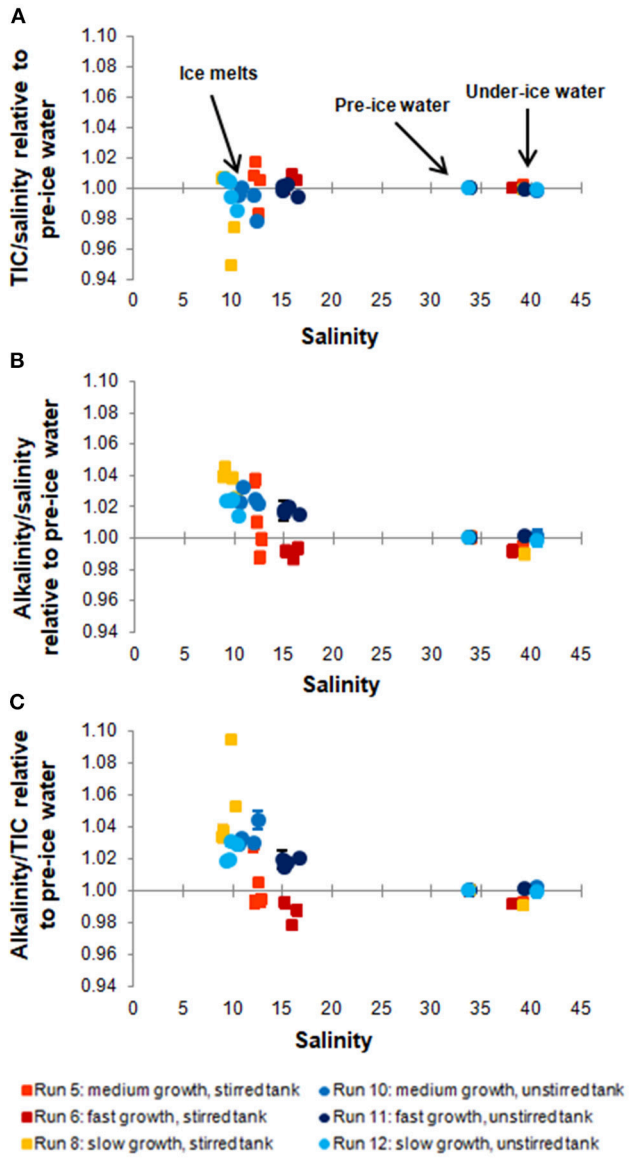

FIGURE 3 | Ratios between TIC and salinity **(A)**, A_T and salinity **(B),** and A_T and TIC **(C)** of the sampled ice melts, pre-ice, and under-ice water. For all experimental runs, the data points were normalized to the ratio of the pre-ice water sample, so as to illustrate changes in the ratios during ice growth. Uncertainties were calculated from deviations between replicates.

in the A_T to TIC ratio in the ice melts of up to 9.4%. This is contrary to expectations of increased ikaite precipitation at lower temperatures/higher brine salinities, but might be caused by the insufficient removal of dissolved CO_2 from the ice during faster ice growth, which is required to achieve ikaite supersaturation (Papadimitriou et al., 2013). The apparent increase in $CaCO_3$ precipitation at slower ice growth could therefore be related to the increased permeability at these higher temperatures, possibly leading to more efficient removal of CO_2 by outgassing, or simply due to the longer duration of the run, which allowed more CO_2 to escape. This is further supported by pCO_2 values measured in the ice during this run, which were lower than for other runs (König, 2017). Conversely, apparently smaller ikaite precipitation in ice samples in the other runs may simply be due to their shorter runtimes, which may not have been sufficient to allow substantial ikaite precipitation. Papadimitriou et al. (2014) reported that 1–3 weeks, depending on ice temperature, is needed for ikaite precipitation to reach steady state in sea ice.

Despite the generally high A_T in our seawater due to contamination, the *absolute* A_T to TIC ratios in the ice melt samples of our experiments (average of 1.09 ± 0.02, with a maximum of 1.16) are generally at the lower end of ratios measured in the field, where values of up to 2.2 have been reported (Rysgaard et al., 2007, 2009). However, our values are comparable to those measured in young or newly formed natural and artificial ice (Rysgaard et al., 2007, 2009; Fransson et al., 2015; Geilfus et al., 2016), which further highlights the importance of incubation time for ikaite precipitation. Some ice melts from the two colder, stirred runs (Run 5 and 6) show an inverse pattern from that of the warm run (Run 8), i.e., a relative increase in ice TIC combined with a decrease in A_T. This might have been caused by either increased retention of CO_2 in the ice (e.g., in the form of bubbles), or unidentified deficiencies in sampling and/or analyses. Transport of ikaite from the ice to the underlying water, as suggested by Geilfus et al. (2016), would also explain the relative decrease in ice A_T compared to TIC. However, as no corresponding increase in underwater A_T was detected, and since the permeability in ice was likely too low at our experimental temperatures, we believe this process is not responsible for the relative decrease in ice A_T we detected.

Time Series Variations

While the water samples only provide point measurements at the beginning and end of the experiments, DIC and A_T calculated from sensor pH and pCO_2 allow us to examine changes in the water over the entire experimental period and to compare their development to those of salinity and ice thickness (**Figure 4**). Comparing TIC, A_T, salinity, and ice thickness (**Figures 4A,B**), the parameter curves appear to be very similar. At the fastest ice growth rate (Run 6; **Figure 4**, left column), all four parameters increase nearly linearly over the whole experiment, while for the two experiments at slower ice growth rates, the increase in all three parameters was initially faster and then slowed over the course of the run. It is worth noting that for salinity, the increase was somewhat delayed for all three experiments compared to ice thickness. This was not the case for the TIC and A_T, which appeared to increase even before the surface was ice covered. While an increase in TIC during this period is conceivable due to increased uptake of CO_2 from the air, and has indeed been observed during a similar experiment by Kotovitch et al. (2016), a significant increase in A_T is unrealistic. Furthermore, no such increase was observed for the pre-ice water samples, and it is therefore likely an artifact of the CO_2 system calculations, coupled with the different response times of the sensors. We were only able to estimate the response time for the HydroC sensor and calculations with time-lag corrected sensor data did not provide useful insight (König, 2017).

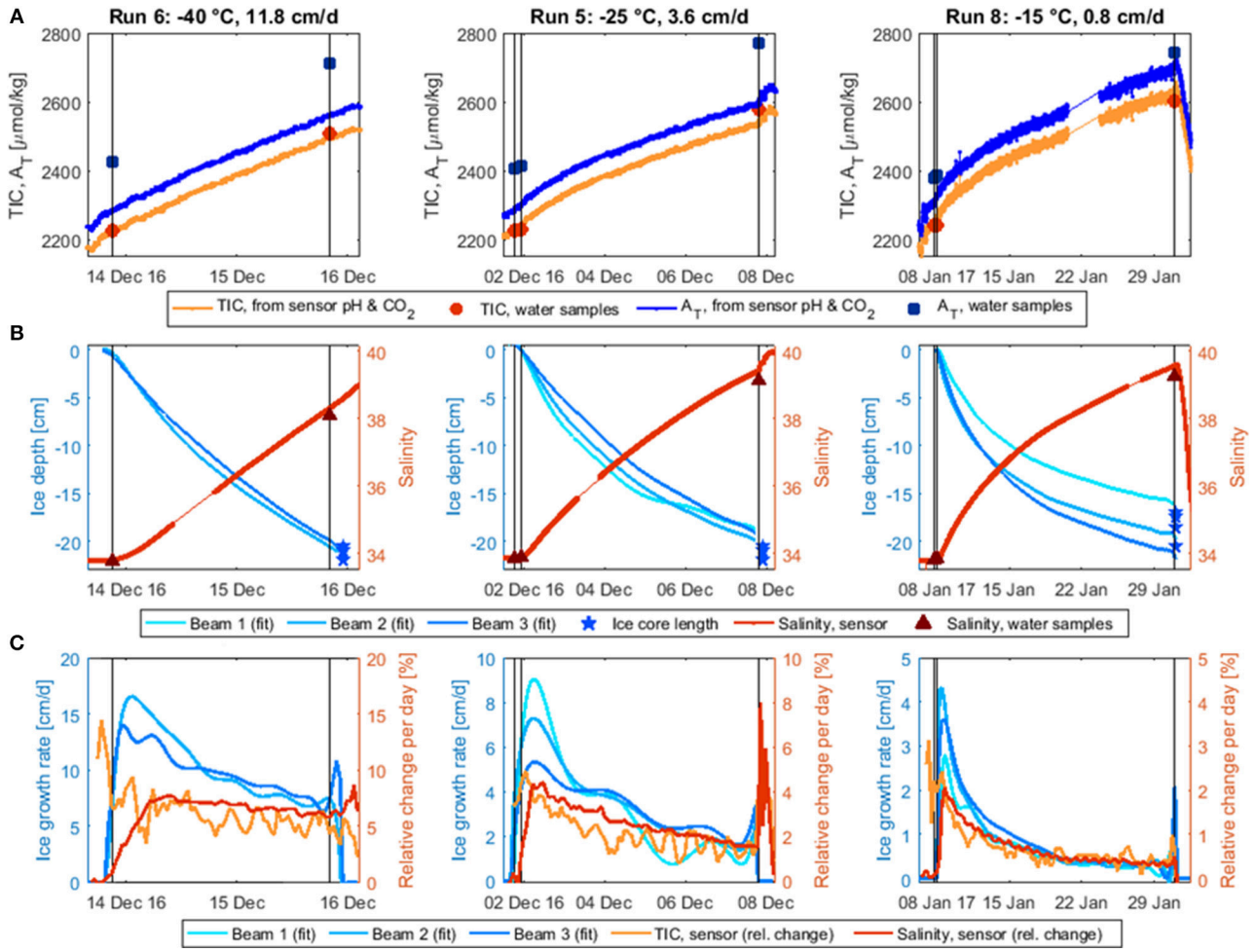

FIGURE 4 | Temporal development of water TIC, A_T **(A)**, water salinity, and ice depth (**B**; fitted curves from the three Dopbeam sonars) during the three stirred experimental runs as well as the corresponding water sample measurements. TIC and A_T were calculated from the HydroC pCO_2 and the (corrected) external pH of SeaFET 245. Water A_T increased before the experiments started, possibly due to some electrochemical process associated with the sensors and equipment in the tank at initial deployment; note that seawater was added to the tank between runs 6 and 8 (**Table 1**), reducing the relative impact of the alkalinity contaminant. **(C)** Ice growth rate (cm/d) derived from Dopbeam-measured ice depth and daily rates of change in salinity (dS/S per day) and TIC (dTIC/TIC per day). Note different vertical and horizontal scales. Black vertical lines indicate water sampling.

To better compare the temporal changes in TIC, salinity, and ice thickness, rates of change were calculated over time intervals adapted to the duration of the run (**Figure 4C**): 1.5 h for Run 5, 45 min for Run 6, 6 h for Run 8. For TIC and salinity, normalized change rates were calculated, e.g., $d\overline{S} = dS/S$, using the data curves, which were averaged over the corresponding time interval for this purpose. As the calculated TIC curve was still very noisy, it was further averaged over four adjacent data points. For ice thickness, the change rate (i.e., growth rate) was derived from curve fits to the Dopbeam sonar data.

The ice growth rates decreased significantly over the course of each experiment, due to the insulating effect of the overlying ice (**Figure 4C**), by more than a factor of five for the slower two experiments and by half for the fastest experiment. Salinity and TIC appeared to increase more steadily over the course of the experiments. This implies a decoupling between ice growth and desalination rates, which can also be observed by comparing the timing of the peak desalination rate, which occurred later than the fastest ice growth rate in all three runs. The discrepancy between peak ice growth and desalination was largest for the fastest ice growth experiment, where the maximum increase in salinity was observed when the ice thickness was 5–6 cm. In the slower two experiments, salinity increased most at ice thicknesses of 0.5–2 cm (Run 8) and 1.5–3 cm (Run 5). These findings are consistent with mushy layer theory, which predicts a delayed onset of brine drainage (Wettlaufer et al., 1997; Notz and Worster, 2009). However, while the *peak* in the desalination rate appears to be delayed, salinity did begin increasing as soon as the first ice had formed, thereby contradicting the mushy layer predictions. This instantaneous increase could be related to the constant mixing of the tank during these three experiments, which could have disrupted

the ice-water boundary layer, as described by Loose et al. (2011).

The rate of change in TIC is harder to interpret, due to the aforementioned difficulties with the sensor CO_2 system calculations, which led to unrealistic increases in A_T and TIC at the beginning of the experiments. Focusing only on the ice growth period (i.e., the time after the last pre-ice water sample was taken), it appears as if TIC was increasing more rapidly than salinity during initial ice growth, but more slowly after that. While this could be an artifact of CO_2 system calculations, it might also be due to a dissimilar behavior of the CO_2 gas and the dissolved salts, as was observed for conservative gas tracers in similar experiments by Loose et al. (2009), who suggested that the differences were related to the faster diffusion of gas away from the ice-water interface. In our case, this process may have been further supported by a slight, additional cooling of the under-ice water (i.e., from approximately -1° to -2°C; König, 2017) and the concomitant increase in gas solubility.

Brine Drainage at Different Growth Rates

The data collected during the experiments without stirring in the tank provide insight into brine release processes, and the temperature dependent differences we observed have potentially important consequences with regard to increasing air temperatures in polar regions. These findings are mainly based on the backscatter data obtained from the Dopbeam sonars, which indeed seemed able to detect brine release from the ice and were further supported by changes in other parameters.

As indicated by the rates of change in the salinity signal (**Figure 4C**), the maximum desalination from the ice occurred in the early stages of each (stirred) run, but after the maximum ice growth rate had been reached. Similarly, the backscatter signal from the Dopbeam sensors shows a relatively undisturbed, clearly defined ice-water interface up until an ice thickness of about 5–10 cm, after which brine draining out of the ice starts to cloud the strong backscatter signal from the ice, indicating periods of relatively strong brine release (**Figure 5A**). This delayed onset of the maximum brine drainage is in agreement with predictions of the mushy-layer theory, as discussed above.

The blurring of the ice-water interface due to brine drainage is more pronounced for the two coldest experiments, either due to more intense outflow of brine or higher density differences between brine and underlying water, causing a more efficient reflection of the sonar pulses. The notion that brine released during the colder experiments is denser than for the warmer run is further supported by areas of intense backscatter in the water further away from the ice-water interface, as well as temperature measurements in the water column.

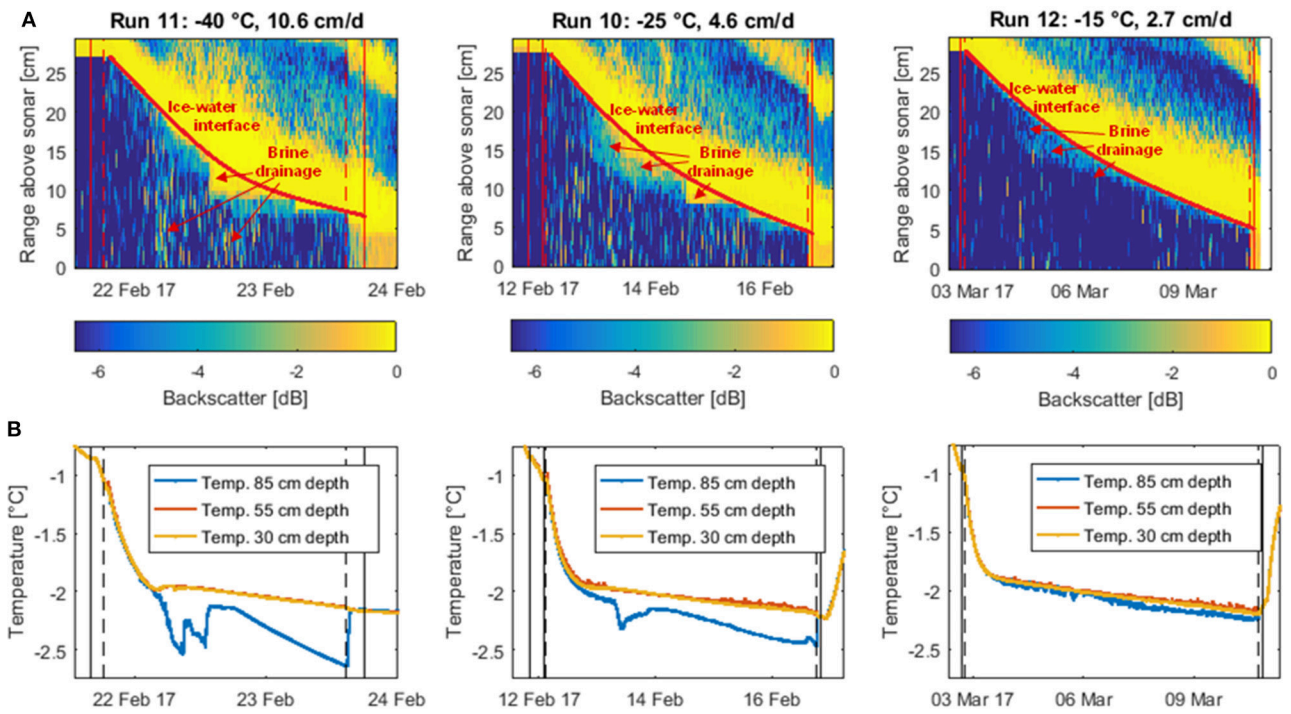

FIGURE 5 | Backscatter profiles **(A)** and water temperature time series **(B)** of the three unstirred experiments. The backscatter profiles based on data from the most sensitive Dopbeam sonar were obtained using the difference between the backscatter signal (at each point in time and distance from the sonar) and the maximum backscatter signal of that run. Thus, less negative values indicate stronger backscatter. The strong backscatter signal from the top left to the bottom right corner of each figure represents the descending ice front. The temperature curves were obtained from sensors installed at three different depths in the water, one below the ice (30 cm depth, yellow), one in the middle of the water column (55 cm depth, red), and one at the bottom of the tank (85 cm depth, blue). Solid vertical lines indicate water (and later ice) sampling, dashed vertical lines the switching off (at the start) and on (at the end) of the stirring in the tank.

While for the warmest unstirred experiment (Run 12), the relatively weak backscatter signal attributed to brine drainage is restricted to the uppermost centimeters of the water column, we find that for the colder two runs, the sonar signal is also scattered back at deeper depths. Furthermore, the temperature signals of sensors installed at three different depths within the water column suggest that during colder runs, the tank was more stratified (**Figure 5B**). For the colder two runs, abrupt changes in the temperature curve of the bottom sensor coincide with the apparent brine drainage patterns we observed in the backscatter data, suggesting that during the intense brine release period at about 5–10 cm ice thickness, some plumes might have been sufficiently dense to reach the bottom of the tank. No such changes were observed during the warmest run, implying a lack of depth-penetrating brine plumes during this experiment. This finding has potentially far-reaching implications for carbon transport to lower water layers with the so-called "brine pump" (section Implications for future sea ice carbon export, below).

However, as no salinity sensor was deployed at depth, the evidence for more effective vertical brine transport at faster ice growth rates (or colder air temperatures) is circumstantial. Nevertheless, given the potential impact on carbon sequestration of this brine transport, we suggest that further experiments should be conducted with additional probes (as well as in deeper tanks) to resolve the salinity profile across the water column.

Carbon Budget

The results of the carbon budget calculations are shown in **Figure 6**. For both sets of runs, the majority of TIC (53–72%) was released to the under-ice water, whereas the rest (28–47%) remained in the ice, and exchange with air was negligible. This is in agreement with previous mass balance studies, which found

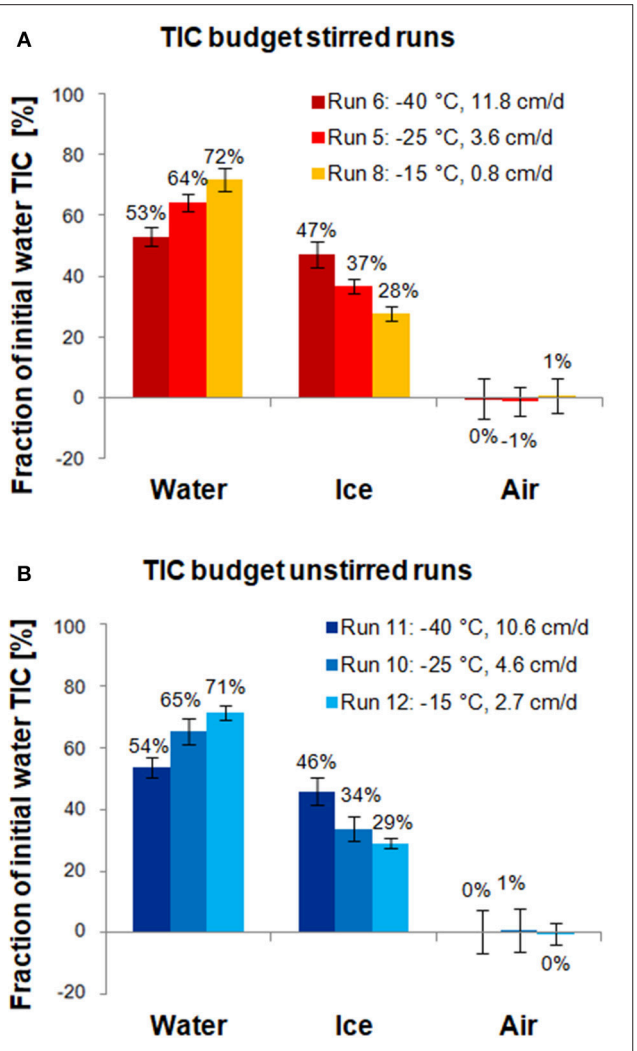

FIGURE 6 | Carbon budgets for stirred runs **(A)** and unstirred runs **(B)**. Bars show how much of the TIC initially in the water ultimately converted into ice ends up in the final under-ice water, ice, and air, respectively (Section Carbon Budget). Error bars were computed from uncertainties in water and ice TIC, initial water mass, and ice mass (propagated from salinity measurements).

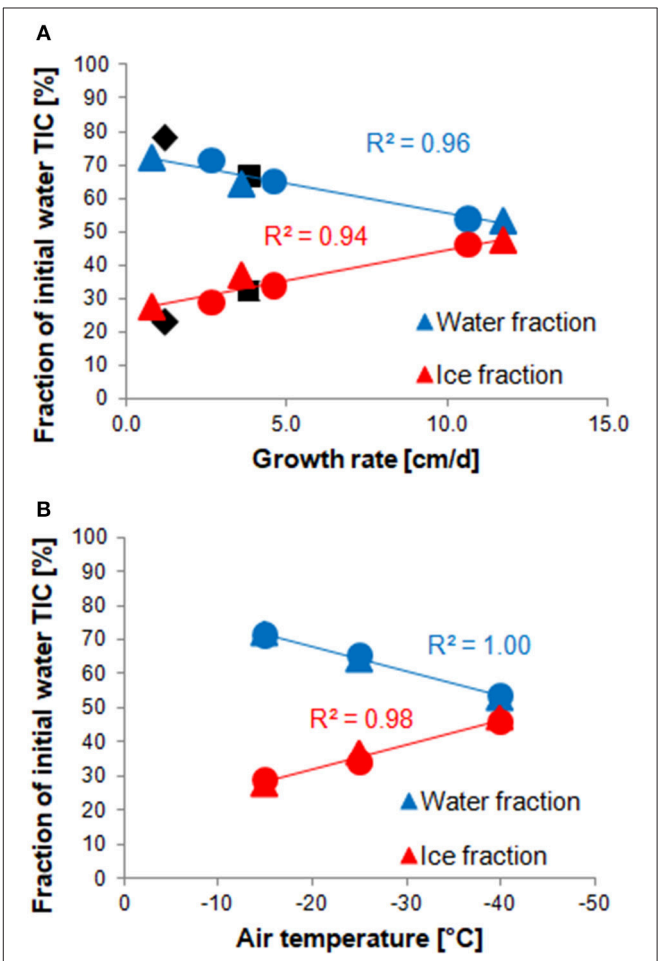

FIGURE 7 | Correlations between the TIC fraction in water (blue) or ice (red) and the average ice growth rate **(A)** or the ambient temperature **(B)** of each experiment. Values from stirred runs are marked with round, those from unstirred runs with triangular, symbols. Values measured by previous studies are shown in black, but have not been used for the regression. Black diamonds show values presented by Rysgaard et al. (2007), squares are the (average) results of Nomura et al. (2006). The air temperatures shown in panel B are average values measured during each run, as listed in **Table S1**.

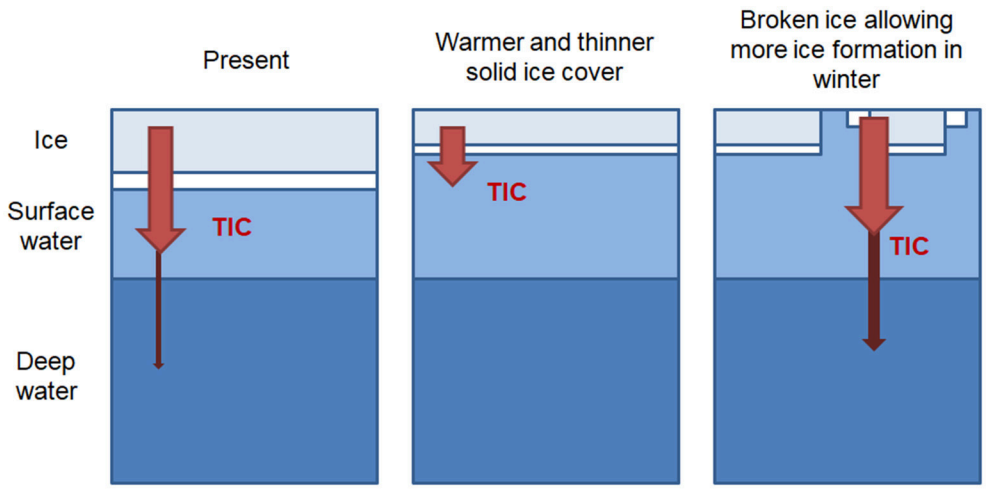

FIGURE 8 | Schematic illustration of the implications of our findings for future scenarios conditions. A thinner and warmer, but complete ice cover and a decrease in total sea ice production leads to a decrease in TIC export to deep water layers. Increased openings within the sea ice cover during winter increase total sea-ice production and export of TIC to deeper water layers.

that of all TIC released from the ice, only a small fraction escaped to the air (<0.1 to 1.1%), while the majority (89.9 to >99.9%) was transported to the underlying water (Nomura et al., 2006; Rysgaard et al., 2007; Sejr et al., 2011).The uncertainty was larger for the air than for water and ice fractions, because the air fraction was estimated from the results of the other fractions. In general, uncertainties in the carbon budget were dominated by the heterogeneity of the ice, which lead to uncertainties in ice TIC and salinity.

Both stirred and unstirred runs show very similar TIC redistribution patterns: in the fastest ice growth experiments, the ice phase contains nearly half of the initial TIC (47 and 46% for stirred and unstirred runs, respectively) but only less than a third in the slowest growth experiments (28 and 29%, respectively). This is in agreement with expectations that higher growth rates lead to less efficient desalination of the ice, and that TIC largely follows salinity. Carbon budget numbers reported in previous laboratory studies for similar growth rates appear to be in line with the values observed for our experiments (**Figure 7**).

Interestingly, the TIC redistribution appears to be less dependent on the growth rate than the ambient temperature at which the experiments were run. The slowest experiment (Run 8), for instance, shows a very similar distribution to Run 12, which was run at the same temperature, despite a more than three times lower growth rate. Thus, there is a better (linear) correlation between TIC fractions in water and ice with ambient temperature than with growth rate (**Figure 7**). Perhaps this reflects the importance of a temperature gradient within the ice in retaining brine and gases.

Implications for Future Sea Ice Carbon Export

Due to large uncertainties in future sea-ice extent and volume (e.g., Meier, 2016; Stammerjohn and Maksym, 2016), meaningful estimates of the total future carbon export from sea ice are difficult. However, the implications of our findings for future potential sea-ice conditions are summarized in **Figure 8**. In the baseline, "present day" case the majority of TIC released from the sea ice remains in the surface layer, with only a small fraction exported to depth, as predicted in the modeling studies of Grimm et al. (2016) and Moreau et al. (2016).

In cases where warmer air temperatures result in a solid ice cover that is warmer and thinner the expected increase in TIC release (per unit of ice) is canceled out by the decrease in total ice production. Furthermore, export of TIC to the deep ocean is reduced due to the less sufficiently dense brine.

On the other hand, a thinner ice cover also leads to a more mobile, broken ice cover during the winter, with more leads and possibly polynyas. In this case, sea-ice and brine production may actually increase. In addition, that brine and the associated TIC may be exported deeper into the water column, thereby enhancing deepwater formation and carbon sequestration.

It is important to note that these simple future scenarios neglect crucial impacts such as changes to ocean circulation, or the related biological systems. However, they again stress the importance of open water within the sea ice cover, which may not only enhance gas exchange (Loose et al., 2009; Else et al., 2011), but also facilitate export of carbon out of the surface layer (Grimm et al., 2016; this study).

CONCLUSION AND PERSPECTIVES

Sea ice growth experiments conducted in a cold laboratory showed that there is a connection between ice growth rates and the redistribution of TIC between the ice and the water underneath. This differential redistribution was evident from discrete water and ice samples, and also visible in continuous time series recorded by underwater sensors. A budgetary approach showed that at higher ice growth rates, relatively more of the initial TIC remains in the ice phase than at slower growth

rates (46–47% compared to 28–29%), and the TIC redistribution appeared to depend more on the ambient temperature at which the ice formed than on the ice growth rate. For all experiments, most TIC was rejected into the under-ice water (53–72%, depending on the temperature), while exchange with the air was insignificant, relative to our experimental uncertainties.

The TIC redistribution appeared to be dominated by brine drainage processes, as indicated by a good correlation between TIC and salinity in the ice and water. Minor deviations between the two parameters were likely due to $CaCO_3$ precipitation in ice and/or CO_2 exchange with the air. Temperature and Doppler backscatter data suggest that whereas more TIC is exported from the ice at higher temperatures (slower ice formation rates), the vertical extent of that transport (e.g., to the bottom of the mixed layer) might be more efficient when ice is formed at colder temperatures (at a faster growth rate). For a more satisfactory assessment of the potential for TIC export to deeper water layers, the stratification and brine release processes should be examined more closely, ideally by the installation of additional salinity probes in the water and possibly the ice.

DATA AVAILABILITY

The data used in this laboratory-based study are included in this manuscript and König (2017).

AUTHOR CONTRIBUTIONS

DK designed and conducted the experiments with substantial guidance from LM and support from KS. SV provided, installed, and processed the data of the Dopbeam sensors. DK conducted chemical analyses, processed all datasets, and drafted the manuscript. All authors contributed to manuscript editing and revision.

FUNDING

This project was supported by the Fisheries and Oceans Canada Arctic Sciences Fund. Further financial support was provided by the Zeno Karl Schindler Foundation in the form of a master thesis grant, and by the ETH Zurich Financial Aid Office, which granted a personal travel allowance to DK.

ACKNOWLEDGMENTS

We would like to thank the staff of the Institute of Ocean Sciences for their support, especially Kenny Scozzafava and Jasmine Wietzke for salinity analyses, Marty Davelaar for help with the TIC and alkalinity analyses, and Sarah Zimmermann and Jonathan Velarde for help with ice coring. Further thanks are due to Nicolas Gruber for his support during the master's thesis this paper is based on, and to him and his group, as well as the BEPSII community for all the fruitful discussions during the preparation of this manuscript.

SUPPLEMENTARY MATERIAL

The Supplementary Material for this article can be found online at: https://www.frontiersin.org/articles/10.3389/feart.2018.00234/full#supplementary-material

REFERENCES

Anderson, L. G., Falck, E., Jones, E. P., Jutterström, S., and Swift, J. H. (2004). Enhanced uptake of atmospheric CO_2 during freezing of seawater: a field study in Storfjorden, Svalbard. *J. Geophys. Res. Oceans* 109:C06004. doi: 10.1029/2003JC002120

Barber, D. G., Ehn, J. K., Pućko, M., Rysgaard, S., Deming, J. W., Bowman, J. S., et al. (2014). Frost flowers on young Arctic sea ice: the climatic, chemical, and microbial significance of an emerging ice type. *J. Geophys. Res. Atmos.* 119, 11593–11612. doi: 10.1002/2014JD021736

Cai, W.-J., and Wang, Y. (1998). The chemistry, fluxes, and sources of carbon dioxide in the estuarine waters of the Satilla and Altamaha Rivers, Georgia. *Limnol. Oceanogr.* 43, 657–668. doi: 10.4319/lo.1998.43.4.0657

Clayton, T. D., and Byrne, R. H. (1993). Spectrophotometric seawater pH measurements: total hydrogen ion concentration scale calibration of m-cresol purple and at-sea results. *Deep Sea Res. Part I Oceanogr. Res. Papers* 40, 2115–2129. doi: 10.1016/0967-0637(93)90048-8

Cox, G., and Weeks, W. (1975). *Brine Drainage and Initial Salt Entrapment in Sodium Chloride Ice.* CRREL Res. Rep. 345., Hanover, NH: U.S. Army Cold Regions Research and Engineering Laboratory.

Dickson, A. G. (1990). Standard potential of the reaction: $AgCl(s) + 1/2\ H_2(g) = Ag(s) + HCl(aq)$, and the standard acidity constant of the ion HSO_4 in synthetic sea water from 273.15 to 318.15 K. *J. Chem. Thermodyn.* 22, 113–127. doi: 10.1016/0021-9614(90)90074-Z

Dickson, A. G., Sabine, C. L., and Christian, J. R., (eds.). (2007). *Guide to Best Practices for Ocean CO2 Measurements*. Sidney, BC: North Pacific Marine Science Organization, PICES Special Publication 3.

Eicken, H. (1992). Salinity profiles of Antarctic sea ice: field data and model results. *J. Geophys. Res. Oceans* 97, 15545–15557. doi: 10.1029/92JC01588

Else, B. G. T., Papakyriakou, T. N., Galley, R. J., Drennan, W. M., Miller, L. A., and Thomas, H. (2011). Wintertime CO_2 fluxes in an Arctic polynya using eddy covariance: evidence for enhanced air-sea gas transfer during ice formation. *J. Geophys. Res. Oceans* 116:C00G03. doi: 10.1029/2010JC006760

Feltham, D. L., Untersteiner, N., Wettlaufer, J. S., and Worster, M. G. (2006). Sea ice is a mushy layer. *Geophys. Res. Lett.* 33:L14501. doi: 10.1029/2006GL026290

Fietzek, P., Fiedler, B., Steinhoff, T., and Körtzinger, A. (2014). *In situ* quality assessment of a novel underwater pCO_2 sensor based on membrane equilibration and NDIR Spectrometry. *J. Atmosph. Oceanic Technol.* 31, 181–196. doi: 10.1175/JTECH-D-13-00083.1

Fransson, A., Chierici, M., Abrahamsson, K., Andersson, M., Granfors, A., Gardfeldt, K., et al. (2015). CO_2-system development in young sea ice and CO_2 gas exchange at the ice/air interface mediated by brine and frost flowers in Kongsfjorden, Spitsbergen. *Ann. Glaciol.* 56, 245–257. doi: 10.3189/2015AoG69A563

Geilfus, N.X., Carnat, G., Dieckmann, G. S., Halden, N., Nehrke, G., Papakyriakou, T., et al. (2013). First estimates of the contribution of $CaCO_3$ precipitation to the release of CO_2 to the atmosphere during young sea ice growth. *J. Geophys.Res. Oceans* 118, 244–255. doi: 10.1029/2012JC007980

Geilfus, N. X., Galley, R. J., Else, B. G. T., Campbell, K., Papakyriakou, T., Crabeck, O., et al. (2016). Estimates of ikaite export from sea ice to the underlying seawater in a sea ice–seawater mesocosm. *Cryosphere* 10, 2173–2189. doi: 10.5194/tc-10-2173-2016

Gough, A. J., Mahoney, A. R., Langhorne, P. J., Williams, M. J. M., and Haskell, T. G. (2012). Sea ice salinity and structure: a winter time series of salinity and its distribution. *J. Geophys. Res. Oceans* 117:C03008. doi: 10.1029/2011JC007527

Griewank, P. J., and Notz, D. (2013). Insights into brine dynamics and sea ice desalination from a 1-D model study of gravity drainage. *J. Geophys. Res. Oceans* 118, 3370–3386. doi: 10.1002/jgrc.20247

Grimm, R., Notz, D., Rysgaard, S., Glud, R., and Six, K. D. (2016). Assessment of the sea ice carbon pump: insights from a three-dimensional ocean-sea-ice biogeochemical model (MPIOM/HAMOCC). *Elementa* 4:000136. doi: 10.12952/journal.elementa.000136

Johnson, K. M., Wills, K. D., Butler, D. B., Johnson, W. K., and Wong, C. S. (1993). Coulometric total carbon dioxide analysis for marine studies: maximizing the performance of an automated gas extraction system and coulometric detector. *Marine Chem.* 44, 167–187. doi: 10.1016/0304-4203(93)90201-X

Jones, E. P., and Coote, A. R. (1981). Oceanic CO_2 produced by the precipitation of $CaCO_3$ from brines in sea ice. *J. Geophys. Res. Oceans* 86, 11041–11043. doi: 10.1029/JC086iC11p11041

König, D. (2017). *Carbon Dynamics during the Formation of Sea Ice at Different Growth Rates.* Master thesis, Swiss Federal Institute of Technology Switzerland.

Kotovitch, M., Moreau, S., Zhou, J., Vancoppenolle, M., Dieckmann, G. S., Evers, K.-U., et al. (2016). Air-ice carbon pathways inferred from a sea ice tank experiment. *Elementa* 4:000112. doi: 10.12952/journal.elementa.000112

Loose, B., McGillis, W. R., Schlosser, P., Perovich, D., and Takahashi, T. (2009). Effects of freezing, growth, and ice cover on gas transport processes in laboratory seawater experiments. *Geophys. Res. Lett.* 36:L05603. doi: 10.1029/2008GL036318

Loose, B., Miller, L. A., Elliott, S., and Papakyriakou, T. (2011). Sea ice biogeochemistry and material transport across the frozen interface. *Oceanography* 24, 202–218. doi: 10.5670/oceanog.2011.72

Martz, T. R., Connery, J. G., and Johnson, K. S. (2010). Testing the honeywell Durafet® for seawater pH applications. *Limnol. Oceanograp. Methods* 8, 172–184. doi: 10.4319/lom.2010.8.172

Meier, W. N. (2016). "Losing Arctic sea ice: observations of the recent decline and the long-term context," in *Sea Ice,* ed D. N. Thomas (Chichester: John Wiley), 290–303.

Miller, L. A., Carnat, G., Else, B. G. T., Sutherland, N., and Papakyriakou, T. N. (2011). Carbonate system evolution at the Arctic Ocean surface during autumn freeze-up. *J. Geophys. Res. Oceans* 116:C00G04. doi: 10.1029/2011JC007143

Miller, L. A., Fripiat, F., Else, B. G. T., Bowman, J. S., Brown, K. A., Collins, R. E., et al. (2015). Methods for biogeochemical studies of sea ice: the state of the art, caveats, and recommendations. *Elem. Sci. Anth.* 3:000038. doi: 10.12952/journal.elementa.000038

Millero, F. J., DiTrolio, B., Suarez, A. F., and Lando, G. (2009). Spectroscopic measurements of the pH in NaCl brines. *Geochim. Cosmochim. Acta* 73, 3109–3114. doi: 10.1016/j.gca.2009.01.037

Millero, F. J., and Poisson, A. (1981). International one-atmosphere equation of state of seawater. *Deep Sea Res. Part A. Oceanogr. Res. Papers* 28, 625–629. doi: 10.1016/0198-0149(81)90122-9

Moreau, S., Vancoppenolle, M., Bopp, L., Aumont, O., Madec, G., Delille, B., et al. (2016). Assessment of the sea-ice carbon pump: Insights from a three-dimensional ocean-sea-ice biogeochemical model (NEMO-LIM-PISCES). *Elem. Sci. Anth.* 4:000122. doi: 10.12952/journal.elementa.000122

Moreau, S., Vancoppenolle, M., Delille, B., Tison, J.-L., Zhou, J., Kotovitch, M., et al. (2015). Drivers of inorganic carbon dynamics in first-year sea ice: a model study. *J. Geophys. Res.Oceans* 120, 471–495. doi: 10.1002/2014JC010388

Nakawo, M., and Sinha, N. K. (1981). Growth rate and salinity profile of first-year sea ice in the high arctic. *J. Glaciol.* 27, 315–330. doi: 10.1017/S0022143000015409

Nomura, D., Granskog, M. A., Fransson, A., Chierici, M., Silyakova, A., Ohshima, K. I., et al. (2018). CO_2 flux over young and snow-covered Arctic pack ice in winter and spring. *Biogeosciences* 15, 3331–3343. doi: 10.5194/bg-15-3331-2018

Nomura, D., Yoshikawa-Inoue, H., and Toyota, T. (2006). The effect of sea-ice growth on air–sea CO_2 flux in a tank experiment. *Tellus B* 58, 418–426. doi: 10.1111/j.1600-0889.2006.00204.x

Notz, D., and Worster, M. G. (2009). Desalination processes of sea ice revisited. *J. Geophys. Res. Oceans* 114. doi: 10.1029/2008JC004885

Papadimitriou, S., Kennedy, H., Kennedy, P., and Thomas, D. N. (2013). Ikaite solubility in seawater-derived brines at 1 atm and sub-zero temperatures to 265 K. *Geochim. Cosmochim. Acta* 109, 241–253. doi: 10.1016/j.gca.2013.01.044

Papadimitriou, S., Kennedy, H., Kennedy, P., and Thomas, D. N. (2014). Kinetics of ikaite precipitation and dissolution in seawater-derived brines at sub-zero temperatures to 265 K. *Geochim. Cosmochim. Acta* 140, 199–211. doi: 10.1016/j.gca.2014.05.031

Parmentier, F.-J. W., Christensen, T. R., Sorensen, L. L., Rysgaard, S., McGuire, A. D., Miller, P. A., et al. (2013). The impact of lower sea-ice extent on Arctic greenhouse-gas exchange. *Nature Clim. Change* 3, 195–202. doi: 10.1038/nclimate1784

Petrich, C., and Eicken, H. (2016). "Overview of sea ice growth and properties," in *Sea Ice,* ed D. N. Thomas (Chichester: John Wiley), 1–41.

Rysgaard, S., Bendtsen, J., Delille, B., Dieckmann, G. S., Glud, R. N., Kennedy, H., et al. (2011). Sea ice contribution to the air–sea CO_2 exchange in the Arctic and Southern Oceans. *Tellus B* 63, 823–830. doi: 10.3402/tellusb.v63i5.16409

Rysgaard, S., Bendtsen, J., Pedersen, L. T., Ramløv, H., and Glud, R. N. (2009). Increased CO_2 uptake due to sea ice growth and decay in the Nordic Seas. *J. Geophys. Res. Oceans* 114:C09011. doi: 10.1029/2008JC005088

Rysgaard, S., Glud, R. N., Sejr, M. K., Bendtsen, J., and Christensen, P. B. (2007). Inorganic carbon transport during sea ice growth and decay: a carbon pump in polar seas. *J. Geophys. Res. Oceans* 112:C03016. doi: 10.1029/2006JC003572

Sejr, M. K., Krause-Jensen, D., Rysgaard, S., Sørensen, L. L., Christensen, P. B., and Glud, R. N. (2011). Air–sea flux of CO_2 in arctic coastal waters influenced by glacial melt water and sea ice. *Tellus B* 63, 815–822. doi: 10.1111/j.1600-0889.2011.00540.x

Stammerjohn, S., and Maksym, T. (2016). "Gaining (and losing) Antarctic sea ice: variability, trends and mechanisms," in *Sea Ice,* ed D. N. Thomas (Chichester: John Wiley), 261–289.

Stephens, B. B., and Keeling, R. F. (2000). The influence of Antarctic sea ice on glacial–interglacial CO_2 variations. *Nature* 404:171. doi: 10.1038/35004556

Tison, J.L., Haas, C., Gowing, M. M., Sleewaegen, S., and Bernard, A. (2002). Tank study of physico-chemical controls on gas content and composition during growth of young sea ice. *J. Glaciol.* 48, 177–191. doi: 10.3189/172756502781831377

Uppström, L. R. (1974). The boron/chlorinity ratio of deep-sea water from the Pacific Ocean. *Deep Sea Res. Oceanogr. Abstracts* 21, 161–162. doi: 10.1016/0011-7471(74)90074-6

Vagle, S., Gemmrich, J., and Czerski, H. (2012). Reduced upper ocean turbulence and changes to bubble size distributions during large downward heat flux events. *J. Geophys. Res. Oceans* 117:C00H16. doi: 10.1029/2011JC007308

van Heuven, S. D., Pierrot, J. W. B., Rae, E. L., and Wallace, D. W. R. (2011). *MATLAB Program Developed for CO_2 System Calculations*. Oak Ridge, Tennessee: U.S. Department of Energy, Carbon Dioxide Information Analysis Center, Oak Ridge National Laboratory.

Vancoppenolle, M., Meiners, K. M., Michel, C., Bopp, L., Brabant, F., Carnat, G., et al. (2013). Role of sea ice in global biogeochemical cycles: emerging views and challenges. *Quat. Sci. Rev.* 79, 207–230. doi: 10.1016/j.quascirev.2013.04.011

Wettlaufer, J., Worster, M. G., and Huppert, H. E. (1997). Natural convection during solidification of an alloy from above with application to the evolution of sea ice. *J. Fluid Mech.* 344, 291–316. doi: 10.1017/S0022112097006022

Conflict of Interest Statement: The authors declare that the research was conducted in the absence of any commercial or financial relationships that could be construed as a potential conflict of interest.

frontiers in Earth Science

ORIGINAL RESEARCH
published: 22 February 2019
doi: 10.3389/feart.2019.00022

Application of Sentinel-2 MSI in Arctic Research: Evaluating the Performance of Atmospheric Correction Approaches Over Arctic Sea Ice

Marcel König[1]*, *Martin Hieronymi*[2] *and Natascha Oppelt*[1]

[1] Earth Observation and Modelling, Department of Geography, Kiel University, Kiel, Germany, [2] Institute of Coastal Research, Helmholtz-Zentrum Geesthacht, Geesthacht, Germany

Multispectral remote sensing may be a powerful tool for areal retrieval of biogeophysical parameters in the Arctic sea ice. The MultiSpectral Instrument on board the Sentinel-2 (S-2) satellites of the European Space Agency offers new possibilities for Arctic research; S-2A and S-2B provide 13 spectral bands between 443 and 2,202 nm and spatial resolutions between 10 and 60 m, which may enable the monitoring of large areas of Arctic sea ice. For an accurate retrieval of parameters such as surface albedo, the elimination of atmospheric influences in the data is essential. We therefore provide an evaluation of five currently available atmospheric correction processors for S-2 (ACOLITE, ATCOR, iCOR, Polymer, and Sen2Cor). We evaluate the results of the different processors using *in situ* spectral measurements of ice and snow and open water gathered north of Svalbard during RV Polarstern cruise PS106.1 in summer 2017. We used spectral shapes to assess performance for ice and snow surfaces. For open water, we additionally evaluated intensities. ACOLITE, ATCOR, and iCOR performed well over sea ice and Polymer generated the best results over open water. ATCOR, iCOR and Sen2Cor failed in the image-based retrieval of atmospheric parameters (aerosol optical thickness, water vapor). ACOLITE estimated AOT within the uncertainty range of AERONET measurements. Parameterization based on external data, therefore, was necessary to obtain reliable results. To illustrate consequences of processor selection on secondary products we computed average surface reflectance of six bands and normalized difference melt index (NDMI) on an image subset. Medians of average reflectance and NDMI range from 0.80–0.97 to 0.12–0.18 while medians for TOA are 0.75 and 0.06, respectively.

Keywords: remote sensing, atmospheric correction, sea ice, Arctic, Sentinel-2

OPEN ACCESS

Edited by:
Benjamin Allen Lange, Freshwater Institute, Fisheries and Oceans Canada, Canada

Reviewed by:
Mallik Mahmud, University of Calgary, Canada
Shujie Wang, Lamont Doherty Earth Observatory (LDEO), United States
John Alec Casey, York University, Canada

***Correspondence:**
Marcel König
koenig@geographie.uni-kiel.de

Specialty section:
This article was submitted to Cryospheric Sciences, a section of the journal Frontiers in Earth Science

Received: *27 July 2018*
Accepted: *04 February 2019*
Published: *22 February 2019*

Citation:
König M, Hieronymi M and Oppelt N (2019) Application of Sentinel-2 MSI in Arctic Research: Evaluating the Performance of Atmospheric Correction Approaches Over Arctic Sea Ice. Front. Earth Sci. 7:22. doi: 10.3389/feart.2019.00022

INTRODUCTION

The limited accessibility of Arctic sea ice makes satellite remote sensing an important tool for synoptic observations in this region. The retrieval of parameters, such as the spectral albedo of sea ice or snow and properties of melt ponds and leads, relies on spectral information; the retrieval of optical properties of target surfaces and waterbodies therefore is necessary. Optical sensors

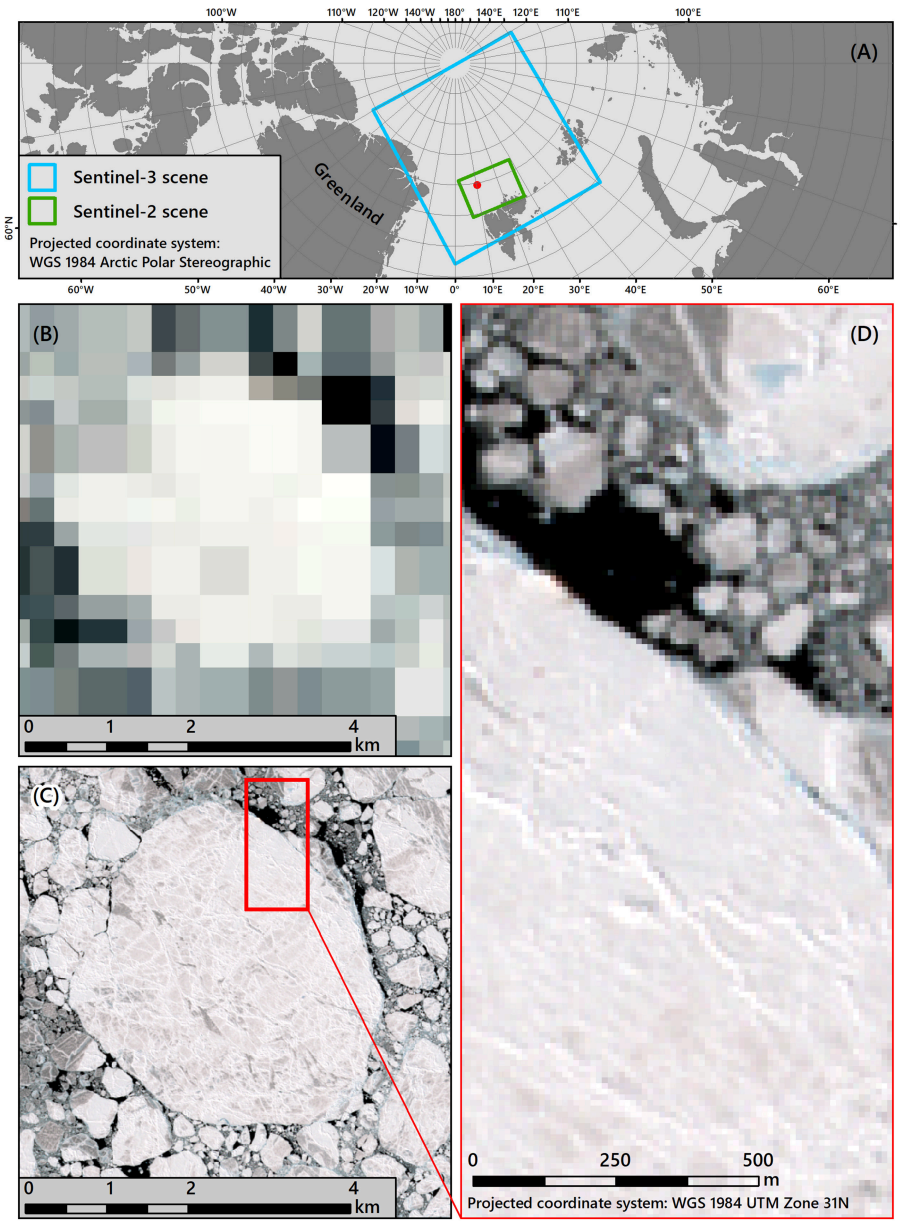

FIGURE 1 | Comparison of Sentinel-2A (S-2A) and−3A (S-3A) spatial coverage and resolution [contains modified Copernicus Sentinel data (2017) processed by ESA/EOM]. **(A)** Coverage of S-3A/OLCI and S-2A/MSI scenes, the red dot indicates the location of **(B)**. **(B)** Ice floe acquired with S-3A/OLCI (300 m, RGB: 665, 560, and 490 nm) at 2017-06-10 14:00:15 UTC. **(C)** The same floe acquired with S-2A (10 m, RGB: 665, 560, and 490 nm) at 2017-06-10 14:58:01 UTC. **(D)** S-2A details.

such as the Advanced Visible High Resolution Radiometer (AVHRR; e.g., Huck et al. (2007)) and the MODerate Resolution Imaging Spectroradiometer (MODIS; e.g., Rösel et al. (2012), Tschudi et al. (2008)) have long been used in Arctic research (Pope et al., 2014; Nasonova et al., 2017) providing observations of different parameters such as sea ice extent, sea ice thickness and albedo. The Sentinel-3 satellites (S-3) from the European Space Agency's (ESA) Copernicus program, carrying the Ocean and Land Color Instrument (OLCI), continue this tradition (Donlon et al., 2012; Malenovský et al., 2012). Recently, Istomina and Heygster (2017) published a retrieval algorithm for sea ice albedo and melt pond fraction from S-3/OLCI observations. Despite a high temporal and spatial coverage of the abovementioned sensors (swath widths: AVHRR = 2,900 km, MODIS = 2,330 km, S-3/OLCI = 1,270 km), their coarse spatial resolution (AVHRR: 1.1–4 km, MODIS: 250–1,000 m, S-3/OLCI: 300 m) impedes detailed observations of sea ice features such as melt ponds and ridges, which exist at spatial scales of meters to tens of meters (**Figure 1**). Studies based on optical sensors with a higher spatial resolution (≤30 m),

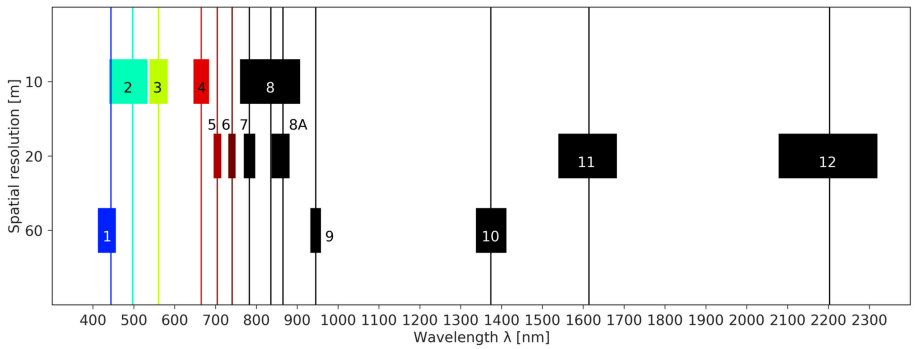

FIGURE 2 | S-2A MSI band widths, central wavelengths and spatial resolutions.

however, are rare. Markus et al. (2002) demonstrated the potential of Landsat 7 ETM+ (L-7; 30 m) for the classification of summertime sea ice surface conditions and retrieved the spatial distribution of ponded/unponded ice and open water (Markus et al., 2003), while Landy et al. (2014) used this sensor to observe sea ice development. Rösel (2013) underlined that high resolution satellite data enable determining melting features on Arctic sea ice and provide a basis for the comparison with coarse resolution satellite data. The ETM+ 8-bit sensor, however, showed saturation problems in the contrast-rich Arctic environment (Bindschadler et al., 2008; Rösel, 2013).

ESA's Sentinel-2 mission (S-2) offers new opportunities for optical sensors in the Landsat-like spatial domain. S-2 consists of the twin satellites S-2A and S-2B, launched in 2015 and 2017, respectively. Both satellites are equipped with the MultiSpectral Instrument (MSI), which provides 13 spectral bands with a 12-bit radiometric resolution in the wavelength region from 443 to 2,202 nm. Depending on the band, spatial resolution varies between 10, 20, and 60 m (European Space Agency, 2015, 2018a). **Figure 2** illustrates the spatial and spectral settings of S-2A. Compared to L-7, S-2 has a larger swath width (290 km) and geographical coverage reaches up to 83° north. The two S-2 satellites are shifted by 180° on the same orbit, which results in a return period of 5 days. In higher latitudes, overlapping swaths further increase the return period to up to one image per day (European Space Agency, 2015, 2018b; Copernicus EO Support, personal communication). Due to the terrestrial focus of the S-2 mission, geographical coverage in the Arctic Ocean is currently limited to areas around islands but areas of interest may be added to the Mission baseline "if sufficient resources are identified" (European Space Agency, 2015). Malenovský et al. (2012) mentioned the potential of S-2 for albedo retrieval, derivation of snow properties and mapping of polynyas and leads; nevertheless, they also highlighted the demand for "precise corrections for atmospheric propagation, topography and directional reflectance behavior" (Malenovský et al., 2012), pointing to the importance of atmospheric correction (AC) of optical remote sensing data. Zege et al. (2015) also emphasized the importance of AC for the retrieval of melt pond fraction and surface albedo.

Radiative transfer through the atmosphere is strongly influenced by Rayleigh and Mie scattering as well as aerosol and gas absorption. This combination is particularly challenging over water areas, where the atmospheric path radiance is typically >85% of the total signal in oceanic waters, >60% in sediment-rich waters, and >94% in very dark waters (IOCCG, 2010). Low sun-zenith angles (>70°) and correspondingly long atmospheric paths further aggravate the processing of data at the beginning and the end of summer in high latitudes (IOCCG, 2015). An adequate AC is therefore essential for the derivation of physical surface properties and follow-up multi-temporal analyses. Another challenge resulting from atmospheric transfer and the scattering of radiation is the neighboring or adjacency effect, i.e., the scattering of light from neighboring surfaces into the sensors field of view resulting in information overlay (Sterckx et al., 2015b). Adjacency effects depend on the brightness contrast between a target pixel and its neighborhood (Richter et al., 2006). The Arctic sea ice is a mix of snow, ice, melt ponds and ocean water, with typical broadband albedos in the visible wavelength region (VIS) ranging from >0.90 for fresh snow to <0.05–0.1 for ocean water (Perovich et al., 1998). Moreover, while being negligible for wavelength regions >1.5 µm, the adjacency effect increases with shorter wavelengths (Richter and Schläpfer, 2017), i.e., the wavelength region used for water remote sensing is heavily affected. Due to the characteristic spatial mixture and high contrasts of deep, clear ocean waters, melt ponds, bright ice and snow surfaces in the sea ice, we expect the adjacency effect to have a large impact on S-2 imagery of Arctic sea ice.

Several AC processors are available for S-2, and some papers already compared processors for lakes (e.g., Dörnhöfer et al., 2016; Martins et al., 2017). Only recently, Doxani et al. (2018) performed an inter-comparison of AC processors for different surface types in temperate and tropical zones. Yet, to our knowledge, no study exists for Arctic sea ice; therefore, the objective of this paper is to evaluate the performance of AC processors for S-2 over different surface types in the Arctic sea ice. For this, we processed S-2A data applying five AC processors (ACOLITE, ATCOR, iCOR, Polymer, and Sen2Cor) and evaluated the results using *in situ* data from open water and ice floe surface measurements acquired during an RV

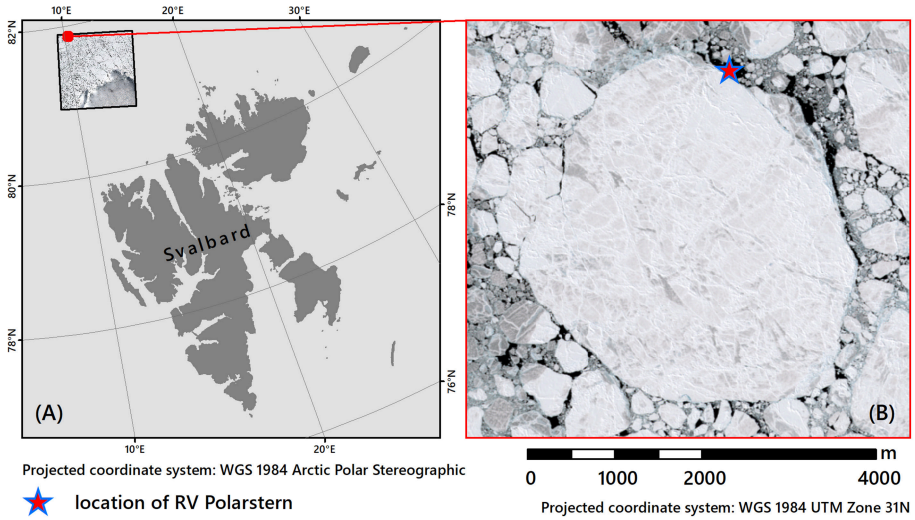

FIGURE 3 | Location of S-2 granule **(A)** and ice floe **(B)** in the Arctic Ocean on June 10, 2017.

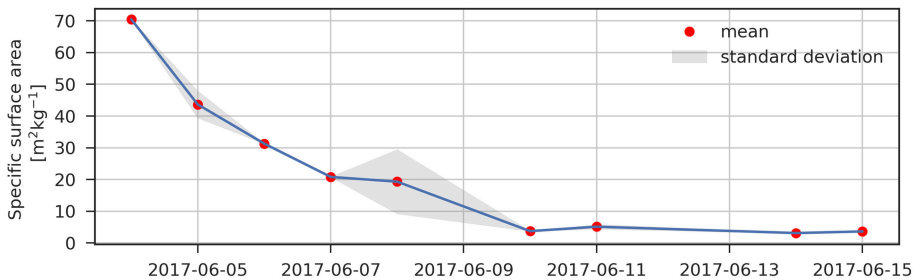

FIGURE 4 | Specific surface area of snow at different locations between 2017-06-04 and 2017-06-15.

Polarstern cruise in June 2017. We further investigate the influence of different AC processors on the retrieval of apparent optical properties, i.e., surface reflectance and remote sensing reflectance, which are used to retrieve parameters such as the spectral albedo or NDMI.

METHODS

Study Area

Cruise Overview

During cruise PS106.1 RV Polarstern was moored to an ice floe north of Svalbard between June 3 and 16, 2017 (**Figure 3**). At the beginning of the measurement period, snow and white ice covered most of the floe. Some few ponds had already formed at pressure ridges but we did not observe any pond formation on the flat parts of the floe; bare ice was exposed only very occasionally. Neither ponds nor bare ice were present near the measurement sites. Melting, however, started during the measurement period. The specific surface area of snow samples from the top 1–2 cm has been analyzed with an IceCube (A2 Photonic Sensors, France) at different locations in the area of interest. Snow melt results in a decrease of the snow's specific surface area. **Figure 4** illustrates that melt occurred between June 4 and 10.

Atmospheric Parameters

To provide input data for the different AC processors, we used sun photometer measurements conducted on board of RV Polarstern and published in the Maritime Aerosol Network (AERONET-MAN, Holben et al., 1998). For later analysis, we computed the aerosol optical thickness (AOT) at 550 nm from the sun photometer measurements as:

$$\beta = \frac{AOT_\lambda}{(\lambda/550)^{-\alpha}} \quad (1)$$

with β being turbidity, i.e., AOT at 550 nm, AOT_λ being the mean AOT at λ (500 nm) and α being the mean Angstrom exponent between 440 and 870 nm. We further used data from the weather station on board RV Polarstern (Schmithüsen, 2018). **Table 1** summarizes minimum, maximum, mean and standard deviation of the atmospheric parameters used to atmospherically correct the S-2 data acquired on June 10, 2017 (details on S-2 data are provided in section Sentinel-2 Data).

TABLE 1 | Atmospheric parameters.

Parameter	Unit	Min	Mean (± standard deviation)	Max	Data source
Aerosol optical thickness at 550 nm	[–]	0.0217	0.0231 (±0.0029)	0.0317	AERONET Microtops Level 2.0 data
Water vapor	cm	1.1066	1.1415 (±0.0226)	1.1881	AERONET Microtops Level 2.0 data
Visibility	km	∼60	65.00 (±2.2)	∼70	Weather station on board RV Polarstern

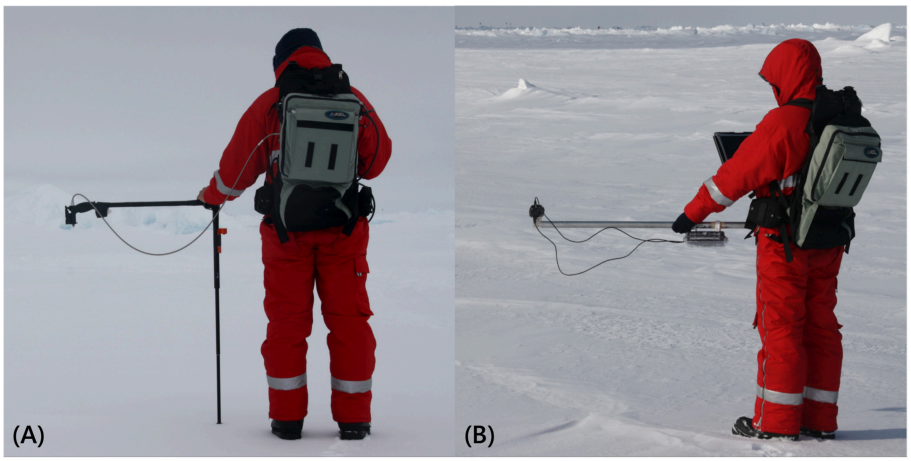

FIGURE 5 | Measurement setups for ASD **(A)** and Ocean Optics **(B)** spectrometers. Photos: Natascha Oppelt.

In Situ Data

To validate the results of the AC processors, we performed radiometric measurements of snow and ice covered areas (section Snow and Ice Measurements on the Floe) as well as open water (section Open-Water Measurements). Simultaneously to the radiometric open water measurements, we took water samples for water constituent analysis (section Water Sampling). All measurements have been localized with Global Positioning System (GPS) measurements (section Positioning of Sampling Points).

Radiometric Measurements

Snow and ice measurements on the floe

For spectral measurements on the floe, we used an ASD LabSpec5000 spectrometer (Analytical Spectral Devices Inc., United States), covering the wavelength region from 350 to 2,500 nm with a 1 nm spectral sampling rate. The ASD was equipped with an optical fiber with a 23° field of view (FOV) mounted to a pistol grip attached to a pole to avoid influences of the polar suits during the measurements (**Figure 5A**). We used a Labsphere Spectralon reflectance standard with 95% diffuse reflectance (Labsphere Inc., United States) as white reference. In addition, we used a set of Ocean Optics STS-VIS spectrometers (Ocean Optics Inc., United States). The setup consists of two synchronized spectrometers; one pointing downwards with a 1° FOV and the other, equipped with a diffusor, pointing upwards to track planar incoming radiation. Both instruments cover a wavelength region from 340 to 820 nm with a spectral sampling rate <1 nm. The spectrometers have also been attached to the end of a pole to avoid influences of the polar suits on the measurements (**Figure 5B**). For the Ocean Optics Instruments, we used a Labsphere Spectralon 99% diffuse reflectance standard (Labsphere Inc., United States) as white reference. For both instrument setups, we took reference measurements at intervals <10 min and when illumination conditions changed. Before conducting a white reference measurement with the ASD, we measured the Spectralon panel to control whether illumination has changed since the last reference measurement. If we detected changes, we performed a visual quality check on all measurements since the previous white reference and deleted spectra with unusual shapes. We corrected the Ocean Optics measurements for irradiance changes using the upwards pointing sensor. To account for the spatial heterogeneity within one S-2 pixel, we either walked around during the measurement process or performed measurements at different sites that we chose randomly. **Table 2** summarizes measurement dates, instruments and illumination conditions.

Open-water measurements

In open-sea water of a polynya, we conducted radiometric measurements from the deck of the vessel using three hyperspectral (380–950 nm) RAMSES sensors (TriOS GmbH, Germany). The sensors were arranged to measure downwelling irradiance (E_d), upwelling radiance just above the water surface (L_u; sensor viewing angle of 40° with 90° azimuth angle to the sun), and corresponding sky radiance (L_{sky}). We

TABLE 2 | Illumination conditions and instruments used.

Date	Instrument(s) used	Illumination conditions
2017-06-05	ASD	Diffuse, solar disk invisible
2017-06-07	ASD, OO	Variable
2017-06-09	OO	Diffuse, solar disk invisible
2017-06-10	RAMSES	Clear sky
2017-06-15	ASD, OO	Diffuse, solar disk visible

ASD, Analytical Spectral Devices spectrometer; OO, Ocean Optics spectrometer.

calculated remote sensing reflectance, R_{rs}, according to the following equation:

$$R_{rs}\left(40^\circ,\ 90^\circ\right) = \frac{L_u\left(40^\circ,\ 90^\circ\right) - \rho\, L_{sky}\left(40^\circ,\ 90^\circ\right)}{E_d} \quad (2)$$

The sea surface reflectance factor, ρ, depends on the sun-viewing geometry and wind-dependent roughness of the surface. Wind was light to moderate, but the limited fetch reduced roughness (mean square slope of the waves) compared to open sea. We applied the usually recommended surface reflactance factor of Mobley (1999) to determine the mean reflectance, in this case $\rho = 0.0272$. Moreover, we applied four different surface reflectance factors between 0.0176 and 0.03 (Mobley, 2015; Hieronymi, 2016) to account for potential effects of reduced roughness and polarization. This methodical variability together with temporal changes of the single measurements were taken into account to determine the standard deviation of the *in situ* measurements.

We resampled all field spectra to S-2A bands using the spectral response functions and central wavelengths (European Space Agency, 2018a,c).

Water Sampling

We took water samples from the polynya simultaneously to the radiometric measurements. Water samples were filtrated and optically analyzed in the ship's laboratory. We determined the spectral absorption properties using a PSICAM (Röttgers and Doerffer, 2007), a QFT-ICAM (Röttgers et al., 2016), and a Liquid Waveguide Capillary Cell (World Precision Instruments, United States). During the S-2A acquisition on June 10, the −1.7°C cold seawater had a salinity of ∼34 PSU. The particle concentration was very low, yielding a total particulate absorption coefficient at 440 nm, $a_p(440)$ of approximately 0.013 m^{-1}. The colored dissolved organic matter (*CDOM*) absorption at 440 nm, $a_{cdom}(440)$, was 0.038 m^{-1}. The spectral shape of the particulate absorption indicates only to the presence of organic phytoplankton particles and no sediments; there is no significant particulate and CDOM absorption in the near infrared (>700 nm). The chlorophyll-a concentration (*Chl-a*) from the photometric measurements was 0.19 (±0.1) mg m^{-3}; additional measurements with an AlgaeTorch (bbe Moldaenke GmbH, Germany) yielded *Chl* between 0.2 and 0.3 mg m^{-3}. These results confirm that the sampled water was very clear during the measurement period.

Positioning of Sampling Points

During the measurement period (**Table 2**) the ice floe drifted several tens of kilometers. To relocate all field measurements in a satellite image, we performed a drift-correction. Three stationary GPS devices constantly tracked floe movement in a 10-s interval. Additionally, we determined the locations of all sampling points with GPS measurements (F5521gw, Ericsson, Sweden; Galaxy S7, Samsung, South Korea; eTrex 10, Garmin, United States) in the World Geodetic System 1984 reference system. To locate all measurements from different dates and times in a single satellite image, we first applied a Savitzky-Golay filter to smooth the positioning data of each of the stationary GPS devices; then we used a second order polynomial to interpolate points in a 1-s interval. In this way, we could allocate every field measurement to three stationary GPS positions. Using this data, we computed the distances from every field measurement position to each of the three stationary GPS devices at the respective time of data acquisition ($t_{in\ situ}$). To find the measurement locations on the floe at the time of satellite overpass ($t_{satellite}$) we fit the distances to the three stationary GPS devices at $t_{satellite}$ to the distances computed at $t_{in\ situ}$ using the method of least squares. Finally, we performed a visual quality control.

Sentinel-2 Data

On June 10, 2017, clear sky conditions allowed acquisition of S-2A data of the floe at 14:58:01 UTC. For this study, we used the S-2 L1C top of atmosphere (TOA) reflectance product (processing baseline: 02.05; European Space Agency, 2015). For AC evaluation, we used S-2 bands which are in the spectral range of the field instruments, i.e. S-2A bands 2–7 (490–783 nm) for sea ice surfaces and bands 2–7 plus band 8A (490–865 nm) for the open water surface. All processors provide a 10 m output, except ATCOR. Which only offers a 20 m output. To provide spatially comparable results, we therefore downsampled 10 m output data to a spatial resolution of 20 m by 2 × 2 pixel block averaging.

Regions of Interest

In general, a point-by-pixel comparison is necessary for an accurate validation of remote sensing data via *in situ* measurements. With a steadily drifting floe, however, we are unable to assess precise accuracies of GPS measurements and trilateration; we therefore dismissed a point-based validation. Instead, we defined a region of interest (ROI) for each measurement Section by computing a circular buffer with a 20 m radius around all GPS points belonging to one measurement section. We defined all pixels intersecting the respective buffer area to be one ROI. **Table 3** lists the respective number of pixels and field spectra as well as the measurement device used for each ROI.

Regarding the RAMSES measurements, we manually defined one ROI in the open water area next to RV Polarstern and excluded pixels with unusual shape presumably influenced by floating ice. **Figure 6** illustrates locations of the respective ROIs.

Atmospheric Correction Processors

For our study, we selected common, publicly available AC algorithms. The level of user-controlled parametrization depends

TABLE 3 | Number of pixels, number of *in situ* spectra and measurement device.

ROI	Date	No. of spectra	No. of pixels	Device
05A	2017-06-05	411	12	ASD
05B	2017-06-05	686	15	ASD
05C	2017-06-05	346	16	ASD
07A	2017-06-07	177	18	ASD
07B	2017-06-07	400	32	OO
07C	2017-06-07	100	24	OO
09A	2017-06-09	150	20	OO
10A	2017-06-10	>1,000	15	RAMSES
15A	2017-06-15	330	20	ASD
15B	2017-06-15	60	9	ASD
15C	2017-06-15	60	17	ASD
15D	2017-06-15	180	27	OO

OO, Ocean Optics; ASD, Analytical Spectral Devices spectrometer for each ROI (Figure 3 shows the locations of ROIs).

on the respective processor and is described in the following. **Table 4** summarizes the most relevant parameters.

ACOLITE is developed at the Royal Belgian Institute of Natural Sciences and includes AC processors specifically designed for aquatic applications, e.g., it addresses diffuse sky reflectance at the water surface. We used the most recent version that applies a new dark spectrum fitting AC by default (Vanhellemont, submitted). The algorithm consists of five steps (Vanhellemont and Ruddick, 2018): (1) Correction of atmospheric gas transmittance and sky reflectance in the TOA signal; (2) Construction of a dark spectrum using the darkest pixels in each band; (3) Estimation of AOT at 550 nm for different aerosol models (continental, maritime) by linearly interpolating path reflectance from look up tables (LUTs) generated with the Second Simulation of a Satellite Signal in the Solar Spectrum–Vector (6SV) radiative transfer model (Vermote et al., 1997); (4) Retaining the band resulting in the lowest AOT for each aerosol model; (5) AC with band and model combination resulting in overall lowest AOT. This approach is presumably more appropriate for ice surfaces than the black short-wave infrared approach of previous versions (Vanhellemont and Ruddick, 2015). Information on precipitable water, atmospheric pressure and ozone concentration are obtained from ancillary data. Adjacency effects are to some extent addressed in the aerosol correction procedure, but are not entirely extinguished (Vanhellemont and Ruddick, 2018). We used the default parameterization but changed the WV default value to 1.14 cm according to the AERONET data. The output of ACOLITE may be images of different reflectances such as surface reflectance or R_{rs} with a 10 m spatial resolution, which was downsampled afterwards.

ATCOR (Atmospheric/Topographic Correction for Satellite Imagery; Richter and Schläpfer, 2017) uses pre-calculated LUTs computed with the Moderate-Resolution Atmospheric Radiance and Transmittance Model–version 5 (MODTRAN 5) (Berk et al., 2008) and image-based retrievals of atmospheric properties. The LUTs cover four aerosol models (rural, urban, maritime, and desert) and six water vapor column contents (0.4–5.0 cm). Varying ozone concentrations are addressed via an extra ozone database. The dense dark vegetation method is used to derive AOT and the aerosol type can be estimated by comparison of derived path radiance with MODTRAN standard aerosol types. WV is estimated using the Atmospheric Pre-corrected Differential Absorption algorithm. The resulting unit is "bottom of atmosphere" (BOA) reflectance (Richter and Schläpfer, 2017). The interface of ATCOR guides the user through the parametrization of the processor, which enables to address emerging problems. The small number of dark pixels in the image hampered an image-based retrieval of aerosol type and AOT. A WV map could be generated, but values near the vessel were high (∼1.8 cm) compared to the AERONET data. To parametrize the processor in accordance to the AERONET data, we therefore selected the pre-defined maritime aerosol type and a stable WV of 1.0 cm, which is the closest selectable default value, compared to the AERONET data. Visibility as a measure for AOT was set to 65 km. ATCOR considers adjacency effects as averaged reflectance of the neighborhood of a pixel (Richter and Schläpfer, 2017); its impact therefore depends on the difference in reflectance of a pixel and its neighborhood and decreases exponentially with increasing distance. Thus, for recurrent spatial patterns, adjacency effects remain similar at different spatial scales; consequently, the absolute range of the adjacency correction is uncritical. Therefore, we selected a typical range of 1 km (Richter and Schläpfer, 2017). The number of adjacency zones remained unchanged (1). We further applied a cirrus correction and selected the 20 m spatial resolution output.

In this study, we also used iCOR version 0.1 in ESA's Sentinel Application Platform (SNAP; v5.0). iCOR, previously known as OPERA (Sterckx et al., 2015a), is an AC processor for land and water as it accounts for the non-Lambertian reflectance of water surfaces. The iCOR workflow comprises four steps (De Keukelaere et al., 2018): (1) Classification of land/water pixels; (2) AOT retrieval over land following the approach in Guanter (2006), and extension to adjacent water pixels assuming a spatially homogeneous atmosphere; (3) adjacency correction; (4) AC using pre-calculated MODTRAN 5 LUTs based on a rural aerosol model (De Keukelaere et al., 2018). In the current iCOR SNAP version, WV is fixed to 2.0 cm. Over water the adjacency effect is corrected using the SIMilarity Environment Correction (SIMEC) approach (Sterckx et al., 2015b) while over land the user defines a fixed range (Sterckx et al., 2015a; VITO, 2017). We applied the adjacency correction and increased the default adjacency window for land surfaces to three pixels (tests with larger values introduced a reflectance peak at 705 nm). Further, we adjusted the default AOT value to 0.02 according to the AERONET data. Besides that, we used the default parameter setting. iCOR returns BOA reflectances in the native resolution of the respective band.

The polynomial-based atmospheric correction algorithm Polymer (Hygeos France; Steinmetz et al., 2011) is an AC processor for water bodies applicable to multiple sensors, including MSI and OLCI. Polymer is a spectral matching algorithm, which decouples the reflectance signal of the water body from atmospheric and water surface reflectance. It makes

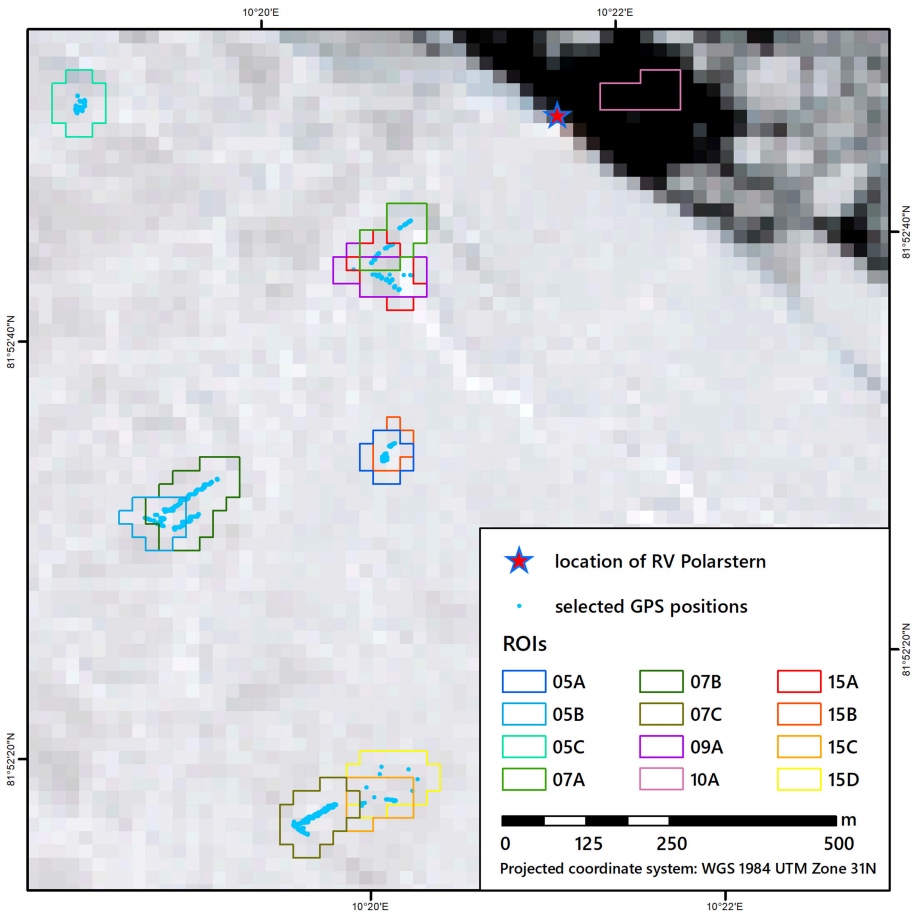

FIGURE 6 | ROI locations on the investigated floe. Background: S-2A stretched pseudo-true color RGB image (RGB: 665, 560, and 490 nm, spatial resolution: 20 m) acquired at 2017-06-10 14:58:01 UTC.

TABLE 4 | Parametrization of AC processors used in this study.

Processor	Version	References	LUT radiative transfer model	Applied aerosol model	AOT retrieval	WV retrieval	Adjacency correction
ACOLITE	20180419	(Vanhellemont, 2018; Vanhellemont and Ruddick, 2018)	6SV	Image based: continental	Dark spectrum fitting	Ancillary data	No
ATCOR-2	9.1.2	(Richter and Schläpfer, 2017)	MODTRAN 5	User-defined: maritime	User-defined visibility: 65 km	User defined: 1.0 cm	Yes
iCOR	0.1	(Sterckx et al., 2015a; VITO, 2017; De Keukelaere et al., 2018)	MODTRAN 5	Fixed: rural	Image-based	Fixed: 2.0 cm	Yes
Polymer	4.0	(Steinmetz et al., 2011)	Successive Order of Scattering	None (polynomial model for atmospheric path reflectance)	Iterative coupled ocean-atmosphere optimization scheme	No	Yes, through atmospheric correction
Sen2Cor	2.4.0.	(Müller-Wilm, 2016)	libRadtran	User-defined: maritime	Image-based	Image-based	Yes

use of the observation that the sum of atmospheric path reflectance and adjacency effects can be approximated by a polynomial consisting of three terms that address (1) non-spectral scattering or reflection, (2) fine aerosol scattering and (3) molecular scattering and adjacency effects, and does not require an aerosol model (IOCCG, 2015). One of the strengths of Polymer is the possibility to retrieve R_{rs} in presence of sun glint, which leads to a higher yield of evaluable pixels compared to other algorithms. Recently, the Polymer algorithm has been modified to improve results in high latitudes (Steinmetz and

Ramon, 2018). In the processing chain, non-water surfaces are masked, i.e., Polymer has only been applied to ROI 10A. For this study, the Polymer 10 m outputs were projected and resampled to the Sentinel-2 grid using the Nearest Neighbor approach, and spatially downsampled to 20 m resolution by 2 × 2 pixel block averaging.

Sen2Cor is the Sentinel-2 Level-2A Prototype processor for land surfaces. For this paper, we used the stand-alone version of Sen2Cor 2.4.0, which also allows for an image-based retrieval of atmospheric parameters. Water vapor is derived with the Atmospheric Pre-corrected Differential Absorption algorithm applied to S-2 bands 8A and 9. Sen2Cor estimates AOT by means of the dense dark vegetation method using the relation of the reflectance in bands 4, 2, and 12. The image-derived atmospheric parameters are then associated with pre-computed LUTs generated by a libRadtran based radiative transfer model. The LUTs include two atmospheric models (mid-latitude summer and winter), two aerosol types (maritime, rural), six or four different WV column values and six ozone concentrations (Müller-Wilm, 2016). We chose the maritime aerosol type and selected the mid-latitude winter model atmosphere as suggested in Harris Geospatial Solutions Inc (2018). We activated the variable visibility option and changed the default value to 65 km.

Performance Measures

We performed the spectral measurements on the floe within 5 days before and after the satellite acquisition. Illumination conditions therefore differed for field measurements and the satellite observation (see section Radiometric Measurements) which may affect measurement results (Malinka et al., 2016). Moreover, due to the different spectrometer setups described in section Snow and Ice Measurements on the Floe, ASD and Ocean Optics show varying sensitivities to changing illumination conditions. The different FOVs result in varying sensitivities to changing sensor-surface geometries. An inter-comparison of ASD and Ocean Optics under field conditions revealed mean differences in surface reflectance of about 0.1; a comparison of *in situ* spectra and BOA reflectances by means of classic performance metrics such as bias or root mean squared error therefore is unreasonable.

To identify systematic differences between the respective processors, i.e., the average tendency of the BOA reflectance to be larger or smaller than TOA reflectance, we computed the percentage bias (PBIAS) as

$$PBIAS = 100 \cdot \frac{\sum_{i=1}^{n} (R^{AC}(\lambda_i) - R^{TOA}(\lambda_i))}{\sum_{i=1}^{n} (R^{TOA}(\lambda_i))} \quad (3)$$

with R^{AC} and R^{TOA} being the bottom and top of atmosphere reflectance at band λ_i, respectively; n is the number of bands.

Compared to the absolute values, spectral shapes are more stable, especially at the beginning of the melt season and for the visible wavelength regions (Perovich, 1994). We therefore evaluated the spectral shapes of ice and snow measurements on the floe, computing the slope between two adjacent bands and then calculate the slopes' Mean Absolute Error (slope MAE):

$$slope\ MAE = \frac{1}{n} \sum_{i=1}^{n} \left| S^{AC}(\lambda_i, \lambda_{i+1}) - S^{in\ situ}(\lambda_i, \lambda_{i+1}) \right| \quad (4)$$

with $S^{AC}(\lambda_i, \lambda_{i+1})$ being the slope of the BOA reflectance outputs of the respective AC processor and $S^{in\ situ}(\lambda_i, \lambda_{i+1})$ being the slope of the resampled *in situ* reflectance between band λ_i and band λ_{i+1}, respectively; n is the number of band pairs. We further calculated the coefficient of determination (r^2) as the square of Pearson's correlation coefficient to evaluate linear correlations between the respective AC BOA output and the *in situ* measurement:

$$r^2 = \left(\frac{\sum_{i=1}^{n} \left(R^{in\ situ}(\lambda_i) - \overline{R^{in\ situ}} \right) \cdot \left(R^{AC}(\lambda_i) - \overline{R^{AC}} \right)}{\sqrt{\sum_{i=1}^{n} \left(R^{in\ situ}(\lambda_i) - \overline{R^{in\ situ}} \right)^2} \cdot \sqrt{\sum_{i=1}^{n} \left(R^{AC}(\lambda_i) - \overline{R^{AC}} \right)^2}} \right)^2 \quad (5)$$

with R^{AC} being the output of the respective AC processor and $R^{in\ situ}$ being the reflectance of the resampled *in situ* spectrum at band λ_i (band 2–7); n is the number of bands.

For deep polynya water, we performed measurements of R_{rs} from the deck of the vessel parallel to the satellite overpass under clear-sky conditions. No white referencing was necessary due to the measurement setup, which already integrates changes in illumination conditions. We therefore compared resulting reflectance intensities. ACOLITE calculates R_{rs}, while ATCOR, iCOR, SEN2COR and Polymer yield surface reflectances. The surface reflectances were transformed into R_{rs} following (Mobley et al., 2018):

$$R_{rs} = \frac{R^{AC}}{\pi} \quad (6)$$

with R^{AC} being the surface reflectance output of the respective AC processor. We then computed MAE to account for differences in reflectance intensity according to:

$$MAE = \frac{1}{n} \sum_{i=1}^{n} \left| R_{rs}^{AC}(\lambda_i) - R_{rs}^{in\ situ}(\lambda_i) \right| \quad (7)$$

with R_{rs}^{AC} being Rrs of the respective AC processor and $R_{rs}^{in\ situ}$ being Rrs of the resampled *in situ* spectrum at band λ_i (band 2–8A); n is the number of bands. To evaluate correspondence in spectral shapes, we computed slope MAE and r^2, replacing surface reflectance with Rrs and expanding S-2A band selection by band 8A.

RESULTS

Due to the different measurement designs described above, we discuss the results for open water as well as snow and ice surfaces separately.

Snow and Ice Surfaces

Figures 7A,C,E illustrates the mean shape and intensity of S2-A TOA reflectances, BOA reflectances of the respective AC

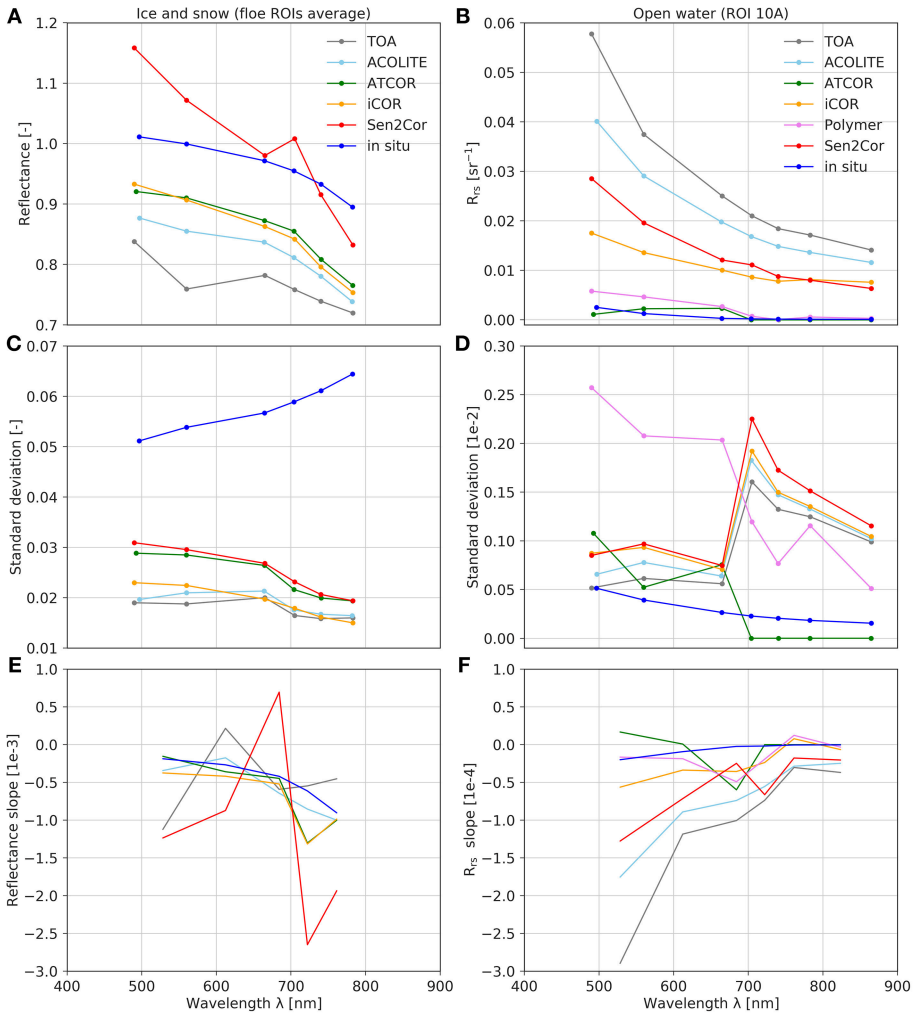

FIGURE 7 | Mean resampled *in situ* spectrum, S-2A TOA spectrum and BOA outputs of different AC processors for ice and snow ROIs **(A)**, respective standard deviations **(C)** and spectral slopes **(E)**. Mean resampled *in situ* spectrum, S-2A TOA and BOA R_{rs} outputs of different AC processors for the open water ROI 10A **(B)**, respective standard deviations **(D)** and spectral slopes **(F)**.

processors and resampled *in situ* spectra from snow and ice surfaces. Due to the low variance, we computed the mean spectra of all ROIs on the floe. *In situ* spectra show the typical shapes of snow and ice with maximum reflectances in the blue-green wavelength region and a decrease toward longer wavelengths. Maximum mean *in situ* reflectances at band 2 (490 nm) range from approximately 0.8–1.1 with high standard deviations presumably resulting from a high spatial variability on sub-pixel scale. Values are in line with field measurements from other studies (e.g., Perovich, 1998; Goyens et al., 2018). In comparison to the TOA spectrum, BOA spectra for all AC processors show increased reflectances over the entire spectrum. For each ROI, Sen2Cor produces the highest BOA reflectances, also indicated by high PBIAS values (**Table 5**). On average, Sen2Cor BOA reflectances are about 30 % higher than TOA reflectances. BOA reflectances of iCOR (mean PBIAS: 10.8%) and ATCOR (mean PBIAS: 11.7%) are generally lower than Sen2Cor values and resemble each other in intensity and shape. Yet, in comparison to iCOR, ATCOR BOA reflectances decrease slightly with shorter wavelengths. ACOLITE BOA reflectances are lowest for all ROIs and only 6.6% higher than TOA reflectances, on average. **Figure 7E** illustrates the slopes of the respective spectra showing largest differences for Sen2Cor (mean slope MAE: 1.17E-03); high slope MAE values in **Table 5** confirm this observation. For iCOR (mean slope MAE: 2.64E-04) and ATCOR (mean slope MAE: 2.29E-04), **Figure 7E** highlights differences in bands 2–4 and similarities in bands 5–7. Overall, ACOLITE fits the shape of the resampled *in situ* spectrum best, also indicated by low slope MAE values in **Table 5** (mean slope MAE: 1.92E-04). Coefficients of determination in **Table 5** confirm this trend and are highest for ACOLITE (mean r^2: 0.9758), followed by ATCOR (mean r^2: 0.9728) and iCOR (mean r^2: 0.9702), while Sen2Cor shows the weakest linear relationship (mean r^2: 0.9137), on average.

TABLE 5 | Performance measures of resampled mean *in situ* and BOA spectra for different ROIs on the ice floe.

ROI	AC Processor	PBIAS	r^2	Slope MAE
05A	ACOLITE	6.6	0.994026	1.41E-04
	ATCOR	12.2	0.988867	2.07E-04
	iCOR	11.0	0.981445	2.90E-04
	Sen2Cor	30.0	0.919942	1.20E-03
05B	ACOLITE	6.6	0.980658	1.90E-04
	ATCOR	11.5	0.986336	1.71E-04
	iCOR	9.3	0.987513	2.29E-04
	Sen2Cor	29.8	0.923357	1.17E-03
05C	ACOLITE	6.6	0.970177	1.61E-04
	ATCOR	12.2	0.977065	2.27E-04
	iCOR	12.5	0.982563	2.46E-04
	Sen2Cor	29.5	0.923	1.16E-03
07A	ACOLITE	6.6	0.981395	2.09E-04
	ATCOR	12.2	0.975791	2.74E-04
	iCOR	11.7	0.948195	3.71E-04
	Sen2Cor	29.6	0.893718	1.22E-03
07B	ACOLITE	6.6	0.986113	2.71E-04
	ATCOR	11.7	0.981915	3.16E-04
	iCOR	10.4	0.989948	3.70E-04
	Sen2Cor	29.9	0.938893	1.25E-03
07C	ACOLITE	6.6	0.877007	4.20E-04
	ATCOR	10.4	0.844808	4.55E-04
	iCOR	9.5	0.815684	4.98E-04
	Sen2Cor	29.9	0.758376	1.35E-03
09A	ACOLITE	6.6	0.99323	1.38E-04
	ATCOR	12.5	0.995584	1.45E-04
	iCOR	11.4	0.993827	1.35E-04
	Sen2Cor	29.8	0.94577	9.98E-04
15A	ACOLITE	6.6	0.990641	1.98E-04
	ATCOR	12.4	0.994046	2.41E-04
	iCOR	12.7	0.985452	2.95E-04
	Sen2Cor	29.8	0.938485	1.18E-03
15B	ACOLITE	6.6	0.985177	1.26E-04
	ATCOR	12.2	0.990944	1.64E-04
	iCOR	11.0	0.994962	1.62E-04
	Sen2Cor	30.0	0.943851	1.06E-03
15C	ACOLITE	6.6	0.988243	1.44E-04
	ATCOR	10.3	0.985885	1.49E-04
	iCOR	9.9	0.994527	1.74E-04
	Sen2Cor	29.8	0.927905	1.13E-03
15D	ACOLITE	6.6	0.987401	1.12E-04
	ATCOR	10.5	0.980002	1.69E-04
	iCOR	9.7	0.997854	1.39E-04
	Sen2Cor	29.8	0.937539	1.13E-03
Mean	ACOLITE	6.6	0.975824	1.92E-04
	ATCOR	11.7	0.972840	2.29E-04
	iCOR	10.8	0.970179	2.64E-04
	Sen2Cor	29.8	0.913712	1.17E-03

Open Water

Figures 7B,D,F illustrates the results for the open water measurements. It is obvious that ACOLITE and Sen2Cor

TABLE 6 | Performance measures of resampled mean *in situ* and R_{rs} spectra for respective AC processors in comparison with mean resampled *in situ* spectrum at ROI 10A.

AC Processor	MAE	r^2	Slope MAE
ACOLITE	0.0202	0.9613	6.88E-05
ATCOR	0.0007	0.1848	1.78E-05
iCOR	0.0098	0.9709	2.17E-05
Polymer	0.0015	0.8497	1.54E-05
Sen2Cor	0.0128	0.9657	4.90E-05

intensities are one order of magnitude higher than the *in situ* values, also demonstrated by high MAE values in **Table 6**. High coefficients of determination (r^2∼0.96), however, indicate a strong linear correlation between resampled *in situ* and R_{rs} spectra, although the spectral slope is different (slope MAE in **Table 6** and **Figure 7**). iCOR average R_{rs} is almost 10 times higher than average *in situ* data (MAE∼0.01), but spectral shape is more similar compared to ACOLITE and Sen2Cor indicated by a small slope MAE (2.17E-05) and high r^2 (∼0.97). Polymer retrieved R_{rs} are in the same order of magnitude as measured R_{rs}, illustrated by a small MAE of 0.0015, while ACOLITE, iCOR and Sen2Cor overestimate R_{rs}. The lowest slope MAE (1.54E-05) indicates that Polymer resembles the shape of the *in situ* spectrum most accurately. The comparably weak correlation (r^2∼0.85) results from a drop of the spectrum in bands 5–8A (**Figure 7B**). The ATCOR output is also in the correct order of magnitude over the full spectrum and has the smallest MAE and a comparable low slope MAE. It has to be noted, however, that the spectral shape in the visible range differs, also indicated by a weak linear correlation (r^2∼0.18). The slope MAE is higher than for Polymer, highlighting the difference in shape in visible bands 2 (490 nm) to 4 (665 nm).

Application Examples

To illustrate the consequences of different ACs on parameter retrieval, we computed the average BOA reflectance from band 2 to 7 (490–782 nm) as a rough approximation to broadband albedo (**Figure 8**). In addition, we calculated NDMI, which can be used as a proxy for melt pond fraction (Istomina and Heygster, 2017) according to

$$NDMI = \frac{\lambda_{Green} - \lambda_{NIR}}{\lambda_{Green} + \lambda_{NIR}} \quad (8)$$

where λ_{Green} is S-2 band 3 (560 nm) and λ_{NIR} is S-2 band 8A (865 nm) from the respective AC product. Theoretically, NDMI values range from −1 to +1. Due to the specific reflectance characteristics of the different sea ice surfaces in these wavelength regions the value range, however, is practically limited to values >0. Increasing values indicate an increasing melt pond fraction. **Figure 8** illustrates that the AC processor influences parameter retrieval and, in reverse, that the application rules the choice of AC processor. Note that median TOA reflectance of the floe surface is 0.75, and BOA reflectances are approximately 0.80 in the ACOLITE product and ∼0.84 in the ATCOR and

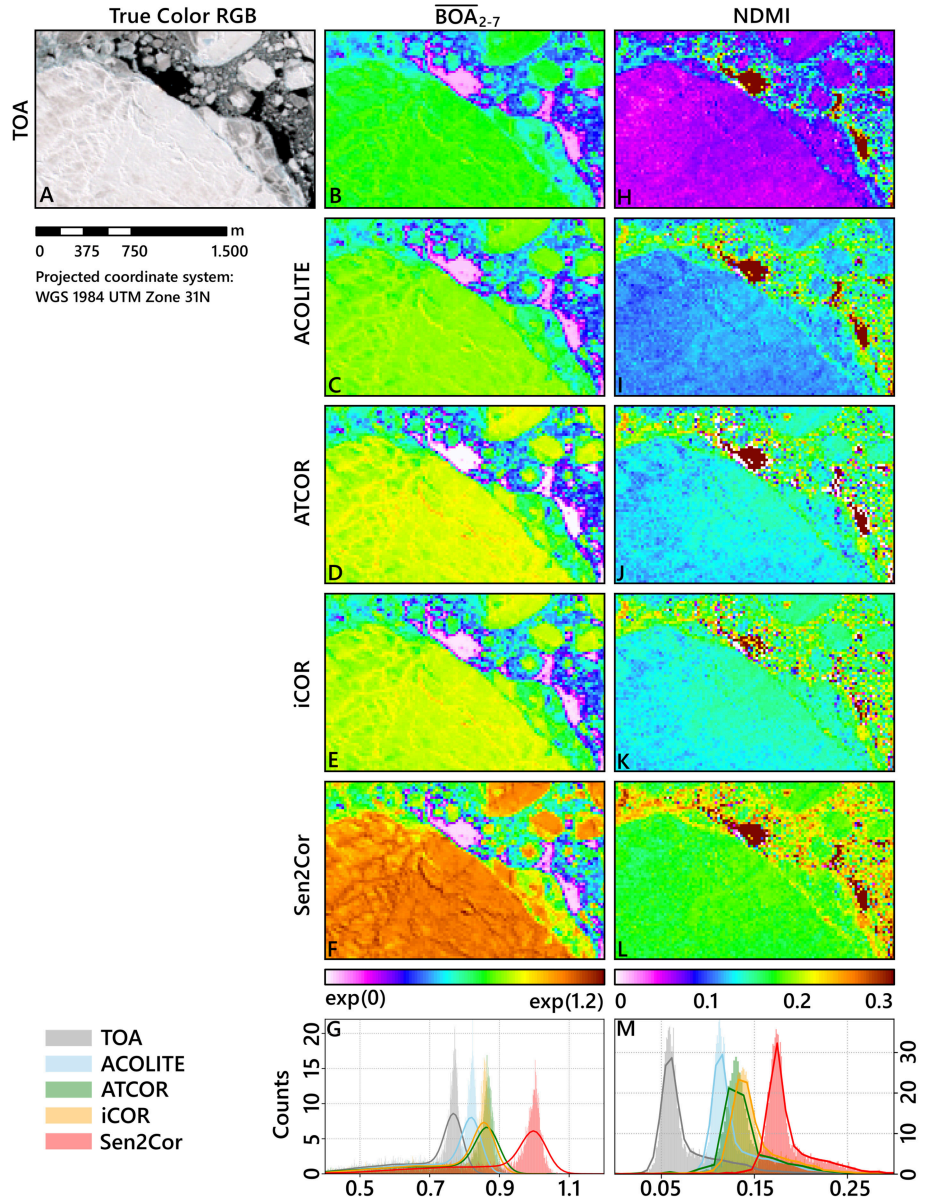

FIGURE 8 | True color RGB image **(A)**; band 2–7 average of TOA **(B)** and BOA **(C–F)**; NDMI results for TOA **(H)** and BOA **(I–L)**; and histograms of the respective parameters for the image subset **(G,M)**.

iCOR products, reaching 0.97 in the Sen2Cor product. In general, NDMI results show the same pattern, whereas median NDMI values are lowest for TOA (0.06), followed by ACOLITE (0.12), ATCOR (0.13), iCOR (0.14), and Sen2Cor (0.18). This corresponds to the spectral behavior illustrated in **Figure 7**.

DISCUSSION

Comparability of Field and Satellite Data

The comparison of field spectroscopy and satellite observations involves a number of difficulties, which particularly applies to remote regions such as the Arctic where ideal measurement opportunities and coincident satellite overpasses are rare. We conducted spectral measurements of the floe surface within a period of ±5 days of the satellite overpass under varying illumination conditions and possibly changing surface properties due to the onset of melt. We postulate, however, that an analysis of spectral shapes is reasonable as the anisotropic reflectance factor of snow at nadir is ∼1 (Perovich, 1994) and the shape of the spectral albedo is constant under different illumination angles (Malinka et al., 2016). For snow surfaces, Goyens et al. (2018) and Bourgeois et al. (2006) observed no significant relationship between variations in reflectance anisotropy with illumination conditions for sun zenith angles <65°. In addition,

the effect of melt on the spectral shape of nadir reflectance of snow and ice is comparably low in the VIS (Perovich, 1994, 1998). Nevertheless, we are unable to exclude potential differences in spectral slope due to melt processes. Besides the temporal differences, it is challenging to represent the spatial variability within a 20 m × 20 m area measured by S2-A via field measurements, even when measured at different locations. Moreover, a re-location of the measurement positions on a drifting floe in combination with spatial uncertainties of both GPS devices and satellite image positioning exacerbates a point-by-pixel comparison. For this reason, we included surrounding pixels into the analysis. However, this method is vulnerable to extreme spectral features in a ROI that can have a great impact on the average spectrum. The standard deviations of the ROIs located on the floe, however, are small indicating low spectral variability (**Figure 7C**); we therefore assume the ROI approach to be a valid method for evaluating the AC processors. ROI 10A over open water was defined manually and excluded pixel with unusual shape, presumably resulting from sub-pixel contamination due to floating ice. This pre-selection may substantially influence the outcome of the study, as pixel with expected shape are preselected. The pre-selection, however, avoids integration of extreme spectral features, which may have a major influence on the average spectrum due to sub-pixel contamination.

Quality of *In Situ* Data

For some ROIs, field spectrometer data show reflectances >1.0, although both field spectrometer setups were calibrated with reflectance standards. The Ocean Optics setup also enabled the correction of illumination changes. For ASD measurements, we surveyed changes in illumination by measuring the reflectance standards before each subsequent calibration. We manually deleted ASD measurements affected by illumination changes, i.e., spectra with unusual shape. Successive spectra with stable shape showing reflectances >1.0, however, remained in the dataset. In addition to the differences regarding sensitivity to changes in illumination, both setups vary regarding their FOVs. The smaller FOV of the Ocean Optics makes it more vulnerable to twisting of the pole and anisotropic effects due to ice surface topography. An inter-comparison of spectrometers in the field revealed that Ocean Optics reflectance values are ∼0.1 higher than ASD reflectances, on average, while the spectral shape was very similar. Warren (1982) stated that cloud cover affects both the spectral distribution of irradiance and the effective incident zenith angle, which causes an increase in all-wave snow albedo of up to 11%. Painter and Dozier (2004) attributed reflectances >1.0 to anisotropic effects of snow, which depend on the sun zenith angle, the grain size and the viewing geometry. Anisotropic effects may also have influenced the measurements described by Goyens et al. (2018) and Perovich (1998), who report reflectances >1.0 at approximately 400 nm measured under clear sky conditions. Peltoniemi et al. (2005) included snow wetness as an additional parameter influencing the spectral albedo and anisotropic behavior of snow and ice surfaces. As we evaluate the spectra only regarding to their shape, however, results remain unaffected by values >1.0. Analysis of water samples in the deep-water polynia show no significant absorption or scattering of the water constituents in the near infrared spectral range (>700 nm). Accordingly, beyond the visible range, measured R_{rs} is smaller than 1.5×10^{-4}, i.e., near zero (black) in the near infrared. Measurements influenced by ice floating into the FOV of the RAMSES spectrometer were excluded from the evaluation. The AERONET AOT values (∼0.02) are within the range reported for typical Arctic background aerosol concentrations, with values between 0.02 and 0.08 (Tomasi et al., 2012; IOCCG, 2015).

AC Processors

Differences between BOA or R_{rs} products may originate from the different processors, the integrated LUTs, different parameterization and image-based parameter retrieval regarding WV content, aerosol type and AOT, or different adjacency correction schemes, and the interplay of these components. Varying options for the user to modify the parameterization further complicate a direct comparison. Moreover, some of the processors are still under development and not yet entirely documented which hinders a detailed reasoning.

The LUTs applied in the AC processors have been generated with different radiative transfer models (MODTRAN 5, 6SV, libRadtran, and Successive Order of Scattering). These models differ regarding the implementation of physical equations, approximation of the radiative transfer equation and subroutines which can result in differences (e.g., Callieco and Dell'Acqua, 2011). Evaluating the impact of a certain radiative transfer model on AC, however, is beyond the scope of this study. The aerosol models covered by the pre-calculated LUTs cover common aerosol types. The options, however, differ between the AC processors (section Atmospheric Correction Processors). It is questionable how well these models represent Arctic aerosol components, e.g., mineral dust, sulfate aerosols and sea salt (at Barrow, Alaska; Tomasi et al., 2012; IOCCG, 2015). In late spring and summer, a phenomenon known as Arctic Haze results from anthropogenic aerosol accumulation in winter is common and occasionally aerosols from forest fires or volcanic eruptions are observed (IOCCG, 2015). To analyze the impact of the aerosol model we conducted a sensitivity analysis with different aerosol models in ATCOR. For the desert, maritime and rural aerosol models, differences in the VIS bands for the bright snow and ice surfaces were ∼2%, while the urban aerosol model resulted in an increase of ∼5–10% reflectance.

ACOLITE is designed for aquatic applications; the main differences compared to other AC processors are the AOT retrieval by the dark spectrum fitting algorithm and the consideration of skyglint. Its performance over ice surfaces, however, is good regarding the shape of BOA reflectance spectra. For sea ice surfaces differences in surface reflectance due to skyglint correction are <0.02. No water vapor and ozone values could be obtained from ancillary data, which might due to the developmental state of the processor; thus, the default values were used for AC and it remains unclear if the retrieval of water vapor and ozone in the Arctic from ancillary data is possible. Given the applied parameterization, the dark spectrum fitting algorithm results in the application of a continental aerosol model and an

AOT of 0.0084 at 550 nm, i.e., comparably close to the measured value of 0.02 (AERONET-MAN reports uncertainties ≤0.02 per band; NASA Goddard Space Flight Center, 2017). We assume that the high R_{rs} values over water result from adjacency effects, which are not addressed by ACOLITE.

ATCOR performs well over ice surfaces while its performance over open water is poor as the spectral shapes of BOA and *in situ* data do not correspond. Due to the lack of dark pixels in the S2-A data set we defined AOT by visibility (65 km), illustrating that the dark vegetation method is unsuitable for AOT retrieval in this image. For WV, image-based retrieval resulted in an overestimation of WV (∼1.8 cm). We therefore defined a default value (1.0 cm) referring to the AERONET data. Few pixels (1.2–1.4%) of bands 5–9 show negative reflectance values at open water areas, which may be caused by underestimated visibility, the aerosol type or calibration issues. Application of haze removal was not possible due to the small amount of clear pixels (<4%). Increasing the visibility parameter (up to 120 km) only had negligible consequences for the snow and ice surfaces and did not improve the spectral shape of open water pixels. This corresponds to Huck et al. (2007) who found that increasing visibility in a 6S forward simulation for AVHRR only affects open water surfaces. Changing the WV content from 1.8 to 1.0 cm had a significant influence, especially in S-2 bands that cover WV absorption features, i.e., band 8 (842 nm), band 9 (940 nm), and also band 5 (705 nm). For simulated Sea-viewing Wide Field-of-view Sensor (SeaWiFS) like spectra at the edge between sea ice and open water, Bélanger et al. (2007) found contaminations due to the adjacency effect up to 24 km off the ice edge resulting in unreliable results in derived chlorophyll concentrations and optical properties of open ocean water. Bulgarelli and Zibordi (2018) found that for S-2/MSI adjacency effects caused by highly reflecting surfaces (e.g., snow) are theoretically detectable at least 20 km off the coast in mid-latitude coastal environments. In contrast to these simulations, the area of interest is characterized by a small-scale mixture of snow, ice, melt ponds and open water, where spatial patterns and average reflectance are similar on different spatial scales. To check whether this statement applies for sea ice, we tested different ranges (1, 3, 5, and 10 km) and results confirmed that the influence is negligible for the spectral shape of the snow surface and intensity of open water pixels.

iCOR addresses the requirements for aquatic and terrestrial surfaces including a correction of adjacency effects. iCOR was unable to assess AOT from the image as the retrieval algorithm relies on vegetation and soil pixels (De Keukelaere et al., 2018), questioning the suitability of this approach for the Arctic sea ice in the absence of *in situ* AOT values. Even though, the fixed WV column height of 2.0 cm showed good results over ice, iCOR's unknown sensitivity to WV aggravates AC processor inter-comparison. The good performance over water compared to ACOLITE and Sen2Cor is probably attributed to the correction of adjacency effects using the SIMEC algorithm. For the application of SIMEC, Sterckx et al. (2015b) point out that aerosol information (AOT and aerosol model) should be either estimated using a land-based aerosol retrieval or from sun photometer data. While we used AERONET data to set the default AOT, we could not parameterize the aerosol type. Further, SIMEC is based on the assumption that reflectance differences between water and surrounding surfaces are strongest in the NIR, which is true for vegetated surfaces but not for ice, where differences are strongest in the VIS. We found that iCOR is very sensitive to changes in AOT. Increasing AOT from 0.02 to 0.1 resulted in an overcorrection and, consequently, a decrease of the spectrum matching the *in situ* measurements very well (slope MAE ∼8.49E-06).

Polymer performs best over water and produces reasonable results even in the high contrast Arctic sea ice matching findings of Steinmetz and Ramon (2018). It is robust to adjacency effects because the atmospheric model fits any spectrally smooth non-water component (Steinmetz and Ramon, 2018).The manual definition of ROI 10A guaranteed that we only considered deep-water pixels, which may also be important for the good performance of Polymer. Nevertheless, we observe a high spectral variability in the VIS bands. Moreover, some negative values appear in the red-edge and NIR regions. Sub-pixel contamination due to floating ice should be corrected due to its spectrally-flat contribution to the reflectance signal.

Usually, Sen2Cor applies image-based retrievals to generate maps of AOT and WV. The lack of dark pixels in the S-2A image, however, prohibited an AOT retrieval based on the DDV method; thus, AOT was estimated from the provided visibility (65 km). Values for scene average WV and AOT at 550 nm are 1.51 cm and 0.132, respectively. Compared to the AERONET data, however, both values are very high. A further test with a fixed visibility of 120 km, corresponding to an AOT of ∼0.0780, as proposed by Pflug et al. (2016) as a good practice for clear air and low AOT over Antarctica, did not improve the results for BOA reflectance and R_{rs} significantly. The increased BOA reflectance in comparison to the other processors fit findings of Li et al. (2018) who report that surface reflectance derived with Sen2Cor is generally overestimated, in particular for bright pixels. The high values over water may be attributed to the lacking correction of skyglint and adjacency effects or the provided LUTs.

A general challenge in high latitudes is the low sun elevation throughout long periods of the year. Huck et al. (2007) found that the solar zenith angle has a major influence on the retrieved TOA reflectance of a nadir-viewing sensor. The low reflectance levels of water bodies further increase this effect, because atmospheric path length increases with decreasing sun elevation. Consequently, the amount of energy absorbed in the atmosphere increases while the amount that arrives at the Earth's surface decreases. At the same time, the amount of light that is specularly reflected at the water surface increases with decreasing sun elevation, while a lower amount is transmitted into the water body. As a consequence, the water body scatters less light toward the sensor (Hieronymi, 2013). Further, the influence of surface roughness on the transmission of light into the waterbody increases with sun zenith angle which challenge wind speed-dependent AC (Hieronymi, 2016). When the sun is close to the horizon, adjacent ice floes may also have a shading effect. The same applies for ice floes, where shadows of ridges increase with lower sun elevation and anisotropic effects increase for sun-zenith angles >65° (Bourgeois et al., 2006). Another issue regarding low sun elevation is the limitation of most

processors to sun zenith angles ≤70°. The reason is that the LUTs are generated with radiative transfer models that base on the assumption of a plane parallel atmosphere rather than an actual spherical-shell atmosphere (IOCCG, 2015). Since in our study the sun zenith angle is 62.5°, we assume that this effect is negligible.

Sentinel-2A Data

Typically, reflectance spectra of snow and ice (like *in situ* spectra) are characterized by a steady decrease from the blue domain toward longer wavelength regions. S-2A TOA spectra, however, show a steep decrease from band 2 to 3 (490 and 560 nm, respectively), followed by an increase from band 3 to 4 (560–665 nm; **Figure 7A**). A comparison of BOA reflectance spectra with typical spectra found in literature (e.g., Perovich, 1994, 1998) indicates that ACOLITE, ATCOR and iCOR produce realistic results. As described in section Comparability of Field and Satellite Data, however, melt processes may have caused reflectance changes between *in situ* and satellite data. Thus, the evaluation of BOA spectral shape is challenging. In general, however, BOA shapes of ACOLITE, ATCOR, and iCOR are similar to the shape of the *in situ* spectra, i.e., the differences in slope MAE and r^2 are small. The shapes of Sen2Cor BOA reflectances do not resemble the typical shapes of snow and ice spectra as they show a steep decrease from the blue wavelength region toward longer wavelengths, interrupted by a local peak in band 5 at 705 nm. Furthermore, Sen2Cor is the only processor that produces reflectance values >1.0. Nadir reflectances of snow and white ice may exceed 1.0 in the blue part of the electromagnetic spectrum (e.g., Perovich, 1994; Goyens et al., 2018) but Sen2Cor BOA reflectances exceed 1.0 even in bands 3 and 4 (560 and 665 nm, respectively). This may result from anisotropic effects due to snow parameters or floe topography and matches observations of Li et al. (2018) who found that Sen2Cor overestimates BOA reflectance; ACOLITE, ATCOR, and iCOR BOA reflectance values, however, are <1.0 in all bands.

Application Examples

As indicated in section Application Examples, the choice of AC processor influences parameter retrieval. The differences in BOA reflectance illustrated in **Figure 7** have a great impact on NDMI and surface albedo (**Figure 8**), which is roughly approximated here by the mean BOA reflectance of bands 2–7 (490–783 nm). The shifted peaks in the histograms refer to the offset-like behavior of the spectra from different AC processors illustrated in **Figure 7**. The example illustrates well that the application of a certain AC processor and resulting BOA reflectances affects the retrieval of geophysical parameters from S-2A imagery.

CONCLUSION

ESA's S-2 mission shows high potential to assist sea ice research. The high spatial resolution allows detailed observation of small-scale sea ice features such as ridges and melt ponds. Thus, S-2 can be used to bridge the spatial scale between *in situ* observations and very high spatial resolution imagery, e.g., from airborne sensors, to coarse resolution sensors such as Sentinel-3. Even though geographical coverage in the Arctic Ocean is currently limited to areas close to the shore, coverage may be extended on request (European Space Agency, 2015). The temporal scale may be bridged either by comparison of identical granules from multiple dates or by multiple images of the same floe. For all subsequent applications such as change detection and time series analysis, however, AC is a crucial step in the processing chain of S-2 data as it is a requirement for an accurate retrieval of geophysical parameters.

We applied five AC processors for S-2 (i.e., ACOLITE, ATCOR, iCOR, Polymer, and Sen2Cor) to a S-2A dataset acquired north of Svalbard on June 10, 2017 and analyzed the results for snow and ice surfaces as well as for deep-water areas. For this dataset, the ACOLITE dark spectrum fitting algorithm resembled the shape of the mean resampled *in situ* spectra of the floe surface in the wavelength region 490–783 nm most accurately, closely followed by ATCOR and iCOR. Considering potential influences of melt on the spectral slope, a conclusive assessment, however, is challenging as ACOLITE, ATCOR and iCOR resembled the typical shape of snow reflectance. Results of this study, however, indicate that the present version of Sen2Cor is unsuitable for applications in the Arctic sea ice.

Due to the field measurement setup, our study was incapable of evaluating AC quality in terms of absolute intensities. Hence, future validation measurements on sea ice are necessary. Field measurements of the water surface concurrent to the S-2A overpass allowed a direct comparison of *in situ* data and AC products. Coefficients of determination indicate a strong linear relationship between the mean resampled *in situ* spectrum and ACOLITE, iCOR, and Sen2Cor BOA reflectances, respectively; their spectral slope, however, differs and intensities are one order of magnitude higher. Regarding absolute intensities and slope MAE, Polymer produced the best results, while ATCOR performed poorly over open-water areas. At the time of the S-2A overpass, existing ponds were too small to be included in this study. Future investigations should therefore also address the applicability of AC processors on optically shallow melt pond water.

We further demonstrated the influence of different AC processors on the retrieval of geophysical parameters. Depending on the processor, medians of average reflectances and NDMI for an image subset range from 0.80 to 0.97, and 0.12 to 0.18, respectively. Medians of average reflectance and NDMI are 0.75 and 0.06, respectively. We expect the impact on models that rely on absolute intensities instead of ratios to be even higher. In our study, the retrieval of AOT was critical. The absence of surface types such as dense dark vegetation (which are relevant for image-based retrieval of atmospheric parameters such as AOT) turned out as a general issue for all processors. ATCOR, Sen2Cor, and iCOR failed to retrieve aerosol information from the image, AOT estimated by the new ACOLITE dark spectrum fitting algorithm, however, was in the margin of uncertainty of the AERONET data. Sensitivity analyses with ATCOR and Sen2Cor, however, indicate that AOT, i.e., visibility, is not a limiting

factor regarding bright ice surface BOA reflectance. Apparently, the influence of AOT on the spectral shape is negligible if some threshold ($\leq$65 km) is exceeded. Image-based retrieval of WV by ATCOR and Sen2Cor and sun photometer data also discorded. With lacking sun photometer data, information about total columnar WV and ozone for processor parameterization, we therefore recommend using predefined aerosol models over ice; nevertheless, we strongly underline the need for image-based retrievals for scenes only containing Arctic sea ice. We further encourage the implementation of an Arctic Background aerosol model (Tomasi et al., 2007) as done by Zege et al. (2015) into existing processors. Until then, the integration of ancillary data might improve BOA retrieval. Yet, further tests are necessary to estimate the quality and availability of ancillary data in the Arctic.

Our study showed that AOT has a large impact on optically deep water. Since Polymer is independent from AOT and aerosol type estimation and insensitive to adjacency effects, it shows a huge potential for the Arctic Ocean. Further field studies, however, should be carried out to explore its capabilities, e.g., for the detection of algae blooms; and extrapolation of the atmospheric signal to adjacent ice floes may also enable AC of ice and snow surfaces. Similarly to Bélanger et al. (2007) and Huck et al. (2007), a sensitivity analysis based on forward modeling of atmospheric transfer to generate S-2A like TOA signals from *in situ* measurements may also support the improvement of existing processors.

DATA AVAILABILITY

Reflectance measurements, positions and regions of interest are available at the PANGAEA data repository under doi.pangaea.de/10.1594/PANGAEA.898552.

AUTHOR CONTRIBUTIONS

MK, MH, and NO conceived and designed the study. MK wrote the paper and conducted image and data processing and analysis. MH processed RAMSES data, analyzed water samples and contributed the respective passages. All authors contributed equally in reviewing and finalizing the manuscript.

ACKNOWLEDGMENTS

We acknowledge the support of captain Wunderlich, the crew and the chief scientists Andreas Macke and Hauke Flores of RV Polarstern cruise AWI_PS106_00. We want to thank Peter Gege, Gerit Birnbaum and Niels Fuchs for their contributions to the field measurements. We are grateful to Marcel Nicolaus and the AWI Sea Ice Physics team for providing stationary GPS measurements on the floe and Rüdiger Röttgers from Helmholtz-Zentrum Geesthacht for helping with the analysis of optical water properties. We also thank François Steinmetz from HYGEOS for providing Polymer data, Quinten Vanhellemont from RBINS for his help with ACOLITE, Sindy Sterckx from VITO for her explanations regarding iCOR and Sebastian Riedel for his support regarding AOT data. We acknowledge the efforts of the AERONET-MAN and the colleagues from TROPOS for the sun photometer measurements and thank ESA for providing Sentinel-2 data. We further thank Marco Zanatta and the AC^3 project for providing IceCube data and three reviewers for their thorough examination and helpful comments. MH was partly funded by the EnMAP scientific preparation program (FKZ: 50EE1718). We acknowledge financial support by Land Schleswig-Holstein within the funding programme Open Access Publikationsfonds.

REFERENCES

Bélanger, S., Ehn, J. K., and Babin, M. (2007). Impact of sea ice on the retrieval of water-leaving reflectance, chlorophyll a concentration and inherent optical properties from satellite ocean color data. *Remote Sens. Environ.* 111, 51–68. doi: 10.1016/j.rse.2007.03.013

Berk, A., Anderson, G. P., Acharya, P. K., and Shettle, E. P. (2008). *MODTRAN 5.2.0.0 User's Manual*. Burlington, MA; Hanscom, MA: Spectral Sciences Inc.; Air Force Research Laboratory.

Bindschadler, R., Vornberger, P., Fleming, A., Fox, A., Mullins, J., Binnie, D., et al. (2008). The landsat image Mosaic of Antarctica. *Remote Sens. Environ.* 112, 4214–4226. doi: 10.1016/j.rse.2008.07.006

Bourgeois, C. S., Calanca, P., and Ohmura, A. (2006). A field study of the hemispherical directional reflectance factor and spectral albedo of dry snow. *J. Geophys. Res. Atmos.* 111, 1–13. doi: 10.1029/2006JD007296

Bulgarelli, B., and Zibordi, G. (2018). On the detectability of adjacency effects in ocean color remote sensing of mid-latitude coastal environments by SeaWiFS, MODIS-A, MERIS, OLCI, OLI and MSI. *Remote Sens. Environ.* 209, 423–438. doi: 10.1016/j.rse.2017.12.021

Callieco, F., and Dell'Acqua, F. (2011). A comparison between two radiative transfer models for atmospheric correction over a wide range of wavelengths. *Int. J. Remote Sens.* 32, 1357–1370. doi: 10.1080/01431160903547999

De Keukelaere, L., Sterckx, S., Adriaensen, S., Knaeps, E., Reusen, I., Giardino, C., et al. (2018). Atmospheric correction of Landsat-8/OLI and Sentinel-2/MSI data using iCOR algorithm: validation for coastal and inland waters. *Eur. J. Remote Sens.* 51, 525–542. doi: 10.1080/22797254.2018.1457937

Donlon, C., Berruti, B., Buongiorno, A., Ferreira, M. H., Féménias, P., Frerick, J., et al. (2012). The Global Monitoring for Environment and Security (GMES) Sentinel-3 mission. *Remote Sens. Environ.* 120, 37–57. doi: 10.1016/j.rse.2011.07.024

Dörnhöfer, K., Göritz, A., Gege, P., Pflug, B., and Oppelt, N. (2016). Water constituents and water depth retrieval from sentinel-2A—A first evaluation in an Oligotrophic Lake. *Remote Sens.* 8:941. doi: 10.3390/rs8110941

Doxani, G., Vermote, E., Roger, J., Gascon, F., Adriaensen, S., Frantz, D., et al. (2018). Atmospheric correction inter-comparison exercise. *Remote Sens.* 10, 1–18. doi: 10.3390/rs10020352

European Space Agency (2015). *Sentinel-2 User Handbook. 1–64*. Available online at: https://earth.esa.int/documents/247904/685211/Sentinel-2_User_Handbook

European Space Agency (2018a). *Resolution and Swath. Sentin. Online*. Available online at: https://sentinel.esa.int/web/sentinel/missions/sentinel-2/instrument-payload/resolution-and-swath (Accessed May 28, 2018).

European Space Agency (2018b). *Revisit and Coverage. Sentin. Online*. Available online at: https://sentinel.esa.int/web/sentinel/user-guides/sentinel-2-msi/revisit-coverage (Accessed Nov 1, 2018).

European Space Agency (2018c). *Sentinel-2 Spectral Response Functions (S2-SRF). Sentin. Online*. Available online at: https://earth.esa.int/web/sentinel/user-guides/sentinel-2-msi/document-library/-/asset_publisher/Wk0TKajiISaR/content/sentinel-2a-spectral-responses (Accessed May 3, 2018).

Goyens, C., Marty, S., Leymarie, E., Antoine, D., Babin, M., and Bélanger, S. (2018). High angular resolution measurements of the anisotropy of

reflectance of sea ice and snow. *Earth Sp. Sci.* 5, 30–47. doi: 10.1002/2017EA000332

Guanter, L. (2006). *New Algorithms for Atmospheric Correction and Retrieval of Biophysical Parameters in Earth Observation*. Application to ENVISAT/MERIS Data, Doctoral thesis, Universitat de Valéncia, Departament de Física de la Terra i Termodinàmica.

Harris Geospatial Solutions Inc (2018). *Fast Line-of-sight Atmospheric Analysis of Hypercubes (FLAASH)*. Available online at: https://www.harrisgeospatial.com/docs/FLAASH.html (Accessed May 3, 2018).

Hieronymi, M. (2013). Monte Carlo code for the study of the dynamic light field at the wavy atmosphere-ocean interface. *J. Eur. Opt. Soc. Rapid Publ.* 8:13039. doi: 10.2971/jeos.2013.13039

Hieronymi, M. (2016). Polarized reflectance and transmittance distribution functions of the ocean surface. *Opt. Express* 24:A1045. doi: 10.1364/OE.24.0A1045

Holben, B. N., Eck, T. F., Slutsker, I., Tanré, D., Buis, J. P., Setzer, A., et al. (1998). AERONET—A federated instrument network and data archive for aerosol characterization. *Remote Sens. Environ.* 66, 1–16. doi: 10.1016/S0034-4257(98)00031-5

Huck, P., Light, B., Eicken, H., and Haller, M. (2007). Mapping sediment-laden sea ice in the Arctic using AVHRR remote-sensing data: atmospheric correction and determination of reflectances as a function of ice type and sediment load. *Remote Sens. Environ.* 107, 484–495. doi: 10.1016/j.rse.2006.10.002

IOCCG (2010). *Atmospheric Correction for Remotely-Sensed Ocean-Colour Products*. Available online at: http://www.ioccg.org/reports/report10.pdf.

IOCCG (2015). *Ocean Colour Remote Sensing in Polar Seas*. eds M. Babin, K. Arrigo, S. Bélanger, and M.-H. Forget Dartmouth. Dartmouth, NS: IOCCG.

Istomina, L. and Heygster, G. (2017). *Retrieval Algorithm for Albedo and Melt Pond Fraction from Sentinel-3 Observations.* EU Project SPICES Deliverable D5.1. Available online at: https://www.h2020-spices.eu/publications/ (Accessed May 29, 2018).

Landy, J., Ehn, J., Shields, M., and Barber, D. (2014). Surface and melt pond evolution on landfast first-year sea ice in the Canadian Arctic Archipelago. *J. Geophys. Res. Ocean.* 119, 3054–3075. doi: 10.1002/2013JC009617

Li, Y., Chen, J., Ma, Q., Zhang, H. K., and Liu, J. (2018). Evaluation of sentinel-2A surface reflectance derived using Sen2Cor in North America. *IEEE J. Sel. Top. Appl. Earth Obs. Remote Sens.* 11, 1997–2021. doi: 10.1109/JSTARS.2018.2835823

Malenovský, Z., Rott, H., Cihlar, J., Schaepman, M. E., García-Santos, G., Fernandes, R., et al. (2012). Sentinels for science: potential of Sentinel-1,−2, and−3 missions for scientific observations of ocean, cryosphere, and land. *Remote Sens. Environ.* 120, 91–101. doi: 10.1016/j.rse.2011.09.026

Malinka, A., Zege, E., Heygster, G., and Istomina, L. (2016). Reflective properties of white sea ice and snow. *Cryosph* 10, 2541–2557. doi: 10.5194/tc-10-2541-2016

Markus, T., Cavalieri, D. J., and Ivanoff, A. (2002). The potential of using Landsat 7 ETM+ for the classification of sea-ice surface conditions during summer. *Ann. Glaciol.* 34, 415–419. doi: 10.3189/172756402781817536

Markus, T., Cavalieri, D. J., Tschudi, M. A., and Ivanoff, A. (2003). Comparison of aerial video and Landsat 7 data over ponded sea ice. *Remote Sens. Environ.* 86, 458–469. doi: 10.1016/S0034-4257(03)00124-X

Martins, V. S., Barbosa, C. C. F., de Carvalho, L. A. S., Jorge, D. S. F., Lobo, F., d. L., and de Moraes Novo, E. M. L. (2017). Assessment of atmospheric correction methods for sentinel-2 MSI images applied to Amazon floodplain lakes. *Remote Sens.* 9:322. doi: 10.3390/rs9040322

Mobley, C. D. (1999). Estimation of the remote-sensing reflectance from above-surface measurements. *Appl. Opt.* 38, 7442. doi: 10.1364/AO.38.007442

Mobley, C. D. (2015). Polarized reflectance and transmittance properties of windblown sea surfaces. *Appl. Opt.* 54, 4828. doi: 10.1364/AO.54.004828

Mobley, C. D., Boss, E., and Roesler, C. (2018). *Ocean Optics Web Book*. Available online at: http://www.oceanopticsbook.info/ (Accessed May 17, 2018).

Müller-Wilm, U. (2016). *Sentinel-2 MSI–Level-2A Prototype Processor Installation and User Manual*. Eur. Sp. Agency, (Special Publ. ESA SP 49, 1–51).

NASA Goddard Space Flight Center (2017). *AERONET MARITIME AEROSOL NETWORK*. Available online at: https://aeronet.gsfc.nasa.gov/new_web/maritime_aerosol_network.html (Accessed November 19, 2018).

Nasonova, S., Scharien, R., Haas, C., and Howell, S. (2017). Linking regional winter sea ice thickness and surface roughness to spring melt pond fraction on Landfast Arctic Sea Ice. *Remote Sens.* 10:37. doi: 10.3390/rs10010037

Painter, T. H., and Dozier, J. (2004). The effect of anisotropic reflectance on imaging spectroscopy of snow properties. *Remote Sens. Environ.* 89, 409–422. doi: 10.1016/j.rse.2003.09.007

Peltoniemi, J. I., Kaasalainen, S., Näränen, J., Matikainen, L., and Piironen, J. (2005). Measurement of directional and spectral signatures of light reflectance by snow. *IEEE Trans. Geosci. Remote Sens.* 43, 2294–2304. doi: 10.1109/TGRS.2005.855131

Perovich, D. K. (1994). Light reflection from sea ice during the onset of melt. *J. Geophys. Res.* 99, 3351–3359. doi: 10.1029/93JC03397

Perovich, D. K. (1998). Observations of the polarization of light reflected from sea ice. *J. Geophys. Res. Ocean.* 103, 5563–5575. doi: 10.1029/97JC01615

Perovich, D. K., Roesler, C. S., and Pegau, W. S. (1998). Variability in Arctic sea ice optical properties. *J. Geophys. Res. Ocean.* 103, 1193–1208. doi: 10.1029/97JC01614

Pflug, B., Bieniarz, J., Debaecker, V., Louis, J., and Müller-Wilms, U. (2016). "Some Experience Using SEN2COR," in *Geophysical Research Abstracts. EGU General Assembly 2016, 17–22. Apr. 2016*, (Vienna).

Pope, A., Rees, W. G., Fox, A. J., and Fleming, A. (2014). Open access data in polar and cryospheric remote sensing. *Remote Sens.* 6, 6183–6220. doi: 10.3390/rs6076183

Richter, R., Bachmann, M., Dorigo, W., and Müller, A. (2006). Influence of the adjacency effect on ground reflectance measurements. *IEEE Geosci. Remote Sens. Lett.* 3, 565–569. doi: 10.1109/LGRS.2006.882146

Richter, R., and Schläpfer, D. (2017). "Atmospheric/Topographic Correction for Satellite Imagery (ATCOR-2/3 User Guide)," in *ATCOR-2/3 User Guide, Version 9.1.2* (Wil), 1–71.

Rösel, A. (2013). Detection of *Melt Ponds on Arctic Sea Ice with Optical Satellite Data*. Berlin; Heidelberg: Springer Berlin Heidelberg.

Rösel, A., Kaleschke, L., and Birnbaum, G. (2012). Melt ponds on Arctic sea ice determined from MODIS satellite data using an artificial neural network. *Cryosphere* 6, 431–446. doi: 10.5194/tc-6-431-2012

Röttgers, R., and Doerffer, R. (2007). Measurements of optical absorption by chromophoric dissolved organic matter using a point-source integrating-cavity absorption meter. *Limnol. Oceanogr. Methods* 5, 126–135. doi: 10.4319/lom.2007.5.126

Röttgers, R., Doxaran, D., and Dupouy, C. (2016). Quantitative filter technique measurements of spectral light absorption by aquatic particles using a portable integrating cavity absorption meter (QFT-ICAM). *Opt. Express* 24:A1. doi: 10.1364/OE.24.0000A1

Schmithüsen, H. (2018). *Continuous meteorological surface measurement during POLARSTERN cruise PS106.1 (ARK-XXXI/1.1)*. Bremerhaven: Alfred Wegener Institute, Helmholtz Centre for Polar and Marine Research. doi: 10.1594/PANGAEA.886302

Steinmetz, F., Deschamps, P.-Y., and Ramon, D. (2011). Atmospheric correction in presence of sun glint: application to MERIS. *Opt. Express* 19:9783. doi: 10.1364/OE.19.009783

Steinmetz, F., and Ramon, D. (2018). "Sentinel-2 MSI and Sentinel-3 OLCI consistent ocean colour products using POLYMER," in *Proceedings 10778, Remote Sensing of the Open and Coastal Ocean and Inland Waters; 107780E* (Honolulu, HI).

Sterckx, S., Knaeps, E., Adriaensen, S., Reusen, I., De Keukelaere, L., and Hunter, P. (2015a). Opera : an atmospheric correction for land and water. *Proc. Sentin. Sci. Work.* 734, 3–6.

Sterckx, S., Knaeps, S., Kratzer, S., and Ruddick, K. (2015b). SIMilarity Environment Correction (SIMEC) applied to MERIS data over inland and coastal waters. *Remote Sens. Environ.* 157, 96–110. doi: 10.1016/j.rse.2014.06.017

Tomasi, C., Lupi, A., Mazzola, M., Stone, R. S., Dutton, E. G., Herber, A., et al. (2012). An update on polar aerosol optical properties using POLAR-AOD and other measurements performed during the International Polar Year. *Atmos. Environ.* 52, 29–47. doi: 10.1016/j.atmosenv.2012.02.055

Tomasi, C., Vitale, V., Lupi, A., Di Carmine, C., Campanelli, M., Herber, A., et al. (2007). Aerosols in polar regions: a historical overview based on optical depth and *in situ* observations. *J. Geophys. Res. Atmos.* 112, 1–28. doi: 10.1029/2007JD008432

Tschudi, M. A., Maslanik, J. A., and Perovich, D. K. (2008). Derivation of melt pond coverage on Arctic sea ice using MODIS observations. *Remote Sens. Environ.* 112, 2605–2614. doi: 10.1016/j.rse.2007.12.009

Vanhellemont, Q. (2018). *ACOLITE Python User Manual*. Brussels: RBINS.

Vanhellemont, Q., and Ruddick, K. (2015). Advantages of high quality SWIR bands for ocean colour processing: examples from Landsat-8. *Remote Sens. Environ.* 161, 89–106. doi: 10.1016/j.rse.2015.02.007

Vanhellemont, Q., and Ruddick, K. (2018). Atmospheric correction of metre-scale optical satellite data for inland and coastal water applications. *Remote Sens. Environ.* 216, 586–597. doi: 10.1016/j.rse.2018.07.015

Vermote, E. F., Tanré, D., Deuzé, J. L., Herman, M., and Morcrette, J.-J. (1997). Second simulation of the satellite signal in the solar spectrum, 6s: an overview. *IEEE Trans. Geosci. Remote Sens.* 35, 675–686. doi: 10.1109/36.581987

VITO (2017). *iCOR plugin for SNAP toolbox, SOFTWARE USER MANUAL, VERSION 1.0*. Mol: VITO.

Warren, S. G. (1982). Optical Properties of Snow. *Rev. Geophys. Sp. Phys.* 20, 67–89. doi: 10.1029/RG020i001p00067

Zege, E., Malinka, A., Katsev, I., Prikhach, A., Heygster, G., Istomina, L., et al. (2015). Algorithm to retrieve the melt pond fraction and the spectral albedo of Arctic summer ice from satellite optical data. *Remote Sens. Environ.* 163, 153–164. doi: 10.1016/j.rse.2015.03.012

Conflict of Interest Statement: The authors declare that the research was conducted in the absence of any commercial or financial relationships that could be construed as a potential conflict of interest.

frontiers in Earth Science

ORIGINAL RESEARCH
published: 13 December 2018
doi: 10.3389/feart.2018.00226

Spring Succession and Vertical Export of Diatoms and IP_{25} in a Seasonally Ice-Covered High Arctic Fjord

Audrey Limoges[1,2], Guillaume Massé[3], Kaarina Weckström[1,4], Michel Poulin[5], Marianne Ellegaard[6], Maija Heikkilä[4], Nicolas-Xavier Geilfus[7], Mikael K. Sejr[8], Søren Rysgaard[7,8] and Sofia Ribeiro[1]*

[1] Department of Glaciology and Climate, Geological Survey of Denmark and Greenland, Copenhagen, Denmark, [2] Department of Earth Sciences, University of New Brunswick, Fredericton, NB, Canada, [3] Department of Biology, TAKUVIK, CNRS and Université Laval, Quebec, QC, Canada, [4] Ecosystems and Environment Research Programme, Environmental Change Research Unit, University of Helsinki, Helsinki, Finland, [5] Research and Collections, Canadian Museum of Nature, Ottawa, ON, Canada, [6] Department of Plant and Environmental Sciences, University of Copenhagen, Copenhagen, Denmark, [7] Centre for Earth Observation Science, Department of Environment and Geography, University of Manitoba, Winnipeg, MB, Canada, [8] Arctic Research Centre, Aarhus University, Aarhus, Denmark

OPEN ACCESS

Edited by:
Hauke Flores, Helmholtz-Gemeinschaft Deutscher Forschungszentren (HZ), Germany

Reviewed by:
Katrin Schmidt, Plymouth University, United Kingdom
Gesine Mollenhauer, Alfred Wegener Institute, Germany

***Correspondence:**
Audrey Limoges
audrey.limoges@unb.ca

Specialty section:
This article was submitted to Cryospheric Sciences, a section of the journal Frontiers in Earth Science

Received: *29 June 2018*
Accepted: *26 November 2018*
Published: *13 December 2018*

Citation:
Limoges A, Massé G, Weckström K, Poulin M, Ellegaard M, Heikkilä M, Geilfus N-X, Sejr MK, Rysgaard S and Ribeiro S (2018) Spring Succession and Vertical Export of Diatoms and IP_{25} in a Seasonally Ice-Covered High Arctic Fjord. Front. Earth Sci. 6:226. doi: 10.3389/feart.2018.00226

The biomarker IP_{25} and fossil diatom assemblages preserved in seafloor sediments are commonly used as proxies for paleo Arctic sea-ice reconstructions, but how their production varies over the seasons and is exported to the sediment remains unclear. We analyzed IP_{25} concentrations and diatom assemblages from a 5-week consecutive series of sea-ice cores and compared the results with sediment trap and surface sediment samples collected at the same site in the Young Sound fjord, Northeast Greenland. Our aim was to investigate the dynamics of diatom colonization of the spring sea ice and the *in situ* production of IP_{25}. Additionally, selected diatom taxa observed in the sea-ice samples were isolated from in-ice assemblages and their lipid composition was analyzed via gas chromatography-mass spectrometry. We confirm that *Haslea spicula* (and not the closely related species *H. crucigeroides*) is an IP_{25}-producer. All three known IP_{25}-producing taxa (*Haslea spicula*, *H. kjellmanii*, and *Pleurosigma stuxbergii* var. *rhomboides*) were present in Young Sound sea-ice and the low IP_{25} concentrations measured in the sea-ice (0.44–0.72 pg mL^{-1}) were consistent with the low abundance of these source species (0.21–9.66 valves mL^{-1}). Total sympagic diatom production also remained very low (21–985 valves mL^{-1}), suggesting that the fjord's sea ice did not provide an optimal physical-chemical environment for diatoms to thrive. Temporal changes in the sympagic diatom community were also observed, with an early presence of the pelagic *Thalassiosira hyperborea* and subsequent dominance of pennate taxa, including *Nitzschia* and *Navicula* species, *Fossula arctica* and *Stauronella arctica*. The assemblages observed during and after the seasonal ice melt consisted primarily of *Fossula arctica*, *Fragilariopsis oceanica*, *Thalassiosira antarctica* var. *borealis* (resting spores), and *Chaetoceros* spp. (vegetative cells and resting spores). The seafloor sediment assemblages largely reflected the melt and post-melt planktic production and were dominated by the resting spores of the centric *Chaetoceros* spp. and *Thalassiosira*

antarctica var. *borealis*, and the pennate *Fragilariopsis oceanica*, *Fossula arctica*, and *Fragilariopsis reginae-jahniae*. This study documents that IP_{25} is produced in Young Sound, and that the weak fingerprint of sea ice in the sediment appears to be primarily due to the limited sea-ice diatom biomass.

Keywords: climate change, Arctic sea-ice, HBIs, diatoms, paleoenvironmental reconstructions, climate proxy, Northeast Greenland

INTRODUCTION

The reliable reconstruction of past sea-ice variability in polar regions is a key prerequisite for climate model development. Due to its effects on the Earth's radiative properties (e.g., Curry et al., 1995), ocean heat transport (e.g., Jahn and Holland, 2013; Tomas et al., 2016), and the stability of tidewater outlet glaciers (e.g., Bendtsen et al., 2017), the rapid sea-ice decline associated with current climate warming can contribute to further changes in the climate system (e.g., Serreze and Barry, 2011). Our ability to fully evaluate and comprehend these impacts is however impaired by the scarcity and short time span of monitoring data. This paucity of long-term information about the interactions between climate and sea ice has motivated the development of methods that are based on the study of tracers preserved in seafloor sediments. Thorough reviews of sea-ice proxies, including their strengths, and shortcoming are presented in Polyak et al. (2010) and de Vernal et al. (2013). Proxy records enable us to extend sea-ice data several millennia back in time and make it possible to define environmental variability at a (multi-) decadal resolution.

The bottom horizon of sea-ice, in particular the 1–3 cm above the ice-water interface (Brown et al., 2011), forms the habitat of diatom species that produce a fossilizable molecular biomarker, IP_{25} (Ice Proxy with 25 carbon atoms; Belt et al., 2007), and sedimentary IP_{25} quantifications have become a widely-applied approach to reconstruct past seasonal sea-ice conditions in the Northern Hemisphere (e.g., Massé et al., 2008; Andrews et al., 2009; Vare et al., 2009; Belt et al., 2010; Müller et al., 2012; Cabedo-Sanz and Belt, 2016). This mono-unsaturated highly branched isoprenoid (HBI) alkene is biosynthesized in the sea-ice matrix by a restricted number of common pan-Arctic diatoms belonging to the *Haslea* and *Pleurosigma* genera (Brown et al., 2014) and is deposited in underlying sediments when the ice melts, in spring, or summer. The source-specific nature and high preservation potential (see however Rontani et al., 2018) of this organic molecular compound makes it a useful biomarker for the reconstruction of past sea-ice conditions. Additionally, since the frustules of sympagic diatoms are generally weakly silicified and do not preserve well in the sediment, IP_{25} constitutes one of the rare direct lines of evidence for the past presence of annually formed sea ice. In fully marine settings, high levels of sedimentary IP_{25} content are generally reported to reflect long-lasting seasonal sea-ice, polynya, or marginal ice zone conditions, whereas the absence of IP_{25} can either indicate perennial sea-ice cover or open water (e.g., Belt and Müller, 2013). Downcore changes in the sedimentary IP_{25} concentrations from a given location are therefore typically interpreted to reflect temporal fluctuations in the sea-ice conditions.

However, recent studies have shown that the sedimentary concentrations of IP_{25} in coastal areas influenced by freshwater runoff are lower than expected, thus showing a mismatch with overlying sea-ice cover extent (Xiao et al., 2013; Hörner et al., 2016; Ribeiro et al., 2017; Limoges et al., 2018). Despite the growing number of IP_{25}-based sea-ice reconstructions, only a limited number of studies have, to date, investigated the ecophysiological and environmental parameters that determine IP_{25} production (e.g., Brown et al., 2011, 2014), raising concerns about the interpretation of IP_{25} as a quantitative indicator of sea-ice cover, and the possible limitations to its application in the Arctic (Belt and Müller, 2013).

Here, we present a two-step investigation based on (1) biomarker and diatom analyses of sea-ice cores, sediment trap, and seafloor sediment samples from the Young Sound, a high Artic fjord located in northeastern Greenland, and (2) targeted diatom culture experiments. The Greenland Ecosystem Monitoring (GEM) programme has carried out systematic measurements in the Young Sound–Tyrolerfjord system since 2003 (Rysgaard and Glud, 2007), providing a robust record of the variability in environmental conditions (e.g., irradiance, salinity) which can be reproduced in the laboratory. This approach provides valuable insight into (i) the IP_{25} production in spring sea-ice, (ii) temporal trends in spring diatom assemblage composition and abundance in the sea ice, (iii) vertical transfer of diatom valves and IP_{25} from ice to sediments, and (iv) production of HBIs by a selection of sympagic diatom species. This study aims to improve paleoenvironmental interpretations for the Arctic region based on diatom-derived proxies.

ENVIRONMENTAL SETTING

The Young Sound is located in northeastern Greenland (74°N — 20°W) (**Figure 1**) and, together with the Tyrolerfjord, forms a ca. 90 km long, and 2–7 km wide fjord system connected to the Greenland Sea. Along the eastern shelf of Greenland, the coastal waters are influenced by the East Greenland Current, which consists of Polar Surface Waters of low temperature (< 0°C), and salinity (<34.4‰), overlying relatively warmer (0–2°C), saline (>34‰), Atlantic waters (>150 m depth) (Boone et al., 2018). In the fjord system, however, a shallow sill of ca. 45 m depth located at the entrance to the fjord forms a natural topographic barrier that prevents the entrainment of more saline Atlantic waters.

The transmittance of light into the surface-waters is attenuated by sea ice and the overlying snow from ca. late-October to mid-July (**Figure 2**). In late July, any remaining sea ice is typically flushed out of the fjord. The duration of the ensuing open-water season has increased since 2000 and currently lasts

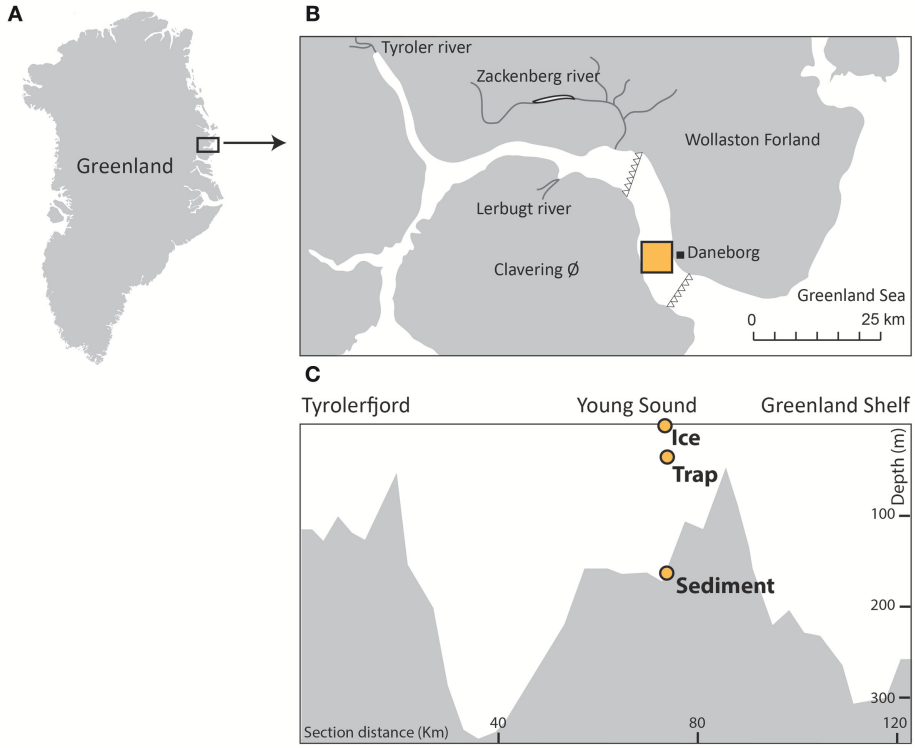

FIGURE 1 | (A) Location of the study area, in Northeast Greenland, **(B)** enlarged map of the Young-Sound-Tyrolerfjord system showing the main rivers and sampling site, and **(C)** bathymetry (m) from the inner to the outer fjord region and position of the sampling stations. The white triangles show the approximate position of the July sea-ice edge (modified from Ribeiro et al., 2017).

~3 months, until late October or early November. A continuous time series of temperature and salinity in the vicinity of our study location is presented in Boone et al. (2018) and underlines a stepwise freshening of the fjord's subsurface and deep waters from 2003 to 2015 (see also Sejr et al., 2017). The fjord's hydrography also experiences important seasonal variation in salinity, with values ranging from 17 to 33.4‰, and 32.25 to 32.50‰, respectively, in the summer, and winter of 2013–2014 (Boone et al., 2018). Both the seasonal sea-ice melt and river runoff (0.63–1.57 $km^3\ yr^{-1}$; Mernild et al., 2007) contribute to the formation of a shallow surface lens of fresher water (5–10 m; S<25‰) from the end of June to July (Rysgaard et al., 1999; Sejr et al., 2017). In August, the sediment discharge associated with the Tyroler, Lerbugt, and Zachenberg rivers creates turbid plumes that cause poor light conditions, especially in the inner part of the fjord (Kroon et al., 2017; Ribeiro et al., 2017) (see **Figure 1**). The Zachenberg river alone can discharge sediment loads of the order of 16.1–130 $\times\ 10^6$ kg yr^{-1} (Jensen et al., 2014).

Sea-ice algal productivity is very low and only represents <1% of the total annual pelagic primary production in the fjord (Rysgaard et al., 2001). Monitoring of the summer planktic protist communities across the Young Sound–Tyrolerfjord system from 2009 to 2012 revealed clear spatial and temporal heterogeneities in the assemblages, largely associated with the strong gradients in surface temperature, and salinity within the system (Krawczyk et al., 2015). Diatoms were generally the most important group within the assemblages and as such play a predominant role in the fjord's primary production.

MATERIALS AND METHODS

Sea-ice Core Samples

Multiple cores of landfast first-year ice were retrieved from the outer part of the Young Sound, near the Daneborg research station (74°18.979′N, 20°17.623′W) (**Figure 1**) over five consecutive weeks during Spring 2014, using a SIPRE corer of 7.6 cm diameter. Sea ice temperature was measured *in-situ*, immediately after extraction of the ice cores using a calibrated temperature probe (Testo 720, ±0.1°C precision) inserted into pre-drilled holes (2.5 cm intervals), perpendicular to core sides. Bulk sea-ice salinity was determined on melted sea-ice sections using a calibrated Thermo Scientific Orion portable salinometer WP-84TPS with a precision of ±0.1. Salinity is reported on the psu scale (practical salinity scale). *In-situ* temperature and salinity measurements for the bottom 10 cm of the ice cores are shown in **Figure 3**. In line with the progressive seasonal ice melt, core lengths decreased from 1.43 m in 26 May to 1.33 m in 23 June (**Table 1**, **Figure 3**). Concomitantly, snow cover thickness steadily declined from 61 to 14 cm over the same period (**Table 1**, **Figure 3**). The last core was collected ~1 month before the ice break-up. Ice

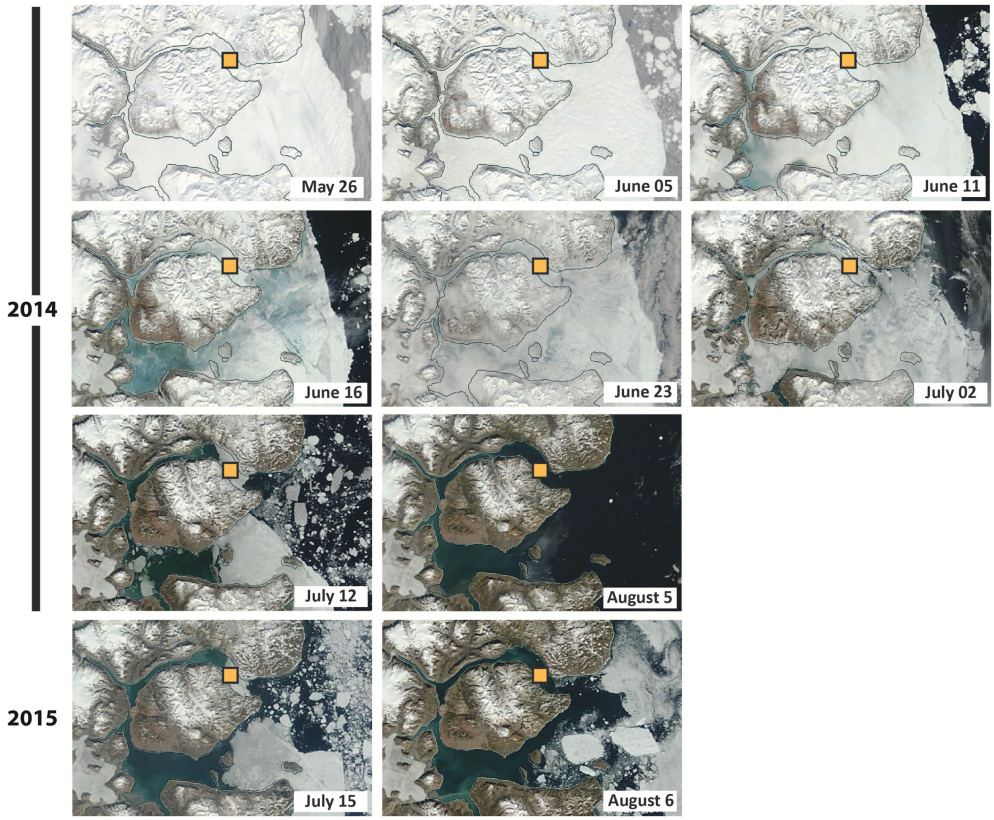

FIGURE 2 | Seasonal sea-ice conditions (based on MODIS imagery) for the years 2014 and 2015. The sampling area is indicated by the yellow square.

core samples were transported from Greenland and stored at −80°C, at the Arctic Research Center, in Aarhus University until processed.

The bottom 10 cm of the ice cores was melted in glass beakers and placed in a refrigerator at 4°C and in the dark for 24 h. When possible, replicates of the ice cores were pooled together (**Table 1**). In the samples reserved for taxonomic examinations, cells were allowed to settle onto the bottom of the beakers, and fixed with acidic Lugol's solution. For the IP_{25} analyses, melted samples were filtered through a Whatman GF/F 47 filter, and the filters frozen at −80°C.

Trap and Seafloor Sediments

A PPS4/3 sediment trap with automated year-round sampling was deployed at 37 m (74.322°N 20.269°W) at the GEM Program (**Figure 1C**). Prior to launching, the collector cups were filled with Whatman GF/F filtered seawater, mercuric chloride ($HgCl_2$), and adjusted to a salinity of 40 ‰ using a solution of sodium chloride (NaCl). The mean current velocity at the trap location is lower than 2 cm s^{-1} (Rysgaard et al., 2003), therefore permitting an efficient trapping of sinking particles. For preservation purposes, $HgCl_2$ was also added after sample recovery (see sampling manual MarineBasis program; Rysgaard et al., 2009). Samples were stored in a cool room (4°C) until analysis.

The time intervals of interest for this study covered by the sediment trap samples are as follows: (1) 24 April to 3 June 2014; (2) 1 July to 4 August 2014, and (3) 15 July to 4 August 2015. As such, the first sediment trap collected sinking particles before the ice melt, and the two others provide a comparison of the particles that were trapped during, and after the ice melt of both 2014 and 2015.

For comparison, we used the topmost (0–1 cm) interval of a sediment core collected in 2014 from 163 m water depth (Rumohr lot core number YS163_R1, collected at 74.3097°N, 20.3°W) (**Figure 1C**). The sediment was freeze-dried and kept at −80°C until further processing. The IP_{25} data from this site is given by Ribeiro et al. (2017, site YST2).

Culture Experiment

Individual diatoms were isolated from natural sea-ice samples (bottom 5 cm of sea-ice cores) collected from Churchill in Hudson Bay, Manitoba in 2005, and Allen Bay, near Resolute Bay, Nunavut in 2013. The sea-ice cores were drilled with a Kovacs Mark III corer of 9 cm diameter. The bottom 5 cm were sectioned using a stainless-steel surgical saw and placed in a cooler with 0.2 µm filtered seawater and stored in the dark below 4°C until the ice melted. Single cells were isolated under the microscope and placed in culture plates filled with Guillard F/2 enriched seawater. Plates were then stored in a cooled (0°C)

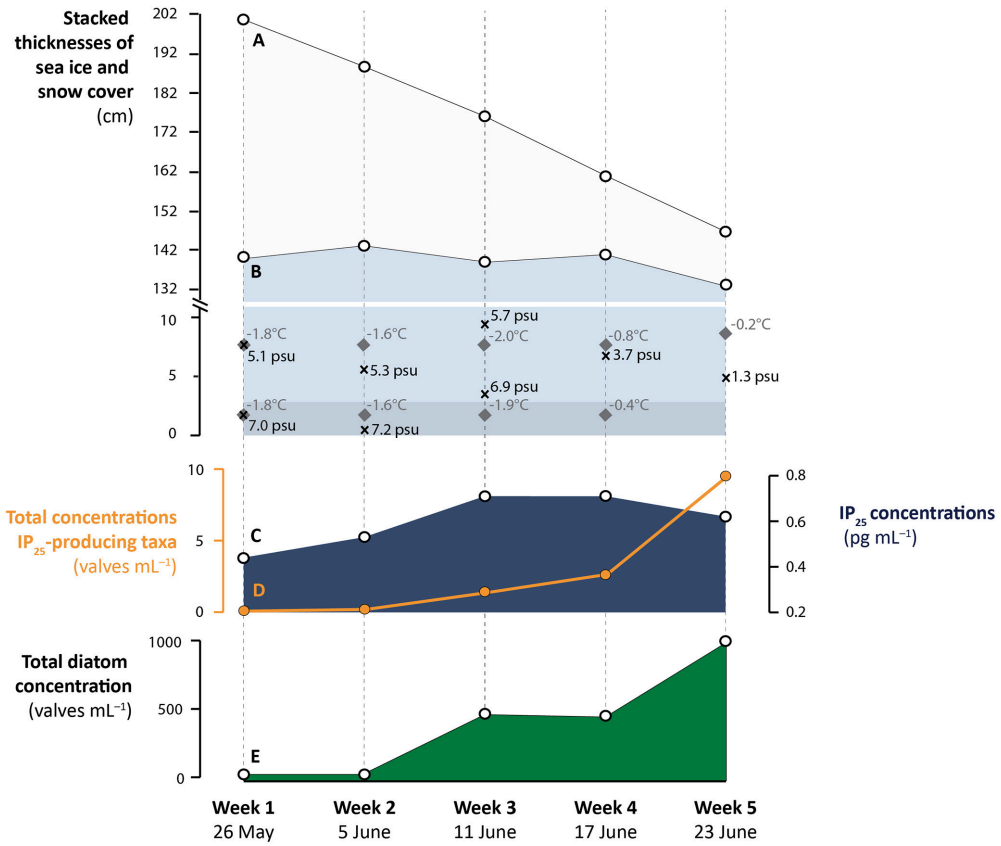

FIGURE 3 | Temporal changes of **(A)** snow cover thickness (cm), **(B)** sea-ice thickness (cm) and *in situ* measurements of salinity (psu; cross symbol) and temperature (°C; diamond symbol) for the bottom 10 cm of sea-ice cores: note the break and different scaling in the vertical axis. The shaded area at the bottom 3 cm of the ice corresponds to the habitat of IP_{25}-producing diatom species, according to Brown et al. (2011), **(C)** IP_{25} concentrations (pg mL^{-1}), **(D)** total concentrations of IP_{25}-producing taxa (valves mL^{-1}), and **(E)** total diatom concentrations (valves mL^{-1}), during the five consecutive weeks of sea-ice sampling in 2014.

plant culture chamber during several weeks until sufficient cells were obtained to transfer the culture into a 250 mL Erlenmeyer flask containing 125 mL of F/2 enriched seawater (salinity of 30‰). After some weeks, sufficient biomass was obtained to carry out both taxonomic identification and hydrocarbon analysis. Cells from each flask were then re-suspended using magnetic stirrers and a 50 mL aliquot filtered using GF/F filters. Filters were then inserted in an 8 mL glass vial and stored at −20°C until analysis. The lipid composition of the different species was determined following the method described in section Biomarker analysis. Results presented here refer specifically to the diatom taxa that were identified in the sea-ice samples from both Canada (Manitoba, Nunavut) and Greenland (Young Sound).

Diatom Identification and Quantification

Three endemic diatom species/species complexes responsible for the production of the lipid IP_{25} were identified by Brown et al. (2014): *Pleurosigma stuxbergii* var. *rhomboides*, *Haslea kjellmanii*, and *Haslea crucigeroides*, and/or *H. spicula*. Due to their morphological similarity, it was not possible during the experiment undertaken by Brown et al. (2014) to determine whether both *H. crucigeroides* and *H. spicula* produce IP_{25}. These two pennate diatoms both have lanceolate valves. The variation in valve width between *H. crucigeroides* and *H. spicula* is 13–17 µm and 7–10 µm, respectively. The shape of the distal parts of their valves is also different: *H. crucigeroides* has sub-rostrate beak-like ends, while *H. spicula* has acutely rounded or pointed ends. Furthermore, the number of transapical striae in 10 µm differs between the two species: *H. spicula* has 25–30 striae in 10 µm, while *H. crucigeroides* has ca. 20–24 striae in 10 µm (Hustedt, 1961; Snoeijs, 1993; Snoeijs and Vilbaste, 1994; Snoeijs and Potapova, 1995; Snoeijs and Kasperoviciene, 1996; Snoeijs and Balashova, 1998; Witkowski et al., 2000). The striation in *Haslea* is characterized by a transapical pattern crossed at right angle by a longitudinal pattern. Therefore, there are 18–22 transapical and 21–28 longitudinal striae in *H. crucigeroides*, and 25–30 transapical and >40 longitudinal striae in *H. spicula*. The literature reported only refers to light microscope observations; the range of striae above are from SEM examination of Arctic sea-ice samples (M. Poulin, personal observation). To resolve the morphological differences between *H. crucigeroides* and *H. spicula*, droplets of sea-ice samples were examined using a scanning electron microscope (SEM; Environmental SEM Quanta 200, FEI). Aliquots of the original

TABLE 1 | Sampling date, ice and snow thicknesses (cm), number of sea-ice core replicates and corresponding total volume filtered for IP_{25} measurements, number of sea-ice core replicates and corresponding initial volume used for diatom counts, and total concentrations of diatoms, IP_{25}-producing diatom taxa, *Haslea spicula*, *H. kjellmanii* and *Pleurosigma stuxbergii* var. *rhomboides* (valves mL^{-1} or valves g^{-1}) and IP_{25} concentration (pg mL^{-1} or ng g^{-1}) corresponding to the sea-ice, sediment trap and surface sediment samples.

	Sampling date	Ice thickness (cm)	Snow thickness (cm)	Number sea-ice replicates IP_{25}	Volume filtered for IP_{25} measurements (mL)	Number sea-ice replicates diatom counts	Initial volume samples for diatom counts (mL)	Total diatom concentration (valve mL^{-1})	Total concentration IP_{25}-producing taxa (valve mL^{-1})	Concentration *H. spicula* (valve mL^{-1})	Concentration *H. kjellmanii* (valve mL^{-1})	Concentration *P. stuxbergii* var. *rhomboides* (valve mL^{-1})	IP_{25} concentrations (pg mL^{-1})	
SI-W1	26 Mai 2014	140	61	2	1080	1	575	21	0.21	0.10	0.00	0.10	0.4 ± 0.2	Sea ice
SI-W2	5 June 2014	143	46	4	2375	2	500	26	0.33	0.33	0.00	0.00	0.5 ± 0.05	
SI-W3	11 June 2014	139	37.5	4	2475	2	600	459	1.49	0.00	1.49	0.00	0.7 ± 0.03	
SI-W4	17 June 2014	141	20	4	1615	2	550	441	2.78	2.78	0.00	0.00	0.7 ± 0.1	
SI-W5	23 June 2014	133	14	4	2430	2	630	985	9.66	9.66	0.00	0.00	0.6 ± 0.05	

	Sampling interval	Total concentration IP_{25}-producing taxa (valve g^{-1})	Concentration *H. spicula* (valve g^{-1})	Concentration *H. kjellmanii* (valve g^{-1})	Concentration *P. stuxbergii* var. *rhomboides* (valve g^{-1})	IP_{25} concentrations (ng g^{-1})	
TS1	24 April–3 June 2014	0	0	0	0	Not analyzed	Trap sediment
TS2	1 July–4 August 2014	0	0	0	0	Not analyzed	
TS3	15 July–4 August 2015	0	0	0	0	Not analyzed	

Site	Total concentration IP_{25}-producing taxa (valve g^{-1})	Concentration *H. spicula* (valve g^{-1})	Concentration *H. kjellmanii* (valve g^{-1})	Concentration *P. stuxbergii* var. *rhomboides* (valve g^{-1})	IP_{25} concentrations (ng g^{-1})	
YST2	0	0	0	0	20.69	S. Sediment

sea-ice samples were dehydrated through a graded series of ethanol and critical point dried. The samples were then mounted on aluminum stubs and coated with a gold/palladium mixture (instrument: FISONS, Polaron SC7640).

Species identification and cell counts were also carried out in light microscopy (Leica DMLB) at 1000× magnification. Sea-ice samples were prepared following the procedure described in Lundholm et al. (2002). Samples were oxidized using hydrogen peroxide (H_2O_2 30%) and a saturated aqueous solution of potassium permanganate ($KMnO_4$) in order to remove organic material. After 24 h, samples were cleared by addition of a saturated aqueous solution of oxalic acid ($COOH_2$) and then washed several times with distilled water. Total sea-ice diatom concentrations were determined by addition of sample aliquots to a Sedgewick-Rafter counting chamber.

Permanent diatom microscope slides were prepared from the trap and surface sediment samples, following standard methodologies (Battarbee et al., 2001). These are stored at the Geological Survey of Denmark and Greenland and available upon request. In brief, the sediment was treated with hydrogen peroxide (H_2O_2, 30%) and hydrochloric acid (HCl, 25%) in order to remove the organic material and carbonates, respectively. The test tubes in which samples were treated were subsequently filled with distilled water and left to settle for 12 h. Residues were then washed (and left to settle) several times using demineralized water. A few drops of the final suspension were allowed to dry on a cover slip and subsequently mounted in Naphrax™ for observation. Identification and quantification of diatom valves were performed in light microscopy (Leica DMLB) using phase contrast optics, at a 1000x magnification.

In order to assess the degree of similarity between the diatom assemblages from the sea-ice, sediment traps, and surface sediment samples, classical cluster analysis using an unweighted pair-group average (UPGMA) clustering algorithm and a Euclidean similarity index was carried out using the software PAST3.12 (Hammer et al., 2001).

Biomarker Analysis

Samples for IP_{25} analysis were processed following the protocol described by Belt et al. (2007). An internal standard (7-hexylnonadecane) was added to the melted ice sample and to ∼0.5 g of the freeze-dried and homogenized sediment samples before analytical treatment. For both sample types, total lipids were ultrasonically extracted (3 times) using a mixture of dichloromethane (DCM: CH_2Cl_2) and methanol (MeOH) (2:1, v/v). Extracts were pooled together, and the solvent was removed by evaporation under a slow stream of nitrogen. The total extract was subsequently suspended in hexane and purified through open column chromatography (SiO_2). HBIs were eluted using hexane (8 mL). Procedural blanks and standard sediments were analyzed every 15 samples.

Hydrocarbon fractions were analyzed using an Agilent 7890 gas chromatograph (GC) fitted with 30 m fused silica Agilent J&C GC columns (0.25 mm internal diameter and 0.25 μm phase thickness) and coupled to an Agilent 5975C Series mass selective detector. Oven temperatures were programmed as follows: 40–300°C at 10°C min^{-1}, followed by an isothermal interval at 300°C for 10 min. The data were collected using ChemStation and analyzed using MassHunter quantification software. IP_{25} was identified on the basis of retention time and comparison of mass spectra with authenticated standards. Abundances were obtained by comparison of individual GC-mass spectrometry responses against those of the internal standard and concentrations are reported in pg mL^{-1} and ng g^{-1} for the ice and sediment samples, respectively. Response factors of the internal standard vs. IP_{25} were determined prior and after each analytical sequence (every 15 samples). The extraction and analytical error on the measurements, determined from measurements of standard sediments is of ± 8%.

RESULTS

Culture Experiments

Thirteen of the diatom taxa observed in the sympagic assemblages from Young Sound were isolated from natural sea-ice samples. These included some of the taxa that typically dominate Arctic sea-ice assemblages (e.g., *Nitzschia frigida*; Poulin et al., 2011). The hydrocarbon composition of all 13 taxa was analyzed (**Table 2**). The IP_{25} compound was only identified in cultures of the diatom *H. spicula*. Analysis of their hydrocarbon fractions indicates that *H. crucigeroides* and *H. vitrea* do not produce IP_{25}, but C_{25} tri- and quadri-unsaturated HBI isomers (**Figure 4**). For all the other diatom taxa analyzed, neither IP_{25}, nor other HBI isomers were detected (**Table 2**).

Sea-ice Diatom Succession and IP_{25} Production

In total, 55 diatom taxa belonging to 24 genera were identified in the ice samples (**Supplementary Material**). Total sea-ice diatom concentrations increased from ca. 21 valves mL^{-1} on 26 May to 985 valves mL^{-1} on 23 June (see **Table 1**, **Figure 3**). The rate of increase was not constant and appeared to be driven in part by changes in sea-ice thickness during the sampling period. The low diatom concentration suggests that the initial stages of sympagic productivity were captured by the first ice samples. The subsequent increase in diatom cells was accompanied by marked changes in the community composition (**Figure 5**). From 26 May to 5 June, the sea-ice assemblages were dominated by centric taxa, notably *Thalassiosira hyperborea* (50% of the assemblage). Dominant taxa also included *Navicula* (17%) and *Nitszchia* (10%) species (see **Table 2** for complete species list). The relative contribution of the centric diatoms then decreased drastically from 11 June, when *Nitzschia frigida* reached a relative abundance of 76%. On 17 June, the assemblages were dominated by *Nitzschia frigida* (37%), *Navicula* spp. (32%), and *Fossula arctica* (10%). Finally, on 23 June, *Nitzschia* spp. was still abundant but the assemblages were largely dominated by *Stauronella arctica* (72%), which had only contributed to a small fraction of the previous assemblages. The highest number of species ($N = 41$) (see **Table 2**) was identified in the ice sample collected on 5 June (the second sampling week).

The presence of the three known IP_{25}-producing taxa (*Haslea spicula, H. kjellmanii,* and *Pleurosigma stuxbergii* var.

TABLE 2 | List of diatom taxa encountered in sea-ice, sediment trap and surface sediment samples from the Young Sound fjord.

	Samples Young Sound			Culture
	ICE	**TRAP**	**SED.**	**HBIs**
CENTRIC DIATOMS				
Actinocyclus curvatulus Janisch		3	x	
Bacterosira bathyomphala spore	2		x	
Chaetoceros spp.				no
Chaetoceros spp. spore	1, 2, 3, 4, 5		x	
Melosira arctica Dickie	1, 2			
Minidiscus proschkinae (Makarova) Park & Lee	2			
Porosira glacialis (Grunow) Jørgensen	2			
Skeletonema cf. *costatum* (Greville) Cleve	2			
Thalassiosira antarctica var. *borealis* Fryxell, Doucette & Hubbard	2		x	
T. antarctica var. *borealis* spore		1, 2, 3	x	
T. bulbosa Syvertsen	2			
T. gravida Cleve	2			
T. hyalina (Grunow) Gran		3	x	
T. hyperborea (Grunow) Hasle	1, 2, 3, 4, 5			
T. nordenskioeldii Cleve		2, 3	x	no
T. oceanica Hasle	1			
T. pacifica Grunow & Angst		2		
Thalassiosira spp.	1, 2, 3	1, 3	x	no
PENNATE DIATOMS				
Amphora spp.		1	x	
Bacillaria socialis (Gregory) Ralfs		1		
Biremis solitaria (Cleve) Witkowski, Lange-Bertalot & Metzeltin	1, 2, 4			
Biremis spp.		1		
Cocconeis costata Gregory		1, 3	x	
C. peltoides Hustedt		1		
C. scutellum Ehrenberg		1, 2 ,3	x	
Cylindrotheca closterium (Ehrenberg) Reimann & Lewin	2			
Diploneis didyma (Ehrenberg) Ehrenberg		1		
D. litoralis var. *clathrata* (Østrup) Cleve	2, 3, 4, 5	2		
D. nitescens (Gregory) Cleve		1		
D. subcincta (A. Schmidt) Cleve		1		
Entomoneis kjellmanii (Cleve) Poulin & Cardinal	1, 2			no
E. pseudoduplex Osada & Kobayasi	2			
Entomoneis sp.1	2			
Fallacia clepsidroides Witkowski		1		
Fossula arctica Hasle, Syvertsen & von Quillfeldt	1, 2, 3, 4, 5	1, 2, 3	x	
Fragilaria cf. *barbararum* Witkowski, Metzeltin & Lange-Bertalot	1, 2, 4, 5	1, 2, 3	x	
Fragilaria spp.		1, 2		
Fragilariopsis cylindrus (Grunow ex Cleve) Frenguelli	1, 2, 5	2, 3	x	
F. oceanica (Cleve) Hasle	1, 2, 3, 4	1, 2, 3	x	no
F. reginae-jahniae Witkoswki, Lange-Bertalot & Metzeltin		2, 3	x	
F. pseudonana (Hasle) Hasle		2, 3		
Grammatophora arcuata Ehrenberg		1		
Gyrosigma spp.		1		
Haslea crucigeroides (Hustedt) Simonsen	2, 5			C25:3, C25:4
**H. kjellmanii* (Cleve) Simonsen	3, 4			
**H. spicula* (Hichie) Bukhtiyarova	1, 2, 3, 4, 5			IP_{25}

(Continued)

TABLE 2 | Continued

	Samples Young Sound			Culture
	ICE	**TRAP**	**SED.**	**HBIs**
H. vitrea (Cleve) Simonsen	4			C25:3, C25:4
Haslea sp. 1	2			
*Lyrella spectabilis (*Gregory) Mann		1		
Navicula directa (W. Smith) Ralfs	1, 2	2		
N. gelida Grunow	3			
N. kariana var. *frigida* (Grunow) Cleve	1, 2, 4			
N. lineola Grunow	1, 2, 3, 4			
N. lineola var. *perlepida* (Grunow) Cleve	2, 3, 4			
N. cf. *oestrupii* Cleve	1, 3, 4			
N. pellucidula Hustedt	1, 2, 3, 4			
N. transitans Cleve	2, 4	2		
N. vanhoeffenii Gran	1, 2, 3, 4, 5	1		no
N. veneta Kützing	2			
Navicula spp.	1, 2, 3, 4, 5	1, 2, 3	x	no
Nitzschia angularis W. Smith	1, 4, 5			
N. frigida Grunow	1, 2, 3, 4, 5			no
N. gelida Cleve & Grunow	2, 3, 4			
N. neofrigida Medlin	1, 4, 5			
Nitzschia spp.	1, 2, 3, 4, 5	1, 3		no
Opephora marina (Gregory) Petit			x	
Pauliella taeniata (Grunow) Round & Basson	1, 2	3	x	no
Pinnularia quadratarea var. *constricta* (Østrup) Gran	2			
P. quadratarea var. *minor* (Grunow) Cleve	1, 4	2		
Pinnularia spp.	1	3		
Planothidium delicatulum-group		1, 3	x	
Planothidium lemmermannii (Hustedt) Morales		2		
**Pleurosigma stuxbergii* var. *rhomboides* (Cleve) Cleve	1			
Pleurosigma spp.	1	1		no
Psammodictyon roridum (Giffen) Mann		1		
Pseudofallacia tenera (Hustedt) Liu, Kociolek & Wang		1		
Pseudogomphonema septentrionale (Østrup) Medlin	1			
Pseudo-nitzschia seriata (Cleve) H. Peragallo		2, 3		
Rhoicosphenia marina (Kützing) M. Schmidt		1		
Stauroneis radissonii Poulin & Cardinal	1, 2, 3, 4, 5			
Stauroneis sp.1	4			
Stauroneis spp.		1, 3		
Stauronella arctica (Hustedt) Lange-Bertalot	1, 2, 3, 4, 5	2		
S. cf. *decipiens* (Hustedt) Lange-Bertalot	2			
Stenoneis wojtek-kowalskii Witkowski, Lange-Bertalot & Metzeltin	1, 4, 5			
Stenoneis spp.	1			
Tabularia tabulata (C. Agardh) Snoeijs		1, 2	x	
Thalassionema nitzschioides (Grunow) Mereschkowsky		1		
Trachyneis aspera (Ehrenberg) Cleve		1		
Thalassiothrix longissima Cleve & Grunow		1		
Ulnaria ulna (Nitzsch) Compère		1		

*The numbers correspond to the sea-ice or sediment trap samples in which they were found (refer to **Table 1**).*
*The x is used to mark the presence of the different taxa in the surface sediment sample. Typical sympagic taxa for which the HBI content was analyzed in the culture experiment are identified. The * indicates the IP_{25}-producing species according to Brown et al. (2014).*

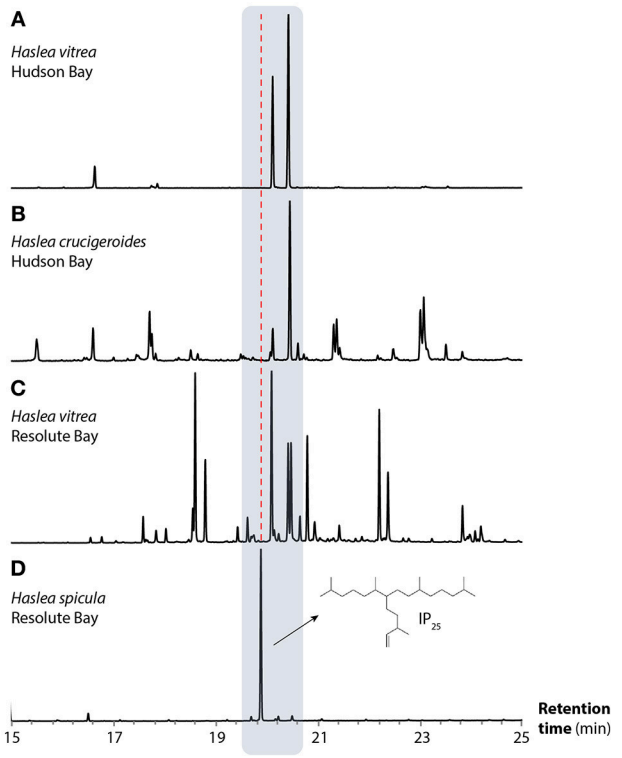

FIGURE 4 | Partial GC-MS TIC chromatograms of hydrocarbon extracts obtained from *Haslea* spp. cultures: **(A)** *Haslea vitrea* isolated from sea-ice collected from Churchill, Hudson Bay, **(B)** *Haslea crucigeroides* (Hudson Bay), **(C)** *Haslea vitrea* (Resolute Bay), and **(D)** *Haslea spicula* (Resolute Bay). The structure of IP_{25} is also illustrated. The x axis corresponds to the retention time (min.). The gray box shows the chromatograms corresponding to HBIs, and the red dashed line shows that of IP_{25}. Amongst the species shown here, only *H. spicula* produces IP_{25}.

rhomboides) was validated through SEM observation. *Haslea crucigeroides,* which, like *H. vitrea* produces HBIs but not IP_{25}, was also observed (**Table 1**). The overall relative abundance of the three IP_{25}-producing taxa remained rather low over the five sampling weeks, with values ranging from 0.3 to 1.3%. This translated into total concentrations rising from 0.21 to 9.66 valves mL^{-1}. In line with these low numbers, measured concentrations of the lipid biomarker IP_{25} were rather low during the entire sampling interval (from 0.4 to 0.7 pg mL^{-1}, **Table 1**). The concentrations of IP_{25} and abundance of IP_{25}-producing species followed distinct trends over time (**Figure 3**).

Trap and Seafloor Sediments

The sediment trap collected particles during the intervals preceding (i) and during/following (ii) the seasonal ice melt:

(i) 24 April to 3 June 2014

A total of 33 taxa were identified (**Supplementary Material**). This assemblage was largely dominated by pennate diatom taxa including *Cocconeis* spp. (40%) and *Navicula* spp. (7%). The resting spores of both *Chaetoceros* spp. and *Thalassiosira antarctica* var. *borealis* contributed to 7 and 4% of the assemblage, respectively (**Figure 5**). Furthermore, although *T. hyperborea* and *Nitzschia* spp. were important contributors to the ice assemblages, they were virtually absent from the sediment trap sample. The high abundance of benthic diatoms of the genus *Cocconeis* Ehrenberg in the sediment trap and its low abundance in the above sea-ice communities was likely due to events of resuspension of seafloor sediments.

(ii) 1 July to 4 August 2014; and 15 July to 4 August 2015

Both assemblages had a total of 20 taxa (**Supplementary Material**). Total centric diatoms, with important contributions of *Chaetoceros* spp. (vegetative cells and resting spores) and *Thalassiosira antarctica* var. *borealis* (resting spores), represented 36 and 61% of the assemblages in 2014 and 2015, respectively (**Figure 5**). The species *Fossula arctica* (23 and 14%), *Fragilariopsis oceanica* (20 and 11%), *F. cylindrus* (9 and 5%), and *F. reginae-jahniae* (5 and 2%) were also significant contributors to the assemblages.

None of the IP_{25}-producing diatom taxa were observed in any of the sediment trap samples analyzed.

In the seafloor sediment sample, a total of 21 taxa belonging to 14 genera were identified (**Supplementary Material**). Resting spores of *Chaetoceros* spp. dominated the assemblage (32%). Other important taxa included *Fragilariopsis oceanica* (20%), *Fossula arctica* (18%), *Thalassiosira antarctica* var. *borealis* (resting spores) (9%), and *Fragilariopsis reginae-jahniae* (7%) (**Figure 5**). Neither IP_{25}-producing diatom taxa, nor *Nitzschia* spp. were recovered from the surface sediment sample. *Navicula* spp. represented ca. 2% of this assemblage.

The sedimentary IP_{25} content was 20.69 ng g^{-1} dry sediment or 1.56 μg g^{-1} TOC (data from Ribeiro et al., 2017).

DISCUSSION

Seasonality of the Diatom Flora

The sea-ice algal assemblages were marked by rapid compositional shifts, with an initial dominance, and with low absolute concentrations, of the centric diatom *Thalassiosira hyperborea*. This species was also reported in sea-ice from other Arctic regions influenced by river discharge (Hasle and Lange, 1989). At our study site, its relative abundance decreased promptly, and this species was not identified in the sea-ice samples from the subsequent sampling weeks. It is therefore possible that these cells became entrapped in the sea-ice when it formed during the preceding autumn. The most steady and significant contributors to the sea-ice communities were taxa belonging to the pennate genera *Nitzschia* Hassall and *Navicula* Bory. The latter were further characterized by high species diversity (**Table 2**). In this respect, the assemblages from the studied fjord are comparable to those from other seasonally sea-ice covered Arctic regions where these two genera, and especially *Nitzschia frigida*, are typically found in the sea-ice (e.g., Medlin and Hasle, 1990; Syvertsen, 1991; Rózanska et al., 2009; Poulin et al., 2011; Leu et al., 2015; Olsen et al., 2017). The high relative abundance of the pennate *Stauronella arctica* during the last sampling week was however surprising since this species

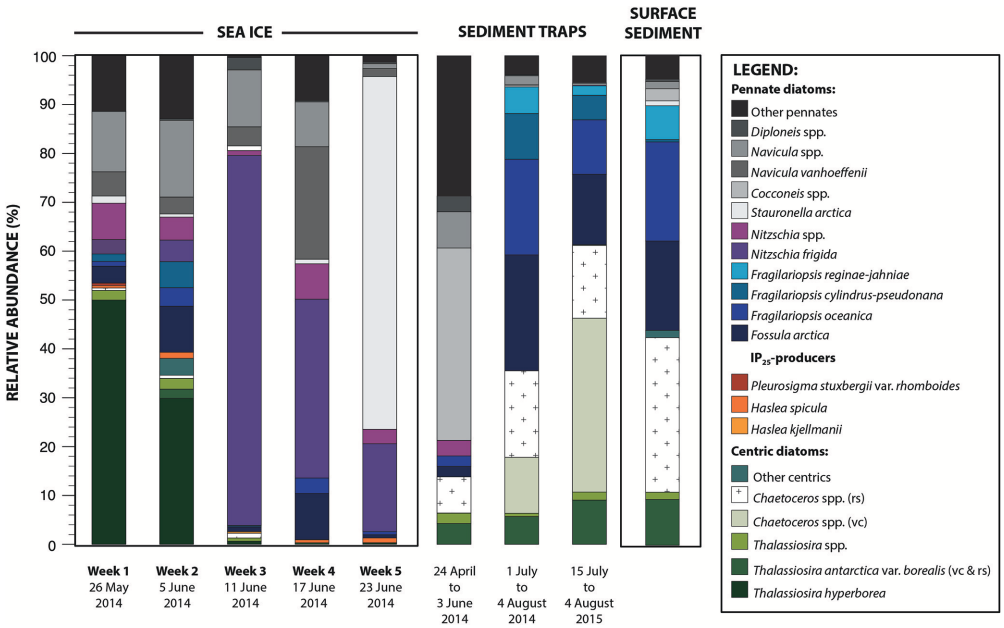

FIGURE 5 | Relative abundance (%) of the diatom taxa in the (i) sea-ice, (ii) sediment trap, and (iii) surface sediment samples. This figure illustrates the diatom succession and vertical transfer of the valves to the seafloor sediment. Sampling dates are indicated under each sample. vc, vegetative cell; rs, resting spore.

has, to our knowledge, never been reported to dominate sea-ice assemblages in the Arctic.

Although *Fossula arctica*, *Fragilariopsis cylindrus*, and *F. oceanica* contributed to the sea-ice flora, their highest relative abundances were found in the trap and surface sediment samples. This suggests that, in this study area, their growth was likely favored during the final stage of sea-ice retreat, and in the surface-water environment resulting from melt (e.g., cold and low-salinity). This is coherent with observations from other sea-ice covered regions that have associated these species with the pelagic vernal bloom (e.g., Kang and Fryxell, 1992; Hasle et al., 1996; von Quillfeldt, 2000, 2004). By contrast to the *Fragilariopsis* species mentioned above, *F. reginae-jahniae* was only observed in the trap and surface sediment samples, suggesting that it colonizes the sea-ice or surface-waters later in the season. The high abundances of both vegetative cells and resting spores of *Chaetoceros* Ehrenberg in the two July sediment traps suggest that more open conditions are required for these to thrive. Blooms of colonial centric *Chaetoceros* spp. have been reported to occur along the marginal ice zone (e.g., Wassmann et al., 1999), but are often found at highest concentrations later in the season (e.g., von Quillfeldt, 2000; Krawczyk et al., 2014). The production of resting spores can occur massively over a short period of time (e.g., Rembauville et al., 2018), as part of a survival strategy that includes a benthic reservoir of resistant cells that can function as inoculum for the next growing season. In the North Water polynya, *Chaetoceros* sp. produce large quantities of fast sinking resting spores as a response to nutrient depletion, allowing the population to be sustained for an extended period of time (Booth et al., 2002). Overall, observations made here are in line with those reported by Krawczyk et al. (2015), showing alternating dominance of *Fragilariopsis* spp. and *Chaetoceros* spp. in the pelagic protist assemblages of Young Sound, in July/August of 2010–2012 and 2009–2011, respectively.

Vertical Export of IP_{25} and Diatom Valves

Several diatom genera identified from the sea-ice, notably *Nitzschia*, *Haslea* Simonsen, and *Navicula*, were only sporadically observed in the trap and surface sediment samples, and most of the time as fragments. From our dataset, it is difficult to determine whether their absence or low representation in the sediments was primarily due to degradation during vertical sinking or caused by a "dilution effect" due to the dominance of the main spring blooming species. Our observations are however consistent with studies from other Arctic regions where these are generally rare or absent (e.g., Moros et al., 2006; Sha et al., 2014; Krawczyk et al., 2017). Similarly, the weakly silicified vegetative cells of *Chaetoceros* spp., that were important contributors to the phytoplankton community as illustrated by their high abundance in the second set of trap samples, were not reported from the surface sediment sample. Compared to the vegetative cells, the resting spores of *Chaetoceros* can be 3–4 times more silicified (Rynearson et al., 2013), allowing them to sink more rapidly toward the seafloor. They have been proven to be more resistant to bacterial degradation (Kuwata and Takahashi, 1990) and remain intact after being digested by zooplankton (Kuwata and Tsuda, 2005). All of these factors favor their export to, and preservation in, the seafloor sediments.

All the diatom taxa that were identified from the surface sediments were also observed either in the sea-ice or sediment trap samples. Classical cluster analysis shows that the diatom assemblage from the surface sediment sample was most similar

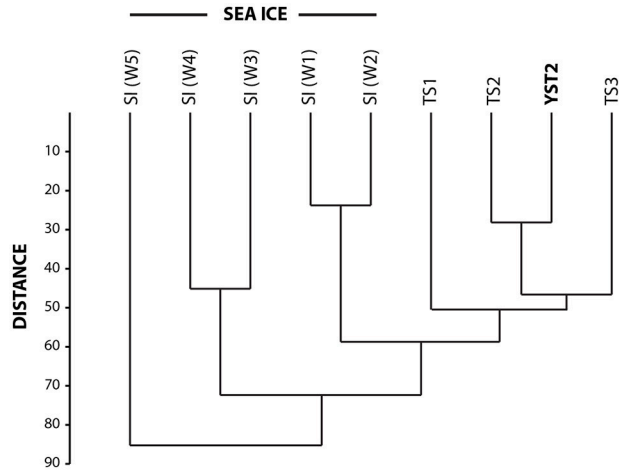

FIGURE 6 | Dendrogram resulting from the cluster analysis. SI, sea-ice sample; TS, sediment trap samples; and YST2, surface sediment sample.

to that of the sediment trap sample that covers the interval from 1 July to 4 August 2014, which represents the melt and post-melt diatom production (**Figure 6**). This is coherent with data from Rysgaard et al. (2001) showing that ice algae only contribute to a minor fraction (<1%) of the total pelagic primary production in the fjord.

Although the sedimentary IP_{25} (20.69 ng g^{-1} dry sediment or 1.56 μg g^{-1} TOC) content was relatively low, i.e., up to 7 times lower than the values reported from other marine Arctic settings where sea-ice lasts throughout spring/summer (e.g., Müller et al., 2011; Xiao et al., 2015), it is comparable to the values reported from other regions influenced by river or meltwater runoff (e.g., Xiao et al., 2013; Limoges et al., 2018). The low IP_{25} concentrations in the sediments are consistent with the low concentrations of IP_{25}-producing taxa found in the fjord's sea-ice. During the fourth and fifth week of sampling, while the total abundance of IP_{25}-producing species increased, IP_{25} concentrations measured from sea-ice stabilized and decreased (**Figure 3**). The absence of a relationship between the concentrations of IP_{25}-producing species and the lipid IP_{25} in the sea-ice samples may arise from (i) intra-specific differences in the production of IP_{25} and subtle changes in the relative contribution of the different IP_{25}-producing species in sea-ice, and/or (ii) changes in the intracellular biosynthesis of IP_{25} in response to environmental conditions (e.g., light intensity, salinity, temperature, nutrients, etc.). We note that Brown et al. (2014) measured relatively similar intracellular IP_{25} concentration (ranging from ca. 0.6 to 3.8 pg $cell^{-1}$) for each of the IP_{25}-producing diatom taxa investigated. Here, the potential impact of those parameters other than sea-ice presence on the intracellular IP_{25} biosynthesis cannot be excluded nor quantified individually, and we recognize that further studies would be needed to address this. Since the abundance of IP_{25}-producing species increases in parallel to a slight decrease in the salinity of the sea-ice bottom (**Figure 3**), our data do not indicate a direct adverse impact of low-salinity on the abundance of IP_{25}-producing species, but neither rule out a potential effect of low-salinity on IP_{25} synthesis.

Implications for Paleo-Environmental Studies

The main contributors to the surface sediment assemblage were resting spores of the centric diatom *Chaetoceros* and *Thalassiosira antarctica* var. *borealis*, and the pennate *Fossula arctica, Fragilariopsis oceanica,* and *F. reginae-jahniae*. All of these (except *F. reginae-jahniae*) were minor components of the sea-ice communities, but their peak abundances occurred during or following ice melt. Based on previous work (e.g., von Quillfeldt, 2000, 2001), the pennate *Fossula arctica*, and *Fragilariopsis oceanica*, as well as *Fragilariopsis cylindrus*, which have been frequently used as sea-ice indicator species in paleoceanographic studies, occur earlier in the spring and appear to reflect the cold and low surface salinity conditions of the marginal ice zone. *Thalassiosira antarctica* var. *borealis* and *Chaetoceros* spp. on the other hand generally bloom later in the season, when the cold and low-salinity surface layer is breaking up and the mixing layer is deeper. These successional characteristics of diatom communities are important to take into account when interpreting palaeo-records from Arctic regions.

The confirmed presence of three IP_{25}-producing species (*Haslea spicula, H. kjellmanii,* and *Pleurosigma stuxbergii* var. *rhomboides*) in the Young Sound together with the detection of IP_{25} in the sea-ice samples is of critical importance because it provides direct evidence for *in-situ* production of IP_{25} in this fjord, even though some additional advection of the biomarker from offshore waters cannot be excluded. The weak IP_{25} sedimentary fingerprint does not appear to be the result of diagenetic processes during vertical transfer toward the sediment but is rather consistent with low overall diatom production and low abundance of IP_{25}-producing species in the fjord ice. In Young Sound, total sea-ice diatom concentrations increased from 21 to 985 valves mL^{-1} (or ca. 11 to 493 cells mL^{-1}) over the five sampling weeks, which is markedly lower than what is reported from other Arctic regions. For example, Hsiao (1980) reported total diatom concentrations of up to ca. 40,000 cells mL^{-1} in the bottom 10 cm of sea-ice cores collected in May 1972 from Husky Lakes (formerly known as Eskimo Lakes), Northwest Territories, Canada. Riedel et al. (2003) also reported concentrations of more than 100,000 cells mL^{-1} in the bottom 3–5 cm of sea-ice cores collected in May 2001 from McDougall Sound, near Resolute Bay, Nunavut. We must note that these differences could be due, in part, to significant spatio-temporal variabilities in-ice biomass (e.g., Lange et al., 2017), and limited ice sampling here. The low production in Young Sound is also possibly related to the ecological needs of the different diatom species and environmental parameters, other than the simple presence of sea-ice (e.g., nutrient levels, light, temperature, salinity, etc.), that affect their growth and steer the assemblage composition. The relative abundance of IP_{25}-producing species (0.3 to 1.3% of sympagic assemblages) is at the low end of the range reported from a number of sites in

the Arctic by (Brown et al. (2014), their Table 3). This suggests that Young Sound is only marginally suitable for the growth of IP_{25}-producing species. Importantly, it has been shown that the bottom horizon of sea-ice (0–3 cm) is strongly affected by the properties of the under-ice surface-water (e.g., Reeburgh, 1984). Poulin et al. (1983) and Gosselin et al. (1986) suggested that lower under-ice salinity negatively influences the settlement efficiency of sympagic microalgal populations, through its role in shaping the microstructure of the ice. Such interplay between salinity, ice porosity, and sea-ice algal colonization was observed in coastal sea-ice, in the Gulf of Finland (Granskog et al., 2005). Although it might be challenging to mimic sea-ice conditions in the laboratory, carefully designed culture experiments are recommended to test the growth and IP_{25} production of the source species under different environmental conditions. In particular, cultures under salinity conditions that are similar to those observed in fjords influenced by meltwater during spring/summer are needed.

In light of the observations made here, as well as in other studies documenting the modern distribution of IP_{25} in sediments from areas influenced by freshwater (Xiao et al., 2013; Hörner et al., 2016; Ribeiro et al., 2017; Limoges et al., 2018), we recommend careful interpretation of paleo sea-ice records based on the sedimentary IP_{25} signal in regions that are susceptible to significant inter-annual, but also longer-term changes in salinity. Lower salinities may influence the structural nature of sea-ice and its propensity to sustain algal growth, including IP_{25}-producing diatom species. As stated above, it is also plausible that low-salinity conditions, as well as other parameters (e.g., light intensity, nutrient levels) influence IP_{25} synthesis and intracellular concentration in these species. To summarize, in fjords and coastal embayment regions, the presence of IP_{25} may for now be regarded as a signal of presence of seasonal sea-ice, rather than a robust indicator of variability in sea-ice concentration. In all cases, multi-proxy approaches are preferred to allow for a more critical evaluation of the paleo-environmental signal derived from this biomarker.

CONCLUSIONS

The spring diatom succession was captured by the sea-ice and sediment trap samples. An important shift in the composition of the assemblages was recorded, with an early diatom colonization by the centric *Thalassiosira hyperborea*, which was rapidly replaced by pennate diatoms belonging to *Nitzschia* and *Navicula* species, and *Stauronella arctica*. *Fossula arctica,* other *Fragilariopsis*, *Thalassiosira antarctica* var. *borealis* spores, and *Chaetoceros* spp. (vegetative cells and resting spores) appeared to thrive in the melt and post-melt environment. The surface sediment diatom assemblages were dominated by the pennate diatoms *Fragilariopsis oceanica*, *Fossula arctica*, *Fragilariopsis reginae-jahniae* and the resting spores of the centric diatoms *Thalassiosira antarctica* var. *borealis* and *Chaetoceros* spp. The paleo-environmental signal preserved by the diatom assemblages in the surface sediment therefore primarily reflected the melt and post-melt sea-surface conditions.

This study confirms the *in-situ* production of the sea-ice biomarker IP_{25} in this fjord system and that *Haslea spicula* is one of the species responsible for the production of the sea-ice biomarker IP_{25}. *Haslea crucigeroides*, like *H. vitrea*, produced other HBIs (including triene) but not IP_{25}. Finally, while IP_{25} is produced in seasonally sea-ice covered coastal environments with freshwater influence, it may not reflect variability in sea-ice concentrations. In the Young Sound, the growth of IP_{25}-producing diatom taxa, and possibly also their cellular IP_{25} synthesis, appear to be affected by the physico-chemical conditions (e.g., light, salinity, nutrient levels) that prevail in the sea-ice microenvironment.

AUTHOR CONTRIBUTIONS

This study was conceptualized by SRi and designed by SRi, GM, KW, and AL. Sampling and *in-situ* measurements were done by N-XG, MS, and SRy. Preparations and analyses were done by KW, GM, ME, and AL. Interpretation of the results was done by SRi, KW, GM, MP, and AL. The manuscript was written by AL with intellectual additions, discussions and revisions by all other co-authors (GM, KW, MP, ME, MH, N-XG, MS, SRy, and SRi). All authors provided their approval for the publication of this manuscript.

ACKNOWLEDGMENTS

This study received financial support from the Villum Foundation, Denmark (grant VKR023454 to SRi). Fieldwork was funded by the Arctic Research Center at Aarhus University. We are grateful to Tage Dalsgaard for help in the laboratory. AL and GM received financial support from NSERC-discovery grant (grants RGPIN-2018-03984 & RGPIN-2016-05945). MH and KW acknowledge funding from the Academy of Finland (grants 296895 and 307282). SR was funded by the Canada Excellence Research Chair Program. Finally, we acknowledge the constructive comments of two reviewers and handing editor, Dr. Flores.

SUPPLEMENTARY MATERIAL

The Supplementary Material for this article can be found online at: https://www.frontiersin.org/articles/10.3389/feart.2018.00226/full#supplementary-material

REFERENCES

Andrews, J. T., Belt, S. T., Olafsdottir, S., Massé, G., and Vare, L. L. (2009). Sea ice and climate variability for NW Iceland/Denmark Strait over the last 2000 cal yr BP. *Holocene* 19, 775–784. doi: 10.1177/0959683609105302

Battarbee, R. W., Jones, V. J., Flower, R. J., Cameron, N. G., Bennion, H., Carvalho, L., et al. (2001). "Tracking environmental change using lake sediments," in *Terrestrial, Algal, and Siliceous Indicators,* Vol. 3, eds J. Diatoms and P. Smol Dordrecht (Netherlands: Kluwer), 155–202. doi: 10.1007/0-306-47668-1_8

Belt, S. T., Massé, G., Rowland, S. J., Poulin, M., Michel, C., and Leblanc, B. (2007). A novel chemical fossil of palaeo sea ice: IP_{25}. *Org. Geochem.* 38, 16–27. doi: 10.1016/j.orggeochem.2006.09.013

Belt, S. T., and Müller, J. (2013). The Arctic sea ice biomarker IP_{25}: a review of current understanding, recommendations for future research and applications in palaeo sea ice reconstructions. *Quat. Sci. Rev.* 79, 9–25. doi: 10.1016/j.quascirev.2012.12.001

Belt, S. T., Vare, L., Massé, G., Manners, H. R., Price, J. C., MacLachlan, S. E., et al. (2010). Striking similarities in temporal changes to spring sea ice occurrence across the central Canadian Arctic Archipelago over the last 7000 years. *Quat. Sci. Rev.* 29, 3489–3504. doi: 10.1016/j.quascirev.2010.06.041

Bendtsen, J., Mortensen, J., Lennert, K., Ehn, J. K., Boone, W., Galindo, V., et al. (2017). Sea ice breakup and marine melt of a retreating tidewater outlet glacier in northeast Greenland (81°N). *Sci. Rep.* 7:4941. doi: 10.1038/s41598-017-05089-3

Boone, W., Rysgaard, S., Carlson, D. F., Meire, L., Kirillov, S., Mortensen, J., et al. (2018). Coastal freshening prevents fjord bottom water renewal in Northeast Greenland: a mooring study from 2003 to 2015. *Geophys. Res. Lett.* 45, 2726–2733. doi: 10.1002/2017GL076591

Booth, B. C., Larouche, P., Bélanger,. S., Klein, B., Amiel, D., and Mei, Z. P. (2002). Dynamics of *Chaetoceros socialis* blooms in the North water. *Deep-Sea Res. II* 49, 5003–5025. doi: 10.1016/S0967-0645(02)00175-3

Brown, T. A., Belt, S., Philippe, B., Mundy, C. J., Massé, G., Poulin, M., et al. (2011). Temporal and vertical variations of lipid biomarkers during a bottom ice diatom bloom in the Canadian Beaufort Sea: further evidence for the use of the IP_{25} biomarker as a proxy for spring Arctic sea ice. *Polar. Biol.* 34, 1857–1868. doi: 10.1007/s00300-010-0942-5

Brown, T. A., Belt, S. T., Tatarek, A., and Mundy, C. J. (2014). Source identification of the Arctic sea ice proxy IP_{25}. *Nat. Commun.* 5:4197. doi: 10.1038/ncomms5197

Cabedo-Sanz, P., and Belt, S. T. (2016). Seasonal sea ice variability in eastern Fram Strait over the last 2,000 years. *Arktos* 2:22. doi: 10.1007/s41063-016-0023-2

Curry, J. A., Schramm, J. L., and Ebert, E. E. (1995). Sea ice-albedo climate feedback mechanism. *J. Clim.* 8, 240–247. doi: 10.1175/1520-0442(1995)008<0240:SIACFM>2.0.CO;2

de Vernal, A., Gersonde, R., Goosse, H., Seidenkrantz, M. S., and Wolff, E. W. (2013). Sea ice in the paleoclimate system: the challenge of reconstructing sea ice from proxies – An introduction. *Quat. Sci. Rev.* 79, 1–8. doi: 10.1016/j.quascirev.2013.08.009

Gosselin, M., Legendre, L., Therriault, J. C., Demers, S., and Rochet, M. (1986). Physical control of the horizontal patchiness of sea-ice microalgae. *Mar. Ecol. Progr. Ser.* 29, 289–298. doi: 10.3354/meps029289

Granskog, M. A., Kaartokallio, H., Thomas, D. N., and Kuosa, H. (2005). Influence of freshwater inflow on the inorganic nutrient and dissolved organic matter within coastal sea ice and underlying waters in the Gulf of Finland (Baltic Sea). Estuar. *Coast. Shelf Sci.* 65, 109–122.

Hammer, Ø., Harper, D. A. T., and Ryan, P. D. (2001). *PAST: Paleontological Statistics Software Package for Education.* Oslo.

Hasle, G. R., and Lange, C. B. (1989). Freshwater and brackish water *Thalassiosira* (*Bacillariophyceae*): taxa with tangentially undulated valves. *Phycologia* 28, 120–135. doi: 10.2216/i0031-8884-28-1-120.1

Hasle, G. R., Syvertsen, E. E., and von Quillfeldt, C. H. (1996). *Fossula arctica* gen nov., spec. nov., a marine Arctic araphid diatom. *Diatom Res.* 11, 261–272. doi: 10.1080/0269249X.1996.9705383

Hörner, T., Stein, R., Fahl, K., and Birgel, D. (2016). Post-glacial variability of sea ice cover, river run-off and biological production in the western Laptev Sea (Arctic Ocean)—a high-resolution biomarker study. *Quat. Sci. Rev.* 143, 133–149. doi: 10.1016/j.quascirev.2016.04.011

Hsiao, S. I. C. (1980). Quantitative composition, distribution, community structure and standing stock of sea ice microalgae in the Canadian Arctic. *Arctic* 33, 768–793. doi: 10.14430/arctic2595

Hustedt, F. (1961). "Die Kieselalgen Deutschlands, Österreichs und der Schweiz," in *Kryptogamenflora von Deutschland, Österreich und der Schweiz, Band 7, Teil 3, Lief. 1*, ed. L. Rabenhorsts (Leipzig: Akademische Verlagsgesellschaft), 1–160.

Jahn, A., and Holland, M. M. (2013). Implications of Arctic sea ice changes for North Atlantic deep convection and the meridional overturning circulation in CCSM4-CMIP5 simulations. *Geophys. Res. Lett.* 40, 1206–1211. doi: 10.1002/grl.50183

Jensen, L. M., Christensen, T. R., and Schmidt, N. M. (2014). *Zackenberg Ecological Research Operations, 19th Annual Report 2013.* Roskilde: DCE-Danish Centre for Environment and Energy, Aarhus University. 130.

Kang, S. H., and Fryxell, G. A. (1992). *Fragilariopsis cylindrus* (Grunow) Krieger - The most abundant diatom in water column assemblages of Antarctic marginal ice-edge zones. *Polar Biol.* 12, 609–627. doi: 10.1007/BF00236984

Krawczyk, D. W., Arendt, K. E., Juul-Pedersen, T., Sejr, M. K., Blicher, M. E., and Jakobsen, H. H. (2015). Spatial and temporal distribution of planktonic protists in the East Greenland fjord and offshore waters. *Mar. Ecol. Prog. Ser.* 538, 99–116. doi: 10.3354/meps11439

Krawczyk, D. W., Witkowski, A., Moros, M., Lloyd, J. M., Høyer, J. L., Miettinen, A., et al. (2017). Quantitative reconstruction of Holocene sea ice and sea surface temperature off West Greenland from the first regional diatom data set. *Paleoceanography* 32, 18–40. doi: 10.1002/2016PA003003

Krawczyk, D. W., Witkowski, A., Waniek, J. J., Wroniecki, M., and Harff, J. (2014). Description of diatoms from the Southwest to West Greenland coastal and open marine waters. *Polar Biol.* 37, 1589–1606. doi: 10.1007/s00300-014-1546-2

Kroon, A., Abermann, J., Bendixen, M., Lund, M., Sigsgaard, C., Skov, K., et al. (2017). Deltas, freshwater discharge, and waves along the Young Sound, NE Greenland. *Ambio* 16, 132–145. doi: 10.1007/s13280-016-0869-3

Kuwata, A., and Takahashi, M. (1990). Life-form population responses of a marine planktonic diatom, *Chaetoceros pseudocurvisetus*, to oligotrophication in regionally upwelled water. *Mar. Biol.* 107, 503–512. doi: 10.1007/BF01313435

Kuwata, A., and Tsuda, A. (2005). Selection and viability after ingestion of vegetative cells, resting spores and resting cells of the marine diatom, *Chaetoceros pseudocurvisetus*, by two copepods. *J. Exp. Mar. Biol. Ecol.* 322, 143–151. doi: 10.1016/j.jembe.2005.02.013

Lange, B. A., Katlein, C., Castellani, G., Fernández-Méndez, M., Nicolaus, M., Peeken, I., et al. (2017). Characterizing spatial variability of ice aglal chlorophyll a and net primary production between sea ice habitats using horizontal profiling platforms. *Front. Mar. Sci.* 4:349. doi: 10.3389/fmars.2017.00349

Leu, E., Mundy, C. J., Assmy, P., Campbell, K., Gabrielsen, T. M., Gosselin, M., et al. (2015). Arctic spring awakening - steering principles behind the phenology of vernal ice blooms. *Prog. Oceanogr.* 139, 151–170. doi: 10.1016/j.pocean.2015.07.012

Limoges, A., Ribeiro, S., Weckström, K., Heikkilä, M., Zamelczyk, K., Andersen, T. J., et al. (2018). Linking the modern distribution of biogenic proxies in High Arctic Greenland shelf sediments to sea ice, primary production, and Arctic-Atlantic inflow. *J. Geophys. Res.* 123, 760–786. doi: 10.1002/2017JG003840

Lundholm, N., Daugbjerg, N., and Moestrup, Ø. (2002). Phylogeny of the Bacillariaceae with emphasis on the genus *Pseudo-nitzschia* (*Bacillariophyceae*) based on partial LSU rDNA. *Eur. J. Phycol.* 37, 115–134. doi: 10.1017/S096702620100347X

Massé, G., Rowland, S. J., Sicre, M. A., Jacob, J., Jansen, E., and Belt, S. T. (2008). Abrupt climate changes for Iceland during the last millennium: evidence from high resolution sea ice reconstructions. *Earth Planet. Sci. Lett.* 269, 565–569. doi: 10.1016/j.epsl.2008.03.017

Medlin, L. K., and Hasle, G. R. (1990). Some *Nitzschia* and related diatom species from fast ice samples in the Arctic and Antarctic. *Polar Biol.* 10, 451–479. doi: 10.1007/BF00233693

Mernild, S. H., Sigsgaard, C., Rasch, M., Hasholt, B., Hansen, B. U., Stjernholm, M., et al. (2007). "Climate, river discharge and suspended sediment transport in the Zackenberg River drainage basin and Young Sound/Tyrolerfjord, Northeast Greenland., 1995-2003," in *Carbon Cycling in Arctic marine ecosystems. Case study Young Sound*, eds S. Rysgaard, R. N. Glud, and T. M. Roberts (Leine: Meddr. Grøland), 24–43.

Moros, M., Jensen, K. G., and Kuijpers, A. (2006). Mid- to late-Holocene hydrological and climatic variability in Disko Bugt, central West Greenland. *Holocene* 16, 357–367. doi: 10.1191/0959683606hl933rp

Müller, J., Wagner, A., Fahl, K., Stein, R., Prange, M., and Lohmann, G. (2011). Towards quantitative sea ice reconstructions in the northern North Atlantic: a combined biomarker and numerical modelling approach. *Earth Planet. Sci. Lett.* 306, 137–148. doi: 10.1016/j.epsl.2011.04.011

Müller, J., Werner, K., Stein, R., Fahl, K., Moros, M., and Jansen, E. (2012). Holocene cooling culminates in sea ice oscillations in Fram Strait. *Quat. Sci. Rev.* 47, 1–14. doi: 10.1016/j.quascirev.2012.04.024

Olsen, L. S., Laney, S. R., Duarte, P., Kauko, H. M., Fernandez-Mendez, M., Mundy, C. J., et al. (2017). The seeding of ice algal blooms in Arctic pack ice:

the multiyear ice seed repository hypothesis. *J. Geophys. Res.* 122, 1529–1548. doi: 10.1002/2016JG003668

Polyak, L., Alley, R. B., Andrews, J. T., Brigham-Grette, J., Cronin, T. M., Darby, D. A., et al. (2010). History of sea ice in the Arctic. *Quat. Sci. Rev.* 29, 1757–1778. doi: 10.1016/j.quascirev.2010.02.010

Poulin, M., Cardinal, A., and Legendre, L. (1983). Réponse d'une communauté de diatomées de glace à un gradient de salinité (baie d'Hudson). *Mar. Biol.* 76, 191–202.

Poulin, M., Daugbjerg, N., Gradinger, R., Ilyash, L., Ratkova, T., and von Quillfeldt, C. (2011). The pan-Arctic biodiversity of marine pelagic and sea-ice unicellular eukaryotes: a first-attempt assessment. *Mar. Biodiv.* 41, 13–28. doi: 10.1007/s12526-010-0058-8

Reeburgh, W. S. (1984). Fluxes associated with brine motion in growing sea ice. *Polar Biol.* 3, 29–33.

Rembauville, M., Blain, S., Manno, C., Tarling, G., Thompson, A., Wolf, G., et al. (2018). The role of diatom resting spores in pelagic–benthic coupling in the Southern Ocean. *Biogeosciences* 15, 3071–3084. doi: 10.5194/bg-15-3071-2018

Ribeiro, S., Sejr, M. K., Limoges, A., Heikkilä, M., Andersen, T. J., Tallberg, P., et al. (2017). Sea ice and primary production proxies in surface sediments from a High Arctic Greenland fjord: spatial distribution and implications for palaeoenvironmental studies. *Ambio* 26 (Suppl. 1), 106–118. doi: 10.1007/s13280-016-0894-2

Riedel, A., Michel, C., Poulin, M., and Lessard, S. (2003). Taxonomy and abundance of microalgae and protists at a first-year sea ice station near Resolute Bay, Nunavut, Spring to early Summer 2001. *Can. Data Rep. Hydrogr. Ocean Sci.* 159, 1–53.

Rontani, J. F., Belt, S. T., and Amiraux, R. (2018). Biotic and abiotic degradation of the sea ice diatom biomarker IP_{25} and selected algal sterols in near-surface Arctic sediments. *Org. Geochem.* 118, 73–88. doi: 10.1016/j.orggeochem.2018.01.003

Rózanska, M., Gosselin, M., Poulin, M., Wiktor, J. M., and Michel, C. (2009). Influence of environmental factors on the development of bottom ice protist communities during the winter-spring transition. *Mar. Ecol. Prog. Ser.* 386, 43–59. doi: 10.3354/meps08092

Rynearson, T. A., Richardson, K., Lampitt, R. S., Sieracki, M. E., Poulton, A. J., Lyngsgaard, M. M., et al. (2013). Major contribution of diatom resting spores to vertical flux in the sub-polar North Atlantic. *Deep-Sea Res. I* 82, 60–71. doi: 10.1016/j.dsr.2013.07.013

Rysgaard, S., and Glud, R. N. (2007). Carbon cycling in Arctic marine ecosystems: case study - young sound. *Meddelelser om Grønland. Bioscience* 58, 176–191.

Rysgaard, S., Kühl, M., Glud, R. N., and Hansen, J. W. (2001). Biomass, production and horizontal patchiness of sea ice algae in a high-Arctic fjord (Young Sound, NE Greenland). *Mar. Ecol. Prog. Ser.* 223, 15–26. doi: 10.3354/meps223015

Rysgaard, S., Nielsen, T. G., and Hansen, B. W. (1999). Seasonal variation in nutrients, pelagic primary production and grazing in a high-Arctic coastal marine ecosystem, Young Sound, Northeast Greenland. *Mar. Ecol. Prog. Ser.* 179, 13–25. doi: 10.3354/meps179013

Rysgaard, S., Sejr, M. K., Frandsen, E. R., Frederiksen, M., Arendt, K., and Mikkelsen, D. M. (2009). *The Zackenberg Marine Monitoring Programme: Sampling Manual for the Annual Summer Field Campaign.* Greenland Institute of Natural Resources and National Environmental Research Institute, Denmark.

Rysgaard, S., Vang, T., Stjernholm, M., Rasmussen, B., Windelin, A., and Kiilsholm, S. (2003). Physical conditions, carbon transport, and climate change impacts in a Northeast Greenland Fjord. *Arct. Antarct. Alp. Res.* 35, 301–312. doi: 10.1657/1523-0430(2003)035[0301:PCCTAC]2.0.CO;2

Sejr, M. K., Stedmon, C. A., Bendtesen, J., Abermann, J., Juul-Pedersen, T., Mortensen, J., et al. (2017). Evidence of local and regional freshening of Northeast Greenland coastal waters. *Sci. Rep.* 7:13183. doi: 10.1038/s41598-017-10610-9

Serreze, M. C., and Barry, R. G. (2011). Processes and impacts of Arctic amplification: a research synthesis. *Glob. Planet. Change* 77, 85–96. doi: 10.1016/j.gloplacha.2011.03.004

Sha, L., Jiang, H., Seidenkrantz, M. S., Knudsen, K. L., Olsen, J., Kuijpers, A., et al. (2014). A diatom-based sea-ice reconstruction for the Vaigat Strait (Disko Bugt, West Greenland) over the last 5000 yr. *Palaeogeogr. Palaeoclimatol. Palaeoecol.* 403, 66–79. doi: 10.1016/j.palaeo.2014.03.028

Snoeijs, P. (1993). *Intercalibration and Distribution of Diatom Species in the Baltic Sea,* Vol. 1, Uppsala: Opulus Press; Baltic Marine Biologist Publication 16a.

Snoeijs, P., and Balashova, N. (1998). *Intercalibration and Distribution of Diatom Species in the Baltic Sea,* Vol. 5. Uppsala: Opulus Press; Baltic Marine Biologist Publication 16e.

Snoeijs, P., and Kasperoviciene, J. (1996). *Intercalibration and Distribution of Diatom Species in the Baltic Sea*, Vol. 4. Uppsala: Opulus Press; Baltic Marine Biologist Publication 16d.

Snoeijs, P., and Potapova, M. (1995). *Intercalibration and Distribution of Diatom Species in the Baltic Sea*, Vol. 3. Uppsala: Opulus Press; Baltic Marine Biologist Publication 16c.

Snoeijs, P., and Vilbaste, S. (1994). *Intercalibration and Distribution of Diatom Species in the Baltic Sea*. Vol. 2. Uppsala: Opulus Press; Baltic Marine Biologist Publication 16b.

Syvertsen, E. E. (1991). Ice algae in the Barents Sea: types of assemblages, origin fate and role in the ice-edge phytoplankton bloom. *Polar Res.* 10, 277–288. doi: 10.3402/polar.v10i1.6746

Tomas, R. A., Deser, C., and Sun, L. (2016). The role of ocean heat transport in the global climate response to projected Arctic sea ice loss. *J. Clim.* 29, 6841–6859. doi: 10.1175/JCLI-D-15-0651.1

Vare, L. L., Massé, G., Gregory, T. R., Smart, C. W., and Belt, S. T. (2009). Sea ice variations in the central Canadian Arctic Archipelago during the Holocene. *Quat. Sci. Rev.* 28, 1354–1366. doi: 10.1016/j.quascirev.2009.01.013

von Quillfeldt, C. H. (2000). Common diatom species in Arctic spring blooms: their distribution and abundance. *Bot. Mar.* 43, 499–516. doi: 10.1515/BOT.2000.050

von Quillfeldt, C. H. (2001). Identification of some easily confused common diatom species in Arctic spring blooms. *Bot. Mar.* 44, 375–389. doi: 10.1515/BOT.2001.048

von Quillfeldt, C. H. (2004). The diatom *Fragilariopsis cylindrus* and its potential as an indicator species for cold water rather than for sea ice. *Vie et Milieu* 5, 137–143.

Wassmann, P., Ratkova, T., Andreassen, I., Vernet, M., Pedersen, G., and Rey, F. (1999). Spring bloom development in the marginal ice zone and the central Barents Sea. *Mar. Ecol.* 20, 321–246. doi: 10.1046/j.1439-0485.1999.2034081.x

Witkowski, A., Lange-Bertalot, H., and Metzeltin, D. (2000). Diatom flora of marine coasts. *I. Iconogr. Diatomol.* 7, 1–925.

Xiao, X., Fahl, K., Müller, J., and Stein, R. (2015). Sea-ice distribution in the modern Arctic Ocean: biomarker records from trans-Arctic Ocean surface sediments. *Geochim. Cosmochim. Acta* 155, 16–29. doi: 10.1016/j.gca.2015.01.029

Xiao, X., Fahl, K., and Stein, R. (2013). Biomarker distribution in surface sediments from the Kara and Laptev seas (Arctic Ocean): indicators for organic-carbon sources and sea-ice coverage. *Quat. Sci. Rev.* 79, 40–52. doi: 10.1016/j.quascirev.2012.11.028

Conflict of Interest Statement: The authors declare that the research was conducted in the absence of any commercial or financial relationships that could be construed as a potential conflict of interest.

frontiers in Marine Science

ORIGINAL RESEARCH
published: 06 June 2018
doi: 10.3389/fmars.2018.00199

Algal Colonization of Young Arctic Sea Ice in Spring

Hanna M. Kauko[1,2], Lasse M. Olsen[1], Pedro Duarte[1], Ilka Peeken[3], Mats A. Granskog[1], Geir Johnsen[4,5], Mar Fernández-Méndez[1], Alexey K. Pavlov[1], Christopher J. Mundy[6] and Philipp Assmy[1]*

[1] Norwegian Polar Institute, Fram Centre, Tromsø, Norway, [2] Trondheim Biological Station, Department of Biology, Norwegian University of Science and Technology, Trondheim, Norway, [3] Alfred Wegener Institute Helmholtz Centre for Polar and Marine Research, Bremerhaven, Germany, [4] Centre for Autonomous Marine Operations and Systems, Trondheim Biological Station, Department of Biology, Norwegian University of Science and Technology, Trondheim, Norway, [5] University Centre in Svalbard, Longyearbyen, Norway, [6] Centre for Earth Observation Science, University of Manitoba, Winnipeg, MB, Canada

The importance of newly formed sea ice in spring is likely to increase with formation of leads in a more dynamic Arctic icescape. We followed the ice algal species succession in young ice (≤0.27 m) in spring at high temporal resolution (sampling every second day for 1 month in May–June 2015) in the Arctic Ocean north of Svalbard. We document the early development of the ice algal community based on species abundance and chemotaxonomic marker pigments, and relate the young-ice algal community to the communities in the under-ice water column and the surrounding older ice. The seeding source seemed to vary between algal groups. Dinoflagellates were concluded to originate from the water column and diatoms from the surrounding older ice, which emphasizes the importance of older ice as a seeding source over deep oceanic regions and in early spring when algal abundance in the water column is low. In total, 120 taxa (80 identified to species or genus level) were recorded in the young ice. The protist community developed over the study period from a ciliate, flagellate, and dinoflagellate dominated community to one dominated by pennate diatoms. Environmental variables such as light were not a strong driver for the community composition, based on statistical analysis and comparison to the surrounding thicker ice with low light transmission. The photoprotective carotenoids to Chl *a* ratio increased over time to levels found in other high-light habitats, which shows that the algae were able to acclimate to the light levels of the thin ice. The development into a pennate diatom-dominated community, similar to the older ice, suggests that successional patterns tend toward ice-associated algae fairly independent of environmental conditions like light availability, season or ice type, and that biological traits, including morphological and physiological specialization to the sea ice habitat, play an important role in colonization of the sea ice environment. However, recruitment of ice-associated algae could be negatively affected by the ongoing loss of older ice, which acts as a seeding repository.

Keywords: sea-ice algae, young ice, Arctic, N-ICE2015, pigments, succession

OPEN ACCESS

Edited by:
Janne-Markus Rintala, University of Helsinki, Finland

Reviewed by:
Daria Martynova, Zoological Institute (RAS), Russia
Klaus Martin Meiners, Australian Antarctic Division, Australia

****Correspondence:***
Hanna M. Kauko
hanna.kauko@npolar.no;
hanna.kauko@alumni.helsinki.fi

Specialty section:
This article was submitted to Marine Ecosystem Ecology, a section of the journal Frontiers in Marine Science

Received: *23 March 2018*
Accepted: *18 May 2018*
Published: *06 June 2018*

Citation:
Kauko HM, Olsen LM, Duarte P, Peeken I, Granskog MA, Johnsen G, Fernández-Méndez M, Pavlov AK, Mundy CJ and Assmy P (2018) Algal Colonization of Young Arctic Sea Ice in Spring. Front. Mar. Sci. 5:199. doi: 10.3389/fmars.2018.00199

INTRODUCTION

The Arctic icescape is changing rapidly, which affects the whole marine system (Meier et al., 2014). Primary production or algal species dynamics and habitats are altered for example by a shorter ice season (Arrigo and van Dijken, 2015) and likely by the reduction of multi-year ice (Lange et al., 2017; Olsen et al., 2017b). The sea ice is also more dynamic and vulnerable to wind forcing (Itkin et al., 2017), which can alter the habitat of ice algae. In the Arctic, ice algae contribute to the annual primary production to a varying degree (<1–60%) depending on season and region (Gosselin et al., 1997; Rysgaard and Nielsen, 2006; Fernández-Méndez et al., 2015). Based on modeling, an estimated 7.5% of annual Arctic primary production is attributed to ice algae (Dupont, 2012). Ice algae also constitute a highly concentrated food source early in the growth season (e.g., Søreide et al., 2010), and thus are a crucial part of Arctic marine foodwebs.

Algae are incorporated into sea ice when it forms through, for example, sieving by growing (Syvertsen, 1991; Lund-Hansen et al., 2017) or rising ice crystals (Reimnitz et al., 1990). Waves, currents, vertical mixing, and other physical factors enhance the entrainment: encounter rates between particles and ice crystals are increased by mixing of crystals into water and water movement through forming ice (Weissenberger and Grossmann, 1998) and along irregularities in bottom-ice topography(Krembs et al., 2002; Lund-Hansen et al., 2017). Frazil ice, which is formed under turbulent conditions (Petrich and Eicken, 2010), was observed to have higher foraminifera abundance than congelation ice (Dieckmann et al., 1990). Also active migration of motile species, and growth even under low irradiances contribute to inhabiting the ice and may be important under calm conditions (Melnikov, 1995; Weissenberger, 1998). In field studies, ice formation has been observed to preferentially retain larger cells (Gradinger and Ikävalko, 1998; Riedel et al., 2007; Rózanska et al., 2008). Further, exopolymeric substances produced by the algae make the cell surfaces sticky and may enhance their incorporation into the ice (Meiners et al., 2003; Riedel et al., 2007).

The main sources of algal species in newly formed sea ice are cells in the water column (pelagic), the sea floor (benthic), or the surrounding older ice (sympagic). Some studies have compared sea ice and water column communities during autumn freeze-up and concluded that the communities differ already during the initial phase of ice formation, suggesting that the seeding community was present in the water column only intermittently (Tuschling et al., 2000; Werner et al., 2007; Niemi et al., 2011). Differences in sea ice communities were observed based on proximity to land i.e., benthic habitats (Ratkova and Wassmann, 2005). Olsen et al. (2017b) suggested that multi-year ice can act as a seed repository, harboring algal cells from a previous growing season that can colonize new ice. In a Greenland fjord the bottom ice algal bloom was formed via spring colonization by phytoplankton, facilitated by increased surface roughness in growing ice crystals (Lund-Hansen et al., 2017). The algal assemblage in new sea ice (ice thickness $\leq$0.03 m) from the Beaufort Sea was similar to the one in the water column, but became different in older stages of ice (Rózanska et al., 2008). Both ice melting and freezing seem to trigger increased species exchange between the water column and sea ice (Hardge et al., 2017). Thus the ice algal community apparently can have many origins, but their relative importance for ice algal recruitment is still not well-known.

Community development can be investigated in light of characteristics of the species present and environmental conditions affecting the species. Further, the number of observed species and how evenly abundance is distributed among the species describe communities (Peet, 1974). Succession refers to changes in species composition and abundance over time. Concepts of species succession (reviewed in McCook, 1994) are derived from work with plant and rocky bottom communities and aim to explain the mechanisms that lead to a certain type of community after disturbance of a site, such as modification of the site by early-colonizing species.

Previous sea ice colonization studies of new and young ice have been conducted in autumn or winter, or in mesocosm experiments (see references above). However, with the ongoing changes in the Arctic icescape, new ice formation during the main algal growth season will possibly increase and offer new habitats for the sympagic communities. Contrary to autumn, light intensity increases during spring, and in spring young ice is a high-light environment compared to older ice with thick snow cover (Kauko et al., 2017), or new ice formed in autumn or winter. Algae in general face an ever-fluctuating light climate, altered e.g., by changing cloud and snow covers. To balance incoming irradiance with the capacity of the photosynthetic apparatus, algae need photoacclimation mechanisms such as adjustment of the cellular pigment pool (reviewed in Brunet et al., 2011). In response to increasing irradiance, changes in the fraction of light-harvesting pigments (LHP) and photoprotective carotenoids (PPC) occur. The latter do not channel the absorbed energy to photosynthesis but dissipate it as heat, thus protecting the photosystems from excess light. The ratios of PPCs to LHP give information on physiology and light history of cells. In addition, many LHP are specific to certain algal groups and can serve as a proxy for taxonomic composition (reviewed in Jeffrey et al., 2011), including those of ice algal communities (Alou-Font et al., 2013).

Increasing light availability due to sea ice retreat has been shown to alter phytoplankton dynamics in the Arctic Ocean using ocean color remote sensing (Arrigo and van Dijken, 2015), but similar large-scale studies are not yet possible for the sea ice habitat due to lack of suitable methods. We have made an effort to understand physical and biological processes in a high-light, young sea ice environment in a refrozen lead during Arctic spring. In a previous study, we have shown that the biomass in the young ice in the refrozen lead was similar to the surrounding older and thicker ice while the light climate was very different, and that algae in the young ice had high concentrations of ultraviolet (UV)-protecting pigments (Kauko et al., 2017). In this paper, we investigate the colonization of the young ice by ice algae and how that relates both to the possible seeding sources, and to the light environment and other environmental conditions. We further examine light acclimation by investigating the photoprotective carotenoids synthetized by

the algae. The objectives of the study were to describe the succession of ice algal species and algal pigment concentrations in young sea ice formed in spring, identify the most important drivers for the algal succession, and compare the young ice community with the surrounding older ice and water column to identify the seeding source.

METHODS

Field Sampling

Young ice (thickness 0.17–0.27 m; Petrich and Eicken, 2010) in a recently refrozen lead was sampled during the Norwegian young sea ICE (N-ICE2015) expedition in the pack ice north of Svalbard at 80.5–82.4°N (**Figure 1A**) in spring 2015 (Granskog et al., 2016, 2018). Ice coring was conducted from early May, a few days after ice reformed over the whole lead, to the beginning of June (Supplementary Table 1) when the ice in the lead broke up. Ice cores for biological samples were first collected close to the edge of the lead (4 and 6 May) and thereafter 13 times (7 May−3 June; approximately every second day) along a transect (five coring sites, three cores pooled at each site) toward the center of the lead (**Figure 1B**). On subsequent sampling days, the transect was moved 2–3 m to the side in order to sample undisturbed ice. Ice cores were melted onboard overnight in the dark at room temperature and unbuffered (Rintala et al., 2014). After 18 May, the ice cores were divided into two sections, where the bottom section was always 0.10 m thick and the top section constituted the remaining part of the core (0.09–0.17 m thick). Salinity of the melted ice cores was measured with a WTW Cond 3110 probe (WTW Wissenschaftlich-Technische Werkstätten GmbH, Weilheim, Germany). Brine salinity was calculated from ice temperature (Cox and Weeks, 1986; Leppäranta and Manninen, 1988). The method for ice core stratigraphy studies is described in Olsen et al. (2017b) and based on Lange (1988). Incoming and ice-transmitted planar downwelling spectral irradiance was measured with two Ramses ACC-VIS spectroradiometers (TriOS Mess- und Datentechnik GmbH, Rastede, Germany) for the wavelength range 320–950 nm (irradiance data are available from Taskjelle et al., 2016). Sampling on the lead is described in detail in Kauko et al. (2017) and biochemical and basic physical data can be found in Assmy et al. (2017a). First-year ice (FYI) and second-year ice (SYI) were sampled weekly and melted by the same procedure (Olsen et al., 2017b). Two cores were pooled and the bottom 0.20 m were cut into 0.10 m long sections and the remaining ice core into 0.20 m sections (all SYI and first FYI coring) or two equal sections (rest of FYI). The water column was sampled via CTD rosettes (one operated from the ship and one through a hole on the adjacent ice floe) twice per week (Assmy et al., 2017b).

Laboratory Methods

From the melted ice core sections 190 mL samples were fixed with glutaraldehyde and 20% hexamethylenetetramine-buffered formaldehyde at final concentrations of 0.1 and 1%, respectively. The samples were stored dark and cool in 200 mL brown glass bottles. Sub-samples were settled in 10 mL Utermöhl sedimentation chambers (HYDRO-BIOS©, Kiel, Germany) for 48 h. Subsequently, protists were identified and counted on a Nikon Ti-U inverted light microscope by the Utermöhl method (Edler and Elbrächter, 2010). Cells were counted in transects. At least 50 cells of the dominant species were counted in each sample (error of ±28% according to Edler and Elbrächter, 2010). Microscopy count data can be found in Olsen et al. (2017a). Abundances (cells L^{-1}) were converted to biomass (mg carbon m^{-3}) using biovolume calculations (Hillebrand et al., 1999) and carbon conversion factors (Menden-Deuer and Lessard, 2000).

Additional samples from the melted ice cores were taken to analyze the algal pigment composition, including diagnostic marker pigments and pigments related to the xanthophyll cycle. For this 100–300 mL melted ice was filtered through 25 mm GF/F filters and shock frozen in liquid nitrogen. The samples were stored at −80°C until analysis. Pigments were analyzed by reverse-phase high performance liquid chromatography (HPLC) using a VARIAN Microsorb-MV3 C8 column (4.6 × 100 mm) and HPLC-grade solvents (Merck), a Waters 1,525 binary pump equipped with an auto sampler (OPTIMAS™), a Waters photodiode array detector (2,996) and the EMPOWER software. For further details see Tran et al. (2013). The ice core samples were melted overnight in darkness and therefore the ratios of the pigments involved in the xanthophyll cycle do not strictly resemble the sampling moment, but together represent a pool of photoprotective carotenoids and are here reported as a sum concentration. HPLC data can be found in Assmy et al. (2017a). An overview of marker pigments and chemotaxonomy can be found in Jeffrey et al. (2011), Higgins et al. (2011), and in the data sheets of Roy et al. (2011). A review of pigments involved in the photoacclimation process can be found in Brunet et al. (2011).

Statistical Methods

Statistical analyses were performed with R (R Core Team, 2017). Data from young ice (including all coring sites and vertical sections, 110 samples) were compared to water column data down to 50 m (23 April−4 June, 69 samples from 17 CTD casts) and to data from the surrounding SYI/FYI (all vertical sections, 22 April−5 June, 74 samples from 11 cores).

Non-metric multidimensional scaling (NMDS), performed with the function *isoMDS* in the MASS package (Venables and Ripley, 2002), was used to investigate the algal community similarity between the different environments based on algal abundance (counts). The count data were first square-root transformed and Bray-Curtis dissimilarity was used for the scaling (calculated with the vegan package; Oksanen et al., 2017).

Shannon's diversity indices (H) were calculated for the species count data with the function *diversity* in the vegan package, defined as $H = -\text{sum}\ (p_i \ln p_i)$, where p_i is the proportion of individuals of species i. Pielou's species evenness (J) was calculated as $J = H/H_{max}$, where H_{max} is a maximum diversity index. Further, $H_{max} = \log_2(S)$, where S is the species richness (species number).

To relate the ice algal species abundance in the young ice to environmental variables, canonical correspondence analysis (CCA; suitable for count data) was performed and additionally function *envfit* was used to fit the environmental variables on NMDS analysis of the young ice. Both were performed with the

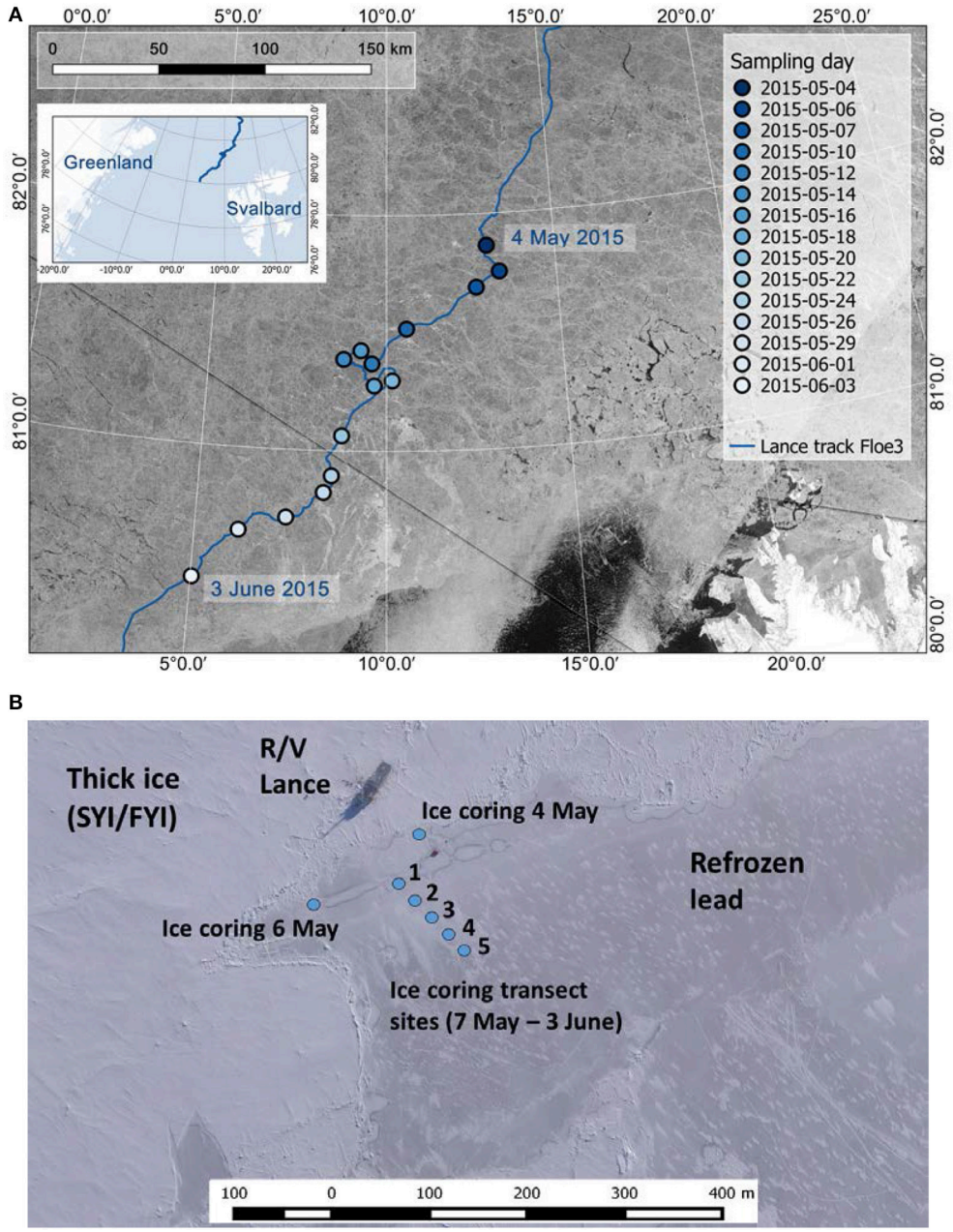

FIGURE 1 | (A) Study area with the drift trajectory of R/V Lance and sampling location on each sampling day. **(B)** Ice coring locations on the young ice in the lead. In **(A)** satellite image (taken on 25 May 2015) source: RADARSAT-2 image provided by NSC/KSAT under the Norwegian-Canadian RADARSAT agreement. RADARSAT-2 Data and Products © MacDonald, Dettwiler and Associates Ltd (2013). All Rights Reserved. RADARSAT is an official mark of the Canadian Space Agency. Map created by the Norwegian Polar Institute/Max König. Aerial image in **(B)** (taken on 23 May 2015): Vasily Kustov and Sergey Semenov (Arctic and Antarctic Research Institute, St. Petersburg, Russia). Maps modified from Kauko et al. (2017).

vegan package and all samples (110) and species were included in the analysis. Environmental variables included snow thickness (indicative also for light intensity) and bulk salinity. Surface water column nitrate concentration (silicate did not change over the sampling period) correlated strongly with bulk salinity of the sea ice and was excluded from further analysis. Bulk salinity therefore also represents the water column nitrate dynamics. There were unfortunately no nutrient samples from the lead ice. Likewise, temperature values, which enable calculation of brine salinity, were not available for the whole period, thus bulk salinity was used. Ice thickness could indicate ice melting events and therefore changes in the physical habitat, but because of strong correlation with snow thickness it was not included in the analysis. The variable snow thickness thus represents several

environmental variables that co-vary, including average in-ice irradiance of the past 48 h, which was calculated for the sampling events. The environmental data were standardized prior to usage by subtracting the mean and then dividing by standard deviation.

The function *anosim* in the vegan package was used to test if variation in the count data was higher between the sampling days than between the ice coring sites on the young ice, to justify the use of averages of the five coring sites.

In time series figures for the days when ice cores were sectioned in two, first a volumetric average of the ice core bottom and top section values (biomass and pigment concentrations) was calculated, and thereafter an average of the five ice coring sites. For 4 and 6 May, averages could be calculated from four and two ice cores, respectively. In the case of pigment to Chl *a* ratios (w: w), the ratio was calculated before averaging the ice core bottom and top sections.

RESULTS

Environmental Conditions

A lead next to the research vessel Lance opened on 23 April. Within the next 3 days, the lead was opening and closing, until it got gradually frozen over by 1 May (width ∼400 m). New ice formed first on the side closest to the vessel, on which the ice coring transect was located. Initially, the edge of the lead was characterized by windblown slush and small ice pieces that congealed to a solid ice cover. By the time of sampling, the ice had reached young ice stage and was thick enough to safely work on. The first ice cores for physical measurements were taken on 1 May at the very edge of the lead (same site as on 4 May; **Figure 1B**). At this site on 1 May, the ice was composed of 0.09 m granular ice in the top half and 0.07 m columnar ice in the bottom. Ice temperatures ranged from −2.0 to −4.2°C and bulk salinities from 9.3 to 10.0. On the site that was sampled on 6 May, the ice consisted of 0.03 m granular ice at the top and 0.14 m columnar ice below. Temperatures ranged from −2.1 to −4.5°C and bulk salinities from 10.3 to 14.9. Brine salinity was up to 78.9 at 0.03 m below the ice core top. For the ice coring transect (7 May onwards; **Figure 1B**), ice structure and other physical properties are reported in detail by Kauko et al. (2017). In short, ice thicknesses ranged from 0.17 to 0.27 m, and increased until 20 May after which a reduction was observed. Sites 2 and 3 had the highest proportion of granular ice (0.17 m on 26 May, compared to 0.05–0.08 m columnar ice) and sites 1 and 5 the lowest (0.04–0.05 m granular ice on 26 May, compared to 0.17–0.195 m columnar ice). Snow thicknesses ranged from 0.01 to 0.06 m. Bulk salinity decreased on average (average of 5 sites) from 7.8 to 5.3 during the sampling period and brine salinities ranged from 23.9 to 52.2 (18 May−1 June). Under-ice downwelling irradiance E_d(PAR) in the photosynthetically active radiation range (PAR, 400–700 nm) was on average 114 μmol photons m^{-2} s^{-1} and ranged from 30 to 350 μmol photons m^{-2} s^{-1} for the period from 12 May to 3 June.

The surrounding ice floe was a composite ice floe consisting of SYI and FYI with a modal ice thickness of 1.2 m and modal snow thickness of 0.45 m (Rösel et al., 2018). Ice temperature and other physical properties are described in Olsen et al. (2017b). Snow depths at the SYI coring site ranged from 0.40 to 0.50 m and at the FYI coring site they were 0.20 m (Olsen et al., 2017b). Irradiance was an order of magnitude lower under FYI than under young ice, and under SYI compared to FYI, with measured irradiances of 0.1–1 μmol photons m^{-2} s^{-1} under SYI and calculated irradiances of 1–20 μmol photons m^{-2} s^{-1} under FYI (Olsen et al., 2017b). Oceanographic conditions of the study area, with Polar Surface Water in the surface, are described in Meyer et al. (2017). Bottom depths during the young ice sampling period varied between 600 and 1,932 m, with shallowest depths occurring toward the end of the study when the ice floe drifted over the Yermak Plateau.

Ice Algal Succession

Temporal Trends in Young Ice

In total, 120 taxa (including e.g., different size categories of flagellates, but excluding cysts) comprising 80 species (including protists identified to species or genus level) were recorded in the young ice samples over the study period. The taxa for all environments are listed in Supplementary Table 2. The community in young ice comprised 54 diatom taxa (45 species), 20 dinoflagellate taxa (15 species), 35 flagellate taxa (15 species), and 11 ciliate taxa (5 species). In this section and section Temporal Trends in Xanthophyll Cycle Pigments, presented values are averages of four ice cores (4 May), two ice cores (6 May), or five coring sites (unless site is specified) where three cores were pooled at each site (transect sampling 7 May onwards; see map in **Figure 1B**). For 18 May and onwards, volumetric averages of ice core bottom and top section values are shown (see section Methods).

In the beginning of the study period, the young ice protist biomass (mg C m^{-3}) and abundance were largely dominated by the ciliate *Mesodinium rubrum* and the cryptophyte chloroplasts (called symbionts hereafter) it had incorporated (**Figure 2** and Supplementary Figure 1). Ciliate cells were presumably damaged during sampling causing release of the symbionts. From 12 May onwards diatoms and dinoflagellates became more prevalent, and together made up almost 70% of the biomass on 12 May. Biomass of ciliates and symbionts decreased thereafter, except on 16 and 20 May. Both flagellates and dinoflagellates biomass increased from early May, but diatoms exponentially increased to over 90% of the total biomass by 3 June, whereas dinoflagellates generally comprised <10% of the biomass. Maximum diatom biomass was 600 mg C m^{-3} on 1 June.

Fucoxanthin, indicative of diatoms, was the most abundant chemotaxonomic marker pigment and increased over the sampling period from 0.01 to 1.26 mg m^{-3} (**Figure 3B**). In terms of marker pigment to Chl *a* ratios, fucoxanthin, and peridinin (a marker for dinoflagellates) showed a contrasting picture during the transect sampling (**Figures 4A,B**). Initially, the peridinin to Chl *a* ratio was high at 0.22 on 7 May, and declined to 0.01 on 1 June. The fucoxanthin to Chl *a* ratio showed the opposite trend, increasing from 0.04 to 0.27.

Species succession was also observed within the diatom community. At the beginning of the transect sampling (7 May onwards) centric diatoms were dominant (**Figure 5A**) and comprised more than 70% of the diatom biomass until

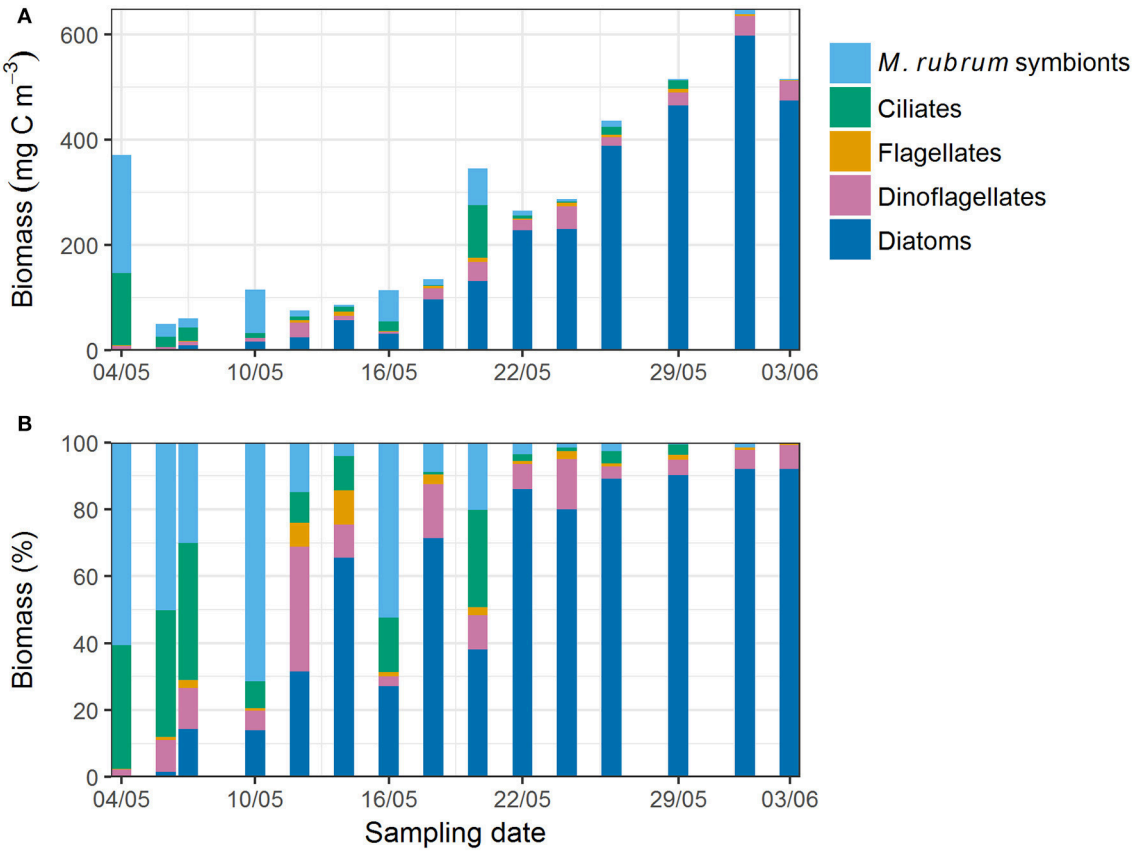

FIGURE 2 | (A) Absolute and **(B)** relative protist biomass in young ice estimated from microscopy counts.

14 May. From 22 May onwards, centric diatoms generally accounted for <60% of diatom biomass, while pennate diatoms increased and dominated (>80% of diatom biomass) from 29 May onwards. The most prevalent taxa among the centric diatoms were *Porosira glacialis* and *Thalassiosira gravida/antarctica* var. *borealis*, and among the pennate diatoms *Nitzschia frigida/neofrigida* (**Figure 6A**), *Fragilariopsis cylindrus* (**Figure 6B**), *Navicula* spp. (**Figure 6C**), and *Pseudo-nitzschia* spp. *Navicula pelagica* appeared in the samples after 18 May. *Fragilariopsis cylindrus* was especially abundant in the middle of the sampling period in terms of cell numbers (Supplementary Figure 2a). On the last two sampling days, *N. frigida/neofrigida* accounted for the highest biomass (ca. 30%) of any individual species.

Cysts accounted for more than 60% of the dinoflagellate biomass on 9 of the 15 sampling days. Cysts of *Polarella glacialis* (**Figure 6E**) occurred throughout the sampling period (**Figure 5B**, Supplementary Figure 2b) and comprised more than 90% of the dinoflagellate biomass on 3 June (35 mg C m^{-3}). Besides cysts, *Gymnodinium* spp. and unidentified dinoflagellates in the size range 10–20 μm were the most prevalent groups among the dinoflagellates.

Unidentified flagellates in the size categories 3–7 and 7–10 μm comprised more than 50% of the flagellate biomass on most sampling days (**Figure 5C**). Prymnesiophytes, consisting of mainly unidentified Coccolithales, peaked on 14 May but were observed on most sampling days. *Phaeocystis pouchetii* was observed from 16 May onwards to a varying degree (biomass <1 mg C m^{-3}). Prasinophytes (**Figure 6F**) and cryptophytes (other than the *M. rubrum* symbionts) were present at low biomass on most sampling days. Chlorophytes were observed only on 4 sampling days. Statocysts of the chrysophyte algae *Dinobryon* sp. were present especially in the latter half of the sampling period (Supplementary Figure 2c).

For Chl *b*, which is found in chlorophytes, prasinophytes, and euglenophytes, concentrations were generally low, up to 0.11 mg m^{-3} on 26 May (**Figure 3D**) and before the transect sampling on 4 May (not shown). The Chl *b* to Chl *a* ratio was highest on 18 May (0.05; **Figure 4C**) and before the coring transect sampling on 6 May (0.07; Supplementary Figure 3c). Alloxanthin (a cryptophyte marker pigment) concentration was at times high: up to 1.72 mg m^{-3} on site 5 on 20 May (**Figure 3E**), and 1.5 mg m^{-3} in one of the ice cores on 4 May. The alloxanthin to Chl *a* ratio was highest on 6 May (Supplementary Figure 3d). Also gyroxanthin diester (found mainly in dinoflagellates) and β,ε-carotene (α-carotene; found in cryptophytes) had marked peaks on site 5 on 20 May (0.15 and 0.84 mg m^{-3}, respectively; **Figures 3F,G**) and before the transect sampling, but otherwise

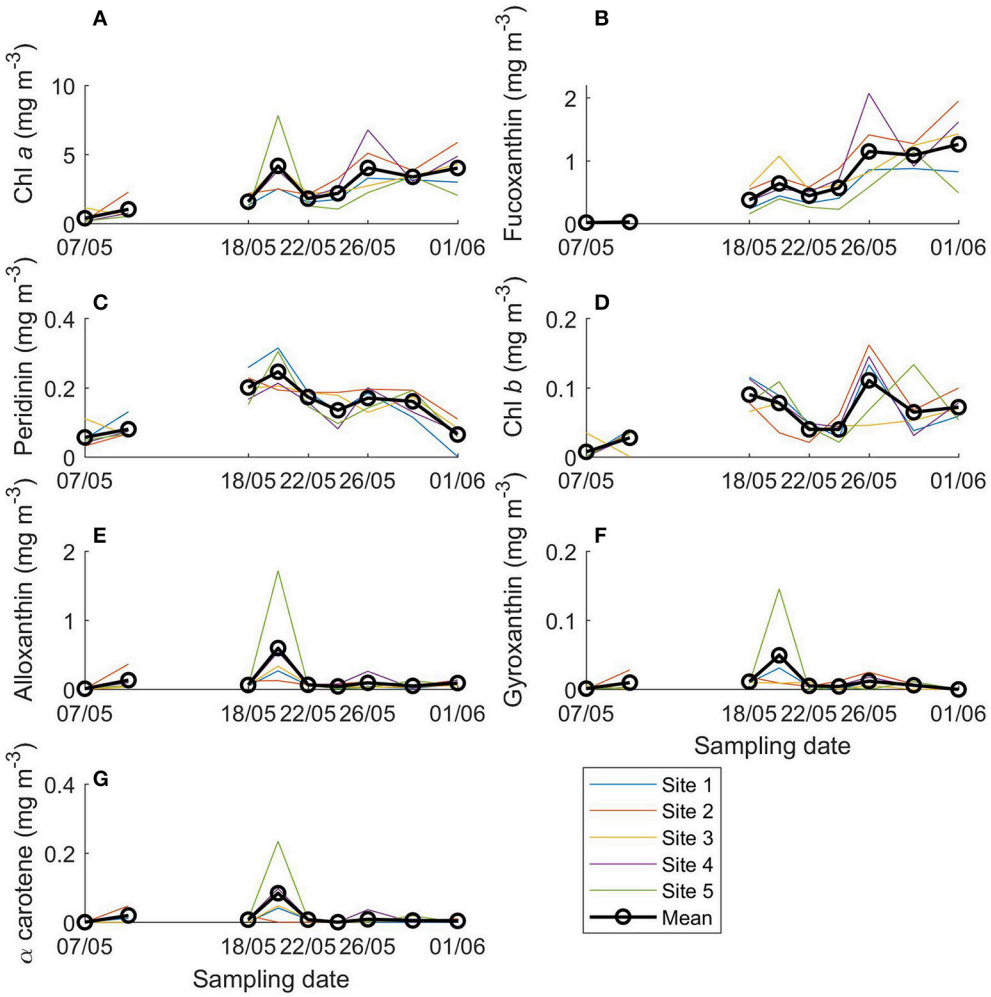

FIGURE 3 | Concentrations of main algal pigments in young ice during the ice coring transect study (7 May onwards). **(A)** Chlorophyll (Chl) *a*, **(B)** fucoxanthin, **(C)** peridinin, **(D)** chlorophyll *b*, **(E)** alloxanthin, **(F)** gyroxanthin diester, and **(G)** α carotene.

had low concentrations during the transect sampling period. The patterns were similar for ratios of these pigments to Chl *a*, but the ratios were low after 24 May (**Figures 4D–F**). Other pigments are shown in Supplementary Figures 4–6 (they were low in concentration or without taxonomic information). No chlorophyll degradation products such as chlorophyllide *a* (algae senescence) or phaeopigments (e.g., phaeophorbide *a*, indicative of grazing) were detected in the samples.

Differences Between Ice Core Bottom and Top Sections in Young Ice

In the previous paragraphs, values were reported for the ice core bottom and top section together (volumetric mean of the values) to be able to investigate the sampling period as a whole (ice core sectioning started on 18 May). In general, abundance and biomass of the species and groups were higher in the ice core bottom sections than in top sections. There were some exceptions, most notably for cysts of the dinoflagellate *Polarella glacialis* and the *Dinobryon* sp. statocysts (**Figure 7**). In terms of relative biomass (Supplementary Figure 7), centric diatoms had a higher contribution in the ice core top sections than in bottom sections. Pennate diatoms had a higher contribution in bottom sections than in top sections, although these also increased and dominated over time in the top sections. For flagellates and dinoflagellates, biomass was low and patterns were not as clear (except for the cysts). Pigment concentrations were likewise in general higher in bottom sections than in top sections. Differences in pigment to Chl *a* ratio between the bottom and top sections are shown in Supplementary Figures 3, 6. Fucoxanthin had higher ratios to Chl *a* in the bottom sections. Gyroxanthin diester, α-carotene, dinoxanthin, and neoxanthin were absent from the top sections, whereas Chl c_3 was only found in top sections.

Comparison of Community Structure Between Habitats

Ice algal community patterns in SYI and FYI are described in Olsen et al. (2017b) and reveal the dominance of pennate

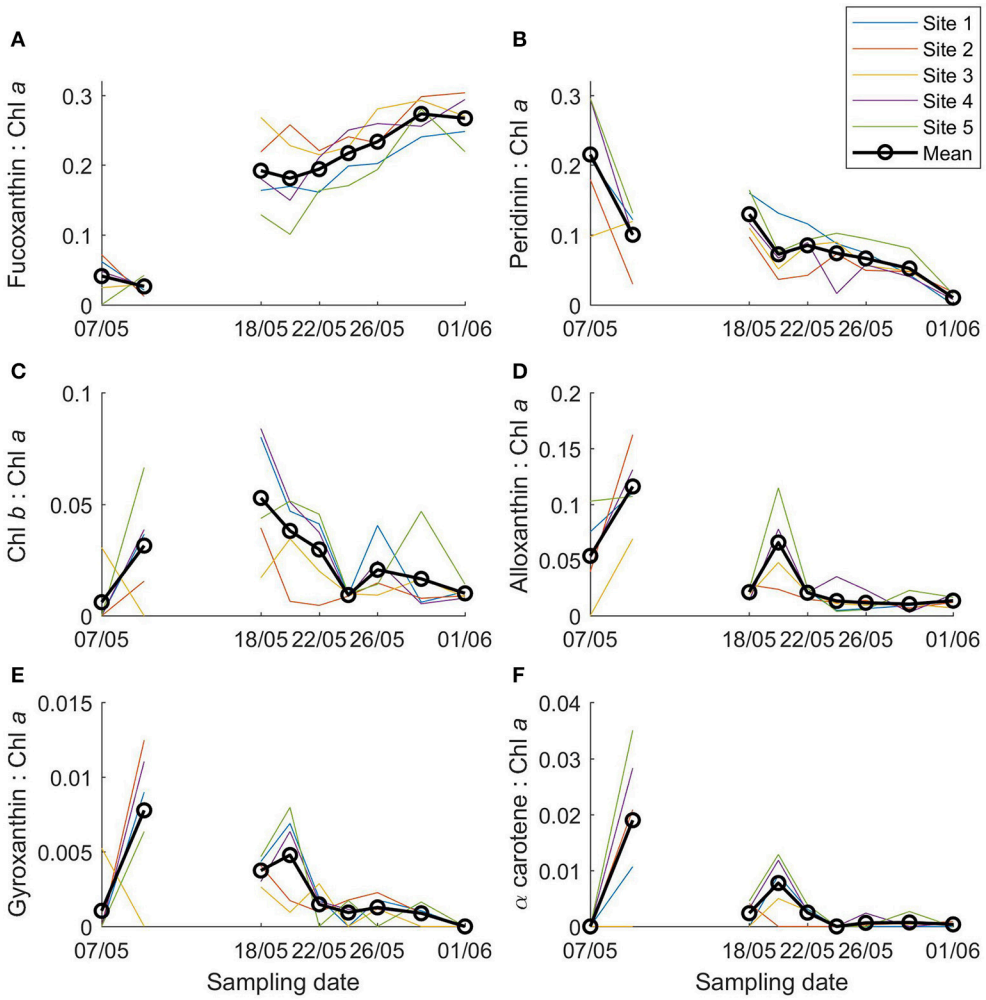

FIGURE 4 | Ratios of main algal pigments to Chl *a* in young ice during the ice coring transect study (7 May onwards). **(A)** Fucoxanthin: Chl *a*, **(B)** peridinin: Chl *a*, **(C)** Chl *b:* Chl *a*, **(D)** alloxanthin: Chl *a*, **(E)** gyroxanthin diester: Chl *a*, and **(F)** α carotene: Chl *a*.

diatoms, especially *N. frigida*, and show that resting cysts were also prominent. In the water column, Chl *a* concentration was low (<0.5 mg m^{-3}) until 25 May when we encountered an under-ice phytoplankton bloom (maximum Chl *a* concentration 7.5 mg m^{-3}) dominated by the haptophyte *P. pouchetii* (Assmy et al., 2017b).

The count data are available in Olsen et al. (2017a). These show that during the early sampling period (22 April−7 May), dinoflagellate abundance in the water column was on average 14-fold higher (average ± standard deviation 1,391 ± 1,217%) compared to diatom abundance. In the surrounding SYI (no FYI sampled at this time period), dinoflagellate abundance was one fourth (24 ± 53%) of diatom abundance. In SYI, 42 diatom, 8 dinoflagellate, and 16 other flagellate taxa (taxonomic level ranging from single species to size categories of flagellates) were identified during this time. In the water column, 8 diatom, 17 dinoflagellate, and 12 other flagellate taxa were identified (Olsen et al., 2017a).

In the early young ice samples (4 May−7 May), 15 diatom (11 of them being pennate species), 12 dinoflagellate, and 9 other flagellate taxa were found, but most taxa were present only in one or two samples. Of these taxa we identified those that were also found in either the water column (samples from 26 April−5 May), SYI (30 April and 7 May) or in both habitats during the re-freezing of the lead and early sampling. Of these, nearly all the dinoflagellates were only found in the water column except for three taxa that were in addition found in four SYI samples. Cysts were found only in SYI and not in the water column. All diatoms were found only in SYI except for two taxa that were also found in one water column sample each, and *N. frigida/neofrigida* in several samples. *N. frigida/neofrigida* was however 1,500 times more abundant in SYI than in the water column.

Temporal Trends in Xanthophyll Cycle Pigments

The photoprotective pigments diadinoxanthin and diatoxanthin increased in both concentration and ratio to Chl *a* over the sampling period, especially compared to the early transect sampling (7 and 10 May; **Figures 8A,C**). The combined concentration increased from 0.01 to 0.87 mg m^{-3} and the ratio

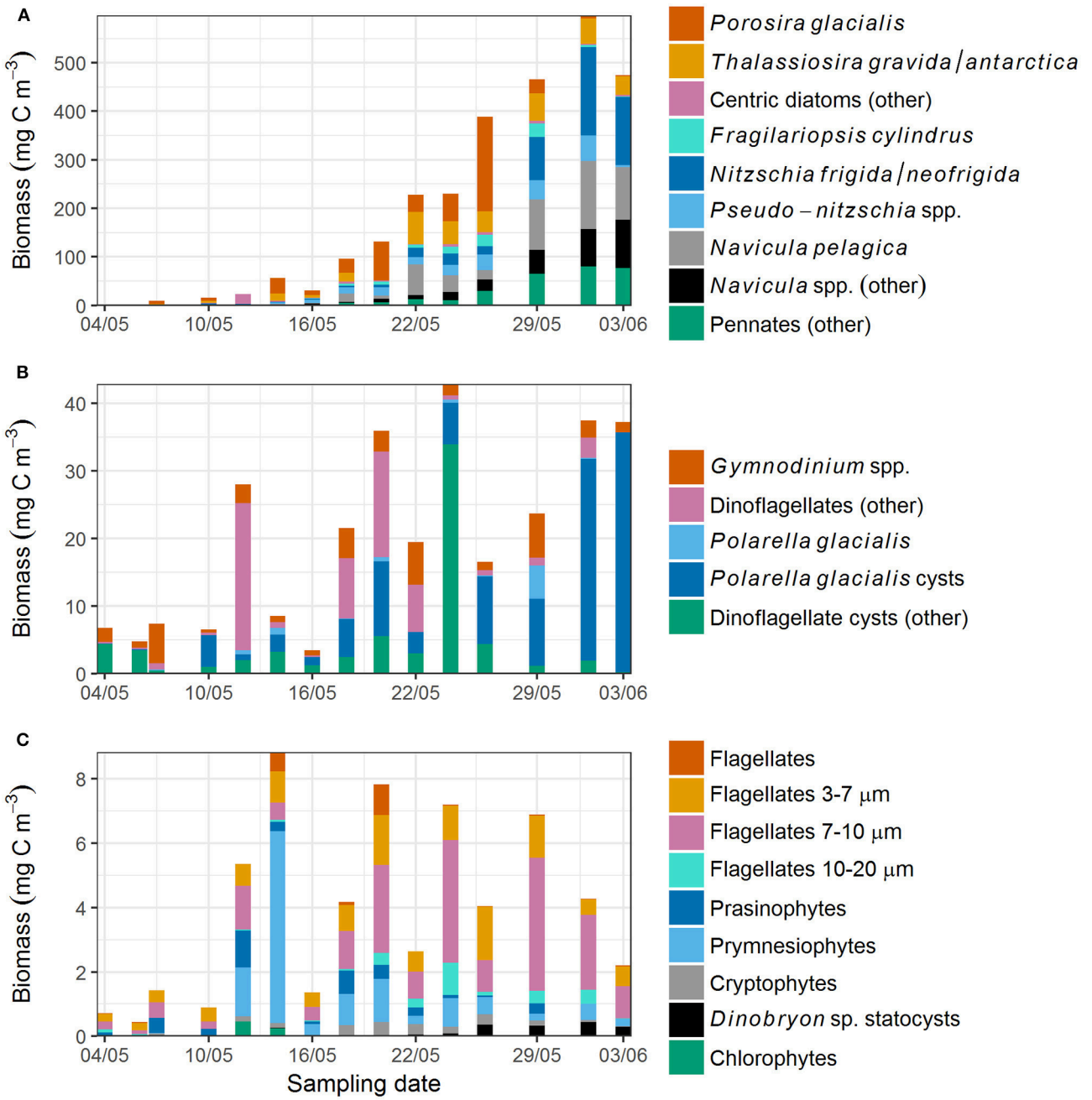

FIGURE 5 | (A) Diatom, **(B)** dinoflagellate, and **(C)** flagellate biomass in young ice. In **(A)**, *Porosira glacialis* and *Thalassiosira gravida/antarctica* are centric diatoms, and the remaining species are pennate diatoms. Note the varying y-axis scale.

of diadinoxanthin+diatoxanthin to Chl *a* from 0.05 to 0.20 over the transect sampling period. Ratios were similar between the ice bottom and top sections (average ± standard deviation for bottom sections 0.19 ± 0.06 and for top sections 0.20 ± 0.07; Supplementary Figure 8a).

Violaxanthin+zeaxanthin concentration and ratio to Chl *a* varied greatly with peaks around 6, 18–20 and 24–29 May (**Figures 8B,D**, Supplementary Figure 8b). The concentration was on average below 0.03 mg m^{-3} and the ratio to Chl *a* was mostly below 0.02.

Statistical Analysis of Community Similarity and Succession

Each habitat—young ice, SYI/FYI, and water column—formed distinct clusters in the NMDS analysis investigating community similarity (**Figure 9**). In the young ice, a temporal shift in species composition is evident (indicated by the coloring) and the samples approach the SYI/FYI group. Ice core bottom and top section samples are on different sides of the young ice samples group (symbols not shown). For thick ice or water column, neither consistent

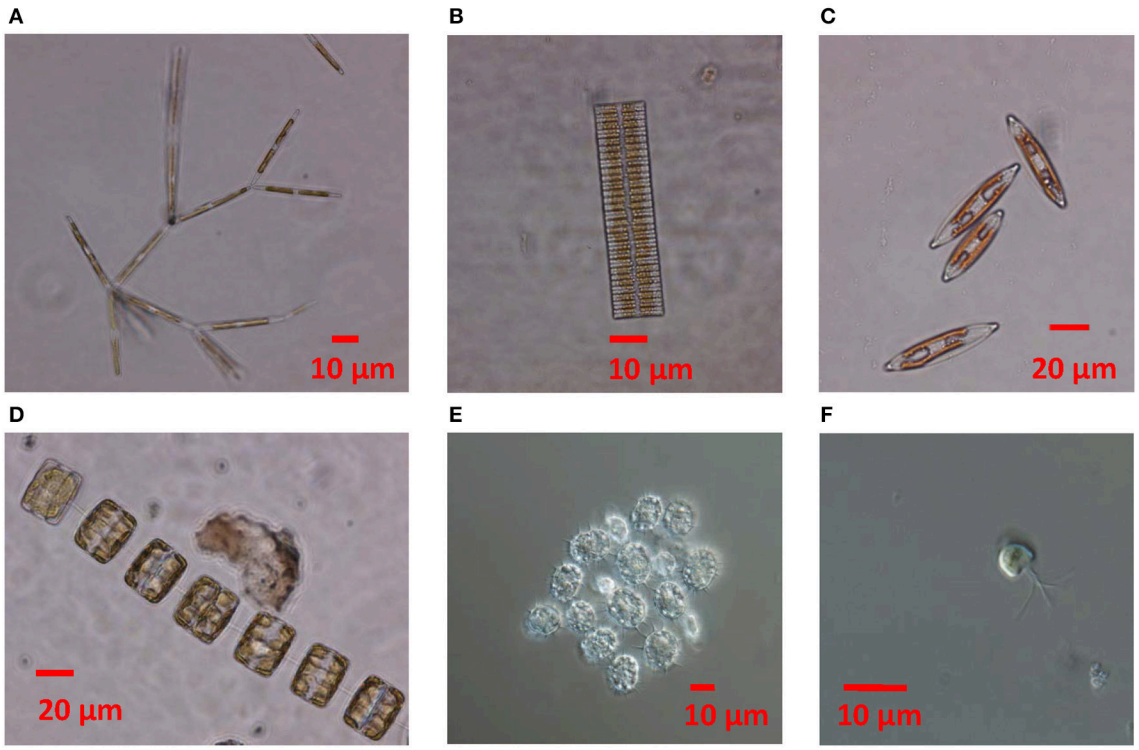

FIGURE 6 | Micrographs showing **(A)** *Nitzschia frigida*, **(B)** *Fragilariopsis cylindrus*, **(C)** *Navicula* sp., **(D)** *Thalassiosira* sp., **(E)** cysts of the dinoflagellate *Polarella glacialis*, **(F)** prasinophyte *Pyramimonas* sp.

vertical (symbols not shown) nor temporal patterns were seen.

The range of Shannon's diversity indices, calculated from species abundance data, was similar in all three environments: 0.01–2.73, 0–2.72, and 0–2.86 for young ice, SYI/FYI and water column, respectively (Supplementary Table 3). When SYI and FYI were treated separately, SYI had a lower diversity range of 0.32–2.46. The young ice had the lowest indices at the beginning of the sampling period whereas the water column samples with lowest diversity were from the latter half of the period (Supplementary Figure 9a). In the SYI/FYI samples, no clear temporal pattern was visible in the diversity index. In general, there was large variation in the indicators (species diversity, richness, and evenness), but species richness increased over time in all habitats (Supplementary Figures 9c,d) and evenness decreased in the water column (Supplementary Figures 9e,f). When the taxon *M. rubrum* symbionts was removed from the dataset (their abundance was likely affected by bursting of *M. rubrum* cells during sampling), evenness had a decreasing trend also in young ice. Furthermore, the early low diversity indices of the young ice disappeared (Supplementary Figure 9b) and the range shifted to 0.84–2.74. Diversity in the young ice was not significantly higher in the ice core top sections than in the bottom sections after removal of the symbionts.

The environmental variables snow thickness and bulk ice salinity (representing several co-varying environmental variables, see section Methods) accounted for 17% of the variance in ice algal abundance in the young ice (CCA in Supplementary Figure 10). The first axis accounted for 16.7% and the second for 0.6% of the variation. The variable bulk salinity aligned close to the first axis and snow thickness close to the second axis. The first axis is parallel to the temporal gradient of the samples (indicated by color in the figure). When the environmental variables were fitted on unconstrained ordination (NMDS for young ice), the patterns were similar and bulk salinity was significantly correlated but snow thickness was not significant.

The sampling days in the young ice differed significantly from each other ($p = 0.001$, $R = 0.41$) for the algal count data, whereas the ice coring sites did not ($p = 0.98$, $R = -0.02$). It is therefore valid to use averages of the coring sites to show the temporal patterns in the young ice biomass and abundance figures.

DISCUSSION

Origin of the Young Ice Community

When new ice forms, cells present in the water column are incorporated into the sea ice. Previous studies have however suggested that not only phytoplankton but also benthic habitats and possibly surrounding ice are sources of ice algae (Ratkova and Wassmann, 2005; Olsen et al., 2017b). In our study, the most probable seeding sources were the water column and surrounding SYI/FYI communities, since the bottom depths at the time of re-freezing were between 1,300 and 2,000 m.

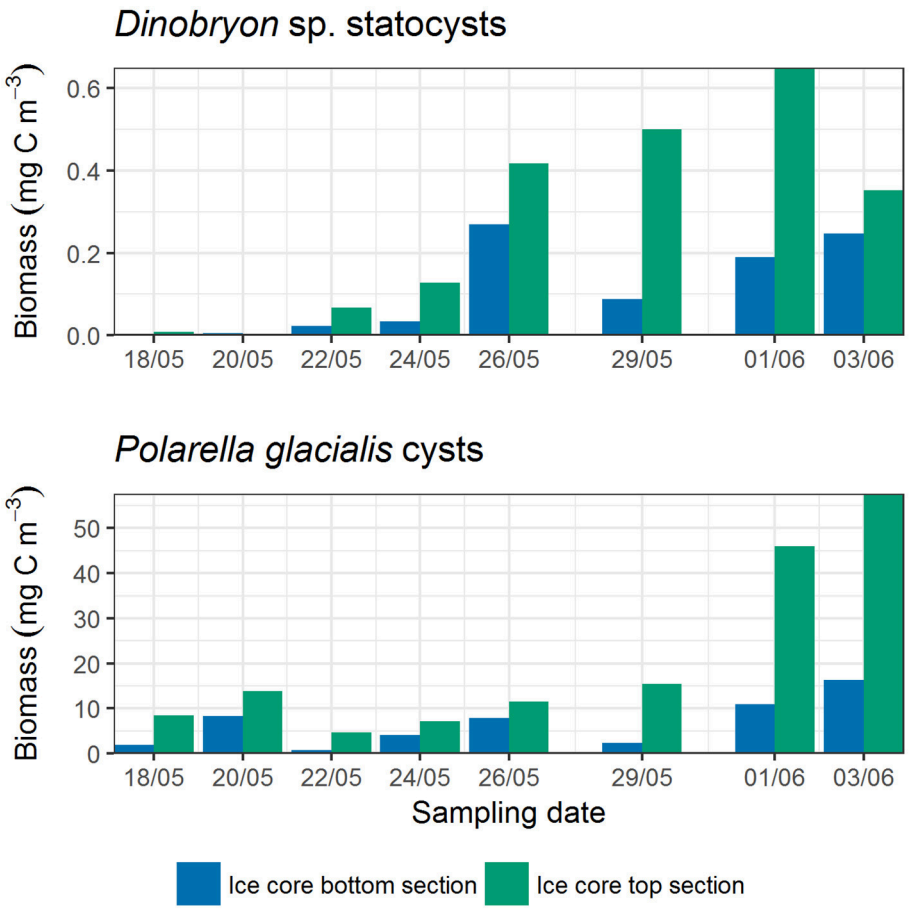

FIGURE 7 | Differences in cyst biomass between ice core bottom and top sections. Ice cores were sectioned from 18 May onwards.

Transport of algae from the shelf waters was not likely as the ice floe was drifting on Polar Surface Water (Meyer et al., 2017). During the re-freezing of the lead and early sampling of the young ice, the algal community in SYI consisted mainly of diatoms and the water column community mainly of dinoflagellates.

The dinoflagellates present in the early young ice samples were in addition found mainly in the water column (and not in SYI). The diatoms, by contrast, were found almost exclusively in SYI except for *N. frigida/neofrigida*. This species is tightly associated with ice, and considering the difference in abundance between SYI and water column, the cells in the water column likely originated from the ice. Olsen et al. (2017b) presented a seeding repository hypothesis for *N. frigida*, suggesting that ice algae from the previous growing season are trapped in the ice and survive over the winter in multi-year ice (MYI), and in the following growing season are able to seed the surrounding new ice. Given our findings, we suggest that the majority of the diatoms in the young ice originated from the surrounding thick ice, although most likely transported via the under-ice water column, while the main source of dinoflagellates was the water column. An additional route for ice-associated species might have been the wind-blown ice pieces that were observed in the lead and were incorporated in the young ice cover. The granular ice that was observed in the ice core top may in turn indicate that the initial ice formed in turbulent conditions, which are favorable for cell harvesting (Dieckmann et al., 1990; Weissenberger and Grossmann, 1998).

In the NMDS analysis each of the habitats (young ice, SYI/FYI, and water column) formed distinct clusters (**Figure 9**). As discussed above, the cells in the young ice are likely to have initially originated from both the water column and older ice. The separation from water column samples means that algae are either selectively incorporated into ice as found in previous studies (Gradinger and Ikävalko, 1998; Riedel et al., 2007; Rózanska et al., 2008), or that community changes happened almost immediately during the first week after ice formation. It was observed that the ice algal community resembled the water column community in new ice ($\leq$0.03 m) but differed in young ice (0.17–0.21 m; Rózanska et al., 2008). Survival in the new habitat may be different; changes for example in salinity and light regime are substantial when moving from the water column to the ice. Brine salinity in the young ice on 6 May was up to 79, and when in ice, algae are subject to a more stable and

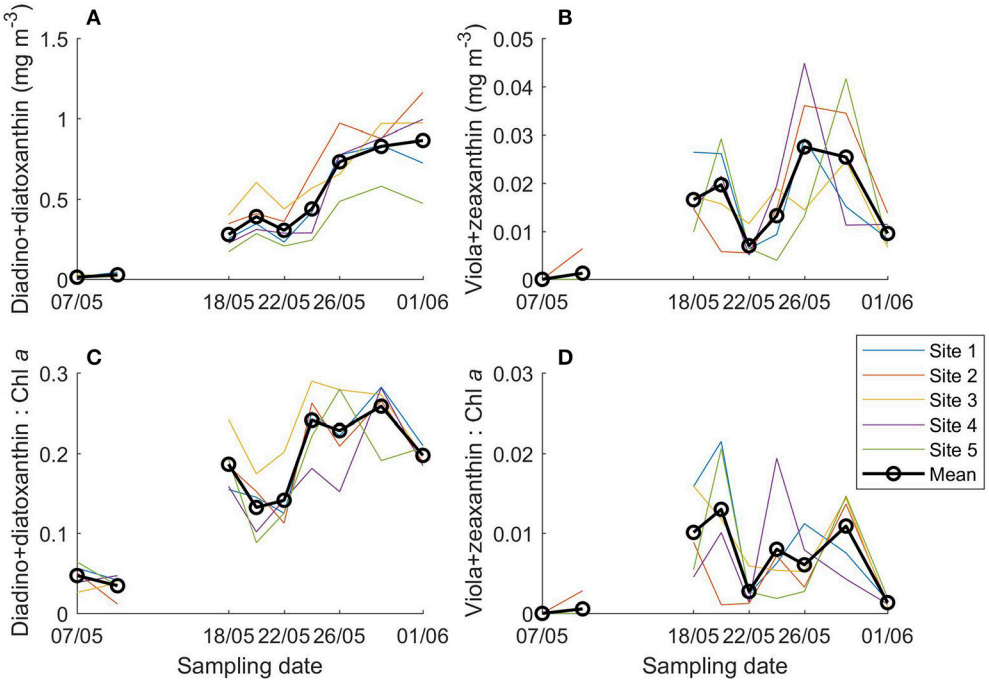

FIGURE 8 | Photoprotective xanthophyll cycle pigments concentration **(A,B)** and ratio to Chl *a* **(C,D)** in young ice during the ice coring transect study (7 May onwards).

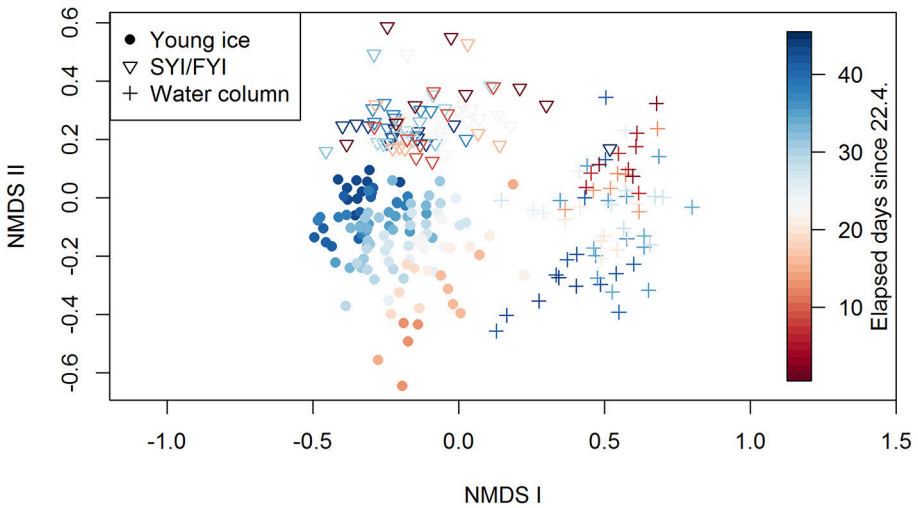

FIGURE 9 | Results of the NMDS analysis showing the grouping of young ice, SYI/FYI, and water column groups. The stress value of the plot is 16.6%.

intense light exposure than in the water column. Niemi et al. (2011) observed higher average number of taxa in new ice (1–6 days old) compared to older stages of ice (35+ days old), which could indicate that several species did not survive as the ice grew older. However, considering the long time gap other processes might have also played a role. Our water column taxonomy samples may also have missed the uppermost water layer, where the transport between ice habitats possibly occurs. Hardge et al. (2017) showed that the algal community at 1 m depth below ice was more similar to the deeper water column than to the FYI and MYI in the Central Arctic Ocean.

Separation of young ice from the SYI/FYI in the ordination (**Figure 9**) shows that the community in the young ice was not identical to the older ice. In the SYI/FYI group, no temporal patterns and thus succession was observed. In contrast, the young ice samples displayed a temporal trend in community composition, indicating that we were able to report the species succession in this habitat. The late young ice samples started to

resemble the SYI/FYI samples and became increasingly distinct from the water column samples, indicating that the young ice community evolved toward a more mature ice algal community.

This study indicates that surrounding ice is an important seeding source at a time of year when the water column has low algal, and especially low diatom, abundance. Ratkova and Wassmann (2005) observed that land-fast sea ice in the White Sea was dominated by pennate diatoms, whereas pack-ice communities in northern Barents Sea were dominated by flagellates, dinoflagellates and centric diatoms, pointing to the importance of sediments as another source for pennate diatoms. As Olsen et al. (2017b) suggest, MYI has an important role as a source in deep areas where the sediment repository is distant. Thus for the ice algal communities to mature to the typical pennate diatom community (Leu et al., 2015; van Leeuwe et al., 2018), contact with previous seasons' populations seems important, and in large parts of the Arctic, particularly the Central Basin, older ice likely plays a crucial role. This is further supported by the observations of Niemi et al. (2011), who found that the timing of ice formation did not determine the community composition in Cape Bathurst flaw lead in the Beaufort Sea, where new ice forms in leads throughout the winter and is surrounded by older first-year land-fast and pack ice. Two thirds of the taxa found in new ice (<6 days old) were not found in the water column but in older ice in their study. Even when phytoplankton is present during sea ice freezing in autumn, the sea ice community differs from the water column, showing that phytoplankton may not be the main source (Werner et al., 2007). In conclusion, timing of freezing (e.g., climate change caused later sea ice freezing in autumn) would be less important than proximity to sediments or older ice (i.e., existence of MYI) for the colonization of future ice algal assemblages.

Ice Algal Succession

From Ciliates and Flagellates to Pennate Diatoms

Biomass in the young ice increased over time but the species composition also changed considerably. On the first sampling days the protist community consisted mainly of ciliates, flagellates, and dinoflagellates, which gradually changed to dominance of pennate diatoms. The most prominent early colonizer of the young ice was the ciliate *M. rubrum*. Cryptophyte chloroplast symbionts of the ciliate (for review on the acquired phototrophy see Hansen et al., 2013) dominated in the young ice at the beginning of the study. *M. rubrum* was also found in the water column in the study region. The high abundance of the free symbionts is an artifact caused by disintegration of *M. rubrum* cells during sampling and fixation (Crawford, 1989), but it shows that *M. rubrum* was not limited to the under-ice water column but some cells also actively entered the ice. The symbionts contributed to a high concentration of the cryptophyte marker pigment alloxanthin, thus in this case alloxanthin indicates *M. rubrum* rather than free-living cryptophytes. The biomass of other cryptophytes was less than 6% of the symbiont biomass (not shown). In the first sampling days, alloxanthin had the highest marker pigment to Chl *a* ratios, confirming a high contribution of *M. rubrum* to the protist community.

The pigment gyroxanthin diester is usually associated with dinoflagellates and is also reported from one pelagophyte and two coccolithophore species (Table 14.2 in Johnsen et al., 2011). In the Arctic, it has previously been associated with the coccolithophore *Emiliana huxleyi* (Pettersen et al., 2011). In our samples, however, gyroxanthin diester seemed to be mainly associated with cryptophytes: temporal patterns of gyroxanthin diester were nearly identical to those of alloxanthin and α carotene, the marker pigments usually associated with cryptophytes (see **Figures 3E–G**, Supplementary Figures 3d–f). In contrast, neither pigments found in dinoflagellates (peridinin, dinoxanthin), pelagophytes (19′-butanoyloxyfucoxanthin; but-fuco), or haptophytes (Chl c_3 found for example in coccolithophores) had similar patterns to gyroxanthin diester. Moreover, Chl c_3 was only found in ice core top sections, whereas gyroxanthin diester only occurred in bottom sections (after ice core sectioning started), which shows that these two pigments were not co-located. Considering that most of the cryptophyte biomass originated from the *M. rubrum* symbionts, gyroxanthin diester seems to be associated with the cryptophyte-*M. rubrum* complex. In the samples where alloxanthin was present but gyroxanthin diester was not, other cryptophytes could be the alloxanthin source. This new observation has implications for using this pigment as an indicator for toxic dinoflagellates or *E. huxleyi* (Pettersen et al., 2011), but more studies are needed to confirm the findings.

Besides *M. rubrum*, dinoflagellates were initially important in the young ice. In terms of marker pigment to Chl *a* ratios, peridinin-containing dinoflagellates were relatively as important in the beginning of the transect sampling as fucoxanthin containing algae (e.g., diatoms) at the end of the study. Fucoxanthin is considered to originate mainly from diatoms because the microscopy analysis confirmed the high abundance of diatoms and another source of fucoxanthin, haptophytes, can be considered to be of minor importance due to the low concentration of the associated pigment Chl c_3. Dinoflagellates have been shown to increase in a post-bloom situation in FYI (Alou-Font et al., 2013) but our study shows that they can also contribute substantially to the young ice community at the beginning of its formation when the total algal biomass in the ice is still low. Total biomass of diatoms was much higher at the end of the study period than the initial dinoflagellate biomass. Diatom biomass was low at the beginning and mainly formed by centric diatoms, but from mid-May diatoms had a higher contribution to biomass than dinoflagellates and the fucoxanthin to Chl *a* ratio also increased over the sampling period. Centric diatoms were not very abundant (Supplementary Figure 2a), and throughout the sampling less abundant than pennate diatoms, but because of their relatively high biomass per cell they were prominent in biomass time series. At the end of the sampling, pennate diatoms clearly dominated also in terms of biomass and in the ice core top sections. The successional patterns are summarized in **Figure 10**. The group composition of the ice algal community is also reflected in the algal absorption spectra (Kauko et al., 2017 their Figure 3). The shoulders in the absorption spectra at 460 and 490 nm, caused by carotenoids and chlorophylls c_1 and c_2,

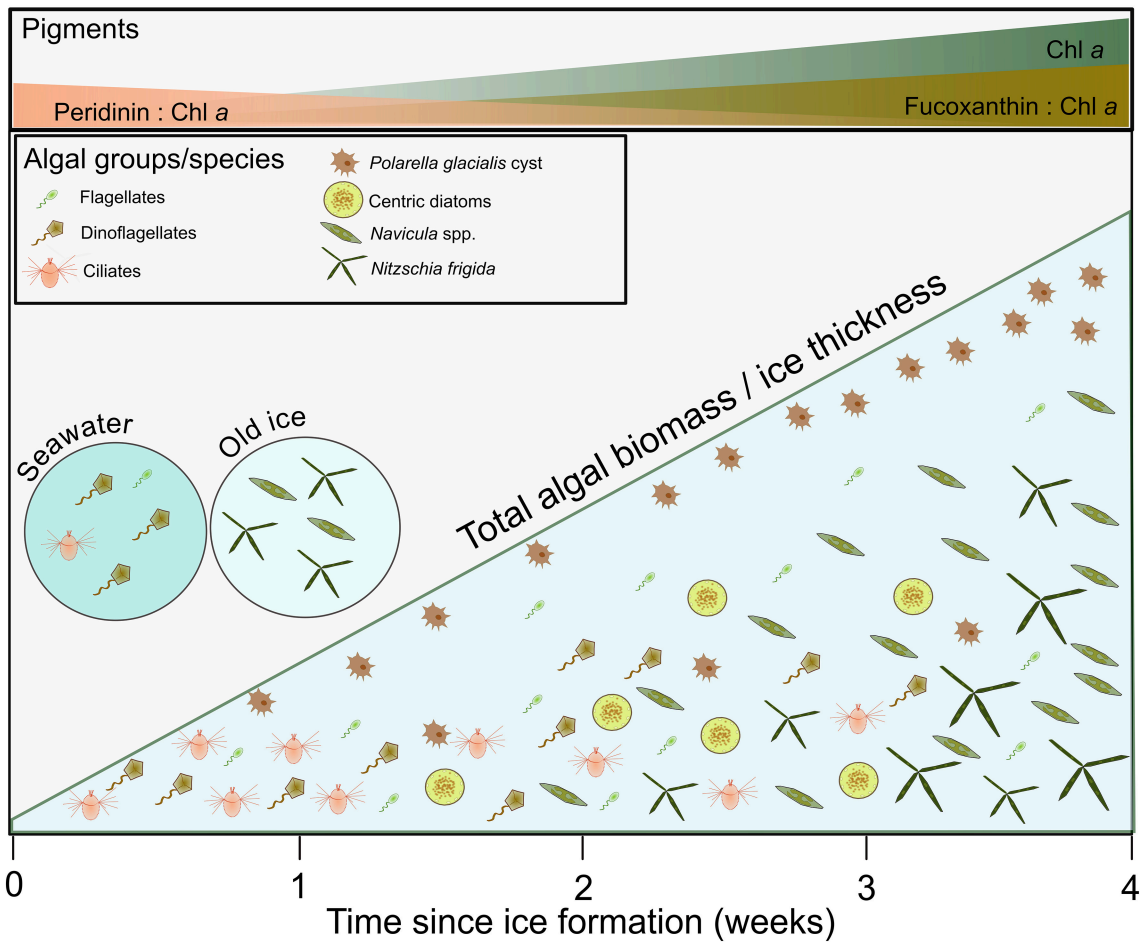

FIGURE 10 | A schematic showing the main successional patterns in the young ice and species composition in the source habitats old ice (i.e., SYI) and seawater (circles on the left). At the beginning, the young ice community had low biomass and was characterized by ciliates, dinoflagellates, and flagellates. Over a month, it developed toward dominance of pennate diatoms (especially *Navicula* spp. and *Nitzschia frigida*). Pennate diatoms eventually dominated also over centric diatoms. Cysts of *Polarella glacialis* were predominantly found in the top layer of the ice. Biomass in the bottom of the ice was typically higher than in the top part (coarsely indicated by the amount of icons within the young ice triangle), and increased over time (the diagonal line represents both increase in biomass and ice thickness in the young ice). In top panel the main patterns of algal marker pigment to Chl *a* ratios are shown, which show the succession from dinoflagellates (type I, peridinin) to diatoms (fucoxanthin).

and the exact wavelength of the *in vivo* red peak of Chl *a* (672–674 nm) are typical for diatoms and dinoflagellates (Johnsen and Sakshaug, 2007).

Chl *b* was the most prominent of the flagellate marker pigments, in addition to the cryptophyte pigments mentioned earlier. In our study Chl *b* likely originated mainly from prasinophytes since they were more abundant and frequent than chlorophytes based on microscopy counts (euglenophytes were not observed). Both based on biomass and low marker pigment concentrations (neoxanthin and lutein), these groups were rare. A fraction of the flagellate group was probably heterotrophic and therefore did not contribute to the marker pigments concentrations, which would also explain why dinoflagellates were relatively more prominent in pigment than count data in the early sampling period. Flagellate abundance could have been underestimated due to the unbuffered melting method used in this study (Garrison and Buck, 1986), but the concomitantly low flagellate marker pigment concentrations also indicate that they had a minor contribution to the ice algal biomass in the young ice, given that chloroplasts are retained on the sample filter.

Species succession from flagellates to diatoms was also observed over a few months in a mesocosm experiment where sea ice was formed from artificial sea water enriched with brine collected in Fram Strait (Weissenberger, 1998). Rózanska et al. (2008) observed that pennate diatoms were more abundant than centric diatoms or dinoflagellates in young ice (0.17–0.21 m thick) formed in fall in the Beaufort Sea, whereas the opposite was observed for new ice and nilas (thickness <0.08 m). Likewise,

Hegseth (1992) observed a succession from centric to pennate diatoms by studying pack ice floes of different age in Barents Sea, but the age of the different floes differed more than the time span of our sampling period. In some studies, however, new ice was already dominated by pennate diatoms (Okolodkov, 1992; Niemi et al., 2011) or centric diatoms became more abundant than pennates over the growth season (Galindo et al., 2017; Campbell et al., 2018). In general, pennate diatom dominance is a main succession stage during blooming bottom ice algal communities (Leu et al., 2015; van Leeuwe et al., 2018).

Cyst Formation

Cyst or resting stage formation are a part of the life cycle of many algae and are among others an adaptation to survive variable environmental conditions (Von Dassow and Montresor, 2011). In our study, cysts of the dinoflagellate *Polarella glacialis* and statocysts of the chrysophyte *Dinobryon* sp. were more abundant in the ice core top sections than in the bottom sections. The higher abundance of cysts from these groups in the upper ice was also found in previous studies (Stoecker et al., 1992, 1997; Garrison and Close, 1993; Gradinger, 1999; Werner et al., 2007). The cyst abundance and biomass increased over the sampling period, whereas vegetative cells were observed to a far lesser extent. This suggest that these species, after a short growth period in the ice, respond with rapid encystment. The pattern was observed throughout the entire sampling period, which means that algae encyst at the top of the ice core already before the main melting season in spring. This encystment seems to have occurred somewhat earlier than in studies from Antarctica (Stoecker et al., 1992; Garrison and Close, 1993), however, conditions in the young ice with thin snow cover and high irradiance may resemble a melting ice environment thus triggering encystment. The strong increase of *P. glacialis* cysts on the two last sampling days could also be a response to ice melt (ice thickness decreased). This encystment pattern over the whole period may however suggest that cysts are used as a dispersion strategy in addition to overwintering, as suggested by Stoecker et al. (1998). Inhabiting the ice surface would maximize dispersal distance, as that is the most likely part to survive longest and travel furthest. The mechanism to seek the surface could simply be controlled by light, as light intensity is higher further up in the ice. Cysts do not seem to have active Chl *a* (Stoecker et al., 1997) and presumably the photosynthetic apparatus is reduced, which explains the decline in peridinin concentration in our samples (**Figure 3C**) although biomass of the *P. glacialis* cysts increased (**Figure 5B**), and that peaks in dinoflagellate biomass and peridinin concentration do not always match (for *P. glacialis* pigments see Thomson et al., 2004). Thus for understanding survival strategies of sea ice biota, microscopic observations are important.

Species Diversity

Species richness increased over time in all habitats, and cumulative species number (Supplementary Figure 11) showed that the young ice community did not reach a plateau in species richness (if only species that were found on all days after they appeared were taken into account). In the ice habitats there were however no clear diversity changes over time (after removal of the symbionts) despite the increase in species richness. Shannon's diversity index indicates how difficult it is to predict the identity of a specimen taken randomly from the community, and Pielou's evenness describes how similar the abundances of the different species are (Peet, 1974), thus both species richness and evenness affect diversity. The low diversity indices and species evenness in the water column co-occur with the *P. pouchetii* under-ice bloom (Assmy et al., 2017b). The diversity pattern in the young ice case can be explained by the decrease in the species evenness: there are more species present, but some also become more dominant. Furthermore, in SYI the dominance seems to be stronger, because of lower evenness (and diversity) than in young ice or FYI. Thus ice algal communities seem to move in the course of succession toward lower diversity because of lower evenness at least during the bloom season. Alou-Font et al. (2013) observed that diversity did not vary between FYI sites with different snow cover (and thus light), but was lowest during peak bloom and highest during post bloom. MYI seems however to be important for the ice algal diversity: in a molecular study in Central Arctic Ocean, highest proportions of unique taxa (unique to ice as compared to melt ponds and water column) were found in MYI (Hardge et al., 2017). Compared to other studies of newly formed ice (that had less frequent sampling events than this study), the number of taxa was much higher in our case, spring young ice (120 taxa and 80 species), than in Beaufort Sea in autumn new ice ($\leq$6 days old; 46 taxa and 21 species; Niemi et al., 2011) or in autumn new ice, nilas, and young ice (ice thickness $\leq$ 0.21 m; 32–48 taxa and 18–26 species; Rózanska et al., 2008).

Drivers of Ice Algal Succession in Young Ice

In the young ice, there was a clear species succession as seen both in biomass and pigment concentration and also in the NMDS analysis. The main abiotic factors did not explain the variation in ice algal abundance to a great degree (17% of variation accounted for in constrained ordination; Supplementary Figure 10). Thus irradiance (indicated by snow thickness) does not seem to be a strong controlling factor of species succession. The significant correlation of bulk salinity with the unconstrained ordination (NMDS) is likely affected by the clear temporal patterns of bulk salinity caused by desalinization of the ice (Figure 2 in Kauko et al., 2017). The alignment of the first axis (in both ordinations) with the temporal gradient in the samples indicates that the main axis, along which the community varies is a temporal axis. Likewise, the correlation of water column nitrate with bulk salinity is likely caused by the temporal patterns, including strong nitrate drawdown during the under-ice phytoplankton bloom encountered in the latter half of the sampling period (Assmy et al., 2017b). Furthermore, bulk ($<$15; $<$9 during transect sampling) or brine salinities ($<$79; $<$52 during transect sampling) were not extreme in the young ice (this study and Kauko et al., 2017). Absence of grazing marker pigments (e.g., phaeophorbide *a*) indicate low grazing pressure. This and the weak control by the abiotic factors included here suggest that biotic factors, and moreover species traits and interactions advantageous for the sea ice environment, were likely important in community development (see Section Adaptation to Environmental Conditions and Morphology). This

conclusion is consistent with that the general pattern of diatom dominance (particularly pennate diatoms) in sea ice is similar across the Arctic (Poulin et al., 2011; Leu et al., 2015), despite a wide range in environmental conditions.

Irradiance

It should be noted that irradiance levels in our young ice case (on average 114 and range 30–350 μmol photons m^{-2} s^{-1}) were relatively high throughout the study period (Kauko et al., 2017). Light has been observed to impact community composition when experimentally perturbed (Enberg et al., 2015) or under different snow cover (Rózanska et al., 2009; Alou-Font et al., 2013). Alou-Font et al. (2013) observed no dinoflagellates under thick snow cover (lower light), but in our case they were found in both ice types. It has been suggested that higher abundance of centric compared to pennate diatoms in sea ice was due to higher light availability (Majaneva et al., 2017; Campbell et al., 2018). Exclusion of UV radiation led to biomass increase of *N. fridiga* in experiments (Enberg et al., 2015). In our samples, however, pennate diatoms dominated toward the end also in the young ice and in ice core top sections, i.e., under high irradiance. Thus in our study, this comparison, in addition to the statistical analysis, does not point to an important role of light in terms of community composition.

Nevertheless, photoacclimation is needed for the algae to be able to colonize new ice in spring. High irradiance can inhibit growth in non-acclimated cells (Mangoni et al., 2009; Juhl and Krembs, 2010). On the other hand, high irradiance likely enables more rapid growth in acclimated communities and dispersion in the ice in spring than in autumn. Ice algae have been considered to be highly shade adapted (Thomas and Dieckmann, 2002) and they can grow in very low light (<0.17 μmol photons m^{-2} s^{-1}; Hancke et al., 2018). Detailed studies on the photoacclimation capacities of ice algae conclude however that they have high plasticity regarding growth irradiance, aided to a large degree by the photoprotective xanthophyll cycle (Robinson et al., 1997; Petrou et al., 2011; Galindo et al., 2017). In our study, the xanthophyll cycle pigments diadino- and diatoxanthin showed an increasing trend both in concentration and ratio to Chl *a*, and thus show a response to increasing irradiance levels (Kauko et al., 2017 and Supplementary Figure 12). Diadino- and diatoxanthin are found in for example diatoms, dinoflagellates, and haptophytes (see Table 11.1 in Brunet et al., 2011) and thus represent the photoprotective mechanism of the majority of algae found in our samples. Other xanthophyll cycle pigments (violaxanthin and zeaxanthin, found e.g., in chlorophytes) were detected in our samples but in low concentrations and with a variable pattern, reflecting the low biomass of these algae in the samples in addition to the light exposure history. A similar seasonal increase in the photoprotective pigment pool in ice algae was also observed in FYI in the Canadian Arctic (Alou-Font et al., 2013; Galindo et al., 2017). The diadinoxanthin + diatoxanthin to Chl *a* ratios in our samples were in the range of what has been previously reported for surface habitats (ponds and slush) on Antarctic sea ice (Arrigo et al., 2014) or under thin snow cover in the Arctic (Alou-Font et al., 2013; Galindo et al., 2017). The average ratio was however similar in the surrounding FYI (data now shown) with much lower light levels [E_d(PAR) 1–20 μmol photons m^{-2} s^{-1}] than in the young ice (Olsen et al., 2017b). The ratios found in surrounding SYI [E_d(PAR) <1 μmol photons m^{-2} s^{-1}] were on average lower and similar to those in interior and bottom ice habitats in Arrigo et al. (2014).

The photoprotective pigment to Chl *a* ratios were not significantly different between the ice core top and bottom sections despite higher light exposure in the former. Based on radiative transfer modeling for 26 May (Kauko et al., 2017), the E_d(PAR) difference between the bottom and top 0.01 m of ice was >450 μmol photons m^{-2} s^{-1}. Alou-Font et al. (2013) found differences in photoprotective pigment to Chl *a* ratios already for irradiance levels of 26 and <10 μmol photons m^{-2} s^{-1} (between different snow covers). In our case the surrounding thick SYI had diadino- + diatoxanthin to Chl *a* ratios that were significantly lower in the bottom 0.20 m of the ice column, despite thick snow cover and thus high light attenuation also at the top of the ice column. These seemingly contradictory results suggest that the photoprotective pigment expression is controlled by more factors than purely light intensity, or that in many cases the expression is not fine-tuned but rather responds to broad categories or thresholds in light intensity (consider also the similarity between young ice and FYI in our case), or temporally integrated doses. When it comes to the photosynthetic pigments in our samples, differences between the young ice sections were again visible. Fucoxanthin to Chl *a* and Chl c_2 to Chl *a* ratios (the most prominent light harvesting pigments in our samples) were higher in ice core bottom sections. In lower light, algae increase the amount of photosynthetic pigments to effectively harvest the available light (Brunet et al., 2011).

Adaptation to Environmental Conditions and Morphology

The succession of the ice algal community, from a flagellate-dinoflagellate to a diatom dominated community, and within the diatoms from centric to pennate diatoms, indicates that sea ice communities evolve toward a more ice-adapted species community over time during a bloom. This was also suggested by Syvertsen (1991), based on changes in ice algal community composition from the ice edge northwards in the Barents Sea, i.e., from younger to older ice. The temporal patterns thus can be affected by the traits of the different species. When ice is formed, the species composition reflects what was present in the water column at the time of ice formation. Over time, selection occurs based on adaptation to the conditions in the ice and competition between species. *N. frigida* with the arborescent colonies, and other pennate species with attaching and gliding capabilities, are well adapted to life in brine channels, which to a certain degree resemble benthic habitats. Furthermore, they are adapted to the growth conditions: for example *N. frigida* grows exponentially even at very low temperatures and high salinities (Aletsee and Jahnke, 1992). *Fragilariopsis* species were in experiments found to be more tolerant to high salinities than a chlorophyte species (Søgaard et al., 2011) and are known to produce antifreeze proteins (Bayer-Giraldi et al., 2010). Additional biotic factors might also play a role in species succession; abundance of *F. cylindrus* (formerly *Nitzschia cylindrus*) was observed to decrease in connection with parasitic infection in the Beaufort Sea (Horner and

Schrader, 1982). The exponential increase of the major pennate diatoms in our study indicates that the growth conditions were favorable for them. However, when the seeding stock is low, they and especially *N. frigida* needed time to become dominant even at close to maximum growth rates (Olsen et al., 2017b).

Dinoflagellates in general are not considered as typical ice algae, but the brine community in upper ice in Antarctic land-fast ice can be dominated by dinoflagellates (Stoecker et al., 1992). Stoecker et al. (1997) reported that dinoflagellates and chrysophytes excysted and started photosyntethizing under extreme conditions (in terms of salinity and temperature) in the upper ice layers early in the season. Stoecker et al. (1998) observed that as the ice warmed, flagellates were replaced by pennate diatoms also in the upper ice. Dinoflagellates seem to be outcompeted by diatoms in the lower parts of ice and during more favorable growth conditions, but some species have evolved capacities to survive and find a niche. Resting cysts are a major component of the life cycle of ice-associated dinoflagellates (see discussion and references in section Cyst formation).

The pennate diatom *F. cylindrus* was, in terms of cell counts, an important species and had an exponential apparent growth rate until 29 May. Thereafter cell numbers declined strongly, possibly due to melting of ice (ice thickness began to decrease), which may have flushed the cells out. The ribbon shaped colonies may not be as optimal for attaching to the ice matrix as e.g., colonies of *N. frigida*. Otherwise it is well-adapted: Petrou et al. (2012) studied the photophysiology of *F. cylindrus* under temperature and nutrient stress and noticed that cell division rates decreased under nitrogen depletion, but physiological changes allowed for greater photoprotective capacity and photosynthetic efficiency was maintained. *Fragiolariopsis* species are also prominent ice algal species throughout the Arctic (Leu et al., 2015). However, *F. cylindrus* (and other small diatoms) in Antarctica was observed in experiments to synthetize mycosporine-like amino acids (MAAs) only in trace amounts that were not sufficient for effective UV protection (Riegger and Robinson, 1997), which could be a competitive disadvantage compared to species with higher amounts of MAAs. Judging by the high MAA to Chl *a* ratios found in the young ice in our case (Kauko et al., 2017), algae were investing strongly in UV protection. Thus both physical changes in the ice (melting) as well as physiological reasons (UV protection) could be responsible for the decline in this species during the study period. Likewise, centric diatoms (morphology shown in **Figure 6D**) were possibly affected by ice melting at the end of the study period.

In summary, the ice algal succession in young ice appears to start in a stochastic manner and then follows patterns that are dependent on the traits of the species present, resulting in differential adaptation to the ice habitat and its conditions (different succession concepts reviewed in McCook, 1994). Initially, species are likely to arrive in ice in a relatively random order based on abundances in the water column, which again are based on proximity to suitable source habitats such as older ice and water column bloom status. Once in ice, traits that provide a competitive advantage in the ice habitat determine the success of species to further grow and spread. Since the diatoms that were found in our early young ice were rarely observed in the water column, it suggests that the relatively few cells that came into contact with the young ice were successful in inhabiting and growing in the ice. Facilitation of the later arrivals by the early colonizers (see Connell and Slatyer, 1977) could occur as biologically produced extracellular polysaccharide substances have been observed to change the microstructure of growing ice (Krembs et al., 2011). Some degree of inhibition of later arrivals by early colonizers could also occur based on nutrient consumption, and in some cases because of allelopathy.

CONCLUSIONS

Our study provides the first observations of algal species succession in newly formed sea ice in spring. By following the same ice floe over an extended period of time we could observe the species succession at a high temporal resolution. The ice algal community originated both from the underlying water column and surrounding older ice, pointing to the importance of older ice as a seeding source. The community developed from a more mixed community toward dominance by ice-adapted pennate diatoms such as *N. frigida*. Overall the succession seemed to be determined more by the traits of the species than by variable abiotic factors. The colonization of the high light environment of young ice in spring is further aided by photoprotective carotenoids. The main trends in community succession were revealed also with marker pigment concentrations, with a fucoxanthin to Chl *a* ratio (indicative of diatoms) increase from 0.04 to 0.27 over the sampling period and low flagellate marker pigment concentrations. The pigment approach misses, however, the species succession within diatoms due to similar pigments, and patterns in cyst biomass due to lack of active photosynthesis in cysts. Cysts dominated the dinoflagellate biomass (>60%) on the majority of the sampling days. Cysts of the dinoflagellate *P. glacialis* were predominantly found in the top layers of the ice and were more prominent than the vegetative cells already in early May, which points to an important role of ice as a cyst repository and suggests that cysts may be used as a dispersion mechanism. With the decline in Arctic sea ice cover, loss of MYI and as ice retreats further away from the shelves, dispersal of ice algal species may be compromised, which could lead to changes in the relative importance of the dominant ice algal species. Based on this and previous studies, the source of pennate diatoms in new ice often seems to derive from surface sediments or older ice, whereas the time of freezing or environmental conditions play a smaller role in determining the community composition. In conclusion, the springtime young-ice algal community developed in less than a month into a typical, pennate diatom dominated community, when surrounding older sea ice can act as a seeding source.

AUTHOR CONTRIBUTIONS

PA, PD, MG, and CM planned the field work; PA, PD, MG, CM, HK, LO, MF-M, and AP conducted the field work; HK and

LO worked up the taxonomy data and planned the study; IP analyzed and processed the HPLC samples and HK worked up the data with the help of GJ and CM; MF-M made the schematics; HK did the statistical analysis and wrote the manuscript, and all co-authors contributed to the final version.

FUNDING

The N-ICE2015 campaign was made possible by the N-ICE project, supported by the Centre of Ice, Climate and Ecosystems at the Norwegian Polar Institute. HK, LO, PA, PD, MG, CM, and GJ were supported by the Research Council of Norway project Boom or Bust (no. 244646). GJ was supported by the Research Council of Norway project AMOS (no. 223254). CM was supported by the Natural Sciences and Engineering Council of Canada Discovery grant. MG and AP were supported by the Research Council of Norway project STASIS (no. 221961) and by the Polish-Norwegian Research Program operated by the National Centre for Research and Development under the Norwegian Financial Mechanism 2009–2014 in the frame of Project Contract Pol-Nor/197511/40/ 2013, CDOM-HEAT. MF-M and PA were supported by the Program Arktis 2030 funded by the Ministry of Foreign Affairs and Ministry of Climate and Environment, Norway (project ID Arctic). IP was funded by the PACES (Polar Regions and Coasts in a Changing Earth System) program of the Helmholtz Association.

ACKNOWLEDGMENTS

We would like to thank the captains and crew of RV Lance, and fellow scientists on N-ICE2015 for assistance. We acknowledge Jozef Wiktor, Magdalena Rózanska-Pluta, and Agnieszka Tatarek from the Institute of Oceanology of the Polish Academy of Sciences for species identification and enumeration, N-ICE2015 snow/ice team for ice temperature data, Anja Rösel for organizing the ice stratigraphy work, Torbjørn Taskjelle and Stephen Hudson for work with the irradiance data, and Max König for providing the map. Data used in the study is available through the Norwegian Polar Data Centre (Assmy et al., 2017a; Olsen et al., 2017a).

SUPPLEMENTARY MATERIAL

The Supplementary Material for this article can be found online at: https://www.frontiersin.org/articles/10.3389/fmars.2018.00199/full#supplementary-material

REFERENCES

Aletsee, L., and Jahnke, J. (1992). Growth and productivity of the psychrophilic marine diatoms *Thalassiosira antarctica* Comber and *Nitzschia frigida* Grunow in batch cultures at temperatures below the freezing point of sea water. *Polar Biol.* 11, 643–647. doi: 10.1007/BF00237960

Alou-Font, E., Mundy, C. J., Roy, S., Gosselin, M., and Agustí. S. (2013). Snow cover affects ice algal pigment composition in the coastal Arctic Ocean during spring. *Mar. Ecol. Prog. Ser.* 474, 89–104. doi: 10.3354/meps10107

Arrigo, K. R., Brown, Z. W., and Mills, M. M. (2014). Sea ice algal biomass and physiology in the Amundsen Sea, Antarctica. *Elem. Sci. Anthr.* 2:28. doi: 10.12952/journal.elementa.000028

Arrigo, K. R., and van Dijken, G. L. (2015). Continued increases in Arctic ocean primary production. *Prog. Oceanogr.* 136, 60–70. doi: 10.1016/j.pocean.2015.05.002

Assmy, P., Duarte, P., Dujardin, J., Fernández-Méndez, M., Fransson, A., Hodgson, R., et al. (2017a). *N-ICE2015 sea ice biogeochemistry [Data set]*. Tromsø: Norwegian Polar Data Centre. doi: 10.21334/npolar.2017.d3e93b31

Assmy, P., Fernández-Méndez, M., Duarte, P., Meyer, A., Randelhoff, A., Mundy, C. J., et al. (2017b). Leads in Arctic pack ice enable early phytoplankton blooms below snow-covered sea ice. *Sci. Rep.* 7:40850. doi: 10.1038/srep40850

Bayer-Giraldi, M., Uhlig, C., John, U., Mock, T., and Valentin, K. (2010). Antifreeze proteins in polar sea ice diatoms: diversity and gene expression in the genus Fragilariopsis. *Environ. Microbiol.* 12, 1041–1052. doi: 10.1111/j.1462-2920.2009.02149.x

Brunet, C., Johnsen, G., Lavaud, J., and Roy, S. (2011). "Pigments and photoacclimation processes," in *Phytoplankton Pigments - Characterization, Chemotaxonomy and Applications in Oceanography*, eds S. Roy, C. A. L. Lewellyn, E. S. Egeland, and G. Johnsen (Cambridge: Cambridge University Press), 445–471.

Campbell, K., Mundy, C. J., Belzile, C., Delaforge, A., and Rysgaard, S. (2018). Seasonal dynamics of algal and bacterial communities in Arctic sea ice under variable snow cover. *Polar Biol.* 41, 41–58. doi: 10.1007/s00300-017-2168-2

Connell, J., and Slatyer, R. O. (1977). Mechanisms of succession in natural communities and their role in community stability and organization. *Am. Nat.* 111, 1119–1144.

Cox, G. F. N., and Weeks, W. F. (1986). Changes in the salinity and porosity of sea-ice samples during shipping and storage. *J. Glaciol.* 32, 371–375.

Crawford, D. W. (1989). *Mesodinium rubrum*: the phytoplankter that wasn't. *Mar. Ecol. Prog. Ser.* 58, 161–174. doi: 10.3354/meps058161

Dieckmann, G. S., Spindler, M., Lange, M. A., Ackley, S. F., and Eicken, H. (1990). "Sea ice. a habitat for the foraminifer *Neogloboquadrina pachyderma*? in sea ice properties and processes," in *Proceedings of the W. F. Weeks Sea Ice Symposium, CRREL Monograph 90-1*, eds S. F. Ackley and W. F. Weeks (Hanover, NH: Cold Regions Research Engineering Laboratory), 86–92.

Dupont, F. (2012). Impact of sea-ice biology on overall primary production in a biophysical model of the pan-Arctic Ocean. *J. Geophys. Res. Oceans* 117, 1–18. doi: 10.1029/2011JC006983

Edler, L., and Elbrächter, M. (2010). "The Utermöhl method for quantitative phytoplankton analysis," in *Microscopic and Molecular Methods for Quantative Phytoplankton analysis*, eds B. Karlson, C. Cusack, and E. Bresnan (Paris: Intergovernmental Oceanographic Commission of UNESCO), 13–20.

Enberg, S., Piiparinen, J., Majaneva, M., Vähätalo, A. V., Autio, R., and Rintala, J.-M. (2015). Solar PAR and UVR modify the community composition and photosynthetic activity of sea ice algae. *FEMS Microbiol. Ecol.* 91, 1–11. doi: 10.1093/femsec/fiv102

Fernández-Méndez, M., Katlein, C., Rabe, B., Nicolaus, M., Peeken, I., Bakker, K., et al. (2015). Photosynthetic production in the central Arctic Ocean during the record sea-ice minimum in 2012. *Biogeosciences* 12, 3525–3549. doi: 10.5194/bg-12-3525-2015

Galindo, V., Gosselin, M., Lavaud, J., Mundy, C. J., Else, B., Ehn, J., et al. (2017). Pigment composition and photoprotection of Arctic sea ice algae during spring. *Mar. Ecol. Prog. Ser.* 585, 49–69. doi: 10.3354/meps1239

Garrison, D. L., and Buck, K. R. (1986). Organism losses during ice melting: a serious bias in sea ice community studies. *Polar Biol.* 6, 237–239. doi: 10.1007/BF00443401

Garrison, D. L., and Close, A. R. (1993). Winter ecology of the sea-ice biota in Weddell sea pack ice. *Mar. Ecol. Ser.* 96, 17–31.

Gosselin, M., Levasseur, M., Wheeler, P. A., Horner, R. A., and Booth, B. C. (1997). New measurements of phytoplankton and ice algal production in the Arctic Ocean. *Deep. Res. Part II Top. Stud. Oceanogr.* 44, 1623–1644. doi: 10.1016/S0967-0645(97)00054-4

Gradinger, R. (1999). Vertical fine structure of the biomass and composition of algal communities in Arctic pack ice. *Mar. Biol.* 133, 745–754.

Gradinger, R., and Ikävalko, J. (1998). Organism incorporation into newly forming Arctic sea ice in the Greenland Sea. *J. Plankton Res.* 20, 871–886. doi: 10.1093/plankt/20.5.871

Granskog, M. A., Assmy, P., Gerland, S., Spreen, G., Steen, H., and Smedsrud, L. H. (2016). Arctic research on thin ice: consequences of Arctic sea ice loss. *Eos. Trans. AGU* 97, 22–26. doi: 10.1029/2016EO044097

Granskog, M. A., Fer, I., Rinke, A., and Steen, H. (2018). Atmosphere-ice-ocean-ecosystem processes in a thinner Arctic sea ice regime: the Norwegian young sea ICE (N-ICE2015) expedition. *J. Geophys. Res. Ocean* 123, 1586–1594. doi: 10.1002/2017JC013328

Hancke, K., Lund-Hansen, L. C., Lamare, M. L., Pedersen, S. H., King, M. D., Andersen, P., et al. (2018). Extreme low light requirement for algae growth underneath sea ice : a case study from Station Nord, NE Greenland. *J. Geophys. Res. Oceans* 123, 985–1000. doi: 10.1002/2017JC013263

Hansen, P. J., Nielsen, L. T., Johnson, M., Berge, T., and Flynn, K. J. (2013). Acquired phototrophy in *Mesodinium* and *Dinophysis* - a review of cellular organization, prey selectivity, nutrient uptake and bioenergetics. *Harmful Algae* 28, 126–139. doi: 10.1016/j.hal.2013.06.004

Hardge, K., Peeken, I., Neuhaus, S., Lange, B. A., Stock, A., Stoeck, T., et al. (2017). The importance of sea ice for exchange of habitat-specific protist communities in the Central Arctic Ocean. *J. Mar. Syst.* 165, 124–138. doi: 10.1016/j.jmarsys.2016.10.004

Hegseth, E. N. (1992). Sub-ice algal assemblages of the Barents Sea: species composition, chemical composition, and growth rates. *Polar Biol.* 12, 485–496.

Higgins, H. W., Wright, S. W., and Schlüter, L. (2011). "Quantative interpretation of chemotaxonomic pigment data," in *Phytoplankton Pigments - Characterization, Chemotaxonomy and Applications in Oceanography*, eds S. Roy, C. A. LLewellyn, E. S. Egeland, and G. Johnsen (Cambridge: Cambridge University Press), 257–313.

Hillebrand, H., Dürselen, C.-D., Kirschtel, D., Pollingher, U., and Zohary, T. (1999). Biovolume calculation for pelagic and benthic microalgae. *J. Phycol.* 35, 403–424. doi: 10.1046/j.1529-8817.1999.3520403.x

Horner, R., and Schrader, G. C. (1982). Relative contributions of ice algae, phytoplankton, and benthic microalgae to primary production in nearshore regions of the Beaufort Sea. *Arctic* 35, 485–503. doi: 10.14430/arctic2356

Itkin, P., Spreen, G., Cheng, B., Doble, M., Girard-Ardhuin, F., Haapala, J., et al. (2017). Thin ice and storms: a case study of sea ice deformation from buoy arrays deployed during N-ICE2015. *J. Geophys. Res. Ocean.* 122, 4661–4674. doi: 10.1002/2016JC012403

Jeffrey, S. W., Wright, S. W., and Zapata, M. (2011). "Microalgal classes and their signature pigments," in *Phytoplankton Pigments - Characterization, Chemotaxonomy and Applications in Oceanography*, eds S. Roy, C. A. LLewellyn, E. S. Egeland, and G. Johnsen (Cambridge: Cambridge University Press), 3–77.

Johnsen, G., Moline, M. A., Pettersson, L. H., Pinckney, J., Pozdnyakov, D. V., Egeland, E. S., et al. (2011). "Optical monitoring of phytoplankton bloom pigment signatures," in *Phytoplankton Pigments - Characterization, Chemotaxonomy and Applications in Oceanography*, eds S. Roy, C. A. LLewellyn, E. S. Egeland, and G. Johnsen (Cambridge, UK: Cambridge University Press), 538–581.

Johnsen, G., and Sakshaug, E. (2007). Biooptical characteristics of PSII and PSI in 33 species (13 pigment groups) of marine phytoplankton, and the relevance for pulse-amplitude-modulated and fast-repetition-rate fluorometry. *J. Phycol.* 43, 1236–1251. doi: 10.1111/j.1529-8817.2007.00422.x

Juhl, A. R., and Krembs, C. (2010). Effects of snow removal and algal photoacclimation on growth and export of ice algae. *Polar Biol.* 33, 1057–1065. doi: 10.1007/s00300-010-0784-1

Kauko, H. M., Taskjelle, T., Assmy, P., Pavlov, A. K., Mundy, C. J., Duarte, P., et al. (2017). Windows in Arctic sea ice: light transmission and ice algae in a refrozen lead. *J. Geophys. Res. Biogeosci.* 122, 1486–1505. doi: 10.1002/2016JG003626

Krembs, C., Eicken, H., and Deming, J. W. (2011). Exopolymer alteration of physical properties of sea ice and implications for ice habitability and biogeochemistry in a warmer Arctic. *Proc. Natl. Acad. Sci. U.S.A.* 108, 3653–3658. doi: 10.1073/pnas.1100701108

Krembs, C., Tuschling, K., and von Juterzenka, K. (2002). The topography of the ice-water interface - its influence on the colonization of sea ice by algae. *Polar Biol.* 25, 106–117. doi: 10.1007/s003000100318

Lange, B. A., Flores, H., Michel, C., Beckers, J. F., Bublitz, A., Casey, J. A., et al. (2017). Pan-Arctic sea ice-algal chl *a* biomass and suitable habitat are largely underestimated for multiyear ice. *Glob. Chang. Biol.* 23, 4581–4597. doi: 10.1111/gcb.13742

Lange, M. A. (1988). Basic properties of Antarctic sea ice as revealed by textural analysis of ice cores. *Ann. Glaciol.* 10, 95–101.

Leppäranta, M., and Manninen, T. (1988). The brine and gas content of sea ice with attention to low salinities and high temperatures. *Finnish Inst. Mar. Res. Intern. Rep.* 2, 1–14.

Leu, E., Mundy, C. J., Assmy, P., Campbell, K., Gabrielsen, T. M., Gosselin, M., et al. (2015). Arctic spring awakening–steering principles behind the phenology of vernal ice algal blooms. *Prog. Oceanogr.* 139, 151–170. doi: 10.1016/j.pocean.2015.07.012

Lund-Hansen, L. C., Hawes, I., Nielsen, M. H., and Sorrell, B. K. (2017). Is colonization of sea ice by diatoms facilitated by increased surface roughness in growing ice crystals? *Polar Biol.* 40, 593–602. doi: 10.1007/s00300-016-1981-3

Majaneva, M., Blomster, J., Müller, S., Autio, R., Majaneva, S., Hyytiäinen, K., et al. (2017). Sea-ice eukaryotes of the Gulf of Finland, Baltic Sea, and evidence for herbivory on weakly shade-adapted ice algae. *Eur. J. Protistol.* 57, 1–15. doi: 10.1016/j.ejop.2016.10.005

Mangoni, O., Carrada, G. C., Modigh, M., Catalano, G., and Saggiomo, V. (2009). Photoacclimation in Antarctic bottom ice algae: an experimental approach. *Polar Biol.* 32, 325–335. doi: 10.1007/s00300-008-0517-x

McCook, L. J. (1994). Understanding ecological community succession: causal models and theories, a review. *Vegetatio* 110, 115–147.

Meier, W. N., Hovelsrud, G. K., van Oort, B. E. H., Key, J. R., Kovacs, K. M., Michel, C., et al. (2014). Actic sea ice in transformation: a review of recent observed changes and impacts on biology and human activity. *Rev. Geophys.* 51, 185–217. doi: 10.1002/2013RG000431

Meiners, K., Gradinger, R., Fehling, J., Civitarese, G., and Spindler, M. (2003). Vertical distribution of exopolymer particles in sea ice of the Fram Strait (Arctic) during autumn. *Mar. Ecol. Prog. Ser.* 248, 1–13. doi: 10.3354/meps248001

Melnikov, I. A. (1995). An *in situ* experimental study of young sea ice formation on an Antarctic lead. *J. Geophys. Res.* 100, 4673–4680.

Menden-Deuer, S., and Lessard, E. J. (2000). Carbon to volume relationship for dinoflagellates, diatoms and other protist plankton. *Limnol. Oceanogr.* 45, 569–579. doi: 10.4319/lo.2000.45.3.0569

Meyer, A., Sundfjord, A., Fer, I., Provost, C., Villacieros Robineau, N., Koenig, Z., et al. (2017). Winter to summer oceanographic observations in the Arctic Ocean north of Svalbard. *J. Geophys. Res. Ocean.* 122, 6218–6237. doi: 10.1002/2016JC012391

Niemi, A., Michel, C., Hille, K., and Poulin, M. (2011). Protist assemblages in winter sea ice: setting the stage for the spring ice algal bloom. *Polar Biol.* 34, 1803–1817. doi: 10.1007/s00300-011-1059-1

Okolodkov, Y. B. (1992). Cryopelagic flora of the Chukchi, East Siberian and Laptev Seas. *Proc. NIPR Symp. Polar Biol.* 5, 28–43.

Oksanen, J., Blanchet, F. G., Friendly, M., Kindt, R., Legendre, P., McGlinn, D., et al. (2017). *Vegan: Community Ecology Package*. Available online at: https://cran.r-project.org/package=vegan

Olsen, L. M., Assmy, P., Duarte, P., Laney, S. R., Fernández-Méndez, M., Kauko, H. M., et al. (2017a). *N-ICE2015 Phytoplankton and Ice Algae Taxonomy and Abundance [Data set]*. Tromsø: Norwegian Polar Data Centre. doi: 10.21334/npolar.2017.dc61cb24

Olsen, L. M., Laney, S. R., Duarte, P., Kauko, H. M., Fernández-Méndez, M., Mundy, C. J., et al. (2017b). The seeding of ice algal blooms in Arctic pack ice: the multiyear ice seed repository hypothesis. *J. Geophys. Res. Biogeosci.* 122, 1–20. doi: 10.1002/2016JG003668

Peet, R. K. (1974). The measurement of species diversity. *Annu. Rev. Ecol. Syst.* 5, 285–307.

Petrich, C., and Eicken, H. (2010). "Growth, structure and properties of sea ice," in *Sea Ice*, eds D. N. Thomas and G. S. Dieckmann (Oxford, UK: Wiley-Blackwell), 23–77.

Petrou, K., Hill, R., Doblin, M. A., McMinn, A., Johnson, R., Wright, S. W., et al. (2011). Photoprotection of sea-ice microalgal communities from the east Antarctic pack ice. *J. Phycol.* 47, 77–86. doi: 10.1111/j.1529-8817.2010.00944.x

Petrou, K., Kranz, S. A., Doblin, M. A., and Ralph, P. J. (2012). Photophysiological responses of *Fragilariopsis cylindrus* (Bacillariophyceae) to nitrogen depletion at two temperatures. *J. Phycol.* 48, 127–136. doi: 10.1111/j.1529-8817.2011.01107.x

Pettersen, R., Johnsen, G., Berge, J., and Hovland, E. K. (2011). Phytoplankton chemotaxonomy in waters around the Svalbard archipelago reveals high amounts of Chl *b* and presence of gyroxanthin-diester. *Polar Biol.* 34, 627–635. doi: 10.1007/s00300-010-0917-6

Poulin, M., Daugbjerg, N., Gradinger, R., Ilyash, L., Ratkova, T., and von Quillfeldt, C. (2011). The pan-Arctic biodiversity of marine pelagic and sea-ice unicellular eukaryotes: a first-attempt assessment. *Mar. Biodivers.* 41, 13–28. doi: 10.1007/s.12526-010-0058-8

R Core Team (2017). *R: A Language and Environment for Statistical Computing*. Vienna: R Foundation for Statistical Computing. Available online at: https://www.R-project.org/

Ratkova, T. N., and Wassmann, P. (2005). Sea ice algae in the White and Barents seas: composition and origin. *Polar Res.* 24, 95–110. doi: 10.1111/j.1751-8369.2005.tb00143.x

Reimnitz, E., Kempema, E. W., Weber, W. S., Clayton, J. R., and Payne, J. R. (1990). "Suspended-matter scavenging by rising frazil ice," in *Sea Ice Properties and Processes, Proceedings of the W. F. Weeks Sea Ice Symposium, CRREL Monograph 90-1*, eds S. F. Ackley and W. F. Weeks (Hanover, NH: Cold Regions Research Engineering Laboratory), 97–100.

Riedel, A., Michel, C., Gosselin, M., and LeBlanc, B. (2007). Enrichment of nutrients, exopolymeric substances and microorganisms in newly formed sea ice on the Mackenzie shelf. *Mar. Ecol. Prog. Ser.* 342, 55–67. doi: 10.3354/meps342055

Riegger, L., and Robinson, D. (1997). Photoinduction of UV-absorbing compounds in Antarctic diatoms and *Phaeocystis antarctica*. *Mar. Ecol. Prog. Ser.* 160, 13–25. doi: 10.3354/meps160013

Rintala, J.-M., Piiparinen, J., Blomster, J., Majaneva, M., Müller, S., Uusikivi, J., et al. (2014). Fast direct melting of brackish sea-ice samples results in biologically more accurate results than slow buffered melting. *Polar Biol.* 37, 1811–1822. doi: 10.1007/s00300-014-1563-1

Robinson, D. H., Kolber, Z., and Sullivan, C. W. (1997). Photophysiology and photoacclimation in surface sea ice algae from McMurdo Sound, Antarctica. *Mar. Ecol. Prog. Ser.* 147, 243–256. doi: 10.3354/meps147243

Rösel, A., Itkin, P., King, J., Divine, D., Wang, C., Granskog, M. A., et al. (2018). Thin sea ice, thick snow and widespread negative freeboard observed during N-ICE2015 north of Svalbard. *J. Geophys. Res. Ocean* 123, 1–21. doi: 10.1002/2017JC012865

Roy, S., Lewellyn, C. A., Egeland, E. S., and Johnsen, G., (eds) (2011). *Phytoplankton Pigments - Characterization, Chemotaxonomy and Applications in Oceanography, 1st Edn*. Cambridge: Cambridge University Press.

Rózanska, M., Gosselin, M., Poulin, M., Wiktor, J. M., and Michel, C. (2009). Influence of environmental factors on the development of bottom ice protist communities during the winter-spring transition. *Mar. Ecol. Prog. Ser.* 386, 43–59. doi: 10.3354/meps08092

Rózanska, M., Poulin, M., and Gosselin, M. (2008). Protist entrapment in newly formed sea ice in the Coastal Arctic Ocean. *J. Mar. Syst.* 74, 887–901. doi: 10.1016/j.jmarsys.2007.11.009

Rysgaard, S., and Nielsen, T. G. (2006). Carbon cycling in a high-arctic marine ecosystem-Young Sound, NE Greenland. *Prog. Oceanogr.* 71, 426–445. doi: 10.1016/j.pocean.2006.09.004

Søgaard, D. H., Hansen, P. J., Rysgaard, S., and Glud, R. N. (2011). Growth limitation of three Arctic sea ice algal species: effects of salinity, pH, and inorganic carbon availability. *Polar Biol.* 34, 1157–1165. doi: 10.1007/s00300-011-0976-3

Søreide, J. E., Leu, E., Berge, J., Graeve, M., and Falk-Petersen, S. (2010). Timing of blooms, algal food quality and *Calanus glacialis* reproduction and growth in a changing Arctic. *Glob. Chang. Biol.* 16, 3154–3163. doi: 10.1111/j.1365-2486.2010.02175.x

Stoecker, D. K., Buck, K. R., and Putt, M. (1992). Changes in the sea-ice brine community during the spring- summer transition, McMurdo Sound, Antarctica. I. Photosynthetic protists. *Mar. Ecol. Prog. Ser. Ser.* 84, 265–278.

Stoecker, D. K., Gustafson, D. E., Black, M. M. D., and Baier, C. T. (1998). Population dynamics of microalgae in the upper land-fast sea ice at a snow-free location. *J. Phycol.* 34, 60–69. doi: 10.1046/j.1529-8817.1998.340060.x

Stoecker, D. K., Gustafson, D. E., Merrell, J. R., Black, M. M. D., and Baier, C. T. (1997). Excystment and growth of chrysophytes and dinoflagellates at low temperatures and high salinities in Antarctic sea-ice. *J. Phycol.* 33, 585–595. doi: 10.1111/j.0022-3646.1997.00585.x

Syvertsen, E. E. (1991). Ice algae in the Barents Sea: types of assemblages, origin, fate and role in the ice-edge phytoplankton bloom. *Polar Res.* 10, 277–288. doi: 10.1111/j.1751-8369.1991.tb00653.x

Taskjelle, T., Hudson, S. R., Pavlov, A. K., and Granskog, M. A. (2016). *N-ICE2015 Surface and Under-Ice Spectral Shortwave Radiation Data [Data set]*. Tromsø: Norwegian Polar Data Centre. doi: 10.21334/npolar.2016.9089792e

Thomas, D. N., and Dieckmann, G. S. (2002). Antarctic sea ice - a habitat for extremophiles. *Science* 295, 641–644. doi: 10.1126/science.1063391

Thomson, P. G., Wright, S. W., Bolch, C. J. S., Nichols, P. D., Skerratt, J. H., and McMinn, A. (2004). Antarctic distribution, pigment and lipid composition, and molecular identification of the brine dinoflagellate *Polarella glacialis* (Dinophyceae). *J. Phycol.* 40, 867–873. doi: 10.1111/j.1529-8817.2004.03169.x

Tran, S., Bonsang, B., Gros, V., Peeken, I., Sarda-Esteve, R., Bernhardt, A., et al. (2013). A survey of carbon monoxide and non-methane hydrocarbons in the Arctic Ocean during summer 2010. *Biogeosciences* 10, 1909–1935. doi: 10.5194/bg-10-1909-2013

Tuschling, K. V., Juterzenka, K., Okolodkov, Y. B., and Anoshkin, A. (2000). Composition and distribution of the pelagic and sympagic algal assemblages in the Laptev Sea during autumnal freeze-up. *J. Plankton Res.* 22, 843–864. doi: 10.1093/plankt/22.5.843

van Leeuwe, M. A., Tedesco, L., Arrigo, K. R., Assmy, P., Campbell, K., Meiners, K. M., et al. (2018). Microalgal community structure and primary production in Arctic and Antarctic sea ice: a synthesis. *Elem. Sci. Anthr.* 6:4. doi: 10.1525/elementa.267

Venables, W. N., and Ripley, B. D. (2002). *Modern Applied Statistics With S, 4th Edn*. New York, NY: Springer.

Von Dassow, P., and Montresor, M. (2011). Unveiling the mysteries of phytoplankton life cycles: patterns and opportunities behind complexity. *J. Plankton Res.* 33, 3–12. doi: 10.1093/plankt/fbq137

Weissenberger, J. (1998). Arctic Sea ice biota: design and evaluation of a mesocosm experiment. *Polar Biol.* 19, 151–159.

Weissenberger, J., and Grossmann, S. (1998). Experimental formation of sea ice: importance of water circulation and wave action for incorporation of phytoplankton and bacteria. *Polar Biol.* 20, 178–188. doi: 10.1007/s003000050294

Werner, I., Ikävalko, J., and Schünemann, H. (2007). Sea-ice algae in Arctic pack ice during late winter. *Polar Biol.* 30, 1493–1504. doi: 10.1007/s00300-007-0310-2

Conflict of Interest Statement: The authors declare that the research was conducted in the absence of any commercial or financial relationships that could be construed as a potential conflict of interest.

frontiers in Earth Science

ORIGINAL RESEARCH
published: 15 March 2018
doi: 10.3389/feart.2018.00022

Organic Matter Controls of Iron Incorporation in Growing Sea Ice

Julie Janssens[1,2,3]*, *Klaus M. Meiners*[2,3], *Ashley T. Townsend*[4] *and Delphine Lannuzel*[1,2]

[1] Institute for Marine and Antarctic Studies, University of Tasmania, Hobart, TAS, Australia, [2] Antarctic Climate and Ecosystems Cooperative Research Centre, University of Tasmania, Hobart, TAS, Australia, [3] Australian Antarctic Division, Department of the Environment and Energy, Kingston, TAS, Australia, [4] Central Science Laboratory, University of Tasmania, Hobart, TAS, Australia

This study presents the first laboratory-controlled sea-ice growth experiment conducted under trace metal clean conditions. The role played by organic matter in the incorporation of iron (Fe) into sea ice was investigated by means of laboratory ice-growth experiments using a titanium cold-finger apparatus. Experiments were also conducted to understand the role of extracellular polymeric substances (EPS) in the enrichment of ammonium in sea ice. Sea ice was grown from several seawater solutions containing different quantities and qualities of particulate Fe (PFe), dissolved Fe (DFe) and organic matter. Sea ice and seawater were analyzed for particulate organic carbon and nitrogen, macro-nutrients, EPS, PFe, and DFe, and particulate aluminum. The experiments showed that biogenic PFe is preferentially incorporated into sea ice compared to lithogenic PFe. Furthermore, sea ice grown from ultra-violet (UV) and non-UV treated seawaters exhibits contrasting incorporation rates of organic matter and Fe. Whereas, the effects of UV-treatments were not always significant, we do find indications that the type or organic matter controls the enrichment of Fe in forming sea ice. Specifically, we come to the conclusion that the incorporation of DFe is favored by the presence of organic ligands in the source solution.

Keywords: sea ice, iron, EPS, organic matter, organic ligands, incorporation, Antarctica

OPEN ACCESS

Edited by:
Benjamin Allen Lange, Fisheries and Oceans Canada, Canada

Reviewed by:
Maria A. Van Leeuwe, University of Groningen, Netherlands
Andrea Niemi, Fisheries and Oceans Canada, Canada

***Correspondence:**
Julie Janssens
julie.janssens@csiro.au

Specialty section:
This article was submitted to Cryospheric Sciences, a section of the journal Frontiers in Earth Science

Received: *17 September 2017*
Accepted: *26 February 2018*
Published: *15 March 2018*

Citation:
Janssens J, Meiners KM, Townsend AT and Lannuzel D (2018) Organic Matter Controls of Iron Incorporation in Growing Sea Ice. Front. Earth Sci. 6:22. doi: 10.3389/feart.2018.00022

INTRODUCTION

Sea ice is an important reservoir of iron (Fe) in the Southern Ocean (e.g., Sedwick and DiTullio, 1997; Lancelot et al., 2009; Lannuzel et al., 2010; Wang et al., 2014). Every spring, Fe contained in sea ice is released into surface waters and can trigger phytoplankton blooms in the marginal ice zone. This seasonal event represents an important source of food for higher trophic levels and potentially contributes to the biological pump in the Southern Ocean (Sullivan et al., 1993; Lannuzel et al., 2007, 2010). Climate predictions suggest sea-ice extent and volume will decrease by 24 and 34%, respectively by 2100 (Arzel et al., 2006). The effect of these changes on sea-ice biogeochemical processes, and most importantly on the uptake of carbon dioxide (CO_2) in the Southern Ocean, remains enigmatic. It is therefore of primary importance to gain a mechanistic understanding of the processes leading to Fe enrichment in sea ice. This step is necessary to adequately represent ice-associated iron biogeochemistry in numerical models.

The co-occurrence of enrichment of organic matter and Fe in sea ice suggests that they are coupled (Grotti et al., 2005; Lannuzel et al., 2007, 2008, 2014a; van der Merwe et al., 2009, 2011a,b; de Jong et al., 2013, 2015; Janssens et al., 2016). It has been proposed that the Fe

concentration in the ice depends on the Fe concentration in the parent seawater during sea-ice formation (van der Merwe et al., 2009). Dissolved organic ligands, potentially in the form of extracellular polymeric substances (EPS), are thought to control the distribution of dissolved Fe (DFe) in sea ice and might be a crucial vector of Fe enrichment in forming sea ice (Lannuzel et al., 2015; Genovese et al., in review).

EPS are produced by algae and bacteria (Meiners et al., 2004; Mancuso Nichols et al., 2005b; Meiners and Michel, 2017) and have been found to be enriched in sea ice compared to seawater (e.g., Krembs et al., 2002a, 2011; Meiners et al., 2003, 2004; Riedel et al., 2006; van der Merwe et al., 2009; Underwood et al., 2010; Ewert and Deming, 2011; Aslam et al., 2012; Janssens et al., 2016). EPS are a good candidate for metallic anion binding (Croot and Johansson, 2000; Verdugo et al., 2004) given their high stickiness and negatively charged surfaces (Decho, 1990; Underwood et al., 2010). EPS exist in a continuum of sizes from dissolved and colloidal to particulate fractions (Verdugo et al., 2004), and therefore may control the enrichment of all Fe size fractions in sea ice.

Janssens et al. (2016) showed that sea-ice formation leads to concomitant physical enrichment of EPS, particulate organic matter and Fe, with larger particles being preferentially enriched compared to smaller particles during an *in situ* ice-growth experiment. Nonetheless the simultaneous investigation of physical, chemical and biological processes in field conditions is extremely difficult given the complex interactions between them. In this context, laboratory ice-growth experiments are valuable to isolate specific processes. Laboratory experiments allow the formation of sea ice in a controlled environment and from chosen source solutions.

Ice tank experiments and laboratory ice-growth experiment are numerous (e.g., INTERICE experiments in Germany—e.g., Weissenberger and Grossmann, 1998; Krembs et al., 2002b; Geilfus et al., 2012; Zhou et al., 2014; CRREL experiments in the United State of America—e.g., Kovacs, 1996; Loose et al., 2009; or SERF experiments in Canada—e.g., Galley et al., 2013; Else et al., 2015). To our knowledge, none of these studies have been conducted under the trace metal clean conditions needed to study Fe-associated processes. This study aims at understanding the basic processes leading to the incorporation of Fe into growing sea ice, and specifically the role of organic matter as a carrier of Fe. Experiments were performed using a titanium (Ti) cold-finger apparatus (Kuiper et al., 2003; Ewert and Deming, 2011) tailored for use under carbon and trace metal non-contaminating conditions. Experiments were conducted to understand the role of EPS in the enrichment of ammonium (NH_4^+) in sea ice (Zhou et al., 2013) and the role of organic matter in the enrichment of Fe in sea ice. We first hypothesize that the quality and quantity of EPS control the rate of incorporation of particulate organic carbon (POC) and NH_4^+ into sea ice. We tested this hypothesis by undertaking a set of experiments using surface water (assumed freshly formed EPS) and deep water (assumed old/preformed EPS), where we quantified the incorporation of EPS, organic matter and inorganic macro-nutrients [hereafter referred as macro-nutrients: nitrate+nitrite: NO_2+NO_3 $=NO_x$, silicic acid: $Si(OH)_4^-$, phosphate: PO_4^{3-}, and ammonium: NH_4^+)] into sea ice. Our second hypothesis was that organic matter is required to incorporate Fe into sea ice. We tested this by undertaking a second set of experiments targeting the role that organic matter plays in the enrichment of Fe (DFe and particulate Fe, PFe) into sea ice using UV and non-UV treated seawater. The addition of desert dusts and sea-ice algae in the source solutions was also carried out to investigate the difference between lithogenic and biogenic PFe incorporation in sea ice. To our knowledge, this work constitutes the first laboratory-based ice-growth experiments conducted under trace metal clean conditions.

METHODS

Experiments

Ice Texture Experiments

The first set of experiments, *Ice texture Exp.*, was conducted onboard RV *Polarstern*, and aimed at identifying the effects of different ice growth rates on ice crystal structure, i.e., ice texture. Seawater used for these experiments was collected during a winter cruise in the Weddell Sea onboard the RV *Polarstern* (ANT-XXIX/6, Lemke and Participants, 2014), using the ship water intake line. The ice was grown at −10, −15, and −20°C, for 24, 8, and 6.45 h respectively, and processed for ice texture analysis onboard the ship (**Table 1**).

Extracellular Polymeric Substances, POC, PON, and Macro-Nutrient Experiments

A second set of experiments, *EPS, POC, PON,* and *macro-nut. Exp.*, was run during the same voyage. Seawater was collected using the ship water intake line, a CTD or a peristaltic pump (E/S Portable Sampler, Masterflex) at different locations and different water depths (**Table 1**) to study the incorporation of EPS, POC, and particulate organic nitrogen (PON) and inorganic macro-nutrients (NO_2+NO_3 $=NO_x$, $Si(OH)_4^-$, PO_4^{3-}, and NH_4^+) into sea ice. The first source solution was surface seawater (Surface SW, ship water intake line). The second source solution was deep seawater (Deep SW) collected with the CTD at 4,300 m depth. In the third source solution (Surface SW + XG), 5 mg L^{-1} of xanthan gum (XG) from *Xanthomonas campestris* (Sigma-Aldrich) was added to the surface seawater sampled with a peristaltic pump (E/S Portable Sampler, Masterflex) at the ice-water interface. To achieve this, a stock solution of 1,000 mg L^{-1} XG was made and sonicated for 60 min using a Bandelin Sonopuls sonicator. The stock solution was then diluted 10 times in Ultra High Purity (UHP) water (Millipore, Gradient A10) and sonicated for 30 min before being added to the surface seawater.

Abbreviations: DFe, dissolved iron; EI, enrichment indices; EPS, extracellular polymeric substances; EPS, POC, PON and macro-nut. Exp., extracellular polymeric substances, POC, PON, and macro-nutrients experiments; Fe, iron; FEP, teflon fluorinated ethylene propylene; Ice texture Exp., ice texture experiment; Iron Exp., iron experiment; NOx, nitrate+nitrite; NH_4^+, ammonium; PAl, particulate aluminum; PFe, particulate iron; PO_4^{3-}, phosphate; POC, particulate organic carbon; PON, particulate organic nitrogen; $SiOH_4^-$, silicic acid; SW, seawater; UHP, ultra high purity; UV, ultraviolet; XG, xanthan gum; DOM, dissolved organic matter; DOC, dissolved organic carbon; CO_2, carbon dioxide.

TABLE 1 | Summary of the different cold-finger experiments.

Experiment name	Treatment name	Source solution	Addition and treatment	Freezing T (°C)	Parameters
Ice texture Exp.	Texture −10°C	RV *Polarstern* SW intake line, Weddell Sea	–	−10	Ice fabrics and dimensions of the ice formed
	Texture −15°C		–	−15	
	Texture −20°C		–	−20	
EPS, POC, PON and macro-nut. Exp.	Surface SW	RV *Polarstern* SW intake line, 67°39 S, 5°31 W	–	−15	Salinity, POC, macro-nutrients and EPS
	Deep SW	Deep SW (4,300 m), 68°01 S, 6°40 W	–		
	Surface SW + XG	Surface SW, 67°11 S, 13°14 W	5 mg/L Xanthan gum		
Iron Exp.	FSW + PFe	Pre-filtered (0.4 μm) surface SW from Trumpeter Bay, (Tasmania), 43°16 S, 147°39 E	30 μM PFe	−15	Salinity, PFe, PAl, DFe, POC, PON
	UV-FSW + PFe		30 μM PFe + 15 min UV		
	FSW + DFe		30 μM DFe		
	UV-FSW + DFe		30 μM DFe + 15 min UV		
	FSW + Algae		Sea ice algae		

In each experiment seawater was collected at different locations and different treatments were used as source solution. SW, seawater; XG, xanthan gum; POC and PON, particulate organic carbon and nitrogen; EPS, extracellular polymeric substances, FSW, filtered seawater; UV, ultra-violet; DFe, dissolved Fe; PFe, particulate Fe; PAl, particulate aluminum.

Iron Experiments

A third set of experiments, *Iron Exp.*, aimed at assessing the role of organic matter in the incorporation of Fe into growing sea ice. Experiments were conducted under trace metal clean conditions at the University of Tasmania. Surface seawater was collected on the 9th of October 2015 from Trumpeter Bay, (Tasmania: 43°16 S, 147°39 E) using a shoreline, and stored in acid-clean low-density polyethylene (LDPE, Nalgene) carboys. The sampling depth was approximately 2.5 m. In the home laboratory, seawater was filtered through polycarbonate (PC) membranes (Sterlitech, pore size: 0.4 μm) at low vacuum (<0.13 bar) using an acid-clean PC filtration apparatus (Sartorius) under a class-100 laminar flow hood (AirClean 600 PCR workstation, Model 300 Controller, AirClean System).

Filtered seawater (FSW) was divided into separate bottles for separate sets of treatments. Triplicate bottles were then spiked with different types of Fe. Added concentrations were selected to reach detectable Fe signals during analyses, despite the small volume of sea ice formed and remaining seawater. The first source solution, "FSW + PFe," was obtained by adding 30 μM of lithogenic PFe (PFe > 0.4 μm) to the FSW. Dust particles < 20 μm were used, collected in the Atacama desert, Chile (European Southern Observatory, Paranal), assuming a composition of 5% (w:w) of Fe, similar to the Earth's Crust (Taylor, 1964).

A second source solution, "FSW + DFe," was obtained by adding 30 μM of DFe (DFe < 0.4 μm) into the FSW using a commercial solution of 1,000 ppm of $FeCl_3$ (Merck).

Two complementary sets of experiments were run after UV-treatment of the FSW. This UV exposure step ensured the destruction of any dissolved organic matter (DOM) present in the solution (Queroue et al., 2014). Filtered seawater was dispensed into acid-clean 0.5 L Teflon fluorinated ethylene propylene (FEP) bottles (Nalgene) and placed between ultraviolet lamps inside a black PVC chamber for 15 min. After UV exposure, PFe or DFe was added to the source solution following the steps adopted in treatments "FSW + PFe" and "FSW + DFe." The latter treatments are referred to as "UV-FSW + PFe" and "UV-FSW + DFe."

A final experiment was carried out using FSW to which 44 mL of melted bottom sea ice containing algae was added. The ice sample was collected at Davis station, Antarctica in November 2015 and maintained under optimum growth conditions in the IMAS culture room until the start of the experiment. This treatment, named "FSW + Algae," aimed at studying the incorporation of biogenic PFe in sea ice. A list of the treatments is given in **Table 1**.

Sea-Ice Growth Set-Up

The experimental set-up and manipulations were conducted in a custom-made clean plastic bubble in a 4°C cold room onboard RV *Polarstern* (*Ice texture Exp.*, *EPS, POC, PON, and macro-nut. Exp.);* and under a class-100 laminar flow hood (AirClean 600 PCR workstation, Model 300 Controller, AirClean System) in a 4°C cold room in the home-laboratory for experiments on the incorporation of Fe and organic matter (*Iron Exp.).* Ice was grown using a cold-finger apparatus first described by Kuiper et al. (2003) and Ewert and Deming (2011), modified for use under carbon and trace metal non-contaminant conditions. The cold-finger was fully made of titanium (Ti) and cooled with a circulating bath (Wise Circu, WCR-P22) using ethanol as coolant (**Figure 1**).

The cold-finger was immersed straight in a custom-cut square acid-clean 2 L PC container (Nalgene) filled with different source solutions of seawater (**Table 1**). The PC container was placed into an insulated box made of foam insulation sheet (TechLite®) and placed on a magnetic stirrer to insure the homogeneity of the source solutions during the experiments.

At the end of each 8-h experiment, the ice was carefully removed from the remaining seawater and extracted from the

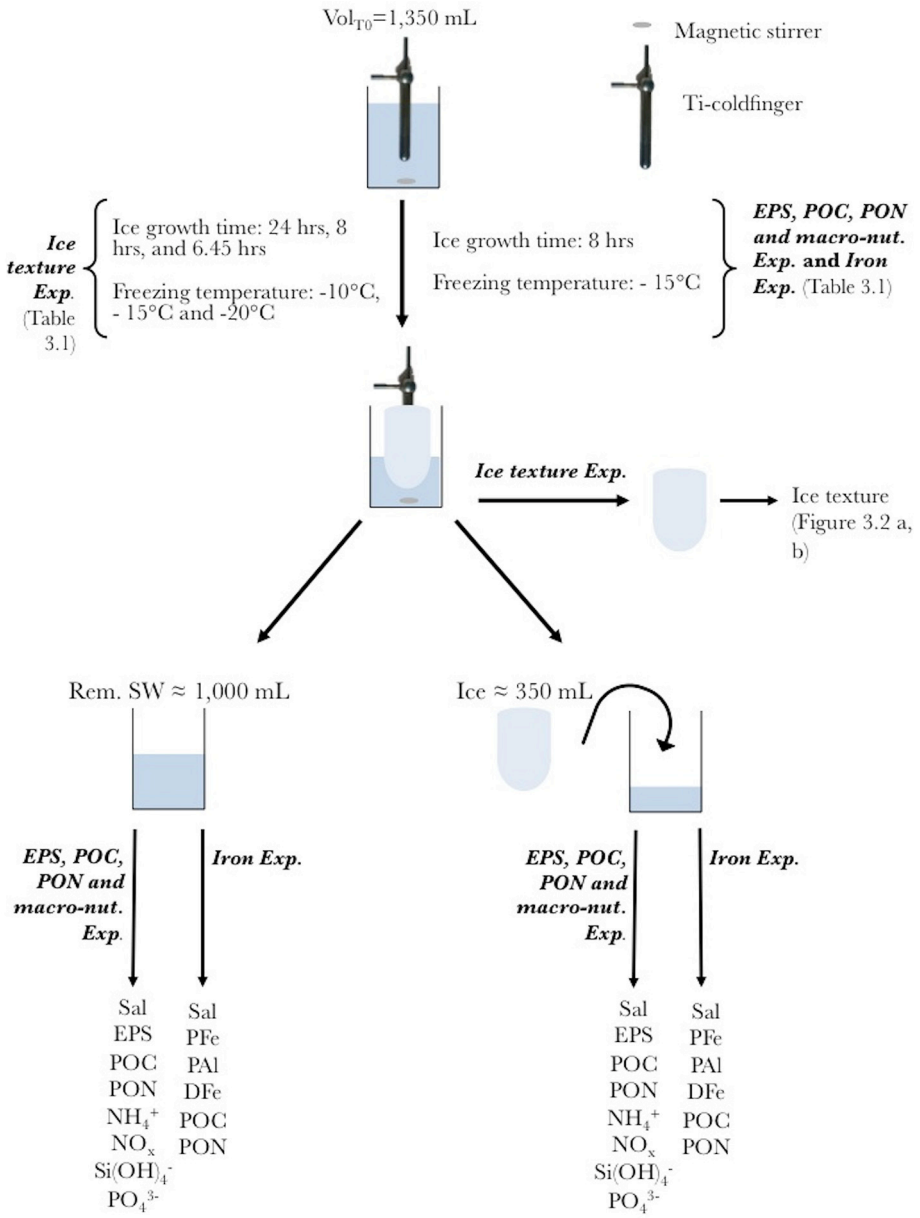

FIGURE 1 | Schematic of the cold-finger experiment for the Ice texture Experiment (*Ice texture Exp.*), the Extracellular polymeric substances, POC, PON, and macro-nutrients experiment (*EPS, POC, PON,* and *macro-nut Exp.*) and the iron experiment (*Iron Exp.*). The entire set-up was placed in a custom-made clean plastic bubble (*Ice texture Exp.* and *EPS, POC, PON,* and *macro-nut. Exp.*), or under a laminar flow hood (*Iron Exp.*). The cold-finger was connected to a circulating water bath with ethanol (not shown). Experiments were run in triplicate. For each experiment the volume at T_0 was 1,350 mL. The ice was formed at −10, −15, and −20°C for 24, 8, and 6.45 h respectively for the *Ice texture Exp.*, and −15°C for 8 h for the *EPS, POC, PON,* and *marco-nut. Exp.* and the *Iron Exp*. Once formed, the ice was removed from the cold-finger, and processed for ice texture (*Ice texture Exp.*), or allowed to melt in the dark at room temperature before further processing (*EPS, POC, PON,* and *macro-nut. Exp.* and *Iron Exp.*). Both remaining seawater (Rem. SW) and ice were processed for parameters described in the method section.

cold-finger. Ice was allowed to melt at room temperature in an acid-clean PC container, following methods from Rintala et al. (2014). A diagram of the experimental set-up and workflow is shown in **Figure 1**. Both remaining seawater and melted ice were analyzed for the list of parameters described below. Prior to each treatment a T_0 sample was collected for measurements of the same parameters in the source solution.

Physical Variables: Salinity and Ice Texture

Salinities (practical salinity, S_P) of seawater, bulk ice (melted bulk-ice sample) and remaining seawater were measured using a portable salinity probe (YSI Incorporated model 30, precision ± 0.1). Vertical and horizontal thin sections of the ice were prepared following the method of Langway (1958). Thin sections were observed through 2 cross-polarized filters and

photographed following methods described in detail in Janssens et al. (2016).

Biogeochemical Variables

Extracellular Polymeric Substances

Melted ice and seawater samples were homogenized and filtered onto 25 mm diameter PC membranes (0.4 μm, Millipore) under low vacuum (<0.13 bar) to avoid cell lysis. Filters were stained with 500 μL of a solution of Alcian Blue (AB, GX8 Sigma, 0.02% AB in 0.06% acetic acid). Excess dye was removed by rinsing the membrane with 2 mL of UHP water (Millipore, Gradient A10). Membranes were then stored individually at −20°C in the dark until analysis. Concentrations were determined colorimetrically using the method of Passow and Alldredge (1995) and modified by van der Merwe et al. (2009). Concentrations were computed using the filter capture efficiency of 4% from van der Merwe et al. (2009).

Dissolved and Particulate Organic Material and Macro-Nutrients

All glassware used for POC and PON analysis were soaked in a 2% (v:v) HCl solution (analytical grade Merck EMSURE Germany), rinsed with UHP water, wrapped in aluminum foil and combusted at 450°C for 4 h. In between triplicates and treatments, glassware was rinsed with UHP water, soaked in a 2% (v:v) HCl solution (analytical grade, Merck EMSURE Germany) for 8 h and rinsed thoroughly with UHP water. Samples for POC and PON were filtered onto pre-combusted 25 mm quartz filters (Sartorius). A 20 mL subsample of the filtrate was collected and stored at −20°C in the dark until analysis for macro-nutrient concentrations (NO_x, $Si(OH)_4^-$, PO_4^{3-}, and NH_4^+). POC and PON samples were stored at −20°C in the dark until analysis. After acidification of the filters [30 μL of 10 % (v:v) HCl, Ajax Finichem] to remove inorganic carbon, POC and PON concentrations were determined using a Thermo Finnigan EA 1112 Series Flash Elemental Analyzer (precision 1%) at Central Science Laboratory (CSL, University of Tasmania). Silicic acid was analyzed using a photometric analyzer (Aquakem 250) and PO_4^{3-}, NO_x, and NH_4^+ were analyzed with a Lachat Flow injection analyzer following the methods of Grasshoff et al. (2009). Detection limits were 0.1 and 0.002 mg L^{-1} for each method, respectively.

Iron and Aluminum

All sampling LDPE bottles, PC containers, PC filtration sets, petri-dishes and other equipment in contact with the samples were cleaned following GEOTRACES recommendations (Cutter et al., 2017). Polycarbonate membranes for PFe and PAl were soaked in 10% (v:v) ultrapure HCl for a week, thoroughly rinsed with UHP water (Barnstead International, NANOpure Diamond polisher) and stored in UHP water until use. Before and between treatments and triplicates, the cold-finger was thoroughly rinsed with UHP water. Between triplicates, equipment used for Fe filtrations was thoroughly rinsed with UHP water, soaked in a 10% (v:v) HCl solution for 16 h and rinsed 5 times with UHP water.

Immediately after removing the ice from the PC bottle, the remaining seawater was filtered onto 0.4 μm pore size 47 mm diameter PC membrane filters (Sterlitech) using an acid-clean PC filtration set (Sartorius) under gentle vacuum (<0.13 bar). The filter was collected for measurements of PFe and PAl (particles > 0.4 μm) concentrations, and placed in acid-clean polystyrene petri-dishes. 60 mL of the filtrate was collected in LDPE bottles (Nalgene) and acidified to pH 1.8 with ultrapure HCl (Seastar from Choice Analytics) for DFe analysis. Once fully melted, the same process was applied to the melted sea ice. Filters were stored individually in acid-clean petri-dishes, triple bagged and kept at −20°C in the dark until analysis. The LDPE bottles containing the dissolved fraction were triple bagged and kept at ambient temperature until analysis.

Filters for PFe and PAl determination were digested using a mixture of strong acids following the method described in Bowie et al. (2010). Dissolved Fe samples were diluted 10 times to reduce sea salt matrix interferences effects during analysis. Particulate metals and DFe concentrations were then measured at the Central Science Laboratory (University of Tasmania) using a Sector Field Inductively Coupled Plasma Mass Spectrometer (ICP-MS, Element 2), following methods described in Bowie et al. (2010).

Segregation Coefficient and Enrichment Index

The partition coefficient, K_{eff} is used to describe the proportion of solute that is retained in sea ice.

$$K_{effX} = [X]_{ice}/[X]_{source}$$

where $[X]_{ice}$ and $[X]_{source}$ is the concentration of the component X in the ice and in the source solution, respectively.

To assess the enrichment of each component in the ice compared to sea salt, the enrichment index was calculated (EI_x, Gradinger and Ikävalko, 1998).

$$EI_x = [Sal]_{source}/[Sal]_{ice}.\,[X]_{ice}/[X]_{source}$$

where $[Sal]_{source}$ is the salinity of the source solution, and $[Sal]_{ice}$ is the salinity of the ice. Enrichment index of 1, <1 or >1 will correspond to conservative, depletion or enrichment, respectively, of the component X as compared to bulk salinity.

Statistical Analysis

All statistical analyses were conducted using the statistical software R (version 3.3.3, R development Core Team, 2017). Differences in treatments were tested with standard analysis of variance (ANOVA) after log-transforming the response parameters to stabilize the variance (graphical diagnosis: Residuals vs. Fitted values, Normal quantiles vs. Standardized residuals, Scale location and Constant leverage). ANOVA was followed by a single-step multiple comparison Tukey-Honest Significant Differences (Tukey-HSD) procedure to determine which treatments differ. When the ANOVA showed no evidence of treatments differences for EIs, a *t*-test was performed to assess if the overall mean (of all treatments) of the EI was different from 1.

RESULTS

Ice Texture and Salinity

The ice texture was dominated by columnar ice (**Figures 2A,B**). The texture reflected the geometry of the cold-finger. Except for small differences in the size of the ice crystals, temperature had no effect on the geometry of the ice crystals.

Salinities of bulk-ice samples, as well as in the remaining seawater, were consistent throughout the experiments, with a mean bulk-ice salinity of 14.5 ± 1.3 S_P (mean ± standard deviation (*SD*), $n = 24$), and a mean salinity of 39.6 ± 1.3 ($n = 24$) for remaining seawater. The different growth temperatures applied to the samples resulted in similar partition coefficients (mean $K_{eff} = 0.32 \pm 0.07$, $n = 3$).

Extracellular Polymeric Substances, POC, PON, and Macro-Nutrients Experiments

Enrichment Indices of Macro-Nutrients and EPS

Figure 3 shows the enrichment indices for EPS and macro-nutrients in sea ice grown from Surface SW, Deep SW and Surface SW + XG. The horizontal line marks the EI = 1 (i.e., conservative incorporation). Results show that $Si(OH)_4^-$, NO_x, and PO_4^{3-} behave conservatively during sea-ice formation, whatever the source solution may be. Enrichment indices were close or equal to one for the macro-nutrients in Surface SW, Deep SW and Surface SW + XG (mean ± *SD* = 1.0 ± 0.09, $n = 9$), except NH_4^+ that was enriched in the ice in each treatment. The largest signal was observed for NH_4^+, which is clearly enriched in sea ice compared to seawater, especially in the deep samples (**Figure 3**). We observed moderate evidence of a difference in incorporation of NH_4^+ between treatments (ANOVA $F = 5.28$, $P = 0.082$). A Tukey-HSD multiple comparison procedure showed that only the Deep SW and Surface SW + XG treatments could be distinguished ($P = 0.07$). EPS enrichment was variable and showed no significant differences (ANOVA $F = 2.03$, $P = 0.212$) between treatments. The highest EI_{EPS} was observed in the Surface SW treatment and the lowest EI_{EPS} was observed in the Deep SW treatment (**Figure 3**). The Deep SW experiment had the highest $EI_{NH_4^+}$ and also the lowest EI_{EPS}.

Enrichment Indices of POC and PON

All EI_{POC} and EI_{PON} were well above 1 indicating an enrichment of POC and PON in newly-formed ice (**Figure 4**). Mean EI_{POC} and EI_{PON} were 50.5 ± 35.7 ($n = 9$) and 8.9 ± 6.4 ($n = 9$), respectively. There is no evidence of treatment difference for EI_{POC} (ANOVA $F = 1.99$, $P = 0.186$), and strong evidence of treatment difference for EI_{PON} (ANOVA $F = 11.23$, $P = 0.005$; Tukey-HSD Surface SW + XG and Deep SW, $P = 0.038$; Tukey-HSD Surface SW + XG and Surface SW, $P = 0.005$).

Iron Experiments

Enrichment Indices of PFe and DFe

Figure 5 shows the enrichment indices for DFe and PFe in sea ice grown from the five different source solutions. The horizontal line marks the EI = 1 (i.e., conservative incorporation). Results show that DFe and PFe do not behave conservatively during sea-ice formation in any of the source solutions. Dissolved Fe was slightly enriched in sea ice compared to the source seawater solution in each treatment ($EI_{DFe} > 1$, *t*-test confidence level 95%, $P = 0.002$) and relatively stable between treatments (mean $EI_{DFe} = 2.2 \pm 0.9$, **Figure 5**) with no evidence that EI_{DFe} differed across treatment groups (ANOVA $F = 1.85$, $P = 0.196$).

We observed a strong evidence of difference in incorporation of PFe between treatments (ANOVA $F = 5.17$, $P = 0.035$). The UV-FSW + DFe and FSW + Algae treatments groups could be distinguished at the 0.05 level (Tukey-HSD, $P = 0.02$). Ice was enriched in PFe in the treatments where lithogenic or biogenic PFe was added: FSW + PFe ($EI_{PFe} = 1.3 \pm 1.41$, $n = 3$) and FSW + Algae ($EI_{PFe} = 4.7 \pm 2.8$, $n = 3$; **Figure 5**). When lithogenic PFe was added and UV treatment applied, less PFe was incorporated in sea ice (UV-FSW + PFe, $EI_{PFe} = 0.5 \pm 0.3$, $n = 3$) than without UV-treatment. The treatment where biogenic PFe was added (FSW + Algae) showed the highest EI_{PFe} of all treatments ($EI_{PFe} = 4.7 \pm 2.8$, $n = 3$).

Enrichment Indices of POC and PON

Particulate organic matter (POC and PON) was more enriched in sea ice in treatments where PFe was added than in treatments where DFe was added (EI_{POC}: ANOVA, $F = 23.14$, $P = 0.003$; and EI_{PON}: ANOVA, $F = 24.57$, $P = 0.000$). Unlike other parameters, POC was the only compound showing a higher EI in UV-treated than in its non-UV treated equivalent. The enrichment index of PON was always lower than EI_{POC} (ANOVA, $F = 4.48$, $P = 0.040$; **Figure 6**).

Overall, the FSW + DFe and UV-FSW + DFe treatments had the lowest EIs and the lowest variability with EI_{PON} of 1.1 ± 0.7, $n = 3$ and 0.8 ± 0.5, $n = 3$, respectively.

The treatments with addition of lithogenic and biogenic PFe, and no UV treatment (FSW + PFe and FSW + Algae) were the only ones where enrichment in all compounds (DFe, PFe, POC, and PON) was observed relative to the source solution (**Figures 5**, **6**). This was not the case for the treatments where DFe was added (FSW + DFe and UV-FSW + DFe), or when UV light was applied, where, depending on the compound, enrichment or depletion was observed.

Particulate Fe to Particulate Al Ratios

Aluminum can be used as a tracer of lithogenic Fe inputs (Lannuzel et al., 2014a). The PFe/PAl molar ratio in the ice was elevated in all treatments compared to the Earth crustal ratio of 0.33 (Taylor, 1964). Two different patterns were observed: In the treatments with addition of PFe (FSW + PFe, UV-FSW + PFe and FSW + Algae), PFe/PAl was higher in the ice than in the remaining seawater (**Figure 7A**), however, this was not statistically significant (ANOVA $F = 0.68$, $P = 0.423$). In these treatments, the PFe/PAl ratios in the ice were up to 2 times higher than the crustal ratio (**Figure 7A**). In the treatment with DFe addition (FSW + DFe and UV-FSW + DFe) the PFe/PAl ratio in the ice was lower than in the remaining seawater (ANOVA $F = 9.60$, $P = 0.011$). In these experiments with addition of DFe, the PFe/PAl ratios were two to three orders of magnitudes higher than the crustal ratio (**Figure 7B**).

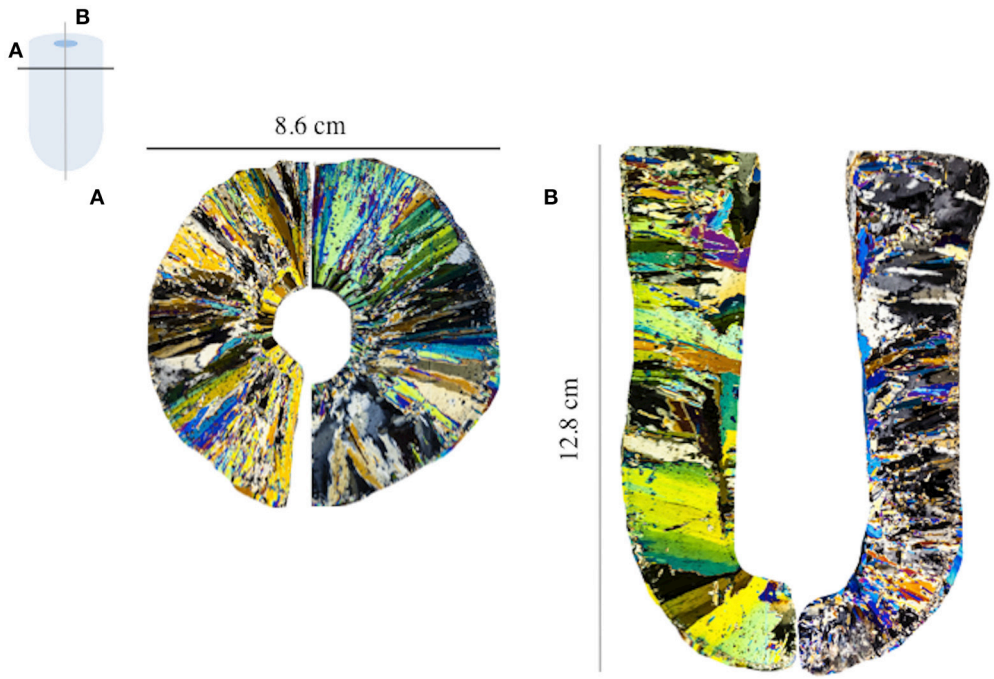

FIGURE 2 | Thin section of **(A)** the horizontal (black line) and **(B)** vertical (gray line) cross-section of the sea ice grown at −15°C. Each colors represents an individual ice crystal seen through cross-polarized light.

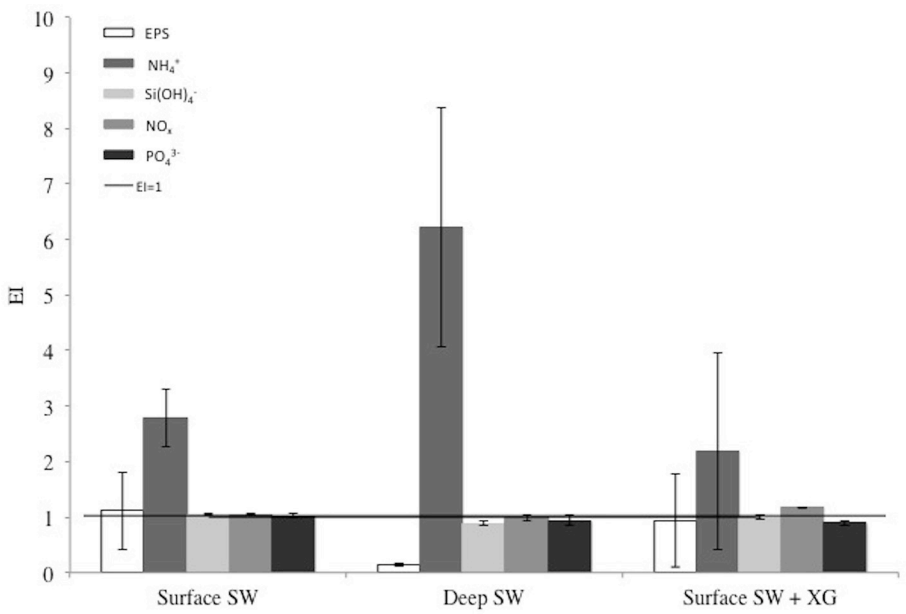

FIGURE 3 | Enrichment indices (EI) of extracellular polymeric substances (EPS), ammonium (NH_4^+), silicic acid ($Si(OH)_4^-$), nitrate + nitrite (NO_x), and phosphates (PO_4^{3-}) in the *EPS, POC, PON, and macro-nut. Exp*. The error bars represent the standard deviation between triplicates ($n = 3$). The black line shows the limit between enrichment (EI>1) or depletion (EI<1) of each compound.

DISCUSSION

The similarity in bulk ice and remaining seawater salinities between the different sets of experiments shows the reproducibility of our experimental set-up. Despite the unusual ice texture of the samples (horizontal ice crystals), representative processes of the natural environment are shown with the conservative behavior (i.e., relative to salt) of macro-nutrients,

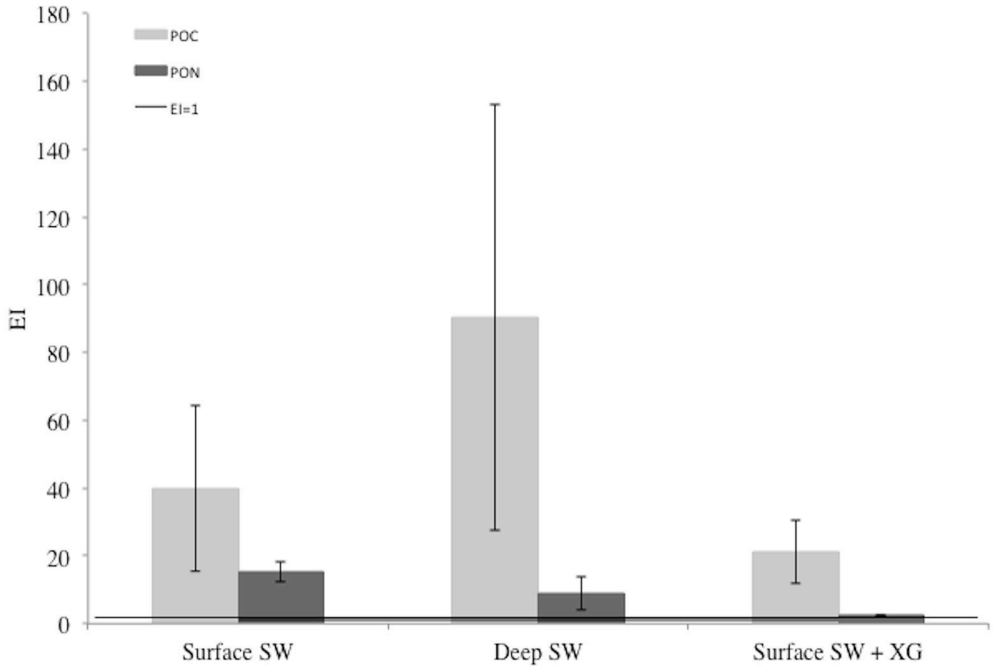

FIGURE 4 | Enrichment indices (EI) of particulate organic carbon (POC) and nitrogen (PON) in the *EPS, POC, PON,* and *macro-nut. Exp*. The error bars represent the standard deviation between triplicates ($n = 3$). The black line shows the limit between enrichment (EI>1) or depletion (EI<1) of POC or PON.

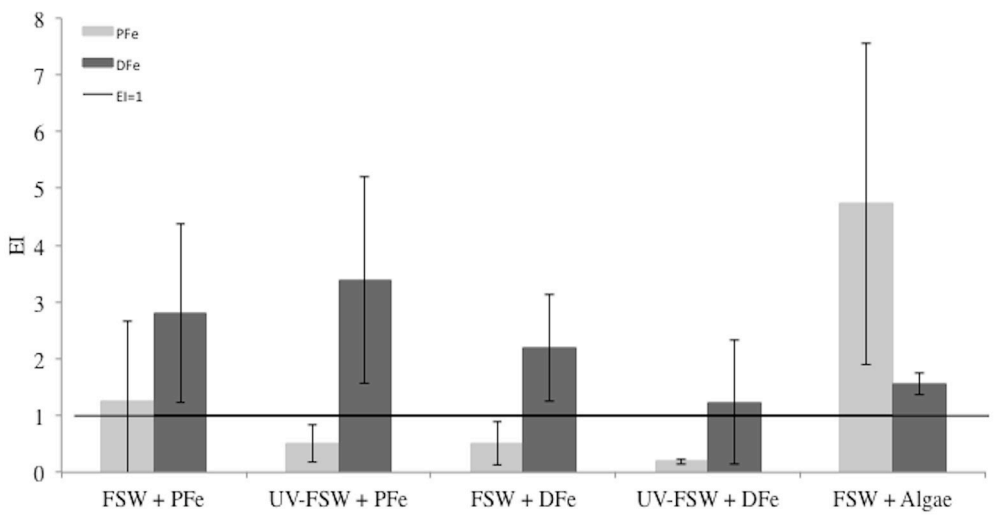

FIGURE 5 | Enrichment indices (EI) of particulate iron (PFe) and dissolved iron (DFe) in each treatment of the *Iron Exp*. The error bars represent the standard deviation between triplicates ($n = 3$). The black line shows the limit between enrichment (EI>1) or depletion (EI<1) of PFe or DFe.

except NH_4^+ as previously observed in natural young ice samples (Janssens et al., 2016) and sea-ice tank experiments (Zhou et al., 2014). In this study, the geometry of the ice crystal grown at 3 different temperatures in the *Ice texture Exp*. do not show any difference. This indicates that selection of the freezing temperature for the next set of experiments did not influence estimated EIs. The freezing temperature was chosen to resemble a realistic temperature encountered in the field in winter, but was somewhat constrained by the minimum temperature of the circulating water bath.

Extracellular Polymeric Substances, POC, PON, and Macro-Nutrients Experiments

POC, PON, and EPS

EPS from deep seawater were the least enriched in the ice, although it had the highest initial concentration (0.10 μg xeq

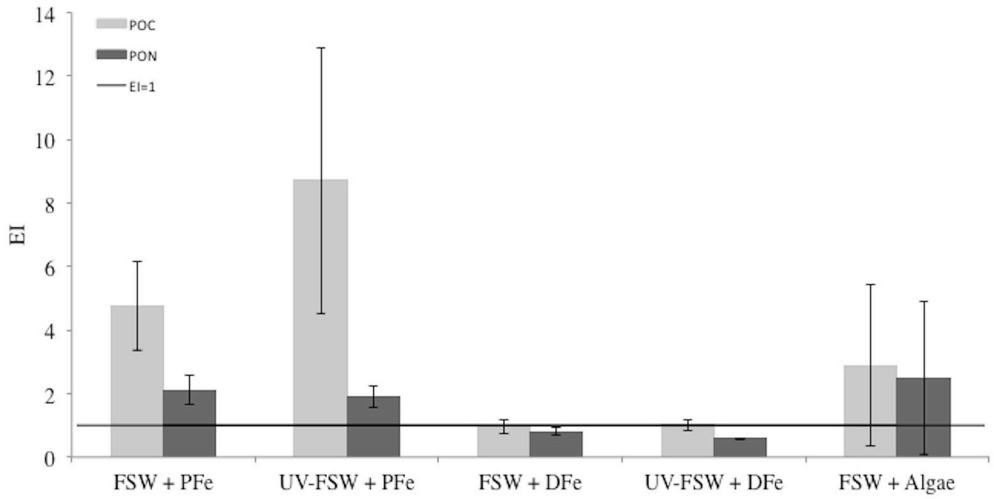

FIGURE 6 | Enrichment indices (EI) for POC and PON in each treatment of the *Iron Exp*. The error bars represent the standard deviation between triplicates ($n = 3$). The black line shows the limit between enrichment (EI>1) or depletion (EI<1) of POC or PON.

L^{-1}). Also, the addition of XG, a reference standard for EPS in marine environments (Passow and Alldredge, 1995), did not show a preferential enrichment compared to the natural EPS in other treatments. Deep-sea bacteria have been found to produce EPS (Mancuso Nichols et al., 2005b), and it could be that deep-water EPS have different surface properties (e.g., number of anionic groups) or molecular weights than EPS produced in surface waters. Decho (1990) reported that physico-chemical characteristics of EPS are influenced by their tertiary structure, which is dependent on the frequency and type of functional groups presence on the EPS. This could also affect the incorporation efficiency, with stickier EPS being more enriched (Meiners and Michel, 2017). These divergences in surface properties of EPS could also play an important role in the incorporation of NH_4^+ in this experiment. The highest NH_4^+ enrichment was found when EI_{EPS} was the lowest (**Figure 3**). EPS have a negatively charged surface due to the high content of poly-anionic sugars. They are stabilized by the presence of cations (such as e.g., K^+ and Ca^{2+}) (Kloareg and Quatrano, 1988; Verdugo et al., 2004). Also, the sticky properties of EPS determine the interaction of EPS with other components of the marine environment (Passow, 2002). Some authors (e.g., Krembs et al., 2002a; Meiners and Michel, 2017) have suggested that the negatively charged EPS would complex with NH_4^+, and helped by their stickiness, lead to the enrichment of NH_4^+ and EPS in the ice (Fripiat et al., 2017). However, the lack of correlation between EPS and NH_4^+ in our study does not support this hypothesis, and further study is needed to decipher this process. Microbial regeneration of NH_4^+ has been previously observed in young sea ice (Riedel et al., 2007). However, due to the short duration of our experiment we believe microbial regeneration alone cannot fully explain the enrichment of NH_4^+ in the ice. In an ice tank study, Krembs et al. (2011) found that concentrations of EPS were higher in the ice when *Melosira arctica*, a diatom found in Arctic sea ice, was added to the source solution compared to ice grown from saline solution containing different concentrations of XG, even if the concentration of XG was higher than the concentration of EPS produced by the diatom. Similarly, using a cold-finger apparatus similar to ours, Ewert and Deming (2011) showed that only native EPS produced by a cold-adapted marine bacterium (commonly found in sea ice) was preferentially incorporated in sea ice. Our results indicating that EPS from surface seawater are enriched in sea ice when compared to deep seawater are consistent with these previous findings, suggesting that the quality of EPS is a key parameter for its entrapment into sea ice.

Higher EI_{POC} than EI_{PON} are in line with previous reports of high POC and PON concentrations in young Antarctic sea ice (Janssens et al., 2016). In our laboratory study, POC and PON were more enriched in experiments using Antarctic unfiltered seawater compared with experiments conducted with filtered source solutions from Tasmania (*Iron* Exp.). The presence of biogenic material (phytoplankton, bacteria and EPS) in the unfiltered Antarctic sample could explain this higher enrichment compared to the filtered Tasmanian seawater sample. Also, similar to EPS, the quality of POC may control the degree of enrichment in sea ice. Due to its location, the coastal Tasmanian sampling site is under influence of terrestrial inputs bringing large amounts of allochtonous material to the pool of organic matter. This is in contrast to the Antarctic sampling sites, where the organic matter in the water column is mainly autochtonous. Zhou et al. (2014) showed that riverine DOM was less enriched in sea ice compared to autochtonous DOM, due to different molecular compositions, different affinity with other compounds, and with sea ice. Similarly, Müller et al. (2013) showed that the degree of dissolved organic carbon (DOC) enrichment depends on the chemical characteristics of the DOM. Our results suggest that the POC of potential terrestrial origin is less enriched in sea ice than the autochtonous Antarctic POC, by an order of magnitude. The reason why the POC is preferentially

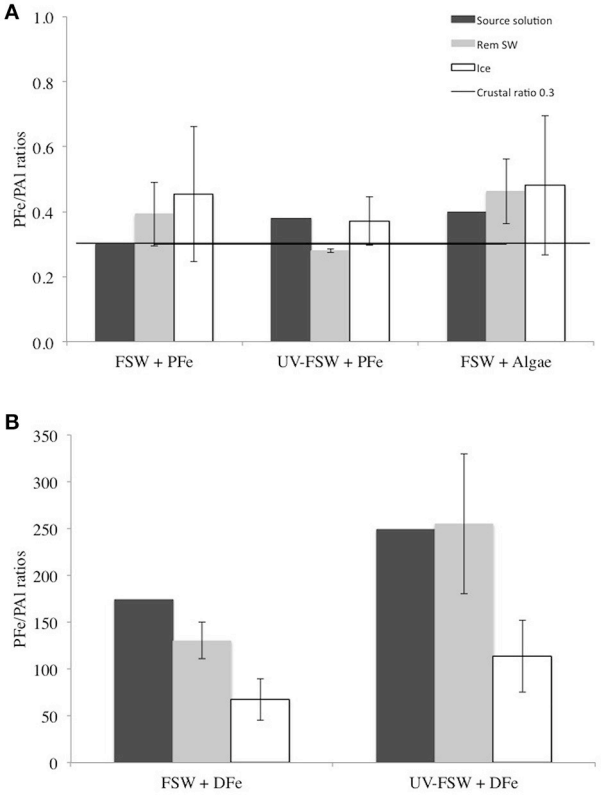

FIGURE 7 | PFe/PAl ratio in the source solution (dark gray), the remaining seawater (light gray) and in the ice (white) in **(A)** FSW + PFe, UV FSW + PFe and FSW + Algae treatments, and **(B)** FSW + DFe and UV FSW + DFe treatments. The dark line represents the Earth crustal PFe/PAl ratio (Taylor, 1964). The error bars represent the standard deviation between triplicates ($n = 3$).

incorporated in the ice compared to PON remains unclear at this stage and this needs further investigations. One idea is EPS might have a higher POC/PON ratio or the organic matter in the ice comprises a mixed composition of live and dead material, with a higher carbon content relative to nitrogen.

Iron Experiments

Lithogenic vs. Biogenic Iron: Role of EPS Produced by Ice Algae and Bacteria

The EI_{PFe} in FSW + Algae was found to be up to 4 times higher than in any other treatment, suggesting a better incorporation of the biogenic PFe compared to the lithogenic PFe. The bottom ice sample added to the FSW + Algae treatment was dominated by pennate diatoms such a *Nitzschia stellata, N. lecointei, Fragillariopsis spec.,* and *Entomoneis kjellmanii* (Andreas Seger and Fraser Kennedy, personal communication). The large size of algal cells compared to the dust sample, may have lead to the preferential enrichment of biogenic PFe relative to lithogenic PFe. The added dusts were sieved through 20 μm nylon mesh, while mentioned diatom species can be as large as 150 μm in cell size (Scott and Marchant, 2005), and can also form colonies and ribbon-chain like assemblages (Scott and Marchant, 2005; Aslam et al., 2012). Better incorporation of larger cells and impurities has been previously observed in natural young sea ice (Gradinger and Ikävalko, 1998; Riedel et al., 2007; Rózanska et al., 2008; Janssens et al., 2016).

Algal-bound EPS could also play a role in the incorporation of PFe into sea ice. Assemblages of diatoms are predominant in autotrophic-dominated sea-ice habitats and known to be associated to, and the main producers of, EPS (Krembs and Engel, 2001; Meiners et al., 2003, 2004; Mancuso Nichols et al., 2005a,b; Underwood et al., 2010, 2013). Particulate EPS have been shown to be likely of algal origin and quickly enriched into sea ice (Meiners et al., 2003; Riedel et al., 2007). EPS enrichment has been previously observed in cold-finger (Ewert and Deming, 2011) and ice tank experiments (Krembs et al., 2011). Negatively charged EPS (Decho, 1990; Mancuso Nichols et al., 2005a) are considered to be important in binding cationic metals like Fe^{3+} and Fe^{2+}. In return, Fe provides some stability to the EPS network by acting as bridging ions (e.g., Brown and Lester, 1982; Decho, 1990).

Finally, EPS are two to four orders of magnitude stickier than other particles (Passow, 2002), therefore potentially further helping the adhesion of PFe to ice surfaces. One can therefore assume that EPS were an important component of the added melted bottom ice sample to the source solution in the FSW + Algae treatment, contributing to the preferential enrichment in biogenic PFe compared to lithogenic PFe. Krembs et al. (2011) showed that the presence of EPS in the ice changes the microstructure of the ice and alters it physical properties. Thus, it is also possible that these modified properties are beneficial for PFe incorporation (more adapted shape of the pores and an increased internal sea ice surface area) but this requires further investigation.

The DFe fraction was less affected by the addition of algae than the PFe fraction. EPS range in size from sub-microns to hundreds of microns in the marine environment (Passow and Alldredge, 1995). EPS produced by sea-ice algae are known to be in the colloidal and soluble form (Aslam et al., 2012). In this study, a size distinction of 0.4 μm was used to define the dissolved and particulate fractions. This definition is however operationally defined and organic matter actually consists of a size continuum spanning across the soluble, colloidal and particulate size fractions. The colloidal material is operationally in the dissolved fraction as it is defined as the fraction that can pass through a filter with pore size of 0.1 to 0.46 μm (Chin et al., 1998). van der Merwe et al. (2009) suggested that organically-bound DFe in the ice shows reduced loss to the water column when brine drainage occurs by being associated with particles or cells (Sunda, 2001). The retention of DFe by EPS could explain the lower EI_{DFe} in the UV-treated FSW + DFe experiment.

Effect of UV Treatment on Fe Incorporation Efficiency: Importance of Organic Ligands

When subject to high UV exposure, DOM is degraded and ultimately transformed into carbon dioxide (CO_2) and water (H_2O). The UV- and non UV-treated experiments aimed at understanding the role of organic matter, including organic

ligands such as EPS, in the incorporation of Fe into sea ice. It has been shown that photochemical reactions alter the concentration and reactivity of the organic ligands involved in the complexation/solubilisation of trace metals (Moffett, 1995). More specifically, photochemical reduction of organically bound Fe decreases ligand-binding strength, rendering the complexed Fe more labile and increasing its bioavailability (Barbeau et al., 2001).

In this study, Fe was added to seawater solutions after UV treatment. While results between UV and non-UV treatments were not statistically significant, different enrichment behaviors for Fe and organic matter were observed between UV-treated and non-UV treated source solutions. The lack of statistical significance is a result of the large variance of the data set compared to the limited size of the data set. Further studies are needed to elucidate the full impact of UV treatment on the incorporation of organic matter into sea ice.

Nevertheless, as expected, DFe (and PFe) enrichment decreased when UV treatment was applied to FSW + DFe. This experiment suggests that the presence and quality of organic matter influences the incorporation of DFe into growing sea ice. However, DFe enrichment increased when UV treatment was applied to FSW + PFe. In the former treatments, the DFe was not present in excess; as such precipitation of DFe into PFe was not observed (see section Conversion of Dissolved Fe to Particulate Form). It is suggested that, in the latter case, the UV treatment resulted in the release of dissolved organic ligands from the degradation of particulate organic matter. These "newly-formed" ligands were then able to complex DFe and carry DFe into sea ice leading to higher EI_{DFe} in UV-FSW + PFe than in FSW + PFe, where dissolved organic ligands were more sparse. The difference in enrichment efficiency of DFe in (UV-)FSW+ PFe and (UV-)FSW + DFe by a combined effect of "ligand saturation" and precipitation of DFe into PFe can be explained in this way (see section Conversion of Dissolved Fe to Particulate Form). The UV-broken bound effect might have been compensated by the production of new dissolved organic ligands available for DFe. However, not enough dissolved organic ligands were present in solution to keep the added 30 μM of DFe in solution in the FSW + DFe treatment. Free DFe remaining in seawater therefore precipitated into PFe (see section Conversion of Dissolved Fe to Particulate Form), leading to the high PFe/PAl ratios observed.

As observed in the case of DFe incorporation in the (UV-)FSW + DFe treatments, PFe enrichment decreased when UV treatment was applied to FSW + PFe and FSW + DFe. This indicates the role of organic matter in the incorporation of PFe in growing sea ice. Unlike EI_{PFe} and EI_{DFe}, EI_{POC} increased when UV treatment was applied to FSW + PFe. It has been proposed that UV-B radiation breaks down not only DOC but also POC (UNEP, 1999), although the effect of UV on particulate organic matter is not clearly defined. Results here show that UV could impact on the quality of POC (including EPS) leading to different incorporation behaviors. It is likely that the POC becomes smaller when UV is applied and is then more easily incorporated into the ice. This argument however contradicts what has been previously observed in the field, where large particles are preferentially incorporated in sea ice (Gradinger and Ikävalko, 1998; Riedel et al., 2007; Lannuzel et al., 2014b; Janssens et al., 2016).

One explanation is that UV-radiation changes the physico-chemical properties of organic matter in a way that the PFe-organic matter binding capacity would be reduced, but the enrichment of POC would be favored. Organic-free PFe would therefore be hardly incorporated, while the UV-induced modifications in the POC facilitate its incorporation. It has been shown that the binding potential of EPS is greatly influenced by their physico-chemical properties (Krembs and Deming, 2008; Verdugo, 2012), which are likely to be altered by UV irradiation. Therefore, more than the size, the important factor for enrichment of particles would be their physico-chemical properties and the tertiary structure/molecular composition/shape of the particles. Zhou et al. (2014) suggested that organic matter is initially incorporated as particulate organic matter and then converted into DOM once in the ice. This process may be observed in the FSW + Algae treatment, with the transformation of POC into DOC by heterotrophic organisms, leading to lower EI_{POC} than in (UV-)FSW + PFe. However, we note that 8 h of incubation time may not be sufficient for significant transformation. Zhou et al. (2014) also showed that different quality of DOC impacts the incorporation efficiency. It is suggested that this mechanism is also applicable to particulate constituents as discussed in section Lithogenic vs. Biogenic Iron: Role of EPS Produced by Ice Algae and Bacteria.

Conversion of Dissolved Fe to Particulate Form

The PFe/PAl ratios measured in the samples can give an indication on the level of conversion of DFe into PFe. The addition of DFe into seawater led to very high PFe/PAl ratios in the FSW + DFe and UV-FSW + DFe experiments (**Figure 7B**). A significant amount of DFe (30 μM) was added to these 2 solutions, without addition of organic ligands (e.g., EDTA) to balance the addition of DFe and keep it in solution. Organic ligands can be produced *in situ* by sea-ice algae and bacteria (Lannuzel et al., 2015) or supplied externally from e.g., sediment resuspension (Croot and Johansson, 2000; Buck et al., 2007). EDTA is synthetically produced and is therefore not an adequate model ligand of the natural environment.

The conversion observed here of the non-organically bound excess of DFe into the PFe pool (Lannuzel et al., 2014a, 2015), leads to the high PFe/PAl ratios observed. This process was even more expressed in the UV-FSW + DFe treatment, where the UV exposure likely broke the bounds of the Fe-ligand complexes already present in the source solution before addition of DFe. The newly formed PFe and remaining DFe could be then less prone to incorporation into sea ice, as observed by lower EI_{PFe} and EI_{DFe}. Two explanations are possible: (1) As previously mentioned in the preceding section, biogenic PFe (low in these experiments) is preferentially enriched in the newly-formed ice compared to lithogenic PFe. A decoupling between biogenic and lithogenic PFe incorporation could be observed. EPS have been proposed to be acting as a "plug," retaining salinity in the ice (Krembs et al., 2011). If the biogenic PFe is incorporated first, helped by the association to, and then retained in the ice by EPS, the incorporation of lithogenic PFe might not be as efficient and

could reach a concentration threshold in the ice. The association of Fe with EPS, as well as the space available in the brine channel system would therefore determine the incorporation, retention, and threshold of PFe in the ice.

(2) Organic ligands may play a key role in transferring DFe from seawater to sea ice. Organically-bound Fe would take advantage of the properties of the particles it is attached to, to get trapped in the ice as discussed previously (section Effect of UV Treatment on Fe Incorporation Efficiency: Importance of Organic Ligands).

It is difficult to distinguish the contribution of each process in these experiments and it is likely a combination of both. We note that Fe concentrations in these experiments were above the range of concentrations encountered in the Southern Ocean, although they are in the range of concentration found in Antarctic fast ice (Grotti et al., 2001; van der Merwe et al., 2011a,b; Noble et al., 2013). All conclusions in this study are derived from a high concentration scenario in regards to added DFe and PFe, but nonetheless, our results provide key information on the general chemistry of the involved processes.

Limitations of Laboratory Ice-Growth Experiments

Laboratory experiments offer a unique opportunity to study ice growth from its initial stage of ice formation while the history of a natural ice floe is difficult to assess. Laboratory experiments allow the isolation of processes occurring at the onset of ice formation, and the study of the influence of specific parameters, while controlling others. Most importantly, replicate measurements are possible in the laboratory while field sampling of a natural ice floe always carries the uncertainty of high spatial heterogeneity (e.g., Meiners et al., 2012, 2017; Williams et al., 2015).

However laboratory based ice-growth experiments also present some drawbacks. First, ice growth is limited in space (a few cm^3) and time (a few hours). In the cold-finger case, the geometry of the system is different from natural ice. Ice crystals are mainly growing horizontally (**Figure 2**), while natural columnar ice exhibits vertical ice crystals. Nonetheless, the good agreement between laboratory-based results and field studies shows that the initial incorporation of solutes and particles over a short period of time is not affected by the geometry of the ice. The cold-finger set-up is, therefore, a useful tool to complete field data and isolate processes to gain a mechanistic understanding of sea-ice biogeochemical processes.

CONCLUSION

This study represents the first study of processes of Fe enrichment in sea ice under laboratory conditions. The investigation suggests an important role of EPS and POC in the enrichment of PFe in sea ice. Results also indicated that large particles of biogenic PFe derived from sea ice algae are preferentially enriched compared to smaller particles of lithogenic PFe derived from continental dust. Combined these results indicate that rather than the quantity, it is the quality of EPS and POC that determines their rate of entrapment in the ice, with autochtonous POC being more enriched than allochtonous POC. The mechanisms remain unclear, but characterizations of these particles would be a step forward to understand the complex links between Fe and organic matter incorporation into sea ice. The quality of particulate organic matter determines its association with PFe, and ultimately the efficiency of PFe incorporation in sea ice. UV treatment likely alters organic matter and modifies its association with Fe (PFe and DFe). This ultimately affects their degree of enrichment. In the context of changing sea-ice environments, it is important to clearly identify the drivers and to quantify the processes that affect ice-associated Fe and carbon biogeochemical cycling in polar waters.

AUTHOR CONTRIBUTIONS

JJ, KM, and DL: contributed to conception and design; JJ, KM, AT, and DL: contributed to acquisition of data; JJ, KM, AT, and DL: contributed to analysis and interpretation of data; JJ, KM, AT, and DL: drafted and revised the article; JJ, KM, AT, and DL: approved the submitted version for publication.

FUNDING

This work was funded by the Australian Research Council (LE0989539 and DE120100030), the Australian Government's Cooperative Research Centres Programme through the Antarctic Climate & Ecosystems Cooperative Research Centre (ACE CRC) and the Australian Antarctic Science (AAS) projects 4051 and 4298. JJ was supported by the Quantitative Antarctic Science Program jointly led by the University of Tasmania and the Australian Antarctic Division.

ACKNOWLEDGMENTS

The authors thank the officers and crew of *RV Polarstern* for their logistical support, as well as the colleagues from the biogeochemical group during the AWECS voyage. We thank Rob King and Tasha Waller from the Australian Antarctic Division for assistance with the collection of the seawater used in the *Iron Experiment*. We also thank Simon Wotherspoon for assistance with the statistical analysis.

REFERENCES

Arzel, O., Fichefet, T., and Goosse, H. (2006). Sea ice evolution over the 20th and 21th centuries as simulated by current AOGCMs. *Ocean Model* 12, 401–415. doi: 10.1016/j.ocemod.2005.08.002

Aslam, S. N., Cresswell-Maynard, T., Thomas, D. N., and Underwood, G. J. C. (2012). Production and characterization of the intra- and extracellular carbohydrates and polymeric substances (EPS) of three sea-ice diatom species, and evidence for a cryoprotective role for EPS. *J. Phycol.* 48, 1494–1509. doi: 10.1111/jpy.12004

Barbeau, K., Rue, E. L., Bruland, K. W., and Butler, A. (2001). Photochemical cycling of iron in the surface ocean mediated by microbial iron(III)-binding ligands. *Nature* 413, 409–413. doi: 10.1038/35096545

Bowie, A. R., Townsend, A. T., Lannuzel, D., Remenyi, T. A., and van der Merwe, P. (2010). Modern sampling and analytical methods for the determination of trace elements in marine particulate material using magnetic sector inductively coupled plasma-mass spectrometry. *Anal. Chim. Acta* 676, 15–27. doi: 10.1016/j.aca.2010.07.037

Brown, M. J., and Lester, J. N. (1982). Role of bacterial extracellular polymers in metal uptake in pure culture and activated sludge-1. Effect of metal concentration. *Water Res.* 16, 1539–1548. doi: 10.1016/0043-1354(82)90206-8

Buck, K. N., Lohan, M. C., Berger, C. J. M., and Bruland, K. W. (2007). Dissolved iron speciation in two distinct river plumes and an estuary: implications for riverine iron supply. *Limnol. Oceanogr.* 52, 843–855. doi: 10.4319/lo.2007.52.2.0843

Chin, W.-C., Orellana, M. V., and Verdugo, P. (1998). Spontaneous assembly of marine dissolved organic matter into polymer gels. *Nature* 391, 568–572. doi: 10.1038/35345

Croot, P. L., and Johansson, M. (2000). Determination of iron speciation by cathodic stripping voltammetry in seawater using the competing ligand. *Electroanalysis* 12, 565–576. doi: 10.1002/(SICI)1521-4109(200005)12:8<565::AID-ELAN565>3.0.CO;2-L

Cutter, G., Andersson, P., Codispoti, L., Croot, P., Francois, R., Lohan, M., et al. (2017). Sampling and sample-handling protocols for GEOTRACES cruises. Available at: http://www.geotraces.org/libraries/documents/Intercalibration/Cookbook.pdf

Decho, A. W. (1990). Microbial exopolymer in ocean environments: their roles in food webs and marine processes. *Ocean Mar. Biol. Annu. Rev.* 28, 73–153.

de Jong, J., Schoemann, V., Maricq, N., Mattielli, N., Langhorne, P., Haskell, T., et al. (2013). Iron in land-fast sea ice of McMurdo Sound derived from sediment resuspension and wind-blown dust attributes to primary productivity in the Ross Sea, Antarctica. *Mar. Chem.* 157, 24–40. doi: 10.1016/j.marchem.2013.07.001

de Jong, J. T. M., Stammerjohn, S. E., Ackley, S. F., Tison, J.-L., Mattielli, N., and Schoemann, V. (2015). Sources and fluxes of dissolved iron in the Bellingshausen Sea (West Antarctica): the importance of sea ice, icebergs and the continental margin. *Mar. Chem.* 177, 518–535. doi: 10.1016/j.marchem.2015.08.004

Else, B., Rysgaard, S., Attard, K., Campbell, K., Crabeck, O., Galley, R., et al. (2015). Under-ice eddy covariance flux measurements of heat, salt, momentum, and dissolved oxygen in an artificial sea ice pool. *Cold Reg. Sci. Technol.* 119, 158–169. doi: 10.1016/j.coldregions.2015.06.018

Ewert, M., and Deming, J. W. (2011). Selective retention in saline ice of extracellular polysaccharides produced by the cold-adapted marine bacterium Colwellia psychrerythraea strain 34H. *Ann. Glaciol.* 52, 111–117. doi: 10.3189/172756411795931868

Fripiat, F., Meiners, K. M., Vancoppenolle, M., Papadimitriou, S., Thomas, D. N., Ackley, S. F., et al. (2017). Macro-nutrients concentrations in Antarctic paci ice: overall patterns and overlooked processes. *Elem. Sci. Anthr.* 5:13. doi: 10.1525/elementa.217

Galley, R., Else, B., Geilfus, N.-X., Hare, A., Isleifson, D., Ryner, L., et al. (2013). Morphology and distribution of liquid inclusions in young sea ice as imaged by magnetic resonance. *Cryosph. Discuss.* 7, 4977–5006. doi: 10.5194/tcd-7-4977-2013

Geilfus, N.-X., Delille, B., Verbeke, V., and Tison, J.-L. (2012). Towards a method for high vertical resolution measurements of the partial pressure of CO_2 within bulk sea ice. *J. Glaciol.* 58, 287–300. doi: 10.3189/2012JoG11J071

Gradinger, R., and Ikävalko, J. (1998). Organism incorporation into newly forming Arctic sea ice in the Greenland Sea. *J. Plankton Res.* 20, 871–886. doi: 10.1093/plankt/20.5.871

Grasshoff, K., Kremling, K., and Ehrhardt, M. (2009). *Methods of Seawater Analysis, 3rd Edn.* Weinheim; New York, NY; Chiester; Brisbane, QLD; Singapore; Toronto, ON: Wiley-VCH.

Grotti, M., Soggia, F., Abelmoschi, M. L., Rivaro, P., Magi, E., and Frache, R. (2001). Temporal distribution of trace metals in Antarctic coastal waters. *Mar. Chem.* 76, 189–209. doi: 10.1016/S0304-4203(01)00063-9

Grotti, M., Soggia, F., Ianni, C., and Frache, R. (2005). Trace metals distributions in coastal sea ice of Terra Nova Bay, Ross Sea, Antarctica. *Antarct. Sci.* 17, 289–300. doi: 10.1017/S0954102005002695

Janssens, J., Meiners, K. M., Tison, J.-L., Dieckmann, G., Delille, B., and Lannuzel, D. (2016). Incorporation of iron and organic matter into young Antarctic sea ice during its initial growth stages. *Elem. Sci. Anthr.* 4:123. doi: 10.12952/journal.elementa.000123

Kloareg, B., and Quatrano, R. S. (1988). Structure of the cell walls of marine algae and ecophysiological functions of the matrix polysaccharides. *Oceanogr. Mar. Biol. Annu. Rev.* 26, 259–315.

Kovacs, A. (1996). *Sea Ice. Part 1. Bulk Salinity Versus Ice Floe Thickness*. CRREL report; 96-7. Hanover, NH: US Army Cold Regions Research and Engineering Laboratory.

Krembs, C., and Deming, J. W. (2008). "The role of exopolymers in microbial adaptation to sea ice," in *Psychrophiles: From Biodiversity to Biotechnology*, eds R. Margesin, F. Schinner, J. C. Marx, and C. Gerday (New York, NY: Springer-Verlag), 247–264.

Krembs, C., Eicken, H., and Deming, J. W. (2011). Exopolymer alteration of physical properties of sea ice and implications for ice habitability and biogeochemistry in a warmer Arctic. *Proc. Natl. Acad. Sci. U.S.A.* 108, 3653–3658. doi: 10.1073/pnas.1100701108

Krembs, C., Eicken, H., Junge, K., and Deming, J. W. (2002a). High concentrations of exopolymeric substances in Arctic winter sea ice: implications for the polar ocean carbon cycle and cryoprotection of diatoms. *Deep Res. Part I Oceanogr. Res.* 49, 2163–2181. doi: 10.1016/S0967-0637(02)00122-X

Krembs, C., and Engel, A. (2001). Abundance and variability of microorganisms and transparent exopolymer particles across the ice-water interface of melting first-year sea ice in the Laptev Sea (Arctic). *Mar. Biol.* 138, 173–185. doi: 10.1007/s002270000396

Krembs, C., Tuschling, K., and Juterzenka, K. (2002b). The topography of the ice-water interface - its influence on the colonization of sea ice by algae. *Polar Biol.* 25, 106–117. doi: 10.1007/s003000100318

Kuiper, M. J., Lankin, C., Gauthier, S. Y., Walker, V. K., and Davies, P. L. (2003). Purification of antifreeze proteins by adsorption to ice. *Biochem. Biophys. Res. Commun.* 300, 645–648. doi: 10.1016/S0006-291X(02)02900-5

Lancelot, C., de Montety, A., Goosse, H., Becquevort, S., Schoemann, V., Pasquer, B., et al. (2009). Spatial distribution of the iron supply to phytoplankton in the Southern Ocean: a model study. *Biogeosciences* 6, 4919–4962. doi: 10.5194/bgd-6-4919-2009

Langway, C. (1958). *Ice Fabrics and the Universal Stage*. Wilmette, IL: U.S. Snow, Ice and Permafrost Research Establishment.

Lannuzel, D., Chever, F., van der Merwe, P. C., Janssens, J., Roukaerts, A., Cavagna, A.-J., et al. (2014a). Iron biogeochemistry in Antarctic pack ice during SIPEX-2. *Deep Sea Res. Part II Top. Stud. Oceanogr.* 131, 111–122. doi: 10.1016/j.dsr2.2014.12.003

Lannuzel, D., Grotti, M., Abelmoschi, M. L., and van der Merwe, P. (2015). Organic ligands control the concentrations of dissolved iron in Antarctic sea ice. *Mar. Chem.* 174, 120–130. doi: 10.1016/j.marchem.2015.05.005

Lannuzel, D., Schoemann, V., de Jong, J., Chou, L., Delille, B., Becquevort, S., et al. (2008). Iron study during a time series in the western Weddell pack ice. *Mar. Chem.* 108, 85–95. doi: 10.1016/j.marchem.2007.10.006

Lannuzel, D., Schoemann, V., de Jong, J., Pasquer, B., van der Merwe, P., Masson, F., et al. (2010). Distribution of dissolved iron in Antarctic sea ice: spatial, seasonal, and inter-annual variability. *J. Geophys. Res.* 115:G03022. doi: 10.1029/2009JG001031

Lannuzel, D., Schoemann, V., de Jong, J., Tison, J.-L., and Chou, L. (2007). Distribution and biogeochemical behaviour of iron in the East Antarctic sea ice. *Mar. Chem.* 106, 18–32. doi: 10.1016/j.marchem.2006.06.010

Lannuzel, D., van der Merwe, P. C., Townsend, A. T., and Bowie, A. R. (2014b). Size fractionation of iron, manganese and aluminium in Antarctic fast ice reveals a lithogenic origin and low iron solubility. *Mar. Chem.* 161, 47–56. doi: 10.1016/j.marchem.2014.02.006

Lemke, P. and Participants of the ANT-XXIX/6 cruise. (2014). *The Expedition of the Research Vessel "Polarstern" to the Antarctic in 2013 (ANT-XXIX/6)*. Berichte zur Polar-und Meeresforschung, Helmoltz Gemeinschaft, Bremerhaven, 679.

Loose, B., McGillis, W. R., Schlosser, P., Perovich, D., and Takahashi, T. (2009). Effects of freezing, growth, and ice cover on gas transport processes in laboratory seawater experiments. *Geophys. Res. Lett.* 36, 1–5. doi: 10.1029/2008GL036318

Mancuso Nichols, C. A., Garon Lardière, S., Bowman, J. P., Nichols, P. D., Gibson, J. A. E., and Guézennec, J. (2005a). Chemical characterization of exopolysaccharides from Antarctic marine bacteria. *Microb. Ecol.* 49, 578–589. doi: 10.1007/s00248-004-0093-8

Mancuso Nichols, C. A., Guezennec, J., and Bowman, J. P. (2005b). Bacterial exopolysaccharides from extreme marine environments with special

consideration of the Southern Ocean, sea ice, and deep-sea hydrothermal vents: a review. *Mar. Biotechnol.* 7, 253–271. doi: 10.1007/s10126-004-5118-2

Meiners, K., Brinkmeyer, R., Granskog, M. A., and Lindfors, A. (2004). Abundance, size distribution and bacterial colonization of exopolymer particles in Antarctic sea ice (Bellingshausen Sea). *Aquat. Microb. Ecol.* 35, 283–296. doi: 10.3354/ame035283

Meiners, K., Gradinger, R., Fehling, J., Civitarese, G., and Spindler, M. (2003). Vertical distribution of exopolymer particles in sea ice of the Fram Strait (Arctic) during autumn. *Mar. Ecol. Prog. Ser.* 248, 1–13. doi: 10.3354/meps248001

Meiners, K. M., Arndt, S., Bestley, S., Krumpen, T., Ricker, R., Milnes, M. et al. (2017). Antarctic pack ice algae distribution: floe-scale spatial variability and predictability from physical parameters. *Geophys. Res. Lett.* 44, 7382–7390. doi: 10.1002/2017GL074346

Meiners, K. M., and Michel, C. (2017). "Dynamics of nutrients, dissolved organic matter and exopolymers in sea ice," in *Sea Ice 3rd Edn,* ed D. N. Thomas (Chichester: John Wiley & Sons), 415–432.

Meiners, K. M., Vancoppenolle, M., Thanassekos, S., Dieckmann, G. S., Thomas, D. N., Tison, J.-L., et al. (2012). Chlorophyll a in Antarctic sea ice from historical ice core data. *Geophys. Res. Lett.* 39:L21602. doi: 10.1029/2012GL053478

Moffett, J. W. (1995). Temporal and spatial variability of copper speciation in the Sargasso Sea. *Deep Res. Part. I Oceanogr. Res.* 42, 1273–1295. doi: 10.1016/0967-0637(95)00060-J

Müller, S., Vähätalo, A. V., Stedmon, C. A., Granskog, M. A., Norman, L., Aslam, S. N., et al. (2013). Selective incorporation of dissolved organic matter (DOM) during sea ice formation. *Mar. Chem.* 155, 148–157. doi: 10.1016/j.marchem.2013.06.008

Noble, A. E., Moran, D. M., Allen, A. E., and Saito, M. A. (2013). Dissolved and particulate trace metal micronutrients under the McMurdo Sound seasonal sea ice: Basal sea ice communities as a capacitor for iron. *Front. Chem.* 1:25. doi: 10.3389/fchem.2013.00025

Passow, U. (2002). Transparent exopolymer particles (TEP) in aquatic environments. *Prog. Oceanogr.* 55, 287–333. doi: 10.1016/S0079-6611(02)00138-6

Passow, U., and Alldredge, A. L. (1995). A dye-binding assay for the spectrophotometric measurement of transparent exopolymer particles (TEP). *Limnol. Oceanogr.* 40, 1326–1335. doi: 10.4319/lo.1995.40.7.1326

Queroue, F., Townsend, A., van der Merwe, P., Lannuzel, D., Sarthou, G., Bucciarelli, E., et al. (2014). Advances in the offline trace metal extraction of Mn, Co, Ni, Cu, Cd, and Pb from open ocean seawater samples with determination by sector field ICP-MS analysis. *Anal. Methods* 6, 2837–2847. doi: 10.1039/C3AY41312H

Riedel, A., Michel, C., and Gosselin, M. (2006). Seasonal study of sea-ice exopolymeric substances on the Mackenzie shelf: implications for transport of sea-ice bacteria and algae. *Aquat. Microb. Ecol.* 45, 195–206. doi: 10.3354/ame045195

Riedel, A., Michel, C., Gosselin, M., and LeBlanc, B. (2007). Enrichment of nutrients, exopolymeric substances and microorganisms in newly formed sea ice on the Mackenzie shelf. *Mar. Ecol. Prog. Ser.* 342, 55–67. doi: 10.3354/meps342055

Rintala, J. M., Piiparinen, J., Blomster, J., Majavena, M., Müller, S., Uusikivi, J., et al. (2014). Fast direct melting of brackish sea-ice samples results in biologically more accurate results than slow buffered melting. *Polar Biol.* 37, 1811–1822. doi: 10.1007/s00300-014-1563-1

Rózanska, M., Poulin, M., and Gosselin, M. (2008). Protist entrapment in newly formed sea ice in the coastal Arctic Ocean. *J. Mar. Syst.* 74, 887–901. doi: 10.1016/j.jmarsys.2007.11.009

Scott, J. F., and Marchant, J. H. (2005). *Antarctic Marine Protists.* Canberra; Hobart: Australian Biological Ressources Study; Australian Antarctic Division.

Sedwick, P. N., and DiTullio, R. (1997). Regulation of algal blooms in Antarctic shelf waters by the release of iron from melting sea ice. *Geophys. Res. Lett.* 24, 2515–2518. doi: 10.1029/97GL02596

Sullivan, C. W., Arrigo, K. R., McClain, C. R., Comiso, J. C., and Firestone, J. (1993). Distributions of phytoplankton blooms in the Southern Ocean. *Science* 262, 1832–1837. doi: 10.1126/science.262.5141.1832

Sunda, W. G. (2001). "Bioavailability and bioaccumulation of iron in the sea," in *The Biogeochemistry of Iron in Seawater*, IUPAC Series on Analytical and physical chemistry of environment systems, eds D. R. Turner and K. H. Hunter (Chichester, UK; West Sussex: Wiley), 41–84.

Taylor, S. R. (1964). Abundance of chemical elements in the continental crust: a new table. *Geochim. Cosmochim. Acta* 28, 1273–1285. doi: 10.1016/0016-7037(64)90129-2

Underwood, G. J. C., Aslam, S. N., Michel, C., Niemi, A., Norman, L., Meiners, K. M., et al. (2013). Broad-scale predictability of carbohydrates and exopolymers in Antarctic and Arctic sea ice. *Proc. Natl. Acad. Sci. U.S.A.* 110, 15734–15739. doi: 10.1073/pnas.1302870110

Underwood, G. J. C., Fietz, S., Papadimitriou, S., Thomas, D. N., and Dieckmann, G. (2010). Distribution and composition of dissolved extracellular polymeric substances (EPS) in Antarctic sea ice. *Mar. Ecol. Prog. Ser.* 404, 1–19. doi: 10.3354/meps08557

UNEP (1999). *Executive Summary of the 1998 Report of the Environmental Assessment Panel, in Synthesis of the Reports of the Scientific, Environmental Effects, and Technologies and Economic Assessment Panels of the Montreal protocol*, UNEP, United Nations Environment Programme Ozone secretariat.

van der Merwe, P., Lannuzel, D., Bowie, A. R., Mancuso Nichols, C. A. and Meiners, K. M. (2011a). Iron fractionation in pack and fast ice in East Antarctica: temporal decoupling between the release of dissolved and particulate iron during spring melt. *Deep Sea Res II.* 58, 1222–1236. doi: 10.1016/j.dsr2.2010.10.036

van der Merwe, P., Lannuzel, D., Bowie, A. R., and Meiners, K. M. (2011b). High temporal resolution observations of spring fast ice melt and seawater iron enrichment in East Antarctica. *J. Geophys. Res.* 116:G03017. doi: 10.1029/2010JG001628

van der Merwe, P., Lannuzel, D., Mancuso Nichols, C. A., Meiners, K., Heil, P., Norman, L., et al. (2009). Biogeochemical observations during the winter–spring transition in East Antarctic sea ice: evidence of iron and exopolysaccharide controls. *Mar. Chem.* 115, 163–175. doi: 10.1016/j.marchem.2009.08.001

Verdugo, P. (2012). Marine microgels. *Ann. Rev. Mar. Sci.* 4, 375–400. doi: 10.1146/annurev-marine-120709-142759

Verdugo, P., Alldredge, A., Azam, F., Kirchman, D., Passow, U., and Santschi, P. (2004). The oceanic gel phase: a bridge in the DOM-POM continuum. *Mar. Chem.* 92, 67–85. doi: 10.1016/j.marchem.2004.06.017

Wang, S., Bailey, D., Lindsay, K., Moore, K., and Holland, M. (2014). Impacts of sea ice on the marine iron cycle and phytoplankton productivity. *Biogeosciences* 11, 4713–4731. doi: 10.5194/bg-11-4713-2014

Weissenberger, J., and Grossmann, S. (1998). Experimental formation of sea ice: importance of water circulation and wave action for incorporation of phytoplankton and bacteria. *Polar Biol.* 20, 178–188. doi: 10.1007/s003000050294

Williams, G., Maksym, T., Wilkinson, J., Kunz, K., Murphy, C., Kimball, P., et al. (2015). Thick and deformed Antarctic sea ice mapped with autonomous underwater vehicles. *Nat. Geosci.* 8, 61–67. doi: 10.1038/ngeo2299

Zhou, J., Delille, B., Eicken, H., Vancoppenolle, M., Brabant, F., Carnat, G., et al. (2013). Physical and biogeochemical properties in landfast sea ice (Barrow, Alaska): insights on brine and gas dynamics across seasons. *J. Geophys. Res.* 118, 3172–3189. doi: 10.1002/jgrc.20232

Zhou, J., Delille, B., Kaartokallio, H., Kattner, G., Kuosa, H., Tison, J.-L., et al. (2014). Physical and bacterial controls on inorganic nutrients and dissolved organic carbon during a sea ice growth and decay experiment. *Mar. Chem.* 166, 59–69. doi: 10.1016/j.marchem.2014.09.013

Conflict of Interest Statement: The authors declare that the research was conducted in the absence of any commercial or financial relationships that could be construed as a potential conflict of interest.

The reviewer, MV, declared a past co-authorship with one of the authors, KM, to the handling editor.

The reviewer, AN, and handling editor declared their shared affiliation.

Advantages of publishing in Frontiers

OPEN ACCESS
Articles are free to read for greatest visibility and readership

FAST PUBLICATION
Around 90 days from submission to decision

HIGH QUALITY PEER-REVIEW
Rigorous, collaborative, and constructive peer-review

TRANSPARENT PEER-REVIEW
Editors and reviewers acknowledged by name on published articles

Frontiers
Avenue du Tribunal-Fédéral 34
1005 Lausanne | Switzerland

Visit us: www.frontiersin.org
Contact us: info@frontiersin.org | +41 21 510 17 00

REPRODUCIBILITY OF RESEARCH
Support open data and methods to enhance research reproducibility

DIGITAL PUBLISHING
Articles designed for optimal readership across devices

FOLLOW US
@frontiersin

IMPACT METRICS
Advanced article metrics track visibility across digital media

EXTENSIVE PROMOTION
Marketing and promotion of impactful research

LOOP RESEARCH NETWORK
Our network increases your article's readership